106 Springer Proceedings in Physics

W. Wu
H. S. Yu
(Eds.)

Modern Trends in Geomechanics

Springer

SPRINGER PROCEEDINGS IN PHYSICS 106

SPRINGER PROCEEDINGS IN PHYSICS

87 **Proceedings of the 25th International Conference on the Physics of Semiconductors**
Editors: N. Miura and T. Ando

88 **Starburst Galaxies**
Near and Far
Editors: L. Tacconi and D. Lutz

89 **Computer Simulation Studies in Condensed-Matter Physics XIV**
Editors: D.P. Landau, S.P. Lewis, and H.-B. Schüttler

90 **Computer Simulation Studies in Condensed-Matter Physics XV**
Editors: D.P. Landau, S.P. Lewis, and H.-B. Schüttler

91 **The Dense Interstellar Medium in Galaxies**
Editors: S. Pfalzner, C. Kramer, C. Straubmeier, and A. Heithausen

92 **Beyond the Standard Model 2003**
Editor: H.V. Klapdor-Kleingrothaus

93 **ISSMGE**
Experimental Studies
Editor: T. Schanz

94 **ISSMGE**
Numerical and Theoretical Approaches
Editor: T. Schanz

95 **Computer Simulation Studies in Condensed-Matter Physics XVI**
Editors: D.P. Landau, S.P. Lewis, and H.-B. Schüttler

96 **Electromagnetics in a Complex World**
Editors: I.M. Pinto, V. Galdi, and L.B. Felsen

97 **Fields, Networks, Computational Methods and Systems in Modern Electrodynamics**
A Tribute to Leopold B. Felsen
Editors: P. Russer and M. Mongiardo

98 **Particle Physics and the Universe**
Proceedings of the 9th Adriatic Meeting, Sept. 2003, Dubrovnik
Editors: J. Trampetić and J. Wess

99 **Cosmic Explosions**
On the 10th Anniversary of SN1993J (IAU Colloquium 192)
Editors: J. M. Marcaide and K. W. Weiler

100 **Lasers in the Conservation of Artworks**
LACONA V Proceedings, Osnabrück, Germany, Sept. 15–18, 2003
Editors: K. Dickmann, C. Fotakis, and J.F. Asmus

101 **Progress in Turbulence**
Editors: J. Peinke, A. Kittel, S. Barth, and M. Oberlack

102 **Adaptive Optics for Industry and Medicine**
Proceedings of the 4th International Workshop
Editor: U. Wittrock

103 **Computer Simulation Studies in Condensed-Matter Physics XVII**
Editors: D.P. Landau, S.P. Lewis, and H.-B. Schüttler

104 **Complex Computing-Networks**
Brain-like and Wave-oriented Electrodynamic Algorithms
Editors: I.C. Göknar and L. Sevgi

105 **Computer Simulation Studies in Condensed-Matter Physics XVIII**
Editors: D.P. Landau, S.P. Lewis, and H.-B. Schüttler

106 **Modern Trends in Geomechanics**
Editors: W. Wu and H.S. Yu

107 **Microscopy of Semiconductor Materials**
Proceedings of the 14th Conference, July 25–29, 2005, Leeds, UK
Editors: T. Cullis and J. Huchison

Volumes 60–86 are listed at the end of the book.

W. Wu H.S. Yu
(Eds.)

Modern Trends in Geomechanics

With 260 Figures, 2 in Color, and 40 Tables

Springer

Professor Dr.-Ing. Wei Wu
Director of the Institute of Geotechnical Engineering
University of Natural Resources and Applied Life Sciences Vienna
Feistmantelstr. 4, 1180 Vienna, Austria
E-mail: wei.wu@boku.ac.at

Professor Hai-Sui Yu
School of Civil Engineering
University of Nottingham
Nottingham, NG7 2RD, UK
E-mail: hai-sui.yu@nottingham.ac.uk

ISSN 0930-8989

ISBN-10 3-540-25135-9 Springer Berlin Heidelberg New York

ISBN-13 978-3-540-25135-4 Springer Berlin Heidelberg New York

Library of Congress Control Number: 2006921401

Springer is a part of Springer Science+Business Media.

springer.com

Printed in The Netherlands

Prodcution: SPI Publisher Services
Cover concept: eStudio Calamar Steinen
Cover production: *design & production* GmbH, Heidelberg

Printed on acid-free paper SPIN: 11350200 89/3100/SPI 5 4 3 2 1 0

Preface

This book is a collection of 31 papers presented at the International Workshop on Modern Trends in Geomechanics, held on 27–29 June 2005 in Vienna. This workshop was run under the motto to bring together different schools of thought in geomechanics research. The workshop was attended by about 50 participants from 15 countries. Besides the presentations, the workshop also offered welcoming occasions for stimulating discussions.

The contributions in this book cover a wide range of topics from applied mathematics to geoengineering applications, reflecting the breadth and depth of geomechanics research. The articles are peer reviewed and arranged in six parts: general aspects, constitutive modelling, micromechanics, analytical and numerical methods, granular materials and engineering applications.

We would like to thank all contributors for their diligence to provide timely their contributions. The generous support received from the following organizations is gratefully acknowledged:

- Alpine Mayreder Construction Ltd
- Bank Austria – Credit Institute
- Austrian Geomechanics Society

Our thanks also go to the managing editors at Springer, in particular Ms. Heather King and Dr. Thomas Ditzinger, who have enabled the quality publication of this book at reasonable price. Last but not least, we would like to express our thanks to our co-workers in Vienna and Nottingham for their help during the workshop. In particular, our secretaries, Anke Priewasser (Vienna) and Caroline Dolby (Nottingham), deserve our heartfelt thanks for their effort in organising the workshop and compiling this book.

W. Wu — Vienna

H-S. Yu — Nottingham

Contents

Part I General Aspects

Energy Methods for Constitutive Modelling in Geomechanics
I.F. Collins and A.T.T. Tai 3

Physical Background of Hypoplasticity
Gerd Gudehus 17

Thermodynamics of Porous Continua
G.T. Houlsby and A.M. Puzrin 39

Effective Stress Formulation of Unsaturated Soil Mechanics
F. Molenkamp 61

Progress in Binary Medium Modeling of Geological Materials
Z.-J. Shen 77

Part II Constitutive Modelling

Generic Constitutive Ingredients in CSSM Models for Sands
Y.F. Dafalias, A.G. Papadimitriou, X.S. LI, and M.T. Manzari 103

State Boundary Surface in Hypoplasticity
D. Mašín and I. Herle 117

Modelling of Bonded Soils with Unstable Structure
R. Nova 129

An Evaluation of Different Constitutive Models to Predict the Directional Response of a Reconstituted Fine-Grained Soil
C. Tamagnini, D. Mašin, D. Costanzo, and G. Viggiani 143

Two Elastoplastic Models for Small and Large Strains and Their Use in Engineering Practise
P.A. Vermeer, R. Schwab, and T. Benz 159

Elastic Visco-Plastic Models for the Time-Dependent Stress–Strain Behaviour of Geomaterials
J.-H. Yin 175

Part III Micromechanics

Micro-Polar Effects under Monotonic and Cyclic Shearing
E. Bauer, J. Tejchman, S.F. Tantono, and W. Huang 193

Modeling the Postlocalization Regime with Local Second Gradient Models: Nonuniqueness of Solutions and Nonpersistent Shear Bands
P. Bésuelle and R. Chambon 209

Confined Compression and Rod Penetration of a Dense Granular Medium: Discrete Element Modelling and Validation
Y.C. Chung and J.Y. Ooi 223

Application of Discrete Element Method to Geomechanics
M. Jiang, H.-S. Yu 241

The Role of Particle Crushing in Granular Materials
G. R. McDowell 271

Micromechanical Study of Damage and Permeability Variation in Brittle Rocks
J.J. Zhou, J.F. Shao, and D. Lydzba 289

Part IV Analytical and Numerical Methods

Hydrologically Driven Slope Failure Initiation in Variably Saturated Porous Media
R.I. Borja, G. Oettl, B.A. Ebel and K. Loague 303

A Survey of Some Mathematical Results for Highly Frictional Granular Materials
G.M. Cox, N. Thamwattana and J.M. Hill 313

Double-Slip and Spin: Dilatant Shear in a Reduced Cosserat Model
D. Harris 329

The Linear Matching Method for Limit and Shakedown Analysis
A.R.S. Ponter and M. Boulbibane 347

On Recent Analytical Results for Advective Transport in Fluid-Saturated Porous Media
A.P.S. Selvadurai 361

Part V Granular Materials: Theory and Experiment

Unusual Soil Behaviour and its Challenge to Constitutive Modelling
J. Chu 377

Histotropy of Hostun RF Loose Sand
T. Doanh, Z. Finge, S. Boucq, and Ph. Dubujet 399

Incremental Nonlinearity in Phenomenological and Multiscale Constitutive Relations
F. Nicot and F. Darve 413

Long-term Deformations in Soils due to Cyclic Loading
A. Niemunis, T. Wichtmann, and T. Triantafyllidis 427

On the Factors Affecting the Formation of Shear Band Systems in Non-Cohesive Soils Under Extensional Strain
T. Triantafyllidis, H. Wolf, and D. König 463

Acceleration Waves in Hypoplasticity - 2D Analysis
B. Weingartner, V.A. Osinov and W. Wu 485

Part VI Engineering Applications

Static and Cyclic Behavior of a Silty Sand According to Tests on Undisturbed Samples
A.B. Huang and Y.T. Huang 503

The Role of Analysis in Non-Displacement Pile Design
R. Salgado 521

Assessment of Uncertainties in Wellbore Stability Analysis
Y. Sheng, D. Reddish, and Z. Lu 541

Part I

General Aspects

Energy Methods for Constitutive Modelling in Geomechanics

I.F. Collins and A.T.T. Tai

School of Engineering, University of Auckland, New Zealand
i.collins@auckland.ac.nz

1 Introduction

Some of the earliest applications of energy arguments to develop conceptual models for the behaviour of soils, sands and other geomaterials are those establishing stress–dilatancy relations due to Taylor [35] and Rowe [31]. The original formulations of the Cam Clay, critical state models was based upon concepts of the plastic dissipation of energy. More recently, energy arguments, based upon the laws of thermodynamics have been used to establish general procedures for constitutive modelling [37]. One of the best known thermomechanics formulations is due to Rice [29]. However this has a built in "normality structure" and is not appropriate for frictional geomaterials which commonly exhibit non-normal flow rules. Here we use the line of development described in the books by Ziegler [40], Maugin [21] and papers by Collins and Houlsby (1997) and Houlsby and Puzrin [18], who coined the term "hyper-plasticity" for this approach. The characterizing feature of the hyper-plastic approach is that the complete elastic–plastic constitutive behaviour, including yield conditions and flow rules, can be determined from two thermomechanical potentials, the free energy and the dissipation rate.

2 The Extant Approach to Critical State Soil Mechanics

The original approach to critical state soil mechanics [23, 24, 30, 32] was based on the plastic work equation:

$$\hat{W}^{\mathrm{P}} = p\dot{e}_{\mathrm{v}}^{\mathrm{P}} + q\dot{e}_{\gamma}^{\mathrm{P}} = Mp\dot{e}_{\gamma}^{\mathrm{P}} = \hat{\Phi}, \tag{1}$$

where we are using the standard notation for triaxial tests. All stresses are to be interpreted as effective stresses. This relation equates $\hat{W}^{\mathrm{P}}$, the rate of plastic work, to $\hat{\Phi}$, the rate of energy dissipation. The latter being assumed to be entirely due to frictional shearing, M being a frictional coefficient. (Note we

are here, for simplicity, assuming the plastic shear strain rates are positive.) In using (1) the rate of elastic work is tacitly assumed to be balanced by the rate of change of the recoverable, elastic free energy. This equation can be rewritten as:

$$\eta \equiv \frac{q}{p} = M + \tan\,\psi, \text{where } \tan\psi \equiv -\frac{\dot{e}_{\mathrm{v}}^{\mathrm{P}}}{\dot{e}_{\gamma}^{\mathrm{P}}}, \tag{2}$$

where ψ is the dilation angle. In this form the relation is equivalent to Taylor's [35] stress–dilatancy equation, demonstrating that as a result of dilation the "strength" of the soil is increased by the additive factor $\tan\psi$. Schofield and Wroth [32] then identified that the dilation angle defines the normal to the plastic potential, so that (2) can again be rewritten as:

$$\frac{q}{p} = M + \frac{\mathrm{d}q}{\mathrm{d}p}, \text{which integrates to give } q = Mp\,\ln\left(\frac{p_{\mathrm{c}}}{p}\right). \tag{3}$$

Drucker's postulate or the maximum work hypothesis was then invoked to identify the plastic potential and the yield locus and hence predicted a normal flow rule. As is well known the yield loci (3), of what is now known as "original Cam Clay", have a vertex on the pressure axis, where $p = p_{\mathrm{c}}$. It was further assumed that this consolidation pressure is a unique function $p_{\mathrm{c}}(e)$ of e – the voids ratio. This function describes the expansion or contraction of the yield loci. It should be noted that although this, and the other classical critical state soil models are frequently referred to as being "isotropic hardening models", they do in fact contain a "kinematics hardening" component in the sense that they translate along the pressure axis as well as expand isotropically, although, of course, they do describe isotropic material behaviour. This observation is important since the physical origins of kinematics and isotropic hardening are very different [36].

Analysis of this model showed that if a loading programme was continued sufficiently far, a soil element would eventually reach a critical "state", at which the element would continue to shear, but under constant stresses and without change in volume. These critical states lay on unique "failure" line, $q = Mp$ in the stress plane and on a unique curve $p = (1/2)p_{\mathrm{c}}(e)$ in the (p, e) plane. This curve is usually assumed to be a straight line either in the $(\ln\ p,\ e)$ or $(\ln\ p, \ln\ v)$ plane. These critical lines separate domains of compactive (loose or wet) and dilative (dense or dry) behaviour. This model was a major advance as it combined the classical idea of Coulomb failure, Casegrande's concept of a critical void ratio and Taylor's model of Reynolds dilatancy .

However some of the specific properties of the model, such as the vertex, were deemed to be unsatisfactory by some, and Burland [3] and Roscoe and Burland [30] produced the "modified Cam Clay" model, by postulating a plastic work equation, which includes volumetric dissipation

$$p\dot{e}_{\mathrm{v}}^{\mathrm{P}} + q\dot{e}_{\gamma}^{\mathrm{P}} = p\sqrt{\dot{e}_{\mathrm{v}}^{\mathrm{P}^2} + \mathrm{M}^2\dot{e}_{\gamma}^{\mathrm{P}^2}}, \tag{4}$$

which, using the extant procedure, predicts a yield locus and associated flow rule ("stress–dilatancy relation") of the form:

$$q^2 - M^2 p(p_c - p) = 0, \text{ and } \tan\psi = \frac{\eta^2 - M^2}{2\eta}. \tag{5}$$

The yield loci are now elliptical, and do not have vertices, but the stress–dilatancy relation is now markedly different from Taylor's. Nevertheless the new yield loci are found to be more in accord with experiment, at least for lightly over-consolidated clays.

3 A Critique of the Extant Procedure

Here we are concerned with the validity of the arguments, illustrated earlier, which were used to establish the yield condition and flow rule, from a postulated dissipation function. Although they have been used by a number of subsequent workers, they are open to three major criticisms:

(a) The plastic work equations (1) and (4) identify the plastic work rate with the rate of energy dissipation. This is not generally true [6, 7]. In the current class of models, in which a soil state is defined by the elastic and plastic strains, the free energy function Ψ in general, depends on the plastic as well as the elastic strain. The free energy is frequently assumed to be decoupled and can be written as the sum of two state functions $\Psi^{\mathrm{E}}(e^{\mathrm{E}}_{ij}) + \Psi^{\mathrm{P}}(e^{\mathrm{P}}_{ij})$ [9, 10, 36]. The plastic work equation should hence be written as:

$$\hat{W}^{\mathrm{P}} = \dot{\Psi}^{\mathrm{P}} + \hat{\Phi}, \text{ where } \hat{\Phi} \geq 0. \tag{6}$$

Physically this extra term Ψ^{P} represents that proportion of the elastic energy stored at the micro-level, within the grains, that is not recovered during elastic unloading. Instead it is trapped as a result of the "grain rearrangement" associated with the plastic deformation. It is frequently referred to as "frozen elastic energy" or "stored plastic work" [7, 13, 36]. It can only be recovered under reversed plastic loading. It would seem to be of more importance in clays than sands, since, in addition to the effect of grain rearrangement, energy can be stored at the micro-level within elastically deformed platelets within the flocculated particle structure as suggested by Bjerrum [2]. The rate of change of the plastic part of the free energy can be used to define the shift or back stresses

$$\dot{\Psi}^{\mathrm{P}} \equiv p_{\mathrm{S}}\dot{e}^{\mathrm{P}}_{\mathrm{v}} + q_{\mathrm{S}}\dot{e}^{\mathrm{P}}_{\gamma} \tag{7}$$

These stresses control the kinematics aspects of the material hardening.

(b) The use of the current pressure p in the expression for dissipation means that the dissipation mechanism is unaffected by pre-consolidation, and the

material has no memory. Whilst this would seem appropriate for sands at confining pressures low enough not to induce crushing, it would not seem apt for clays or crushable sands, whose structure is significantly affected by prior consolidation. In fact the hyper-plastic thermomechanical procedure when applied to the dissipation functions in (1) and (4), result in open ended, "Coulomb-type" yield loci, with no pre-consolidation pressure as shown by Collins and Hilder [8].

(c) The "dissipative stresses" $p_{\rm D}$ and $q_{\rm D}$ can be defined by

$$p_{\rm D}\dot{e}_{\rm v}^{\rm P} + q_{\rm D}\dot{e}_{\gamma}^{\rm P} = \hat{\Phi}. \tag{8}$$

Thus, whilst it is the inner product of the plastic strain rate with the *actual* stress, which gives the plastic work rate, it is the inner product with the *dissipative* stress, which gives the dissipation rate. The rate independence of a material requires its dissipation function to be homogeneous of degree 1 in the plastic strain rates. One of the most powerful and useful results of hyper-plastic thermomechanics is that for such materials, the *dissipative stresses* must lie on a yield locus, whenever dissipation occurs, and that the plastic strain rates are given by a normal flow rule *in dissipative stress space*. The yield function in *true stress space* can then be found by using the shift stresses. When the dissipation function involves the actual pressure, the flow rule is non-associated in true stress space as shown by Collins and Houlsby and Collins [6, 9]. The flow rule is hence determined by the thermodynamic potentials and one does not have to invoke any extraneous normality, or other flow rule, hypothesis in this procedure.

4 The Hyper-Plastic Thermomechanical Procedure

The basic plastic work equation (6) can be written as:

$$\hat{W}^{\rm P} = p\dot{e}_{\rm v}^{\rm P} + q\dot{e}_{\gamma}^{\rm P} = p_{\rm S}\dot{e}_{\rm v}^{\rm P} + p_{\rm D}\dot{e}_{\rm v}^{\rm P} + q_{\rm D}\dot{e}_{\gamma}^{\rm P}, \tag{9}$$

where $p_{\rm S} \equiv \partial\Psi^{\rm P}/\partial e_{\rm v}^{\rm P}$ is the shift pressure. Here we are assuming that the plastic *shear* strains do not induce any "frozen elastic energy". A view supported by the experiments of Luong [20] and Okada and Nemat-Nasser [26], so that $\Psi^{\rm P}$ is independent of $e_{\gamma}^{\rm P}$. It follows that

$$p = p_{\rm S} + p_{\rm D} \text{ and } q = q_{\rm D}. \tag{10}$$

To generate the modified Cam Clay model we will choose the dissipation potential to be

$$\hat{\Phi} = p_{\rm cd}\sqrt{\dot{e}_{\rm v}^{\rm P2} + M^2\dot{e}_{\gamma}^{\rm P2}}, \tag{11}$$

where $p_{\rm cd}(e_{\rm v}^{\rm P})$ is that part of the consolidation pressure which causes dissipation. Using Euler's theorem , dissipative stresses are hence given by

$$p_{\rm D} \equiv \frac{\partial\hat{\Phi}}{\partial\dot{e}_{\rm v}^{\rm P}} = \frac{p_{\rm cd}^2\dot{e}_{\rm v}^{\rm P}}{\hat{\Phi}}, \text{ and } q_{\rm D} \equiv \frac{\partial\hat{\Phi}}{\partial\dot{e}_{\gamma}^{\rm P}} = \frac{p_{\rm cd}^2M^2\dot{e}_{\gamma}^{\rm P}}{\hat{\Phi}}. \tag{12}$$

Eliminating the strain rates from (11) and (12), gives the elliptical, dissipative yield condition and associated flow rule:

$$\frac{p_{\mathrm{D}}^2}{p_{\mathrm{cd}}^2} + \frac{q_{\mathrm{D}}^2}{M^2 p_{\mathrm{cd}}^2} = 1 \text{ and } \tan\psi \equiv -\frac{\dot{e}_{\mathrm{v}}^{\mathrm{P}}}{\dot{e}_{\gamma}^{\mathrm{P}}} = \frac{M^2 p_{\mathrm{D}}}{q_D}, \tag{13}$$

which using (10) gives the elliptical yield loci in true stress space:

$$\frac{(p - p_{\mathrm{S}})^2}{p_{\mathrm{cd}}^2} + \frac{q^2}{M^2 p_{\mathrm{cd}}^2} = 1. \tag{14}$$

When $q = 0$, yielding occurs when $p = p_{\mathrm{S}} \pm p_{\mathrm{cd}}$, so that if we insist that the yield loci all go through the origin, $p_{\mathrm{S}} = p_{\mathrm{cd}}$, and the consolidation pressure is $p_{\mathrm{C}} = 2p_{\mathrm{S}}$, and (14) reduces to (5), the yield condition for modified Cam Clay. Note that if we do not make this assumption, we can generate "bubble models" in which *both* ends of the yield locus translate. Hardening or softening is governed by the function $p_{\mathrm{S}}(e_{\mathrm{v}}^{\mathrm{P}})$, or equivalently by $p_{\mathrm{C}}(e_{\mathrm{v}}^{\mathrm{P}})$, which are known from the critical state (or normal consolidation) lines in the (v, p) plane. Note that on the critical state line $q = Mp, p = p_{\mathrm{S}}$ and $\dot{e}_{\mathrm{v}}^{\mathrm{P}}$ and p_{D} are both zero. It is very important to appreciate that since the shift stresses are derived from the free energy function, they are functions only of the *current plastic strains*. The dissipative stresses however are derived from the dissipation function, which depends on the *current rate of change of the plastic strains*. The relation between the pressure and the plastic volume strain is hence unique, whenever the dissipative pressure is zero. As illustrated earlier, this always happens on the critical state line (CSL) for isotropic models, but, as will be seen, this is not the case when anisotropy is induced. Since the pressure is also a unique function of the elastic volume strain, it follows that the critical state line (CSL) in (v, p) space is also unique for isotropic models.

It should also be noted that the earlier theory assumes that dissipation is governed by the same function for plastic compaction ($\dot{e}_{\mathrm{v}}^{\mathrm{P}} > 0$) as for dilation ($\dot{e}_{\mathrm{v}}^{\mathrm{P}} < 0$).

An unsatisfactory aspect of this model is that the shear component of the dissipation in (11), is $Mp_{\mathrm{cd}}\dot{e}_{\gamma}^{\mathrm{P}}$ instead of $Mp\dot{e}_{\gamma}^{\mathrm{P}}$ as would seem more appropriate when modelling frictional behaviour. In consequence Collins and Hilder (2002) investigated an extended two-parameter family of generalized, isotropic critical state models, which include modified Cam Clay and the frictional extension suggested earlier as special cases. The dissipation function is taken to be

$$\hat{\Phi} = \sqrt{A^2 \dot{e}_{\mathrm{v}}^{\mathrm{P}2} + M^2 B^2 \dot{e}_{\gamma}^{\mathrm{P}2}}, \tag{15}$$

where A and B are linear functions in p and p_{S}:

$$A = (1 - \gamma)p + p_{\mathrm{S}} \text{ and } B = (1 - \alpha)p + \alpha p_{\mathrm{S}}, \tag{16}$$

where α and γ are parameters with values in the interval {0,1}. Both parameters are 1 for modified Cam Clay. The resulting yield loci, are still elliptical,

with an associated flow rule, in dissipative stress space

$$\frac{p_{\mathrm{D}}^2}{A^2} + \frac{q_{\mathrm{D}}^2}{M^2 B^2} = 1 \tan\,\psi \equiv -\frac{\dot{e}_{\mathrm{v}}^{\mathrm{P}}}{\dot{e}_{\gamma}^{\mathrm{P}}} = -\frac{M^2 p_{\mathrm{D}}}{q_{\mathrm{D}}}\frac{B^2}{A^2}, \tag{17}$$

but are transformed into different shaped curves in true stress space, since A and B now also depend on the true pressure p

$$\frac{(p-p_{\mathrm{S}})^2}{A^2} + \frac{q^2}{M^2 B^2} = 1 \tag{18}$$

and the flow rule is no longer associated.

In all cases the critical state is reached when $p_{\mathrm{D}} = 0, p = p_{\mathrm{S}}$ and $q = Mp$. Moreover the volumetric plastic strain rate is zero so that the dissipation is purely frictional, and the rate of change of the frozen energy is also zero, i.e. $\dot{\Psi}^{\mathrm{P}}(e_{\mathrm{v}}^{\mathrm{p}}) = 0$ Frozen elastic energy is created on the contractive, hardening, loose (wet) side of critical, but released on the dilative, softening, dense (dry) side. As noted earlier, the CSL for all these models is also unique in (v, p) plane.

Putting $q = 0$ in (), the consolidation pressure is seen to be $p_{\mathrm{C}} = rp_{\mathrm{S}}$, where $r = 2/\gamma$ is the "spacing ratio" [23, 39]. The parameter γ is hence a measure of the "length" of the yield locus, whilst α is a "tear drop" parameter. As α decreases from unity, the locus becomes less elliptical and more tear drop shaped as illustrated in Fig. 1. The Coulomb model is recovered when both parameters and p_{S} are zero

The elliptical dissipative yield locus can be given a parametric representation

$$p_{\mathrm{D}} \equiv p - p_{\mathrm{S}} = A\,\sin\,\varpi \text{ and } q_{\mathrm{D}} \equiv q = MB\,\cos\,\varpi. \tag{19}$$

The yield condition can hence be expressed in terms of the parametric angle ϖ using (17) and (19):

$$\xi \equiv \frac{p_{\mathrm{S}}}{p} = \frac{(1-(1-\gamma)\sin\varpi)}{1+\sin\varpi}, \eta \equiv \frac{q}{p} = M\frac{[1+(1-2\alpha+\alpha\gamma)\sin\varpi)]\cos\varpi}{1+\sin\varpi}. \tag{20}$$

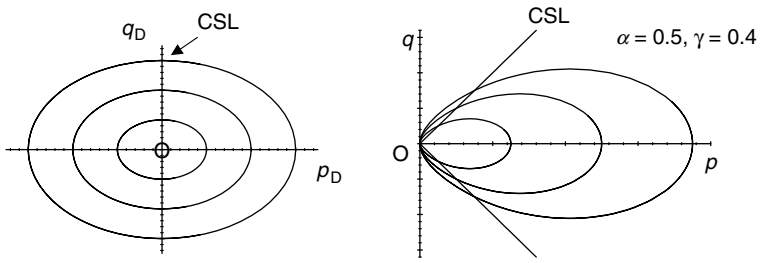

Fig. 1. Yield loci in dissipative and true stress planes, isotropic model

This is a parametric form of the yield condition for an isotropic material, which, provided the plastic behaviour is governed by angles and not by a yield stress, can always be written in the form $\eta = F(\xi)$. This follows from elementary dimensional analysis. The parameter ξ is essentially the "state parameter" of Been and Jefferies [1], as it is a measure of displacement from the critical state line in the voids ratio–pressure plane. The stress ratio and dilatancy angle depend just upon ξ. A similar state pressure index has been used by Wang et al. [38]. As pointed out by Sladen et al. [34] this is, in fact, an essential feature of *all* isotropic critical state models. In the thermomechanical formulation it is more convenient to use the angle ϖ as the fundamental, isotropic state parameter. This is a measure of the angular displacement from the critical state, where $\varpi = 0$, in the dissipative stress diagram.

For this extended class of critical state models the dilatancy angle is given by

$$\tan\,\psi = -M\,\frac{[1 + (1 - 2\alpha + \alpha\gamma)\sin\varpi)]\tan\varpi}{(2-\gamma)}. \tag{21}$$

This extended family of critical state models was originally developed on purely phenomenological grounds. However Collins [6] has recently shown that the new parameters: α and γ, can be given micro-mechanical interpretations, using a bi-modal model, based upon the discrete element method (DEM) findings of Radjai et al. [27]. The micro-mechanical representative volume element (RVE) is assumed to consist of a strong network, consisting of force chains, and a complementary weak network, where the direct stresses are lower, but the grains are more readily able to shear. It is found that α is the volume fraction of force chains, whilst γ depends on the fraction of the mean pressure, which is carried by the force chains.

5 Reynold's Dilatancy and Induced Anisotropy

The flow rules of isotropic models such as those discussed earlier are frequently interpreted as "stress–dilatancy relations". However, with the exception of that for original Cam Clay, these are not compatible with the original ideas of Reynolds [28]. It has been appreciated for some time, that dilation induced by shearing is accompanied by the development of anisotropy. This anisotropy is due to the reorientation of contact normals between particles, the development of anisotropic distribution of voids, and the reorientation of individual grains. To model this behaviour, the volumetric plastic strain rate is regarded as the sum of two parts as outlined in Collins [7]. One, denoted by $\dot{e}^{\mathrm{P}}_{\mathrm{vir}}$, is the irreversible strain rate resulting from changes in the current stress, and is that predicted by an isotropic theory, such as that outlined earlier. The second part is the induced or reversible plastic volume strain rate, which arises as a result of shearing and is given by

$$\dot{e}^{\mathrm{P}}_{\mathrm{vin}} = -\tan\ \theta\ \dot{e}_{\gamma^{\mathrm{P}}}, \tag{22}$$

where θ is termed the "induced dilatancy angle". This division of the plastic volume strain rate is very similar to that proposed by Nixon and Chandler [25] or Shamoto et al. [33] when modelling cyclic behaviour. As will be seen θ is also a measure of the induced anisotropy. Following Kanatani, Goddard and Bashir, Houlsby and Collins and Muhunthan [11, 15, 17, 19], we will regard this induced dilatancy as an *internal constraint*, which *does no work* and does not dissipate or store any energy. This is because if the grains were rigid and frictionless, the work needed to induce Reynolds dilatancy would be zero, in the quasi-static, weightless limit.

The basic plastic work equation is hence now written as:

$$p\dot{e}_{\mathrm{v}}^{\mathrm{P}} + q\dot{e}_{\gamma}^{\mathrm{P}} = p_{\mathrm{S}}\dot{e}_{\mathrm{vir}}^{\mathrm{P}} + \{p_{\mathrm{R}}\dot{e}_{\mathrm{vin}}^{\mathrm{P}} + q_{\mathrm{R}}\dot{e}_{\gamma}^{\mathrm{P}}\} + \{\overline{p}_{\mathrm{D}}\dot{e}_{\mathrm{vir}}^{\mathrm{P}} + \overline{q}_{\mathrm{D}}\dot{e}_{\gamma}^{\mathrm{P}}\}. \tag{23}$$

The first term on the right-hand side is the rate of change of frozen elastic energy given by the rate of change of the plastic part of the free energy function. This is independent of the plastic shear strain and only depends on the irreversible part of the volumetric plastic strain. Hence $p_{\mathrm{S}} = p_{\mathrm{S}}(e_{\mathrm{vir}}^{\mathrm{P}})$. The second term is the rate of working associated with Reynolds dilatancy, which, as stated, must be zero. Hence, the reaction stresses must satisfy

$$q_{\mathrm{R}} = p_{\mathrm{R}} \tan \theta. \tag{24}$$

This model is a refinement of that presented by Collins and Muhunthan [11], in that the distinction between the reaction and shift stresses is more precisely defined. The third term is the rate of dissipation, which, like the free energy, does not depend on the induced volume changes. Note the definition of the dissipative stresses $\overline{p}_{\mathrm{D}}$ and $\overline{q}_{\mathrm{D}}$ differs from that we have used in (8). From (23) we see that the two sets of stresses are related by

$$\overline{p}_{\mathrm{D}} = p_{\mathrm{D}} \text{ and } \overline{q}_{\mathrm{D}} = q_{\mathrm{D}} - \tan \theta \; p_{\mathrm{D}}. \tag{25}$$

By equating like plastic strain rate terms in this work equation we deduce

$$p = p_{\mathrm{R}}, p = p_{\mathrm{S}} + \overline{p}_{\mathrm{D}} \text{ and } q = q_{\mathrm{R}} + \overline{q}_{\mathrm{D}}. \tag{26}$$

From these equations we deduce that the stress ratio is

$$\frac{q}{p} = \frac{\overline{q}_{\mathrm{D}}}{p} + \tan \theta. \tag{27}$$

The first term on the right-hand side is the "intrinsic strength" associated with the dissipative yield function, the second is the "extra strength" arising from the induced dilatancy and accompanying anisotropy. We can now apply the general procedure to determine the yield loci, flow rule, etc. to develop the anisotropic extension of the general class of models discussed earlier. However, here, for illustrative purposes we will only consider modified Cam Clay, for

which the dissipation function is

$$\hat{\Phi} = p_{\rm cd}\sqrt{(\dot{e}^{\rm P}_{\rm vir})^2 + (Me^{\rm P}_{\gamma})^2} = p_{\rm cd}\sqrt{(\dot{e}^{\rm P}_{\rm v} + \tan\theta\,\dot{e}_{\gamma})^2 + (Me^{\rm P}_{\gamma})^2}. \tag{28}$$

This is similar to the dissipation function originally proposed by Dafalias [14] to model anisotropic behaviour. Here M is not necessarily a constant, but, like θ, can evolve with the deformation. Application of the standard procedure shows that the elliptical dissipative yield loci are given by

$$\frac{\overline{p}^2_{\rm D}}{p^2_{\rm cd}} + \frac{\overline{q}^2_{\rm D}}{M^2p^2_{\rm cd}} = 1 \text{ or } \frac{p^2_{\rm D}}{p^2_{\rm cd}} + \frac{(q_{\rm D} - \tan\,\theta\; p_{\rm D})^2}{M^2p^2_{\rm cd}} = 1. \tag{29}$$

With parametric representations

$$p_{\rm D} = \overline{p}_{\rm D} = p_{\rm cd}\sin\varpi, \overline{q}_{\rm D} = Mp_{\rm cd}\,\cos\varpi,\; q_{\rm D} = p_{\rm cd}(M\,\cos\,\varpi + \tan\,\theta\,\sin\varpi. \tag{30}$$

The yield loci in $(\overline{p}_{\rm D}, \overline{q}_{\rm D})$ space are the same as illustrated in Fig. 1. The "barred" dissipative stress plane, hence describes the isotropic part of the deformation, and the associated, normal flow rule give the isotropic part of the dilation. In the $(p_{\rm D}, q_{\rm D})$ plane the ellipses are rotated, as illustrated in Fig. 2, and the flow rule in this plane gives the *total* dilation, thus:

$$\tan\overline{\psi}\;\equiv -\frac{\dot{e}^{\rm P}_{\rm vir}}{\dot{e}^{\rm P}_{\gamma}} = -M\,\tan\,\varpi, \tag{31}$$

$$\text{and}\quad \tan\psi\;\equiv -\frac{\dot{e}^{\rm P}_{\rm v}}{\dot{e}^{\rm P}_{\gamma}} = \tan\theta + \tan\overline{\psi} = \tan\theta - {\rm M}\tan\varpi. \tag{32}$$

In terms of total effective stresses, the yield loci are

$$\frac{(p - p_{\rm S})^2}{p^2_{\rm S}} + \frac{(q - p\tan\theta)^2}{M^2p^2_{\rm S}} = 1, \tag{33}$$

or in parametric form

$$\frac{p_{\rm S}}{p} = 1/(1+\sin\varpi),\text{ and }\frac{q}{p} = \tan\theta + {\rm M}\frac{\cos\varpi}{1+\sin\varpi}. \tag{34}$$

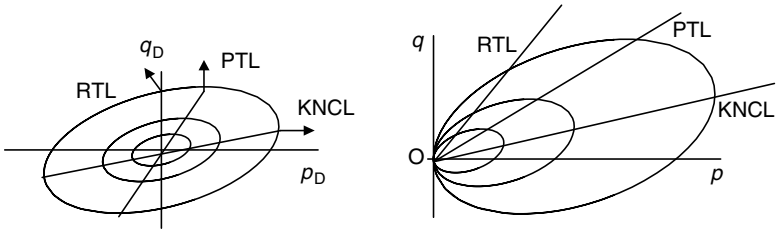

Fig. 2. Yield loci in dissipative and true stress planes, anisotropic model

Eliminating θ between (32) and (34) gives the general stress–dilatancy relation:

$$\frac{q}{p} = \tan\psi + M \sec\varpi. \tag{35}$$

(Note that we have again identified $p_{\rm S}$ and $p_{\rm cd}$, to ensure that the origin lies upon the yield loci, as in the isotropic theory.) The state of the soil is hence defined by the (isotropic) state parameter ϖ, or equivalently $p_{\rm S}/p$, and θ, which is a fabric parameter, dependent on the degree of anisotropy. In Fig. 2 the kinematics normal consolidation line (KNCL), where $\dot{e}_\gamma = 0$ and $\varpi = \pi/2$, has slope θ, in the (q, p) plane. The CSL of the isotopic models now splits into two lines. On one, the total plastic dilation angle and plastic volume strain rate are zero. This is the phase transition line (PTL) encountered in undrained tests. On this line the dilative strains induced by the Reynolds' effect are exactly, counterbalanced by the compactive strains induced by stress changes. For Modified Cam Clay (MCC), the slope of this line is $\overline{M}$ and the dissipation rate is $p_{\rm S}\overline{M}\dot{e}^{\rm P}_\gamma$, where $\overline{M} = \sqrt{M^2 + \tan^2\theta}$.

On the second line, corresponding to the point where $p_{\rm D} = 0$ and $\varpi = 0$ in Fig. 2 the irreversible volumetric strain rate, due to stress changes is zero, so that the deformation is entirely as envisaged by Reynolds. On this line $\psi = \theta$, as the only volume changes are those induced by shear. For this reason Collins [7] suggested that this line be termed the Reynolds–Taylor line (RTL). From (34) or (35), the slope of this line is given by the classic Taylor relation:

$$\frac{q}{p} = \tan\theta + M = \tan\psi + M, \tag{36}$$

though here, we are working within an anisotropic framework. The dissipative pressure is zero on the RTL, so that $p = p_{\rm S}$, and hence *the pressure is a unique function* of $e^{\rm P}_{\rm vir}$. The Reynolds–Taylor state is hence represented by a unique line in the $(e^{\rm P}_{\rm vir}, p)$ plane. Assuming a value for the spacing ratio, this line and hence the kinematic hardening function, $p_{\rm S}(e^{\rm P}_{\rm vir})$, can be determined from isotropic compression tests. Although the material is dilating on this line, this dilation does not dissipate any energy and the dissipation is given by (1), as originally envisaged by Schofield and Wroth [32]. It is of course important to emphasize that the values of θ and M are path dependent and all these lines in the (p, q) plane rotate as the deformation proceeds. In a drained test, the final position of the RTL corresponds to the ultimate failure line, whilst in an un-drained test it gives the ultimate or asymptotic state line of Gudehus et al. [16] and Chu [4] and Lo [5]. The main object of this chapter has been to describe a physically motivated, theoretical framework. Detailed applications to the modelling of sand, will be presented elsewhere.

6 Achievements and Ongoing Research

To date the main achievements are:

(a) The use of the hyper-plastic thermomechanical formulation provides a rich, mathematical structure for systematically developing models of

geomaterials. In particular it is providing a new energy interpretation of the classical critical state models.

(b) An extended family of critical state models have been developed, which better models the behaviour of clays and sands.

(c) The flow rule and yield loci are determined from the assumed form of the thermodynamic potentials. Much of the arbitrariness of the choice of these functions has been removed.

(d) The distinction between "Reynolds dilatancy" and plastic flow rules has been emphasized.

(e) Induced anisotropy is seen as a natural consequence of dilatancy.

(f) Definite statements can be made about the uniqueness of "critical lines" in (e, p) space.

(g) Micro-mechanical concepts can be included in the formulation of the thermodynamic potentials. Specifically, aspects of the force chain structure can be included, by introducing two new parameters, which affect the shape of the yield loci and form of the flow rule.

The main limitations of the current analyses are:

(a) Attention has been focused on single surface models. Whilst there are no difficulties in extending the general procedures to multi-surface, subloading and bounding surface models, the exact forms of the free energy potentials, which govern the translation of these surfaces still need to be determined. A particularly important aspect is the modelling of particle re-arrangement and of grain crushing.

(b) The analyses presume that the strain can be regarded as the sum of an elastic and plastic strain, and that these strains can be used as state variables. It also assumes that the free energy can be separated into elastic and plastic components. Analysis of the homogenization procedure, assuming continuous stress and strain fields at the micro-level, show that these assumptions are only strictly valid when the micro-elasticity, arising from the grain deformations is *linear* [12, 22]. When the micro-elastic behaviour is non-linear, it is no longer possible to treat elastic and plastic strains as state variables. Instead, the elastic–plastic decomposition must be performed on the *strain rate,* and the resulting elastic and plastic strains are path dependent.

(c) Whilst the models take account of the freezing of elastic energy and the bimodal nature of the stress and strain distributions at the meso-level, they do not account for the detailed behaviour at the micro-level. Specifically they do not account for the complexity of individual grain interactions.

References

1. Been, K. and Jefferies, M.G. (1985). A state parameter for sands. Geotechnique 35, No. 2, 99–112

2. Bjerrum, L. (1966). Progressive failure in slopes of overconsolidated plastic clay shales. The Terzhagi Lectures, 1963–1972. (1974) American Society of Civil Engineers, New York
3. Burland, J.B. (1965). The yielding and dilation of clay. Correspondence, Geotechnique, 15, 211–214
4. Chu, J. (1995). An experimental examination of the critical state and similar concepts for granular materials. Can. Geotech. J. 32, 1065–1075
5. Chu, J. and Lo, S.-C.R. (1994). Asymptotic behaviour of a granular soil in strain path testing. Geotechnique, 44, No. 1, 65–82
6. Collins, I.F. (2005a). Elastic/plastic models for soils and sands. Int. J. Mech. Sci., 47, No. 4, 493-508
7. Collins, I.F. (2005b). The concept of stored plastic work or frozen elastic energy in soil mechanics. Geotechnique 55, No. 5, 373–382.
8. Collins, I.F. and Hilder, T. (2002). A theoretical framework for constructing elastic/plastic constitutive models for triaxial tests. Int. J. Numer. Anal. Methods Geomech. 26, 1313–1347
9. Collins, I.F. and Houlsby, G.T. (1997). Application of thermomechanical principles to the modelling of geotechnical materials. Proc. R. Soc. Lond. A 453, 1975–2001
10. Collins, I.F. and Kelly, P.A. (2002). A thermomechanical analysis of a family of soil models. Geotechnique, 52, No. 7, 507–518
11. Collins, I.F. and Muhunthan, B. (2003). The relationship between stress–dilatancy, anisotropy and plastic dissipation for granular materials. Geotechnique 53, No. 7, 611–618
12. Collins, I.F. and Tai, A. (2005). What has thermomechanics to offer geomechanics? Proc. of 11th International Conference on Computer Methods and Advances in Geomechanics, Ed. G. Barla and M. Barala, Torino, Italy 19–24 June, Vol 1, 281–288.
13. Coussy, O. (1995). Mechanics of porous continua. Wiley Chichester, New York
14. Dafalias, Y.F. (1986). An anisotropic critical state clay plasticity model. Mech. Res. Commun. 13, 341–347
15. Goddard, J.D. and Bashir, Y.M. (1990). On Reynolds dilatancy. Recent developments in Structured Continua, Vol. 2. eds D, DeKee and P.N. Kaloni, Longmans New York, 23–35
16. Gudehus, G., Goldscheider, M. and Winter, H. (1977). Mechanical properties of sand and clay and numerical integration methods: some sources of errors and bounds on accuracy. Finite Elements in Geomechanics (ed Gudehus), 121–150
17. Houlsby, G.T. (1993). Interpretation of dilation as a kinematic constraint. Modern Approaches to Plasticity, ed D. Kolymbas, Elsevier, New York, 119–138
18. Houlsby, G.T. and Puzrin, A.M. (2000). A thermomechanical framework for constitutive models for rate-independent dissipative materials. Int. J. Plasticity, 16, 1017–1047
19. Kanatani K.-I. (1982). Mechanical foundation of the plastic deformation of granular materials. Proceedings IUTAM Conference.on Deformation and Failure of Granular Materials, Delft, 119–127
20. Luong, M.P. (1986). Characteristic threshold and infrared vibrothermography of sand. Geotech. Testing J. ASTM, 80–86
21. Maugin, G.A. (1992). The thermomechanics of plasticity and fracture, Cambridge University Press, Cambridge

22. Mroz, Z. (1973). Mathematical Models of Inelastic Material Behaviour, University of Waterloo Press
23. Muir Wood, D. (1990). Soil Behaviour and Critical State Soil Mechanics. Cambridge University Press, Cambridge
24. Muir Wood, D. (2002). Constitutive cladistics: the progeny of critical state soil mechanics. Constitutive and Centrifugal Modeling: Two Extremes, Springman (ed), Swets & Zeitlinger, Lisse
25. Nixon, S.A. and Chandler, H.W. (1999). On the elasticity and plasticity of dilatatant granular materials. J. Mech. Phys. Solids, 47, 1397–1408
26. Okada, N and Nemat-Nasser, S. (1994). Energy dissipation in inelastic flow of saturated cohesionless granular media. Geotechnique, 44, No. 1, 1–19
27. Radjai, F., Wolf, D.E., Jean, M. and Moreau, J.-J. (1998). Bimodal character of stress transmission in granular packings. Phys. Rev. Lett., 80, No. 1, 61–64
28. Reynolds, O. (1885). On the dilatancy of media composed of rigid particles in contact, with experimental illustrations. Phil. Mag. 20, 469–482
29. Rice, J. (1971) Inelastic constitutive relations for solids: an internal-variable theory and its application to metal plasticity. J. Mech. Phys. Solids. 19, 433–455
30. Roscoe, K.H. and Burland, J.B. (1968). On the generalized stress–strain behaviour of "wet clay". Engineering Plasticity, ed J Heyman and F.A. Leckie, Cambridge, Cambridge University Press, 535–609
31. Rowe, P. W. (1962). The stress–dilatancy relation for static equilibrium of an assembly of particles in contact, Proc. R. Soc. A 269, 500–527
32. Schofield, A. N. and Wroth, C. P. (1968). Critical State Soil Mechanics, McGraw-Hill New York, London
33. Shamoto, Y., Zhang, J.-M., and Goto, S. (1997). Mechanism of large post-liquefaction deformation in saturated sand. Soils Foundations, 37, 71–80
34. Sladen, J.A., Krahn, J. and Hollander, R.D. (1986). A state parameter for sands. (Correspondence on paper by Been, K and Jefferies, M.G, (1985). Geotechnique 35, No. 2, 99–112) Geotechnique 36, No. 1, 123–124
35. Taylor, D.W. (1948). Fundamentals of Soil Mechanics. Wiley New York
36. Ulm, F.-J., and Coussy, O. (2003). Mechanics and durability of solids, Vol. 1. Prentice Hall New Jersey
37. Voyiadjis, G.Z. and Song, C.R. (2005). A. coupled micro-mechanical based model for saturated soils. Mech. Res. Commun. 32, 490–503
38. Wang, Z.-L., Dafalias, Y.F., Li, X.-S. and Makdisi, F.I. (2002). State pressure index for modeling sand behavior. ASCE, J. Geotech. Environ. Eng. 128, No. 6, 511–519
39. Yu, H.-S. (1998). CASM: a unified state parameter model for clay and sand. Int. J. Num. Anal. Meth. Geomech. 22, 621–653
40. Ziegler, H. (1983). An Introduction to Thermomechanics (2nd edition), North Holland, Amsterdam

Physical Background of Hypoplasticity

Gerd Gudehus

Institute of Soil Mechanics and Rock Mechanics, University of Karlsruhe
Gerd.Gudehus@ibf.uni-karlsruhe.de

1 Introduction

No other concept was and is as successful in Soil Mechanics as hypoplasticity. This is due to a sound physical background, as will be briefly outlined in this chapter. A reviewer's response to my first proposal more than 30 years ago was "Terzaghi completed Soil Mechanics 1925, so there is no need for further research". In fact Terzaghi contributed a lot to our science, but certainly he did not complete it. With hypoplasticity we have joined the mainstream of Physics.

"Original hypoplasticity" was chosen as title of Sect. 2 as there are some common features with Schofield's [55] "Original Cam Clay". The concept of asymptotic states was taken over, but it was formulated in a more consistent manner. Percolations appear instead of thermodynamic phase transitions. Polar quantities are introduced for state limits with localizations in Sect. 3. This can lead to pattern formation or deterministic chaos. The intergranular strain is also introduced by means of state limits (Sect. 4). It renders possible a kind of interpolation between hypoelastic and hypoplastic behaviour.

To a certain extent hypoplasticity is supported by statistical granular dynamics simulations. The main difference to molecular dynamics is that granular encounters are not conservative: there is no potential for the intergranular forces, and the grains are changed every time. Therefore there is no Hamiltonian, and thus no dynamic equilibrium with temperature and state functions as potentials. Instead, external drift with energy input can lead to state limits independently of the start. These are represented by *attractors*, i.e. asymptotic solutions of the hypoplastic relations. This requires that certain properties of the grains are permanent although they undergo dislocations near contacts, so abrasion and fragmentation are neglected.

Clay particles are less regular and far softer even than angular calcite grains. Certain properties of them must nevertheless be permanent as proportional compression and isochoric shearing of remoulded saturated clay can lead to asymptotic states independently of the start. Cracking is indicated as

a third kind of state limit of Cam Clay, it can be specified by hypoplasticity. Viscosity of the particles plays a significant role, this is modelled by visco-hypoplasticity (Sect. 5). It is due to thermally activated dislocations of the solid particles. The bound pore water influences the skeleton behaviour as its density is changed with changes of the skeleton (Sect. 6).

Grain skeletons can reveal similar viscous effects as clays, which cannot be explained by thermal activation. This leads to seismo-hypoplasticity with a granular temperature (Sect. 7). The granular dynamics is not yet fully understood. Further open questions arise with unsaturated skeletons and with crushing particles. Hypoplasticity has not reached a dead end (Sect. 8).

2 Original Hypoplasticity

Goldscheider [18] discovered some properties of sand under cuboidal deformations which enhanced the birth of hypoplasticity. First, there is no elastic range, but a limit condition with a flow rule. Second, with constant mean pressure the amount of contractancy after a reversal is bigger than the one of dilatancy before. Third, proportional compressive deformation paths lead to proportional stress paths asymptotically. So I gave up elastoplasticity and pointed out the need of novel constitutive relations with these properties [26].

After frustrating attempts with statistical mechanics Kolymbas [39] proposed constitutive equations of the rate type with the properties outlined above. After this breakthrough lengthy trial and error attempts led to improved representations, but determination and physical meaning of the parameters were not satisfactory. A way out was opened by Kolymbas [40] combining the influences of pressure and density. Bauer [6] and Gudehus [21] proposed pressure-dependent limit void and stress ratios and hypoplastic relations consistent with them. This rendered possible an easy and robust determination of parameters, and more and more validations by model and field tests.

The limit void ratios may be briefly discussed (Fig. 1) in comparison with Critical State Soil Mechanics (CSSM, [56]). Following Casagrande [11], critical states are defined in CSSM as asymptotes for simple shearing with stationary stress ratio

$$\tau/\sigma' = \tan\varphi_{\mathrm{sc}} \tag{1}$$

and void ratio

$$e_{\mathrm{c}} = e_{\mathrm{cr}} - \lambda\,\ln(\sigma'/\sigma_{\mathrm{r}}). \tag{2}$$

The reference stress σ_{r} is chosen at will and thus not objective. Evidently (2) fails for $\sigma' \to 0$ and $\sigma' \to \infty$. In hypoplasticity critical states are defined as asymptotes for isochoric shearing, so the problem of localization is circumvented (Sect. 3). Equation (1) holds again, but

$$e_{\mathrm{c}} = e_{\mathrm{c0}}\,\exp\left[-\left(\frac{3\sigma'}{h_{\mathrm{s}}}\right)^{n}\right] \tag{3}$$

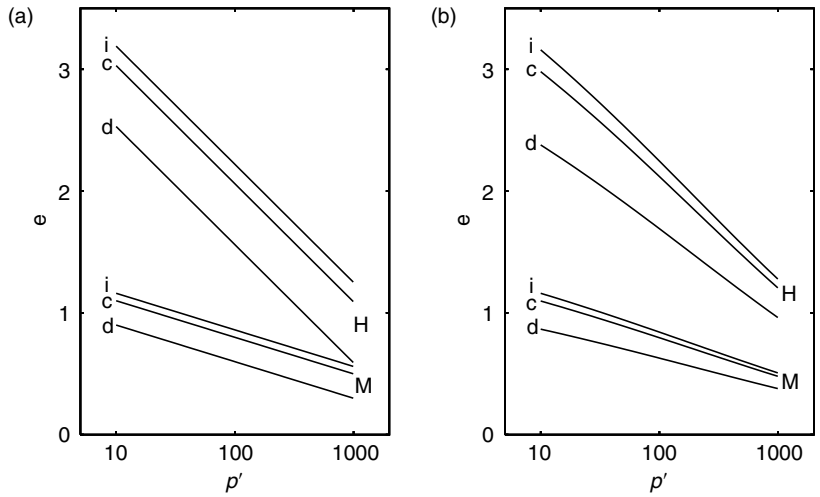

Fig. 1. Pressure-dependent limit rations of highly (H) and moderately (M) plastic clay by CSSM **(a)** and by hypoplasticity **(b)**

is assumed instead of (2). The granulate hardness h_s is objective, it ranges from ca. 100 MPa for angular calcite to ca. 10 GPa for round quartz grains. Near $\sigma' = 0$ (3) can be replaced by

$$\sigma' \approx \frac{1}{3}\, h_\mathrm{s}(1 - e_\mathrm{c}/e_\mathrm{c0})^{1/n}, \tag{4}$$

which is typical of a *percolation* [57]. The index n increases from ca. 0.2 for angular to ca. 0.5 for round grains. Thus it decreases with an increase of the fractal dimension of the grain surface.

For an isotropic compression from a very loose state the void ratio by CSSM tends to (2) with e_ir instead of e_cr, and to (3) with e_i0 instead of e_c0 by hypoplasticity. Thus CSSM implies the conventional virgin compression law that fails for $\sigma' \to 0$ and $\sigma' \to \infty$. The percolation by (4) is known in granular physics [28]. For an oedometric compression the same holds true with a reference void ratio halfway between the ones for critical states and for isotropic compression.

Other stress states can similarly be allowed for in CSSM and in hypoplasticity. The latter implies a critical stress ratio for cylindrical symmetry, wherein φ_sc is related with φ_c by Bauer's [7] formula

$$\tan\varphi_\mathrm{sc} = 2/\sqrt{1 + 3/\sin^2\varphi_\mathrm{c}}\,. \tag{5}$$

Formally (5) is also proposed for peak states, replacing φ_c by φ_p for cylindrical symmetry and φ_sp for simple shearing. Postponing localization (Sect. 3) and cyclic densification (Sect. 4), we consider now state limits with the lowest

possible void ratio, e_d. A cylinder with e_d is capable of uniaxial stress, then it has $\varphi_\mathrm{p} = 90°$, (5) yields $\varphi_\mathrm{sp} = 45°$. In this physically meaningful extreme state of the skeleton, which may then be considered as a kind of dry masonry, there is dilatation without sliding. This replaces the unspecified tensile cracking of CSSM proposed by Schofield [55].

Granular dynamics simulations give partial support to hypoplasticity. Substituting grain contacts by linear normal and shear springs with dry friction, however, misses the pressure–density relationship. Thus at best the lack of an elastic range and a certain influence of e on φ_p and dilatancy can be shown. Only recently the non-linearity due to pressure-dependent contact flats has been allowed for [49]. It corresponds to (4) qualitatively, the asymptotic properties for stationary shearing and proportional compression are reproduced as in hypoplasticity (Fig. 2). Uniaxial stress states have earlier been produced with the same model [61], but with very low e like a jointed rock. Further simulations with $e \approx e_\mathrm{d}$ are advisable to better understand the granular phase transition from skeleton to dry masonry (cf. Sects. 3 and 4).

3 Shear Localization

As outlined already by Cauchy, the symmetric stress tensor named after him is not the only substitute of internal forces. It cannot represent spatial fluctuations (Sect. 4) and polar effects. The polar quantities introduced by the Cosserat brothers were first applied to dislocations of solids. It was realized that they play a role only near surfaces, also those separating a body by localization. The molecules along a liquid surface are polarized and more densely packed, in particular along a cavitation. This holds true also for interfaces between different solids and/or fluids. *Cum grano salis*, i.e. with non-conservative interparticle forces, these statements can be transferred to soils.

For a shear localization it suffices to introduce three polar quantities: rotation rate ω_c minus shearing and rigid body parts, couple stress m_c and non-symmetric part τ_c of shear stress. Hypoplastic relations with these quantities have two additional attractors (Fig. 3): Stationary shearing with constant rate D and ω_c leads to constant stress ratios $m_\mathrm{c}/d_\mathrm{g}\sigma$ and τ_c/σ in addition to $\tau/\sigma = \tan\varphi_\mathrm{sc}$, whereas stationary shearing or proportional compression with $\omega_\mathrm{c} = 0$ leads to $m_\mathrm{c} = 0$ and $\tau_\mathrm{c} = 0$. The mean grain size d_g enters as characteristic length. With these attractors the first attempt was already successful [58], later versions were more elegant [34].

Consider now the evolution of an initially dense slender biaxial sample by shortening (Fig. 4). Minute initial fluctuations of e evolve into a pattern when approaching the peak σ_1. Alongside with it a pattern of m_c with zero mean value evolves. At peak a single shear band arises, the skeletons below and above are only shifted past each other. Shortening of a flat biaxial sample leads to a similar initial pattern, but at peak a zig-zag shear band appears (Fig. 5). With further shortening and dilation the sample is paved by further

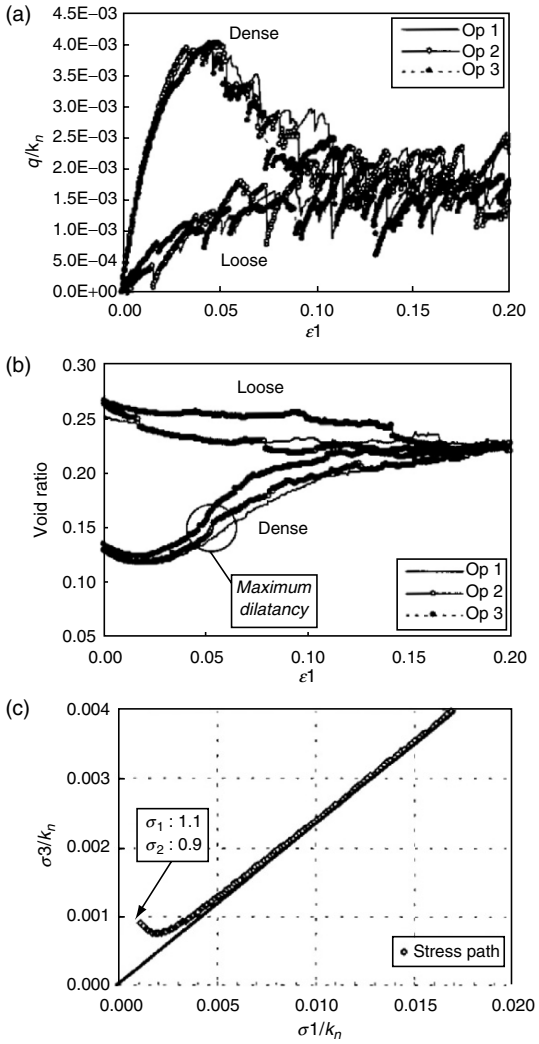

Fig. 2. Simulated response of an assembly of polygons [49] to biaxial shearing with constant pressure **(a, b)** and proportional compression **(c)**

zig-zag bands. In the asymptote there is a fractal spatial fluctuation of m_c around zero and of e around e_c. All this is validated by experiments [25].

Similar *critical phenomena* appear in various non-linear dynamic systems. Thermodynamic systems at critical points, characterized by zero transition energies, generate spatial patterns and obey power laws with universal exponents for deviations from the critical temperature [10]. Far off equilibrium irregular propagations can evolve into coherent waves at a critical point [29]. With modified boundary conditions, a deterministic chaos can evolve from

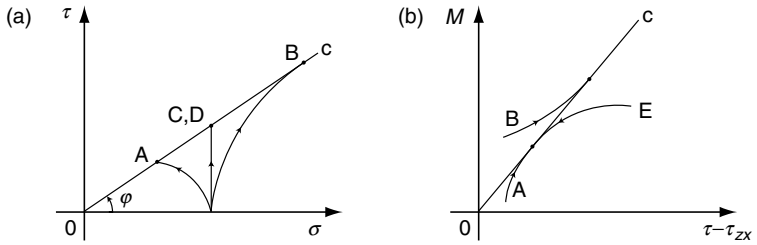

Fig. 3. Attractors of polar stress for stationary shearing with **(a)** and without Cosserat rotation **(b)**

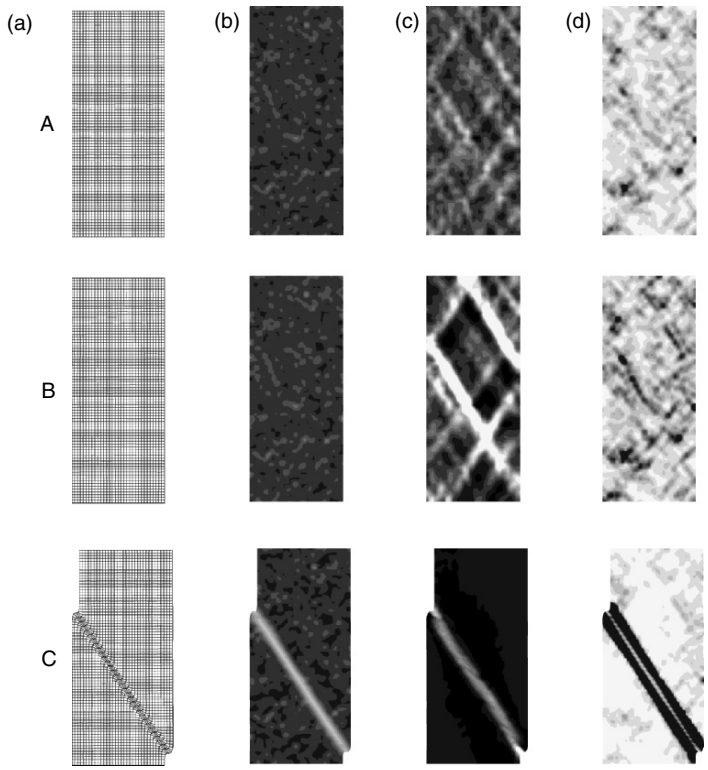

Fig. 4. Evolution of shape **(a)**, density **(b)**, shearing **(c)** and couple stress **(d)** of a biaxial sample, calculated with hypoplasticity [25]

the same critical point. Molecular critical phenomena can also arise with interfaces, e.g. spontaneous capillary condensation or cavitation.

Granular physics was triggered by the discovery of self-organized criticality and $1/f$-spectrum of avalanches from a little sand heap [4]. Later physicists realized the role of density in granular phase transitions. A granular gas without equilibrium was introduced, but grain skeletons posed a harder task. The granular dynamics of shear localization was partly revealed [3]. Average grain

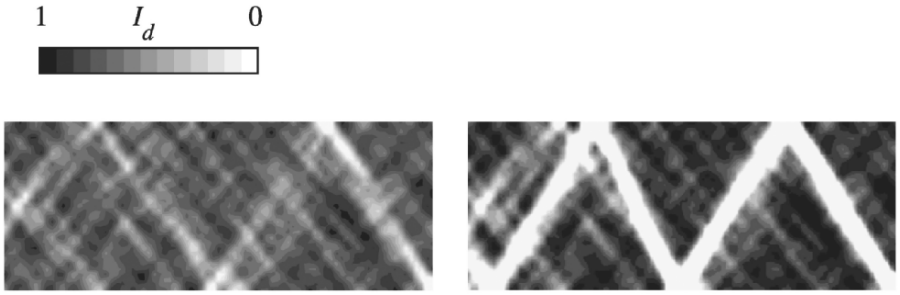

Fig. 5. Evolution of a flat biaxial sample, calculated with hypoplasticity and polar terms [25]

rotations inside shear bands indicate ω_c, whereas they fluctuate around zero outside. m_c and τ_c were derived as averages of suitable grain groups without contact moments [16]. These are important qualitative first steps.

The following interpretation of hypoplasticity in this light is admittedly heuristic. The critical state of a grain skeleton is a kind of critical point: its continuation does not change the average state, the spatial fluctuation is fractal in the range between sample and grain size. It is achieved by uniform shift imposed from the boundaries with constant mean pressure or density. A power law (4) holds near $\sigma = 0$, but counterparts of power laws near a critical temperature are not known.

Peak states of grain skeletons are similar to molecular critical points in so far as they lead to localization along spontaneously arising internal interfaces. Along the middle of a shear band there are no polar quantities, there the state limit is described by a peak stress ratio and dilatancy ratio. Both depend on the instantaneous density index

$$I_d = (e_c - e)/(e_c - e_d), \tag{6}$$

wherein e_c and e_d depend on σ via (3) with $e_{d0} < e_{c0}$ for e_d. I_d enters the evolution equations via $(1 - I_d)^\alpha$ with an exponent α depending on grain roughness, thus a power law holds near critical states. The unattainable state limit with $I_d = 1$, $\varphi_c = 90°$ and maximum dilatancy is an upper bound of peak states.

Peak states imply localization under further boundary shift as thus the dissipation of energy is reduced. The shear zone thickness ranges from grain to body size for I_d from 1 to 0. Polar quantities arise spontaneously along shear bands if these are not enforced along rough boundaries, and can be swept out again if the skeleton is forced towards an overall critical state. For geotechnical boundary conditions this comes up to deterministic chaos more than to self-organization. That's why plastic limit states provide at best crude estimates and the bound theorems do not hold. More research is needed, in particular with hypoplasticity, until such critical phenomena of grain skeletons are properly understood so that they can be technically controlled.

4 Alternating Evolutions of Grain Skeletons

The typical response to cyclic shearing with constant σ' predicted with hypoplasticity shows a step-wise densification and hardening up to periodic asymptotic loops. The lowest e approaches e_d for small amplitudes. With deviator cycles around a critical stress ratio a periodic ratcheting is achieved with $e_\mathrm{d} < e < e_\mathrm{c}$ (Fig. 6). Thus alternating evolutions can lead to periodic butterfly-shaped state loops. These resemble strange attractors of conservative systems, and may also indicate impending deterministic chaos of non-conservative grain skeletons.

Hysteresis and ratcheting are not really as strong as in Fig. 6. This shortcoming of hypoplasticity is overcome with the *intergranular strain* tensor $\boldsymbol{\delta}$ [45]. For sufficiently big monotonous deformations $\boldsymbol{\delta}$ is determined by the tensors $\boldsymbol{\sigma}$ and $\boldsymbol{D}$ of stress and stretching rate and not needed therefore, hypoplasticity then works without it. Many small strain cycles lead to $\boldsymbol{\delta} \to 0$, then the response is hypoelastic, i.e. incrementally linear. Cases in between are covered by an interpolating evolution equation with $\mathrm{tr}(\boldsymbol{D\delta})$ as a switch function. This leads to a less hysteretic alternating evolution (Fig. 7). The observed behaviour in resonant column tests with different amplitudes suffices to determine the parameters for $\boldsymbol{\delta}$ [12].

The need of an internal tensorial variable in addition to the external ones, $\boldsymbol{\sigma}$ and e, was recognized when dealing with the asymptotic response to proportional compression [26]. As outlined earlier, $\boldsymbol{\delta}$ has two attractors, viz. for hypoplastic and hypoelastic behaviour. They can be related with the

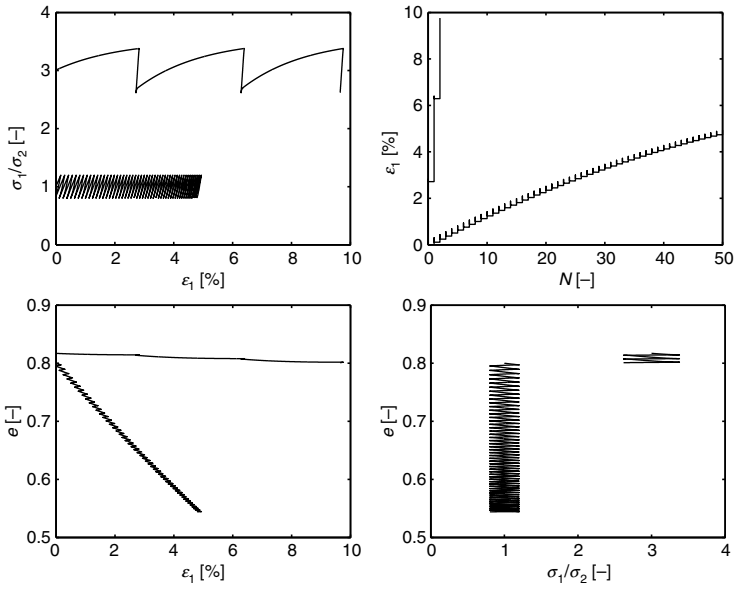

Fig. 6. Ratcheting with constant σ_2, calculated by hypoplasticity

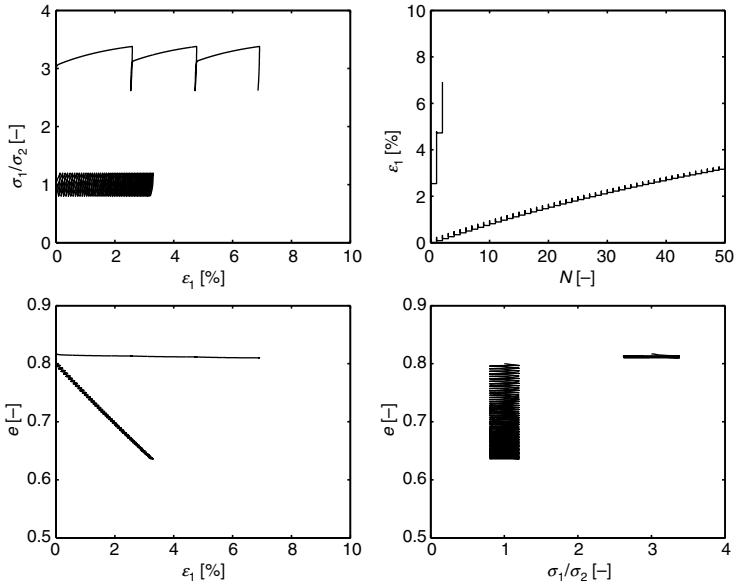

Fig. 7. As Fig. 6, but with intergranular strain

spatial fluctuation of intergranular forces. It is maximal together with $\boldsymbol{\delta}$, then force chains are marked and neighboured grains with low forces are close to sliding [53] so that the skeleton is prone to dissipation. The fluctuation is minimal for $\boldsymbol{\delta} = 0$, then no grains are close to sliding so that the response is non-dissipative. Simulations show for ratcheting that the fluctuation gets stationary somewhere between upper and lower bounds [1].

There is some similarity with a non-porous solid with crystallite dislocations and eigenstress. Thermal annealing is similar to attaining $\min \boldsymbol{\delta}$ by minute oscillations. Solid dislocations are thermally (Sect. 5), granular ones seismically activated (Sect. 6). In both cases a back stress is not physically justified as this would be a spatial mean value. As the spatial fluctuation of intergranular forces is fractal over several grain sizes δ can be independent of the latter. Evidently the deviatoric plastic strain is not a state variable. Elastoplastic relations with nucleating and bounding yield surfaces may at best get objective with suitable infernal variables but even then they are less economic and transparent than hypoplastic ones.

Response envelopes [20] have been and can be of use for further improvement of hypoplastic relations. There is no need for inverse ones which are explicit in strain. The extension to more than two components is straightforward, but not prioritary. The necessity of an elliptic shape was proven by systematic variations [64]. It characterizes the hypoelastic part with a potential, although this cannot uniquely be separated. Granular dynamics simulations may be of use to bridge between the attractors of $\boldsymbol{\delta}$, but not with linear contact springs (cf. end of Sect. 2).

Stability cannot be judged from the incremental response only. The notion local stability is physically irrelevant, even the stability of a sample or a representative volume element cannot be judged without boundary conditions. Along the boundaries there are fluctuations as those represented by polar stresses and $\boldsymbol{\delta}$, and there is also a transmission of chaotic acoustic waves (Sect. 7). As elastic strain rates cannot clearly be separated the net energy for stress cycles is scarcely of use. Plasticity bound theorems do not hold for lack of normality, the existence of statically possible fields is only necessary for stability. Energy balances with assumed kinematic chains can at best yield estimates [19, 21].

The propagation of shear waves is more revealing for stability [48]. The response to repeated waves was simulated with hypoplasticity and validated by shakebox tests and earthquake data [27]. Loss of stability may be revealed by loss of propagation [47], or by the emission of coherent waves [2]. Stability may also be defined by step-wise reduced ratcheting under repeated equal boundary impacts [23]. This corresponds to Liapunov's definition, but a Liapunov function has still to be found.

5 Visco-Hypoplasticity

Rate-independence is assumed in original hypoplasticity, and also with intergranular strain. This is apparently justified if the interaction of grains is rate-independent. Clays and organic soils have softer particles (the name grain is not adequate) so that rate effects are important. Terzaghi [60] reported on creep effects in solid friction experiments and proposed contact flat sizes in proportion to the gross pressure and the inverse of solid strength. Prandtl [52] used the same argument to support Amonton's friction law long before Bowden and Tabor [9]. Based on Arrhenius' law and creep experiments, he derived the equation

$$\tau = \tau_\mathrm{r}[1 + c_1 \ln(\dot{\varepsilon}/c_2)] \tag{7}$$

for the dependence of solid shearing resistance τ on strain rate $\dot{\varepsilon}$. He showed that the two parameters c_1 and c_2 are proportional to the absolute temperature T. This means that plasticity implies *thermally activated non-linear viscosity*. Mitchell et al. [43] showed by creep tests with T-control that (7) works for a saturated clay. Derived activation energies per mole were typical for ceramics, but activated flow units could not be identified. Bjerrum [8] observed resistances to undrained shearing which can be approximated by (7). He also reported on compression and overconsolidation with time for constant σ'. Leinenkugel [42] observed the same rate-dependence and proposed

$$c_\mathrm{u} = \sigma_\mathrm{e} \tan\varphi_\mathrm{sc}[1 + I_\mathrm{v} \ln(\dot{\varepsilon}/\dot{\varepsilon}_\mathrm{r})] \tag{8}$$

with Hvorslev's [37] equivalent stress σ_e. The viscosity index I_v and the reference rate $\dot{\varepsilon}_\mathrm{r}$ correspond to c_1 and c_2 in (8), so both are proportional to

T. With e corresponding to σ' by (2) Leinenkugel [42] could reproduce Bjerrum's [8] statements on delayed compression. He interpreted his findings with the theory of rate processes.

It was repeatedly observed [46] that (1) holds with constant φ_c for stationary shearing independently of $\dot{\varepsilon}$. This is reconciled with Terzaghi's and Prandtl's argument by assuming contact flat sizes that decrease with bigger $\dot{\varepsilon}$ via (7). If $\dot{\varepsilon}$ is increased with constant e both τ and σ' increase so that (1) holds again, this explains (8). Persson [51] derived (8) by assuming thermally activated dislocations of nano-size homogeneous blocks, and related their properties with the factors c_1 and c_2. The dislocation energy of clay particles could thus be related with I_v in (9) [22] via

$$\varepsilon_a \approx k_B T(12 + 1/I_v)\,, \tag{9}$$

yielding realistic values from ca. 0.5 to 3 eV for I_v from 0.06 to 0.01. As with sliding friction [50] the high-frequency submicroscopic oscillations are not at variance with the rate-independence of φ_c.

Rate-dependent state limit void ratios can be approximated by (2) or (3) with σ_r or h_s depending on $\dot{\varepsilon}$ as c_u by (8). Using this h_s, i.e.

$$h_s = h_{sr}[1 + I_v \ln(D/D_r)] \approx h_{sr}(D/D_r)^{I_v} \tag{10}$$

with the modulus D of stretching rate in a hypoplastic relation describes also transitions for monotonous deformations with varying strain rate or effective stress [21]. This does not work, however, for path reversals and relaxation.

Kolymbas [39] proposed a rate-type relation with the second-order stretching rate $\boldsymbol{D}_2$ that reproduces rate-dependence, creep and relaxation. As it requires an initial strain rate and higher-order differences the search went on for simpler relations [64]. Niemunis [44] achieved a breakthrough by combining hypoplasticity with Cam Clay and Perzyna's concept. He employed also the intergranular strain. Even for a diatomaeceous clay the quality is exceptional (Fig. 8). This holds true also for wave propagation [27]. Instead of I_d for granular soils, a suitable OCR is the decisive state variable.

I have proposed a visco-hypoplastic relation on this base without using (2) from Cam Clay [22]. It implies three state limits by (3) with h_s by (10) and is thus physically consistent. An objective reference strain rate, D_r in (10), is proposed. The intergranular strain $\boldsymbol{\delta}$ can also be incorporated in order to improve the response to jumps and reversals. As it represents the spatial fluctuation of interparticle forces the evolution equation for it should allow for viscosity.

Attractors are the backbone of my visco-hypoplastic equations. Three of them are reached with a constant D. They represent the same state limits as in hypoplasticity, but now h_s depends on D. Other than in original hypoplasticity, they can also be reached with constant effective stress and/or strain components, i.e. by creep and/or relaxation. The time-variate D is then given by the instantaneous mean effective pressure and void ratio via (3) and (10).

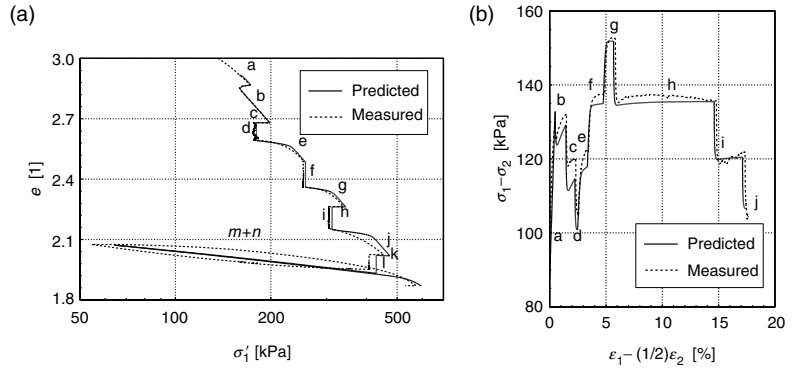

Fig. 8. Compression **(a)** and shearing behaviour **(b)** of a diatomaeceous clay, observed [41] and simulated by visco-hypoplasticity [44]

For pure relaxation and for stabilizing creep a lower bound of h_s is proposed for D below a very low threshold . Thus further attractors can be approached with $D \to 0$ or $t \to \infty$, which may be interpreted as thermodynamic equilibria.

Attractors should also be the core of extended visco-hypoplastic relations. For shear localization this means that the ratios of polar and non-polar stresses reach asymptotic values for constant extended stretching rate, and that asymptotes with decreasing amount can be reached with constant generalized stress. For the intergranular strain there are driven attractors with constant D as for rate-independence, and also autogenous ones for constant components.

Molecular dynamics counterparts of visco-hypoplasticity do not yet exist. Simulations of idealized dilute colloids [15] refer at best to a slurry. Simulations with hard grains and electrolytes may help to understand the influence of the iomic strength in fine-grained soils where macropores delimit the use of hypoplasticity. Not even the identity of clay aggregates is clear. Only their permanence may be deduced from the existence of attractors, in particular critical states.

6 Hydro-Pyknotropy

Terzaghi [59] discovered peculiar properties of water in narrow solid–liquid interfaces. He introduced the notion of bound pore water. Derjaguin and Churayev [13] showed that this "polywater" is denser and far more viscous than normal water. After decades it became clear that it exists only in nano-size diffuse boundary zones. Equilibrium mean-field solutions are used in the DLVO-theory of colloids with spherical particles. Equilibrium solutions have also been proposed for idealized clay aggregates [65], they have little in common with results of molecular dynamics [15] and of force microscopy [38].

There is only little and indirect evidence for the behaviour of bound pore water far off equilibrium. Zou [66] could explain the non-linear permeability

of clays by assuming that the activation energy ε_a of the bound pore water is reduced with increasing rate of shearing. He showed that ε_a can reach ca. $8k_BT \approx 0.2$ eV, which is well above ca. $0.5k_BT$ of free water and well below the dislocation energy of solid particles by (9). Rendulic [54] observed a minute density increase of pore water in triaxial tests. Topolnicki [62] observed density decrease and increase in drained isochoric biaxial tests. The average pore water density was changed up to ca. $\pm 0.5\,\%$ for saturated kaolin clay at $p' \approx 200$ kPa. This indicates that the bound pore water can undergo a dilatant stripping by skeleton deformations, and can also contract.

I have worked out [24] a hypoplastic relation for the relative excess of pore water density,

$$\chi = v_{wo}/v_w - 1, \tag{11}$$

wherein v_w denotes the specific volume of partly bound water, and v_w the one of the free pore water. χ is a measure of *hydro-pyknotropy*, i.e. variable water density. State limit values of χ can be related with the ones of the solid particle skeleton by (2) and (11) via

$$\chi = \kappa_\chi(e_0 - e) \tag{12}$$

with $e_0 = e_{d0}$, e_{c0} or e_{i0} respectively. Thus $\chi = 0$ is assumed for $p' = 0$ and $\chi = \kappa_\chi$ for $p' \to \infty$. $\kappa_\chi \approx 0.2$ was estimated as first approximation.

A rate-type relation links $\dot\chi$ with $\dot e$ and D so that the χ state limit values are attractors alongside with the ones of the skeleton. A second parameter m_χ is chosen so that the dilation ratio of the pore water for $\dot p' = 0$ exceeds the one of the skeleton for OCR ≤ 5 initially, and is lower otherwise. This leads to expulsion or imbibition of pore water for isochoric shearing with OCR < 2, which is rather close to what Topolnicki [62] observed, so there is apparently a first validation.

Starting with OCR $<$ ca. 2, undrained shearing leads to a decrease of p', and thus to an increase of pore water pressure p_w for constant total pressure. This explains the apparent residual friction angle $\varphi_r < \varphi_{sc}$ of highly plastic clay [37], as the low permeability prevents drainage of shear bands whereas the p_w increase is not observed at the sample boundary. It explains also that clays are denser in shear bands than their neighbourhood after tests with OCR $<$ ca. 2 initially [31].

For OCR well above 2 initially and undrained shearing the dilation of the skeleton is restricted to the one of the pore water. This flattens the τ-peak for apparently drained shearing as with localization the locally increased D prevents further drainage towards the shear band. Thus back-calculated peaks come closer to the observed ones [22]. The local suction, which is not observed at the boundaries, explains the densification observed after the test [31]. I also made an attempt to explain cracking by this theory [24]. The necessary condition $\sigma_2' = 0$ normal to a crack can be reached by rapid undrained shearing so that an extreme local dilation of pore water is achieved with $e \to e_d$ by reduction of p'. The crack is oriented by $45° - \varphi_p/2 = 0°$ against the σ'-direction as $\varphi_p = 90°$ holds for e_d state limits (Sect. 2).

An additional condition is that p_w attains the capillary entry pressure p_ce. As p_ce equals the tensile strength of saturated aggregates without net interparticle adhesion, a unaxial undrained tension test can thus be explained and evaluated for e_d. Uniaxial undrained shortening up to axial splitting can likewise be explained. This helps to understand the plastic limit index test: after densification to $e_\mathrm{d} = w_\mathrm{p}\gamma_\mathrm{s}/\gamma_\mathrm{w}$ by rather uniform cyclic shearing the subsequent localized undrained deformation leads to cavitation.

Shrinkage cracking cannot yet be explained in the same manner. The similarity of crack patterns for biaxial extension, undrained shortening and shrinkage suggests a common mechanism. Shear band patterns in clay have much in common with those in sand, but their analysis is more difficult due to skeleton viscosity and filtration [32]. The difficulties increase for cracking, which can be considered as anomalous shear localization. As cracking is a critical phenomenon and a kind of phase transition with percolation, other approaches like with the renormalization group [10] may be more promising.

7 Seismo-Hypoplasticity and Granular Temperature

Rate-independence of grain skeletons is often inferred from the one of interacting grain couples. This is at variance with observations: drained triaxial shortening of quartz sand with jumps of strain rate [14] reveals a shear stress response like a lowly plastic clay (Fig. 9). This can be modelled by visco-hypoplasticity with $I_\mathrm{v} = 0.02$, but the dislocation energy by (9) is too low for quartz. After a D-jump up or down there is an increase or decrease of dilatancy that disappears with further shearing. Creep is observed with constant deviator stress τ that stabilizes with densification for $\tau/\sigma' < \tan\varphi_\mathrm{sc}$.

Stress kinks reported in the same paper indicate a microseismic activity. Ring shear tests with constant mean σ and a local σ-transducer reveal a rate-independent spectrum of such stick-slip events (Fig. 10). Rate-independent kinks are also obtained with granular dynamics simulations. They indicate the repeated building and collapse of force chains [53]. The simulated spectrum is nearly fractal as with earthquakes [61]. Each microseismic event implies acoustic emission with frequencies that increase for smaller grains, normally it fades away long before the next snap-through.

The chaotic part of kinetic energy in an assembly of grains may be interpreted as *granular temperature* T_g [30]. For a granular gas with colliding grains an equation of state can be formulated with T_g although there is no dynamic equilibrium as with conservative interparticle forces [17]. This explains the linear viscosity of strongly shaken grain assemblies as observed by Barkan [5]. The non-linear viscosity of skeletons (Fig. 9) with rate-independent φ_sc [36] requires another approach.

I have proposed seismo-hypoplastic relations with a heuristic T_g [23]. Formally they agree with my visco-hypoplasticity ones (Sect. 5), but I_v and D_r

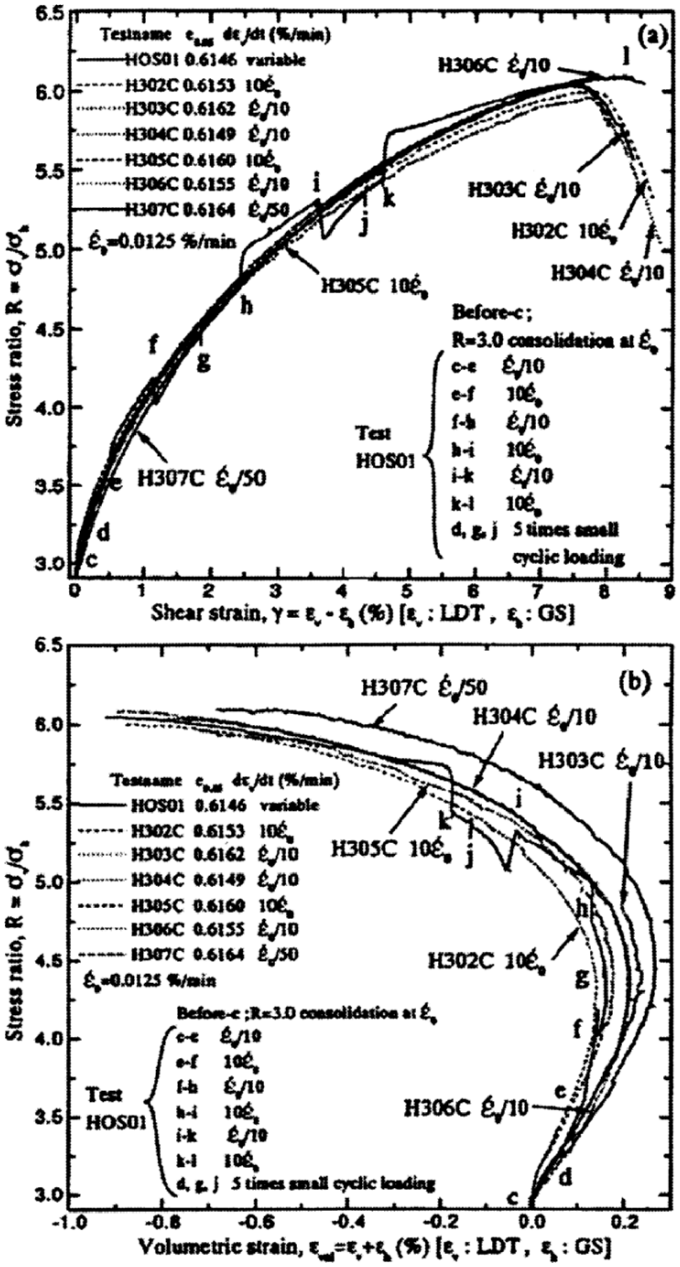

Fig. 9. Response of sand to drained triaxial compression with jumps of strain rate [9]

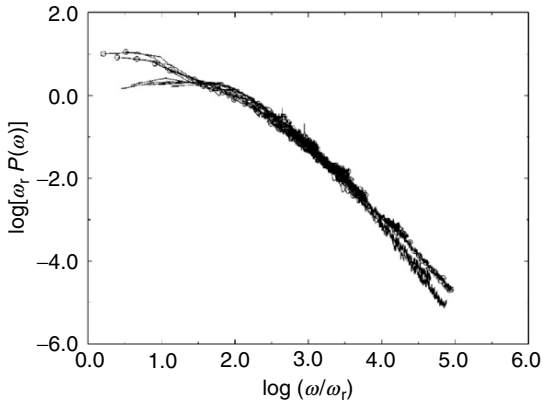

Fig. 10. Spectrum of stress kinks observed with sand in a ring shear apparatus, normalized by the rate of rotation [33]

are proportional to T_g instead of T. With suitable reference values the observed rate-dependence and creep (e.g. Fig. 9) is reproduced. Stabilization or destabilization with decreasing or increasing e and/or τ/σ' is obtained realistically. As the dissipated work per unit of deformation, say 1%, is proportional to σ' for stationary shearing the same is assumed for T_{rg}. Referred to a critical state ($\tau/\sigma' = \tan\varphi_{sc}$) with the same σ' or p', T_g is somewhat bigger for isotropic compression with e_i and zero for e_d state limit (cf. Sect. 2). Thus the solid hardness increases with D by (10). This explains the increase or decrease of dilatancy with an increase or decrease of D for constant σ' or p', and its subsequent decay after the adaption of e with continued shearing.

The granular dynamics may be explained as follows. Imagine first grains with conservative interaction, i.e. without friction and plastic flats. A skeleton of them in a slowly sheared layer with constant σ has $\tau/\sigma > 0$ due to anisotropic intergranular forces. If the acoustic waves due to collisions are absorbed at the boundaries the average kinetic energy T_g is stationary and maximally chaotic, so there is a Boltzmann distribution. (With reflecting boundaries T_g would increase until the skeleton expands to a granular gas.) For shearing with higher D the average grain distance is somewhat higher, and so is e, as T_g impedes the grain encounters. This corresponds to thermally activated dislocations of a sheared solid in a thermostat with $T = 0$, but $T > 0$ inside due to stationary dissipation. Thus T_g is endogenous, and the grain encounters are seismically activated.

Similary as with a granular gas, it is assumed that the chaotic kinetic energy is Boltzmann-distributed also with friction. T_g is proportional to the content of the spectrum of stick-slip kinks normalized by the average strain rate (Fig. 10). As the size distribution of force chains is nearly fractal the spectrum saturates towards the grain size and the sample size. A certain fraction of the mechanical energy input dissipated per unit of deformation is immedi-

ately absorbed by heat, a second mechanical chaotic part is released with each collapse of force chains and radiated, then it is also absorbed by intergranular friction which is thus activated. The proper boundary of a sample or a representative volume element must therefore be permeable for chaotic acoustic waves, which are generated and absorbed in the interior and the environment.

In case of ratcheting by repeated acoustic waves the microseismic activity is pulsating, and so is T_g. Cumulative changes of position, and also of average state for step-wise stabilization or destabilization, are obtained with an average $\overline{T}_g$ per period. Realistic relations of e, σ' and τ/σ' with the number of periods can thus be obtained. They can partly substitute rather cumbersome empirical relations based on cyclic triaxial tests [63]. Thus vibro-hypoplasticity can be used to predict cumulative effects for such a big number of periods that numerical approaches with elasto-hypoplasticity are too cumbersome or numerically unstable. We are carrying out triaxial tests with ratcheting to better understand T_g and its pulsation [35]. As with Fig. 9 stationary ratcheting can be obtained with τ-cycles around $\sigma \tan \varphi_c$. The σ_1-kinks are precisely measured, their spectrum for different amplitudes is revealing. This will also help to better understand the intergranular strain and to improve constitutive relations with it.

8 Concluding Remarks

In the core of all hypoplastic relations are their *attractors*. They represent state limits which characterize phases of the skeleton of solid particles and of the partly adsorbed pore liquid. As the interaction of the solid particles is not conservative the attractors are driven, i.e. they require energy supply to compensate for dissipation. Similar attractors are also obtained with adequate granular dynamics simulations. With thermally activated dislocations skeletons can reach a thermodynamic equilibrium after extremely long time, this is a further attractor. The partly bound pore fluid can reach attractors far off equilibrium, but returns to it in a short time if the skeleton is fixed. Dilatancy and contractancy of skeleton and pore fluid are different in general, both are characteristic of dissipative particle aggregates.

With localization of shear zones the concept of attractors works likewise, but in a more complex manner. Hypoplastic relations extended by polar quantities can thus yield realistic shear zone thickness and patterns. Results of simulations have to be properly averaged to support these findings. With suitable boundary conditions a fractal sequence of shear band patterns is obtained that leads to an overall critical state with fractal spatial fluctuations. A strange attractor could not be found for this evolution, the renormalization group is possibly more adequate for this critical phenomenon far off equilibrium.

For saturated clays rate-dependent attractors can likewise be defined with polar quantities. The evolution of shear bands is linked with dilation of the partly bound fluid if rapid shearing prevents filtration. Otherwise the analysis

gets more complex. The anomalous extreme case of shear localization with lowest void ratio and unaxial effective stress state, combined with capillary entry for cavitation of pore fluid, leads to cracking. For crack patterns strange attractors or renormalization groups have to be developed. This could also open a more profound access to unsaturated soils.

The microseismic activity of grain skeletons justifies a seismo-hypoplastic relation with a granular temperature and attractors. Ratcheting by repeated seismic waves could open a new access to the intergranular strain representing the spatial fluctuation of intergranular forces, again with attractors. The spontaneous emission of coherent acoustic waves is another critical phenomenon that calls for attractors or a renormalization group. Thus a spontaneous collapse could be better controlled.

All these attractors require permanent solid particles. It is not yet known how far this assumption is physically justified, and how it could be overcome without losing the advantage of attractors.

References

1. Alonso-Marroquín F. & Herrmann H.J. (2004) Ratcheting of granular materials. Physical Review Letters 92(5): 054301-1–4
2. Andreotti B. (2004) The song of dunes as a wave-particle mode locking. Physical Review Letters 93(23): 238001-1–4
3. Åström J.A., Herrmann H.J. & Timonen J. (2000) Granular packings and fault zones. Physical Review Letters 84(4): 638–641
4. Bak P., Tang C. & Wiesenfeld K. (1987) Self-organized criticality: an explanation of 1/f noise. Physical Review Letters 59(4): 381–384
5. Barkan D.D. (1962) Dynamics of Bases and Foundations. McGraw-Hill Series in Soils Engineering and Foundations
6. Bauer E. (1996) Calibration of a comprehensive hypoplastic model for granular materials. Soils and Foundations 36(1): 13–26
7. Bauer E. (1997) The critical state concept in hypoplasticity. In: Nineth International Conference on Computer Methods and Advances in Geomechanics. Balkema: 691–696
8. Bjerrum L. (1973) Problems of soil mechanics and construction on soft clays and structurally unstable soils (collapsible, expansive and others). In: Proceedings of the Eigth International Conference on Soil Mechanics and Foundation Engineering 3: 111–159
9. Bowden F.P. & Tabor D. (1967) Friction and Lubrication. Methuen
10. Bruce A. & Wallace D. (1989) Critical point phenomena: universal physics at large length scales. In: Davies P. (ed.) The New Physics. Cambridge University Press Cambridge: 236–267
11. Casagrande A. (1936) Characteristics of cohesionless soils affecting the stability of earth fills. Journal of the Boston Society of Civil Engineers, Contribution to Soil Mechanics
12. Cudmani R.O. (2005) The Application of Numerical Methods to the Solution of Static and Dynamic Geomechanical Problems. In preparation

13. Derjaguin B.V. & Churayev N.V. (1971) Investigation of the Properties of Water II. Journal of Colloid and Interface Science 36(4): 415–426
14. Di Benedetto H., Tatsuoka F. & Ishihara M. (2002) Time-dependent shear deformation characteristics of sand and their constitutive modelling. Soils and Foundations 42(2): 1–22
15. Dijkstra M., Hansen J.-P. & Madden P.A. (1997) Statistical model for the structure and gelation of smectite clay suspensions. Physical Review E 55(3): 3044–3053
16. Ehlers W., Ramm E., Diebels S. & D'Adetta G.A. (2003) From particle ensembles to Cosserat continua: homogenization of contact forces towards stresses and couple stresses. International Journal of Solids and Structures 40: 6681–6702
17. Feynman R.P., Leighton R.B. & Sands M. (1963) The Feynman Lectures on Physics. Addison-Wesley Reading, MA
18. Goldscheider M. (1975) Dilatanzverhalten von Sand bei geknickten Verformungswegen. Mechanics Research Communications 2: 143–148
19. Gudehus G. (1972) Lower and upper bounds for stability of earth-retaining structures. In: Proceedings of the Fifth European Conference on Soil Mechanics and Foundation Engineering: 21–28
20. Gudehus G. (1979) A comparison of some constitutive laws for soils under radially symmetric loading and unloading. In: Wittke W. (ed.) Proceedings of the Third International Conference on Numerical Methods in Geomechanics: 1309–1323
21. Gudehus G. (1993) Spontaneous liquefaction of saturated granular bodies. In: Kolymbas D. (ed.) Workshop on Modern Approaches to Plasticity: 691–714
22. Gudehus G. (2004) A visco-hypoplastic constitutive relation for soft soils. Soils and Foundations 44(4): 11–26
23. Gudehus G. (2005a) Seismo-hypoplasticity with a granular temperature. Granular Matter online
24. Gudehus G. (2005b) Strain rate dependent state limits of saturated clay. In preparation
25. Gudehus G. & Nübel K. (2004) Evolution of shear bands in sand. Géotechnique 54(3): 187–201
26. Gudehus G., Goldscheider M. & Winter H. (1975) Mechanical properties of sand and clay and numerical integration methods: some sources of errors and bounds of accuracy. In: Proceedings of the International Symposium on Numerical Methods in Soil Mechanics and Rock Mechanics: 289–304
27. Gudehus G., Cudmani R.O., Libreros-Bertini A.B. & Bühler M.M. (2004) In-plane and anti-plane strong shaking of soil systems and structures. Soil Dynamics and Earthquake Engineering 24(4): 319–342
28. Guyon E. & Troadec J.-P. (1994) Du sac de billes au tas de sable. Editions Odile Jacob
29. Haken H. (1977) Synergetics – An Introduction. Springer Berlin Heidelberg New York
30. Herrmann H.J. (1993) On the thermodynamics of granular media. Journal de Physique II 3: 427–433
31. Hicher P.Y., Wahyudi H. & Tessier D. (1994) Microstructural analysis of strain localisation in clay. Computers and Geotechnics 16: 205–222
32. Higo Y. (2003) Instability and strain localization analysis of water-saturated clay by elasto-viscoplastic constitutive models. Dissertation, Kyoto University

33. Howell D.W., Behringer R.P. & Veje C.T. (1999) Fluctuations in granular media. Chaos 9(3): 559–572
34. Huang W. & Bauer E. (2002) Numerical investigation of shear localization in a micro-polar hypoplastic material. International Journal on Numerical and Analytical Methods in Geomechanics 27: 325–352
35. Huber G. & Wienbroer H. (2005) Vibro-viscosity and granular temperature of cylindrical grain skeletons–experiments, In: Proceedings of the Fifth International Conference on Powders and Grains
36. Hungr O. & Morgenstern N.R. (1984) High velocity ring shear tests on sand. Géotechnique 34: 415–421
37. Hvorslev M.J. (1937) Über die Festigkeitseigenschaften gestörter bindiger Böden. Ingeniorvidenskabelige Skrifter A Nr.45, Danmarks Naturvidenskabelige Samfund, Dissertation, Kopenhagen
38. Israelachvili J.N. (1985) Intermolecular and Surface Forces. Academic, New York
39. Kolymbas D. (1978) Ein nichtlineares viskoplastisches Stoffgesetz für Böden. Veröffentlichungen des Institutes für Bodenmechanik und Felsmechanik, Heft 77, Universität Karlsruhe
40. Kolymbas D. (1991) An outline of hypoplasticity. Archive of Applied Mechanics 61: 143–151
41. Krieg S. (2000) Viskoses Bodenverhalten von Mudden, Seeton und Klei. Veröffentlichungen des Institutes für Bodenmechanik und Felsmechanik, Heft 150, Universität Karlsruhe
42. Leinenkugel H.J. (1976) Deformations- und Festigkeitsverhalten bindiger Erdstoffe–Experimentelle Ergebnisse und ihre physikalische Bedeutung. Veröffentlichungen des Institutes für Bodenmechanik und Felsmechanik. Heft 66, Universität Karlsruhe
43. Mitchell J.K., Campanella R.G. & Singh A. (1968) Soil creep as a rate process. Journal of Soil Mechanics and Foundation Div., ASCE 94 SM1: 231–259
44. Niemunis A. (2003) Extended Hypoplastic Models for Soils. Schriftenreihe des Institutes für Grundbau und Bodenmechanik, Ruhr-Universität Bochum, Heft 34
45. Niemunis A. & Herle I. (1997) Hypoplastic model for cohesionless soils with elastic strain range. Mechanics of Cohesive-Frictional Materials 2: 279–299
46. Oka F. (1982) Elasto-viscoplastic constitutive equation for overconsolidated clay. In: Dungar R., Pande G.N., Studer J.A. (eds.) Proceedings of the International Symposium on Numerical Models in Geomechanics. Balkema: 147–156
47. Osinev V.A. (1998) Theoretical investigation of large-amplitude waves in granular soils. Soil Dynamics and Earthquake Engineering 17: 13–28
48. Osinev V.A. & Wu W. (2005) Instability and ill-posedness in the deformation of plastic solids: some correlations through simple examples. In: Wang Y., Hutter K. (eds.) Proceedings of the Internatioal Symposium on Trends in Applications of Mathematics to Mechanics
49. Peña A.A., Lizcano A., Alonso-Marroquín & Herrmann H.J. (2004) Numerical simulations of biaxial test using non-spherical particles. Submitted to Mechanics of Cohesive-Frictional Materials
50. Persson B.N.J. (1998) Sliding Friction–Physical Principle and Applicatons. Springer Balin Hieldelberg New York
51. Persson B.N.J. (2000) Theory of time-dependent plastic deformation in disordered solids. Physical Review B 61.9: 5949–5966

52. Prandtl L. (1928) Ein Gedankenmodell zur kinetischen Theorie der festen Körper. Zeitschrift für Angewandte Mathematik und Mechanik 8.2: 85–106
53. Radjaj F., Wolf D.E., Jean M., Roux S. & Moreau J.J. (1997) Force networks in dense granular media. Balkema, Rotterdam: 211–214
54. Rendulic L. (1937) Ein Grundgesetz der Tonmechanik und sein experimenteller Beweis. Der Bauingenieur 18(31|32): 459-467
55. Schofield A. (2002) Re-appraisal of Terzaghi's soil mechanics. In: Proceedings of the 15th International Conference on Soil Mechanics and Geotechnical Engineering 4: 2473–2482
56. Schofield A. & Wroth P. (1968) Critical State Soil Mechanics. McGraw-Hill Series in Soils Engineering and Foundations
57. Stauffer D. & Aharony A. (1991) Introduction to Perlocation Theory. Taylor & Francis London
58. Tejchman J. & Gudehus G. (2001) Shearing of a narrow granular layer with polar quanities. International Journal on Numerical and Analytical Methods in Geomechanics 25(1): 1–28
59. Terzaghi K. (1920) New facts about surface-friction. Physical Review 16(1): 54–61
60. Terzaghi K. (1925) Erdbaumechanik auf bodenphysikalischer Grundlage. Deuticke
61. Tillemans H.-J. & Herrmann H.-J. (1995) Simulating deformations of granular solids under shear. Physika A 217: 261–288
62. Topolnicki M. (1987) Observed stress–strain behaviour of remoulded saturated clay and examination of two constitutive models. Veröffentlichungen des Institutes für Bodenmechanik und Felsmechanik. Heft 107, Universität Karlsruhe
63. Wichtmann T., Niemunis A. & Triantafyllidis Th. (2004) Strain accumulation in sand due to drained uniaxial cyclic loading. In: Triantafyllidis (ed.) International Conference on Cyclic Behaviour of Soils and Liquefaction Phenomena. Balkema, Rotterdam: 233–246
64. Wu W. & Kolymbas D. (2000) Hypoplasticity then and now. In: Kolymbas D. (ed.) Constitutive Modelling of Granular Materials. Springer Barlin Hieldelberg New York: 57–105
65. Zerwer A. & Santamarina J.C. (1994) Double layers in pyrometamorphosed bentonite: index properties and complex permittivity. Applied Clay Science 9: 283–291
66. Zou Y. (1996) A non-linear permeability relation depending on the activation energy of pore liqiud. Géotechnique 46(4): 769-774

Thermodynamics of Porous Continua

G.T. Houlsby* and A.M. Puzrin†

* Department of Engineering Science, Oxford University, UK
guy.houlsby@eng.ox.ac.uk
†Institute of Geotechnical Engineering, ETH Zürich, Switzerland

1 Introduction

In previous papers [2, 5–9] we have developed a theory for plastic materials in which the entire constitutive response is determined by specification of two potential functions. We have termed this approach "hyperplasticity". There are many other areas of continuum mechanics where similar approaches have been made. For instance Ziegler [10] develops theories for viscous materials. Many authors treat flow processes within a thermodynamic context, and frequently make use of a dissipation function. In our previous papers, the special features of rate-independent materials have been the reason for an emphasis that differs somewhat from most treatments of the subject.

We explore in this paper how the hyperplasticity approach can be generalised and set within the context of a wider variety of types of material behaviour. In particular we shall again place an emphasis on the use of two potential functions, and on the use of Legendre transformations to obtain alternative formulations.

When more complex materials are considered, there are two classes of behaviour which are dissipative. The first is associated with fluxes, for instance flow in a porous medium or the flow of electrical current. In these cases the dissipation is associated with the spatial gradient of some variable (e.g. the hydraulic head for flow in a porous medium, the voltage for an electrical problem). The constitutive behaviour is usually described by a linear relationship between the flux and the spatial gradient.

The second type of dissipation is associated with the time variation of internal variables. The plasticity problems treated in our earlier papers are of this character. Viscous behaviour can also be described in this way.

Most treatments of the thermodynamics of dissipative continua concentrate either on fluxes or on rates of change of internal variables. However, whilst the two problems have much in common, they also have important differences. Most obviously one involves a spatial variation and the other a time variation. It is tempting to treat both in the same way, and many authors adopt this approach, using for instance "generalised forces" and "generalised

fluxes". Here we adopt a slightly different approach, keeping separate those variables associated with fluxes, and those associated with internal variables. In this way the different ways that the two types of process appear in the relevant equations can be made clearer.

Rather than considering the possibility of abstract, unspecified fluxes, we find it more useful to develop our approach by considering a concrete example. The case that we take is a very important problem in geomechanics and other fields, namely flow in a porous medium. This serves as a useful example because the flux itself has mass, which introduces a number of features to the problem that need careful treatment. The porous medium has to be treated as consisting of two phases, and there is a partition of the extensive quantities (e.g. internal energy, entropy) between the solid skeleton and fluid phases.

How does our treatment differ from previous work on the mechanics of porous continua? Firstly, and in contrast to comprehensive works such as Coussy [3], de Boer [4], we do not attempt here to set out a fully comprehensive model for porous continua in all their complexity. Instead our purpose is to set out a simple framework, consistent with our earlier work, within which flow phenomena in porous media may be described in terms of conceptual models.

Coussy [3] employs a thermodynamic terminology, but in his approach he uses different energy functions for the skeleton and for the pore fluid. Here we treat the two using the same energy function, which has the advantage of consistency.

de Boer [4] also addresses porous media within a thermodynamic context, including a detailed historical review. However, he places hardly any emphasis on the dissipation in a porous medium, a concept which is absolutely central to treatment adopted here.

For simplicity we prefer, where possible, to adopt a small strain formulation. However, the problem of coupled fluid and skeleton behaviour cannot be treated rigorously within the small strain framework. This is because there is a coupling between strains, fluid flow and density changes, whilst in the small strain formulation the density is treated as a constant. In the following, therefore, it is necessary to move to a large strain formulation. There is a choice between adopting a Lagrangian approach, in which the problem is formulated in terms of initial coordinates, and an Eulerian approach, in which it is formulated within the current coordinates. We adopt the Eulerian approach for much of the following development, since this allows a more direct interpretation of the variables. It will prove necessary, however, to make a transformation to Lagrangian variables for part of the analysis.

In the small strain approach we used in earlier papers (as cited earlier), for convenience all the extensive quantities were defined per unit volume. Since the density was in effect constant this is exactly equivalent to use of extensive quantities per unit mass, but avoids a factor of the density appearing throughout the equations. In large strain analysis it is necessary to use extensive quantities per unit mass, as is usual in thermodynamics, and we adopt this approach below.

2 Notation

We make much use of vectors and tensors, and for these we use the subscript notation. Thus σ_{ij} is a shorthand for a second-order tensor which could be written out in full in matrix form as

$$\begin{bmatrix} \sigma_{11} & \sigma_{12} & \sigma_{13} \\ \sigma_{21} & \sigma_{22} & \sigma_{23} \\ \sigma_{31} & \sigma_{32} & \sigma_{33} \end{bmatrix}.$$

We adopt the summation convention over a repeated index, so that, $\sigma_{ii} \equiv \sigma_{11} + \sigma_{22} + \sigma_{33}$. The unit tensor (Kronecker delta) is given by δ_{ij}, where $\delta_{ij} = 1$ for $i = j$ and $\delta_{ij} = 0$ for $i \neq j$. The deviator of a tensor is indicated by a prime notation, thus $\sigma'_{ij} \equiv \sigma_{ij} - (1/3)\delta_{ij}\sigma_{kk}$.

We denote the time differential by the dot notation, thus $\dot{x} \equiv \partial x/\partial t$. Spatial differentiation is denoted by a comma notation, so that if x_i are the co-ordinate directions, then $y_{,i} \equiv \partial y/\partial x_i$.

As mentioned earlier, we adopt here an Eulerian approach to the description of a material undergoing large strain, i.e. the description of the material is based on the current co-ordinate system. In this it will be necessary to distinguish between the time differential of a variable x at a particular point in space, and the material derivative, which represents the rate of change for an element of the material, which has a current velocity ν_i. We denote the material or convective derivative by $\mathrm{d}x/\mathrm{d}t = \tilde{x} = \dot{x} + x_{,i}\nu_i$. We can note, from this definition, that it follows that the product rule applies to the convective derivative, e.g. the material derivative of xy is $\tilde{x}y + x\tilde{y}$, and we shall make much use of this result in the following.

3 Thermomechanical Framework

3.1 Density Definitions, Velocities and Balance Laws

Consider a volume V fixed in space bounded by a surface S. The unit outward normal to the boundary is n_i. The volume contains porous material with a skeleton material of density ρ^{s} and with a porosity n (volume of voids divided by total volume). Thus the mass of skeleton per unit total volume is $\rho = (1-n)\rho^{\mathrm{s}}$. We should also note that ρ is the "dry density" in soil mechanics terminology.

The velocity of the skeleton at any point is ν_i, so that the mass flux of the skeleton per unit area is $\rho\nu_i$, and the outward mass flux per unit area from V is $\rho\nu_i n_i$. For conservation of mass we can write that the rate of increase of mass within the volume, plus the outward mass flux is zero:

$$\int_V \dot{\rho}\mathrm{d}V + \int_S \rho\nu_i n_i \mathrm{d}S = 0. \tag{1}$$

Applying Gauss's divergence theorem,[1] the above transforms to

$$\int_V (\dot{\rho} + \rho \nu_{i,i}) \mathrm{d}V = 0.$$

Then noting that V is arbitrary, we can write this in local form:

$$\dot{\rho} + (\rho \nu_i)_{,i} = \dot{\rho} + \rho_{,i} \nu_i + \rho \nu_{i,i} = \tilde{\rho} + \rho \nu_{i,i} = 0, \tag{2}$$

which establishes the link between the material rate of change of dry density and the dilatation rate.

A comment is relevant here about the importance of the assumption that the volume V is arbitrary. This is only justified provided that V is large enough so that averaged values of stresses, strains etc. over the volume element are meaningful. Such an element is said to be a "representative volume element". In the context of the mechanics of granular materials this will typically require that the element contains many thousands of particles. At the same time the element must be sufficiently small so that changes of stresses etc. across the element are small. This requirement of course conflicts with the first, and there are classes of problem for which both criteria cannot be satisfied simultaneously. Such problems (e.g. those involving strong localisation) are not amenable to treatment by conventional continuum mechanics, although there are certain techniques that allow the scale at which continuum mechanics can be applied to be pushed ever smaller.

We now allow for the possibility of fluxes of a pore fluid. We shall consider a pore fluid, the amount of which is specified by the parameter w defined as mass of fluid per unit mass of skeleton material (i.e. the water content in soil mechanics terminology). Note that in the study of the mechanics of granular media, a wide variety of different quantities are used to define the amount of fluid present in the porous medium. The flux of the fluid mass is m_i per unit area relative to the skeleton. The total flux vector of the fluid is therefore $m_i + \rho w \nu_i$, and the outward flux of the fluid across the boundary S follows as $(m_i + \rho w \nu_i)\, n_i$.

We note that the mass of fluid per unit volume of skeleton is ρw. It follows that

$$\rho w = n \rho^{\mathrm{w}}, \tag{3}$$

where ρ^{w} is the density of the fluid. The mass flux vector m_i can also be written as:

$$m_i = \rho^{\mathrm{w}} w_i = \rho^{\mathrm{w}} n \left(\nu_i^{\mathrm{w}} - \nu_i\right), \tag{4}$$

where w_i is the Darcy artificial seepage velocity and ν_i^{w} is the average absolute velocity of the fluid.

[1] In the above terminology, Gauss's divergence theorem states that, for any variable x that is continuous and differentiable in V, $\int_S x n_i \mathrm{d}S = \int_V x_{,i} \mathrm{d}V$.

Noting that the mass of the fluid is conserved, there is a balance equation analogous to (1) of the form

$$\int_V \frac{\partial}{\partial t}\left(\rho w\right) \mathrm{d}V + \int_S \left(m_i + \rho w \nu_i\right) n_i \mathrm{d}S = 0, \tag{5}$$

which we can rewrite in local form by using the divergence theorem of Gauss, to obtain the local conservation law:

$$\dot{\rho} w + \rho \dot{w} + m_{i,i} + \rho_{,i} w \nu_i + \rho w_{,i} \nu_i + \rho w \nu_{i,i} = 0 \tag{6}$$

or

$$\rho \tilde{w} + \tilde{\rho} w + m_{i,i} + \rho w \nu_{i,i} = 0, \tag{7}$$

which by virtue of the skeleton mass conservation equation (2) becomes

$$\rho \tilde{w} + m_{i,i} = 0. \tag{8}$$

It is convenient to obtain a combined continuity equation for flow of the skeleton and pore fluid. First we can note $\tilde{\rho} = \tilde{\rho}^{\mathrm{s}}\left(1-n\right) - \rho^{\mathrm{s}} \tilde{n}$ so that we can rewrite the mass continuity equation as

$$\tilde{\rho}^{\mathrm{s}}\left(1-n\right) - \rho^{\mathrm{s}} \tilde{n} + \rho^{\mathrm{s}}\left(1-n\right) \nu_{i,i} = 0. \tag{9}$$

We can also obtain by manipulation of (7):

$$\tilde{\rho}^{\mathrm{w}} n + \rho^{\mathrm{w}} \tilde{n} + \left(\rho^{\mathrm{w}} w_i\right)_{,i} + n \rho^{\mathrm{w}} \nu_{i,i} = 0. \tag{10}$$

Finally dividing (9) by ρ^{s} and (10) by ρ^{w} and adding we obtain:

$$\nu_{i,i} + w_{i,i} + w_i \frac{\rho^{\mathrm{w}}_{,i}}{\rho^{\mathrm{w}}} + n \frac{\tilde{\rho}^{\mathrm{w}}}{\rho^{\mathrm{w}}} + \left(1-n\right) \frac{\tilde{\rho}^{\mathrm{s}}}{\rho^{\mathrm{s}}} = 0. \tag{11}$$

If both the soil grains and the pore fluid are incompressible then this reduces to the simple form $\nu_{i,i} + w_{i,i} = 0$. Introducing $\nu^{\mathrm{w}} = 1/\rho^{\mathrm{w}}$ and $\nu^{\mathrm{s}} = 1/\rho^{\mathrm{s}}$ the continuity equation can also be written $\nu_{i,i} + w_{i,i} = m_i \nu^{\mathrm{w}}_{,i} + \rho w \tilde{\nu}^{\mathrm{w}} + \rho \tilde{\nu}^{\mathrm{s}}$, where

$$\frac{1}{\rho} = \nu = \nu^{\mathrm{s}} + w \nu^{\mathrm{w}}. \tag{12}$$

3.2 Tractions, Stresses, Work and Energy

The tractions (forces per unit area) on the skeleton on the fraction $(1-n)$ of the boundary S are t_i, and the pressure in the pore fluid is p which acts on a fraction n of the boundary. The work done per unit area by the surroundings against the tractions on S is therefore $\left(1-n\right) t_i \nu_i$, and that done against the pore pressure is $-npn_i\nu^{\mathrm{w}}_i$. There are also body forces arising from a gravitational field of strength g_i. The work done per unit volume by the body forces

on the skeleton is $\rho\nu_i g_i$ and on the fluid is $\rho w \nu_i^{\mathrm{w}} g_i$. The heat flux per unit area is q_i, so that the outward heat flux from S per unit area is $q_i n_i$.

As an extensive quantity, the kinetic energy of the whole matter enclosed in volume V may be written as the sum of the kinetic energies of the skeleton and of the fluid:

$$K = \frac{1}{2}\int_V \rho \left(\nu_i\right)^2 \mathrm{d}V + \frac{1}{2}\int_V \rho w \left(\nu_i^{\mathrm{w}}\right)^2 \mathrm{d}V. \tag{13}$$

At this stage we are neglecting the effects of tortuosity, which are due to the fact that the pore fluid must take a tortuous path between the skeleton particles, so that the average speed of the water particles is higher than the magnitude of the average velocity. We shall, however, show how the results can be modified later to take this into effect. Now consider the rate of change of kinetic energy in the volume V, which can be written

$$\begin{aligned}\tilde{K} = & \int_V \frac{\partial}{\partial t}\left[\frac{\rho\nu_i\nu_i}{2} + \frac{\rho w \nu_i^{\mathrm{w}}\nu_i^{\mathrm{w}}}{2}\right]\mathrm{d}V \\ & + \int_S \left[\frac{\rho\nu_i\nu_i}{2}\right]\nu_j n_j \mathrm{d}S + \int_S \left[\frac{\rho w \nu_i^{\mathrm{w}}\nu_i^{\mathrm{w}}}{2}\right]\nu_j^{\mathrm{w}} n_j \mathrm{d}S.\end{aligned} \tag{14}$$

The volume integral reflects changes of the kinetic energy with time in the volume, while the surface integrals account for the kinetic energy brought into the volume due to the skeleton and pore fluid movement through the surface. Applying the theorem of Gauss and grouping the resulting terms it is possible to obtain:

$$\begin{aligned}\tilde{K} = & \int_V \rho\nu_i\left(\dot{\nu}_i + \nu_{i,j}\nu_j\right)\mathrm{d}V + \int_V \left(\dot{\rho} + \rho\nu_{j,j} + \rho_{,\mathrm{j}}\nu_j\right)\left[\frac{\nu_i\nu_i}{2}\right]\mathrm{d}V \\ & + \int_V \rho w \nu_i^{\mathrm{w}}\left(\dot{\nu}_i^{\mathrm{w}} + \nu_{i,j}^{\mathrm{w}}\nu_j^{\mathrm{w}}\right)\mathrm{d}V \\ & + \int_V \left(\dot{\rho}w + \rho\dot{w} + \rho w \nu_{j,j}^{\mathrm{w}} + \rho w_{,j}\nu_j^{\mathrm{w}} + \rho_{,\mathrm{j}} w \nu_j^{\mathrm{w}}\right)\left[\frac{\nu_i^{\mathrm{w}}\nu_i^{\mathrm{w}}}{2}\right]\mathrm{d}V.\end{aligned} \tag{15}$$

Recalling the mass balance equations for skeleton and for fluid (2) and (6), respectively, we note that the second and fourth integrals vanish. We introduce also the definitions of the accelerations of the skeleton and fluid particles, respectively

$$a_i = \tilde{\nu}_i = \dot{\nu}_i + \nu_{i,j}\nu_j, \tag{16}$$

$$a_i^{\mathrm{w}} = \tilde{\nu}_i^{\mathrm{w}} = \dot{\nu}_i^{\mathrm{w}} + \nu_{i,j}^{\mathrm{w}}\nu_j^{\mathrm{w}}, \tag{17}$$

where the material derivative with respect to a fluid particle is denoted by $\dot{x} + x_{,i}\nu_i^{\mathrm{w}} = \tilde{x}$. The expression for the rate of change of kinetic energy becomes

$$\tilde{K} = \int_V (\rho\nu_i a_i + \rho w \nu_i^{\mathrm{w}} a_i^{\mathrm{w}})\,\mathrm{d}V$$
$$= \int_V (\rho a_i + \rho w a_i^{\mathrm{w}})\,\nu_i \mathrm{d}V + \int_V m_i a_i^{\mathrm{w}} \mathrm{d}V. \tag{18}$$

3.3 The First Law

The First Law of Thermodynamics states that there is a variable, called specific internal energy, such that the rate of increase of the internal energy in the volume plus the rate of change of the kinetic energy in this volume is equal to the sum of the rates of energy input at the boundaries plus the rate of work of the body forces in the volume. We attribute a specific internal energy u^{s} to the skeleton and u^{w} to the pore fluid. The first law therefore becomes

$$\int_V \frac{\partial}{\partial t}(\rho u^{\mathrm{s}} + \rho w u^{\mathrm{w}})\,\mathrm{d}V + \int_S (\rho u^{\mathrm{s}} \nu_i + \rho w u^{\mathrm{w}} \nu_i^{\mathrm{w}})\, n_i \mathrm{d}S$$
$$+ \int_V (\rho a_i + \rho w a_i^{\mathrm{w}})\,\nu_i \mathrm{d}V + \int_V m_i a_i^{\mathrm{w}} \mathrm{d}V = \int_S ((1-n)\,t_i \nu_i - n p n_i \nu_i^{\mathrm{w}})\,\mathrm{d}S$$
$$+ \int_V (\rho\nu_i + \rho w \nu_i^{\mathrm{w}})\, g_i \mathrm{d}V + \int_S (-q_i n_i)\,\mathrm{d}S. \tag{19}$$

We can note that the tractions and pore pressure are related to the stresses by $(1-n)\,t_j - n p n_j = \sigma_{ij} n_i$, so that $(1-n)\,t_j \nu_j = \sigma_{ij}\nu_j n_i + n\nu_j^{\mathrm{w}} p n_j - p w_j n_j$ and we can rewrite the above as

$$\int_V \frac{\partial}{\partial t}(\rho u^{\mathrm{s}} + \rho w u^{\mathrm{w}})\,\mathrm{d}V + \int_S (\rho u^{\mathrm{s}} \nu_i + \rho w u^{\mathrm{w}} \nu_i^{\mathrm{w}})\, n_i \mathrm{d}S$$
$$+ \int_V (\rho a_i + \rho w a_i^{\mathrm{w}})\,\nu_i \mathrm{d}V + \int_V m_i a_i^{\mathrm{w}} \mathrm{d}V$$
$$= \int_S (\sigma_{ij}\nu_j - p w_i - q_i)\, n_i \mathrm{d}S + \int_V (\rho\nu_i + \rho w \nu_i^{\mathrm{w}})\, g_i \mathrm{d}V. \tag{20}$$

Applying the divergence theorem of Gauss we obtain the local form

$$\frac{\partial}{\partial t}(\rho u^{\mathrm{s}} + \rho w u^{\mathrm{w}}) + (\rho u^{\mathrm{s}} \nu_i + \rho w u^{\mathrm{w}} \nu_i^{\mathrm{w}})_{,i}$$
$$= (\sigma_{ij}\nu_j - p w_i - q_i)_{,i} + (\rho\nu_i + \rho w \nu_i^{\mathrm{w}})\, g_i$$
$$- (\rho a_i + \rho w a_i^{\mathrm{w}})\,\nu_i - m_i a_i^{\mathrm{w}} \tag{21}$$

and expanding the differentials in the first row of (21) we obtain:

$$\begin{aligned}
&\frac{\mathrm{d}}{\mathrm{d}t}\left(\rho u^{\mathrm{s}}+\rho w u^{\mathrm{w}}\right)+\left(\rho u^{\mathrm{s}}\nu_{i,i}+\rho w u^{\mathrm{w}}\nu_{i,i}\right)+\left(u^{\mathrm{w}}m_i\right)_{,i}\\
&\quad=\frac{\mathrm{d}}{\mathrm{d}t}\left(\rho u^{\mathrm{s}}+\rho w u^{\mathrm{w}}\right)-\left(\tilde{\rho}u^{\mathrm{s}}+\tilde{\rho}w u^{\mathrm{w}}\right)+\left(u^{\mathrm{w}}_{,i}m_i-\rho\tilde{w}u^{\mathrm{w}}\right)\\
&\quad=\rho\tilde{u}^{\mathrm{s}}+\rho w\tilde{u}^{\mathrm{w}}+u^{\mathrm{w}}_{,i}m_i. \qquad (22)
\end{aligned}$$

The second row of (21) may be transformed as follows:

$$\begin{aligned}
&\left(\sigma_{ij}\nu_j-pw_i-q_i\right)_{,i}+\left(\rho\nu_i+\rho w\nu_i^{\mathrm{w}}\right)g_i\\
&\quad=\left(\sigma_{ij,i}+\rho g_j\right)\nu_j+\sigma_{ij}\nu_{j,i}-p_{,i}w_i-pw_{i,i}-q_{i,i}+\rho^{\mathrm{w}}n\nu_i^{\mathrm{w}}g_i\\
&\quad=\left(\sigma_{ij,i}+\rho\left(1+w\right)g_j\right)\nu_j+\sigma_{ij}\nu_{j,i}+\left(\rho^{\mathrm{w}}g_i-p_{,i}\right)w_i-pw_{i,i}-q_{i,i}. \qquad (23)
\end{aligned}$$

We can then decompose $\nu_{i,j}$ into its symmetric and antisymmetric parts, identifying the former as the strain rate and the latter as the vorticity tensor:

$$\mathrm{d}_{ij}=\frac{1}{2}\left(\nu_{i,j}+\nu_{j,i}\right), \qquad (24)$$

$$\omega_{ij}=\frac{1}{2}\left(\nu_{i,j}-\nu_{j,i}\right), \qquad (25)$$

so that after substitution of (22)–(25) into (21) we can write

$$\begin{aligned}
&\rho\tilde{u}^{\mathrm{s}}+\rho w\tilde{u}^{\mathrm{w}}+u^{\mathrm{w}}_{,i}m_i\\
&\quad=\left(\sigma_{ij,i}+\rho\left(1+w\right)g_j-\rho a_j-\rho w a_j^{\mathrm{w}}\right)\nu_j+\sigma_{ij}\omega_{ji}\\
&\qquad+\sigma_{ij}d_{ij}+\left(\rho^{\mathrm{w}}\left(g_i-a_i^{\mathrm{w}}\right)-p_{,i}\right)w_i-pw_{i,i}-q_{i,i}. \qquad (26)
\end{aligned}$$

Equations of Motion

No change in internal energy should, however, be caused by either a rigid body translation or rotation, so that we can conclude that

$$\left(\sigma_{ij,i}+\rho\left(1+w\right)g_{\mathrm{j}}-\rho a_j-\rho w a_j^{\mathrm{w}}\right)\nu_j=0$$

and $\sigma_{ij}\omega_{ji}=0$ for all ν_j and ω_{ij}. These are of course the virtual work forms of the direct and rotational equilibrium conditions. From the latter it follows that the antisymmetric part of σ_{ij} must be zero, i.e. that σ_{ij} is symmetric. This condition is usually referred to as that of complementary shear stresses. From the former it follows that

$$\sigma_{ij,i}+\rho\left(1+w\right)g_j-\rho a_j-\rho w a_j^{\mathrm{w}}=0, \qquad (27)$$

which can be recognised as the equations of motion (or the static equilibrium equations in the case of zero acceleration). Equation (27) expresses the momentum balance for the porous medium considered as a whole, and they

have been derived as a part of formulation rather than postulated. However, this equation is not sufficient for description of the momentum balance of the pore fluid, which cannot be derived until some constitutive statement is made about interaction between the fluid and skeleton. The missing fluid balance equation will later be derived as a part of the formulation.

In view of (27), (26) reduces to

$$\begin{aligned}&\rho\tilde{u}^{\mathrm{s}} + \rho w\tilde{u}^{\mathrm{w}} + u^{\mathrm{w}}_{,i} m_i = \\ &\sigma_{ij} d_{ij} + \left(\rho^{\mathrm{w}}\left(g_i - a^{\mathrm{w}}_i\right) - p_{,i}\right) w_i - p w_{i,i} - q_{i,i}.\end{aligned} \tag{28}$$

3.4 The Second Law

The Second Law of Thermodynamics can be stated in a number of different ways. We state it here in the form that there exists a function of state, the specific entropy s, such that the rate of entropy production is non-negative. We attribute s^{s} to the skeleton and s^{w} to the pore fluid, so that the specific entropy of the whole medium is

$$s = s^{\mathrm{s}} + w s^{\mathrm{w}}. \tag{29}$$

The flux of the entropy η_i is defined by $\eta_i = q_i/\theta$. Unlike the case for the flux of the pore fluid, the total amount of entropy is not conserved. This is expressed by rewriting the fundamental inequality for the entropy in the form

$$\int_V \frac{\partial}{\partial t}\left(\rho s^{\mathrm{s}} + \rho w s^{\mathrm{w}}\right) \mathrm{d}V + \int_S \left(\rho s^{\mathrm{s}} \nu_i + \rho w s^{\mathrm{w}} \nu^{\mathrm{w}}_i\right) n_i \mathrm{d}S \geq \int_S \left(-\frac{q_i}{\theta} n_i\right) \mathrm{d}S. \tag{30}$$

The above equation states that the rate of increase of entropy within the volume, plus the convection of entropy across the boundary is greater than or equal to the entropy flux (from heat flow) into the volume. The additional entropy production is due to dissipative processes.

Applying the divergence theorem we obtain:

$$\frac{\partial}{\partial t}\left(\rho s^{\mathrm{s}} + \rho w s^{\mathrm{w}}\right) + \left(\rho s^{\mathrm{s}} \nu_i + \rho w s^{\mathrm{w}} \nu^{\mathrm{w}}_i + \frac{q_i}{\theta}\right)_{,i} \geq 0, \tag{31}$$

which can be written as

$$\begin{aligned}&\frac{\mathrm{d}}{\mathrm{d}t}\left(\rho s^{\mathrm{s}} + \rho w s^{\mathrm{w}}\right) + \left(\rho s^{\mathrm{s}} \nu_{i,i} + \rho w s^{\mathrm{w}} \nu_{i,i}\right) + \left(s^{\mathrm{w}} m_i\right)_{,i} + \left(\frac{q_i}{\theta}\right)_{,i} \\ &\quad = \frac{\mathrm{d}}{\mathrm{d}t}\left(\rho s^{\mathrm{s}} + \rho w s^{\mathrm{w}}\right) - \left(\tilde{\rho} s^{\mathrm{s}} + \tilde{\rho} w s^{\mathrm{w}}\right) + \left(s^{\mathrm{w}}_{,i} m_i - \rho\tilde{w} s^{\mathrm{w}}\right) + \left(\frac{q_i}{\theta}\right)_{,i} \\ &\quad = \rho\tilde{s}^{\mathrm{s}} + \rho w\tilde{s}^{\mathrm{w}} + s^{\mathrm{w}}_{,i} m_i + \frac{q_{i,i}}{\theta} - \frac{q_i \theta_{,i}}{\theta^2} = \frac{\rho d}{\theta} \geq 0,\end{aligned} \tag{32}$$

where d is the specific dissipation, corresponding to irreversible part of entropy production, and must always be non-negative. We note that in earlier papers

we have used d for just the "mechanical dissipation". The quantity defined as d here includes also the term usually referred to as the "thermal dissipation", which is due to the heat flux. The condition that the total dissipation be non-negative is slightly less restrictive than the earlier requirement that the mechanical dissipation be non-negative.

3.5 Combining the First and Second Laws

We now combine (28) and (32) to obtain:

$$\begin{aligned}\rho\tilde{u}^{\mathrm{s}} + \rho w\tilde{u}^{\mathrm{w}} + \rho d = \sigma_{ij}d_{ij} - pw_{i,i} + \rho\theta\tilde{s}^{\mathrm{s}} + \rho w\theta\tilde{s}^{\mathrm{w}} - \eta_i\theta_{,i} \\ + \left(\rho^{\mathrm{w}}\left(g_i - a_i^{\mathrm{w}}\right) - p_{,i}\right)w_i - \left(u_{,i}^{\mathrm{w}} - \theta s_{,i}^{\mathrm{w}}\right)m_i \end{aligned} \tag{33}$$

which, by virtue of the continuity equation can be written as:

$$\begin{aligned}&\rho\tilde{u}^{\mathrm{s}} + \rho w\tilde{u}^{\mathrm{w}} + \rho d \\ &\quad = \left(\sigma_{ij} + p\delta_{ij}\right)d_{ij} - \rho p\tilde{\nu}^{\mathrm{s}} - \rho w p\tilde{\nu}^{\mathrm{w}} + \rho\theta\tilde{s}^{\mathrm{s}} + \rho w\theta\tilde{s}^{\mathrm{w}} \\ &\qquad - \eta_i\theta_{,i} + \left(g_i - a_i^{\mathrm{w}} - \nu^{\mathrm{w}}p_{,i}\right)m_i - \left(u_{,i}^{\mathrm{w}} - \theta s_{,i}^{\mathrm{w}} + p\nu_{,i}^{\mathrm{w}}\right)m_i. \end{aligned} \tag{34}$$

Defining the total internal energy per mass of skeleton as $u = u^{\mathrm{s}} + wu^{\mathrm{w}}$ we then obtain:

$$\begin{aligned}\tilde{u} + d = \frac{1}{\rho}\left(\sigma_{ij} + p\delta_{ij}\right)d_{ij} - p\tilde{\nu}^{\mathrm{s}} - wp\tilde{\nu}^{\mathrm{w}} + \theta\tilde{s} + w\theta\tilde{s}^{\mathrm{w}} + u^{\mathrm{w}}\tilde{w} \\ + \frac{1}{\rho}\left(g_i - a_i^{\mathrm{w}} - \nu^{\mathrm{w}}p_{,i}\right)m_i - \frac{1}{\rho}\left(u_{,i}^{\mathrm{w}} - \theta s_{,i}^{\mathrm{w}} + p\nu_{,i}^{\mathrm{w}}\right)m_i - \frac{1}{\rho}\eta_i\theta_{,i}. \end{aligned} \tag{35}$$

The left hand side is clearly the sum of a stored term ($\tilde{u}$) and a dissipated term (d). It is tempting therefore to identify it with the total energy input, but this would be incorrect, as that is represented by $\tilde{u}$ itself.

The right hand side of (35) includes three types of term. The first involves the strain rate. The second type involves material differentials, and the third involves fluxes. The presence of the strain rate poses a problem within the Eulerian formulation, as it does not prove to be possible to express the strain rate as a material derivative of any observable quantity. This problem can be avoided by adopting a Lagrangian formulation. We can rewrite:

$$\frac{1}{\rho}\left(\sigma_{ij} + p\delta_{ij}\right)d_{ij} = \frac{1}{\rho_0}\left(\pi_{ij} + p^{\mathrm{L}}\delta_{ij}\right)\dot{\Delta}_{ij}, \tag{36}$$

where π_{ij} is the Piola–Kirchhoff stress tensor and Δ_{ij} is the Green–Lagrange strain defined by $2\Delta_{ij} = P_{ki}P_{kj} - \delta_{ij}$ where $P_{ij} = \partial x_i/\partial X_j$ and x_i and X_i are the current (Eulerian) and initial (Lagrangian) coordinates of a material point measured in a Cartesian system. The initial dry density is ρ_0. It can be shown

that $\pi_{ij} = \det(P_{ij})\, P^{-1}_{ik}\sigma_{kl}P^{-1}_{jl}$ and $\dot{\Delta}_{ij} = P_{ki}d_{kl}P_{lj}$. It is also necessary to introduce the variable $P^{\mathrm{L}} = p\det(P_{ij})\, P^{-1}_{ik}P^{-1}_{ik}$ which is the transformation of the pore pressure to the Lagrangian coordinate system. We note that in the Lagrangian coordinates no distinction is necessary between the time and material derivatives so that $\dot{\Delta}_{ij} = \partial\Delta_{ij}/\partial t = \mathrm{d}\Delta_{ij}/\mathrm{d}t = \tilde{\Delta}_{ij}$.

In principle it would be possible to transform all the other variables to Lagrangian coordinates too, but this has the disadvantage that physical meaning is lost. Since these transformations are not strictly necessary for the following argument we shall leave the remaining terms in their Eulerian form.

We can now write (35) as

$$\begin{aligned}\tilde{u} + d = {} & \frac{1}{\rho_0}\left(\pi_{ij} + p^{\mathrm{L}}\delta_{ij}\right)\tilde{\Delta}_{ij} - p\tilde{\nu}^{\mathrm{s}} - wp\tilde{\nu}^{\mathrm{w}} + \theta\tilde{s} + w\theta\tilde{s}^{\mathrm{w}} + u^{\mathrm{w}}\tilde{w} \\ & + \frac{1}{\rho}\left(g_i - a^{\mathrm{w}}_i - \nu^{\mathrm{w}}p_{,i}\right)m_i - \frac{1}{\rho}\left(u^{\mathrm{w}}_{,i} - \theta s^{\mathrm{w}}_{,i} + p\nu^{\mathrm{w}}_{,i}\right)m_i - \frac{1}{\rho}\eta_i\theta_{,i}.\end{aligned} \tag{37}$$

3.6 The Internal Energy Function

We now adopt the hypothesis that the internal energy is a function of the strains, the entropy, the water content, the extensive quantities ν^{s}, s^{s}, ν^{w} and s^{w}, and certain internal variables α_{ij}. We assume that the function can be decomposed in the form

$$\begin{aligned}u &= u\left(\Delta_{ij}, \alpha_{ij}, \nu^{\mathrm{s}}, s^{\mathrm{s}}, w, \nu^{\mathrm{w}}, s^{\mathrm{w}}\right) \\ &= u^{\mathrm{s}}\left(\Delta_{ij}, \alpha_{ij}, \nu^{\mathrm{s}}, s^{\mathrm{s}}\right) + wu^{\mathrm{w}}\left(\nu^{\mathrm{w}}, s^{\mathrm{w}}\right),\end{aligned} \tag{38}$$

so that

$$\begin{aligned}\tilde{u} &= \frac{\partial u}{\partial\Delta_{ij}}\tilde{\Delta}_{ij} + \frac{\partial u}{\partial\alpha_{ij}}\tilde{\alpha}_{ij} + \frac{\partial u}{\partial\nu^{\mathrm{s}}}\tilde{\nu}^{\mathrm{s}} + \frac{\partial u}{\partial s^{\mathrm{s}}}\tilde{s}^{\mathrm{s}} + \frac{\partial u}{\partial w}\tilde{w} + \frac{\partial u}{\partial\nu^{\mathrm{w}}}\tilde{\nu}^{\mathrm{w}} + \frac{\partial u}{\partial s^{\mathrm{w}}}\tilde{s}^{\mathrm{w}} \\ &= \frac{\partial u^{\mathrm{s}}}{\partial\Delta_{ij}}\tilde{\Delta}_{ij} + \frac{\partial u^{\mathrm{s}}}{\partial\alpha_{ij}}\tilde{\alpha}_{ij} + \frac{\partial u^{\mathrm{s}}}{\partial\nu^{\mathrm{s}}}\tilde{\nu}^{\mathrm{s}} + \frac{\partial u^{\mathrm{s}}}{\partial s^{\mathrm{s}}}\tilde{s}^{\mathrm{s}} + u^{\mathrm{w}}\tilde{w} + w\frac{\partial u^{\mathrm{w}}}{\partial\nu^{\mathrm{w}}}\tilde{\nu}^{\mathrm{w}} + w\frac{\partial u^{\mathrm{w}}}{\partial s^{\mathrm{w}}}\tilde{s}^{\mathrm{w}}.\end{aligned} \tag{39}$$

3.7 The Dissipation Function and Force Potential

We also postulate that the dissipation is a function of the same state variables, but also of $\tilde{\alpha}_{ij}$ (rate of change of internal variable) and of the fluxes, i.e.

$$d = d\left(\Delta_{ij}, \alpha_{ij}, \nu^{\mathrm{s}}, s^{\mathrm{s}}, w, \nu^{\mathrm{w}}, s^{\mathrm{w}}, \tilde{\alpha}_{ij}, m_i, \eta_i\right). \tag{40}$$

We can either derive a force potential z from the dissipation using the procedure described in the Appendix, or we can in fact assume the form of

z and derive d. In either case the force potential is defind such that

$$d = \frac{\partial z}{\partial \tilde{\alpha}_{ij}} \tilde{\alpha}_{ij} + \frac{\partial z}{\partial m_i} m_i + \frac{\partial z}{\partial \eta_i} \eta_i, \tag{41}$$

where z, the force potential, is a function of the same variables as d

$$z = z\left(\Delta_{ij}, \alpha_{ij}, \nu^{\mathrm{s}}, s^{\mathrm{s}}, w, \nu^{\mathrm{w}}, s^{\mathrm{w}}, \tilde{\alpha}_{ij}, m_i, \eta_i\right). \tag{42}$$

3.8 Constitutive Equations

Substituting (39) and (41) into (35), and collecting terms we obtain the most important equation in this paper

$$\begin{aligned} 0 = & \left(\frac{1}{\rho_0}\left(\pi_{ij} + p^{\mathrm{L}}\delta_{ij}\right) - \frac{\partial u^{\mathrm{s}}}{\partial \Delta_{ij}}\right)\tilde{\Delta}_{ij} + \left(-p - \frac{\partial u^{\mathrm{s}}}{\partial \nu^{\mathrm{s}}}\right)\tilde{\nu}^{\mathrm{s}} + \left(\theta - \frac{\partial u^{\mathrm{s}}}{\partial s^{\mathrm{s}}}\right)\tilde{s}^{\mathrm{s}} \\ & + w\left(-p - \frac{\partial u^{\mathrm{w}}}{\partial \nu^{\mathrm{w}}}\right)\tilde{\nu}^{\mathrm{w}} + w\left(\theta - \frac{\partial u^{\mathrm{w}}}{\partial s^{\mathrm{w}}}\right)\tilde{s}^{\mathrm{w}} + \left(-\frac{\partial u^{\mathrm{s}}}{\partial \alpha_{ij}} - \frac{\partial z}{\partial \tilde{\alpha}_{ij}}\right)\tilde{\alpha}_{ij} \\ & + \left(\frac{1}{\rho}\left(g_i - a_i^{\mathrm{w}} - \nu^{\mathrm{w}} p_{,i}\right) - \frac{\partial z}{\partial m_i}\right) m_i + \left(-\frac{1}{\rho}\theta_{,i} - \frac{\partial z}{\partial \eta_i}\right)\eta_i \\ & - \frac{1}{\rho}\left(u_{,i}^{\mathrm{w}} - \theta s_{,i}^{\mathrm{w}} + p\nu_{,i}^{\mathrm{w}}\right) m_i. \end{aligned} \tag{43}$$

Now (43) should be satisfied for any combination of $\tilde{\Delta}_{ij}, \tilde{\alpha}_{ij}, \tilde{\nu}^{\mathrm{s}}, \tilde{s}^{\mathrm{s}}, \tilde{\nu}^{\mathrm{w}}, \tilde{s}^{\mathrm{w}}$, η_i, and m_i since all these quantities are independent of each other, each term in (43) has to be equal to zero independently. Because the internal energy function (38) is independent of $\tilde{\Delta}_{ij}, \tilde{\nu}^{\mathrm{s}}, \tilde{s}^{\mathrm{s}}, \tilde{\nu}^{\mathrm{w}}$ and $\tilde{s}^{\mathrm{w}}$, from the first two rows of (43) it follows that

$$\frac{1}{\rho_0}\left(\pi_{ij} + p^{\mathrm{L}}\delta_{ij}\right) = \frac{\partial u^{\mathrm{s}}}{\partial \Delta_{ij}}, \tag{44}$$

$$-p = \frac{\partial u^{\mathrm{s}}}{\partial \nu^{\mathrm{s}}}, \tag{45}$$

$$\theta = \frac{\partial u^{\mathrm{s}}}{\partial s^{\mathrm{s}}}, \tag{46}$$

$$-p = \frac{\partial u^{\mathrm{w}}}{\partial \nu^{\mathrm{w}}}, \tag{47}$$

$$\theta = \frac{\partial u^{\mathrm{w}}}{\partial s^{\mathrm{w}}}. \tag{48}$$

Considering now a spatial gradient of u^{w}, we can obtain:

$$u_{,i}^{\mathrm{w}} = \frac{\partial u^{\mathrm{w}}}{\partial \nu^{\mathrm{w}}}\nu_{,i}^{\mathrm{w}} + \frac{\partial u^{\mathrm{w}}}{\partial s^{\mathrm{w}}} s_{,i}^{\mathrm{w}} = -p\nu_{,i}^{\mathrm{w}} + \theta s_{,i}^{\mathrm{w}} \tag{49}$$

so that the fourth row of (43) is identically zero.

Equations (44–48) express an essential property of the internal energy function: that it is a potential for stresses and temperature. The basic form of these relationships is well known from hyperelasticity, but the particular expressions here deserve some comment. First note that the intensive quantities of pore pressure and temperature each appear as a partial derivative of the internal energy of the skeleton and of the pore fluid. The fact that both derivatives are related the same value of the intensive variable reflects in effect an assumption of an intimate mixing of the two phases. The temperature of the solids and fluid is assumed to be the same, and the pore pressure acts equally on the solids and the fluid. We later find it convenient (in the context of Legendre transforms of the energy function) to distinguish between the temperatures and pressures derived from the two terms in the potential: one for the particles and one for the fluid. We shall, however, continue to use the assumption of intimate mixing of the two components.

Equation (44) embodies Terzaghi's principle of effective stress for a porous medium. It demonstrates that (for the choice of kinematics variables we have made) the quantity that is work conjugate to the strain rate is not the total stress σ_{ij} but the effective stress $\overline{\sigma}_{ij} = \sigma_{ij} + p\delta_{ij}$ (the positive sign appears because we have followed the tensile positive convention usual in continuum mechanics for the stresses, whilst the pore pressure is positive in compression). The corresponding definition of the Lagrangian effective stress is given by the following equation:

$$\overline{\pi}_{ij} = \pi_{ij} + p^{\mathrm{L}}\delta_{ij}. \tag{50}$$

Unfortunately, an argument similar to that used to develop (44–48) above cannot be applied to the terms in the second and third rows of (43), because the z function does depend on $\tilde{\alpha}_{ij}$, η_i and m_i. Assuming independence of the fluxes and of the rate of the internal variable, only the weaker conditions

$$\left(\frac{\partial u^{\mathrm{s}}}{\partial \alpha_{ij}} + \frac{\partial z}{\partial \tilde{\alpha}_{ij}}\right)\tilde{\alpha}_{ij} = 0;$$

$$\left(\theta_{,i} + \rho\frac{\partial z}{\partial \eta_i}\right)\eta_i = 0;$$

and

$$\left((\nu^{\mathrm{w}}P_{,i} - g_i + a_i^{\mathrm{w}}) + \rho\frac{\partial z}{\partial m_i}\right)m_i = 0$$

can be formally derived from (43).

However, at this stage we restrict ourselves to analysis of models to which stricter conditions (than those described above) can be applied

$$\frac{\partial u}{\partial \alpha_{ij}} + \frac{\partial z}{\partial \tilde{\alpha}_{ij}} = 0, \tag{51}$$

$$\theta_{,i} = -\rho\frac{\partial z}{\partial \eta_i}, \tag{52}$$

$$\nu^{\mathrm{w}}p_{,i} - g_i + a_i^{\mathrm{w}} = -\rho\frac{\partial z}{\partial m_i}. \tag{53}$$

Equation (51) is Ziegler's orthogonality condition, defining visco-plastic constitutive behaviour, (52) is (for an appropriate form of z) the Fourier heat conduction law, while (53) represents the missing equations of motion of the pore fluid, which becomes more obvious after they are rewritten as following:

$$(-p\delta_{ij})_{,i} + \rho^{\mathrm{w}} g_j - \rho^{\mathrm{w}} a_j^{\mathrm{w}} - \rho^{\mathrm{w}} \rho \frac{\partial z}{\partial m_j} = 0, \tag{54}$$

where the third term in the left part can be identified with a "drag" force.

When inertial effects can be neglected, and with an appropriate choice of force potential z, (53) becomes Darcy's law for fluid flow (for constant a fluid of constant density ρ^{w}).

4 Discussion

Equations (44–48) and (51–53) represent a complete set of the constitutive relationships describing the material, which is therefore defined entirely by specification of two scalar potential functions u and z in (38) and (42), respectively. Equations (51–53) are sufficient, but not necessary, to ensure that the laws of thermodynamics are obeyed.

Note that the entire formulation of the constitutive behaviour is based on the following principles:

- The mass conservation laws (1) and (5)
- The First Law of Thermodynamics (19)
- The Second Law of Thermodynamics (30)

and the following assumptions:

- The existence of the internal energy function (38) independent of rigid body translation and rotation.
- The existence of the quasi-homogeneous dissipation function (40) satisfying (41).
- The two above functions should be related through Ziegler's orthogonality condition (51) and the Onsager reciprocity relationships for the fluxes which follow directly from (52) and (53).

Needless to say, the above formulation of the constitutive behaviour is guaranteed to satisfy the laws of thermodynamics. We make no secret of the fact, however, that we have introduced some additional, more restrictive assumptions. It is for the reader to decide whether these restrictions reduce the scope for constitutive modelling to such an extent that the materials that can be described are no longer realistic. We address later, however, some of the advantages that follow from adopting the more restrictive approach. It is our belief that in fact a very wide variety of material response can be described within this framework. Furthermore we are not aware of any specific counterexamples from the physical world, which provide clear evidence that the restrictions imposed above are invalid.

4.1 The Complete Formulation

We summarise the position we have arrived at as follows. The first step is to specify a constitutive model through internal energy and force potential functions

$$\begin{aligned} u &= u\left(\Delta_{ij}, \alpha_{ij}, \nu^{\mathrm{s}}, s^{\mathrm{s}}, w, \nu^{\mathrm{w}}, s^{\mathrm{w}}\right) \\ &= u^{\mathrm{s}}\left(\Delta_{ij}, \alpha_{ij}, \nu^{\mathrm{s}}, s^{\mathrm{s}}\right) + w u^{\mathrm{w}}\left(\nu^{\mathrm{w}}, s^{\mathrm{w}}\right), \end{aligned} \tag{55}$$

$$z = z\left(\Delta_{ij}, \alpha_{ij}, \nu^{\mathrm{s}}, s^{\mathrm{s}}, w, \nu^{\mathrm{w}}, s^{\mathrm{w}}, \tilde{\alpha}_{ij}, m_i, \eta_i\right). \tag{56}$$

Using these functions, the differential relationships in Table 1 are applied. The variables involved in the solution (with the numbers of variables for vector and tensor quantities) are x_i (3), ν_i (3), ν_i^{w} (3), a_i (3), a_i^{w} (3), P_{ij} (9), Δ_{ij} (6), π_{ij} (6), α_{ij} (6), ρ, w, ν^{s}, S^{s}, ν^{w}, S^{w}, p, p^{L}, θ, m_i (3) and η_i (3), that is 57 variables in all. We supplement these with four further formal variables through $\theta = \theta^{\mathrm{s}} = \theta^{\mathrm{w}}$ and $p = p^{\mathrm{s}} = p^{\mathrm{w}}$. The use of these variables allows the Legendre transform of the energy function to be carried out consistently. Specification of initial and boundary conditions completes the formulation.

4.2 Modifications to Account for Tortuosity

Effects of tortuosity have been neglected in the above derivations. It is usual to account for such effects by introducing a tortuosity factor a (see e.g. [3]), which is the ratio between average of the squared microscopic relative velocity of the fluid with respect to the skeleton, and the square of the average of the same quantity. It is straightforward to show that a is a factor always greater than or equal to unity. When this factor is included, the expression for the kinetic energy becomes

$$K = \frac{1}{2}\int_V \rho(\nu_i)^2 \mathrm{d}V + \frac{1}{2}\int_V \rho w\left(\left(\nu_i^{\mathrm{w}}\right)^2 + (a-1)\left(\nu_i^{\mathrm{r}}\right)^2\right)\mathrm{d}V, \tag{57}$$

where $\nu_i^{\mathrm{r}} = \nu_i^{\mathrm{w}} - \nu_i$ is the macroscopic relative velocity of the fluid with respect to the skeleton.

When the additional terms due to this change are followed through to (37), the only change necessary is to replace a_i^{w} in the first term on the second line with a modified acceleration term a_i^{we}, which is defined as:

$$a_i^{\mathrm{we}} = a_i^{\mathrm{w}} + (a-1)\tilde{\nu}_i^{\mathrm{r}} + \frac{1}{2}\tilde{a}\nu_i^{\mathrm{r}}. \tag{58}$$

Note that the term in a_i^{w} in the equation of motion (27) is not altered. In Table 1 the a_i^{w} term in the first equation of motion is unaltered, but that in the second equation of motion is modified to a_i^{we} . Because there is now the additional variable a in the problem, a further equation is now required. This

Table 1. Summary of equations

equation type	equation	no. of equations
differential of free energy (skeleton)	$\pi_{ij} + p^{\mathrm{L}}\delta_{ij} = \rho_0 \partial u^{\mathrm{s}}/\partial \Delta_{ij}$	6
	$-p = \partial u^{\mathrm{s}}/\partial \nu^{\mathrm{s}}$	1
	$\theta^{\mathrm{s}} = \partial u^{\mathrm{s}}/\partial s^{\mathrm{s}}$	1
differentials of free energy (pore fluid)	$-p = \partial u^{\mathrm{w}}/\partial \nu^{\mathrm{w}}\mathrm{c}$	1
	$\theta^{\mathrm{w}} = \partial u^{\mathrm{w}}/\partial s^{\mathrm{w}}$	1
Ziegler's orthogonality condition	$\partial u^{\mathrm{s}}/\partial \alpha_{ij} + \partial z/\partial \tilde{\alpha}_{ij} = 0$	6
heat conduction law	$\theta_{,i} = -\rho \partial z/\partial \eta_i$	3
mass balance equations	$\tilde{\rho} + \rho \nu_{i,i} = 0$	1
	$\rho \tilde{w} + m_{i,i} = 0$	1
Second Law of Thermodynamics	$\theta \left(\tilde{s}^{\mathrm{s}} + w\tilde{s}^{\mathrm{w}} + \frac{1}{\rho} s^{\mathrm{w}}_{,i} m_i + \frac{1}{\rho}\eta_{i,i} \right)$ $= \frac{\partial z}{\partial \tilde{\alpha}_{ij}}\tilde{\alpha}_{ij} + \frac{\partial z}{\partial m_i} m_i + \frac{\partial z}{\partial \eta_i}\eta_i \geq 0$	1
equations of motion	$(P_{jk}\pi_{ik})_{,i} + \rho_0(1+w)g_j = \rho_0(a_j + w a^{\mathrm{w}}_j)$	3
	$\nu^{\mathrm{w}} p, i - g_i + a^{\mathrm{w}}_i = -\rho \partial z/\partial m_i$	3
strain definition	$2\Delta_{ij} = P_{ki}P_{kj} - \delta_{ij}$	6
deformation gradient	$P_{ij} = \partial x_i/\partial X_j$	9
skeleton velocity	$\nu_i = \tilde{x}_i$	3
skeleton acceleration	$a_i = \tilde{\nu}_i$	3
fluid acceleration	$a^{\mathrm{w}}_i = \dot{\nu}^{\mathrm{w}}_i + \nu^{\mathrm{w}}_{i,j}\nu^{\mathrm{w}}_j$	3
mass flux definition	$m_i = \rho w \left(\nu^{\mathrm{w}}_i - \nu_i\right)$	3
density definition	$1/\rho = \nu^{\mathrm{s}} + w\nu^{\mathrm{w}}$	1
Lagrangian pore pressure	$p^{\mathrm{L}} = p \det\left(P_{ij}\right) P^{-1}_{ik} P^{-1}_{ik}$	1
total number of equations		57

would be a constitutive relationship for the tortuosity factor a, which could for instance be expressed as a function of the porosity. Berryman [1] suggests the expression $a = (n+1)/2n$ for a matrix of spherical particles. In terms of the variables in Table 1 this would become $a = \left(\rho w \nu^{\mathrm{w}} + 1\right)/2\rho w \nu^{\mathrm{w}}$.

4.3 Legendre–Fenchel Transforms

In the classical thermodynamics, in addition to the specific internal energy (u), three other energy functions are defined: specific Helmholtz free energy (f), specific enthalpy (h) and specific Gibbs free energy (g). These functions are related to the specific internal energy (55) through a series of Legendre–Fenchel Transformations (see the Appendices in [2] and [8]), as shown in Table 2.

Table 2. Energy potentials for use in large strain continuum mechanics of porous media

internal energy	Helmholtz free energy	enthalpy	Gibbs free energy
$u\left(\Delta_{ij},\alpha_{ij},\nu^{\mathrm{s}},s^{\mathrm{s}},w,\nu^{\mathrm{w}},s^{\mathrm{w}}\right)$	$f\left(\Delta_{ij},\alpha_{ij},\nu^{\mathrm{s}},\theta^{\mathrm{s}},w,\nu^{\mathrm{w}},\theta^{\mathrm{w}}\right)$	$h\left(\pi_{ij},\alpha_{ij},p^{\mathrm{s}},s^{\mathrm{s}},w,p^{\mathrm{w}},s^{\mathrm{w}}\right)$	$g\left(\pi_{ij},\boldsymbol{\alpha}_{ij},p^{\mathrm{s}},\theta^{\mathrm{s}},w,\nu^{\mathrm{w}},\theta^{\mathrm{w}}\right)$
$= u^{\mathrm{s}}\left(\Delta_{ij},\alpha_{ij},\nu^{\mathrm{s}},s^{\mathrm{s}}\right)$	$= f^{\mathrm{s}}\left(\Delta_{ij},\alpha_{ij},\nu^{\mathrm{s}},\theta^{\mathrm{s}}\right)$	$= h^{\mathrm{s}}\left(\pi_{ij},\alpha_{ij},p^{\mathrm{s}},s^{s}\right)$	$= g^{\mathrm{s}}\left(\bar{\pi}_{ij},\alpha_{ij},p^{\mathrm{s}},\theta^{\mathrm{s}}\right)$
$+wu^{\mathrm{w}}\left(\nu^{\mathrm{w}},s^{\mathrm{w}}\right)$	$+wf^{\mathrm{w}}\left(\nu^{\mathrm{w}},\theta^{\mathrm{w}}\right)$	$+wh^{\mathrm{w}}\left(p^{\mathrm{w}},s^{\mathrm{w}}\right)$	$+wg^{\mathrm{w}}\left(p^{\mathrm{w}},\theta^{\mathrm{w}}\right)$
	$f=u-s\theta$	$h=u-\frac{\bar{\pi}_{ij}\Delta_{ij}}{\rho_0}+pv$	$g=u-s\theta\frac{\bar{\pi}_{ij}\Delta_{ij}}{\rho_0}+pv$
	$f^{\mathrm{s}}=u^{\mathrm{s}}-s^{\mathrm{s}}\theta^{\mathrm{s}}$	$h^{\mathrm{s}}=u^{\mathrm{s}}-\frac{\bar{\pi}_{ij}\Delta_{ij}}{\rho_0}+p^{\mathrm{s}}\nu^{s}$	$g^{\mathrm{s}}=u^{\mathrm{s}}-s^{\mathrm{s}}\theta^{\mathrm{s}}\frac{\bar{\pi}_{ij}\Delta_{ij}}{\rho_0}+p^{\mathrm{s}}\nu^{\mathrm{s}}$
	$f^{\mathrm{w}}=u^{\mathrm{w}}-s^{\mathrm{w}}\theta^{\mathrm{w}}$	$h^{\mathrm{w}}=u^{\mathrm{w}}+p^{\mathrm{w}}\nu^{\mathrm{w}}$	$g^{\mathrm{w}}=u^{\mathrm{w}}-s^{\mathrm{w}}\theta^{\mathrm{w}}+p^{\mathrm{w}}\nu^{\mathrm{w}}$
$\pi_{ij}=\pi_{ij}+p^{\mathrm{L}}\delta_{ij}=\rho_0\frac{\partial u^{\mathrm{s}}}{\partial\Delta_{ij}}$	$\pi_{ij}=\pi_{ij}+p^{\mathrm{L}}\delta_{ij}=\rho_0\frac{\partial f^{\mathrm{s}}}{\partial\Delta_{ij}}$	$\Delta_{ij}=-\rho_0\frac{\partial h^{\mathrm{s}}}{\partial\pi_{ij}}$	$\Delta_{ij}=-\rho_0\frac{\partial g^{\mathrm{s}}}{\partial\pi_{ij}}$
$\chi_{ij}=-\rho_0\frac{\partial u^{\mathrm{s}}}{\partial\alpha_{ij}}$	$\chi_{ij}=-\rho_0\frac{\partial f^{\mathrm{s}}}{\partial\alpha_{ij}}$	$\chi_{ij}=-\rho_0\frac{\partial h^{\mathrm{s}}}{\partial\alpha_{ij}}$	$\chi_{ij}=-\rho_0\frac{\partial g^{\mathrm{s}}}{\partial\alpha_{ij}}$
$p^{\mathrm{s}}=\frac{\partial u^{\mathrm{s}}}{\partial\nu^{\mathrm{s}}};\ p^{\mathrm{w}}=\frac{\partial u^{\mathrm{w}}}{\partial\nu^{\mathrm{w}}}$	$p^{\mathrm{s}}=\frac{\partial f^{\mathrm{s}}}{\partial\nu^{\mathrm{s}}};\ p^{\mathrm{w}}=\frac{\partial f^{\mathrm{w}}}{\partial\nu^{\mathrm{w}}}$	$\nu^{\mathrm{s}}=\frac{\partial h^{\mathrm{s}}}{\partial p^{\mathrm{s}}};\ \nu^{\mathrm{w}}=\frac{\partial h^{\mathrm{w}}}{\partial p^{\mathrm{s}}}$	$\nu^{\mathrm{s}}=\frac{\partial g^{\mathrm{s}}}{\partial p^{\mathrm{s}}};\ \nu^{\mathrm{w}}=\frac{\partial g^{\mathrm{w}}}{\partial p^{\mathrm{w}}}$
$\theta^{\mathrm{s}}=\frac{\partial u^{\mathrm{s}}}{\partial\nu_{\mathrm{s}}};\ \theta^{\mathrm{w}}=\frac{\partial u^{\mathrm{w}}}{\partial s^{\mathrm{w}}}$	$s^{\mathrm{s}}=\frac{\partial f^{\mathrm{s}}}{\partial\theta^{\mathrm{s}}};\ s^{\mathrm{w}}=\frac{\partial f^{\mathrm{w}}}{\partial\theta^{\mathrm{w}}}$	$\theta^{\mathrm{s}}=\frac{\partial h^{\mathrm{s}}}{\partial s^{\mathrm{s}}};\ \theta^{\mathrm{w}}=\frac{\partial h^{\mathrm{w}}}{\partial s^{\mathrm{w}}}$	$s^{\mathrm{s}}=\frac{\partial g^{\mathrm{s}}}{\partial\theta^{\mathrm{s}}};\ s^{\mathrm{w}}=\frac{\partial g^{\mathrm{w}}}{\partial\theta^{\mathrm{w}}}$

As demonstrated in Table 2, all the derived energy functions e can be also decomposed into the specific energy functions e^{s} and e^{w} attributed to the skeleton and fluid, respectively. Moreover, by the virtue of (12) and (29), these parts can be transformed independently. Constitutive equations in the last row of Table 2 follow directly as properties of the corresponding Legendre–Fenchel Transformations (see again the Appendices in [2–8]).

The choice of which formulation to use will depend on the application in hand. For instance the four forms of the energy potential in classical thermodynamics are adopted in different cases (e.g. isothermal problems, adiabatic problems etc.).

The dissipation function formulation can be also adjusted to the chosen energy formulation, simply by expressing the force potential z through corresponding variables:

$$\left.\begin{aligned} z &= z^{u}\left(\Delta_{ij}, \alpha_{ij}, \nu_{\mathrm{s}}, s^{\mathrm{s}}, w, \nu_{\mathrm{w}}, s^{\mathrm{w}}, \tilde{\alpha}_{ij}, m_i, \eta_i\right) \\ z &= z^{f}\left(\Delta_{ij}, \alpha_{ij}, \nu_{\mathrm{s}}, \theta^{\mathrm{s}}, w, \nu_{\mathrm{w}}, \theta^{\mathrm{w}}, \tilde{\alpha}_{ij}, m_i, \eta_i\right) \\ z &= z^{h}\left(\overline{\pi}_{ij}, \alpha_{ij}, p^{\mathrm{s}}, s^{\mathrm{s}}, w, p^{\mathrm{w}}, s^{\mathrm{w}}, \tilde{\alpha}_{ij}, m_i, \eta_i\right) \\ z &= z^{g}\left(\overline{\pi}_{ij}, \alpha_{ij}, p^{\mathrm{s}}, \theta^{\mathrm{s}}, w, p^{\mathrm{w}}, \theta^{\mathrm{w}}, \tilde{\alpha}_{ij}, m_i, \eta_i\right) \end{aligned}\right\}. \tag{59}$$

In principle it would be possible to define the dissipation function in terms of a different set of variables than the energy function, but only in rather particular circumstances might this be useful.

4.4 Small Strain Formulation

The displacement vector of a point with initial coordinates X_i is defined by $u_i = x_i - X_i$, so that the deformation gradient can be expressed as $P_{ij} = \delta_{ij} + u_{i,j}$. The assumption of small strains is equivalent to $||u_{i,j}|| << 1$, therefore $\det(P_{ij}) \cong 1 + u_{i,i}$ and, after the higher order terms are neglected, the following simplifications can be applied to the formulation in Table 1:

- $2\Delta_{ij} = P_{ki}P_{kj} - \delta_{ij} \cong u_{i,j} + u_{j,i} = 2\epsilon_{ij}$, where ϵ_{ij} is the linearised strain tensor
- $\pi_{ij} = \det(P_{ij})P^{-1}_{ik}\sigma_{kl}P^{-1}_{jl} \cong \sigma_{ij}$
- $p^{\mathrm{L}} = p\,\det(P_{ij})P^{-1}_{ik}P^{-1}_{ik} \cong p$

The linearised strain tensor can in some circumstances be decomposed into elastic and plastic components $\varepsilon_{ij} = \varepsilon^{\mathrm{e}}_{ij} + \varepsilon^{\mathrm{p}}_{ij}$, and the kinematics internal variable α_{ij} can be associated with the plastic strain tensor $\varepsilon^{\mathrm{p}}_{ij}$.

4.5 Example

The following example describes a conventional thermo-poro-elasto-plastic model which can be applied to describe small strain behaviour of saturated isotropic frictional granular material. The constitutive behaviour is completely

defined by the following two potential functions. The first one is Gibbs free energy function $g = g^{\mathrm{s}} + wg^{\mathrm{w}}$, which we assume to have constant, linear and quadratic terms, written in the following form so that certain constants retain their usual meaning:

$$\begin{aligned} g^{\mathrm{s}} = {} & g_0^{\mathrm{s}} + (p^{\mathrm{s}} - p_0)\,\nu_0^{\mathrm{s}} - (\theta^{\mathrm{s}} - \theta_0)\,s_0^{\mathrm{s}} \\ & - \frac{(p - p_0)^2}{2K^{\mathrm{s}}}\nu_0^{\mathrm{s}} + 3\alpha^{\mathrm{s}}\,(\theta^{\mathrm{s}} - \theta_0)\,(p^{\mathrm{s}} - p_0)\,\nu_0^{\mathrm{s}} - c_p^{\mathrm{s}}\frac{(\theta^{\mathrm{s}} - \theta_0)^2}{2\theta_0} \\ & - \frac{1}{\rho_0}\left(\frac{1}{3K}\frac{\overline{\sigma}_{ii}\overline{\sigma}_{jj}}{6} + \frac{1}{2G}\frac{\overline{\sigma}'_{ij}\overline{\sigma}'_{ij}}{2} + \alpha\,(\theta^{\mathrm{s}} - \theta_0)\,\overline{\sigma}_{kk} + \overline{\sigma}_{ij}\alpha_{ij}\right) \end{aligned} \tag{60}$$

$$\begin{aligned} g^{\mathrm{w}} = {} & g_0^{\mathrm{w}} + (p^{\mathrm{w}} - p_0)\,\nu_0^{\mathrm{w}} - (\theta^{\mathrm{w}} - \theta_0)\,s_0^{\mathrm{w}} \\ & - \frac{(p^{\mathrm{w}} - p_0)^2}{2K^{\mathrm{w}}}\nu_0^{\mathrm{w}} + 3\alpha^{\mathrm{w}}\,(\theta - \theta_0)\,(p^{\mathrm{w}} - p_0)\,\nu_0^{\mathrm{w}} - c_p^{\mathrm{w}}\frac{(\theta^{\mathrm{w}} - \theta_0)^2}{2\theta_0} \end{aligned} \tag{61}$$

where initial values are denoted with the subscript "0", and the constants have the following physical meanings:

- K^{s} and K^{w} are the isothermal bulk moduli of the skeleton particles and fluid, respectively
- $3\alpha^{\mathrm{s}}$ and $3\alpha^{\mathrm{w}}$ are the volumetric thermal expansion coefficients of the skeleton particles and fluid, respectively
- c_p^{s} and c_p^{w} are the mass heat capacity at constant pressure p_0 of the skeleton particles and fluid, respectively
- K and G are the isothermal bulk and shear moduli of the skeleton matrix, respectively
- α is the linear thermal expansion coefficient of the skeleton matrix.

The second function required is the force potential, which we choose in the form

$$z = \frac{\mu\overline{\sigma}_{ii}}{\rho_0}\sqrt{\tilde{\alpha}'_{ij}\tilde{\alpha}'_{ij}} + \frac{\Lambda}{\rho_0}\left(3\beta\sqrt{\tilde{\alpha}'_{ij}\tilde{\alpha}'_{ij}} + \tilde{\alpha}_{ii}\right) + \frac{\nu_{\mathrm{w}}}{2\rho k_m}m_i m_i + \frac{\theta}{2\rho k_\eta}\eta_i\eta_i, \tag{62}$$

where Λ is a Lagrangian multiplier associated with a dilation constraint $c = 3\beta\sqrt{\tilde{\alpha}'_{ij}\tilde{\alpha}'_{ij}} + \tilde{\alpha}_{ii} = 0$. The constants have the following physical meanings:

- k_m is the permeability coefficient.
- k_η is the thermal conductivity coefficient.
- μ and β are the coefficients related to the effective angles of friction ϕ' and dilation ψ obtained in triaxial compression

$$\beta = \frac{2\sqrt{2}\sin\psi}{\sqrt{3}(3 - \sin\psi)}; \mu + \beta = \frac{2\sqrt{2}\sin\phi'}{\sqrt{3}(3 - \sin\phi')}. \tag{63}$$

The following constitutive relationships can be derived from the earlier formulation using the equations from the last column of Table 1:

$$\varepsilon_{ij} = \frac{\overline{\sigma}_{ii}}{3K} + 3\alpha(\theta - \theta_0) + \alpha_{ij};\ \varepsilon'_{ij} = \frac{\overline{\sigma}'_{ij}}{2G} + \alpha'_{ij}, \tag{64}$$

$$\frac{\nu_{\mathrm{s}} - \nu_0^{\mathrm{s}}}{\nu_0^{\mathrm{s}}} = 3\alpha^{\mathrm{s}}\left(\theta^{\mathrm{s}} - \theta_0\right) - \frac{p^{\mathrm{s}} - p_0}{K^{\mathrm{s}}}, \tag{65}$$

$$\frac{\nu_{\mathrm{w}} - \nu_0^{\mathrm{w}}}{\nu_0^{\mathrm{w}}} = 3\alpha^{\mathrm{w}}\left(\theta^{\mathrm{w}} - \theta_0\right) - \frac{p^{\mathrm{w}} - p_0}{K^{\mathrm{w}}}, \tag{66}$$

$$s^{\mathrm{s}} = s_0^{\mathrm{s}} + c_p^{\mathrm{s}}\frac{\left(\theta^{\mathrm{s}} - \theta_0\right)}{\theta_0} - 3\alpha^{\mathrm{s}}\left(p^{\mathrm{s}} - p_0\right)\nu_0^{\mathrm{s}} + \frac{\alpha\overline{\sigma}_{kk}}{\rho_0}, \tag{67}$$

$$s^{\mathrm{w}} = s_0^{\mathrm{w}} + c_p^{\mathrm{w}}\frac{\left(\theta^{\mathrm{w}} - \theta_0\right)}{\theta_0} - 3\alpha^{\mathrm{w}}\left(p^{\mathrm{w}} - p_0\right)\nu_0^{\mathrm{w}}. \tag{68}$$

Equation (64) represents decomposition of the strain tensor into elastic and plastic components, where elastic part is defined by conventional thermoelasticity. Equations (65) and (67) give thermoelastic relationships for the skeleton, while (66) and (68) represent classical thermoelastic relationships for the fluid.

Evolution equations for plastic strains are obtained by defining generalised stress $\overline{\chi}_{ij} = -\rho_0\left(\frac{\partial g^{\mathrm{s}}}{\partial\alpha_{ij}}\right) = \overline{\sigma}_{ij}$ and dissipative generalised stress $\chi_{ij} = -\rho_0\left(\partial z/\partial\tilde{\alpha}_{ij}\right)$, so that

$$\chi'_{ij} = (\mu\overline{\sigma}_{ii} + 3\Lambda\beta)\frac{\tilde{\alpha}'_{ij}}{\sqrt{\alpha'_{ij}\tilde{\alpha}'_{ij}}};\ \chi_{ii} = 3\Lambda \tag{69}$$

and by eliminating $\tilde{\alpha}'_{ij}$ and Λ from (69) we obtain the equation of the yield surface in the dissipative generalised stress space

$$y\left(\overline{\sigma}_{ij}, \chi_{ij}\right) = \sqrt{\chi'_{ij}\chi'_{ij}} - (\mu\overline{\sigma}_{ii} + \beta\chi_{ii}) = 0. \tag{70}$$

The flow rule $\tilde{\alpha}_{ij} = \tilde{\lambda}\partial y/\chi_{ij}$ (where $\tilde{\lambda}$ is a Lagrangian multiplier) follows from the properties of the Legendre–Fenchel Transformation $y = \chi_{ij}\tilde{\alpha}_{ij}/\rho_0 - z = 0$ relating the yield surface to the force potential. When Ziegler's orthogonality condition $\chi_{ij} = \overline{\chi}_{ij}$ is applied to the equations of the yield surface and flow rule, it becomes clear that the behaviour described is equivalent to that of a perfectly plastic model with the Drucker–Prager failure cone defined by an effective angle of internal friction ϕ', and a non-associated flow rule with the plastic potential cone defined by an angle of dilation ψ.

Finally, from (52) and (53), after neglecting inertial effects and substituting $\eta_i = q_i/\theta$ and $m_i = w_i/\nu_{\mathrm{w}}$, it follows:

$$q_i = -k_\eta\theta_{,i}, \tag{71}$$

$$w_i = -k_m\left(\nu_{\mathrm{w}}p_{,i} - g_i\right). \tag{72}$$

Equation (71) is the isotropic Fourier heat conduction law, while for constant ν^{w} (72) becomes the isotropic version of Darcy's law for fluid conduction.

Thus, by employing just two potentials, we have derived a theory for a porous continuum that includes elastic and plastic behaviour of the soil skeleton, with the latter being governed by a frictional criterion and involving dilation and non-associated flow. Thermal expansion and thermal capacity are taken into account for both the skeleton and the pore fluid. Heat conduction and seepage are included in the model, which also embodies the principle of effective stress. The versatility of the approach that we have termed hyperplasticity in describing a wide variety of phenomena relevant to the mechanics of granular materials and porous continua is therefore demonstrated.

5 Conclusions

The theoretical framework presented in this paper extends our previous work to problems involving:

- Large strains
- Fluid flow in porous media
- Heat flow in porous media
- Inertial effects

As in the standard hyperplastic approach, the entire constitutive behaviour is completely defined by specification of two scalar potential functions. However, in the generalised framework these functions also include the properties related to the different phases of the medium and their interaction. The fluid and heat conduction laws are also specified through these potentials, completing the description of the constitutive behaviour of the complex media.

Appendix

For certain simple cases the force potential may be derived using procedures described by Houlsby and Puzrin [6]. For more general cases the following method may be used.

Consider the definition $z(\tau_0\dot{\alpha}_{ij}) = \int_0^{\tau_0} \frac{d(\tau\dot{\alpha}_{ij})}{\tau}\mathrm{d}\tau$. Differentiation with respect to τ_0 gives $\frac{\partial z(\tau_0\dot{\alpha}_{ij})}{\partial(\tau_0\dot{\alpha}_{ij})}\dot{\alpha}_{ij} = \frac{d(\tau_0\dot{\alpha}_{ij})}{\tau_0}$, and setting $\tau_0 = 1$ yields the result $\frac{\partial z(\dot{\alpha}_{ij})}{\partial\dot{\alpha}_{ij}}\dot{\alpha}_{ij} = \chi_{ij}\dot{\alpha}_{ij} = d(\dot{\alpha}_{ij})$. This demonstrates that application of the above definition leads to a potential with the required property that $\chi_{ij} = \partial z/\partial\dot{\alpha}_{ij}$ satisfies $\chi_{ij}\dot{\alpha}_{ij} = d$. Thus by setting $\tau_o = 1$ above we obtain $z(\dot{\alpha}_{ij}) = \int_0^1 \frac{d(\tau\dot{\alpha}_{ij})}{\tau}\mathrm{d}\tau$.

References

1. Berryman, J.G. (1980) "Confirmation of Biot's theory", Applied Physics Letters, Vol. 37, pp 382–384

2. Collins, I.F. and Houlsby, G.T. (1997) "Application of thermomechanical Principles to the modelling of geotechnical materials", Proceedings of Royal Society of London, Series A, Vol. 453, pp 1975–2001
3. Coussy, O. (1995) "Mechanics of Porous Continua", Wiley, New York
4. de Boer, R. (2000) "Theory of Porous Media", Springer, Berlin Heidelberg New York
5. Houlsby, G.T. and Puzrin, A.M. (2000) "A thermomechanical framework for constitutive models for rate-independent dissipative materials", International Journal of Plasticity, Vol. 16, No. 9, pp 1017–1047
6. Houlsby, G.T. and Puzrin, A.M. (2002) "Rate-dependent plasticity models derived from potential functions", Journal of Rheology, Vol. 46, No. 1, pp 113–126
7. Puzrin, A.M. and Houlsby, G.T. (2001a) "Fundamentals of kinematics hardening hyperplasticity", International Journal of Solids and Structures, Vol. 38, No. 21, pp 3771–3794
8. Puzrin, A.M. and Houlsby, G.T. (2001b) "A thermomechanical framework for rate-independent dissipative materials with internal functions", International Journal of Plasticity, Vol. 17, pp 1147–1165
9. Puzrin, A.M. and Houlsby, G.T. (2003) "Rate dependent hyperplasticity with internal functions", Proceedings of the ASCE, Journal of the Engineering Mechanics Division, Vol. 129, No. 3, pp 252–263
10. Ziegler, H. (1977) "An Introduction to Thermomechanics", North Holland, Amsterdam (2nd edition, 1983)

Effective Stress Formulation of Unsaturated Soil Mechanics

F. Molenkamp

Faculty of Civil Engineering and Geosciences, Delft University of Technology, Netherlands
Frans.Molenkamp@CiTG.TUDelft.nl

1 Introduction

The incremental deformation of an unsaturated granular material depends amongst others on the increments of both the total stress and the pore fluid stress, the latter being related to the level of saturation. Despite the complexity of these relations the incremental deformation could still be described by the same material models as already derived for saturated granular materials if the combined effects of the total stress, the pore fluid stress and the level of saturation could be combined in a suction-induced effective stress measure, which would represent the interparticle forces which are at the basis of the definition of the intergranular stress.

In this paper first the various aspects of this suction-induced intergranular stress concept are characterised, taking full account of both the observed behaviour and published fundamental analyses of the combined actions of the pore fluid and pore air on the granular structure. In particular the role of the pore air stress in the definition of the suction-induced intergranular stress is considered in detail. Finally, the resulting rate form of the effective stress–strain relation of a compressible soil skeleton composed of a compressible mineral is formulated.

2 Characteristics of Saturation Versus Suction

Because the moist pore air and pore water with dissolved air are separated by curved interfaces with surface tension, the moist pore air stress p^{g} and the pore water stress p^{w} are different. In case of unsaturated soil the pore water stress p^{w} concerns suction. This suction is related to various quantities, amongst others the water saturation S^{w}, its rate of change ∂S^{w}, the mean grain size d_{50} and the moist pore air stress p^{g}. A possible relation is illustrated in Fig. 1 in terms of the saturation S^{w} versus the dimensionless measure of the pore water suction Ψ

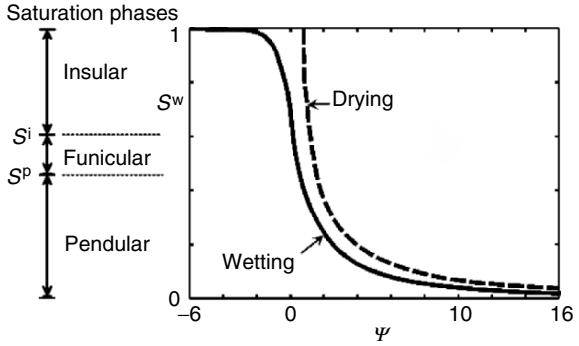

Fig. 1. Hysteretic cycle of wetting and drying in terms of the relation between the saturation S^{w} and the dimensionless pore water suction Ψ. Also the various saturation phases are indicated

$$\Psi = \frac{(p^{\mathrm{w}} - p^{\mathrm{g}})d_{50}}{2\sigma^{\mathrm{s}}} = \frac{\Psi d_{50}}{2\sigma^{\mathrm{s}}}, \tag{1}$$

where σ^{s} is the surface tension of the water–air interface, which for pure water is given by Edlefsen and Andersen [3]

$$\sigma^{\mathrm{s}} = 0.1171 - 0.0001516\ T\ (\mathrm{N\,m^{-1}}) \tag{2}$$

with T being the temperature in (K) and ψ is the capillary pore suction, also known as matric suction, defined by

$$\psi = p^{\mathrm{w}} - p^{\mathrm{g}}. \tag{3}$$

As a consequence of the application of the sign convention of continuum mechanics with tension and stretch being positive, the capillary suction ψ is positive if the pore water stress p^{w} is less compressive, or even tensile, than pore gas stress p^{g} , which can only be negative.

The water saturation S^{w} is considered to depend at least on both the dimensionless suction Ψ and the rate of change of the water saturation ∂S^{w} thus

$$S^{\mathrm{w}} = S^{\mathrm{w}}(p^{\mathrm{w}}, p^{\mathrm{g}}, \partial S^{\mathrm{w}}, d_{50}, \sigma^{\mathrm{s}}) = S^{\mathrm{w}}(\Psi, \partial S^{\mathrm{w}}). \tag{4}$$

The dependence on the rate of change ∂S^{w} is considered to be due to the difference of the liquid–solid contact angle for wetting and drying.

Figure 1 indicates the potential response of the application of repeated cycles of wetting and drying.

Depending on the water saturation S^{w} the following three saturation phases can be distinguished [1], namely:

(a) The *pendular saturation phase* concerns the smaller water saturation range, $0 \leq S^{\mathrm{w}} \leq S^{\mathrm{p}} = \sim 0.4{-}0.7$, in which the pore water occurs in

the form of both liquid bridges and small pockets in the grain surfaces, while the air phase is continuous. The air will often, but not necessarily, be in open contact with the atmosphere. Free flow of both dry air and water vapour can occur.

(b) The *funicular saturation phase*, with both continuous gas and water phases, occurs for water saturation levels in the approximate range $\sim 0.4{-}0.7 = S^{\mathrm{p}} \leq S^{\mathrm{w}} \leq S^{\mathrm{i}} = \sim 0.7{-}0.9$. The gas–water interfaces are in direct contact with the grains and parts of the surface of the grains remain dry, enabling the surface tension to connect the gas–water interfaces to the grains. Therefore these larger gas–water interfaces will move with the soil skeleton and reduce the hydraulic conductivity of the pore structure drastically.

(c) The *insular saturation phase*, in which the pore gas occurs in the form of entrapped gas bubbles within a continuous water phase. Individual bubbles can only fit in the pores of the soil skeleton if the water saturation is sufficiently large, e.g. $\sim 0.7{-}0.9 = S^{\mathrm{i}} \leq S^{\mathrm{w}} \leq 1$, and if the mean bubble diameter d^{b} is sufficiently small, e.g. $d^{\mathrm{b}}/d_{10} < 0.2{-}0.5$, in which d_{10} is the grain size for which the mass of the smaller grains form 10% of the dry soil mass.

For increasing saturation the pore gas stress p^{g} in the pore gas bubbles can increase towards very large pressure, depending on the rates of loading and solution of air in water. In such case the larger pressure will be reached at the instant of implosion of the gas bubbles when reaching full saturation. Therefore for insular saturation the application of the capillary suction ψ according to 3, thus $\psi = p^{\mathrm{w}} - p^{\mathrm{g}}$, in amongst others the relation between the saturation S^{w} and the pore water suction, illustrated in Fig. 1, is not appropriate in general. In fact the pore gas stress p^{g} in the entrapped gas bubbles would cause the capillary suction ψ to reach positive infinity for full saturation rather than about zero as illustrated in Fig. 1. Consequently for the insular saturation range another global suction measure needs to be applied, as

$$\psi^{\mathrm{b}} = p^{\mathrm{w}} - p^{\mathrm{b}} \tag{5}$$

in which p^{b} is the background air stress, which is the pore gas stress in the ground in open contact and equilibrium with the atmospheric air stress at the ground surface.

3 Typical Expressions for Saturation Versus Suction

A popular non-hysteretic model [4] relating the water saturation S^{w} and the capillary pore suction ψ for the insular and funicular saturation phases reads

$$\frac{S^{\mathrm{w}} - S^{\mathrm{r}}}{1 - S^{\mathrm{r}}} = \left(\frac{1}{1 + \{\chi\,\psi\}^{\eta}} \right)^{\frac{\eta-1}{\eta}} ; \quad \chi\,\psi = \left(\left\{ \frac{S^{\mathrm{w}} - S^{\mathrm{r}}}{1 - S^{\mathrm{r}}} \right\}^{\frac{-\eta}{\eta-1}} - 1 \right)^{\frac{1}{\eta}}, \tag{6}$$

where S^{r} is the so-called "residual" degree of saturation. The main simplifying and limiting assumption of this model is that at this residual degree of saturation S^{r} the capillary suction ψ approaches infinity. Apparently both the vapour flow in the pendular saturation phase and the related distribution of the capillary pore suction of the adhered pore water have not been taken into account. The parameter η is a dimensionless exponent and parameter χ is the pore size distribution parameter, also known as the inverse of the capillary pore suction ψ at "air entry". Both parameters η and χ depend on the pore size in terms of the mean grain diameter d_{50}. Typical values for clay, silt and sand (e.g. [4]) of the parameters, S^{r} η, χ and d_{50} have been collected in Table 1. The indicated mean grain diameter d_{50} corresponds to the measured intrinsic permeability κ as expressed (e.g. [8]) by

$$\kappa = C \frac{n^3}{(1-n)^2} d_{50}^2 \tag{7}$$

in which C is a dimensionless factor.

The ranges of saturation and suction corresponding to the parameters in Table 1 are illustrated in Fig. 2a in terms of the saturation S^{w} versus the Briggs logarithm of the dimensionless pore water suction measure Ψ as defined by (1), thus $\log \Psi = \log(\psi d_{50}/(2\sigma^{\mathrm{s}}))$. For each type of soil two extreme curves are shown, one curve for the first parameters of the range in Table 1 and the other curve for the last parameters indicating the ranges.

Figure 2a shows that the steepness of the relations decreases in the sequence from sand, to silt and finally to clay, while the width of the ranges in terms of dimensionless suction measure $\log \Psi$ increases.

Particularly for clay relatively large values of $\log \Psi$ are reached. For decreasing saturation S^{w} the curves become flat when approaching the residual saturation S^{r}. This is consistent with the property of expression (6) that $\chi\psi$ approaches infinity when S^{w} reduces to S^{r}. This clarifies a limitation of expression (6), namely that matrix suction ψ would be infinite if the saturation would equal the residual saturation S^{r}. Apparently this relation cannot describe the suction for decreasing saturation $S^{\mathrm{w}} < S^{\mathrm{r}}$, approaching the dry state $S^{\mathrm{w}} = 0$.

To ensure that the transition between the funicular and pendular saturation phases at saturation $S^{\mathrm{w}} = S^{\mathrm{p}}$ occurs at the specific capillary pore suction

Table 1. Typical ranges of unsaturated soil parameters of (6) for various soils (in accordance with e.g. [4]).

soil type	S^{r}	η	χ	d_{50}
unit	–	–	$\mathrm{m}^2\,\mathrm{N}^{-1}$	m
clay	0.2–0.1	1.2–2	$10^{-6} - 10^{-5}$	$10^{-7} - 10^{-9}$
silt	0.15–0.08	2–4	$10^{-5} - 10^{-4}$	$10^{-5} - 10^{-7}$
sand	0.1–0.05	4–10	$10^{-4} - 5.10^{-4}$	$10^{-3} - 10^{-5}$

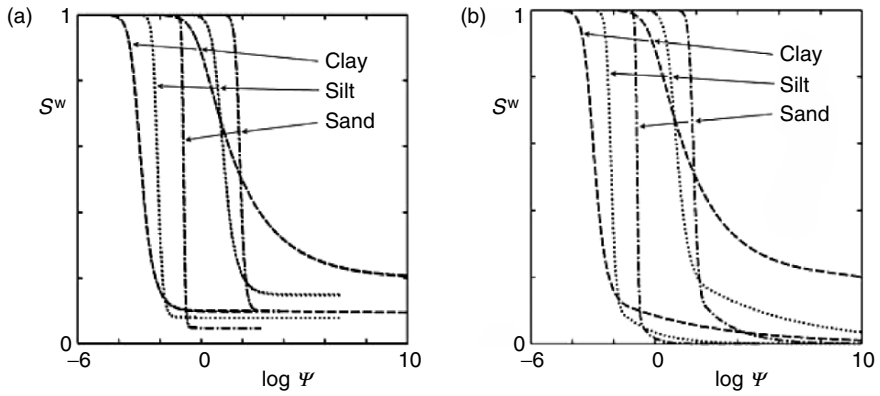

Fig. 2. Saturation S^{w} versus logarithm of dimensionless pore water suction Ψ for various soils with parameter ranges as indicated in Table 1. (**a**) Defined by (6) [4], (**b**) defined by (6), (9) and (12), including pendular phase with transition at saturation $S^{\mathrm{p}} = cS^{\mathrm{r}}$ (13) for factor $c = 1.1$

ψ^{p} the corresponding residual saturation S^{r} can be derived from (6), giving

$$S^{\mathrm{r}} = \left\{ S^{\mathrm{p}} - \left(\frac{1}{1 + \{\chi\, \psi^{\mathrm{p}}\}^{\eta}} \right)^{\frac{\eta-1}{\eta}} \right\} \left\{ 1 - \left(\frac{1}{1 + \{\chi\, \psi^{\mathrm{p}}\}^{\eta}} \right)^{\frac{\eta-1}{\eta}} \right\}^{-1} . \quad (8)$$

It may be noted that this transition occurs when the pore water phase becomes discontinuous and thus the corresponding permeability becomes zero. In the pendular phase $S^{\mathrm{w}} < S^{\mathrm{r}}$ the transport of pore water can only occur as water vapour through the continuous gas phase.

For the continuation of the relation (6) between the saturation S^{w} and the matrix suction ψ into the pendular range good fits to high quality experimental data are essential. For such fits simple relations with a minimum number of additional parameters are needed. The exponential decaying function through the transition point $\psi^{\mathrm{p}}, S^{\mathrm{p}}$ as given by the first expression of (9) has one parameter ζ. From this expression for the slope the second expression of (9) results

$$S^{\mathrm{w}} = S^{\mathrm{p}} \exp\left(-\zeta \, \log\left(\frac{\Psi}{\Psi^{\mathrm{p}}} \right) \right); \quad \frac{\mathrm{d}S^{\mathrm{w}}}{\mathrm{d}\log\Psi} = -\zeta\, S^{\mathrm{w}}. \quad (9)$$

The single parameter ζ cxan be derived from the slope of (6) at this transition point $\psi^{\mathrm{p}}, S^{\mathrm{p}}$, which is expressed by

$$\left. \frac{\mathrm{d}S^{\mathrm{w}}}{\mathrm{d}\psi} \right|^{\mathrm{p}} = -\chi\,(\eta - 1)\,(1 - S^{\mathrm{r}})\,\{\chi\, \psi^{\mathrm{p}}\}^{\eta-1} \left(\frac{1}{1 + \{\chi\, \psi^{\mathrm{p}}\}^{\eta}} \right)^{\frac{2\eta-1}{\eta}} . \quad (10)$$

Elaborating (9) further to obtain the same derivative $dS^{\mathrm{w}}/d\psi|^{\mathrm{p}}$ as in (10) gives

$$\left.\frac{\mathrm{d}S^{\mathrm{w}}}{\mathrm{d}\psi}\right|^{\mathrm{p}} = \left.\frac{\mathrm{d}S^{\mathrm{w}}}{\mathrm{d}\log\Psi}\right|^{\mathrm{p}} \left.\frac{\mathrm{d}\log\Psi}{\mathrm{d}\Psi}\right|^{\mathrm{p}} \frac{\mathrm{d}\Psi}{\mathrm{d}\psi} = -\frac{\zeta\, S^{\mathrm{p}}}{\ln 10\,\psi^{\mathrm{p}}}. \tag{11}$$

From (11) the fitting parameter ζ can be derived as

$$\zeta = -\frac{\ln 10\,\psi^{\mathrm{p}}}{S^{\mathrm{p}}} \left.\frac{\mathrm{d}S^{\mathrm{w}}}{\mathrm{d}\psi}\right|^{\mathrm{p}} \tag{12}$$

in which (10) can be substituted in the last term.

Figure 2b shows the same curves as illustrated in Fig. 2a above the transition point $\psi^{\mathrm{p}}, S^{\mathrm{p}}$ and the curves according to (9) with parameter ζ according to (10) and (12) below this transition point. The transition point $\psi^{\mathrm{p}}, S^{\mathrm{p}}$ is defined by the saturation S^{p} as a factor c times the residual saturation S^{r} as defined by Genuchten [4], namely

$$S^{\mathrm{p}} = c\, S^{\mathrm{r}}. \tag{13}$$

The curves in Fig. 2b have been obtained for the magnitude of factor $c = 1.1$. The first expression of (9) for $S^{\mathrm{w}} < S^{\mathrm{p}}$, illustrated in Fig. 2b, is applicable for the case that for decreasing saturation S^{w} towards the dry state $S^{\mathrm{w}} = 0$ the dimensionless matrix suction Ψ increases towards infinity. However, amongst others due to the roughness of the particles, during decreasing saturation S^{w} in the pendular phase a maximum suction may be reached, after which for continuously decreasing saturation S^{w} this suction may decrease towards zero (e.g. [6]). This aspect of the moisture–grain interaction may be accounted for approximately by the following expression, namely

$$\Psi = \Psi^{\mathrm{p}} \left(\frac{S^{\mathrm{w}}}{S^{\mathrm{p}}}\right)^{\frac{-\ln 10}{\zeta}} f\left[\frac{S^{\mathrm{w}}}{S^{\mathrm{p}}}\right] \tag{14}$$

in which the modification function $f[S^{\mathrm{w}}/S^{\mathrm{p}}]$ reads

$$f\left[\frac{S^{\mathrm{w}}}{S^{\mathrm{p}}}\right] = 2 + \ln\left(\sin\left\{\frac{\pi}{2}\left(\frac{S^{\mathrm{w}}}{S^{\mathrm{p}}}\right)^{\frac{1}{\lambda}}\right\}\right) - \sin\left\{\frac{\pi}{2}\left(\frac{S^{\mathrm{w}}}{S^{\mathrm{p}}}\right)^{\frac{1}{\lambda}}\right\}. \tag{15}$$

The left part of the right hand side of (14) is the inverse of the left expression of (9). The right part, thus the function $f[S^{\mathrm{w}}/S^{\mathrm{p}}]$, concerns a modification function, which has unit magnitude and zero slope at $S^{\mathrm{w}} = S^{\mathrm{p}}$ and minus infinity at $S^{\mathrm{w}} = 0$. The parameter λ (with $\lambda \geq 1$) enables to define the detailed shape of this modifying sine-function.

In Fig. 3a, b the modification of the pendular phase according to (15) of the curves of Fig. 2b is shown for parameters $\lambda = 1$ and $\lambda = 2$, respectively. For decreasing saturation this modification introduces first the occurrence of maximum suctions, which magnitudes decrease with decreasing

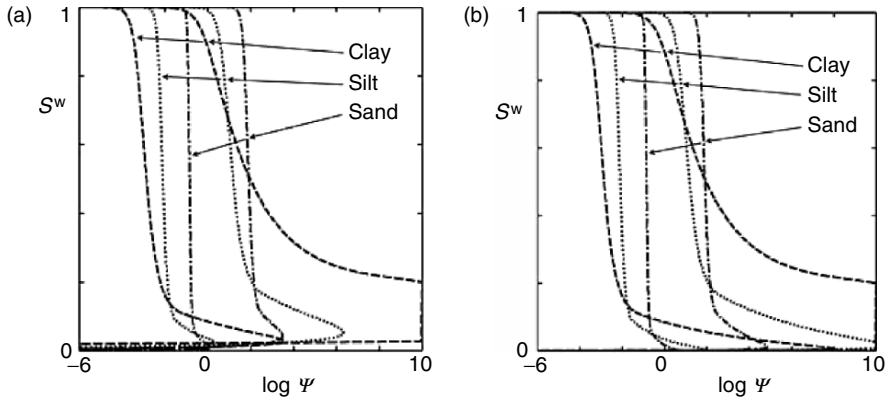

Fig. 3. Saturation S^w versus logarithm of dimensionless pore water suction Ψ for various soils with parameter ranges as indicated in Table 1, defined by (6) [4] for the insular and funicular phases as illustrated in Fig. 2. The pendular phase has been defined by (6), (9) and (12), like in Fig. 2b, but also modified according to (15) for factors: (**a**) $\lambda = 1$, (**b**) $\lambda = 2$

parameter value λ. Subsequently, the dimensionless suction measure $\log \Psi$ decreases monotonically towards minus infinity for the decreasing saturation towards the dry state, while the corresponding suction ψ approaches zero.

It may be noted that this property corresponds to that of dry sand, for which no capillary cohesion is left in the dry state. On the other hand, when clays are allowed to shrink freely during drying-out they can form hard materials with significant cohesion, which suggests that for clays the capillary suction may not become zero at the dry state.

4 Suction-Induced Intergranular Stress Versus Suction

Another basic concept of unsaturated geomaterials is the notion, that the combined action of the pore water suction and the surface tension can be considered to induce interparticle forces, which in an average sense can be expressed in terms of the "effective pore suction" ψ'_{ij}. The "effective pore suction" ψ'_{ij} is considered to depend in an intricate way on the pore water stress p^w, the moist pore air stress p^g, the water saturation S^w and its rate of change ∂S^w, the mean grain size d_{50}, the surface tension σ^s and a fabric tensor of the granular skeleton A_{kl} (e.g. [5–7, 9])

$$\psi'_{ij} = \psi'_{ij}\,(p^w, p^g, S^w, \partial S^w,\, d_{50},\, \sigma^s, A_{kl}) = \psi'_{ij}\,(\Psi,\, \partial S^w,\, A_{kl})\,. \qquad (16)$$

If the capillary pore suction ψ (3) is positive then the normal components of the pore-suction-induced intergranular stress tensor ψ' (16) are compressive, thus negative in continuum mechanics terms.

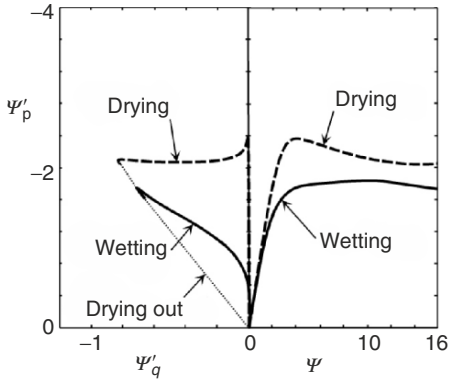

Fig. 4. Possible relations for repeated cycles of wetting and drying in triaxial tests between the dimensionless isotropic and deviatoric "effective pore suction" components Ψ'_p and Ψ'_q according to (17) and (18) and the dimensionless pore water suction Ψ according to (1) and (3)

Some aspects of the relation (16) for the application of repeated cycles of wetting and drying in triaxial tests are illustrated in Fig. 4, involving the possible relations between the isotropic and deviatoric components

$$\psi'_p = \frac{\psi'_{11} + 2\,\psi'_{33}}{3} \quad \text{and} \quad \psi'_q = \psi'_{11} - \psi'_{33} \tag{17}$$

of the "effective pore suction" ψ'_{ij} and the capillary suction ψ as defined by (3). It should be noted that in Fig. 4 in fact the following dimensionless isotropic and deviatoric effective quantities are used, namely

$$\Psi'_p = \frac{\psi'_p\, d_{50}}{2\,\sigma^{\mathrm{s}}} \quad \text{and} \quad \Psi'_q = \frac{\psi'_q\, d_{50}}{2\,\sigma^{\mathrm{s}}}, \tag{18}$$

while for the dimensionless capillary suction Ψ the quantity according to (1) is applied.

The right side part of Fig. 4, illustrating the possible relation between the capillary suction Ψ and the isotropic effective suction Ψ'_p, indicates a smaller Ψ'_p (in absolute terms) during wetting than during drying for the small suction range $\Psi < 16$ as considered. For small suction, say for $\Psi < \sim 2$, the isotropic effective suction Ψ'_p (in absolute terms) is of the same order as the suction Ψ, thus $\Psi'_p \approx -\Psi$. It should also be understood that for increasing pore suction, $\Psi > 16$, the isotropic effective suction Ψ'_p may at least for granular materials eventually approach zero.

The left side part of Fig. 4 illustrates the corresponding effective stress paths in terms of the suction-induced isotropic and deviatoric intergranular stresses Ψ'_p and Ψ'_q, respectively. It should be noted that the latter is due to the combined effects of the anisotropy of the micro-structural fabric of the granular skeleton, for spheres expressed by the fabric tensor $\mathbf{A}$ [5–7, 9] and the pore suctions and surface tension as expressed by the dimensionless pore suction measure Ψ. The left side part of Fig. 4 illustrates that for wetting,

thus decreasing suction Ψ, the deviatoric effective suction Ψ'_q decreases (in absolute terms) faster to zero than the isotropic effective suction Ψ'_p. For drying, starting at full saturation and zero suction Ψ, represented by the origin in Fig. 4, the isotropic effective suction Ψ'_p reaches an absolute maximum at still negligible deviatoric effective suction Ψ'_q, known as the "air entry" stress state. Subsequently the deviatoric effective suction Ψ'_q increases while the isotropic effective suction Ψ'_p decreases (in absolute terms) to reach the maximum deviatoric effective stress level in terms of Ψ'_q/Ψ'_p, depending on the granular fabric, which is to be followed during further "drying out" towards the completely dry state, also represented by the origin.

In general for the smaller saturation levels with a continuous gas phase, e.g. $S^{\mathrm{w}} \ll S^{\mathrm{i}}$, the effective pore suction Ψ'_{ij} is considered to be anisotropic due to the general anisotropic nature of a fabric tensor of the granular skeleton A_{kl}.

It should be understood that the characteristics of unsaturated granular soils in terms of the effective pore suction Ψ'_{ij} as illustrated in Fig. 4 cannot be measured directly. The directly measurable quantities are the total stress tensor σ and the strain tensor ε, apart of earlier mentioned water saturation S^{w} and its rate ∂S^{w}, the pore water stress p^{w}, the pore gas stress p^{g} (or the background air stress p^{b} in (5) for the insular phase) and the mean grain size d_{50}, and thus the scalar dimensionless capillary pore suction Ψ as defined by (1). Therefore the illustrated relations in Fig. 3 can only be deduced by combining the separately measured effective stress–strain behaviour for the fully saturated state and the measured behaviour for unsaturated states, which is a challenge.

5 Specific Definitions for the Pendular and Funicular Saturation Phases

For both the pendular and funicular saturation phases with a continuous air phase the pore gas stress p^{g} may only differ marginally from the background atmospheric air stress p^{b}, which is the gas stress at the considered depth in the ground in equilibrium with the atmospheric stress. In such case the pore water stress p^{w} in the ground can be expressed with respect to the background atmospheric air stress p^{b}, based on (3), by

$$(p^{\mathrm{w}} - p^{\mathrm{b}}) = (p^{\mathrm{w}} - p^{\mathrm{g}}) + (p^{\mathrm{g}} - p^{\mathrm{b}}) = \psi + (p^{\mathrm{g}} - p^{\mathrm{b}}) \tag{19}$$

in which all three stresses p^{w}, p^{g} and p^{b} are measurable and therefore the capillary suction ψ can be determined. In this case the relatively small difference $p^{\mathrm{g}} - p^{\mathrm{b}}$ is involved in driving the flow of the pore gas through the continuous pore air space. For these unsaturated phases the total "intergranular" stress σ^*_{ij} [2] is due to the interparticle forces, induced by both:

- The capillary pore suction $\psi = p^{\mathrm{w}} - p^{\mathrm{g}}$ and as such expressed by the "effective" pore suction Ψ'_{ij} (16).
- The total stress, expressed with respect to the local pore gas stress p^{g}, thus $\sigma_{ij} - p^{\mathrm{g}}\,\delta_{ij}$.

Therefore for the unsaturated case the total "intergranular" stress σ^*_{ij} can be defined by the following sum (see [6, 7])

$$\sigma^*_{ij} = \psi'_{ij} + (\sigma_{ij} - p^{\mathrm{g}}\delta_{ij})\,; \quad (\sigma_{ij} - p^{\mathrm{g}}\delta_{ij}) = \sigma^*_{ij} - \psi'_{ij}. \tag{20}$$

A more general total stress measure concerns the expression with respect to the background atmospheric air stress p^{b}, leading with (20) to

$$\left(\sigma_{ij} - p^{\mathrm{b}}\delta_{ij}\right) = \sigma^*_{ij} - \psi'_{ij} + \left(p^{\mathrm{g}} - p^{\mathrm{b}}\right)\delta_{ij}. \tag{21}$$

To further clarify this definition of the intergranular stress (21) for the pendular and funicular saturation phases, it is compared to the definition of the stress contributions for full saturation, namely

$$\sigma_{ij} = \sigma^*_{ij} + p^{\mathrm{w}}\,\delta_{ij} \tag{22}$$

in which p^{w} is the pore fluid stress for full saturation. To this end, first (22) is repeated while subtracting from the terms on both sides of the equal sign the background isotropic atmospheric air stress $p^{\mathrm{b}}\delta_{ij}$ at the considered depth in the ground (see (19)), leading to

$$\left(\sigma_{ij} - p^{\mathrm{b}}\,\delta_{ij}\right) = \sigma^*_{ij} + \left(p^{\mathrm{w}} - p^{\mathrm{b}}\right)\,\delta_{ij}. \tag{23}$$

Then from the comparison of the right side terms of (21) and (23) follows, that the quantity $(p^{\mathrm{w}} - p^{\mathrm{b}})\delta_{ij}$ for the saturated case changes to $-\psi'_{ij} + (p^{\mathrm{w}} - p^{\mathrm{b}})\delta_{ij}$ for the pendular and funicular saturation phases, thus

$$\left(p^{\mathrm{w}} - p^{\mathrm{b}}\right)\,\delta_{ij} \quad \overset{\text{unsaturation}}{\Rightarrow} \quad -\psi'_{ij} + \left(p^{\mathrm{g}} - p^{\mathrm{b}}\right)\delta_{ij}. \tag{24}$$

Multiplication of all terms of (19) by δ_{ij} and substitution of its last right side term in (24) gives for the change from the saturated case to the pendular and funicular saturation phases

$$\left(p^{\mathrm{w}} - p^{\mathrm{b}}\right)\,\delta_{ij} \quad \overset{\text{unsaturation}}{\Rightarrow} \quad -\psi'_{ij} - \psi\,\delta_{ij} + \left(p^{\mathrm{w}} - p^{\mathrm{b}}\right)\delta_{ij}, \tag{25}$$

from which follows that the pore fluid stress p^{w} for the full saturation phase is replaced by

$$p^{\mathrm{w}}\delta_{ij} \quad \overset{\text{unsaturation}}{\Rightarrow} \quad -\psi'_{ij} - \psi\,\delta_{ij} + p^{\mathrm{w}}\delta_{ij} = -\psi'_{ij} + p^{\mathrm{g}}\delta_{ij} \tag{26}$$

in which the right side term has been obtained after substituting (3). Consequently, in the expression of the intergranular stress σ^* (22) and (23) for full saturation, the pore fluid stress p^{w} changes for both funicular and pendular saturation to the following expression in order to obtain the corresponding intergranular stress σ^* as expressed by (21), namely

$$p^{\mathrm{w}} \quad \overset{\text{unsaturation}}{\Rightarrow} \quad -\frac{\psi'_{ij}\delta_{ij}}{3} + p^{\mathrm{g}}. \tag{27}$$

When approaching the completely dry state $S^{\mathrm{w}} \downarrow 0$ of a cohesionless granular material the suction-induced intergranular stress approaches zero, thus $\psi'_{ij}\delta_{ij} \downarrow 0$. In that case from (27) follows that the pore gas stress p^{g} replaces the pore water stress p^{w}, as could be expected.

6 Specific Definitions for the Insular Saturation Phase

For insular saturation the water phase is continuous and the air phase occurs in the form of entrapped gas bubbles. In this particular case the local capillary pore suction $\psi = p^{\mathrm{w}} - p^{\mathrm{g}}$ according to (3) of the gas bubbles needs to be replaced by a more global measure of the pore suction. Instead of the pore gas stress p^{g} in the entrapped gas bubbles another, at this stage of the derivation yet -unknown, pore stress p^{x}, is to be defined such that the transitions of both the saturation S^{w} and the intergranular stress σ^*_{ij} between full and insular saturation will be smooth. To this end the global pore suction measure ψ^{x}, replacing the capillary suction ψ, is introduced as

$$\psi^{\mathrm{x}} = p^{\mathrm{w}} - p^{\mathrm{x}}. \tag{28}$$

This expression implies that for insular saturation both the saturation S^{w} and the suction-induced intergranular stress ψ'_{ij} are amongst others function of ψ^{x} rather than of ψ.

For the insular saturation phase with entrapped gas bubbles the pore suction-induced part ψ'_{ij} of the intergranular stress σ^*_{ij} cannot depend on the gas stress p^{g} occurring in the gas bubbles. In fact, due to equilibrium the combined effect on particles of the gas stress p^{g} in the gas bubbles and the surface tension σ^{s} of the gas–water interface of the bubbles is identical to that of the pore water stress p^{w} in the continuous water phase. Consequently, gas bubbles adhered to the particle surface exert practically the same force on that surface, as the pore water would do. Therefore for the insular case the total intergranular stress σ^*_{ij} could be expressed with respect to any global gas stress measure p^{x}. This notion results in the following expression for the total intergranular stress σ^*_{ij}, namely

$$\sigma^*_{ij} = \psi'_{ij} + (\sigma_{ij} - p^{\mathrm{x}}\delta_{ij})\,; \quad (\sigma_{ij} - p^{\mathrm{x}}\delta_{ij}) = \sigma^*_{ij} - \psi'_{ij}. \tag{29}$$

To determine this pore gas stress p^{x} in (28) and (29) on the basis of a smooth transition of the intergranular stress σ^* from insular towards full saturation, thus $S^{\mathrm{w}} \uparrow 1$, the intergranular stress σ^* for the insular saturation phase according to (29) is compared to the definition according to (23) for full saturation, namely

$$\sigma^*_{ij} = -\left(p^{\mathrm{w}} - p^{\mathrm{b}}\right)\,\delta_{ij} + \left(\sigma_{ij} - p^{\mathrm{b}}\,\delta_{ij}\right). \tag{30}$$

This comparison shows that $(p^{\mathrm{w}} - p^{\mathrm{g}})\delta_{ij}$ for the saturated case would change to $-\psi'_{ij}$ for insular saturation, thus

$$\left(p^{\mathrm{w}} - p^{\mathrm{b}}\right)\,\delta_{ij} \quad \overset{\text{unsaturation}}{\Rightarrow} \quad -\psi'_{ij}, \tag{31}$$

if p^{x} would be selected equal to the background pore gas stress p^{b}, thus $p^{\mathrm{x}} = p^{\mathrm{b}}$. For a smooth transition from the insular state to full saturation, it is also required that $\psi'_p \approx -\psi^{\mathrm{x}}$, when approaching full saturation $S^{\mathrm{w}} \uparrow 1$, which is

consistent with the illustration in Fig. 4. This condition is expressed by

$$\lim_{S^{\mathrm{w}}\uparrow 1} \psi'_{ij} = -\psi^{\mathrm{x}}\,\delta_{ij}. \tag{32}$$

Substitution of (32) in (31) gives

$$\left(p^{\mathrm{w}} - p^{\mathrm{b}}\right)\,\delta_{ij} \quad \overset{\text{unsaturation: } S^{\mathrm{w}}\uparrow 1}{\Rightarrow} \quad \psi^{\mathrm{x}}\delta_{ij} = \left(p^{\mathrm{w}} - p^{\mathrm{x}}\right)\delta_{ij}, \tag{33}$$

from which also follows for insular saturation, that

$$p^{\mathrm{x}} = p^{\mathrm{b}} \quad \text{and} \quad \psi^{\mathrm{b}} = p^{\mathrm{w}} - p^{\mathrm{b}} \tag{34}$$

in which ψ^{b} is the resulting pore suction measure, replacing the capillary suction ψ for this insular case, which was provisionally indicated earlier in (5).

The intergranular stress σ^* for the pendular and funicular cases according to (21) reads

$$\sigma^*_{ij}\big|^{\text{funicular}} = \psi'_{ij} - \left(p^{\mathrm{g}} - p^{\mathrm{b}}\right)\delta_{ij} + \left(\sigma_{ij} - p^{\mathrm{b}}\delta_{ij}\right). \tag{35}$$

For the insular saturation phase the expression for the intergranular stress according to (29), after substituting (34), thus for $p^{\mathrm{x}} = p^{\mathrm{b}}$, becomes

$$\sigma^*_{ij}\big|^{\text{insular}} = \psi'_{ij} + \left(\sigma_{ij} - p^{\mathrm{b}}\delta_{ij}\right). \tag{36}$$

Subtracting (35) from (36) gives for the change of intergranular stress at the transition between insular and funicular saturation

$$\Delta\sigma^*_{ij} = \sigma^*_{ij}\big|^{\text{insular}} - \sigma^*_{ij}\big|^{\text{funicular}} = \left(p^{\mathrm{g}} - p^{\mathrm{b}}\right)\delta_{ij}. \tag{37}$$

This clarifies that due to the definitions of the pore gas stress at the transition from the funicular to the insular saturation phase, the intergranular stress σ^* changes incrementally according to (37).

On the basis of (31) and (34) the pore fluid stress p^{w} for the full saturation phase is for the insular saturation phase replaced by

$$p^{\mathrm{w}} \quad \overset{\text{unsaturation}}{\Rightarrow} \quad -\frac{\psi'_{ij}\delta_{ij}}{3} + p^{\mathrm{b}}. \tag{38}$$

The measured unsaturated soil behaviour of the kind illustrated in Figs. 1 and 4 will not be affected by the change of definition from capillary pore suction $\psi = p^{\mathrm{w}} - p^{\mathrm{g}}$, according to (3) for the pendular and funicular phases, to the background pore suction ψ^{b} (34) for the insular phase, under the following condition for the transition between the insular and funicular states, namely

$$\text{if} \quad p^{\mathrm{g}} = p^{\mathrm{b}} \quad \text{then} \quad \psi^{\mathrm{b}} = \psi, \tag{39}$$

which is usually satisfied in laboratory experiments to measure soil behaviour.

7 Combined Definitions of Intergranular Stress for all Saturation Phases

The main differences between the above-mentioned definitions concern those of the "intergranular stress" σ^*, defined by (21) for the pendular and funicular saturation phases and (29) with $p^{\mathrm{x}} = p^{\mathrm{b}}$, according to (34), for the insular saturation phase. Consequently, for all unsaturated phases the following general expression of the "intergranular stress" σ^* suffices

$$\sigma^*_{kl} = \sigma_{kl} - p^{\mathrm{wx}}_{kl}, \tag{40}$$

which is similar in form of expression (22) for the saturated case. In (40) the following three cases are distinguished, namely

- For the saturated case with the pore water stress p^{w} (22) gives

$$p^{\mathrm{wx}}_{kl} = p^{\mathrm{w}}\delta_{kl}. \tag{41}$$

- For all unsaturated phases

$$p^{\mathrm{wx}}_{kl} = -\psi'_{kl} + p^{\mathrm{x}}\delta_{kl}. \tag{42}$$

  in which the air stress p^{x} and suction-induced intergranular stress ψ'_{kl} are defined by
- For the pendular and funicular phases, in accordance with (27) and (16), where p^{g} is the local pore gas stress in the continuous air phase

$$p^{\mathrm{x}} = p^{\mathrm{g}}; \quad \psi'_{kl} = f\left\{p^{\mathrm{w}} - p^{\mathrm{g}}, A_{ij,\ldots}\right\}. \tag{43a}$$

- For the insular phase, in accordance with (34), (38) and (31), where p^{b} is the background pore air stress at the considered depth in the ground (19) in equilibrium with the atmospheric air

$$p^{\mathrm{x}} = p^{\mathrm{b}}; \quad \psi'_{kl} = -\left(p^{\mathrm{w}} - p^{\mathrm{b}}\right)\delta_{kl}. \tag{43b}$$

8 Rate Forms of Stress–Strain Relations

For the fully saturated case the strain rate $\partial\varepsilon_{ij}$ of the soil skeleton is related to both the Jaumann rates of the intergranular stress $\partial\sigma^{\mathrm{J}*}_{ij}$ and the pore fluid stress ∂p^{w} and the Jaumann effective stress rate $\partial\sigma^{\mathrm{J}'}{}_{ij}$ [2] by

$$\partial\varepsilon_{ij} = \mathrm{D}^{-1}_{ijkl}\,\partial\sigma^{\mathrm{J}*}_{kl} + \frac{\delta_{ij}\,\partial p^{\mathrm{w}}}{3\,K^{\mathrm{sf}}} = \mathrm{D}^{-1}_{ijkl}\,\partial\sigma^{\mathrm{J}'}_{kl} \tag{44}$$

in which D^{-1}_{ijkl} is the inverse of the tangent elasto-plastic stress–strain matrix of the soil skeleton and K^{sf} concerns the bulk stiffness of the mineral as encountered by the pore fluid stress.

For the above-mentioned unsaturated phases, in the expression of the strain rate $\partial\varepsilon_{ij}$ of the soil skeleton for the saturated phase according to (44) the dependence on the rate of the pore fluid stress ∂p^{w} is replaced for all unsaturated phases in accordance with (42) and (43) by

$$\partial\varepsilon_{ij} = \mathrm{D}^{-1}_{ijkl}\,\partial\sigma^{\mathrm{J}*}_{kl} + \frac{\delta_{ij}}{3\,K^{\mathrm{sf}}}\left(-\frac{\partial\psi'_{kl}\,\delta_{kl}}{3} + \partial p^{\mathrm{x}}\right) = \mathrm{D}^{-1}_{ijkl}\,\partial\sigma^{\mathrm{J}'}_{kl} \tag{45}$$

in which (43) can be substituted when the actual saturation phase is known. Premultiplication of (45) by D_{mnij} and substitution of the tangent bulk stiffness of the soil skeleton $K^{\mathrm{T}} = \delta_{mn}\mathrm{D}_{mnij}\delta_{ij}/9$ results in the following expression of the Jaumann rate of the intergranular stress

$$\partial\sigma^{\mathrm{J}*}_{mn} = \mathrm{D}_{mnkl}\,\partial\varepsilon_{kl} - \delta_{mn}\frac{K^{\mathrm{T}}}{K^{\mathrm{sf}}}\left(-\frac{\partial\psi'_{kl}\,\delta_{kl}}{3} + \partial p^{\mathrm{x}}\right) \tag{46}$$

in which the air stress p^{x} depends on the saturation phase as expressed by (41), (42) or (43).

9 Conclusions

For unsaturated granular materials the physical background and anticipated relations between the water saturation, pore water suction, anisotropic fabric tensor, intergranular stress tensor and pore gas stress are formulated, taking account of observed behaviour and published fundamental analyses. It is shown that the role of the pore gas stress in the definition of the suction-induced intergranular stress σ^* changes from the funicular saturation phase (35) to the insular saturation phase (36). This implies the occurrence of an incremental change of the intergranular stress (37) at the transition between the funicular and insular saturation phases. Finally the effect of the changing role of the pore gas stress for the various saturation phases on the rate form of the effective stress–strain relation of a soil skeleton is clarified.

References

1. Bear J (1972) Dynamics of fluids in porous media, New York, Elsevier
2. Biot MA (1956) General solutions of the equations of elasticity and consolidation for a porous medium, J. Appl. Mech., Tr. ASME, 91–96
3. Edlefsen NE, Anderson ABC (1943) The thermodynamics of soil moisture, Hilgardia, vol. 16, 31–299
4. Genuchten M Th van (1980) A closed form equation for predicting the hydraulic conductivity of unsaturated soils, Soil Sci. Soc. Am. J., vol. 44, 892–898
5. Li XS (2003) Effective stress in unsaturated soil: A microstructural analysis. Géotechnique, vol. 53(2), 273–277

6. Molenkamp F, Nazemi AH (2003a) Interactions between two rough spheres, water bridge and water vapour, Géotechnique, vol. 53(2), 255–264
7. Molenkamp F, Nazemi AH (2003b) Micromechanical considerations of unsaturated pyramidal packing, Géotechnique, vol. 53(2), 195–206
8. Taylor DW (1948) Fundamentals of soil mechanics, Wiley, New York
9. Thornton C (2000) Numerical simulations of deviatoric shear deformation of granular media, Géotechnique, vol. 50(1), 43–53

Progress in Binary Medium Modeling of Geological Materials

Z.-J. Shen

Department of Hydraulic Engineering, Tsinghua University, Beijing, China
zjshen@mail.tsinghua.edu.cn

In this study the mechanism of breakage of structural geological materials under different confining stresses was investigated. Four kinds of failure modes were distinguished: bulging rupture, shearing rupture, shearing crushing, and compression crushing. The basic properties of the mechanical behavior were summarized as elastic deformation, plastic yielding, and brittle rupture, which in other terms can be represented by springs, sliders, and bonded bars, respectively. Based on these assumptions, the geological materials were conceptualized as binary mediums consisting of structural blocks and broken cells, which were named as the bonding element and frictional element, respectively. By assuming that the bonding element was the ideal elasto-brittle body and the frictional element was the elasto-plastic body, and by using the homogenization theory of heterogeneous materials, the stress–strain relations were derived in an integrated form and in an incremental form according to the deformation theory of plasticity and the flow theory of plasticity. In these equations two sets of parameters are included, i.e., breakage coefficients and local stress coefficients. They can be determined by using curve fitting method with experimental data. Equations in the integrated form have been used in some engineering problems, such as the stability of cut slope and wetting deformation of loess foundation.

1 Introduction

R. Hill was probably the earliest pioneer in the study of the stress–strain relationship of a heterogeneous body which consists of two elastic mediums of different moduli [1]. He examined a representative element of such a body with the volume $\nu_1+\nu_2$, where ν_1 and ν_2 are the volumes occupied by the first and second mediums, respectively. Based on the volumetric averaging concept

$$\{\overline{\sigma}\} = (\nu_1\{\overline{\sigma}\}_1 + \nu_2\{\overline{\sigma}\}_2)/(\nu_1+\nu_2), \tag{1a}$$

$$\{\overline{\varepsilon}\} = (\nu_1\{\overline{\varepsilon}\}_1 + \nu_2\{\overline{\varepsilon}\}_2)/(\nu_1+\nu_2) \tag{1b}$$

the following stress–strain relationship can be obtained:

$$\{\overline{\sigma}\} = [D]\{\overline{\varepsilon}\}; [D] = \nu_1[D]_1[A]_1 + \nu_2[D]_2[A]_2, \tag{2a}$$

$$\{\overline{\varepsilon}\} = [D]^{-1}\{\overline{\sigma}\}; [D]^{-1} = \nu_1[D]_1^{-1}{}_1[C]_1 + \nu_2[D]_2^{-1}[C]_2, \tag{2b}$$

where $\overline{\varepsilon}$ and $\overline{\sigma}$ are the averaged strain and stress in the representative element volume. $[D]_1$ and $[D]_2$ are the rigidity matrixes of the two mediums. $[A]_1$ and $[A]_2$ ($[C]_1$ and $[C]_2$) are the local strain (stress) coefficients for the two components, respectively, i.e., $\{\overline{\varepsilon}\}_1 = [A]_1\{\overline{\varepsilon}\}; \{\overline{\varepsilon}\}_2 = [A]_2\{\overline{\varepsilon}\}(\{\overline{\sigma}\}_1 = [C]_1\{\overline{\sigma}\}; \{\overline{\sigma}\}_2 = [C]_2\{\overline{\sigma}\})$, where $\{\overline{\varepsilon}\}_1$ and $\{\overline{\varepsilon}\}_2(\{\overline{\sigma}\}_1$ and $\{\overline{\sigma}\}_2)$ again are the averaged strain (stress) for the medium 1 and medium 2.

In recent years, the homogenization theory of heterogeneous materials has been widely used in different fields of solid mechanics for different materials, such as alloys, composite materials, and concrete. Wang et al. also used the theory to derive a similar equation for composite soils [2]. In these studies only the deformation properties of material were investigated. As for the failure process, damage and fracture mechanics are still the main theories used in predicting the development of micro or macrocracks in homogeneous bodies. In these latter studies, a microelement is nullified if it is broken. However, unlike metals and concrete with which the structures usually work in extension or bending states, structures of geological material generally work in a shear state and a microelement still has frictional resistance after its destruction. Therefore, a concept of transformation must be introduced, instead of the null, for geological materials. Based on the homogenization theory and the transformation concept, the author has recently proposed a new kind of model – binary medium model for geological materials. More than a decade ago when the author introduced damage mechanics into the study of soil mechanics, the concept of microelement transformation had already been used, and a so-called duplex-spring model was proposed [3]. In that model, however, the difference of strain levels in the two media was ignored, i.e., $[A]_1 = [A]_2 = [I]$ was assumed in (2a), where $[I]$ is unit tensor. This means that we had adopted the so-called Voigt assumption as explained in Hill's paper , or a parallel mode as shown in Fig. 1a was used [4]. However, in the newly proposed binary medium model, this assumption is abandoned. In this paper the main achievements in the development of this new model will be introduced.

2 Idealization of Structured Geological Materials

Although the structure of rock bodies has been recognized since the 1960s, the concept of soil structure was advanced much earlier [5]. It has also been well known for a long time that the cohesive resistance and frictional resistance are not mobilized simultaneously, with the latter coming into effect only after a definite amount of deformation has been accumulated which is often accompanied with strain softening due to the loss of cohesive resistance. Therefore,

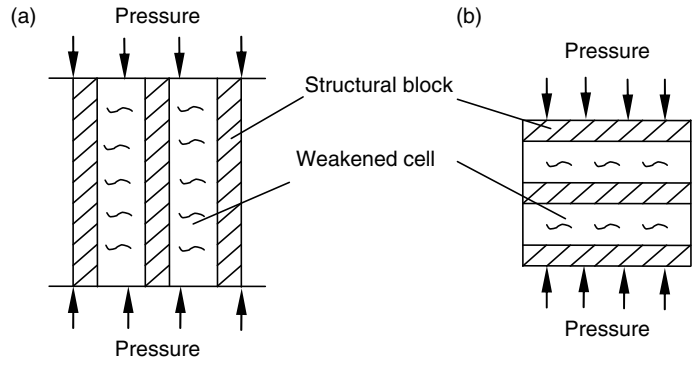

Fig. 1. Load transfer of binary medium material. (**a**) Parallel mode (**b**) string mode

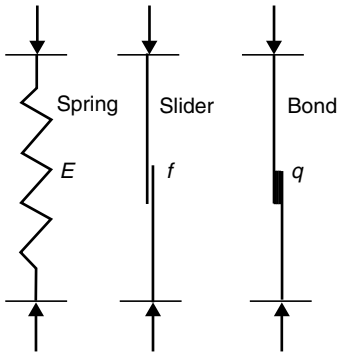

Fig. 2. Basic elements

structural geological materials must be characterized with three properties: elastic deformation, plastic yielding, and brittle cracking. The corresponding three elements are the spring, slider, and bonded bar , which are controlled by modulus E, yield strength f, and break strength q, respectively as shown in Fig. 2. By combining them in different ways, various modes of strain hardening and softening behaviors of samples can be simulated.

Based on these understandings, structural geological materials can be idealized as a binary medium consisting of a bonding element and a frictional element as shown in Fig. 3. The former represents structural bodies, bonding blocks (body element), or rock bridges (face element), while the later represents broken cells, softening bands (body element), or joints and cracks (face element). Accordingly, the process of the failure of geological materials can be characterized as the breakage of a bonding element and its transformation into a frictional element.

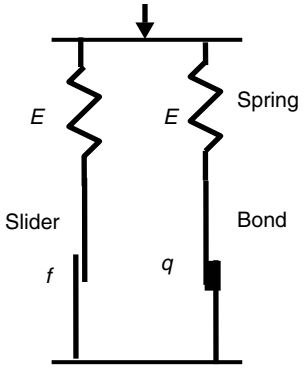

Fig. 3. Binary medium model

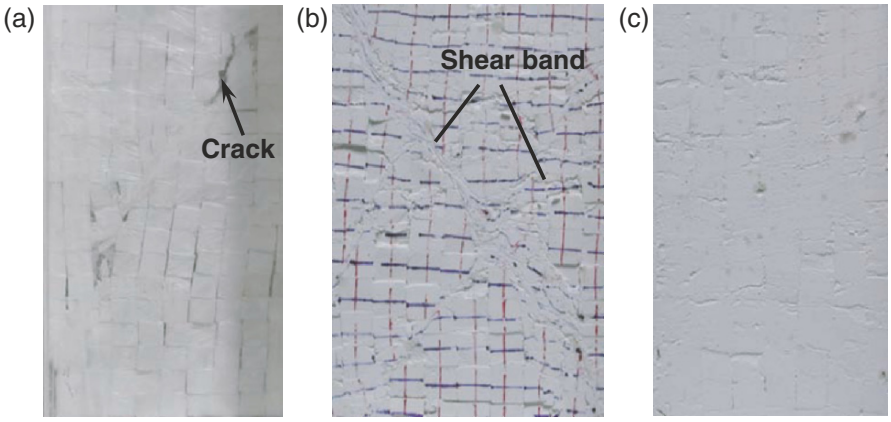

Fig. 4. Failure modes of cubic piled samples. (**a**) 0.03 Mpa (**b**) 0.15 Mpa (**c**) 0.45 Mpa

3 Mechanism of Breakage

The binary medium model is a macroscopic model for practical use. Its key point is to carry out microscopic study on the mechanism of the breakage of bonding blocks. To this aim, samples piled up from small gypsum blocks in cylindrical or rectangular shape have been used for biaxial tests [6]. Figure 4 shows three different failure modes observed in rectangular block samples under different confining stresses. Under low confining stress of 30 kPa, the block columns began to bulge, with cracks opening (see Fig. 4a). Under a moderate lateral stress of 150 kPa, many blocks were broken down, forming two shear bands crossing each other (see Fig. 4b). Finally, when the lateral stress was increased to 450 kPa, almost all of the blocks were broken, as shown in Fig. 4c. Figure 5 shows two breakage modes which were observed in the cylindrical

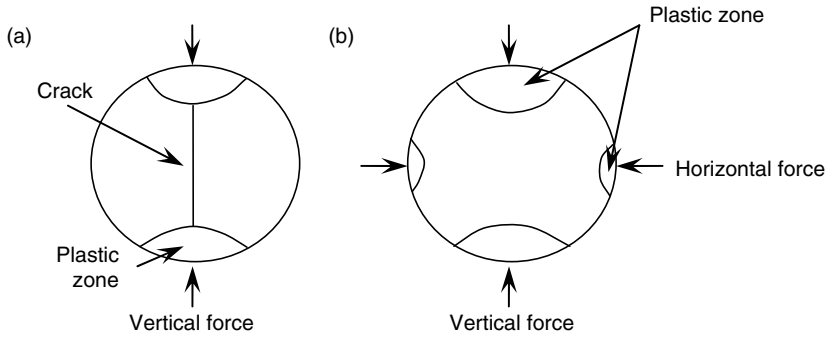

Fig. 5. Failure modes of cylindrical blocks. (**a**) Rupture after local yielding (**b**) local crushing

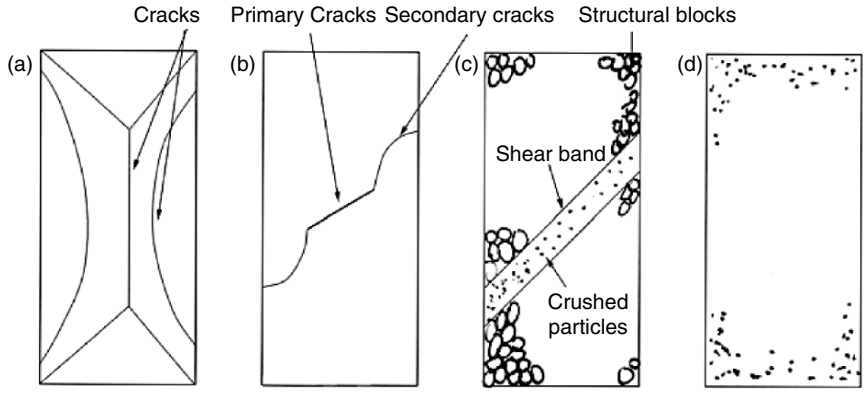

Fig. 6. Failure modes of rock and soil samples. (**a**) Bulging rupture (**b**) shearing rupture (**c**) shearing crushing (**d**) compression crushing

block samples under low and high confining stress. Figure 5a shows a block under low stress that is cracked at the center with two small plastic zones at the contact area. But, as shown in Fig. 5b, the type of block breakage under high confining stress was plastic yielding at four contact areas. Based on these findings and considering the shear rupture mode of rock samples of high strength, we can distinguish two types of breakage modes: rupture and crushing. Furthermore, by linking the confining stress to the compression strength of samples, the following four failure modes can be proposed: (a) bulging rupture, (b) shearing rupture, (c) shearing crushing, and (d) compression crushing, as shown in Fig. 6.

Note that we have also carried out some numerical simulations of the failure process of the samples. Figure 7 presents an example of a numerical simulation, and shows three typical stages of failure of a structural clay sample. In the first stage, the sample deformed elastically, as shown in Fig. 7a. When

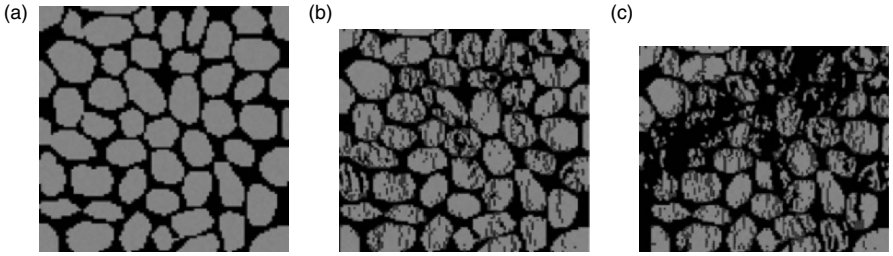

Fig. 7. Numerical simulation of failure process of a structural clay sample. (**a**) Elastic deformation (**b**) cracking and rupture of blocks (white bodies) (**c**) formation of shear bands (black area)

the load was increased further, cracks and ruptures appeared in some blocks (see Fig. 7b). Finally, much of the blocks were broken within some areas, i.e., a shear band formed, as shown in Fig. 7c.

Based on the above findings, we have come to the conclusion that in the process from deformation to failure, both rupture and crushing of structural blocks can take place and also both brittle cracking and plastic yielding exist. Therefore, it seems unreasonable to solely use a single theory or method, such as fracture mechanics or damage mechanics, to solve the complicated phenomena which is involved in the failure of geological materials. We shall call the failure process that includes both rupture and crushing the *breakage process* and we think it is necessary to establish a new branch of geomechanics: *breakage mechanics*. Breakage mechanics can be established based on the binary medium model and has the following salient characteristics in comparison with the current theories:

(a) The bonding element is an elasto-brittle medium, while the frictional element is an elasto-plastic medium. They have totally different natures.
(b) The bonding element becomes frictional element after its breakage, and the simple nullification of them is abandoned.
(c) Both of the elements can be either a body element or a face element.
(d) The key point of examination of the change of a sample's internal structure under loading moves from expansion of the empty area (cracks, voids) to the breakage of the concrete body (bonding blocks, rock bridges).

4 Deformation Theory of Breakage Mechanics

4.1 General Formulation

If we assume the existence of an unique relationship between total stress and total strain for frictional elements, then (2) is still valid but $[D]$ must be regarded as the secant modulus. Let us define $\lambda_{\mathrm{v}} = \nu_2/(\nu_1 + \nu_2)$ as volumetric breakage coefficient. Then (2) becomes

$$\{\overline{\sigma}\} = (1-\lambda_\nu)\{\overline{\sigma}\}_1 + \lambda_\nu\{\overline{\sigma}\}_2 \tag{3a}$$

and

$$\{\overline{\varepsilon}\} = (1-\lambda_\nu)\{\overline{\varepsilon}\}_1 + \lambda_\nu\{\overline{\varepsilon}\}_2. \tag{3b}$$

Without loss of generality we can take $\nu_1 + \nu_2 = 1$. Correspondingly, (1a) can be written as

$$\{\overline{\sigma}\} = ((1-\lambda_\nu)[D]_1[A]_1 + \lambda_\nu[D]_2[A]_2)\,\{\overline{\varepsilon}\}, \tag{4}$$

In isotropic cases $[A]_1$ and $[A]_2$ are scalar and can be written as a_1 and a_2. Then using $\overline{\varepsilon} = (1-\lambda_\nu)\overline{\varepsilon}_1 + \lambda_\nu\overline{\varepsilon}_2$, we can obtain $(1-\lambda_\nu)a_1 = 1-\lambda_\nu a_2$. By substituting them into (4) we obtain

$$\{\overline{\sigma}\} = ((1-b)[D]_1 + b[D]_2)\,\{\overline{\varepsilon}\}, \tag{5}$$

If we define $\{\sigma_\mathrm{i}\} = [D]_1\{\overline{\varepsilon}\}$as bonding stress and $\{\sigma_\mathrm{f}\} = [D]_2\{\overline{\varepsilon}\}$ as frictional stress, then (5) can be further simplified as

$$\{\overline{\sigma}\} = (1-b)\{\sigma_\mathrm{i}\} + b\{\sigma_\mathrm{f}\}, \tag{6}$$

where $b = 1-(1-\lambda_\nu)a_1$ is called the breakage parameter hereafter. It is evident from the failure mechanism shown in Fig. 6 that when a shear band forms the abovementioned single volumetric averaging technique may fail to predict the actual behavior of geological materials. For example, in a mudflow the sliding body may contain a large amount of stones, which may contribute nothing to the slope stability. Therefore, it seems to be necessary in this case to use both volumetric averaging and face averaging techniques.

Let the stress and strain tensors be decomposed into a spherical part, and deviatoric part, respectively. Correspondingly, in parallel with the volumetric breakage coefficient λ_ν, a new facial breakage coefficient λ_s must be introduced. In addition, instead of a pair of local strain matrixes $[A]_1$ and $[A]_2$, two pairs of scalar quantity $a_{\mathrm{s}1}$ and $a_{\mathrm{s}2}$ as well as $a_{\nu 1}$ and $a_{\nu 2}$ will be employed. The averaging equations can be then expressed as follows:

$$\sigma_\mathrm{m} = (1-\lambda_\nu)\sigma_{\mathrm{m}1} + \lambda_\nu\sigma_{\mathrm{m}2} \tag{7a}$$

$$\varepsilon_\nu = (1-\lambda_\nu)\varepsilon_{\nu 1} + \lambda_\nu\varepsilon_{\nu 2} \tag{7b}$$

$$\{s\} = (1-\lambda_\mathrm{s})\{s\}_1 + \lambda_\mathrm{s}\{s\}_2 \tag{8a}$$

$$\{e\} = (1-\lambda_\mathrm{s})\{e\}_1 + \lambda_\mathrm{s}\{e\}_2 \tag{8b}$$

where $\{s\} = \{\sigma\} - \sigma_\mathrm{m}\{\mathrm{I}\}, \{e\} = \{\varepsilon\} - (1/3)\varepsilon_\nu\{\mathrm{I}\}, \{\mathrm{I}\} = \{1\,1\,1\,0\,0\,0\}^\mathrm{T}$. Similarly, the averaging stress–strain relationship can be written as

$$\overline{\sigma}_\mathrm{m} = [(1-b_\nu)K_1 + b_\nu K_2]\overline{\varepsilon}_\nu, \tag{9a}$$

$$\overline{\sigma}_\mathrm{s} = [(1-b_\mathrm{s})G_1 + b_\mathrm{s}G_2]\overline{\varepsilon}_\mathrm{s}, \tag{9b}$$

where $\overline{\sigma}_{\mathrm{m}}$ and $\overline{\sigma}_{\mathrm{s}}$ are the average mean compression stress, and average generalized shear stress, respectively. $\overline{\varepsilon}_{\nu}$ and $\overline{\varepsilon}_{\mathrm{s}}$ are the average volumetric strain and average shear strain, respectively. K_1 and K_2 (G_1 and G_2) are the bulk (shear) moduli for two elements. $b_{\nu} = 1-(1-\lambda_{\nu})a_{\nu 1}$ and $b_{\mathrm{s}} = 1-(1-\lambda_{\mathrm{s}})a_{\mathrm{s}1}$ are two breakage parameters.

In the following we shall call (6) the *single parameter model*, and (9) the *double parameter model*. The corresponding parameter b or parameters b_{ν} and b_{s} are internal variables. They can be determined by a "trial and error" method in a way similar to the determination of hardening parameter in the theory of plasticity.

4.2 An Ideal Model

In this model the assumption of an ideal frictional material will be used, as shown in Fig. 8 [7]. Let E_{i} be the Young's modulus for a bonding element. The Young's modulus for a frictional element can be calculated by $E_{\mathrm{f}} = k\sigma_{3\mathrm{f}}$, where k is a proportional ratio and $\sigma_{3\mathrm{f}}$ is the minor principal stress of the frictional element. Then (4) becomes:

$$\{\overline{\sigma}\} = ((1-b)E_{\mathrm{i}}[P]_{\mathrm{i}} + bk\sigma_{3\mathrm{f}}[P]_{\mathrm{f}})\,\{\overline{\varepsilon}\}, \tag{10}$$

where $[P]_{\mathrm{i}}$ and $[P]_{\mathrm{f}}$ are matrixes only related to Poisson's ratio. The incremental form of this equation will be

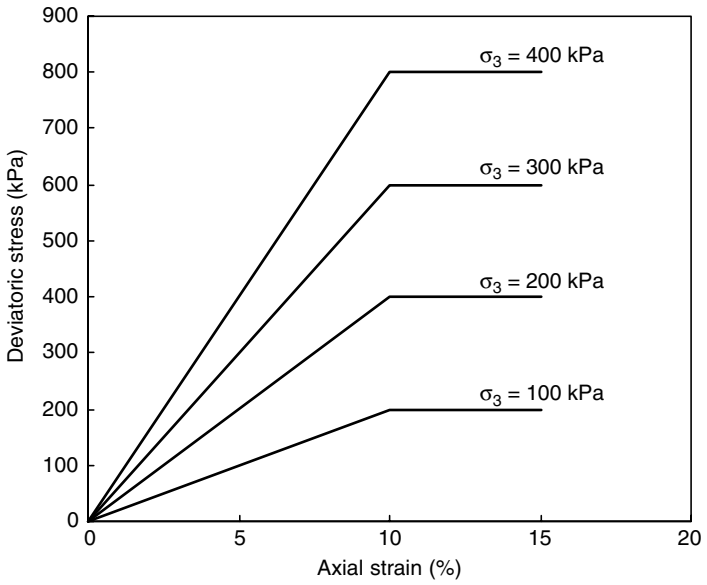

Fig. 8. Ideal frictional material

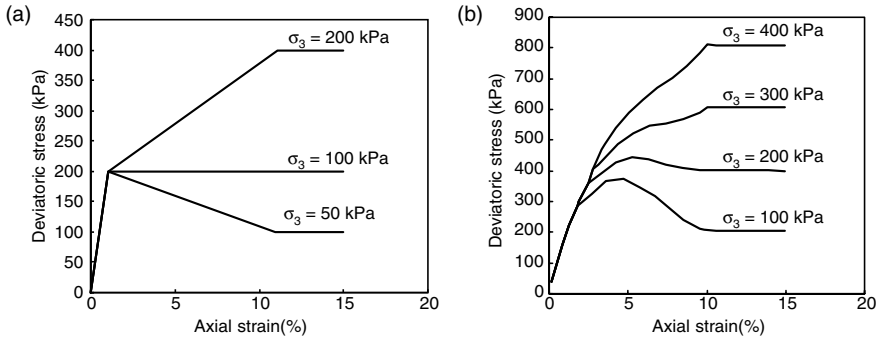

Fig. 9. Stress–strain curves for an ideal geological material obtained by using different evolution laws of parameter b. (**a**) Parabolic law (**b**) hyperbolic law

$$\{\Delta\overline{\sigma}\} = ((1-b)E_{\mathrm{i}}[P]_{\mathrm{i}} + bk\sigma_{3\mathrm{f}}[P]_{\mathrm{f}})\{\Delta\overline{\varepsilon}\} - (\{\sigma_{\mathrm{i}}\} - \{\sigma_{\mathrm{f}}\})\left\{\frac{\partial b}{\partial\widehat{\varepsilon}}\right\}\left\{\frac{\partial\widehat{\varepsilon}}{\partial\varepsilon}\right\}\{\Delta\varepsilon\}\,. \tag{11}$$

For simplicity, let the major principal strain ε_1 be the variable controlling the evolution of breakage parameter b. When a parabolic function or a hyperbolic function between b and ε_1 is used, the computed stress–strain curves under various degree of confining stress are as shown in Fig. 9a, b [7].

4.3 A Model for Over consolidated Clay

Failure in over consolidated clay often happens along a weak band, indicating that it is necessary to use the double parameter assumption. Again the bonding element is assumed to be an elasto-brittle body, but its constrained modulus decreases with the increase of the over consolidation ratio [8]:

$$K_{\mathrm{i}} = \frac{M_{\mathrm{m}}}{R_{\mathrm{c}}^{n}}\frac{1+\nu}{3(1-\nu)}; G_{\mathrm{i}} = \frac{M_{\mathrm{m}}}{R_{\mathrm{c}}^{n}}\frac{1-2\nu}{2(1-\nu)}, \tag{12}$$

where $R_{\mathrm{c}} = \sigma_{\mathrm{c\,max}}/\sigma_{\mathrm{c}}$ is the over consolidation ratio, M_{m} is the constrained modulus when the consolidation stress is equal to the historically maximum consolidation stress $\sigma_{\mathrm{c}} = \sigma_{\mathrm{c\,max}}$, n is a model constant, and v is Poisson's ratio. The volumetric strain and shear strain of the friction element are calculated by

$$\varepsilon_{\nu} = c_{\mathrm{c}} \ln\frac{\sigma_{\mathrm{m}}(1+\chi)}{\sigma'_{\mathrm{m0}}} \tag{13a}$$

and

$$\varepsilon_{\mathrm{s}} = \varepsilon_{\nu}\frac{c_{\mathrm{a}}\eta}{\eta_{\mathrm{c}} - \eta}, \tag{13b}$$

where $\eta = \sigma_{\mathrm{s}}/\sigma_{\mathrm{m}}$, $\chi = c_{\mathrm{d}}\eta^{\mathrm{m}}$ and $\sigma'_{\mathrm{m0}} = \sigma_{\mathrm{m0}}/R_{\mathrm{c}}^{n}$. σ_{m0} is a reference stress when the volumetric strain is 0. η_{c} and the other coefficients are model constants.

The two breakage parameters are proposed as

$$b_\nu = 1 - [1 + c_1\varepsilon_\nu] \exp(-c_1\varepsilon_\nu) \tag{14a}$$

and

$$b_\mathrm{s} = 1 - [1 + c_2\varepsilon_\mathrm{s}] \exp(-c_2\varepsilon_\mathrm{s}), \tag{14b}$$

where c_1 and $_{c2}$ are two other constants. The stress–strain relationship is expressed as follows:

$$\Delta\sigma_\mathrm{m} = ((1 - b_\nu)K_\mathrm{i} + b_\nu K_\mathrm{ft})\,\Delta\varepsilon_\nu - (K_\mathrm{i} - K_\mathrm{fs})\,\frac{\partial b_\nu}{\partial\varepsilon_\nu}\Delta\varepsilon_\nu \tag{15a}$$

and

$$\Delta\sigma_\mathrm{s} = ((1 - b_\mathrm{s})G_\mathrm{i} + b_\mathrm{s}G_\mathrm{ft})\,\Delta\varepsilon_\mathrm{s} - (G_\mathrm{i} - G_\mathrm{fs})\,\frac{\partial b_\mathrm{s}}{\partial\varepsilon_\mathrm{s}}\Delta\varepsilon_\mathrm{s}, \tag{15b}$$

where K_ft and G_ft (K_fs and $_{,}G_\mathrm{fs}$) are tangential (secant) moduli obtained from (13) for volumetric and shear deformation. When the deviatoric stress $\Delta\sigma_\mathrm{s}$ is known, its components can be obtained by using the Plandtl–Reuss law.

4.4 A Model for Loess

Loess frequently collapses due to wetting, which gives rise to deformation in a large area. Therefore, in this case the single volumetric averaging technique can be used [9]. The modulus of the bonding element can be calculated by using an equation similar to (12), in which the degree of saturation S_r will be used instead of the over consolidation ratio R_c

$$K_\mathrm{i} = \frac{M_\mathrm{s}}{S_\mathrm{r}^n}\frac{1+\nu}{3(1-\nu)};\; G_\mathrm{i} = \frac{M_\mathrm{s}}{S_\mathrm{r}^n}\frac{1-2\nu}{2(1-\nu)}, \tag{16}$$

where M_S is the constrained modulus of loess at the saturated state. The stress–strain relationship for a frictional element is the same as shown in (13). Taking into account the fact that the bond in the loess usually is quite low, and the bonding blocks can be destroyed not only under shear stress but also under spherical stress, we shall use the major principal strain as the controlling factor of breakage. Hence the evolution law of the breakage parameter can be expressed by

$$b = 1 - [1 + c_\mathrm{b}\varepsilon_1] \exp(-c_\mathrm{b}\varepsilon_1). \tag{17}$$

The corresponding stress–strain relationship in incremental form then becomes

$$\begin{aligned}\Delta\sigma_\mathrm{m} = {} & ((1 - b)K_\mathrm{i} + bK_\mathrm{ft})\,\Delta\varepsilon_\nu \\ & - (K_\mathrm{i} - K_\mathrm{fs})\,\frac{\partial b}{\partial\varepsilon_1}\frac{\partial\varepsilon_1}{\partial\varepsilon_\nu}\Delta\varepsilon_\nu + \frac{\partial\sigma_\mathrm{m}}{\partial S_\mathrm{r}}\Delta S_\mathrm{r},\end{aligned} \tag{18a}$$

$$\begin{aligned}\Delta\sigma_\mathrm{s} = {} & ((1 - b)G_\mathrm{i} + bG_\mathrm{ft})\,\Delta\varepsilon_\mathrm{s} \\ & - (G_\mathrm{i} - G_\mathrm{fs})\,\frac{\partial b}{\partial\varepsilon_1}\frac{\partial\varepsilon_1}{\partial\varepsilon_\mathrm{s}}\Delta\varepsilon_\mathrm{s} + \frac{\partial\sigma_\mathrm{s}}{\partial S_\mathrm{r}}\Delta S_\mathrm{r},\end{aligned} \tag{18b}$$

in which the third term in the right side of each equation represents the effect due to the increase of degree of saturation ΔS_r.

5 Flow Theory of Breakage Mechanics

In this section the flow theory of plasticity will be used for frictional elements. In this case the local strain coefficient must be regarded as an independent internal variable in parallel with the breakage coefficient.

5.1 General Relationships

Let us consider a representative volume element (RVE). Let $\{\sigma\}_1$ and $\{\varepsilon\}_1$ ($\{\sigma\}_2$ and $\{\varepsilon\}_2$) represent the local stress and local strain tensors of the elasto-brittle (elasto-plastic) elements, respectively. Let $\{\sigma\}$ and $\{\varepsilon\}$ be the average stress and average strain of RVE (the top bar is here omitted for simplicity), and let $[D]_1$ and $[D]_2$ represent the elastic modulus tensors of the two elements. In addition, f_2 and g_2 are used to represent the yield function and potential function for elasto-plastic elements. Then the following stress–strain relationships in incremental form can be obtained:

$$\{\Delta\varepsilon\}_1 = [D]_1^{-1}\{\Delta\sigma\}_1, \tag{19a}$$

$$\{\Delta\varepsilon\}_2 = [D]_2^{-1}\{\Delta\sigma\}_2 + \Delta\lambda\frac{\partial g_2}{\partial\{\sigma\}_2}, \tag{19b}$$

where $\Delta\lambda$ is the plastic multiplier. If f_2 is expressed as

$$f_2(\{\sigma\}_2, h(\{\varepsilon^{\mathrm{p}}\})) = 0, \tag{20}$$

where h is the hardening parameter, then (19b) can be rewritten as

$$\{\Delta\varepsilon\}_2 = [D]_2^{-1}\{\Delta\sigma\}_2 + a\frac{\partial g_2}{\partial\{\sigma\}_2}\left\{\frac{\partial f_2}{\partial\{\sigma\}_2}\right\}^{\mathrm{T}}\{\Delta\sigma\}_2, \tag{21}$$

where a is the plastic coefficient defined by

$$a = -(\frac{\partial f_2}{\partial h}\left\{\frac{\partial h}{\partial\{\varepsilon^{\mathrm{p}}\}}\right\}^{\mathrm{T}}\frac{\partial g_2}{\partial\{\sigma\}_2})^{-1}. \tag{22}$$

The volumetric breakage coefficient of the elasto-plastic part can be expressed by the following relationship:

$$\lambda_\nu = f_1(\{\sigma\}_1). \tag{23}$$

In addition, the local stress coefficient $[C]$ can be expressed as

$$\{\sigma\}_1 = [C]\{\sigma\}, \tag{24}$$

where f_1 and $[C]$ are functions to be determined. The methods of their determination will be discussed later.

Hereafter let $\{\sigma\}^0, \{\varepsilon\}^0, \{\sigma\}_1^0, \{\varepsilon\}_1^0, \{\sigma\}_2^0$, and $\{\varepsilon\}_2^0$ represent the initial average stress and strain, and local stress and strain for the first and the second

element, respectively. Let $\{\Delta\sigma\}$, $\{\Delta\varepsilon\}, \{\Delta\sigma\}_1, \{\Delta\varepsilon\}_1, \{\Delta\sigma\}_2$, and $\{\Delta\varepsilon\}_2$ be the corresponding stress increment and strain increment tensors, respectively. Hence $\{\sigma\}^0 + \{\Delta\sigma\}, \{\varepsilon\}^0 + \{\Delta\varepsilon\}, \{\sigma\}_1^0 + \{\Delta\sigma\}_1$, and $\{\varepsilon\}_1^0 + \{\Delta\varepsilon\}_1, \{\sigma\}_2^0 + \{\Delta\sigma\}_2, \{\varepsilon\}_2^0 + \{\Delta\varepsilon\}_2$ represent the corresponding final stress and strain tensors, respectively. The stress–strain relationship will be deduced in two ways.

5.2 Single Parameter Theory

Let λ_ν^0 be the volumetric breakage coefficient at the initial state, $\Delta\lambda_\nu$ its increment and $\lambda_\nu^0 + \Delta\lambda_\nu$ the new breakage coefficient. Substituting the initial quantities and final quantities into (2a) and (2b), we can obtain the following equation, in which the high order terms are omitted:

$$\{\Delta\sigma\} = \{\Delta\sigma\}_1 + \lambda_\nu^0(\{\Delta\sigma\}_2 - \{\Delta\sigma\}_1) + \Delta\lambda_\nu(\{\sigma\}_2^0 - \{\sigma\}_1^0), \tag{25a}$$

$$\{\Delta\varepsilon\} = \{\Delta\varepsilon\}_1 + \lambda_\nu^0(\{\Delta\varepsilon\}_2 - \{\Delta\varepsilon\}_1) + \Delta\lambda_\nu(\{\varepsilon\}_2^0 - \{\varepsilon\}_1^0). \tag{25b}$$

After obtaining $\{\Delta\sigma\}_2$ from (25a), then using $\{\Delta\varepsilon\}_2 = [D]_{\mathrm{ep}}^{-1}\{\Delta\sigma\}_2$, $\{\Delta\varepsilon\}_1 = [D]_1^{-1}\{\Delta\sigma\}_1$ and $\Delta\lambda_\nu = \left\{\frac{\partial f_1}{\partial\{\sigma\}_1}\right\}^{\mathrm{T}}\{\Delta\sigma\}_1$, and using (3) to eliminate $\{\sigma\}_2^0$ and $\{\varepsilon\}_2^0$, (25b) can be rewritten as

$$\begin{aligned}\{\Delta\varepsilon\} = {} & [D]_{\mathrm{ep}}^{-1}\{\Delta\sigma\} - (1-\lambda_\nu^0)([D]_{\mathrm{ep}}^{-1} - [D]_1^{-1})[A]\{\Delta\sigma\} + \frac{1}{\lambda_\nu^0}([D]_{\mathrm{s}}^{-1} \\ & -[D]_{\mathrm{ep}}^{-1} + [D]_{\mathrm{ep}}^{-1}[C] - [D]_1^{-1}[C])\{\sigma\}^0\{B\}[A]\{\Delta\sigma\},\end{aligned} \tag{26}$$

where

$$[D]_{\mathrm{ep}}^{-1} = [D]_2^{-1} + a\frac{\partial g_2}{\partial\{\sigma\}_2}\left\{\frac{\partial f_2}{\partial\{\sigma\}_2}\right\}^{\mathrm{T}}, \tag{27a}$$

$$\{B\} = \frac{\partial f_1}{\partial\{\sigma\}_1}, \tag{27b}$$

$$[A] = \frac{\partial\{\sigma\}_1}{\partial\{\sigma\}} = [C] + \frac{\partial[C]}{\partial\{\sigma\}}\{\sigma\}. \tag{27c}$$

Equation (26) shows that the total increment strain $\{\Delta\varepsilon\}$ can be expressed in three parts. The first part is the deformation when the whole element is occupied by the elasto-plastic body. The second part is the reduction of deformation due to the existence of the elasto-brittle body. The third part is the deformation due to the increase of $\Delta\lambda_\nu$ i.e., due to the breakage of the elasto-brittle microelement.

5.3 Double Parameter Theory

Similarly, let $\Delta\sigma_{\mathrm{m}}, \Delta\sigma_{\mathrm{m1}}, \Delta\sigma_{\mathrm{m2}}, \Delta\varepsilon_{\nu 1}, \Delta\varepsilon_{\nu 1}, \Delta\varepsilon_{\nu 2}; \{\Delta s\}, \{\Delta s\}_1, \{\Delta s\}_2; \{\Delta e\}$, $\{\Delta e\}_1, \{\Delta e\}_2$, and $\Delta\lambda_\nu, \Delta\lambda_{\mathrm{s}}$ be the corresponding incremental quantities of

the stress and strain tensors; the local stress–strain relationships will be

$$\Delta\varepsilon_{\nu 1} = (1/K_1)\Delta\sigma_{\mathrm{m}1}, \tag{28a}$$

$$\{\Delta e\}_1 = (1/(2G_1))\{\Delta s\}_1, \tag{28b}$$

$$\Delta\varepsilon_{\nu 2} = K_2^{-1}\Delta\sigma_{\mathrm{m}2} + a\frac{\partial g_2}{\partial\sigma_{\mathrm{m}2}}\left(\frac{\partial f_2}{\partial\sigma_{\mathrm{m}2}}\Delta\sigma_{\mathrm{m}2} + \left\{\frac{\partial f_2}{\partial\{s\}_2}\right\}^{\mathrm{T}}\{\Delta s\}_2\right), \tag{29a}$$

$$\{\Delta e\}_2 = \frac{1}{2}G_2^{-1}\{\Delta s\}_2 + a\frac{\partial g_2}{\partial\{s\}_2}\left(\frac{\partial f_2}{\partial\sigma_{\mathrm{m}2}}\Delta\sigma_{\mathrm{m}2} + \left\{\frac{\partial f_2}{\partial\{s\}_2}\right\}^{\mathrm{T}}\{\Delta s\}_2\right), \tag{29b}$$

where K_1 and K_2 (G_1 and G_2) are bulk (shear) moduli for the bonding element and frictional element, respectively. Then (23) and (24) for the breakage function and local stress coefficient become, respectively

$$\lambda_\nu = f_\nu(\{\sigma\}_1); \quad \lambda_{\mathrm{s}} = f_{\mathrm{s}}(\{\sigma\}_1). \tag{30}$$

and

$$\sigma_{\mathrm{m}1} = c_{\mathrm{m}}\sigma_{\mathrm{m}}; \quad \{s\} = c_{\mathrm{s}}\{s\}. \tag{31}$$

Using the procedure similar to the above, the following stress–strain relationships can be obtained:

$$\begin{aligned}
\{\Delta\varepsilon\} = {} & \left(\frac{1}{3}[K]_2^{-1} + \frac{1}{3}[P]_{\mathrm{m}}^{-1} + \frac{\lambda_{\mathrm{s}}^0}{\lambda_\nu^0}[Q_{\mathrm{m}}]^{-1}\right)\Delta\sigma_{\mathrm{m}}\{\mathrm{I}\} \\
& + \left(\frac{1}{2}[G]_2^{-1} + [Q_{\mathrm{s}}]^{-1} + \frac{1}{3}\frac{\lambda_\nu^0}{\lambda_{\mathrm{s}}^0}[P_{\mathrm{s}}]^{-1}\right)\{\Delta s\} \\
& -(1-\lambda_\nu^0)\left(\frac{1}{3}[K]_2^{-1} + \frac{1}{3}[P]_{\mathrm{m}}^{-1} - \frac{1}{3}[K]_1^{-1} + \frac{\lambda_{\mathrm{s}}^0}{\lambda_\nu^0}[Q]_{\mathrm{m}}^{-1}\right)A_{\mathrm{m}}\Delta\sigma_{\mathrm{m}}\{\mathrm{I}\} \\
& -(1-\lambda_{\mathrm{s}}^0)\left(\frac{1}{2}[G]_2^{-1} + [Q]_{\mathrm{s}}^{-1} - \frac{1}{2}[G]_1^{-1} + \frac{1}{3}\frac{\lambda_\nu^0}{\lambda_{\mathrm{s}}^0}[P]_{\mathrm{s}}^{-1}\right)A_{\mathrm{s}}\{\Delta s\} \\
& + \frac{1}{\lambda_\nu^0}\left(\frac{1}{3}[K]_{\mathrm{s}}^{-1} - \frac{1}{3}c_{\mathrm{m}}[K]_1^{-1}\right. \\
& \qquad \left. - \left(\frac{1}{3}[K]_2^{-1} + \frac{1}{3}[P]_{\mathrm{m}}^{-1} + \frac{\lambda_{\mathrm{s}}^0}{\lambda_\nu^0}[Q]_{\mathrm{m}}^{-1}\right)(1-c_{\mathrm{m}})\right)\sigma_{\mathrm{m}}\{\mathrm{I}\}\Delta\lambda_\nu \\
& + \frac{1}{\lambda_{\mathrm{s}}^0}\left(\frac{1}{2}[G]_{\mathrm{s}}^{-1} - \frac{1}{2}c_{\mathrm{s}}[G]_1^{-1}\right. \\
& \qquad \left. - \left(\frac{1}{2}[G]_2^{-1} + [Q]_{\mathrm{s}}^{-1} + \frac{1}{3}\frac{\lambda_\nu^0}{\lambda_{\mathrm{s}}^0}[P_{\mathrm{s}}]^{-1}\right)(1-c_{\mathrm{s}})\right)\{s\}\Delta\lambda_{\mathrm{s}},
\end{aligned} \tag{32}$$

where

$$[K]_1^{-1} = \frac{1}{K_1}[\mathrm{I}], \qquad [G]_1^{-1} = \frac{1}{G_1}[\mathrm{II}], \tag{33a}$$

$$[K]_2^{-1} = \frac{1}{K_2}[\mathrm{I}], \qquad [G]_2^{-1} = \frac{1}{G_2}[\mathrm{II}], \tag{33b}$$

$$[P_\mathrm{m}]^{-1} = a\frac{\partial g_2}{\partial \sigma_{\mathrm{m}2}}\{\mathrm{I}\}\frac{\partial f_2}{\partial \sigma_{\mathrm{m}2}}\{\mathrm{I}\}^\mathrm{t}, \tag{34a}$$

$$[P_\mathrm{s}]^{-1} = a\frac{\partial g_2}{\partial \sigma_{\mathrm{m}2}}\{\mathrm{I}\}\left\{\frac{\partial f_2}{\partial \{s\}_2}\right\}^\mathrm{T}, \tag{34b}$$

$$[Q_\mathrm{m}]^{-1} = a\frac{\partial g_2}{\partial \{s\}_2}\frac{\partial f_2}{\partial \sigma_{\mathrm{m}2}}\{\mathrm{I}\}^\mathrm{T}, \tag{34c}$$

$$[Q_\mathrm{s}]^{-1} = a\frac{\partial g_2}{\partial \{s\}_2}\left\{\frac{\partial f_2}{\partial \{s\}_2}\right\}^\mathrm{T}, \tag{34d}$$

$$[K]_\mathrm{s}^{-1} = \frac{\varepsilon_\nu}{\sigma_\mathrm{m}}[\mathrm{I}], \qquad [G]_\mathrm{s}^{-1} = \frac{2\{e\}}{\{s\}}, \tag{35}$$

$$A_\mathrm{m} = c_\mathrm{m} + \frac{\partial c_\mathrm{m}}{\partial \sigma_\mathrm{m}}\sigma_\mathrm{m}, \qquad A_\mathrm{s} = c_\mathrm{s} + \left\{\frac{\partial c_\mathrm{s}}{\partial \{s\}}\right\}^\mathrm{T}\{s\}, \tag{36}$$

in which

$$[\mathrm{I}] = \begin{bmatrix} 1&0&0&0&0&0\\ 0&1&0&0&0&0\\ 0&0&1&0&0&0\\ 0&0&0&0&0&0\\ 0&0&0&0&0&0\\ 0&0&0&0&0&0 \end{bmatrix} \quad [\mathrm{II}] = \begin{bmatrix} 1&0&0&0&0&0\\ 0&1&0&0&0&0\\ 0&0&1&0&0&0\\ 0&0&0&1&0&0\\ 0&0&0&0&1&0\\ 0&0&0&0&0&1 \end{bmatrix}.$$

The structure of (32) is similar to (26). The first two terms on the right hand represent the deformation when the whole body is regarded as a frictional medium. The middle two terms represent the reduction of deformation due to the existence of a bonding element. The final two terms result from the increase of breakage coefficients $\Delta\lambda_\nu$ and $\Delta\lambda_\mathrm{s}$. Note that for simplicity, representation $\Delta\lambda_\nu$ and $\Delta\lambda_\mathrm{s}$ have not been converted to $\Delta\sigma_\mathrm{m}$ and $\{\Delta s\}$, but the following equations hold

$$\Delta\lambda_\nu = B_{\nu\mathrm{m}}A_\mathrm{m}\Delta\sigma_\mathrm{m} + \{B_\nu\}_\mathrm{s}^\mathrm{T}A_\mathrm{s}\{\Delta s\}, \tag{37a}$$

$$\Delta\lambda_\mathrm{s} = B_\mathrm{sm}A_\mathrm{m}\Delta\sigma_\mathrm{m} + \{B_\mathrm{s}\}_\mathrm{s}^\mathrm{T}A_\mathrm{s}\{\Delta s\}, \tag{37b}$$

where

$$B_{\nu\mathrm{m}} = \frac{\partial f_\nu}{\partial \sigma_{\mathrm{m}1}},\ \{B_\nu\}_\mathrm{s} = \frac{\partial f_\nu}{\partial \{s\}_1},\ B_\mathrm{sm} = \frac{\partial f_\mathrm{s}}{\partial \sigma_{\mathrm{m}1}},\ \{B_\mathrm{s}\}_\mathrm{s} = \frac{\partial f_\mathrm{s}}{\partial \{s\}_1}.$$

5.4 Determination of Structural Parameters

In (26) and (32), four sets of parameters in total need to be determined. The first is the modulus of elasto-brittle material. Theoretically, it can be determined in laboratory by using undisturbed samples. But actually the results are doubtful because of unavoidable disturbance in sampling. Therefore, it is advisable to measure them in situ. The second set contains elastic modulus and hardening parameter of the frictional element, which can be determined in a laboratory by using completely disturbed samples. The third and the fourth sets contain $\lambda_\nu, \lambda_\mathrm{s}$ and c_ν, c_s, respectively. Because they are closely related to the internal structure of the samples, we shall call them structural parameters.

For man-made materials with known internal structures, such as alloys and composite materials, the structural parameters can be determined by theoretical analysis in simple cases or by numerical simulation in complicated cases. But geological materials are natural products, and their internal structure is actually impossible to determine. Therefore, the only realistic method seems to be to determine them indirectly. Briefly, the procedure of determination is recommended as follows: First, assume some empirical functions; then calculate the stress–strain relation curves by using (26) or (32); and finally choose the best one by comparing the calculated results with experimental data.

6 Breakage of Oval Structural Blocks

A mathematical model can be established if a sample is assumed to be a regularly arranged assembly of oval blocks.

6.1 Breakage Criteria for Oval Block

There are two types of breakage in structural blocks: local crushing and total rupture. An oval block can be broken by any of the following three criteria (also see Fig. 10).

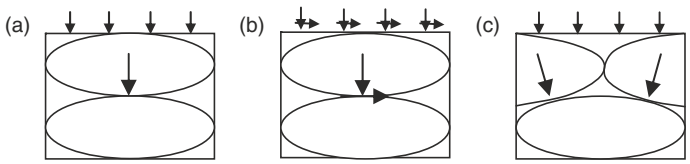

Fig. 10. Breakage of oval blocks. (**a**) Local crushing (**b**) shearing rupture (**c**) bending rupture

Local Crushing Criterion

Let c be the cohesion of the block material, E its Young's modulus, and ν its Poisson's ratio. According to Hertz's contact theory, the following local crushing criterion can be obtained:

$$[\sigma_1]_{\mathrm{I}} = B_{\mathrm{I}} C, \tag{38}$$

$$B_{\mathrm{I}} = \frac{9\pi^3 \xi^3 (1-\nu^2)^2 c^2 r_{\mathrm{a}}^2}{16 E^2 r_{\mathrm{b}}^2}, \tag{39}$$

where B_{I} is called the first breakage factor. In (38) and (39), r_{a} and r_{b} are the radius of the long axis and short axis, respectively. ξ is a coefficient calculated according to the plasticity theory. $[\sigma_1]$ is the nominal major principle stress at the state of the local crushing.

Shearing Rupture Criterion

Let t be the tensile strength of the block material. Then an oval block will be ruptured under the following nominal shear stress:

$$[\tau] = B_{\mathrm{II}} t, \tag{40}$$

where B_{II} is a function of normal stress and is called the second breakage factor.

Bending Rupture Criterion

When two or three blocks are arranged in the most unfavorable state, the bending moment at the center cross-section reaches such a state that tensile fracture happens at the top of the cross-section (see Fig. 10c). The corresponding nominal principal stress will be

$$[\sigma_1]_{\mathrm{III}} = B_{\mathrm{III}} t, \tag{41}$$

$$B_{\mathrm{III}} = \frac{r_b^2}{2 r_a^2}, \tag{42}$$

where B_{III} is called the third-breakage factor.

6.2 Five Steps of the Breakage Process

Five steps can be distinguished in the deformation and failure process of a sample consisting of oval blocks.

Elastic Deformation Stage

The blocks are assumed to deform elastically ahead of local crushing. Let $r_{\mathrm{b}0}$ and r_{b} be the radius of the short axis measured, respectively, before and after deformation. The apparent major principal strain can be calculated as follows:

$$\varepsilon_1 = 1 - \frac{r_{\mathrm{b}}}{r_{\mathrm{b}0}} = (\frac{9(1-\nu^2)^2\sigma_1^2}{2E^2r_{\mathrm{b}}^2})^{1/3}. \tag{43}$$

In the case of $\sigma_1 = [\sigma_1]_{\mathrm{I}}, r_1 = r_{\mathrm{b}1}$ can be determined accordingly.

Filling Hardening Stage

When the major compression stress $\sigma_1 = [\sigma_1]_{\mathrm{I}}$, local crushing occurs. In this stage the crushed material drops from the block bodies and fills the pores between the blocks. If σ_1 increases further, the contact area and strain ε_1 increases consequently. Assume that in the process of local crushing the blocks still keep their oval shape while the radius of their short axis is reduced. Then, at the end of this stage, the radius of the short axis will be

$$r_{\mathrm{b}2} = \frac{\pi(1+\eta)}{6+\pi\eta} r_{\mathrm{b}0}. \tag{44}$$

The corresponding value ε_1 can be calculated by (43), where η is the rate of volume increase after the crushed material has been dropped from the blocks. The stress σ_1 at this time is

$$[\sigma_1]_2 = \frac{9\pi^3\xi^3(1-\nu^2)^2r_{\mathrm{a}}^2}{E^2r_{\mathrm{b}2}^2}. \tag{45}$$

Compression Hardening Stage

When the voids between the blocks are full of the crushed material (the frictional element), the material begins its densification. Then some part of the stress will be sustained by the frictional element, which leads to a further hardening until the subsequent peak stress reaches

$$\sigma_1 = [\sigma_1]_3 = [\sigma_1]_{3\mathrm{i}} + [\sigma_1]_{3\mathrm{f}}. \tag{46}$$

where $[\sigma_1]_{3\mathrm{i}}$ is the stress shared by the block bodies and can be calculated by the aforementioned method. $[\sigma_1]_{3\mathrm{f}}$ is the stress shared by the frictional element and can be determined using the Mohr–Coulomb criterion. At this time $r_1 = r_{\mathrm{b}3}$, and the strain ε_1 is determined again according to (43).

Slip Softening Stage

When the stress shared by the frictional element meets the Mohr–Coulomb criterion, local slipping takes place. This causes to the adjacent blocks to move relatively, and then initiates the total rupture of the blocks. Accompanied with the rupture of the structural blocks, the capacity of the sample against the external load decreases, i.e., strain softening takes place and a shear band forms.

Plastic Flow Stage

When the blocks within the shear band are broken completely, the sample reaches a steady plastic flow state. The stress state in this stage can be determined by the Mohr–Coulomb criterion. Assume that this state will be achieved when the blocks have moved a distance of a half of a block length horizontally. Then the vertical strain at the beginning of this stage can be obtained by

$$\varepsilon_1 = \left(\frac{9(1-\nu^2)^2 \sigma_1^2}{2E^2 r_{\mathrm{b}4}^2} \right)^{1/3} . \tag{47}$$

6.3 Stress–Strain Relationship

According to aforementioned description, the stress–strain curves of a sample under different confining stresses can be obtained. Figure 11 shows clearly that a sample may exhibit softening behavior at low confining stress but hardening behavior at high confining stress. The corresponding relationship between the coefficient of stress concentration and vertical strain ε_1 is shown in Fig. 12. Note that in Fig. 12 the shear banding is not considered. In the calculation,

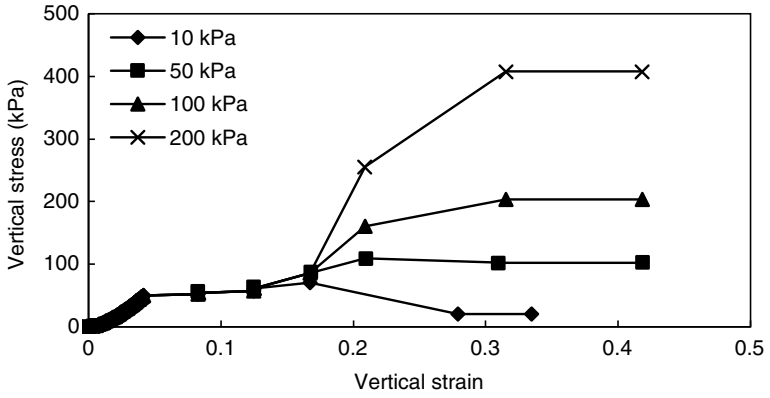

Fig. 11. Stress–strain curves of a block assembled sample

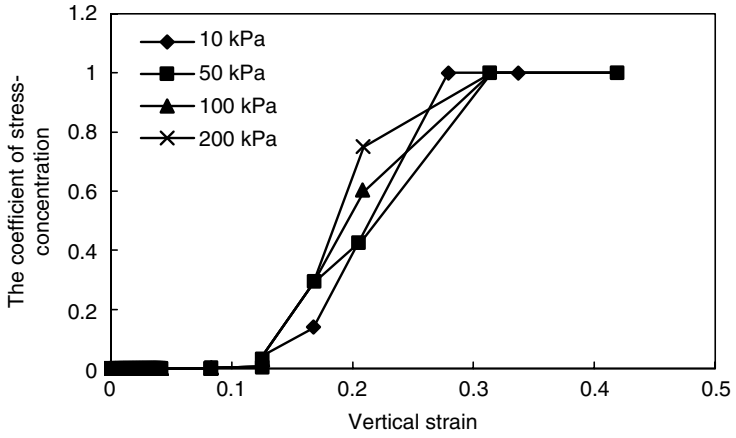

Fig. 12. Relationships between volumetric breakage ratio and vertical strain

the following parameters are used:

$$E = 20,000\,\text{kPa}, k = 20, \nu = 0.3, c = 300\,\text{kPa}, \phi = 20^\circ, \eta = 1.2, \xi = 5.14$$

and the shape of blocks is taken as follows: $r_{\text{a}0} = 10\,\text{cm}, r_{\text{b}0} = 8\text{cm}$.

7 Preliminary Application

7.1 Interpretation of Test Results of Rock Samples

Rock samples exhibit quite different behavior under the action of confining stress. For example, marmoreal samples show strain-softening behavior under low confining stress, but hardening under high confining stress. However, well-cemented sandstone exhibits strain-softening even under high confining stress. In addition, many tests exhibit some irregular fluctuation in their results. The proposed binary model can duplicate these phenomena. If the volumetric breakage function takes the following Weibull's law:

$$\lambda_\nu = 1 - \exp\left[-\left(\frac{\sigma_{\text{d}}}{q_{ee}}\right)^{\text{m}}\right], \tag{48}$$

then we can get some calculated results as shown in Fig. 13. For details, see reference [10].

7.2 Wetting Deformation of Loess Foundations

The above-mentioned binary model has also been incorporated into a FEM code and used to calculate the wetting deformation of a loess foundation under a circular footing with a preload of 200 kPa. The deformed mesh in this simulation is shown in Fig. 14. For details, see [11].

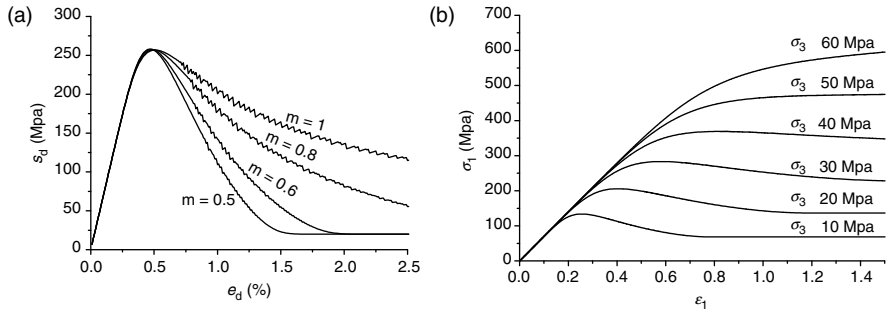

Fig. 13. Stress–strain curves of rock samples. (**a**) Change of value m (**b**) Change of confining stress

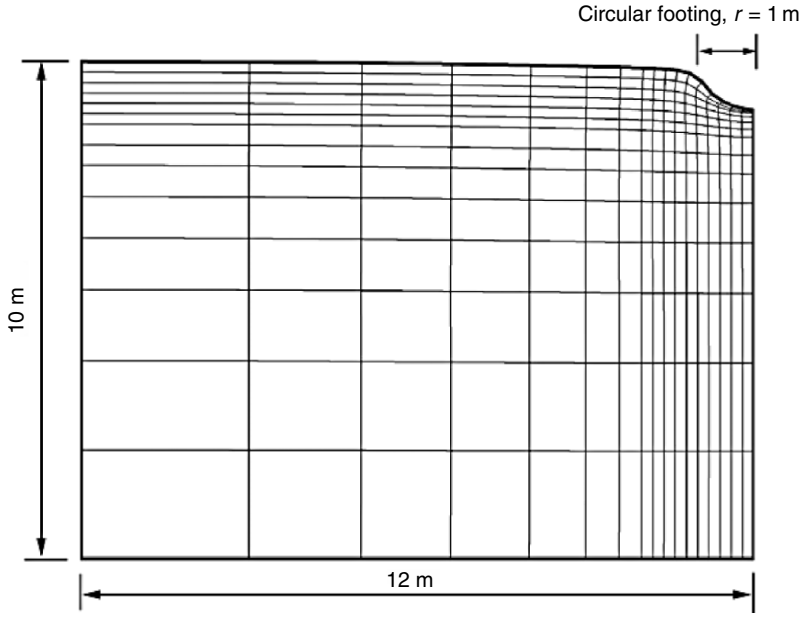

Fig. 14. Wetting deformation of a loess foundation

7.3 Stability of a Cut Slope

The long term stability of cut slopes under natural conditions is still a point of concern in geotechnical engineering. Here the strain softening effect and wetting softening effect due to water infiltration influence each other. There is no effective method available for its analysis. Based on the binary model and reduced suction concept we have proposed a relatively simple method for this purpose. Figures 15 and 16 show the computed results for a cut slope, showing the stability reduction under slow infiltration of rainwater. For details, see [12].

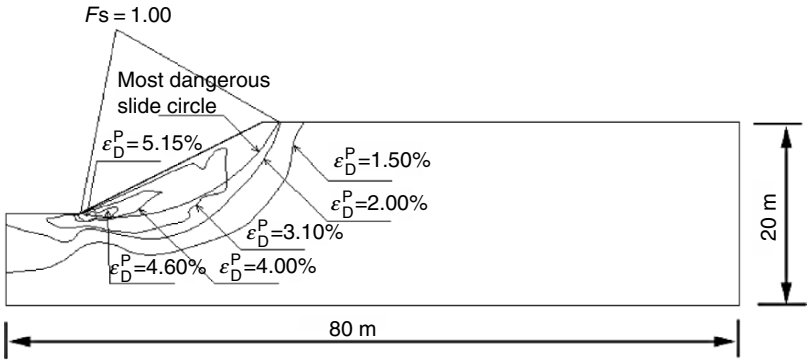

Fig. 15. Stability analysis of a cut slope

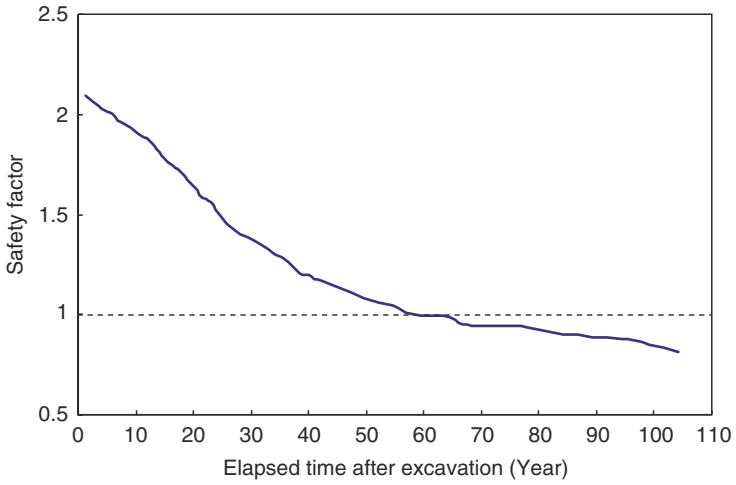

Fig. 16. Decrease of factor of safety with time

8 Conclusions and Further Research

Geological materials are natural products. They have many outstanding properties that are difficult to be modeled by the existing theories that have been based on the concept of a homogeneous medium. The proposed binary medium model was designed to better solve this problem. However, until now our study still takes soils as the main objects. But we hope this model also can be used to simulate the behavior of rock masses. The following are some conclusions from our investigations:

1. The structural geological materials can be conceptualized as a binary medium consisting of a bonding element and a frictional element, which

can be simulated by the elasto-brittle body and elasto-plastic body, respectively.
2. The binary medium is a heterogeneous material and the homogenization theory can be used to derive its averaging stress–strain relationship. In comparison to the traditional theory where only the volumetric averaging technique is used, this paper introduces both volumetric averaging and facial averaging techniques.
3. The breakage of the bonding element is controlled by the local stress on the element. Therefore, it is necessary to establish the evolution law of the local stress coefficient.
4. Breakage coefficients and local stress coefficients are two sets of internal variables. The former is similar to the damage coefficient in damage mechanics, while the latter is to some extent like the stress intensity factor in fracture mechanics. Because it is impossible to observe the internal structure of geological materials in a laboratory by current techniques, only an indirect method can be used in their determination.
5. The numerical simulation examples show that the proposed binary medium model can duplicate many fundamental aspects of stress–strain behavior of geological materials, and seems to be promising in the geotechnical engineering field.

Of course, the above-mentioned results are just preliminary findings. The key points of further research in the future are the mechanism of the breakage of bonding blocks and the evolution law of two sets of internal variable. Regarding these targets, some procedures are under consideration:

- Theoretical analysis to obtain analytical solutions for simple cases.
- Numerical tests by using FEM and DEM to get the evolution laws in some typical cases.
- Physical tests to reveal the breakage mechanism of bonding blocks at both the macroscopic and mesoscopic level including tests of rock and soil samples under various stress paths and various degree of confining stress.

By these three procedures, it is expected that the fundamental framework of breakage mechanics for geological materials can be established in the near future.

Acknowledgments

This research program was supported by the Chinese National Science Foundation (No:10272062). The author appreciates Dr. Minjing Jiang for his contribution in improving the quality of this paper.

References

1. Hill R, Elastic property of reinforced solids: some theoretical principles. Journal of Mechanical Physics Solids, 1963,11: 357–372
2. Wang JG, Leung CF and Ichicawa Y, A simplified homogenization method for composite soils. Computers and Geotechnics, 2002, 29(6): 477–500
3. Shen ZJ, A nonlinear damage model for structured clay (in Chinese). Journal of Nanjing Hydraulic Research Institute, 1993, (4): 247–255
4. Shen ZJ and Chen TL, Breakage mechanics for geological materials: Structure types and load sharing (in Chinese). Chinese Journal of Rock Mechanics and Engineering, 2004, 23(13): 2137–2142
5. Schmertmann JH, The mechanical aging of soil[J]. JGED, ASCE, 1991, 117(GT9): 1288–1330
6. Liu EL, Shen ZJ and Chen TL, Experimental study on the breaking process of bar-like structural bodies (in Chinese). Chinese Journal of Rock Mechanics and Engineering, 2005, 24(8)
7. Shen ZJ, Breakage mechanics for geological materials: an ideal brittle elasto-plastic model (in Chinese). Chinese Journal of Geotechnical Engineering, 2003, 25(3): 253–257
8. Shen ZJ and Deng G, Binary-medium model for over-consolidated clays (in Chinese). Rock and Soil Mechanics, 2003, 24(4): 495–499
9. Shen ZJ and Hu ZQ, A binary medium model for loess (in Chinese). Chinese Journal of Hydraulic Engineering, 2003,(7):1–6
10. Shen ZJ and Chen TL, Simulation of rock deformation and failure by binary medium model (in Chinese). Hydro-Science and Engineering, 2004(1):1–5
11. Shen ZJ, Application of binary medium model in the deformation analysis of loess during wetting (in Chinese). Chinese Journal of Hydraulic Engineering, 2005, 36(2): 129–134
12. Shen ZJ and Sun DW, Deformation and stability analysis of over-consolidated soils based on reduced suction concept (in Chinese). Chinese Journal of Geotechnical Engineering, 2005, 27(1): 105–109

Part II

Constitutive Modelling

Generic Constitutive Ingredients in CSSM Models for Sands

Y.F. Dafalias*, A.G. Papadimitriou†, X.S. LI#, and M.T. Manzari¶

*National Technical University of Athens, Hellas, Greece and University of California at Davis, USA
yfdafalias@ucdavis.edu
†National Technical University of Athens, Hellas, Greece
#Hong Kong University of Science and Technology, Hong Kong
¶George Washington University, USA

Abstract. The dependence of several constitutive quantities of a typical sand plasticity model, such as the peak and phase transformation stress-ratios, the plastic modulus, the dilatancy and the location of the critical state line, on the state parameter ψ and a properly defined scalar-valued measure of inherent fabric anisotropy, yields a constitutive framework within which a chosen model is able to simulate successfully the results of a plethora of loading responses accounting for different densities, confining pressures, orientation of loading directions and sample preparation methods. In parallel, appropriate dependence of the dilatancy or the plastic modulus on an evolving fabric-dilatancy tensor ensures accurate simulation of cyclic loading. The generic nature of such constitutive ingredients is discussed in regards to their use in conjunction with different constitutive models.

1 Introduction

In published works of the authors and their collaborators over the period of last several years on plastic constitutive modeling of sands, a number of novel constitutive ingredients appear. The first ingredient is the dependence of the peak and phase transformation stress-ratios on the state parameter ψ (Been and Jefferies 1985), so that these ratios coincide with the critical stress ratio when the ψ is zero at critical state. The second ingredient is the dependence of the plastic modulus and the dilatancy on a scalar-valued measure A of the relative orientation of inherent fabric anisotropy direction and an appropriate plastic loading direction. And finally, the third ingredient is the dependence of the dilatancy and/or the plastic modulus on the relative orientation of an evolving fabric-dilatancy tensor with the plastic loading direction.

The most important attribute of the foregoing ingredients is that they are generic, in the sense they can be incorporated in different constitutive models, as long as the background constitutive framework is that of critical state soil mechanics (CSSM). This presentation addresses all constitutive modelers, and

its main goal is to present these constitutive ingredients, explain their generic nature, which often is lost within the complexities of the constitutive models they are embedded in, and discuss how they can be used by other researchers in their own constitutive models.

It is important to emphasize that such ingredients are most appropriate (but not exclusively so) for sand constitutive models, which are stress-ratio $\eta = q/p$ driven, in the sense that a change in stress-ratio is the main mechanism of plastic deformation, contrary to clays where loading under a constant stress-ratio η induces a large amount of plastic consolidation. Note that q and p above denote the triaxial stress deviator, $q = \sigma_1 - \sigma_3$, and the mean effective stress, $p = (\sigma_1 + 2\sigma_3)/3$. In the sequel, bold face characters denote second order tensors.

2 Dependence on State Parameter

Plastic strain computations in elastoplasticity generally involve two basic parameters, the plastic modulus K_p and the dilatancy D. In a stress-ratio η driven model in the triaxial space, both parameters can be made functions of η, for example:

$$K_\mathrm{p} = h(M^\mathrm{b} - \eta) \tag{1}$$

$$D = A_\mathrm{d}(M^\mathrm{d} - \eta), \tag{2}$$

where M^b is a "virtual" peak or bounding stress-ratio and M^d is a similarly "virtual" dilatancy or phase transformation stress-ratio. Notice that (1) has the basic ingredient of a bounding surface formulation, where the plastic modulus is a function of the "distance" in stress (ratio) space between the current and the bounding surface states.

Wood et al. [20] proposed to render M^b a function of the state parameter $\psi = e - e_\mathrm{c}$, Been and Jefferies (1985), with e_c the void ratio on the critical state line (CSL) in the $e - p$ space corresponding to the ever-current p, as:

$$M^\mathrm{b} = M - k^\mathrm{b}\psi, \tag{3}$$

where M is the critical state stress-ratio in $q - p$ space, and k^b a material constant. While (3) was proposed by Wood et al. [20] in a triaxial setting for the peak stress ratio, it was not directly linked to an expression for the plastic modulus like (1). Rather it was used in a simple uniaxial simulation of the stress–strain response, where the variable M^b was linked to the development of deviatoric strain under monotonic loading. It was [11] who adopted the above (3) in conjunction with (1) for a multiaxial bounding surface constitutive model formulation of the two-surface kinematics hardening kind, where the generalization of the (variable with ψ) M^b superbly qualifies for a varying in size conical bounding surface in stress space. Most importantly, [11] proposed

also a similar dependence of the dilatancy stress-ratio M^{d} on ψ, which reads

$$M^{\mathrm{d}} = M + k^{\mathrm{d}}\psi \tag{4}$$

with k^{d} another material constant. Equations (3) and (4), in conjunction with (1) and (2), were the novel constitutive ingredients, which enabled the aforementioned general stress-space sand constitutive model to simulate the sand response under drastically different densities and confining pressures, with a single set of model constants for a given sand. In particular, (4) was the element that rendered the model compatible with CSSM premises, as for example having failure occur with no volume change. This is very simply the result of $M^{\mathrm{d}} = M$ for $\psi = 0$ in conjunction with $D = 0$, for $\eta = M$ (critical state). In addition, the dilatant or contractive nature of dense and loose samples is successfully simulated via (2) and (4), while (1) and (3) address the important issue of softening in dense samples, since K_{p} can be positive (hardening), negative (softening), or zero (peak and/or failure stress-ratio).

In a more general consideration of state-dependent dilatancy, Li and Dafalias [6], among other things, proposed an exponential dependence of M^{b} and M^{d} on ψ, i.e., they suggested instead of (3) and (4), the expressions:

$$M^{\mathrm{b}} = M\exp(-n^{\mathrm{b}}\psi) \tag{5}$$

$$M^{\mathrm{d}} = M\exp(n^{\mathrm{d}}\psi) \tag{6}$$

with n^{b} and n^{d} model constants, in lieu of k^{b} and k^{d}, respectively. Equations (5) and (6) have a wider applicability than (3) and (4), although the latter can be used successfully as well.

An illustration of a stress-ratio driven model in the triaxial stress space q–p is provided in Fig. 1, based on Manzari and Dafalias [11]. Observe the shape of the yield surface (open wedge with apex at the origin of axes) and note that it does not move when the stress-ratio η remains constant (stress-ratio η driven). Furthermore, note the lines corresponding to the aforementioned $M^{\mathrm{b}}, M^{\mathrm{d}}$, and M. The example in Fig. 1 corresponds to $\psi < 0$, as it can be easily concluded from the position of the M^{b} and M^{d} lines in regards to the

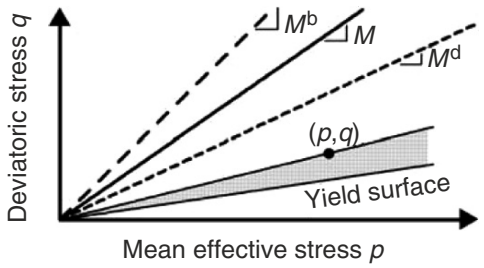

Fig. 1. Yield surface and the M, M^{b}, and M^{d} lines in a stress-ratio driven model

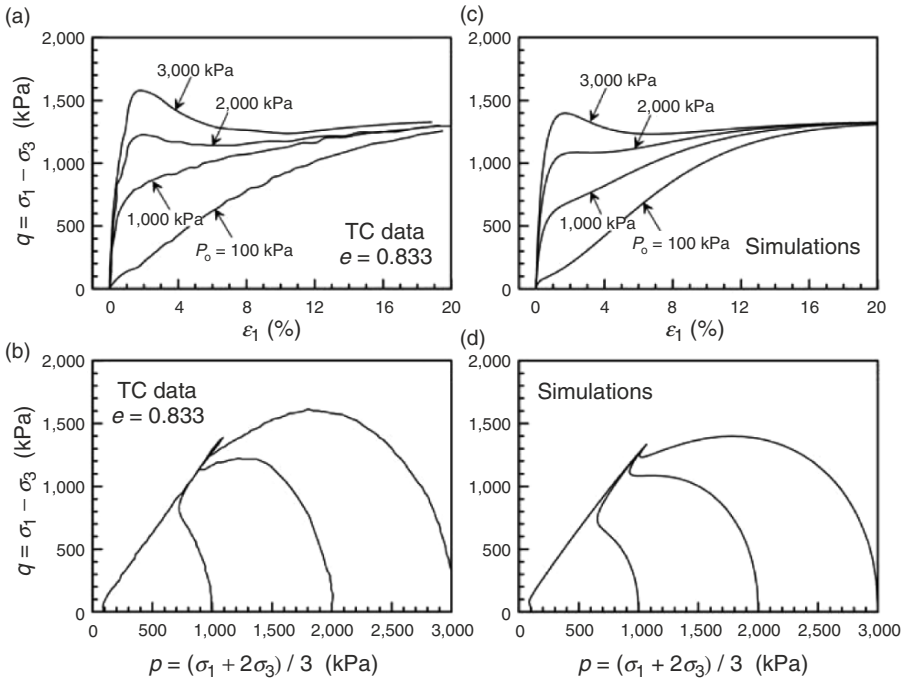

Fig. 2. Experimental results and model simulations for different initial pressures under triaxial compression ($e = 0.833$); Data: Verdugo and Ishihara [16]; Simulations: Dafalias and Manzari [4]

M line and the foregoing equations. As the sand approaches critical state where $\psi = 0$, the M^{b} and M^{d} lines converge on the M line, based on (3) and (4), or (5) and (6) alternatively.

As an example of the predictive abilities of a ψ-dependent stress-ratio η driven model, Fig. 2 presents a comparison between undrained triaxial compression test data and simulations with the pertinent model of Dafalias and Manzari [4]. Observe the large variation in the initial pressure (p_0 varies from 100 to 3,000 kPa), and how well a ψ-dependent stress-ratio η driven model simulates the data with a single set of model constants.

Obviously, the foregoing dependence of M^{b} and M^{d} on ψ presupposes the explicit definition of the CSL equation in the $e - p$ space. This is usually performed with a two-parameter linear – logarithmic relation:

$$e_{\mathrm{c}} = e_0 - \lambda \ln(p/p_{\mathrm{a}}) \tag{7}$$

or for greater accuracy by [9]:

$$e_{\mathrm{c}} = e_0 - \lambda (p/p_{\mathrm{a}})^{\xi}, \tag{8}$$

where e_0, λ, and ξ are model constants and p_{a} is the atmospheric pressure.

Table 1. Usual range of constants for ψ dependence of M^{b} and M^{d}

constant	k^{b}	k^{d}	n^{b}	n^{d}
range	0.8 – 3.0	0.3 – 6.0	0.6 – 2.0	0.2 – 3.5

In closure, based on Papadimitriou et al. [14] and related experience, the usual variation of the constants related to the ψ dependence of M^{b} and M^{d} is given in Table 1.

The very simple constitutive ideas embodied in (3) through (6) can very easily be implemented in other constitutive models where the M^{b} and M^{d} appear. For example, Li et al. [10] modified the bounding surface hypoplasticity model of Wang et al. [18] by rendering M^{d} an exponential function of ψ. In this very simple way, the model was able to predict critical failure without unbounded volume change. Further extending these constitutive concepts, Wang et al. [19] introduced first the state pressure index $I_{\mathrm{p}} = p/p_{\mathrm{c}}$, with p_{c} the p on the CSL at the same e, as an alternative measure to ψ, and subsequently proposed power dependence on I_{p} of the dilatancy and failure lines in $q-p$ space, such lines defined at the same void ratio. In a similar way, many existing stress-ratio driven constitutive models can incorporate the M^{b} and M^{d} (in particular) dependence on ψ or other indices like I_{p}, without altering any other basic constitutive features.

3 Dependence on Inherent Fabric Anisotropy

Abundance of experimental evidence suggests a strong dependence of the sand response on the orientation of the loading in regards to an existing preferred fabric direction, the latter due to settlement formation under gravity. This is the case of inherent sand fabric anisotropy, which must be accounted for in a constitutive modeling approach. The most recent data by Yoshimine et al. [22] and Nakata et al. [12] in a torsional shear apparatus, are very eloquent in showing drastic differences in response, often reaching the level of 300% or more, when the same sand sample is loaded identically with the principal stress directions in various orientations with respect to the vertical axis of sample deposition. One catalytic observation of the aforementioned data, is that the deviatoric strains are almost coaxial with the stress (especially at high stress ratios), thus, suggesting that whatever difference is observed in the stress–strain response, is due to differences in the dilatancy and/or the plastic modulus according to orientation.

The above prompted Li and Dafalias [7] and Dafalias et al. [5] to address the inherent fabric anisotropy in a very simple way. Firstly, an anisotropic scalar-valued state variable A was introduced, properly defined in terms of joint isotropic invariants of an inherent fabric anisotropy tensor $\mathbf{F}$ and a normalized "active" loading direction $\mathbf{n}$. More specifically, given the assumed (and expected) transversely isotropic symmetry of a sample because of the

procedure of preparation, the fabric tensor $\mathbf{F}$ is also transversely isotropic in the bedding plane of the sample, defined in terms of a single constant, a, as:

$$[\mathbf{F}] = \begin{bmatrix} a & 0 & 0 \\ 0 & 1/2(1-a) & 0 \\ 0 & 0 & 1/2(1-a) \end{bmatrix}. \tag{9}$$

The normalized "active" loading direction $\mathbf{n}$ is a matter of definition. For example, one may define a tensor whose eigenvectors coincide with the principal stress direction (e.g., as in Li and Dafalias [7]). Such a choice, would fail however to portray the situation realistically in reverse loading conditions, because the stress itself does not define, in general, the "active" loading direction. Therefore, for models with a yield surface the "active" loading direction $\mathbf{n}$ could be defined in terms of the normal to the yield surface (e.g., as in Dafalias et al. [5]). In cases where there is no yield surface, a loading surface could substitute for the yield surface, as in stress-reversal models (e.g., as in Li and Dafalias [8]).

In general, this definition of A accounts in a natural and straightforward way for the relative orientation of the "active" loading with respect to the fabric. The definitions of A in the foregoing papers are similar, yet different. For example, Dafalias et al. [5] proposed the use of the first joint isotropic invariant of $\mathbf{F}$ and $\mathbf{n}$ for A, as

$$A = g(\theta, c)\mathbf{F} : \mathbf{n}, \tag{10}$$

where θ is the Lode angle related to direction $\mathbf{n}$, c is the absolute ratio of A in triaxial compression (A_{c}) and extension (A_{e}) and g is an interpolation function for the value of A in different loading directions (between A_{c} and A_{e}). The definition of A by Li and Dafalias [7], and its extension for non-proportional loading (e.g., rotational shear) by Li and Dafalias [8], essentially use the second and third joint invariants of $\mathbf{F}$ and $\mathbf{n}$, and are not presented here for reasons of brevity.

In all the foregoing propositions, the plastic modulus K_{p} was made a function of A, by the dependence of the plastic modulus scaling coefficient h, (1), on A. In particular, Dafalias et al. [5] proposed:

$$h = h_{\mathrm{A}} \left[1 + k_{\mathrm{h}} - k_{\mathrm{h}}^{(A_{\mathrm{e}} - A)/(A_{\mathrm{e}} - A_{\mathrm{c}})} \right], \tag{11}$$

where k_{h} is constant expressing the ratio of plastic moduli in triaxial extension and compression. The respective equation of Li and Dafalias [7,8] is linear with respect to A and is again calibrated in terms of constant k_{h}.

Finally, the dilatancy expression D was made function of A in an indirect way, namely by rendering the location of the CSL in the $e{-}p$ space a function of A. This makes the state parameter ψ, and the ψ-dependent M^{d}, according to (4) or (6), indirect functions of A. More specifically, Dafalias et al. [5] proposed a parallel relocation of the CSL, (7) or (8), as a function of A, via:

$$e_0 = e_{\mathrm{A}} \exp\left(-\mathrm{A}\right), \tag{12}$$

where e_A serves as a model constant. Note that the respective equation of Li and Dafalias [7,8] is quadratic with respect to A and requires the calibration of an extra constant k_Γ, but its effect is similar to that of (12).

In order to show the performance of the foregoing simple scheme for introducing the effect of inherent fabric anisotropy in a constitutive model, one has to use appropriate test data. Most appropriate for this purpose are the data of Yoshimine et al. [22] and Nakata et al. [12], where the same loading sequence was applied at different directions with respect to the bedding plane of similarly prepared Toyoura sand samples.

Specifically, these tests were characterized by undrained loading with the same value of the intermediate principal stress ratio $b = (\sigma_2 - \sigma_3)/(\sigma_1 - \sigma_3)$ at different orientations, quantified via the angle α of σ_1 with respect to vertical. As an example of the accuracy of the proposed scheme, Fig. 3 presents a comparison of data and simulations for $b = 0.5$, using the Dafalias et al. [5] model formulation. It has to be underlined that without the proposed anisotropy scheme, the simulations in Fig. 3c,d would collapse into one single curve for each plot.

From another point of view, the effect of inherent fabric anisotropy on sand response may be viewed by comparing measurements from differently

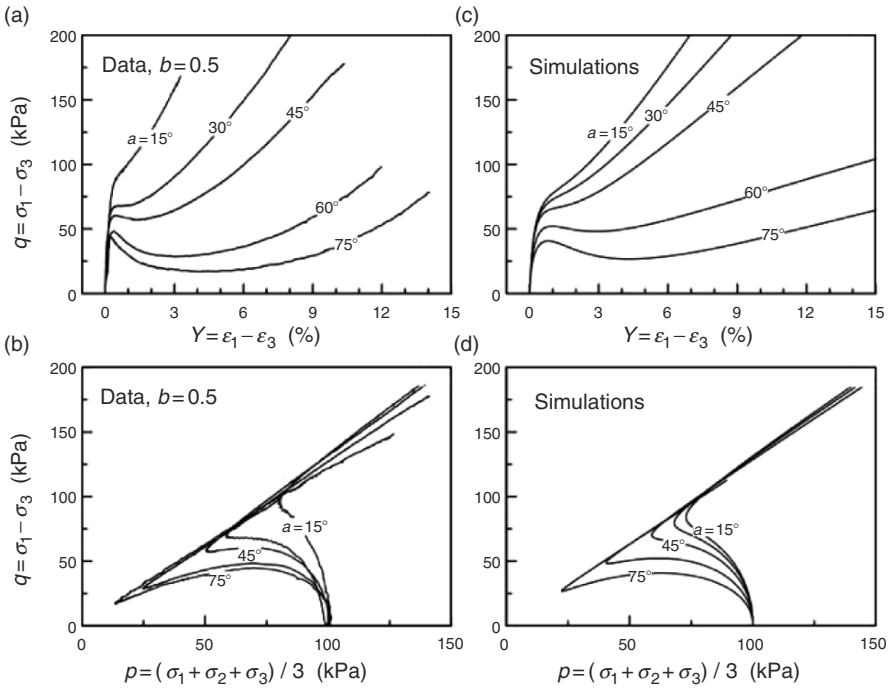

Fig. 3. Experimental results and model simulations for different angles of α at $b = 0.5 (e = 0.82)$; Data: Yoshimine et al. [22]; Simulations: Dafalias et al. [5]

prepared samples of the same sand that undergo the same loading in manner and direction, i.e., the same values of ratio b and angle α. In this case, it is the different initial fabric that differentiates the response and not the direction of loading, as in Fig. 3. Papadimitriou et al. [15] show that the scheme of Dafalias et al. [5] can be used successfully for the simulation of the effect of different initial fabrics on sand response.

For example, Fig. 4 shows a comparison of data and simulations of triaxial compression and extension tests on Toyoura sand samples prepared by four (4) different methods: air pluviation (AP), dry deposition (DD), dry rodding (DR), and wet tamping (WT). The tests show a significant effect of the preparation method on the undrained sand response, which is captured successfully by the simulations.

These successful simulations were made possible by appropriately calibrating the constants related with the proposed anisotropy scheme, i.e., the constants that appear in (9) through (12). More specifically, Papadimitriou et al. [15] show that constants e_{A} and h_{A}, (11) and (12), that govern the overall response are strongly affected by the preparation method, unlike constants a and k_{h}, (9) and (11), that quantify the relative effect of different loading directions and show a weak dependence on the preparation method. In practice, if one wants to capture the effects of sample preparation method for any given sand, he could merely address the variation of constants e_{A} and h_{A} and retain the values of a and k_{h} constant. In other words, the latter two

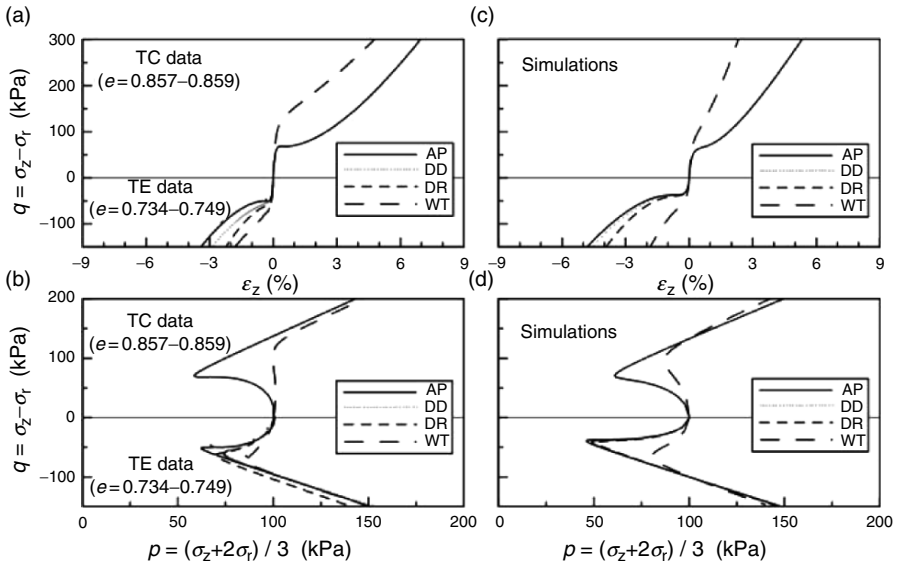

Fig. 4. Effect of sample preparation on undrained triaxial response of Toyoura sand from simulations and data (from [15])

Table 2. Expected range of constants for inherent fabric anisotropy scheme

constant	a	k_{h}	e_{A}	h_{A}
range	0.20–0.32	0.15–0.50	0.75–1.0	2.0–35

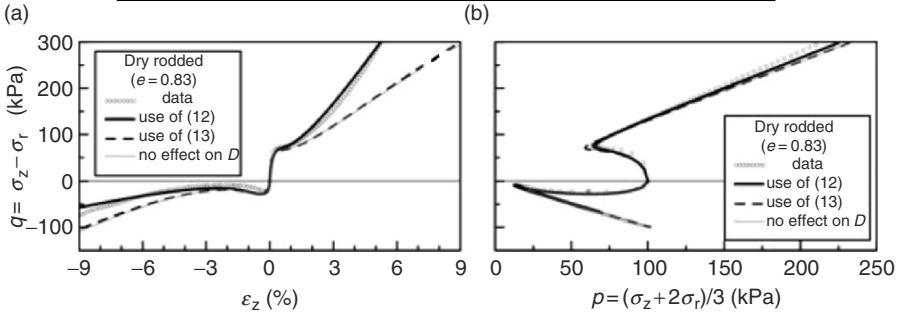

Fig. 5. Comparison of undrained triaxial data to model simulations assuming no effect on D, a unique CSL (use of (13)), or a variable CSL (use of (12)) as a function of inherent fabric anisotropy (based on [15])

constants are related to the "nature" of the sand, i.e., the mineralogy, grain shape and size distribution, and are therefore sand-specific.

Based on related experience, the expected variation of the constants related to the inherent fabric anisotropy scheme is given in Table 2.

The parallel relocation of the CSL in the $e-p$ space as a function of loading direction and manner and/or sample preparation method, obtained via a dependence on A by the very simple (12), is still a debatable issue in the literature, because it violates the uniqueness of the CSL. Thus, it was attempted to account for the effect of inherent fabric anisotropy without violating the uniqueness of the CSL in the following two ways.

First, Papadimitriou et al. [15] used a direct dependence of the dilatancy D, (2), on A, as an alternative to (12), by setting:

$$A_{\mathrm{d}} = A_{\mathrm{A}} \ \exp(\mathrm{A}). \tag{13}$$

Note that in (13) it is the A_{A} that serves as a model constant instead of the e_{A} of (12). It is clear that use of (13) instead of (12) preserves the uniqueness of CSL, or rather its independence from inherent fabric anisotropy effects. As shown in Fig. 5, after appropriate calibration, the effect of this alternative direct dependence of dilatancy D on A becomes important after the quasisteady state and all the way to critical failure, while for the initial parts of loading (up until the quasisteady state) the differences are unimportant. Yet, if the overall response is to be considered, use of (12) instead of (13) yields a much better simulation, as it is evident from Fig. 5, at the price of a non-unique CSL in the $e-p$ space due to its dependence on A.

The second way to preserve the uniqueness of the CSL but account for the effect of inherent fabric anisotropy is to consider only the plastic modulus K_{p}

dependence on A as shown in (11), with no effect of A on D, direct or indirect, i.e., without use of (12) or (13). As shown in Fig. 5, the resulting simulation is almost identical to the one when use of (13) in lieu of (12) was made.

This is the simplest version of the proposed inherent fabric anisotropy scheme, which again may be used successfully only up until the quasisteady state, especially when constant a is near 1/3 (as is $a = 0.31$ for dry rodding in Fig. 5), which renders the $\mathbf{F}$ of (9) almost equal to the identity tensor. Still, its overall simulative capability is much inferior to the case where both (11) and (12) are used. The conclusion at present is that the relocation of the CSL according to (12) appears to play an important role in accounting for the effect of inherent fabric anisotropy on the stress–strain simulations.

Along similar concepts within CSSM, Wan and his collaborators over the last years have worked on incorporating fabric and state parameter effects in various aspects of a critical state model, namely in the mobilized, the peak friction and the dilatancy angles, in the location of the CSL etc, the latest version of which is presented in Wan and Guo [17]. While these works are very interesting due to their direct micromechanical foundation, yet, the approach presented here is simpler for a continuum mechanics modeling.

More importantly it can easily be incorporated in any sand plasticity model, since, by definition, any such model must contain the concepts of plastic modulus K_{p} and dilatancy D, or their equivalent, in its formulation. Even if the exact form of (1) and (2) is not adopted, certainly the peak and phase transformation stress ratios are directly or indirectly part of any constitutive model for sands, in which case (3) and (4), or (5) and (6) can be used. Furthermore, the definition of A is generic, because an "active" loading direction $\mathbf{n}$ can be defined in any such model, while tensor $\mathbf{F}$ is defined independently of the constitutive model at hand.

4 Dependence on Evolving Sand Fabric Anisotropy

In applying the model of Manzari and Dafalias [11] to problems of sand liquefaction, it was realized that under cyclic loading the model was providing a stabilized undrained stress path much before the mean effective stress p reached a value close to zero, thus, hindering the onset of liquefaction. By studying the model performance vs. available experimental data, it was concluded that one of the reasons for this discrepancy, was that after dilation in loading, the subsequent contraction in unloading was not strong enough to generate the characteristic "butterfly" shape of the undrained stress path and the ensuing continuous reduction of the effective p. Available micromechanical considerations in the literature, suggested the following constitutive scheme. A dilatancy tensor $\mathbf{z}$ was introduced, which evolves according to:

$$\dot{\mathbf{z}} = -B \left\langle -\dot{\boldsymbol{\epsilon}}_{\mathrm{v}}^{\mathrm{p}} \right\rangle \left[C\mathbf{n} + \mathbf{z} \right], \tag{14}$$

where $\dot{\boldsymbol{\epsilon}}_{\mathrm{v}}^{\mathrm{p}}$ is the plastic volumetric strain rate, $<>$ are the MacCauley brackets that ensure that tensor $\mathbf{z}$ evolves only during the dilatant phase, while the

minus sign in front of B provides for $\mathbf{z}$ evolution opposite to the "active" loading direction $\mathbf{n}$. Obviously, (14) introduces two (2) new constants, the B that corresponds to the rate of evolution of anisotropy and the C that serves to define the maximum (saturated) value of tensor $\mathbf{z}$, when its rate equals zero.

The coefficient A_{d} of the dilatancy expression D, (2), was made function of tensor $\mathbf{z}$ and the "active" loading direction $\mathbf{n}$, as:

$$A_{\mathrm{d}} = A_0 \left(1 + \langle \mathbf{z}{:}\mathbf{n} \rangle\right). \tag{15}$$

Thus, upon reversal of loading and the ensuing change of sign of $\mathbf{n}$, the term $< \mathbf{z}{:}\mathbf{n} >$ from zero becomes active and enhances the value of A_{d}, and thus of the dilatancy D. This very simple scheme was proven to be very successful in achieving the desired effect of intense pore pressure build-up upon load reversal following dilation Dafalias and Manzari [3, 4]. As an example, Fig. 6 shows that the intensely contractive response of the data after load reversal following dilation can only be captured with the simulation run taking into account the evolving fabric anisotropy ($C = 4$).

In parallel, Papadimitriou and Bouckovalas [13] extended the principle of Papadimitriou et al. [14] and applied an evolving fabric-related multiplier of the coefficient h of the plastic modulus K_{p} expression, (1), i.e.,

$$h = h_0 \frac{1 + \langle z_{\mathrm{p}} \rangle^2}{1 + \langle \mathbf{z}{:}\mathbf{n} \rangle}. \tag{16}$$

The fabric-related tensor $\mathbf{z}$ of the denominator of (16) evolves using (14) and offers similarly good results near liquefaction, since the weakening of K_{p} upon load reversal results in similar trends for undrained loading. In addition to the above, the scalar z_{p} in the numerator of (16) evolves as

$$\dot{z}_{\mathrm{p}} = B\, \dot{\epsilon}_{\mathrm{v}}^{\mathrm{p}} \tag{17}$$

with B being the same as in (14). The numerator of (16) provides realistic rates of accumulation of (volumetric and deviatoric) strains and excess pore pressures during the whole cyclic loading process, from its consolidation state all the way to liquefaction or cyclic mobility. Finally note that Papadimitriou

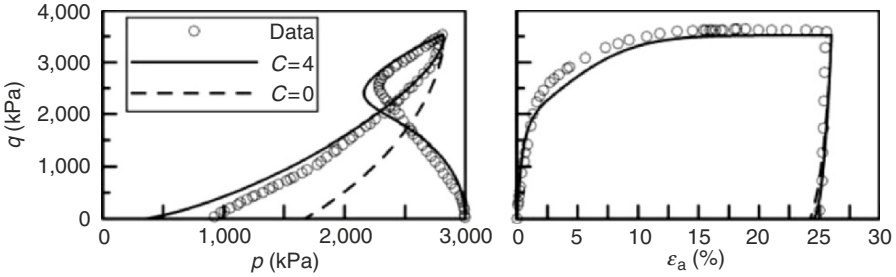

Fig. 6. Comparison of undrained triaxial data to model simulations with $C = 4$ (evolving fabric effect on D) and $C = 0$ (no evolving fabric effect on D); Data: Verdugo and Ishihara [16]; Simulations: Dafalias and Manzari [4]

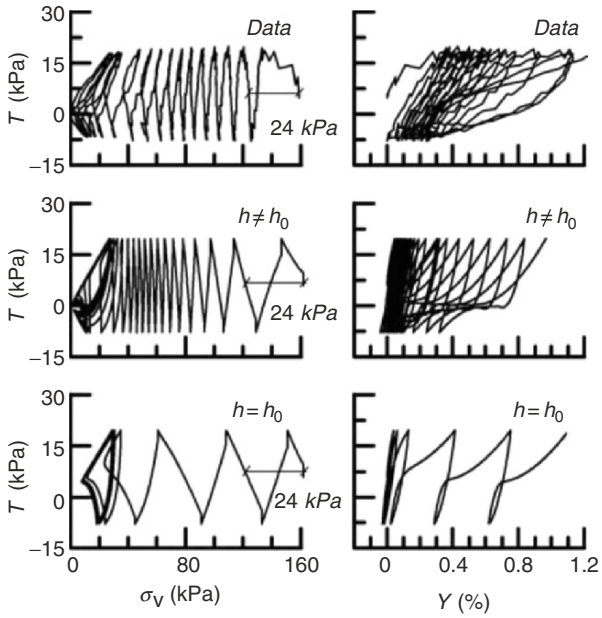

Fig. 7. Comparison of undrained simple shear data to model simulations with $h \neq h_0$ (evolving fabric effect on K_p) and $h = h_0$ (no evolving fabric effect on K_p); Data: Arulmoli et al. [1]; Simulations: Papadimitriou and Bouckovalas [13]

and Bouckovalas [13] relate the values of B and C in (14) and (17) to the stress history, thus facilitating their calibration.

As an example, Fig. 7 shows how this scheme with $h \neq h_0$, (16), simulates successfully the initially decreasing rate of excess pore pressure buildup in the data, as well as its increase near liquefaction. For comparison, observe that without this scheme ($h = h_0$), the simulation is unable to simulate the whole stress history, even if it is appropriately calibrated to yield the same excess pore pressure at the end of the first load cycle (approx. 24 kPa).

Obviously such constitutive schemes can be directly applied to any constitutive model that uses the concepts of loading direction $\mathbf{n}$, dilatancy and plastic modulus.

For example, Yang et al. [21] applied the foregoing principles in proposing a function affecting the dilatancy, which enhances the contractive response upon load reversal following dilative undrained loading.

Acknowledgment

The writers gratefully acknowledge support from the NSF Grant CMS-9800330 of the program directed by the late Clifford Astill and the CMS-0201231 of the program directed by Dr. Richard Fragaszy.

References

1. Arulmoli, K., Muraleetharan, K.K., Hossain, M.M. and Fruth, L.S. (1992): VELACS: verification of liquefaction analyses by centrifuge studies; laboratory testing program – soil data report, *The Earth Technology Corporation*
2. Been, K. and Jefferies, M.G. (1999): A state parameter for sands, *Geotechnique*, 35 (2), 99–112
3. Dafalias, Y.F. and Manzari, M.T. (1999): Modeling of fabric effect on the cyclic loading response of granular soils, *Proceedings of the 13th ASCE Engineering Mechanics Specialty Conference*, 13–16 June, Baltimore, Maryland (in CD-ROM)
4. Dafalias, Y.F. and Manzari, M.T. (2004): A simple plasticity sand model accounting for fabric change effects, *J. Eng. Mech. ASCE*, 130 (6), 622–634
5. Dafalias, Y.F., Papadimitriou, A.G. and Li, X.S. (2004): Sand plasticity model accounting for inherent fabric anisotropy, *J. Eng. Mech. ASCE*, 130 (11), 1319–1333
6. Li, X.S. and Dafalias, Y.F. (2000): Dilatancy for cohesionless soils, *Geotechnique*, 50 (4), 449–460
7. Li, X.S. and Dafalias, Y.F. (2002): Constitutive modeling of inherently anisotropic sand behavior, *J. Geotech. Geoenviron. Eng. ASCE*, 128 (10), 868–880
8. Li, X.S. and Dafalias, Y.F. (2004): A constitutive framework for anisotropic sand including non-proportional loading, *Geotechnique*, 54 (1), 41–55
9. Li, X.S. and Wang, Y. (1998): Linear representation of steady-state line for sand, *J. Geotech. Geoenviron. Eng. ASCE*, 124 (12), 1215–1217
10. Li, X.S., Dafalias, Y.F. and Wang, Z.L. (1999): State dependent dilatancy in critical state constitutive modeling of sand, *Can. Geotech. J.* 36 (4), 599–611
11. Manzari, M.T. and Dafalias, Y.F. (1997): A critical state two-surface plasticity model for sands, *Geotechnique*, 47 (2), 255–272
12. Nakata, Y., Hyodo, M., Murata, H. and Yasufuku, N. (1998): Flow deformation of sands subjected to principal stress rotation, *Soils Found.* 38 (2), 115–128
13. Papadimitriou, A.G. and Bouckovalas, G.D. (2002): Plasticity model for sand under small and large cyclic strains: a multiaxial formulation, *Soil Dyn. Earthquake Eng.* 22 (3), 191–204
14. Papadimitriou, A.G., Bouckovalas, G.D. and Dafalias, Y.F. (2001): Plasticity model for sand under small and large cyclic strains, *J. Geotech. Geoenviron. Eng.* 127 (11), 973–983
15. Papadimitriou, A.G., Dafalias, Y.F. and Yoshimine, M. (2005): Plasticity modeling of the effect of sample preparation method on sand response, *Soils Found.* 40 (2), 109–124
16. Verdugo, R. and Ishihara, K. (1996): The steady state of sandy soils, *Soils Found.* 36 (2), 81–92
17. Wan, R.G. and Guo, P.J. (2004): Stress dilatancy and fabric dependencies on sand behavior, *J. Eng. Mech. ASCE*, 130 (6), 635–645
18. Wang, Z.L., Dafalias, Y.F. and Shen, C.K. (1990): Bounding surface hypoplasticity model for sand, *J. Eng. Mech. ASCE*, 116 (5), 983–1001
19. Wang, Z.L., Dafalias Y.F., Li, X.S. and Makdisi, F.I. (2002): State pressure index for modeling sand behavior, *J. Geotech. Geoenviron. Eng. ASCE*, 128 (6), 511–519

20. Wood, D.M., Belkheir K. and Liu, D.F. (1994): Strain softening and state parameter for sand modeling, *Geotechnique*, 44 (2), 335–339
21. Yang, Z., Elgamal, A. and Parra, E. (2003): Computational model for cyclic mobility and associated shear deformation, *J. Geotech. Geoenviron. Eng. ASCE*, 129 (12), 1119–1127
22. Yoshimine, M., Ishihara, K. and Vargas, W. (1998): Effects of principal stress direction and intermediate principal stress on undrained shear behavior of sand, *Soils Found.* 38 (3), 177–186

State Boundary Surface in Hypoplasticity

D. Mašín* and I. Herle†

*Department of Engineering Geology, Charles University, Prague Czech Republic
masin@natur.cuni.cz
†Institute of Geotechnical Engineering, Technische Universität Dresden, Germany

1 Introduction

Hypoplastic constitutive models have been developed since 1980s and since then they have established a solid base for an alternative description of the soil behaviour, without an explicit definition of yield and potential surfaces, see, e.g. the review by [15]. Recent hypoplastic models [3, 16] include the concept of critical states and have been successfully used in many computations of boundary value problems within coarse-grained soils. The progress of hypoplastic models suitable for the description of fine-grained soils has been delayed. Rate-dependent [4, 13] and rate-independent [6, 8] hypoplastic models for clays promise to follow the success of the development for sand. Nevertheless, a thorough testing of various constitutive aspects is required in order to ensure a correct performance in general conditions of boundary value problems.

One of the key characteristics of soil behaviour, incorporated in different ways in the most of the currently available elasto-plastic constitutive models, is the presence of the surface in the stress–porosity space which bounds all accessible states (state boundary surface). Hypoplastic models do not incorporate the state boundary surface explicitly in the mathematical formulation. However, as demonstrated in [11] for a particular hypoplastic model for clay [8], state boundary surface is predicted implicitly by the constitutive equation as a by-product of the mathematical formulation.

As shown in [11], state boundary surface of a hypoplastic model for clays is sufficiently accurately approximated by the so-called *swept-out-memory* (SOM) surface, a surface in the stress–porosity space which covers asymptotic states (limit states, attractors) achieved after sufficiently long proportional deformation paths. The purpose of this chapter is to provide a mathematical derivation for the limit states of the two particular *endomorphous* hypoplastic models – a hypoplastic model for clays by Mašín [8], which follows from [6] and [13], and a hypoplastic model for granular materials by von Wolffersdorff [16].

2 Basic Properties of Considered Constitutive Models

A complete mathematical formulation of both models considered in the chapter is given in Appendices A and B. In its most general form, mathematical formulation of the models is given by

$$\mathring{\mathbf{T}} = \mathsf{h}\left(\mathbf{T}, \mathbf{D}, e\right), \tag{1}$$

where $\mathring{\mathbf{T}}$ is a co-rotated (Jaumann) stress rate, $\mathbf{T}$ stands for Cauchy's stress tensor, $\mathbf{D}$ is Euler's stretching tensor and e is void ratio. All stresses are considered as effective in the sense of Terzaghi. According to the terminology laid out by Kolymbas [7], models belong to the sub-class of hypoplastic models referred to as *endomorphous*. In addition to the Cauchy stress $\mathbf{T}$, void ratio e is also considered as a state variable. The particular form of the isotropic tensor-valued function h, adopted in constitutive model by [8], follows from [3] and reads

$$\mathring{\mathbf{T}}\left(\mathbf{T}, \mathbf{D}, e\right) = f_s\left(\operatorname{tr}\mathbf{T}\right)\left[\boldsymbol{\mathcal{L}}(\hat{\mathbf{T}}) : \mathbf{D} + f_d\left(\operatorname{tr}\mathbf{T}, \mathrm{e}\right)\mathbf{N}(\hat{\mathbf{T}})\|\mathbf{D}\|\right], \tag{2}$$

where the operator trace is defined by $\operatorname{tr}\mathbf{X} = \mathbf{X}{:}1$ with 1 being the second-order unit tensor, $\hat{\mathbf{T}}$ is the normalised stress defined by $\hat{\mathbf{T}} = \mathbf{T}/\operatorname{tr}\mathbf{T}$, $\|\mathbf{D}\| = \sqrt{\mathbf{D} : \mathbf{D}}$ is the Euclidian norm of $\mathbf{D}$ and the operator arrow is defined as $\overrightarrow{\mathbf{D}} = \mathbf{D}/\|\mathbf{D}\|$. f_s and f_d are *barotropy* and *pyknotropy* factors [3, 16].

The barotropy factor f_s of the hypoplastic model for clays [16] is independent of void ratio e and is a linear function of $\operatorname{tr}\mathbf{T}$. It follows that for a constant value of the pyknotropy factor f_d (i.e. for SOM conditions) the model [14] is positively homogeneous of *degree 1* with respect to stress, i.e.

$$\gamma^2\mathring{\mathbf{T}}\left(\mathbf{T}, \mathbf{D}, e\right) = \mathring{\mathbf{T}}\left(\gamma^2\mathbf{T}, \mathbf{D}, e\right). \tag{3}$$

The barotropy factor of the hypoplastic model for granular materials [16] is a non-linear function of $\operatorname{tr}\mathbf{T}$ *and* void ratio. For this reason the model is not positively homogeneous with respect to stress. However, as discussed in [14], for a constant value of f_d the model is *directionally homogeneous*

$$\overrightarrow{\mathring{\mathbf{T}}}\left(\mathbf{T}, \mathbf{D}, e\right) = \mathring{\mathbf{T}}\left(\gamma^2\mathbf{T}, \mathbf{D}, e\right), \tag{4}$$

which is a sufficient condition to predict asymptotic behaviour [14].

3 Proportional Stress and Strain Paths

Behaviour along proportional stress and strain paths (with $\overrightarrow{\mathbf{D}}$ and $\overrightarrow{\mathbf{T}}$ being constant) is reflected in the so-called SOM states, see Figure 1. These SOM states can also be considered as attractors of the soil behaviour [2].

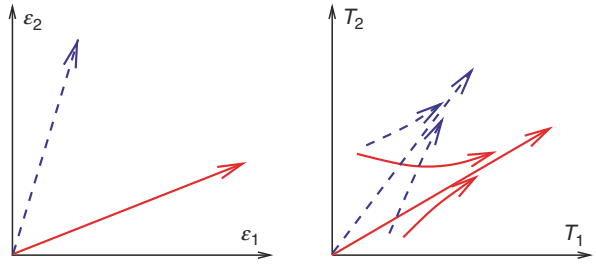

Fig. 1. SOM behaviour: Proportional stress paths for proportional strain paths

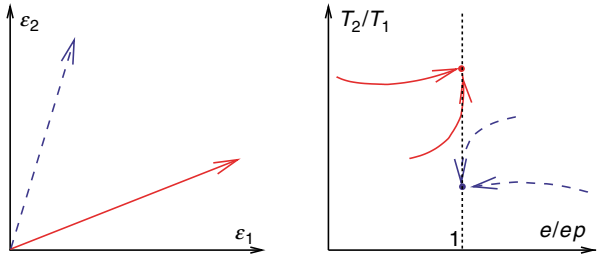

Fig. 2. Extended SOM behaviour including void ratio

The response of a real soil, however, does not depend solely on the stress tensor. Void ratio must be considered as an additional state parameter for both coarse-grained and fine-grained soils.

Except for constant volume (undrained) deformation, void ratio changes along proportional strain paths. In the case of hypoplastic models for pairs of proportional stress and strain paths one can find corresponding void ratios e_p dependent on the mean stress p. Combinations of e_p and p for $\operatorname{tr}\overrightarrow{\mathbf{D}} < 0$ plotted in the e:p space can be denoted as normal compression lines. Their positions in the e:p space may be characterised by the void ratio at vanishing mean stress (for model [16]), or at vanishing logarithm of the mean stress normalised by the reference stress (for model [8]), denoted here as e_{p0}. In this way, extended SOM states which include void ratio can be defined (Figure 2). Critical states can be considered as an example of extended SOM states for strain paths with $\operatorname{tr}\mathbf{D} = 0$, where SOM stress ratio follows from critical friction angle φ_c.

4 Limit State (Swept-Out-Memory) Conditions

As introduced Sect. 3, at extended SOM states the stress rate tensor $\mathring{\mathbf{T}}$ has the same direction as the stress tensor $\mathbf{T}$ and the pyknotropy factor f_d is constant ($\dot{f}_d = 0$) for one particular direction of stretching $\overrightarrow{\mathbf{D}}$. In the present developments, we will search for the value of the pyknotropy factor f_d and

direction of stretching $\overrightarrow{\mathbf{D}}$ which correspond to SOM states for the *given* stress state $\mathbf{T}$. The rate formulation of the considered hypoplastic equations reads

$$\mathring{\mathbf{T}} = f_s \boldsymbol{\mathcal{L}} : \mathbf{D} + f_s f_d \mathbf{N} \|\mathbf{D}\|, \tag{5}$$

which may be, without loss of generality, simplified by assuming f_s being part of constitutive tensors $\boldsymbol{\mathcal{L}}$ and $\mathbf{N}$ and taking $\|\mathbf{D}\| = 1$ (considered models are rate independent–positively homogeneous of degree 1 in $\mathbf{D}$). Therefore

$$\mathring{\mathbf{T}} = \boldsymbol{\mathcal{L}} : \overrightarrow{\mathbf{D}} + f_d \mathbf{N}. \tag{6}$$

At SOM conditions $\mathring{\mathbf{T}} \parallel \mathbf{T}$, so we may introduce a scalar multiplier γ such that

$$\mathring{\mathbf{T}} = \gamma \overrightarrow{\mathbf{T}}. \tag{7}$$

Therefore, SOM conditions are described by

$$\gamma \overrightarrow{\mathbf{T}} = \boldsymbol{\mathcal{L}} : \overrightarrow{\mathbf{D}} + f_d \mathbf{N} \tag{8}$$

with

$$\dot{f}_d = 0. \tag{9}$$

Note that limit states calculated according to (8) and (9) include also proportional strain paths with $\operatorname{tr} \overrightarrow{\mathbf{D}} > 0$ ($\gamma < 0$).

4.1 Hypoplastic Model for Clays

Let us now solve (8) for the hypoplastic constitutive model for clays. The pyknotropy factor f_d of this model is defined as

$$f_d = \left(\frac{2p}{p_{\mathrm{e}}^*} \right)^{\alpha}, \tag{10}$$

where p is the mean stress $p = -\operatorname{tr} \mathbf{T}/3$ and p_{e}^* is the equivalent pressure on the isotropic normal compression line, which is defined to be linear in the $\ln p : \ln(1+e)$ space and follows [1]

$$\ln(1+e) = N - \lambda^* \ln \left(\frac{p_{\mathrm{e}}^*}{p_{\mathrm{r}}} \right), \tag{11}$$

with p_{r} being the reference stress of 1 kPa. Comparison of (10) and (11) reveals that $\dot{f}_d = 0$ is satisfied for any line defined by

$$\ln(1+e) = \text{const.} - \lambda^* \ln \left(\frac{p}{p_{\mathrm{r}}} \right). \tag{12}$$

Time differentiation of (12) yields the rate formulation of normal compression lines, as defined in Sect. 3

$$\frac{\dot{e}}{1+e} = -\frac{\lambda^*}{p}\dot{p}\,. \tag{13}$$

Because

$$\dot{e} = (1+e)\mathrm{tr}\,\overrightarrow{\mathbf{D}}, \tag{14}$$

we have

$$\mathrm{tr}\,\overrightarrow{\mathbf{D}} = -\frac{\lambda^*}{p}\dot{p} = -\lambda^*\frac{\mathrm{tr}\,(\gamma\,\overrightarrow{\mathbf{T}})}{\mathrm{tr}\,\mathbf{T}} = -\frac{\lambda^*\gamma}{\|\mathbf{T}\|}, \tag{15}$$

from which follows the expression for the scalar multiplier γ

$$\gamma = -\|\mathbf{T}\|\frac{\mathrm{tr}\,\overrightarrow{\mathbf{D}}}{\lambda^*}. \tag{16}$$

We see that in the hypoplastic model for clays γ is *independent* of void ratio (independent of the actual value of the pyknotropy factor f_d), which significantly simplifies derivation of the mathematical expression for SOM states.

Equations (16) and (8) may be combined

$$-\frac{\mathbf{T}}{\lambda^*}\mathrm{tr}\,\overrightarrow{\mathbf{D}} = \boldsymbol{\mathcal{L}} : \overrightarrow{\mathbf{D}} + f_d\mathbf{N}. \tag{17}$$

To solve this equation for $\overrightarrow{\mathbf{D}}$ and f_d, we introduce the fourth-order tensor $\boldsymbol{\mathcal{A}}$

$$\boldsymbol{\mathcal{A}} = \boldsymbol{\mathcal{L}} + \frac{1}{\lambda^*}\mathbf{T}\otimes 1, \tag{18}$$

such that

$$\boldsymbol{\mathcal{A}} : \overrightarrow{\mathbf{D}} = \boldsymbol{\mathcal{L}} : \overrightarrow{\mathbf{D}} + \frac{\mathbf{T}}{\lambda^*}\mathrm{tr}\,\overrightarrow{\mathbf{D}} \tag{19}$$

holds. Equation (17) may be therefore written

$$\boldsymbol{\mathcal{A}} : \overrightarrow{\mathbf{D}} + f_d\mathbf{N} = 0. \tag{20}$$

Since $\|\overrightarrow{\mathbf{D}}\| = 1$, we get

$$f_d = \|\boldsymbol{\mathcal{A}}^{-1} : \mathbf{N}\|^{-1} \tag{21}$$

and

$$\overrightarrow{\mathbf{D}} = -\frac{\boldsymbol{\mathcal{A}}^{-1} : \mathbf{N}}{\|\boldsymbol{\mathcal{A}}^{-1} : \mathbf{N}\|}, \tag{22}$$

so we have a direction of stretching $\overrightarrow{\mathbf{D}}$ and the value of pyknotropy factor f_d at SOM surface for any stress level $\mathbf{T}$. Graphical representation of (21) and (22) is demonstrated in Sect. 5.

4.2 Hypoplastic Model for Granular Materials

Solution of (8) and (9) is less straightforward for the hypoplastic model for granular materials. In this case, the pyknotropy factor is defined as

$$f_d = \left(\frac{e - e_d}{e_c - e_d} \right)^{\alpha}, \tag{23}$$

where e_c and e_d are characteristic void ratios which evolve with the mean stress according to

$$\frac{e_c}{e_{c0}} = \frac{e_d}{e_{d0}} = \exp\left[- \left(\frac{3p}{h_s} \right)^n \right]. \tag{24}$$

It follows from (23) and (24) that the pyknotropy factor of a hypoplastic model for granular materials is constant along any line defined by

$$e = (\text{const.}) \exp\left[- \left(\frac{3p}{h_s} \right)^n \right], \tag{25}$$

which leads after time differentiation to

$$\frac{\dot{e}}{e} = \frac{n}{h_s} \mathrm{tr}\, \mathring{\mathbf{T}} \left(\frac{3p}{h_s} \right)^{(n-1)} \tag{26}$$

By combining (26) with (14) and (7) we have

$$\mathrm{tr}\, \overrightarrow{\mathbf{D}} \left(\frac{1+e}{e} \right) = \gamma \frac{n}{h_s} \mathrm{tr}\, \overrightarrow{\mathbf{T}} \left(\frac{3p}{h_s} \right)^{(n-1)}. \tag{27}$$

We see that the value of the scalar multiplier γ of a hypoplastic model for granular materials *depends* on the void ratio, so also on the actual value of the pyknotropy factor f_d. To solve (27) and (8) for $\overrightarrow{\mathbf{D}}$ and f_d, we extract $\overrightarrow{\mathbf{D}}$ from (8) so we have

$$\overrightarrow{\mathbf{D}} = \gamma(\boldsymbol{\mathcal{L}}^{-1} : \overrightarrow{\mathbf{T}}) - f_d(\boldsymbol{\mathcal{L}}^{-1} : \mathbf{N}). \tag{28}$$

Combination of (28) and (27) yields the first equation relating f_d and γ which reads

$$\gamma = - \frac{\left(\frac{1+e}{e} \right) \mathrm{tr}\, \mathbf{B}}{G - \left(\frac{1+e}{e} \right) \mathrm{tr}\, \mathbf{C}} f_d, \tag{29}$$

with

$$\mathbf{B} = \boldsymbol{\mathcal{L}}^{-1} : \mathbf{N}, \tag{30}$$

$$\mathbf{C} = \boldsymbol{\mathcal{L}}^{-1} : \mathbf{T}, \tag{31}$$

$$G = \frac{n}{h_s} \mathrm{tr}\, \overrightarrow{\mathbf{T}} \left(\frac{3p}{h_s} \right)^{(n-1)}. \tag{32}$$

The second necessary equation is found by taking norm of (28). Because $\|\overrightarrow{\mathbf{D}}\| = 1$ we have

$$1 = \|\mathbf{B}\|^2 f_d^2 + \|\mathbf{C}\|^2 \gamma^2 - 2(\mathbf{B}{:}\mathbf{C}) f_d \gamma. \tag{33}$$

Combination of (29) and (33) yields an *implicit* equation for f_d

$$f_d = \sqrt{\left[\|\mathbf{B}\|^2 + \left(\frac{\|\mathbf{C}\|\left(\frac{1+e}{e}\right)\operatorname{tr}\mathbf{B}}{G - \left(\frac{1+e}{e}\right)\operatorname{tr}\mathbf{C}}\right)^2 + \frac{2(\mathbf{B}{:}\mathbf{C})\operatorname{tr}\mathbf{B}\left(\frac{1+e}{e}\right)}{G - \left(\frac{1+e}{e}\right)\operatorname{tr}\mathbf{C}}\right]^{-1}}, \tag{34}$$

where (from (23))

$$e = f_d^{(1/\alpha)}(e_c - e_d) + e_d. \tag{35}$$

Therefore, for hypoplastic model for granular materials explicit formulation for $\overrightarrow{\mathbf{D}}$, f_d and γ cannot be found. Equation (34) may be, however, solved numerically. We search for corresponding e and f_d, while taking into account that also f_s (and, therefore, also $\boldsymbol{\mathcal{L}}$ and $\mathbf{N}$ which include f_s in present developments) changes with e. Results are demonstrated graphically in Sect. 5.

5 Graphical Representation

Graphical representation of outlined equations for limit states is described in detail by Gudehus and Mašín [10]. State limits of both hypoplastic models for clays and for granular materials may be expressed by a graph relating $\overrightarrow{\mathbf{D}}$ and $\overrightarrow{\mathbf{T}}$. For axisymmetric states we define in Rendulic plane angles ψ_σ and $\psi_{\dot\epsilon}$ according to Fig. 3. Special directions in the Rendulic plane of strain rate

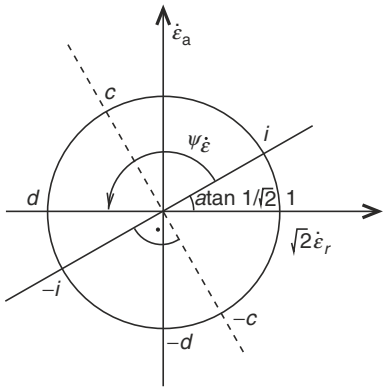

Fig. 3. Definition of angle $\psi_{\dot\epsilon}$ for axisymmetric states in Rendulic plane of $\boldsymbol{\epsilon}$ [10]. Angle ψ_σ is defined accordingly in the Rendulic plane of $\boldsymbol{\sigma}$

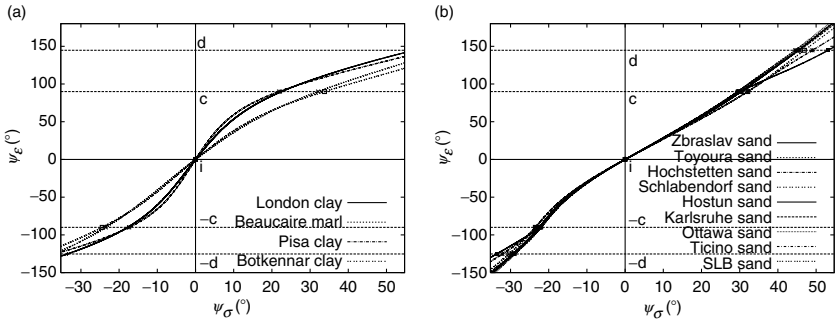

Fig. 4. ψ_σ–$\psi_{\dot{\epsilon}}$ plots for the hypoplastic model for clays (**a**) and hypoplastic model for granular materials (**b**)

Table 1. Parameters of a hypoplastic model for granular materials [5]

soil	φ_c (°)	h_s (MPa)	n	e_{d0}	e_{c0}	e_{i0}	α	β
Zbraslav sand	31	5,700	0.25	0.52	0.82	0.95	0.13	1.00
Toyoura sand	30	2,600	0.27	0.61	0.98	1.10	0.18	1.00
Hochstetten sand	33	1,500	0.28	0.55	0.95	1.05	0.25	1.50
Schlabendorf sand	33	1,600	0.19	0.44	0.85	1.00	0.25	1.00
Hostun sand	31	1,000	0.29	0.61	0.91	1.09	0.13	2.00
Karlsruhe sand	30	5,800	0.28	0.53	0.84	1.00	0.13	1.05
Ottawa sand	30	4,900	0.29	0.49	0.76	0.88	0.10	1.00
Ticino sand	31	5,800	0.31	0.60	0.93	1.05	0.20	1.00
SLB sand	30	8,900	0.33	0.49	0.79	0.90	0.14	1.00

Table 2. Parameters of a hypoplastic model for clays

soil	reference	φ_c (°)	λ^*	κ^*	N	r
London clay	[8]	22.6	0.11	0.014	1.375	0.4
Beaucaire marl	[12]	33	0.057	0.007	0.85	0.4
Pisa clay	[9]	21.9	0.14	0.005	1.56	0.2
Bothkennar clay	[9]	35	0.119	0.002	1.344	0.05

space are denoted by "i" and "−i" (for isotropic compression and extension), "c" and "−c" (for isochoric compression and extension) and "d" and "−d" (for extension with ϵ_a=0 and ϵ_r=0, respectively). ψ_σ versus $\psi_{\dot{\epsilon}}$ plots for both models are shown in Fig. 4. Parameters used for simulations with a hypoplastic model for granular materials follow from [5] (Table 1), parameters of a hypoplastic model for clays have been compiled from different publications (see Table 2 for references).

The second plot used to characterise limit state conditions relates ψ_σ with a function of the pyknotropy factor f_d at limit states. Suitable quantities follow from the formulation of pyknotropy factors of the two models considered ((10) and (23)). The influence of pyknotropy for the model for granular materials

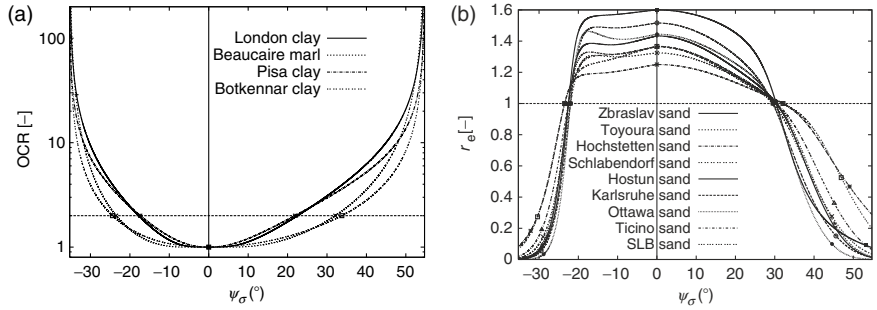

Fig. 5. ψ_σ–OCR and ψ_σ–r_e plots for the hypoplastic model for clays (**a**) and hypoplastic model for granular materials (**b**)

is characterised by a relative void ratio r_e defined as

$$r_\mathrm{e} = \frac{e - e_d}{e_c - e_d}, \tag{36}$$

whereas the degree of over-consolidation for the model for clays may be characterised by over consolidation ratio (OCR), defined as

$$\mathrm{OCR} = \frac{p_\mathrm{e}^*}{p}. \tag{37}$$

Graphs relating ψ_σ with r_e for the model for granular materials and ψ_σ with OCR for the model for clays are in Fig. 5.

6 Conclusions

As pointed out in Sect. 1, limit state conditions are important aspects of soil behaviour which must be predicted by advanced constitutive models. The chapter presented mathematical derivation for SOM (limit) states of the two hypoplastic constitutive models. It has been shown that the hypoplastic model for clays allows for an explicit formulation of limit state conditions. The expression for limit state conditions may be evaluated also for a hypoplastic model for granular materials. In this case, however, the analytical solution of the problem is not available and governing equations must be solved numerically. An experimental check of the limit state loci predicted by the models is a matter of further research. Presented derivations are important for incorporating structural effects into hypoplastic models, as demonstrated in [9] by formulating a hypoplastic model for structured clays.

Acknowledgment

The first author is grateful for the financial support by the research grants SSPI-CT-2003-501837-NOAH'S ARK under the EC 6th FP and GACR 205/03/1467.

Appendix 1

The mathematical structure of the hypoplastic model for clays is discussed in detail in [8]. The constitutive equation in rate form reads

$$\mathring{\mathbf{T}} = f_s \boldsymbol{\mathcal{L}} : \mathbf{D} + f_s f_d \mathbf{N} \|\mathbf{D}\|, \tag{38}$$

where

$$\boldsymbol{\mathcal{L}} = 3\left(c_1 \boldsymbol{\mathcal{I}} + c_2 a^2 \hat{\mathbf{T}} \otimes \hat{\mathbf{T}}\right)\mathbf{N} = \boldsymbol{\mathcal{L}} : \left(-Y \frac{\mathbf{m}}{\|\mathbf{m}\|}\right)\hat{\mathbf{T}} := \frac{\mathbf{T}}{\operatorname{tr}\mathbf{T}}. \tag{39}$$

$\mathbf{1}$ is the second-order identity tensor and $\boldsymbol{\mathcal{I}}$ is the fourth-order identity tensor, with components

$$(\mathcal{I})_{ijkl} := \frac{1}{2}\left(1_{ik}1_{jl} + 1_{il}1_{jk}\right). \tag{40}$$

In (38), the functions $f_s(\operatorname{tr}\mathbf{T})$ (*barotropy* factor) and $f_d(\operatorname{tr}\mathbf{T}, e)$ (*pyknotropy* factor) are given by

$$f_s = -\frac{\operatorname{tr}\mathbf{T}}{\lambda^*}\left(3 + a^2 - 2^\alpha a\sqrt{3}\right)^{-1} \quad f_d = \left[-\frac{2\operatorname{tr}\mathbf{T}}{3p_\mathrm{r}} \exp\left(\frac{\ln(1+e) - N}{\lambda^*}\right)\right]^\alpha, \tag{41}$$

where p_r is the reference stress 1 kPa. The scalar function Y and second-order tensor $\mathbf{m}$ appearing in (39) are given, respectively, by

$$Y = \left(\frac{\sqrt{3}a}{3 + a^2} - 1\right)\frac{(I_1 I_2 + 9I_3)\left(1 - \sin^2\varphi_\mathrm{c}\right)}{8I_3 \sin^2\varphi_\mathrm{c}} + \frac{\sqrt{3}a}{3 + a^2}, \tag{42}$$

in which

$$I_1 := \operatorname{tr}\mathbf{T} \qquad I_2 := \frac{1}{2}\left[\mathbf{T} : \mathbf{T} - (I_1)^2\right] \qquad I_3 := \det\mathbf{T}$$

and

$$\mathbf{m} = -\frac{a}{F}\left[\hat{\mathbf{T}} + \hat{\mathbf{T}}^* - \frac{\hat{\mathbf{T}}}{3}\left(\frac{6\,\hat{\mathbf{T}} : \hat{\mathbf{T}} - 1}{(F/a)^2 + \hat{\mathbf{T}} : \hat{\mathbf{T}}}\right)\right], \tag{43}$$

in which

$$\hat{\mathbf{T}}^* = \hat{\mathbf{T}} - \frac{\mathbf{1}}{3} \qquad F = \sqrt{\frac{1}{8}\tan^2\psi + \frac{2 - \tan^2\psi}{2 + \sqrt{2}\tan\psi\cos 3\theta}} - \frac{1}{2\sqrt{2}}\tan\psi, \tag{44}$$

$$\tan\psi = \sqrt{3}\|\hat{\mathbf{T}}^*\|\cos 3\theta \quad = -\sqrt{6}\frac{\operatorname{tr}\left(\hat{\mathbf{T}}^* \cdot \hat{\mathbf{T}}^* \cdot \hat{\mathbf{T}}^*\right)}{\left(\hat{\mathbf{T}}^* : \hat{\mathbf{T}}^*\right)^{3/2}}. \tag{45}$$

Finally, the scalars a, α, c_1 and c_2 appearing in (39)–(43), are given as functions of the material parameters φ_c, λ^*, κ^* and r by the following relations:

$$a = \frac{\sqrt{3}\,(3-\sin\varphi_c)}{2\sqrt{2}\sin\varphi_c}, \qquad \alpha = \frac{1}{\ln 2}\,\ln\left[\frac{\lambda^*-\kappa^*}{\lambda^*+\kappa^*}\left(\frac{3+a^2}{a\sqrt{3}}\right)\right], \tag{46}$$

$$c_1 = \frac{2\left(3+a^2-2^\alpha a\sqrt{3}\right)}{9r}, \qquad c_2 = 1+(1-c_1)\frac{3}{a^2}. \tag{47}$$

The model requires five constitutive parameters, namely φ_c, λ^*, κ^*, N and r.

Appendix 2

This appendix summarises mathematical formulation of a hypoplastic model for granular materials [16].

The model assumes the following stress-strain relation:

$$\mathring{\mathbf{T}} = f_s\boldsymbol{\mathcal{L}} : \mathbf{D} + f_s f_d \mathbf{N}\|\mathbf{D}\|, \tag{48}$$

with

$$\boldsymbol{\mathcal{L}} = \frac{1}{\hat{\mathbf{T}} : \hat{\mathbf{T}}}\left(F^2\boldsymbol{\mathcal{I}} + a^2\hat{\mathbf{T}}\otimes\hat{\mathbf{T}}\right), \tag{49}$$

$$\mathbf{N} = \frac{Fa}{\hat{\mathbf{T}} : \hat{\mathbf{T}}}\left(\hat{\mathbf{T}} + \hat{\mathbf{T}}^*\right), \tag{50}$$

where $\mathbf{1}$ is a second-order unity tensor, $\mathcal{I}_{ijkl} = \frac{1}{2}\left(1_{ik}1_{jl} + 1_{il}1_{jk}\right)$ is a fourth-order unity tensor and

$$\mathrm{tr}\mathbf{T} = \mathbf{T} : \mathbf{1}, \quad \hat{\mathbf{T}} = \mathbf{T}/\mathrm{tr}\,\mathbf{T}, \quad \hat{\mathbf{T}}^* = \hat{\mathbf{T}} - \mathbf{1}/3, \tag{51}$$

$$a = \frac{\sqrt{3}\,(3-\sin\varphi_c)}{2\sqrt{2}\sin\varphi_c}, F = \sqrt{\frac{1}{8}\tan^2\psi + \frac{2-\tan^2\psi}{2+\sqrt{2}\tan\psi\cos 3\theta}} - \frac{1}{2\sqrt{2}}\tan\psi, \tag{52}$$

with

$$\tan\psi = \sqrt{3}\|\hat{\mathbf{T}}^*\|, \quad \cos 3\theta = -\sqrt{6}, \frac{\mathrm{tr}\left(\hat{\mathbf{T}}^*\cdot\hat{\mathbf{T}}^*\cdot\hat{\mathbf{T}}^*\right)}{\left[\hat{\mathbf{T}}^* : \hat{\mathbf{T}}^*\right]^{3/2}}. \tag{53}$$

The scalar factors f_s and f_d take into account the influence of mean pressure and density

$$f_s = \frac{h_s}{n}\left(\frac{e_i}{e}\right)^\beta \frac{1+e_i}{e_i}\left(\frac{-\mathrm{tr}\,\mathbf{T}}{h_s}\right)^{1-n}\left[3+a^2-a\sqrt{3}\left(\frac{e_{i0}-e_{d0}}{e_{c0}-e_{d0}}\right)^\alpha\right]^{-1}, \tag{54}$$

$$f_d = \left(\frac{e-e_d}{e_c-e_d}\right)^\alpha. \tag{55}$$

The characteristic void ratios – e_i, e_c and e_d decrease with the mean pressure according to the relation

$$\frac{e_i}{e_{i0}} = \frac{e_c}{e_{c0}} = \frac{e_d}{e_{d0}} = \exp\left[-\left(\frac{-\text{tr }\mathbf{T}}{h_s}\right)^n\right]. \tag{56}$$

The model requires eight parameters: ϕ_c, h_s, n, e_{d0}, e_{c0}, e_{i0}, α and β.

References

1. R. Butterfield. A natural compression law for soils. *Géotechnique*, 29(4):469–480, 1979.
2. G. Gudehus. Attractors for granular storage and flow. In *3rd European Symposium – Storage and Flow of Particulate Solids, Paper for the conference 'Partec 95'*, pages 333–345, 1995.
3. G. Gudehus. A comprehensive constitutive equation for granular materials. *Soils and Foundations*, 36(1):1–12, 1996.
4. G. Gudehus. A visco-hypoplastic constitutive relation for soft soils. *Soils and Foundations*, 44(4):11–25, 2004.
5. I. Herle. *Hypoplastizität und granulometrie of einfacher korngerüste*. PhD thesis, Universität Fridericiana in Karlsruhe, 1997.
6. I. Herle and D. Kolymbas. Hypoplasticity for soils with low friction angles. *Computers and Geotechnics*, 31(5):365–373, 2004.
7. D. Kolymbas. An outline of hypoplasticity. *Archive of Applied Mechanics*, 61:143–151, 1991.
8. D. Mašín. A hypoplastic constitutive model for clays. *International Journal for Numerical and Analytical Methods in Geomechanics*, 29(4):311–336, 2005.
9. D. Mašín. A hypoplastic constitutive model for clays with meta-stable structure. Canadian Geotechnical Journal (submitted), 2006.
10. D. Mašín and G. Gudehus. Graphical representation of rate independent constitutive relations for saturated clays. State limites of saturated soils (in preparation), 2006.
11. D. Mašín and I. Herle. State boundary surface of a hypoplastic model for clays. *Computers and Geotechnics*,32(6):400–410 2005.
12. D. Mašín, C. Tamagnini, G. Viggiani, and D. Costanzo. Directional response of a reconstituted fine grained soil. Part II: Performance of different constitutive models. *International Journal for Numerical and Analytical Methods in Geomechanics (accepted)*, 2006.
13. A. Niemunis. A visco-hypoplastic model for clay and its FE implementation. In *Resultats recents en mechanique des sols et des roches XI Colloque Franco-Polonais*. Gdańsk, 1996.
14. A. Niemunis. *Extended hypoplastic models for soils*. Habilitation thesis, Ruhr-University, Bochum, 2002.
15. C. Tamagnini, G. Viggiani, and R. Chambon. A review of two different approaches to hypoplasticity. In D. Kolymbas, editor, *Constitutive Modelling of Granular Materials*, pages 107–144. Springer, Berlin Heidelberg New York, 1999.
16. P.A. von Wolffersdorff. A hypoplastic relation for granular materials with a predefined limit state surface. *Mechanics of Cohesive–Frictional Materials*, 1:251–271, 1996.

Modelling of Bonded Soils with Unstable Structure

R. Nova

Milan University of Technology (Politecnico) Italy
nova@stru.polimi.it

1 Introduction

Since the pioneering works of the School of Cambridge, Schofield and Wroth [17], much progress was made in modelling the behaviour of soils and soft rocks in the framework of hardening plasticity. Models such as those of Lade [6] and Nova and Wood [13] can describe the behaviour of remoulded clay or freshly deposited sand with remarkable accuracy even under complex loading histories. Nova [10], Kavvadas et al. [5] and Rouainia and Wood [16] proposed models for cemented soils or soft rocks. Hueckel and Ma [3] coupled the effects of chemistry to those of mechanics to describe the overall behaviour of clay when subject to loading and to structural changes due to chemical attack. Recently, Nova et al. [14] produced a comprehensive chemo-mechanical model for soft rocks, capable of describing interesting features such as softening–hardening transition or the occurrence of compaction bands under certain circumstances.

Despite these progresses, certain type of soils, characterized by high void ratios and fragile bonds, exhibit special features of behaviour that cannot be easily dealt with even by the most recent and sophisticated models. To this class of soils belong artificial materials such as cemented residues of heavy metal production. For instance Jarofix, a mixture of jarosite (hydrated ferric sulphate rich in heavy ions that may be easily leached away) lime and cement, is a material characterized by very high porosity (more than 70%) and strong but brittle bonds. The experimental behaviour of Jarofix, as reported by Arroyo et al. [1], shows the occurrence of compaction-dominated instabilities. A similar type of behaviour was also observed on a clayey silt, artificially produced by sedimentation as a residue of the washing of the Ticino silty gravel at Lonate [15]. When sedimented and naturally dried such a material must be removed by excavation. Having a very porous structure and brittle bonds, the stability of the fronts poses serious problems and may be cause of worker casualties.

Because of the complexity of their behaviour, the modelling of such materials is a formidable task. In order to get at least a qualitative insight, a very simple basic model is employed here to understand which should be the basic structure of a constitutive model capable of describing the observed instabilities. With the aim of describing more and more sophisticated phenomena with an ever increasing will of quantitative accuracy, in fact, the structure of the modern constitutive models has become more and more complex and the number of constitutive parameters has increased from the original 5 upto 200. It is therefore difficult to understand what is the effective role of each of those parameters.

In this chapter, we go back to the original simplicity with the aim of highlighting which is the role played by the various factors that influence the mechanical behaviour of bonded geomaterials. The original Cam Clay model is first reformulated in terms of strain hardening plasticity. The effects of the existence of intergranular bonds are then taken into account by introducing a single parameter that varies with the plastic strains experienced. It is shown that, depending on the value of some constitutive parameters, softening can occur at very low stress levels giving rise to temporary instabilities. However, hardening can be reactivated for larger strains until failure is achieved at a stress level which is typical for unbonded soils.

2 Reformulation of Cam Clay as a Strain Hardening Model

The mechanical behaviour of soils depends on the loading they have experienced in their previous (geologic or recent) history. The concept of overconsolidation ratio was in fact introduced to delineate between virgin loading and recompression in confined loading conditions (oedometric). This concept was successively extended by introducing the notion of yield locus. This is a surface in the effective stress space that encloses a region, called elastic domain. Soil behaviour for stresses within this region is reversible (elastic), while permanent strains are generated by stress increments directed outwards the current yield locus. As the maximum preconsolidation pressure increases in an oedometric test by increasing the vertical loading, the yield locus evolves and the size of the elastic domain becomes larger and larger with increasing plastic strains.

The first (and simplest) constitutive law capable to cope with this was the so-called Cam Clay model [17]. For the scopes of this chapter this model is here reformulated in terms that are more convenient from the standpoint of hardening plasticity theory.

To make things simple, only axisymmetric stress states are considered. The most convenient stress variables in this case are:

$$p' \equiv \frac{1}{3}(\sigma'_{\mathrm{a}} + 2\sigma'_{\mathrm{r}}), \qquad q = \sigma'_{\mathrm{a}} - \sigma'_{\mathrm{r}}, \tag{1}$$

where the indices a and r stand for axial and radial. The corresponding strain variables are consequently

$$\varepsilon_{\mathrm{v}} = \varepsilon_{\mathrm{a}} + 2\varepsilon_{\mathrm{r}}, \qquad \varepsilon_{\mathrm{d}} = \frac{2}{3}\left(\varepsilon_{\mathrm{a}} - \varepsilon_{\mathrm{r}}\right). \tag{2}$$

The yield locus in the stress plane (and positive q) is assumed to be given by

$$f = q + Mp' \ \ln\left(\frac{p'}{p_{\mathrm{c}}}\right) = 0. \tag{3}$$

The parameter p_{c} controls the size of the elastic domain and depends on the amount of plastic strains experienced. In the simplest version of the model, it depends on volumetric plastic strains, only. To find this relation explicitly, it is possible to make reference to the bilogarithmic expression proposed by Butterfield [2] that links the variation of void ratio, e, to that of the isotropic pressure in a purely isotropic test

$$\ln(1+e) = \ln(1+e_0) - \lambda' \ \ln(p_{\mathrm{c}}) \tag{4}$$

from which one can derive the volumetric strain rate as a function of the increment of p_{c}:

$$\frac{-\dot{e}}{1+e} = \dot{\varepsilon}_{\mathrm{v}} = \lambda' \frac{\dot{p}_{\mathrm{c}}}{p_{\mathrm{c}}}. \tag{5}$$

In a similar way we can assume that, upon unloading, the recovered elastic strain rates are given by

$$\dot{\varepsilon}_{\mathrm{v}}^{\mathrm{e}} = \kappa' \frac{\dot{p}_{\mathrm{c}}}{p_{\mathrm{c}}}, \tag{6}$$

so that the dependence on p_{c} of the plastic volumetric strain rates can be derived

$$\frac{\partial p_{\mathrm{c}}}{\partial \varepsilon_{\mathrm{v}}^{\mathrm{p}}} = \frac{p_{\mathrm{c}}}{(\lambda' - \kappa')}. \tag{7}$$

Equation (7) is the hardening law.

For a generic stress increment, volumetric as well as deviatoric strains take place. As in the original Cam Clay model, in the elastic domain, it is assumed that no recoverable shear strain is possible (i.e. the elastic shear modulus is assumed to be infinitely large). As far as volumetric strains are concerned, (6) is taken as valid for any load increment (it is necessary to assume that below a certain isotropic pressure, p_0, the bulk modulus is constant, however).

It is further assumed that plastic strain rates can be derived from a plastic potential g:

$$\dot{\varepsilon}_{\mathrm{v}}^{\mathrm{p}} = \Lambda \frac{\partial g}{\partial p'}, \qquad \dot{\varepsilon}_{\mathrm{d}}^{\mathrm{p}} = \Lambda \frac{\partial g}{\partial q}, \tag{8}$$

where Λ is a non-negative variable known as plastic multiplier. Equation (8) gives the flow rule.

If g coincides with f (associate flow rule), by defining the stress ratio η as

$$\eta \equiv q/p', \tag{9}$$

and the dilatancy d as

$$d \equiv \frac{\partial \varepsilon_{\mathrm{v}}^{\mathrm{p}}}{\partial \varepsilon_{\mathrm{d}}^{\mathrm{p}}}, \tag{10}$$

it is straightforward to derive from (3) that

$$\eta + d = M. \tag{11}$$

This relation is known as stress–dilatancy relationship.

In general, however, the expression of the yield locus and that of the plastic potential differ (non-associate flow rule). To make things simple, we assume here that the yield locus equation is characterized by a parameter $m < M$, i.e.:

$$f = q + mp' \ln\left(\frac{p'}{p_c}\right) = 0. \tag{12}$$

The value of Λ, for a given stress increment, can be derived by taking into account that plastic strains can occur only if $f = 0$ before and after the stress increment has occurred. Thus

$$\mathrm{d}f = 0 = \frac{\partial f}{\partial p'}\mathrm{d}p' + \frac{\partial f}{\partial q}\mathrm{d}q + \frac{\partial f}{\partial p_c}\mathrm{d}p_c. \tag{13}$$

From (3), (8), (11) and (12), one can eventually derive that

$$\Lambda = \frac{(m-\eta)\mathrm{d}p' + \mathrm{d}q}{mp'(M-\eta)}(\lambda' - \kappa'). \tag{14}$$

By choosing convenient values for M, m, λ' and k', it is possible to simulate soil behaviour in axisymmetric tests. From a qualitative point of view, the agreement between calculated and experimental data is very good, especially for normally consolidated clay specimens. For such a material, it can be shown, for instance, that the behaviour is non-linear and irreversible from the very beginning of the loading process. The maximum stress ratio reached in drained and undrained tests is the same. In drained tests the volumetric strains are positive, i.e. compactive, and the rate of them decreases with increasing deviatoric strain rates until an asymptotic value of the void ratio is reached (critical state). Correspondingly, in undrained tests the pore water pressure increases until an asymptotic value is achieved, again at the critical state. For overconsolidated clay specimens, the agreement is less good, because of the extreme simplicity of the elastic law assumed and of the shape of the yield locus.

The model can predict anyway several features of the observed behaviour of overconsolidated clay, such as the difference between lightly and heavily overconsolidated clays, the variation of the Skempton parameter A_f at failure with the overconsolidation ratio, the occurrence of a peak in deviatoric stresses in drained tests on heavily overconsolidated clay specimens and so on. Cam Clay was the first model capable to treat in a unified framework isotropic and shear loading, drained and undrained tests, normal consolidation and overconsolidation.

The assumption of non-normality allows the occurrence of a peak in an undrained test to occur in the hardening regime. Since in such a test

$$\dot{\varepsilon}_v = \dot{\varepsilon}_v^e + \dot{\varepsilon}_v^p = k'\frac{\dot{p}'}{p'} + \Lambda d = 0 \tag{15}$$

from (14) and (11) one can derive that the stress path is given by

$$\ln \frac{p'}{p_{c0}} = \frac{\eta}{m}\left(1 - \frac{k'}{\lambda'}\right). \tag{16}$$

A peak in q occurs when

$$\frac{\eta}{m} = \frac{1}{1 - \frac{k'}{\lambda'}}. \tag{17}$$

Equation (17) is the equation of a straight line passing through the origin that is called instability line [7]. Equation (17) gives also a simple mean to calibrate the value of the parameter m.

Many geomaterials after an initial compacting phase exhibit some dilatancy. This can be modelled by assuming that hardening depends on both volumetric and deviatoric plastic strains. The hardening rule is modified as in Nova [9]

$$\dot{p}_c = \frac{p_c}{\lambda' - k'}\left\{\dot{\varepsilon}_v^p + \xi\dot{\varepsilon}_d^p\right\}. \tag{18}$$

The physical meaning of ξ is that of the absolute value of the dilatancy at failure in drained tests. In fact when

$$d + \xi = 0, \tag{19}$$

a state at which hardening (or softening) cannot occur any longer is reached (limit state).

From the definition of d and (11) we can derive that the stress ratio at limit state is given by

$$\eta_f = M + \xi. \tag{20}$$

The value of Λ is modified via (12) and (18) as

$$\Lambda = \frac{(m - \eta)\mathrm{d}p' + \mathrm{d}q}{mp'(M - \eta + \xi)}(\lambda' - \kappa'). \tag{21}$$

When $\eta = \eta_f, \Lambda$ therefore tends to infinity (failure). On the other hand, when $\eta = M$ and consequently $d = 0$ we can derive from (6) that in undrained tests p' should not change at this stress ratio level. This means that the stress path either ends at this point (if $\xi = 0$) or has a vertical tangent (if $\xi > 0$). For values of η larger than M the stress path tends therefore towards the positive sense of axis p'. The zero dilatancy line (usually considered as the critical state) coincides therefore with the so called phase transformation line [4].

Finally, since

$$\Lambda = \frac{\frac{m\ \mathrm{d}p'}{p'} + \mathrm{d}\eta}{m(M - \eta + \xi)}(\lambda' - \kappa'), \tag{22}$$

an asymptotic state ($\dot{\eta} = 0$) is reached in undrained loading when

$$\eta = \eta_{\mathrm{u}} = M + \frac{\kappa'}{\lambda'}\xi. \tag{23}$$

It is worth nothing therefore that according to this elementary model drained failure and the asymptotic undrained state do not coincide and the latter is reached for a smaller stress ratio value.

3 Modelling of Bonded Soils

Most natural soils are characterized by diagenetic bonds which can be destroyed by sampling and/or remoulding. In order to model the behaviour of such materials it is necessary to modify the constitutive law presented so far.

From a macroscopic viewpoint, the existence of such bonds is essentially reflected by the occurrence of a non-zero tensile strength. Moreover, the size of the "initial" elastic domain is not only controlled by the maximum past pressure but also by the degree of cementation.

To make things as simple as possible, we disregard here the tensile strength and take account of the size increase of the elastic domain, only. We can therefore define

$$p_{\mathrm{c}} = p_{\mathrm{m}} + p_{\mathrm{s}}, \tag{24}$$

where p_{s} plays exactly the same role of p_{c} for an unbonded soil, while p_{m} is a new parameter that takes account of the intergranular bonding degree. Depending on the mechanical and environmental (i.e. chemical) conditions, the value of p_{m} can remain constant, increase (diagenesis) or decrease (weathering). In general

$$p_{\mathrm{m}} = p_{\mathrm{m}}\left(\varepsilon_{ij}^{\mathrm{p}}, \vartheta_k\right), \tag{25}$$

where $\varepsilon_{ij}^{\mathrm{p}}$ are plastic strains, while ϑ_k indicates a set of non-mechanical parameters (e.g. temperature, time, solute concentration, ...). Figure 1 shows the yield locus for a bonded soil in the compression quadrant of the axisymmetric plane.

The occurrence of plastic strains can be associated to the breaking of the bonds. Therefore the value of p_{m} must decrease with increasing plastic strains. For the sake of simplicity we assume here, in a way analogous to (7), that

$$\frac{\partial p_{\mathrm{m}}}{\partial \varepsilon_{\mathrm{d}}^{\mathrm{p}}} = -\rho_{\mathrm{m}}^{*} p_{\mathrm{m}}, \tag{26}$$

that is more or less equivalent to say that the number of bonds that break when plastic strains take place is proportional to the total bond number. The parameter ρ_{m}^{*} controls the rate of bond degradation.

From (8), (13), (18), (24) and (26), one can derive that

$$\Lambda = \frac{(m-\eta)\mathrm{d}p' + \mathrm{d}q}{H}, \tag{27}$$

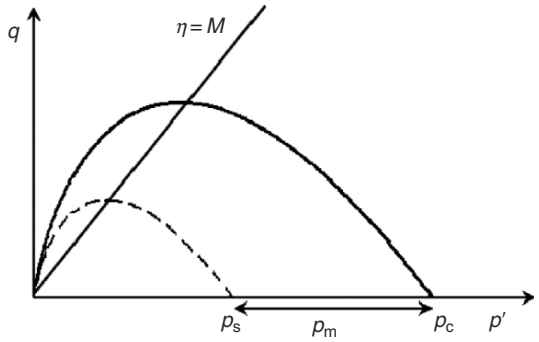

Fig. 1. Yield locus for a bonded soil

where

$$H = -\frac{\partial f}{\partial p_c}\left(\frac{\partial p_c}{\partial p_s}\frac{\partial p_s}{\partial \varepsilon_v^p}\frac{\partial g}{\partial p'} + \frac{\partial p_c}{\partial p_s}\frac{\partial p_s}{\partial \varepsilon_d^p}\frac{\partial g}{\partial q} + \frac{\partial p_c}{\partial p_m}\frac{\partial p_m}{\partial \varepsilon_d^p}\frac{\partial g}{\partial q}\right)$$

$$= \frac{mp'}{p_c}\left(\frac{p_s(M-\eta+\xi)}{\lambda'-\kappa'} - \rho_m^* p_m\right) \tag{28}$$

is the hardening modulus. This can be conceived as the sum of two components. The first one is linked to the plastic volumetric strain and can be positive (hardening) or negative (softening), depending on the sign of the volumetric strains, as is the original Cam Clay model. The second is instead linked to bond degradation and it is always negative.

Defining for the sake of brevity

$$\rho_s = \frac{1}{\lambda'-\kappa'}, \tag{29}$$

the overall value of H depends on the mutual relation between $\rho_s p_s$ and $\rho_m^* p_m$. Note that at the beginning of the shear phase the first term between parentheses can be smaller than the second. Soil can be therefore in a softening state; at a later state, however, p_m decreases while p_s increases so that hardening can be reached again.

This is an unusual situation, but it can actually occur. Consider first, for the sake of simplicity, a p' constant test on a soft rock for which it is assumed the validity of the normality rule ($m = M$) and $\xi = 0$.

Assume that, after isotropic consolidation, the stress state is within the elastic domain, as in Fig. 2. The first loading phase (AB) occurs within the elastic domain and, for the very simple elastic law assumed, neither axial nor volumetric strains take place. At B the specimen yields. For convenient values of the constitutive parameters, H is negative, i.e. the specimen softens under axial strain increase. The occurrence of both volumetric and deviatoric plastic strains, governed by the flow rule, makes p_s increasing while p_m is decreasing, so that the absolute value of H decreases. For a convenient value

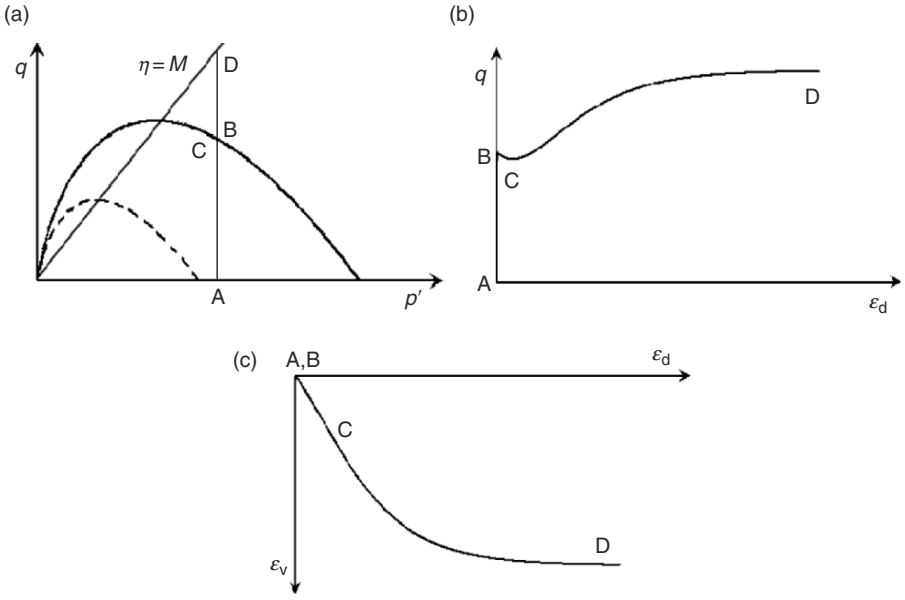

Fig. 2. (**a**) Stress path in a constant isotropic pressure test; (**b**) Calculated deviatoric strains; (**c**) Calculated volumetric strains

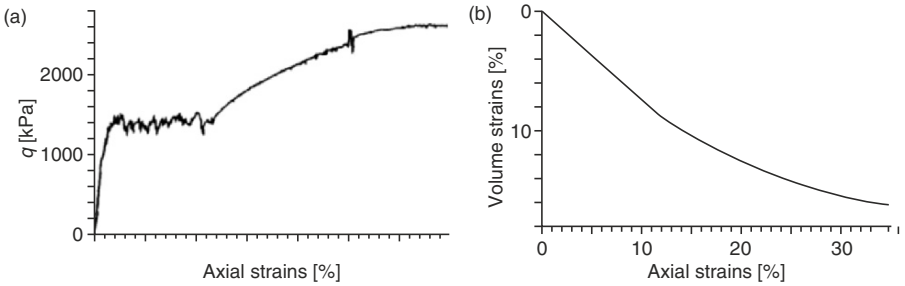

Fig. 3. (**a**) Axial strains in a constant cell pressure test on a specimen of Calcarenite di Gravina; (**b**) Volumetric strains (data after [8])

of the axial strain (point C) the hardening modulus becomes zero. This point is associated with a horizontal tangent of the deviatoric stress–strain law. For larger strains the hardening modulus becomes positive and the deviator stress can increase, until a threshold value associated to critical state is eventually achieved (point D). Figure 3 (after [8]) shows the experimental results (in a constant cell pressure test) in which a clear instability phenomenon followed by hardening is shown.

If the stress state is on the yield locus already after isotropic consolidation, softening starts at the very beginning of the yield phase (Fig. 4), so that

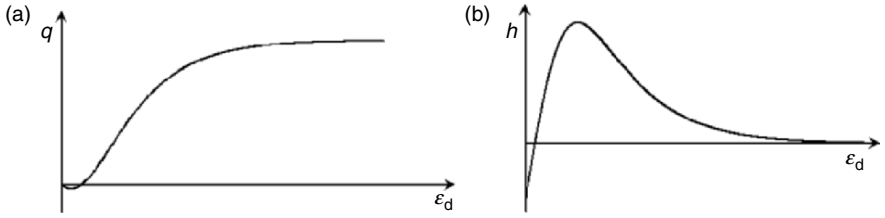

Fig. 4. Deviatoric strains (**a**) and hardening modulus (**b**) in a constant isotropic pressure test with an initial stress state belonging to the yield surface

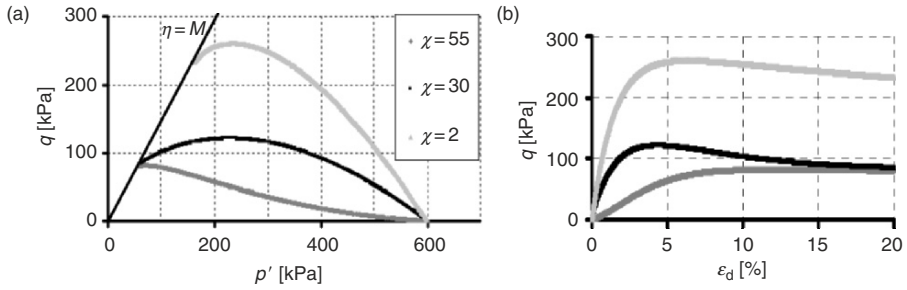

Fig. 5. Calculated stress paths (**a**) and deviatoric strains trends (**b**) obtained in undrained compression tests for different initial values of the ratio χ

negative q values are associated to increasing shear strains. This behaviour cannot be captured by means of an ordinary triaxial apparatus, since the test is actually displacement controlled. It is likely that a non-uniformity in the stress and strain state of the specimen take place, for instance, with the formation of local compaction band. When strains are larger, part of the bonds are destroyed so that p_m is smaller and the material experiences hardening again.

A fully strain controlled test as undrained compression is of particular interest. Figure 5 shows the trend of the effective stress path for $m \neq M$ and different initial values of the ratio

$$\chi = \frac{\rho_m^* p_m}{\rho_s p_s}. \tag{30}$$

We can note that for small values of χ, the behaviour is similar to that of a normally consolidated soil, while for high values of χ the concavity of the stress path changes sign and a remarkable increase in pore water pressure takes place. Note in passing that the use of non-normality allows the peak in q for a stress ratio smaller than the critical state to be modelled. It is very interesting to note that in the undrained test, despite softening takes place, the stress–strain law does not give signs of instability. From (15) we can in fact derive that the tangents to the stress path and the deviatoric stress–strain

curve are given by

$$\mathrm{d}p' = -\frac{M-\eta}{k'h+(M-\eta)(m-\eta)}\mathrm{d}q, \tag{31}$$

$$\mathrm{d}\varepsilon_1 = -\frac{k'}{M-\eta}\frac{\mathrm{d}p'}{p'} = \frac{k'/p'}{k'h+(M-\eta)(m-\eta)}\mathrm{d}q. \tag{32}$$

For negative values of h (but small in absolute value) they are both positive. An apparent hardening behaviour takes place, therefore. However, if

$$h = -\frac{(M-\eta)(m-\eta)}{k'} \tag{33}$$

at constant axial stress, an arbitrary decrease of p', and a corresponding increase of u, can occur. At the same time, axial strain increases.

This result can explain the rather awkward behaviour observed on some Jarofix specimens, as shown in Fig. 6. After having been consolidated to 400 kPa, the drainage was closed. As soon as deviatoric strains were applied, a remarkable increase of the pore water pressure was observed. After a while, the control of the test was regained.

An initially similar type of behaviour was observed on Lonate silt. The concavity of the stress path is always directed in the sense of positive p', what is very unusual. With a convenient set of parameters ($\xi \neq 0$), however, it is possible to reproduce this behaviour in an acceptable way, Fig. 7.

Finally, the effect of χ on the behaviour in oedometric tests can be investigated. Figure 8 shows the predicted stress paths and vertical stress–strain curve for different initial values of χ. For high values of it the stress path makes a curl that corresponds to a peak in the stress–strain curve. As shown by Nova (2003) this phenomenon is associated to the formation of a compaction band. Of course, for such materials, in order to get the calculated behaviour, full strain control is necessary.

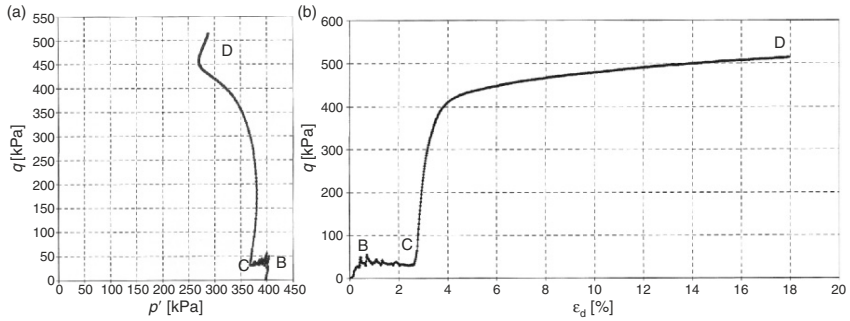

Fig. 6. Stress paths (**a**) and deviatoric strains (**b**) in an undrained compression test on specimens of Jarofix

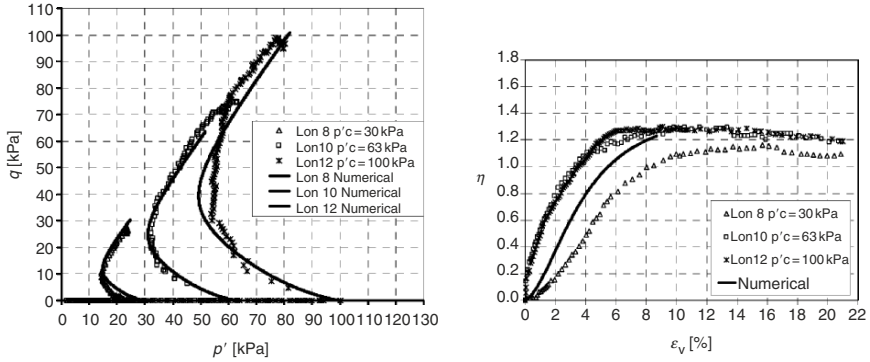

Fig. 7. Experimental and calculated curves related to undrained triaxial tests on Lonate silt (data after [15]): stress paths (**a**) and deviatoric strains (**b**)

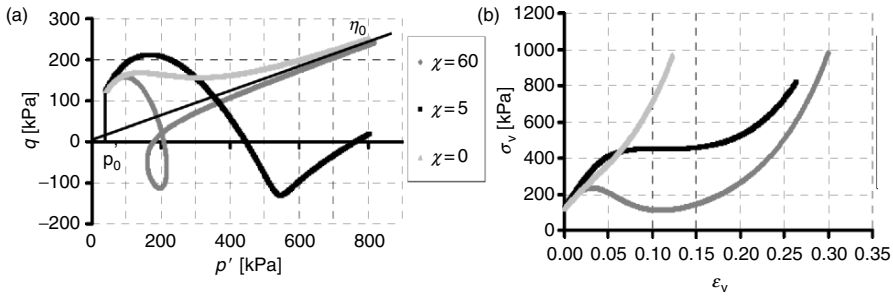

Fig. 8. Calculated stress paths (**a**) and vertical stress trends (**b**) obtained in oedometric tests for different values of the ratio χ

4 Conclusions

Bonded soils with large initial porosity show unusual behaviour when tested in either drained or undrained conditions. The transition from the elastic to the elastoplastic regime can be characterized by a temporarily unstable behaviour, followed by a new hardening phase. In undrained tests, the pore water pressure can increase unlimitedly for certain values of the stress ratio. In the oedometer, loss of control of a load controlled test is possible with the formation of a compaction band.

To model the behaviour of such materials, at least from a qualitative point of view, a small modification of the original Cam Clay model is sufficient. It is enough to assume that hardening depends on two competing "mechanism": compaction and shear.

Compaction is responsible for hardening. Shear strains can at the same time cause hardening of the unbonded fabric and softening of the bonds.

These are in fact assumed to be reduced in number as long as shear strains increase.

The comparisons sketched in this chapter show that with such a simple modification, several features of this unusual behaviour can be captured: instability followed by hardening, large pore water pressure increase in undrained tests, formation of compaction bands in oedometric tests. The key factor is that the hardening modulus can be negative at the very beginning of the shearing process. Despite that, the deviator stress can be increased in undrained conditions. The chosen hardening rules, moreover, tend to progressively erase the effect of bond breaking, while they emphasize hardening due to soil compaction. Hardening then follows softening (and not vice versa) and initial instability is followed by a regular and more usual soil behaviour.

References

1. Arroyo M, Tsige M, Medina L, Cañizal J (2005) Mechanical properties of a stabilized metallurgical waste. Submitted
2. Butterfield R (1979) A natural compression law for soils. Géotechnique 29: 469–480
3. Hueckel T, Ma CM (1991) Plasticity of saturated clays under combined mechanical and environmental loads. In: Desai CS et al. (eds) Constitutive Laws for Engineering Materials, ASME, New York, pp 53–56
4. Ishihara K, Tatsuoka F, Yasuda S (1975) Undrained deformation and liquefaction of sand under cyclic stresses. Soils Foundations 15(1): 29–44
5. Kavvadas M, Anagnostopoulos A, Kalteziotis N (1993) A framework for the mechanical behaviour of cemented Corinth marl. Proceedings of Geotechnical Engineering of Hard Soils–Soft Rocks, Balkema, Rotterdam, pp 577–583
6. Lade PV (1977) Elastoplastic stress–strain theory for cohesionless soil with curved yield surfaces. Int. J. Solids Struct. 13: 1019–1035
7. Lade PV (1992) Static instability and liquefaction on loose fine sandy slopes. J. Geotech. Eng. 118: 51–71
8. Lagioia R, Nova R (1995) An experimental and theoretical study of the behaviour of a calcarenite in triaxial compression. Géotechnique 45(4): 633–648
9. Nova R (1977) On the hardening of soils. Arch. Mech. Stos. 29(3): 445-458
10. Nova R (1992) Mathematical modelling of natural and engineered geomaterials. General lecture 1st E.C.S.M. Munchen, Eur. J. Mech. A/Solids 11: 135–154
11. Nova R (2003) The failure concept in soil mechanics revisited. In: Labuz JF & Drescher A (eds) Bifurcations and Instabilities in Geomechanics. Balkema, Lisse, pp 3–16
12. Nova R, Arroyo M (2005) An attempt to model compaction instabilities in stabilized residues. Proc. Int. Symp. Powders Grains, Stuttgart
13. Nova R, Wood DM (1979) A constitutive model for sand in triaxial compression. Int. J. Num. Anal. Meth. Geomech. 3(3): 255–278
14. Nova R, Castellanza R, Tamagnini C (2003) A constitutive model for bonded geomaterials subject to mechanical and/or chemical degradation. Int. J. Num. Anal. Meth. Geomech. 27(9): 705–732

15. di Prisco C (2005) Studio dei problemi geotecnici di stabilità dei fronti di scavo connessi allo svuotamento di vasche di decantazione. Report Provincia Varese
16. Rouainia M, Wood DM (2000) A kinematic hardening constitutive model for natural clays with loss of structure. Géotechnique 50(2): 153–164
17. Schofield AN, Wroth CP (1968) Critical State Soil Mechanics. McGraw Hill, New York

An Evaluation of Different Constitutive Models to Predict the Directional Response of a Reconstituted Fine-Grained Soil

C. Tamagnini*, D. Mašin†, D. Costanzo#, and G. Viggiani¶

*Università degli Studi di Perugia, Italy
tamag@unipg.it
†Charles University, Prague, Czech Republic
#Politecnico di Torino, Italy
¶Laboratoire 3S, UJF/INPG/CNRS, Grenoble, France

1 Introduction

The directional character of the mechanical response of fine-grained soils, i.e., its dependence on the loading direction, has been the subject of several studies throughout the last decades, including both experimental and theoretical investigations. On the experimental side, some pioneering contributions were provided in the early seventies, see e.g., [17, 37]. Notable examples of more recent contributions can be found in [2, 3, 11, 28].

On the theoretical side, a major improvement of classical plasticity as applied to clays has been provided by the introduction of the so-called nested-surface kinematic hardening theories of plasticity, originating from the works of Prevost [24], Mroz et al. [21], and Hashiguchi [14]. These latter studies were essentially motivated by the need of improving available design approaches for those practical applications where soil is subject to cyclic loading conditions, e.g., earthquake and offshore engineering. Later studies on shear banding in soils as a bifurcation problem [25,27] showed the need to take into account the *incrementally nonlinear* character of the material response – i.e., a dependence of soil tangent stiffness on the strain rate direction, see, e.g., [8, 32] – and motivated the development of a class of constitutive theories which depart from the framework of plasticity and rather can be seen as a generalization of Truesdell theory of hypoelasticity [34]. A distinctive feature of this approach is the absence of any kinematic decomposition of strain rates into reversible and irreversible parts. An important example in this respect is provided by the theory of hypoplasticity, as defined by Kolymbas [15], see also [16].

More generally, it turns out that a proper description of soil behavior as a function of loading direction not only is useful for modeling the response of geotechnical structures to cyclic loading or for analyzing localization phenomena, but it is also a key ingredient in the analysis of any geotechnical structure

where different zones of soil experience widely different stress-paths, both in size and direction, e.g., deep excavations and tunnels. This has been demonstrated in a number of practical applications, e.g., [10, 29, 35, 36].

The objective of this work is to assess the performance of some advanced constitutive models in reproducing the incremental behavior of a soft, normally consolidated clay as observed in laboratory tests performed along a number of different stress-paths, all originating from a common initial state (*stress-probes*). Two particular classes of inelastic models have been selected for the comparison. On the one hand, the three-surface kinematic hardening model proposed in [30, 31] has been chosen as a representative of advanced soil plasticity approaches. On the other hand, three different versions of hypoplasticity have been considered: the CLoE model [5]; the clay K–hypoplastic model recently proposed by [18], and an enhanced version of this last model, embedding the concept of intergranular strain [23] as an additional internal state variable. Finally, the classical modified Cam-Clay model [26] has been also considered for reference. The results obtained from a large program of stress-probing tests on a soft normally consolidated clay [7] are used herein both for the calibration of the five models, and as a benchmark for the evaluation of the models performance.

The details of the experimental program and a complete account of the experimental results are given in [7], and will be only briefly recalled herein. The results obtained from standard isotropic or triaxial compression and extension tests, starting from an isotropic state, have been used for the calibration of the models. The assessment of models performance has been carried out with reference to a different set of data, obtained from axisymmetric stress-probing tests starting from an anisotropic initial stress state. Predicted and observed directional responses are compared in terms of incremental response envelopes, as defined in [33], which provides a global picture of the models performance over a wide range of loading directions.[1]

2 Experimental Program

The material tested (Beaucaire Marl) is a low plasticity silty clay coming from southern France. The tests were performed on reconstituted material, prepared by thoroughly mixing known quantities of natural soil with distilled water, to a water content approximately equal to 1.5 times the liquid limit. The slurry was then consolidated in a large consolidometer up to a nominal vertical effective stress of 75 kPa. Full details of the experimental procedures employed in the testing program are given in [7].

All tests were carried out using a Bishop and Wesley-type triaxial cell, with fully automated feedback-control. Standard soil specimens, 38.1 mm in diameter and 76.2 mm high, were used in all the tests. Axial load was

[1] In the following, the usual sign convention of soil mechanics (compression positive) is adopted throughout. In line with Terzaghi's principle of effective stress, all stresses are *effective* stresses.

measured by means of an internal load cell. Cell and pore water pressures were measured by means of pressure transducers. Assessments of system scatter showed that stresses could be resolved and controlled to within 0.5 kPa. Axial displacements were measured by means of an external LVDT, with a 10 mm range, and an external proximity transducer having a 2 mm range. Internal and external strain measurements were found to be equivalent to all practical purposes, and reliable down to a minimum axial strain of 0.05%. Volume changes were measured by means of an Imperial College-type volume gauge, with a 50 mm^3 range and a resolution of 0.035% in terms of volume strain. The overall accuracy of volume strain measurements, also depending on possible temperature effects and the stiffness of drainage lines, was evaluated to be approximately 0.05%. This figure also applies to radial strains, which were not directly measured, but rather computed from axial and volume strains.

The testing program consisted of 20 drained stress probes (including two backup tests), starting from a common initial stress state and pointing in different directions in the triaxial plane. Two different initial stress states were considered: the first one (state A) is located on the isotropic axis at mean stress $p = 150$ kPa; the second one (state B) is characterized by the same value of p and a deviator stress $q = 60$ kPa. Both states A and B were reached upon stress-controlled consolidation along a constant q/p path ($q/p = 0$ for state A, $q/p = 0.4$ for state B). Each stress probe from an initial state $(\sigma_{a0}, \sigma_{r0})$ is described by the following parametric equations:

$$\Delta\sigma_a := \sigma_a - \sigma_{a0} = R_\sigma \sin\alpha_\sigma \tag{1}$$

$$\sqrt{2}\,\Delta\sigma_r := \sqrt{2}\,\sigma_r - \sigma_{r0} = R_\sigma \cos\alpha_\sigma, \tag{2}$$

where $R_\sigma = \|\Delta\boldsymbol{\sigma}\|$ denotes the norm of the stress increment, and α_σ represents its direction in the Rendulic plane of stress increments ($\Delta\sigma_a : \sqrt{2}\,\Delta\sigma_r$, see Fig. 1a). Each stress probe was continued up to a R_σ value corresponding either to a "failure" state, or to a prescribed maximum value of the cell pressure.

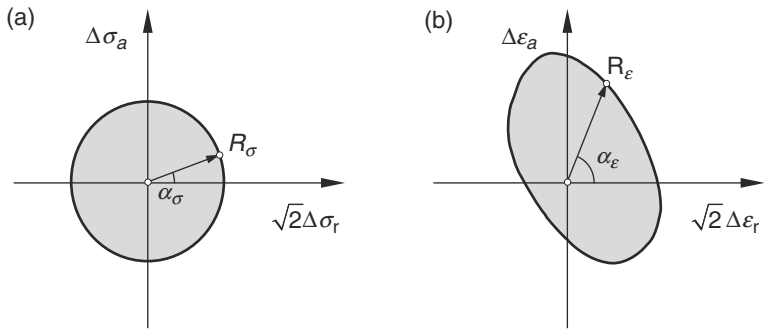

Fig. 1. Response envelope concept: (**a**) input stress probes; (**b**) output strain envelope

Table 1. Details of the experimental stress-probing program, after [7]

test #	initial state	α_σ (deg.)	α_σ^{pq} (deg.)	test #	initial state	α_σ (deg.)	α_σ^{pq} (deg.)
Tx124	A	0	303.69	Tx118	B	0	303.69
Tx128	A	35	0.00	Tx115	B	35	0.00
—	—	—	—	Tx130	B	46	21.91
Tx121	A	90	71.57	Tx132	B	90	71.57
Tx126	A	126	90.00	Tx119	B	126	90.00
—	—	—	—	Tx116	B	154	104.49
Tx123	A	180	123.69	—	—	—	—
Tx127	A	215	180.00	Tx134	B	215	180.00
—	—	—	—	Tx129	B	226	201.91
Tx122	A	270	251.57	Tx117	B	270	251.57
Tx125	A	305	270.00	Tx113	B	305	270.00

All probes were carried out under stress control, applying a constant rate of the stress increment norm approximately equal to $2.5\,\mathrm{kPa\,h^{-1}}$. Note that for each initial state, the testing program included as particular cases convnetional triaxial, constant p and isotropic, compression and extension paths. The loading directions α_σ prescribed for each probe are listed in Table 1. The stress probe direction in the $q:p$ plane, α_σ^{pq}, calculated from the stress invariant increments Δp and Δq as:

$$\Delta p = \frac{1}{3}\left(\Delta\sigma_a + 2\Delta\sigma_r\right); \quad \Delta q = \Delta\sigma_a - \Delta\sigma_r \tag{3}$$

$$\sin\alpha_\sigma^{pq} = \frac{\Delta q}{\sqrt{(\Delta p)^2 + (\Delta q)^2}}; \quad \cos\alpha_\sigma^{pq} = \frac{\Delta p}{\sqrt{(\Delta p)^2 + (\Delta q)^2}} \tag{4}$$

is also reported in the same table. A picture of the stress paths originating from the initial state B in the q:p plane is shown in Fig. 2.

3 Constitutive Models Considered

3.1 3-SKH Model

The 3-SKH model is an advanced example of the kinematic hardening plasticity models for soils. It can be considered an evolution of the classical modified Cam-Clay model [26] and the two-surface kinematic hardening model proposed in [1]. The main feature of the model consists in the introduction of an additional kinematic *history surface* – as defined in [30], see Fig. 3 – motivated by experimental findings about the influence of the recent stress history on soil behavior [2]. The general formulation of the 3-SKH model is given in [31].

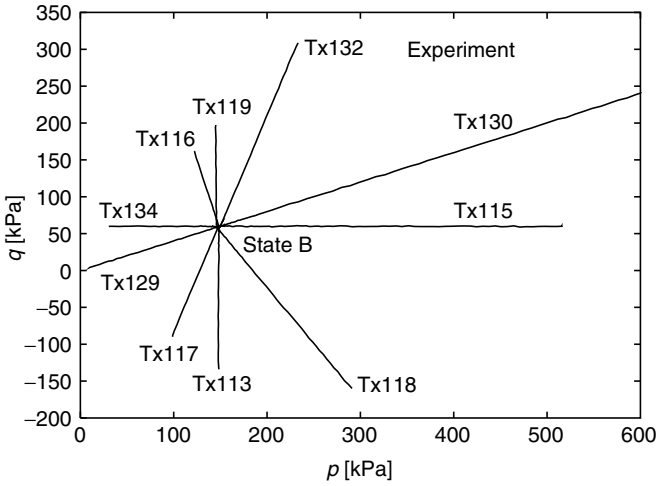

Fig. 2. Experimental stress paths from state B

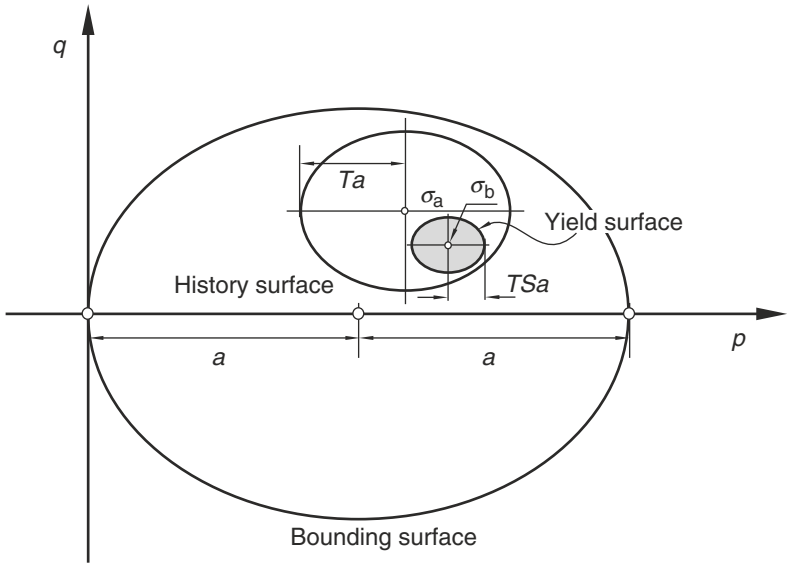

Fig. 3. Sketch of the characteristic surfaces of the 3-SKH model

3.2 CLoE Hypoplastic Model

The hypoplastic model CLoE originates from the pioneering work of Chambon and Desrues on strain localization in incrementally nonlinear materials [4, 9]. The constitutive equation is given, in rate-form, by:

$$\dot{\boldsymbol{\sigma}} = \boldsymbol{\mathcal{A}}(\boldsymbol{\sigma})\dot{\boldsymbol{\epsilon}} + \boldsymbol{b}(\boldsymbol{\sigma})\,\|\dot{\boldsymbol{\epsilon}}\|\,. \tag{5}$$

The first term on the right-hand side yields an incrementally linear response, while the second accounts for incremental nonlinearity via a linear dependence on the norm of the strain rate tensor. To keep the formulation as simple as possible, the set of state variables is limited to the stress tensor $\boldsymbol{\sigma}$.

The two constitutive tensors $\boldsymbol{\mathcal{A}}$ and $\boldsymbol{b}$ appearing in (5) are homogeneous functions of degree one of the stress tensor, for which no explicit expression is assumed. Rather, $\boldsymbol{\mathcal{A}}$ and $\boldsymbol{b}$ are obtained via an interpolation procedure based on the assigned material responses at some suitably defined image points, located along special loading paths (*basic paths*). These are selected among those stress-paths that are experimentally accessible by means of conventional laboratory tests. Details on the mathematical formulation of the material response for the basic paths and on the interpolation procedure are given in [5].

3.3 K–Hypoplastic Models for Clays

The basic formulation of K–hypoplasticity for rate-independent fine-grained soils has been recently developed in [18]. The model combines the mathematical structure of K–hypoplastic models for granular soils – see e.g., [38] and references therein – with key concepts of critical state soil mechanics through the notion of generalised hypoplasticity [22]. The constitutive equation is given, in rate-form, by:

$$\dot{\boldsymbol{\sigma}} = f_s \boldsymbol{\mathcal{L}} : \dot{\boldsymbol{\epsilon}} + f_s f_d \boldsymbol{N}\,\|\dot{\boldsymbol{\epsilon}}\|\,. \tag{6}$$

Explicit, closed-form expressions for the two tensors $\boldsymbol{\mathcal{L}}(\boldsymbol{\sigma})$ and $\boldsymbol{N}(\boldsymbol{\sigma})$ and for the scalar functions $f_s(p)$ and $f_d(p, e)$ are provided in [18]. It must be noted that, although (5) and (6) appear quite similar, a major difference of K–hypoplasticity as compared to CLoE stems from including void ratio in the set of state variables for the material through the pyknotropy factor f_d [13]. This allows the critical state concept to be incorporated in the model response.

The K–hypoplastic model provided by (6) can predict the behavior of fine-grained soils upon monotonic loading at medium to large strain levels. An enhanced version has been also proposed in [18] to improve the model performance in the small-strain range and for cyclic loading conditions. The constitutive equation for the enhanced model reads:

$$\dot{\boldsymbol{\sigma}} = \boldsymbol{\mathcal{M}}\,(\boldsymbol{\sigma}, e, \boldsymbol{\delta}, \boldsymbol{\eta}) : \dot{\boldsymbol{\epsilon}}, \tag{7}$$

where $\boldsymbol{\mathcal{M}}$ is the fourth-order tangent stiffness tensor of the material, $\boldsymbol{\eta} := \dot{\boldsymbol{\epsilon}}/\,\|\dot{\boldsymbol{\epsilon}}\|$ denotes the strain rate direction, and the additional state variable $\boldsymbol{\delta}$ is a symmetric second-order tensor called *intergranular strain* [23].

Let $\rho := \|\boldsymbol{\delta}\| / R$ be a suitable normalized magnitude of $\boldsymbol{\delta}$, R being a scalar model parameter, and

$$\hat{\boldsymbol{\delta}} = \begin{cases} \boldsymbol{\delta}/\|\boldsymbol{\delta}\| & \text{for } \boldsymbol{\delta} \neq \mathbf{0} \\ \mathbf{0} & \text{for } \boldsymbol{\delta} = \mathbf{0} \end{cases} \tag{8}$$

denote intergranular strain direction. The fourth-order tangent stiffness tensor $\boldsymbol{\mathcal{M}}$ is calculated from the constitutive tensors tensors $\boldsymbol{\mathcal{L}}$ and $\boldsymbol{\mathcal{N}}$ defined in (6) and the intergranular strain direction $\hat{\boldsymbol{\delta}}$ via the following interpolation:

$$\boldsymbol{\mathcal{M}} = [\rho^{\chi} m_T + (1 - \rho^{\chi}) m_R] f_s \boldsymbol{\mathcal{L}} + \boldsymbol{\mathcal{B}}, \tag{9}$$

where:

$$\boldsymbol{\mathcal{B}} := \begin{cases} \rho^{\chi}(1 - m_T) f_s \boldsymbol{\mathcal{L}} : \hat{\boldsymbol{\delta}} \otimes \hat{\boldsymbol{\delta}} + \rho^{\chi} f_s f_d \boldsymbol{\mathcal{N}} \otimes \hat{\boldsymbol{\delta}} & (\hat{\boldsymbol{\delta}} : \dot{\boldsymbol{\epsilon}} > 0). \\ \rho^{\chi}(m_R - m_T) f_s \boldsymbol{\mathcal{L}} : \hat{\boldsymbol{\delta}} \otimes \hat{\boldsymbol{\delta}} & (\hat{\boldsymbol{\delta}} : \dot{\boldsymbol{\epsilon}} \leq 0) \end{cases} \tag{10}$$

The evolution equation for the intergranular strain tensor $\boldsymbol{\delta}$ is given by

$$\dot{\boldsymbol{\delta}} = \begin{cases} \left(\boldsymbol{\mathcal{I}} - \hat{\boldsymbol{\delta}} \otimes \hat{\boldsymbol{\delta}} \rho^{\beta_r} \right) : \dot{\boldsymbol{\epsilon}} & (\hat{\boldsymbol{\delta}} : \dot{\boldsymbol{\epsilon}} > 0) \\ \dot{\boldsymbol{\epsilon}} & (\hat{\boldsymbol{\delta}} : \dot{\boldsymbol{\epsilon}} \leq 0) \end{cases} . \tag{11}$$

In (9)–(11), χ, m_T, m_R, and β_r are material constants. Full details of the mathematical structure of the model are provided in [18].

3.4 Calibration of the Models

When comparing the performance of different constitutive models in predicting the observed directional response of the material, a particular care must be taken in the proper selection of the procedure adopted for their calibration. In the present case, this task is somewhat facilitated by the fact that all the constitutive models considered, with the only exception of the CLoE hypoplastic model, incorporate the basic principles of critical state soil mechanics, and thus some of the material constants share the same physical meaning.

In order to separate the data used for the calibration of the different models and the data used for the evaluation of their performance, the material constants of the five models have been determined from the results of the stress probes starting from the isotropic initial state A. This is also consistent with the procedure typically used in practical applications, where most of the experimental data provided by the site investigation refer to isotropically consolidated, drained, or undrained triaxial tests.

For some of the constitutive models considered, the available data from stress probes at point A do not provide enough information to calibrate all the relevant constants. This is the case, for example, of the material parameters controling the response of the 3-SKH model and the enhanced K–hypoplastic model in the very small strain range. In such cases, the choice has been made to evaluate such material constants based on the experience gathered in previous

experimental investigations on similar soils. Although such a choice necessarily introduces a certain degree of subjectivity in the comparative evaluation of the models response, it can still be considered acceptable to our purposes, considering that the typical range of variation of such parameters for different soils is relatively limited, and the model response is not very sensitive to their variation, see e.g., [6, 23].

The calibration procedures are fully detailed in [20]. The resulting sets of material constants adopted for each model are reported in Tables 2 and 3. For the meaning of each constant and the initial values of the state variables adopted in the simulations, the reader is referred to [20].

Table 2. Material constants adopted for MCC, 3-SKH and K–hypoplastic models

material constant	MCC	3-SKH	K–hypo (standard)	K–hypo (enhanced)
N	2.245	–	–	–
λ	0.097	–	–	–
κ	0.017	–	–	–
M	1.33	1.33	–	–
G (MPa)	5.0	–	–	–
N^*	–	0.85	0.85	0.85
λ^*	–	0.057	0.057	0.057
κ^*	–	0.004	0.007	0.007
A	–	653.0	–	–
n	–	0.71	–	–
m	–	0.27	–	–
T	–	0.24	–	–
S	–	0.16	–	–
ψ	–	1.0	–	–
ϕ_c (deg)	–	–	33.0	33.0
r	–	–	0.4	0.4
m_R	–	–	–	3.5
m_T	–	–	–	3.5
R	–	–	–	10^{-4}
β_r	–	–	–	0.2
χ	–	–	–	6.0

Table 3. Material constants adopted for CLoE model

φ_c (deg.)	c (kPa)	χ_{ca} (–)	y_{ca} (–)	y_{rc} (–)	p_{fc} (–)	p_{ref} (kPa)	$\epsilon_{v,\text{ref}}$ (–)	λ_c (–)	φ_e (deg.)
34.0	0	0.17	0.055	3.1	0	147.26	0.0	183.34	33
χ_d (–)	χ_c (–)	χ_{m2} (–)	y_e (–)	p_{fe} (–)	m_c (–)	m_e (–)	n (–)	ω (–)	
−1.0	−0.1	−0.05	0.011	0.02	−0.2	0.0	−0.2	0.36	

4 Observed vs. Predicted Response

In the following, the response of reconstituted Beaucaire Marl to the stress probing program detailed in Table 1 and the predictions of the different models described in Sect. 3 are depicted using the so-called *incremental strain response envelope*, as defined in [33]. Such a representation directly follows from the concept of response envelope – first proposed in [12] – by replacing stress and strain rates with finite-size stress and strain increments. In the general case, an incremental strain response envelope (RE, hereafter) is a "surface" in a six-dimensional space. However, for the particular loading conditions considered, the most natural choice is to represent the section of the REs in the plane of work-conjugated strain increment quantities, $(\Delta\epsilon_a, \sqrt{2}\,\Delta\epsilon_r)$, see Fig. 1b. The size of each strain increment vector defining the RE can be directly interpreted as a directional secant compliance of the material, for the associated loading direction and stress increment magnitude.

Figures 4 and 5 show the computed REs for all the model considered at small to medium stress increment levels ($R_\sigma = 20$, 30, 40, and 50 kPa), and at medium to large stress increment levels ($R_\sigma = 50$ and 90 kPa), respectively. The corresponding experimental REs are also shown on the top left corner of both figures.

For small to medium stress increment levels, the experimental REs indicate that the softest response is associated to those paths which are characterized by a large deviatoric component (e.g., tests Tx119 and Tx113). As R_σ increases, the envelopes progressively shift upward to the left, due to the fact that the initial state is closer to the critical state line for axisymmetric compression than to the corresponding line for axisymmetric extension. For $\eta = 0.4$ loading paths (Tx130 and Tx129), the material response is softer when the probe points in the direction of continued loading, and stiffer upon unloading (i.e., upon full stress path reversal with respect to the consolidation history). In fact, this last path corresponds to the stiffest response of the material. A direct consequence of the above observations is that the experimental REs are markedly nonsymmetric about the origin of the strain increment space.

The predictions of the different models considered appear, from a qualitative standpoint, all in fair agreement with the salient features of the experimental response discussed earlier. The only notable exception is represented by the predictions of CLoE model upon $\eta = 0.4$ loading paths, where – contrary to experimental evidence – no significant difference between secant stiffnesses in compression and extension is observed. From a quantitative standpoint, however, all models appear to significantly underpredict the secant stiffness of the material. The REs predicted by the two elastoplastic models have a convex shape, except for the expected, yet minor irregularity of the Modified Cam-Clay envelopes, close to neutral loading in extension. The REs of the two K–hypoplastic models, and (to a much lesser extent) those of CLoE show

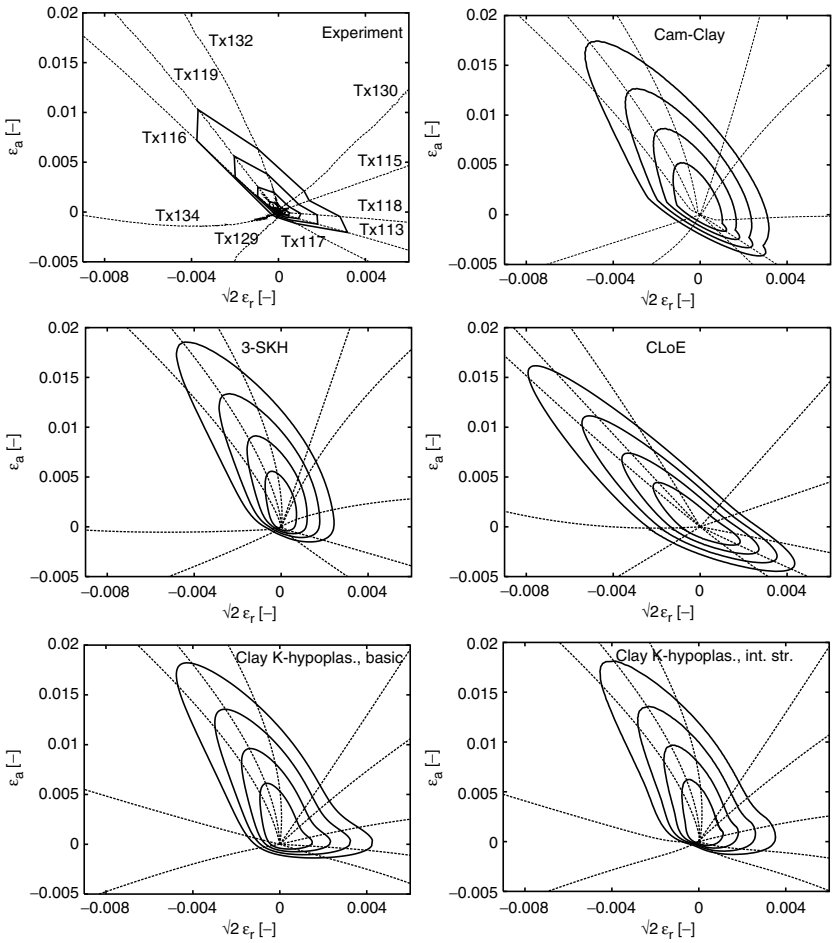

Fig. 4. Experimental vs. simulated strain response envelopes for $R_\sigma = 20$, 30, 40, and 50 kPa

some degree of nonconvexity in a region located around the $\eta = 0.4$ loading direction. This feature is also shown by the two largest experimental REs, although such an observation is based on the results of one single stress-probe.

At large stress increment level ($R_\sigma = 90$ kPa, Fig. 5), both the elastoplastic and the K–hypoplastic models provide response envelopes which appear in fairly good agreement with the experimental results, both from a qualitative and a quantitative point of view. On the contrary, CLoE significantly underestimates soil stiffness for loading paths close to deviatoric compression (Tx116 and Tx119).

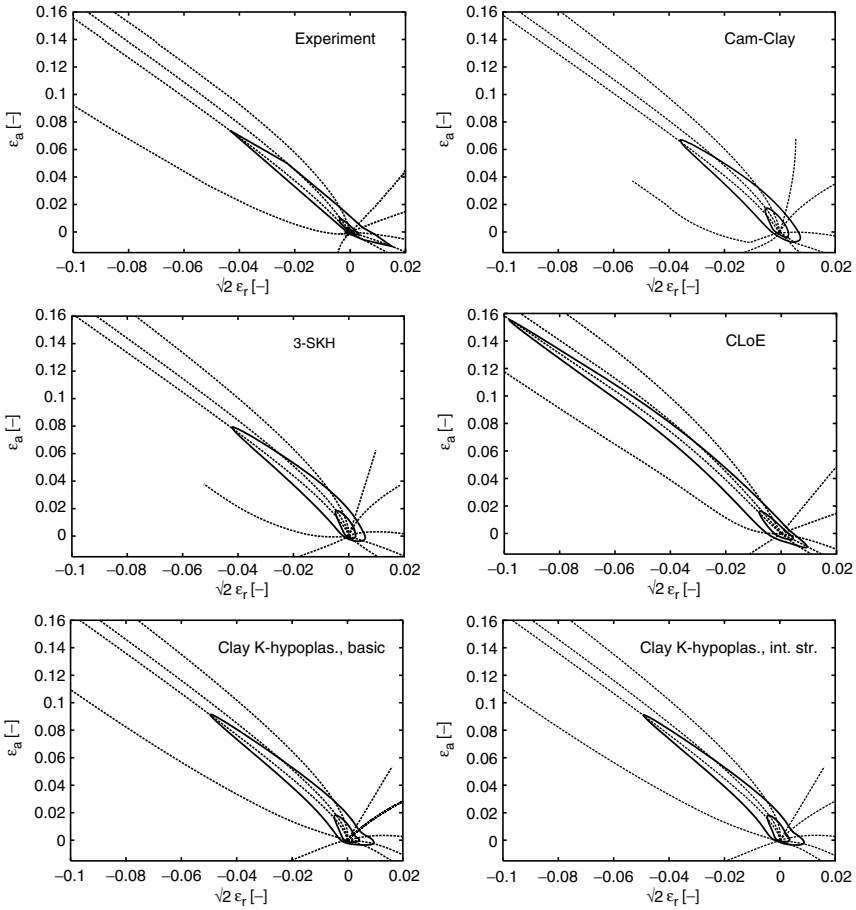

Fig. 5. Experimental vs. simulated strain response envelopes for $R_\sigma = 50$ and 90 kPa

5 Concluding Remarks

The comparative evaluation of the performance of different constitutive models in their application to the quantitative solution of practical engineering problems is a very complex task, which typically requires the consideration of a number of key issues, such as: the capability of reproducing the relevant experimental response; the relative complexity of the calibration procedures; the number and nature of the internal state variables describing the effects of previous loading history; the availability of robust and accurate algorithms for their numerical implementation in FE codes, etc. In this paper, the attention is focused on the qualitative and quantitative agreement between experimentally observed response and model predictions at the element level.

In standard practice, the comparison between model predictions and experimental results is typically done with reference to a limited number of conventional stress paths, whereas the response of the material for different loading conditions is extrapolated in a more or less reasonable way. This can be quite sufficient to assess the model performance in practical applications, whenever the problem at hand is such that most of the soil affected by the imposed loading conditions undergoes very similar stress paths, and one of such paths is included among those explored in the laboratory testing program. Unfortunately, this is only seldom the case in many important applications where an accurate prediction of soil–structure interaction processes and of the displacement field around the structure is required. Notable examples in this respect are provided by deep excavations and shallow tunnels to be realized in urban environments, as in such cases, different zones of soil experience widely different stress-paths, both in size and direction, and the quality of numerical predictions crucially relies on the ability of the constitutive model adopted for the soil to accurately reproduce the material response along all such loading paths.

In this paper, an attempt is made to evaluate the response of different advanced constitutive models for fine-grained soils in more general terms, considering their predictive capabilities over a quite wide range of loading conditions. While the strain response envelopes plotted in Figs. 4 and 5 provide a clear qualitative picture of the performance of the five models considered, a more quantitative comparison of model predictions has been presented in [20] by introducing a suitable scalar measure of the "distance" between model responses and experimental results. Based on such a comparison, the best performance overall appears to be provided by the enhanced K–hypoplastic model and the 3-SKH model, at both small and large strain levels.

As compared to its enhanced version, the performance of the standard K–hypoplastic model is still reasonably good, mainly because the loading programs considered involve only a very limited number of stress reversals. For the application to monotonic (or quasimonotonic) loading conditions, the standard K–hypoplastic model may therefore represent a valid alternative to more complex formulations. On the contrary, the performance of CLoE model appears quite poor as compared to the other elastoplastic or hypoplastic models, particularly for those loading paths involving a significant increase in mean stress. This is not surprising, considering that CLoE is a first-generation hypoplastic model, in which the stress tensor is the only state parameter. For this reason, the mathematical structure of CLoE does not allow to properly distinguish normally consolidated and overconsolidated states, and to correctly describe critical state failure conditions. While CLoE has demonstrated its capability of accurately modeling the response of coarse-grained soils along mainly deviatoric loading paths, see e.g., [5], these limitations obviously make it unfit to model the behavior of soft clays. An attempt to modify the current version of CLoE in order to improve its performance for normally consolidated clays has been recently presented by [19].

It is worth noting that even the predictions of the classical Cam-Clay model for those paths which point outside the initial yield surface are quite good, and essentially equivalent to those obtained with 3-SKH model. This is to be expected, as the soil considered in this study was in a (almost) normally consolidated state.

Both the enhanced K–hypoplastic model and the 3-SKH model are characterized by a relatively limited number of constants, most of which are linked to standard features of clay behavior. In fact, all the constants appearing in these two models can be determined by means of standard laboratory tests, with the only exception of those controling the stiffness of the material at very low strain levels. Of course, the above considerations also apply to the simpler standard K–hypoplastic model for clays, which possesses only five constants, just like the classical Modified Cam-Clay. On the other hand, CLoE model requires a much wider pool of experimental data to determine the relatively large number of constants. Moreover, as CLoE constants typically control more than one specific feature of the material response, they cannot be determined independently. Rather, they have to be found by means of a complex calibration procedure which has to be implemented numerically in a suitable calibration code. This represents a second, major drawback of the CLoE model as compared to the more recent K–hypoplastic models for clays.

Acknowledgment

The second author is grateful for the financial support by the research grants SSPI-CT-2003–501837-NOAH'S ARK under the EC 6th FP and GACR 205/03/1467.

References

1. A. Al Tabbaa and D.M. Wood. An experimentally based "bubble" model for clay. In *Proceeding of 3rd International Conference on Numerical Models in Geomechanics*. Niagara Falls, 1989
2. J.H. Atkinson, D. Richardson, and S.E. Stallebrass. Effects of recent stress history on the stiffness of over–consolidated soil. *Géotechnique*, 40(4):531–540, 1990
3. L. Callisto and G. Calabresi. Mechanical behaviour of a natural soft clay. *Géotechnique*, 48(4):495–513, 1998
4. R. Chambon and J. Desrues. Bifurcation par localisation et non linéarité incrémentale: un example heuristique d'analyse complete. In *Plastic Instability*, pages 101–113, Paris, France, 1985. Presses ENPC
5. R. Chambon, J. Desrues, W. Hammad, and R. Charlier. CLoE, a new rate–type constitutive model for geomaterials. theoretical basis and implementation. *Int. J. Numer. Anal. Methods Geomech.*, 18:253–278, 1994
6. C.R.I. Clayton and G. Heymann. Stiffness of geomaterials at very small strains. *Géotechnique*, 51(3):245–255, 2001

7. D. Costanzo, G. Viggiani, and C. Tamagnini. Directional response of a reconstituted fine–grained soil. Part I: experimental investigation. Int. J. Num. Anal. Meth. Geomech. (in print), 2006
8. F. Darve. The expression of rheological laws in incremental form and the main classes of constitutive equations. In F. Darve, editor, *Geomaterials: Constitutive Equations and Modelling*, pages 123–148. Elsevier, Amsterdam, 1990
9. J. Desrues and R. Chambon. Shear band analysis for granular materials: the question of incremental non–linearity. *Ingenieur–Archiv*, 59:187–196, 1989
10. R.J. Finno, I.S. Harahap, and P.J. Sabatini. Analysis of braced excavations with coupled finite element formulations. *Comput. Geotech.* 12:91–114, 1989
11. J. Graham, M.L. Noonan, and K.V. Lew. Yield states and stress-strain relationships in natural plastic clay. *Can. Geotech. J.*, 20:502–516, 1983
12. G. Gudehus. A comparison of some constitutive laws for soils under radially symmetric loading and unloading. In Wittke, editor, *3rd Int. Conf. Numer. Methods Geomech.*, Aachen, pages 1309–1324. Balkema, Rotterdam, 1979
13. G. Gudehus. A comprehensive constitutive equation for granular materials. *Soils Found.* 36(1):1–12, 1996
14. K. Hashiguchi. Two– and three–surface models of plasticity. In *V International Conferance of Numerical Methods in Geomechanics*, pages 285–292, Nagoya, Japan, 1985. Balkema, Rotterdam
15. D. Kolymbas. An outline of hypoplasticity. *Arch. Appl. Mech.* 61:143–151, 1991
16. J. Lanier, D. Caillerie, R. Chambon, and G. Viggiani. A general formulation of hypoplasticity. *Int. J. Numer. Anal. Methods Geomech.*, 28:1461–1478, 2004
17. P.I. Lewin and J.B. Burland. Stress-probe experiments on saturated normally consolidated clay. *Géotechnique*, 20(1):38–56, 1970
18. D. Mašín. A hypoplastic constitutive model for clays. *Int. J. Numer. Anal. Methods Geomech.*, 29:311–336, 2005
19. D. Mašín, R. Chambon, and J. Desrues. CLoE model modified to predict the behaviour of normally compressed clays. In *Proc. 11th Int. Conf. IACMAG*. Turin, Italy, 2005
20. D. Mašin, C. Tamagnini, D. Costanzo, and G. Viggiani. Directional response of a reconstituted fine–grained soil. Part II: performance of different constitutive models. Int. J. Num. Anal. Meth. Geomech., (in print), 2006
21. Z. Mroz, V.A. Norris, and O.C. Zienkiewicz. An anisotropic hardening model for soils and its application to cyclic loading. *Int. J. Numer. Anal. Methods Geomech.*, 2:203–221, 1978
22. A. Niemunis. *Extended Hypoplastic Models for Soils*. Habilitation thesis, Ruhr-University, Bochum, 2002
23. A. Niemunis and I. Herle. Hypoplastic model for cohesionless soils with elastic strain range. *Mech. Cohesive–Frictional Mater.* 2:279–299, 1997
24. J.H. Prevost. Mathematical modelling of monotonic and cyclic undrained clay behaviour. *Int. J. Numer. Anal. Methods Geomech.*, 1:195–216, 1977
25. J.R. Rice. The localization of plastic deformations. In Koiter, editor, *Theoretical and Applied Mechanics*, pages 207–220. North–Holland, 1976
26. K.H. Roscoe and J.B. Burland. On the generalised stress-strain behaviour of wet clay. In J. Heyman and F.A. Leckie, editors, *Engineering Plasticity*, pages 535–609. Cambridge University Press, Cambridge, 1968
27. J.W. Rudnicki and J.R. Rice. Conditions for the localization of deformation in pressure–sensitive dilatant materials. *J. Mech. Phys. Solids*, 23:371–394, 1975

28. P.R. Smith, R.J. Jardine, and D.W. Hight. The yielding of Bothkennar clay. *Géotechnique*, 42(2):257–274, 1992
29. H.D. St. John, D.M. Potts, R.J. Jardine, and K.G. Higgins. Prediction and performance of ground response due to construction of a deep basement at 60 Victoria Embankment. In G.T. Houlsby and A.N. Schofield, editors, *Predictive Soil Mechanics (Wroth Mem. Symp.)*. Thomas Telford, London, 1993
30. S.E. Stallebrass. *Modelling the effect of recent stress history on the behaviour of overconsolidated soils*. PhD thesis, The City University, London, 1990
31. S.E. Stallebrass and R.N. Taylor. Prediction of ground movements in overconsolidated clay. *Géotechnique*, 47(2):235–253, 1997
32. C. Tamagnini and G. Viggiani. On the incremental non-linearity of soils. Part I: theoretical aspects. *Rivista Italiana di Geotecnica*, 36(1):44–61, 2002
33. C. Tamagnini, G. Viggiani, R. Chambon, and J. Desrues. Evaluation of different strategies for the integration of hypoplastic constitutive equations: Application to the CLoE model. *Mech. Cohesive–Frictional Mater.* 5:263–289, 2002
34. C.A. Truesdell. Hypo–elastic shear. *J. Appl. Phys.* 27:441–447, 1956
35. G. Viggiani and C. Tamagnini. Ground movements around excavations in granular soils: a few remarks on the influence of the constitutive assumptions on FE predictions. *Mech. Cohesive–Frictional Mater.* 5(5):399–423, 2000
36. A.J. Whittle, Y.M.A. Hashash, and R.V. Whitman. Analysis of deep excavation in Boston. *J. Geotech. Engng. ASCE*, 119(1):69–90, 1993
37. D.M. Wood. *Some aspects of the mechanical behavior of Kaolin under truly triaxial conditions of stress and strain*. PhD thesis, Cambridge University, Cambridge, 1974
38. W. Wu and D. Kolymbas. Hypoplasticity then and now. In D. Kolymbas, editor, *Constitutive Modelling of Granular Materials*. Springer, Berlin Heidelberg New York, 2000

Two Elastoplastic Models for Small and Large Strains and Their Use in Engineering Practise

P.A. Vermeer*, R. Schwab†, and T. Benz*,†

*Institute of Geotechnical Engineering, University of Stuttgart, Germany
vermeer@igs.uni-stuttgart.de
†Federal Waterways Engineering and Research Institute, Karlsruhe, Germany

1 Introduction

In computer science, abstraction is defined as the ability of a program to ignore some aspects of the information that it is manipulating, i.e. the ability to focus on the essential. Modern programming styles, such as object oriented programming, support high levels of abstraction on the basis of modularity and structure.

In constitutive modelling, the concepts of structure and modularity can be applied as well. The elastoplastic double hardening model by Vermeer [22] or its successor, the Hardening Soil (HS) model by Schanz et al. [20] are only two examples. Here the main modules are an elastic kernel and two plastic hardening mechanisms: A shear hardening mechanism and a cap hardening mechanism.

Abstraction is an important issue in constitutive modelling, too: *"The art of successful modelling is to include just enough detail for the implied simplification to be reasonable for for the particular application."* (Muir Wood [12]) The appropriate level of abstraction or simplification, however, is difficult to determine. Although it primarily depends on design requirements and the soil type, it also depends on the analysis type (i.e. drained or undrained), load type (i.e. cyclic or monotonic), boundary conditions and many more.

Especially in engineering practise where robust and easy to apply models are needed, the appropriate level of abstraction can sometimes not be met due to a lack of suitable models. Two new models that tentatively close this gap are proposed in this paper. Using the concept of modularity, they are both based on the well known HS model as implemented in the finite element code Plaxis. The new modules are a small strain formulation and an advanced shear hardening formulation for cyclic modelling and improved monotonic deviatoric modelling.

An illustration of the new modules' mode of operation is given by means of simple element tests. Two case studies of large navigable locks at the end of this paper then proof their value also for engineering practise.

2 Model Formulation

2.1 The Hardening Soil Model in a Nutshell

The original HS model was developed by Schanz [19] and Schanz et al. [20] on the basis of the Double Hardening model by Vermeer [22]. Thus, the HS model comprises also ideas by Kondner and Zelasko [8], Duncan and Chang [6], Ohde [13] and Rowe [15]. Standard lab tests as triaxial and oedometer tests spin off the model's basic characteristics. In drained triaxial tests soils exhibit a hyperbolic stress–strain relation during primary loading, where unloading and reloading can be approximated with a linear function. Therefore the HS model introduces a first yield surface that separates between deviatoric primary loading and unloading/reloading. The evolution of this cone type yield surface is such that it is in accordance with the hyperbolic shape of the stress–strain relation as first formulated by Kondner and Zelasko(1963) [8] and subsequently applied by Duncan and Chang [6] in their hypoelastic model. The deviatoric shape of the yield surface is chosen coherent to the applied Mohr-Coulomb failure criterion. In triaxial compression it reads

$$\begin{aligned} f^s_{12} &= \frac{1}{E_{50}} \frac{(\sigma_1 - \sigma_2)}{q_\mathrm{a} - (\sigma_1 - \sigma_2)} - \frac{2(\sigma_1 - \sigma_2)}{E_\mathrm{ur}} - \gamma^\mathrm{ps}, \text{and} \\ f^s_{13} &= \frac{1}{E_{50}} \frac{(\sigma_1 - \sigma_3)}{q_\mathrm{a} - (\sigma_1 - \sigma_3)} - \frac{2(\sigma_1 - \sigma_3)}{E_\mathrm{ur}} - \gamma^\mathrm{ps}, \end{aligned} \tag{1}$$

where q_a is the asymptotic deviatoric stress and γ^ps is the hardening parameter. Since associated plasticity is an unrealistic assumption for most geomaterials an additional plastic potetial of the form

$$\begin{aligned} g^s_{12} &= \frac{(\sigma_1 - \sigma_2)}{2} - \frac{\sigma_1 + \sigma_2}{2} \sin\psi_\mathrm{m}, \text{and} \\ g^s_{13} &= \frac{(\sigma_1 - \sigma_3)}{2} - \frac{\sigma_1 + \sigma_3}{2} \sin\psi_\mathrm{m} \end{aligned} \tag{2}$$

is introduced. Here the mobilized dilatancy angel ψ_m is defined according to Rowe's stress dilatancy theorie [15]

$$\sin\psi_\mathrm{m} = \frac{\sin\varphi_\mathrm{m} - \sin\varphi_\mathrm{cs}}{1 - \sin\varphi_\mathrm{m}\sin\varphi_\mathrm{cs}}, \tag{3}$$

where, φ_cs is the critical state friction angel and the mobilized friction angel φ_m is calculated to

$$\sin\varphi_\mathrm{m} = \frac{\sigma_1 - \sigma_3}{\sigma_1 + \sigma_3 - 2c\ \mathrm{cot}\varphi}. \tag{4}$$

When simulating primary oedometric loading with the cone-type yield surface only, the model acts too stiff. Thus, a second cap-type yield surface of the form

$$f^c = \frac{q^2}{\alpha^2} - p^2 - p_{\mathrm{p}}^2 \tag{5}$$

with the material constant α and the pre-consolidation measure p_{p} is introduced. This cap-type yield surface allows then to distinct between primary volumetric loading and full elastic unloading/reloading. Both yield surfaces are shown in Fig. 1 in principal stress space and in $p-q$ space.

Material parameter input to the model can be separated into strength and stiffness parameters. Strength parameters are the friction angel φ, cohesion c and the dilatancy angel ψ. Material stiffness is defined at a reference stress state p^{ref} by three different moduli: E_{oed}, the tangent oedometer loading modulus which controls mainly the evolution of the cap type yield surface and so the state parameter p_{p}. E_{50}, the secant stiffness at 50% of the ultimate triaxial strength, which controls mainly the evolution of the cone type yield surface or the state variable γ^{ps}. The elastic constants in the area enclosed by the two yield surfaces is given by the unloading/reloading Young's modulus E_{ur} for complete deviatoric unloading and the Poisson's ratio ν_{ur}. An Ohde [13] type power law with exponent m is used to adjust the specified reference stiffness values to the calculated stress state.

2.2 Module I: A Small Strain Overlay Model

Soil stress–strain behaviour is highly non-linear. The maximum soil stiffness can be solely observed at low strain levels, e.g. strains $\leq 10^{-6}$. From there on, stiffness decays so rapidly with almost purely elastic straining that it can not be measured in standard laboratory tests without using bender elements or other specialized equipment such as LVDTs.

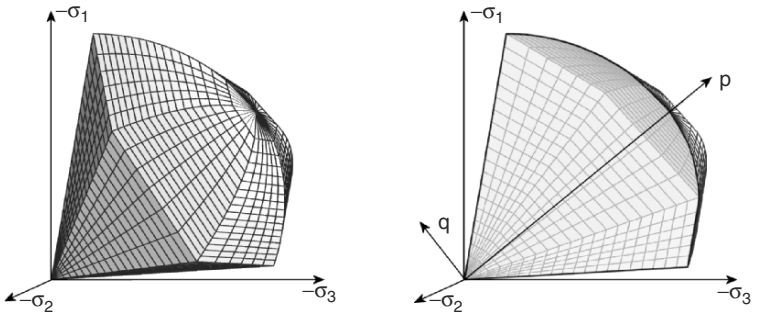

Fig. 1. Yield surfaces of the HS model for cohesionless soil. *Left*: Cap- and cone-type yield surfaces in principal stress space with the cone being in its ultimate Mohr-Coulomb failure criterion position. *Right*: p–q cut through the yield surfaces

The small strain overlay model is a module to include small strain stiffness in many elastoplastic models. The extension of the HS-model with the small strain overlay model is in the following referred to as the *HS-Small* model. Parameter input that is particular to the HS-Small model is discussed at the end of this section. Only an abridged description of the small strain overlay model can be given here. For a detailed model description it is therefore referred to [2].

The small strain overlay model assumes that the decay of small strain stiffness is primarily related to either break up of bonding forces or frictional forces exceeding their elastic limit. Small strain stiffness decay can thus be observed whenever the inter-particle forces in an assembly are reorganized and concentrated. This happens either in primary loading or within a loading history upon a change in load path. As a measure for the disturbance of inter-particle forces the proposed overlay model thus tracks the material's monotonic deviatoric strain history. Strain history is treated as a second order surface in principal strain space. To avoid any possible singularities of the second order surface, a volumetric **1** strain is superimposed to the deviatoric history strain. A geometrical interpretation of second order surfaces in some basic tests is shown in Fig. 2. Here, the small deviatoric strains have been amplified to the power of 10^3 in order to visualize the distortion of the volumetric **1** strain component, which is a perfect sphere in this representation.

From the strain history $\mathbf{H}^i$ st step i and the actual deviatoric strain increment $\Delta\mathbf{e}^{i+1}$ in step $i+1$, determination of the elastic material stiffness is as follows. First, the actual deviatoric strain history is calculated as

$$\mathbf{H}^{i+1} = (\mathbf{T}^i)^{\mathrm{T}}(\mathbf{H}^i + \mathbf{1})\mathbf{T}^i + \Delta\mathbf{e}^{i+1} - \mathbf{1}, \tag{6}$$

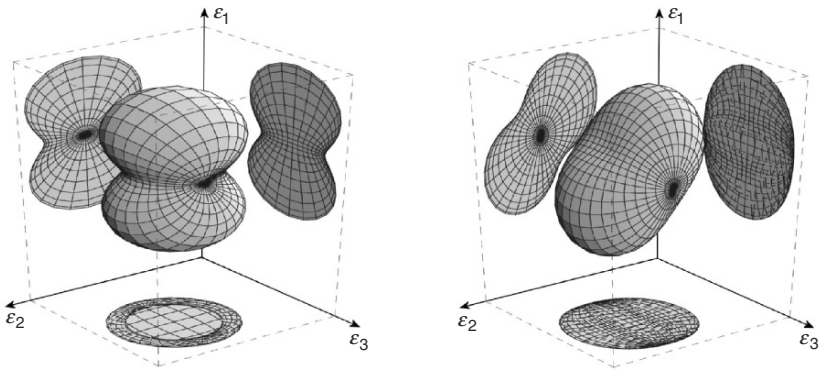

Fig. 2. Strain history interpreted as second order surface in strain space. *Left*: Triaxial extension. *Right:* Simple shear

where $\mathbf{T}^i$ is a transformation matrix that partially or fully resets strain history upon changes in the loading path. The scalar measure $\gamma_{\text{Hist}}^{i+1}$ for the monotonic strain history is then defined as:

$$\gamma_{\text{Hist}}^{i+1} = \sqrt{3}\frac{\|\Delta\mathbf{e}^{i+1}\boldsymbol{\chi}^{\boldsymbol{i+1}}\|}{\|\Delta\mathbf{e}^{i+1}\|} \quad \text{with} \quad \chi_k^{i+1} = \mathbf{n}_{(k)}^{\mathrm{T}}(\mathbf{H}^{i+1} + \mathbf{1})\mathbf{n}_{(k)} - 1, \tag{7}$$

where $\|\dots\|$ denotes the Hilbert-Schmidt norm $\|A\| = \sqrt{a_{ij}a_{ij}}$ and $\mathbf{n}_{(k)}$ are the principal directions of strain increment $\Delta\mathbf{e}^{i+1}$. In a geometric context, (7) is the projection of the strain history onto the actual loading direction.

The magnitude of the overall monotonic strain $\gamma_{\text{Hist}}^{i+1}$ is related to shear stiffness by an approach of Santos and Correia. Based on many test data for sands and clays, Santos proposed in his PhD Thesis [17] two analytical expressions for the upper and lower bounds of normalized stiffness–strain curves. Santos and Correia [18] fitted these two boundary curves with the hyperbolic function

$$G(G_0, \gamma_{0.7}) = \frac{G_0}{1 + a\frac{\gamma}{\gamma_{0.7}}}, \tag{8}$$

where G is the actual shear modulus, G_0 is the initial shear modulus at very small-strains, γ is the applied monotonic shear strain, and $\gamma_{0.7}$ is the shear strain at which the shear modulus has been reduced to $0.7G_0$. A best fit of the two boundary curves is obtained for $a = 0.385$ as shown in Fig. 3.

The proposed degradation curve reaches far into the plastic material domain. In the plastic domain however, stiffness degradation is modelled by material hardening. Therefore, a lower cut-off in the stiffness strain curved is defined at the elastic unloading/reloading shear modulus G_{ur} defined as

$$G_{\text{ur}} = \frac{E_{\text{ur}}}{2(1 + \nu_{\text{ur}})} \tag{9}$$

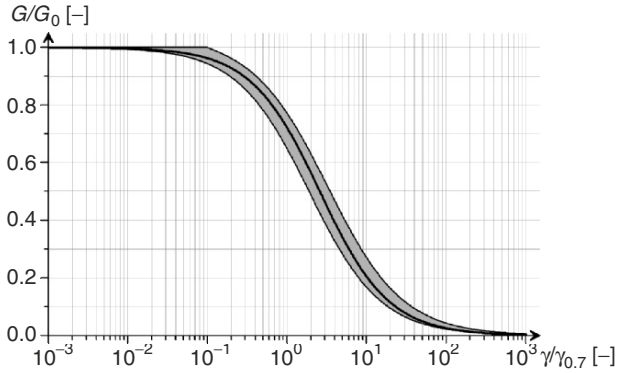

Fig. 3. Normalized stiffness degradation curves G/G_0 over $\gamma/\gamma_{0.7}$ according Santos and Correia. The hyperbolic curve defined within (8) (bold) is shown between its experimentally derived upper and lower bounds. A best fit is obtained for $a = 0.385$

with the elastic constants E_{ur} and ν_{ur}. Thus, G_{ur} is the shear modulus in complete deviatoric unloading. The additional model parameters for the small strain formulation are then G_0, the elastic small strain shear modulus, and the threshold value $\gamma_{0.7}$ in primary loading. In order to obey Massing's rule, this threshold value is internally doubled during unloading/reloading.

2.3 Module II: Double Hardening Bounding Surface Plasticity

An advanced shear hardening module based on the bounding surface plasticity concept by Dafalias [5] is proposed in this section. In combination with the HS-Small model, this new module allows for improved state dependent, or unified modelling as well as cyclic modelling. Although the existing model is altered extensively, the new model is in the following referred to as the *HS-Bound* model. Additional parameter input is needed to specify the material's initial- and critical state, its phase transition, and its cyclic characteristics.

Incorporating the principles of Wood et al. [23], the new shear hardening module allows for unified soil modelling based on the state parameter defined by Been and Jefferies [1]

$$\psi = e - e_{\mathrm{cs}} = e - (e_{\mathrm{cs}}^{\mathrm{ref}} - \lambda \ln(\frac{p}{p^{\mathrm{ref}}})), \tag{10}$$

where λ and $e_{\mathrm{cs}}^{\mathrm{ref}}$ are material constants that define a straight critical-state line in $e - \ln(p)$ space. Whenever enough test data is available, the user can alternatively switch to the modified critical state line proposed by Li and Wang [9]

$$\psi = e - e_{\mathrm{cs}} = e - (e_{\mathrm{cs}}^{\mathrm{ref}} - \lambda_c (\frac{p}{p^{\mathrm{ref}}})^{\xi}) \tag{11}$$

which is a straight line in $e - (\frac{p}{p^{\mathrm{ref}}})^{\xi}$ space.

Material stiffness is now defined as function of stress (Ohde), strain (small strain overlay model), and the distance d_{b} between the actual stress ratio and its image on the bounding surface. The yield surface of the model is a Drucker-Prager cone that is allowed to harden kinematically and isotropically. Figure 4 shows the model surfaces in principal stress space. The deviatoric shapes of the critical(c)-, bounding(b)-, and dilatancy(d) surface are all defined according Papadimitriou and Bouckovalas [14] as

$$g(\Theta, c^{c,b,d}) = \frac{2c^{c,b,d}}{\frac{1+c^{c,b,d}}{2} - \frac{1-c^{c,b,d}}{2}\cos(3\Theta)} - \left(\frac{1+c^{c,b,d}}{2} + \frac{1-c^{c,b,d}}{2}\cos(3\Theta)\right), \tag{12}$$

where Θ is the Lode angle and $c^{c,b,d}$ gives the ratio of extent in triaxial compression M_{c} and triaxial extension M_{e} for the respective surface.

For a given material state ψ and known critical state M^{c} the deviatoric extents M^{b} and M^{d} of the bounding- and dilatancy surfaces, respectively, are

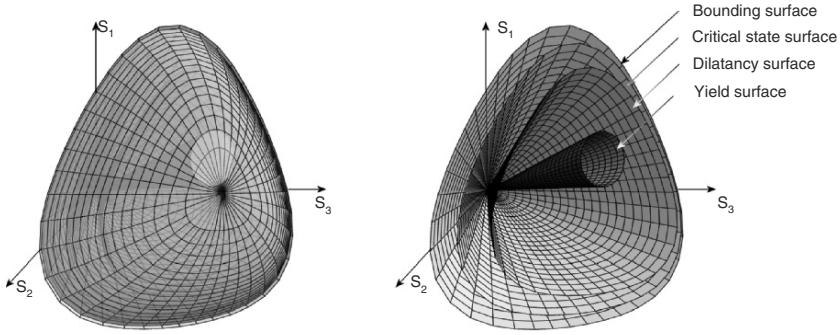

Fig. 4. *Left*: Bounding surface with cap in principal strain space. Only the highlighted cap portion is active. *Right*: View inside the model onto yield-, dilatancy-, critical-, and bounding surface

defined as

$$\begin{aligned} M^{\mathrm{b}} &= M^{\mathrm{c}} + k^{\mathrm{b}}\langle -\psi \rangle \\ M^{\mathrm{d}} &= M^{\mathrm{c}} e^{k^{\mathrm{d}}\psi} \end{aligned} \quad , \tag{13}$$

where k^{b} and k^{d} are material parameters related to material strength. However, the user is not expected to specify these internal parameters. Instead, a user interface is provided that converts the standard strength and stiffness parameters known from the original HS model to the new internal calculation parameters. For stiffness and dilatancy parameters this is done by iterative calculations of triaxial and oedometer tests.

Not specifing an explicit plastic potential surface, dilatancy is defined in close agreement to Li and Dafalias [10] in multiaxial stress–strain space as

$$D = \frac{\mathrm{d}\varepsilon^p_{kk}}{\sqrt{\frac{2}{3}\mathrm{d}e^p_{ij}\mathrm{d}e^p_{ij}}} = Ad_d, \tag{14}$$

where A is an internal material parameter and d_{d} is the distance between the actual stress ratio and its image on the dilatancy surface.

For a description of the used mapping rule and hardening laws it is referred to Papadimitriou and Bouckovalas [14] or Manzari and Dafalias [11] since their equations have been only slightly modified. A new feature of the proposed shear hardening mechanism is the implementation of a stress ratio memory surface and a sweep out of memory function for near failure states of stress. For a description of these important feature for cyclic modelling and a complete model description it is referred to an upcoming publication.

3 Element Tests

The additional features of the new models can be best identified in element tests. Hence, before applying them to boundary value problems as done in Sect. 4, they are first used in triaxial and oedometer tests.

3.1 Small Strain Triaxial Tests

The tests by Rivera and Bard [4] on dense sand comprise static and cyclic (repeated) triaxial loading. In the calculation of the tests presented in Fig. 5 plastic straining has been suppressed. Thus, the small strain overlay is here used as a stand-alone model. Active hardening mechanisms would further decrease stiffness with straining. However, for reasonable material hardening this stiffness decrease can be neglected in the small strain range. For a more detailed discussion on this topic see Benz et al. [2].

In the calculation of the tests by Rivera and Bard it turns out that the model's ability to capture differences between virgin- or monotonic loading and re- or cyclic loading is essential. As shown on the right hand side of Fig. 5, Masing's rule is fulfilled, too.

3.2 Various Tests on Dense and Loose Hostun Sand

Several drained triaxial and oedometer tests on dense and loose Hostun sand are shown in Fig. 6 and Fig. 7. All tests have been either performed at the Laboratoire 3S (the former Institute of Mechanics IMG) in Grenoble or at the Institute of Geotechnical Engineering of Stuttgart University (IGS). Both models, the HS-Small and the HS-Bound model can reproduce the test results reasonably well. However, for the HS-Small model two sets of parameters have to be provided. One set for dense sand and one set for loose sand (Table 1). Apart from the initial void ratio, a single set of parameters is sufficient with the HS-Bound model. Peak and residual strength is then in good agreement with the test data. The concept of unified or state dependent modelling improves

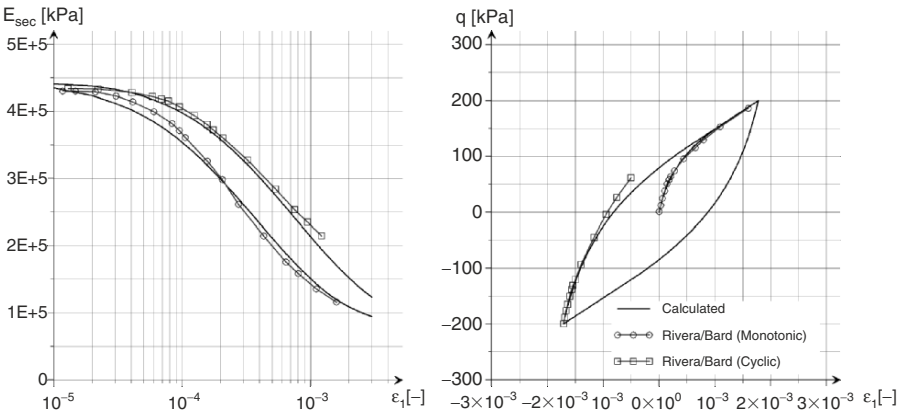

Fig. 5. Triaxial test by Rivera and Bard (in Biarez and Hicher [4]) and its simulation with the small-strain overlay model ($G_{0,\mathrm{ref}} = 125\,\mathrm{MPa}$ at $p_{\mathrm{ref}} = 100\,\mathrm{kPa}, \gamma_{0.7} = 2\mathrm{e}^{-4}$). *Left*: secant stiffness in respect to last reversal point. *Right*: hysteresis loop

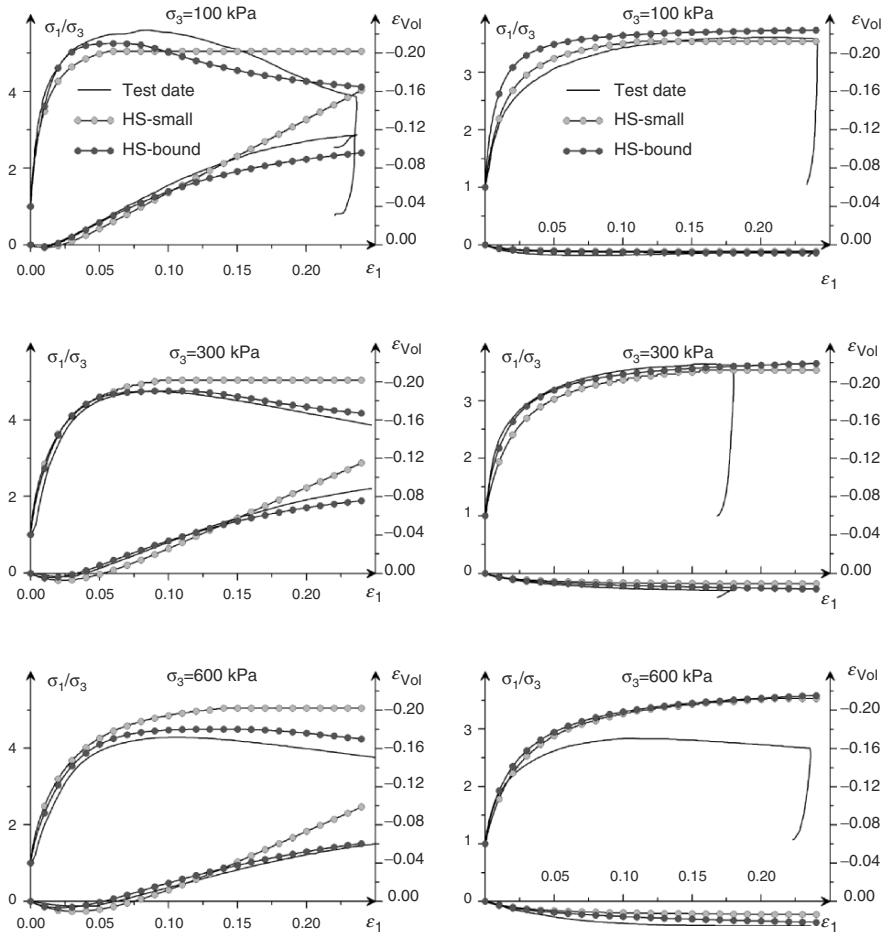

Fig. 6. Triaxial tests on dense (*left column*) and loose (*right column*) Hostun sand with increasing confining pressures from top to bottom

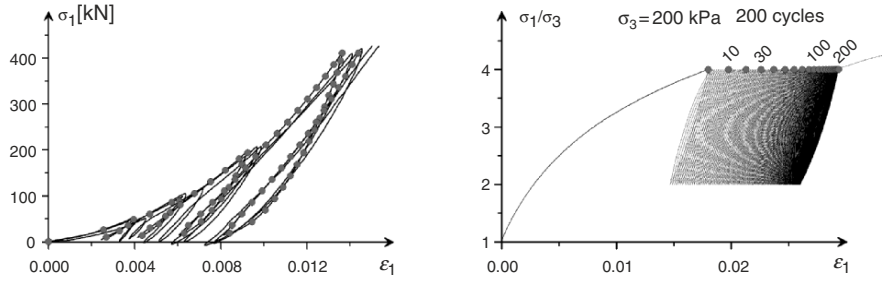

Fig. 7. Oedometer test results (*left*) and cyclic triaxial test results (*right*) on dense Hostun sand from the HS-Bound model

Table 1. Parameters for dense and loose Hostun sand

	E_{50}^{ref} [MPa]	$E_{\text{oed}}^{\text{ref}}$ [MPa]	$E_{\text{ur}}^{\text{ref}}$ [MPa]	c [kPa]	φ [°]	ψ [°]	G_0^{ref} [MPa]	$\gamma_{0.7}$ [−]	m [−]	ν_{ur} [−]
sand(D)	36.0	30.0	90.0	0.0	42	14	150	$2e^{-4}$	0.50	0.20
sand(L)	12.0	16.0	60.0	0.0	34	0	62.5	$1e^{-4}$	0.65	0.20

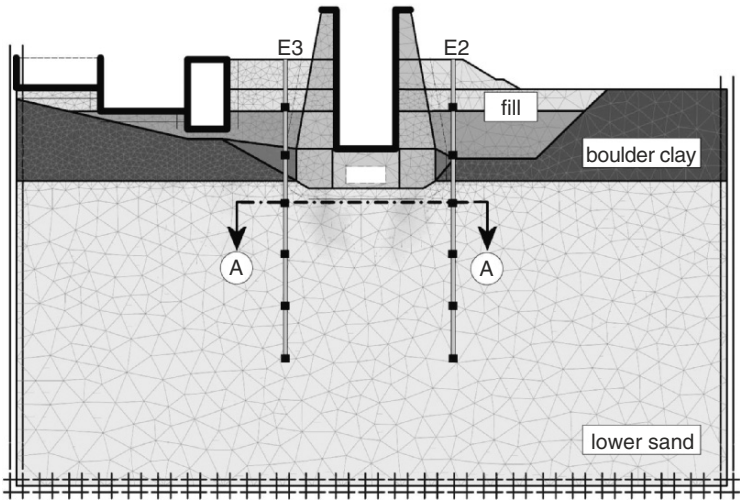

Fig. 8. Finite element model of the navigable lock Uelzen I. Vertical displacements are measured in extensometers E2 and E3 next to the lock

also the volumetric behaviour of the HS-Bound model compared to this of the HS-Small model considerably.

Results of the HS-Bound model in cyclic calculations are shown in Fig. 7. Here an oedometer test and a cyclic triaxial experiment by Tan [21] are modelled in reasonably good agreement with the test data from dense Hostun sand.

4 Boundary Value Problems

4.1 Case Study I: Lock Uelzen I – Settlements

The Elbe Side Canal connects the Mittelland Canal with the river Elbe. The difference in elevation between the Mittelland Canal and the river Elbe of 61 m is divided between the Lock Uelzen and the ship lift Scharnebeck. The Lock Uelzen I with a chamber length of 185 m, a width of 12 m and a lift of 23 m went into operation in 1976. In Fig. 8, a finite element model of the lock Uelzen I with the lock in the middle and the economising basins on the left hand side is presented. The following case study concentrates on the vertical displacements and settlements of the lock due to filling and draining the lock chamber.

Table 2. Soil parameters Uelzen

	γ_{sat} [kNm^{-3}]	k [m(days)$^{-1}$]	E_{50}^{ref} [MPa]	E_{oed}^{ref} [MPa]	E_{ur}^{ref} [MPa]	c [kPa]	φ [°]	ψ [°]	G_0^{ref} [MPa]	$\gamma_{0.7}$ [–]	m [–]
upper fill	21.0	drained	48.0	40.0	144	0	35.0	5.0	166	5e^{-4}	0.50
medium fill	21.0	drained	42.0	35.0	126	0	32.0	2.0	194	3e^{-4}	0.50
lower fill	20.0	drained	36.0	30.0	108	0	30.0	0.0	166	3e^{-4}	0.50
boulder clay	21.5	drained	20.0	16.0	62.0	26	33.0	10.0	105	3e^{-4}	0.80
lower sand	19.0	drained	104	90.0	320	0	43.0	13.0	500	3e^{-4}	0.60

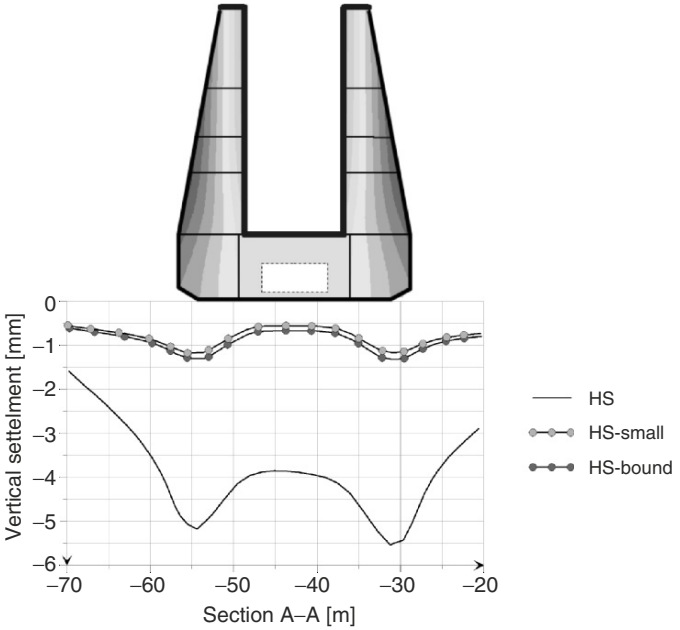

Fig. 9. Vertical settlements in Section A–A due to lock operation

Boulder clay and a lower sand layer present the subsoil at the location. The boulder clay is of semi-solid consistency. The lower sand layer consists of fine to semi grained sand. The strength and density of the sand is remarkably high. Cone resistance q_c is up to and over 100 kNm^{-2}. Soil parameters used in the following calculations are given in Table 2. These parameters have been carefully calibrated i.e. by an back analysis of an excavation right next to the existing lock [7].

From extensometer measurements on both sides of the lock it can be seen that the displacements due to lock operation are nearly elastic. Displacements below 1 mm are measured at the lock's base due to the 23 m water level rise in the lock during operation. Calculated displacement profiles along Section A–A (Fig. 8) are given in Fig. 9. Using the parameters given in Table 2, the original HS model overestimates the vertical displacements by far. These by the HS-Small and HS-Bound models fit the measurements better.

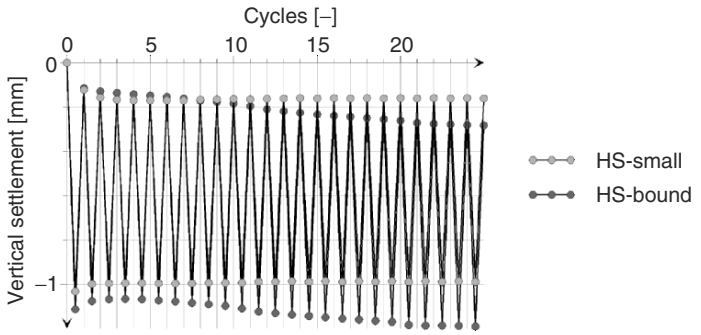

Fig. 10. Calculated vertical displacements in cyclic lock operation

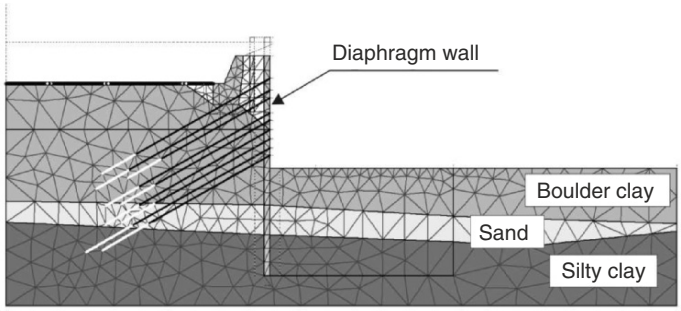

Fig. 11. Finite element mesh of the Suelfeld lock excavation

However, the HS-Small is not adequate to additionally accumulate the small plastic deformations during lock operation. Here a model with advanced shear hardening mechanisms as implemented in the HS-Bound model is to be used. Figure. 10 shows the calculated cyclic response in 25 consecutive operation cycles. A relatively low tolerated numerical error and a well calibrated model are the prerequisites for such calculations. The calculation of many cycles is thus a costly task. However, a cycle skipping algorithm in the form of this proposed in Benz et al. [3] can mitigate this problem. Once, the characteristics of the accumulation curve is established, a pseudo-time viscous law could be used for the further calculation, too.

4.2 Case Study II: Lock Suelfeld – Excavation

The Suelfeld navigable lock on the Mittelland canal is adapted to the new ship generation [16]. For this purpose a new structure is currently built in the place of the southern lock chamber. The excavation is fully housed by diaphragm walls (Fig. 11). The time this paper is written, the excavation works have been finished.

Table 3. Soil parameters Suelfeld

	γ_{sat} [kNm^{-3}]	k [m(day)$^{-1}$]	E_{50}^{ref} [MPa]	E_{oed}^{ref} [MPa]	E_{ur}^{ref} [MPa]	c [kPa]	φ [°]	ψ [°]	G_0^{ref} [MPa]	$\gamma_{0.7}$ [–]	m [–]
sand	20.5	$8.6e^{+0}$	40.0	38.0	300	0	37.5	7.5	375	$3e^{-4}$	0.55
silty clay	21.5	$8.6e^{-4}$	8.5	6.0	23.0	30	32.0	10.0	50.0	$3e^{-4}$	0.90
boulder clay	21.5	$8.6e^{-3}$	8.5	6.2	27.0	6	28.0	6.0	42.0	$3e^{-4}$	0.70

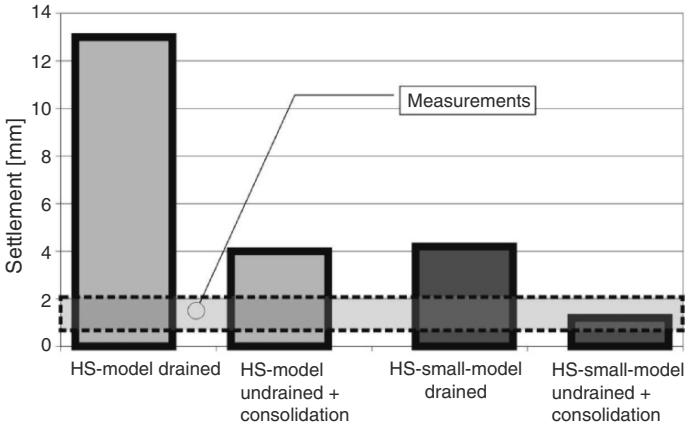

Fig. 12. Computed settlements of the existing lock

At the building site overconsolidated glacial deposits overlie the Lias bedrock: clayey silt, sand and boulder clay. The cohesive layers–silt and boulder clay – were characterized using laboratory tests on undisturbed samples. The soil parameters given in Table 3 have been further refined in a back analysis of the existing lock. Measured vertical displacements of the existing lock during operation are compared to these from finite element analysis (Fig. 12). Only the HS-Small model could provide reasonable results here. The HS-Bound model has not been used in the Suelfeld calculation, yet.

A geotechnical measurement program has been established in order to measure (a) wall deformations, (b) deformations and pore pressure of the adjacent soil masses, (c) forces in anchors and struts, and (d) the excavation bed heave. In order to predict the excavation behaviour and the interaction between the excavation and the neighbouring structures, finite element analysis were performed using the Plaxis code. In Fig. 13 the computed horizontal displacements in the end-of-excavation stage are presented.

The measured maximum horizontal displacement in the section shown in Fig. 13 is 18 mm. The maximum displacement calculated by the HS-Small model in this section is 16 mm. The calculated displacement field over hight is also similar to the measured one. This good agreement is encountered also in the comparison between computed and measured anchor-forces presented

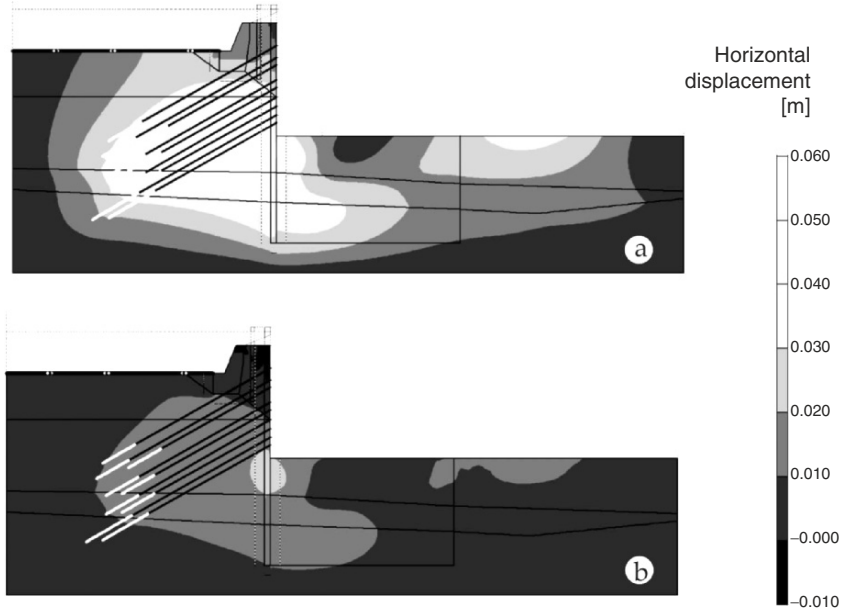

Fig. 13. Computed horizontal displacements: (**a**) HS-model (**b**) HS-Small model

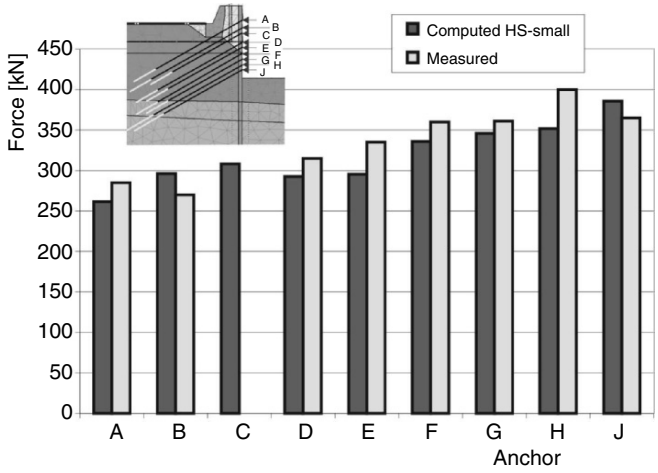

Fig. 14. Comparison between computed and measured anchor-forces (end-of-excavation stage)

in Fig. 14. The original HS model on the other hand gives too large displacement up to 54 mm. The calculated displacement field and anchor-forces are also not in such good agreement as these calculated by the HS-Small model.

5 Conclusions

By a modular extension of the hardening soil (HS) model, two new models with increased complexity have been developed. The HS-Small model adds a small strain stiffness formulation to the functionality of the original HS model. The HS-Bound model adds the same small strain formulation but improves also the shear hardening mechanism of the original HS model. The major difficulty with more complex models is usually parameter selection. Since all HS models are meant for use in engineering practice, they all use the same established set of parameters. The few additional parameters needed for the more advanced models can be extracted from laboratory test data.

Increased model complexity comes along with reduced abstraction. As shown in element tests and in boundary value problems, this tentatively increases the engineers ability to model real soil behaviour. In some analysis this might not be necessary, in others it might. Accumulation of plastic strain in cyclic loading is an example were more complex but still easy to use soil models such as the HS-Bound model are urgently needed. Although model complexity should be always chosen according to the problem it is used in, incorporation of small strain stiffness into numerical analysis can be made a general recommendation in serviceability design. Yet, the HS-Small model enables also the practical working engineer to do so.

References

1. Been K, Jefferies MG (1985) A state parameter for sands. Géotechnique 35(2): 99–112
2. Benz T, Vermeer PA, Schwab R (2005) A small strain overlay model. Int. J. num. Anal. Methods Geomech. submitted
3. Benz T, Schwab R, Vermeer PA (2005) On the numerical modelling of quasi-static cyclic problems. In: Proc. 11th Int. Conf. IACMAG (Turin, Italy)
4. Biarez J, Hicher PY (1994) Elementary Mechanics of Soil Behaviour. A.A.Balkema, Rotterdam
5. Dafalias YF (1986) Bounding surface plasticity, I: mathematical foundation and hypoplasticity. J. Engng. Mech., ASCE 112(9): 966–987
6. Duncan JM, Chang CY (1970) Nonlinear analysis of sterss and strain in soil. J. Soil Mech. Found. Div. ASCE 96: 1629–1653
7. Kayser J, Schwab R (2002) Continuous model validation for a large navigable lock. In: Magnan (ed) Proc. Int Symp Ident and Det of Soil and Rock Para for Geotech Design (Paris). Presses de l'ENPC, Paris, pp 557–564
8. Kondner RL, Zelasko JS (1963) A hyperbolic stress strain formulation for sands. In: Proc. 2nd Pan Am. Int. Conf. Soil Mechods Found. Engng. (Brazil), vol. 1. pp 289–394
9. Li XS, Wang Y (1998) Linear representation of steady-state line for sand. J. Geotech. Geoenviron. Engng., ASCE 124(12): 1215–1217
10. Li XS, Dafalias YF (2000) Dilatancy for cohesionless soils. Géotechnique 50(4): 449–460

11. Manzari MT, Dafalias YF (1997) A critical state two-surface plasticity model for sands. Géotechnique 47(2): 255–272
12. Muir Wood D (2004) Geotechnical modelling. Spon Press, London New Yory
13. Ohde J (1951) Grundbaumechanik, Bd. III. Hütte
14. Papadimitriou AG, Bouckovalas GD (2002) Plasticity model for sand under small and large cyclic strains: a multiaxial formulation. Soil Dyn. Earthquake Eng. 22(1): 191–204
15. Rowe PW (1962) The stress-dilatancy relation for ststic equilibrium of an assmbly of particles in contact. In: Proc. R. Soc. A., No. 269. pp 500–527
16. Saathoff J, Schwab R (2004) Anwendung der Finite-Element-Methode beim Entwurf der neuen Schleuse Sülfeld Süd. In: Proc. of 28th Baugrundtagung, Leipzig. VGE, Essen
17. Santos JA (1999) Soil characterisation by dynamic and cyclic torsional shear tests. Application to the study of piles under lateral static and dynamic loadings. PhD Thesis, Technical University of Lisbon, Portugal
18. Santos JA, Correia AG (2001) Reference threshold shear strain of soil. Its application to obtain an unique strain-dependent shear modulus curve for soil. In: Proc. 15th Int. Conf. Soil Mechods Geotech. Engng. (Istanbul, Turky), vol. 1. pp 267–270
19. Schanz T (1998) Zur Modellierung des mechanischen Verhaltens von Reibungsmaterialien. Habilitation, University of Stuttgart, Germany
20. Schanz T, Vermeer PA, Bonnier PG (1999) The hardening soil model - formulation and verification. In: Brinkgreve (ed) Beyond 2000 in computational geotechnics. Balkema, Rotterdam, pp 281–296
21. Tan CH (1990) Developpement d'un Modele elastoplastique pour le Comportement des Materiaux granulaires sous Sollicitations non monotones complexes. PhD thesis, University of Lille, France
22. Vermeer PA (1978) A double hardening model for sand. Geotechnique 28(4): 413–433
23. Wood DM, Belkheir K, Liu DF (1994) Strain softening and state parameters for sand modelling. Géotechnique 44(2): 335–339

Elastic Visco-Plastic Models for the Time-Dependent Stress–Strain Behaviour of Geomaterials

J.-H. Yin

Department of Civil and Structural Engineering, The Hong Kong Polytechnic University, China
cejhyin@polyu.edu.hk

Abstract. Five elastic visco-plastic (EVP) models for the time-dependent stress–strain behaviour of clayey soils are introduced in the paper. The relations, features and applications of these EVP models are presented and discussed. Methods for determining all model parameters are briefly described. Typical measured and simulated time-dependent stress–strain relationships of clayey soils are compared and discussed.

1 Introduction

Generally speaking, the stress–strain behaviour of all geomaterials is non-linear, irreversible and time-dependent. Geomaterials are natural earth materials including soils and rocks. The time-dependence of the stress–strain behaviour may be ignored under certain conditions, for example, for hard rocks, stiff soils, and sandy soils under low stress levels, but may be significant for these geomaterials under higher deviator stress levels. The time-dependence of the stress–strain behaviour of soft clayey soils and soft rocks is often too significant to be neglected in many cases. Analysis of geotechnical structures directly and indirectly with these geomaterials needs a good understanding and constitutive modelling of the time-dependent stress–strain behaviour of these materials. Many researchers, for example, Bjerrum [2], Graham et al. [3], Leroueril et al. [4] and Yin [8] among others, studied the time effects on the stress–strain behaviour of soils based on odometer and triaxial test results. A number of constitutive models have been suggested for the time-dependent stress–strain behaviour of soils and rocks. Most models are based on the elastic visco-plastic (EVP) modelling framework of Perzyna [5,6]. The five EVP models introduced in this paper were originally developed for clayey soils. One of the models has been extended and applied for a soft rock. All the EVP models have great potential to be extended and used for

describing the time-dependent stress–strain behaviour soft rocks. However, the presentation, calibrations and applications of these models in this paper are still referred to clayey soils.

2 A Classic 1-D EVP Model for 1-D Straining Condition

Bjerrum [2] suggested a conceptual time line model for modelling the delayed compression in 1-D straining (oedometer) condition. Yin and Graham [11,12] defined the "equivalent time", which may be called Bjerrum-Yin-Graham's "equivalent time", and other concepts such as "instant time" lines and "reference time" lines for 1-D applications (see Fig. 1). In the classis model, logarithmic fitting functions are used.

2.1 Instant Time Line (or κ-line)

The instant time line is used to define instantaneous strains. These are assumed to be elastic in this EVP modelling, not elastic–plastic as assumed for

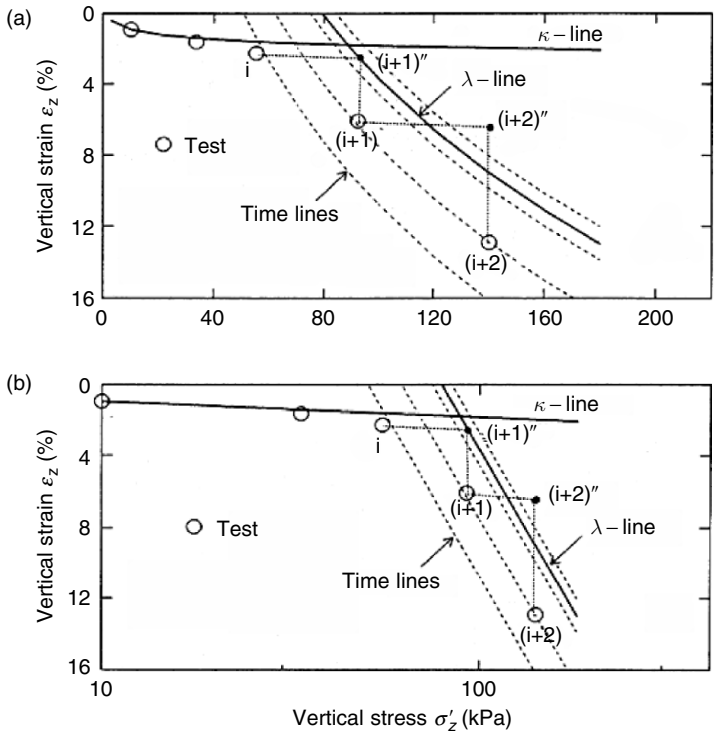

Fig. 1. Relationships of vertical effective stress σ'_z vs. vertical strain ε_z from an oedometer test, κ-line, λ-line and "equivalent time" t_e line, (**a**) σ'_z in arithmetic scale and (**b**) σ'_z in logarithmic scale (after [13])

example by Bjerrum [2]. Strains on the instant time line can be expressed

$$\varepsilon_z^{\mathrm{e}} = \varepsilon_{zi}^{\mathrm{e}} + \frac{\kappa}{V} \ln\left(\frac{\sigma'_z}{\sigma'_{zi}}\right) \tag{1}$$

where σ'_{zi} is a reference vertical effective stress with corresponding vertical strain $\varepsilon_{zi}^{\mathrm{e}}$. In (1), $V = 1 + e_0$ is the specific volume, where e_0 is void ratio. The ratio κ/V is a material parameter used in the same way as in the Cam-Clay models. Equation (1) can be used to fit test data in an overconsolidated range or in unloading/reloading stages of loading. This allows the parameter κ/V to be easily determined from fitting test data (see Fig. 1).

2.2 Reference Time Line (or λ-line)

The reference time line is:

$$\varepsilon_z^{\mathrm{r}} = \varepsilon_{z0}^{\mathrm{r}} + \frac{\lambda}{V} \ln\left(\frac{\sigma'_z}{\sigma'_{z0}}\right), \tag{2}$$

where $\varepsilon_{z0}^{\mathrm{r}}$ is the vertical strain at effective stress $\sigma'_z = \sigma'_{z0}$. In (1), $\varepsilon_{z0}^{\mathrm{r}}$, λ/V and σ'_{z0} are three material parameters. The superscript "r" is used here denoting the reference time line. The reference time line becomes an elastic–plastic compression line as that in the Cam-Clay models [12]. The term λ/V is similar to that used in the Cam-Clay models for defining the elastic–plastic line in isotropically consolidated specimens in a normally consolidated stress range. The parameter σ'_{z0} can be taken as a preconsolidation effective pressure σ'_{zc} with the corresponding strain ε_{zc}, although another point may also be taken. In fact, the two values $\varepsilon_{z0}^{\mathrm{r}}$ and σ'_{z0} determine a point at which the λ-line passes through, for example, point $(\mathrm{i}+1)''$ in Fig. 1b. In this way, the λ-line provides a reference for counting creep time or for calculation of the "equivalent time" which will be discussed later in this section. The later section will describe how the three parameters $\varepsilon_{z0}^{\mathrm{r}}, \lambda/V$ and σ'_{z0} can be determined.

2.3 Creep Compression Strain

Creep strains can be described by

$$\varepsilon_z^{\mathrm{vp}} = \frac{\psi}{V} \ln\left(\frac{t_0 + t_{\mathrm{e}}}{t_0}\right), \tag{3}$$

where ψ/V and t_0 are two material parameters. Note that (3) uses equivalent time t_{e} defined from the reference time line in Fig. 1b and not the time interval corresponding to the real duration of loading. In this way, ψ/V becomes a material constant, and not a parameter, like, the secondary coefficient of consolidation $C_{\alpha\varepsilon}$ that varies with overconsolidation ratio (Yin and Graham 1990). Note that (3) is still defined at $t_{\mathrm{e}} = 0$.

Consider a creep test loaded elastically in Fig. 1 from point i to point (i+1)″ and then allowed to creep to point (i+1) under constant mean effective stress $\sigma'_{z(i+1)}$. Here we have chosen point (i + 1)″ to be on the reference time line. The rationale is the same as that we chose the origin of a coordinate system. If point (i+1)″ is selected to be on the reference time line, creeping from point (i + 1)″ to (i + 1) takes place with the equivalent time t_{e}, which is equal to the real creep duration t since loading from point i to point (i+1)″ takes zero time due to pure elastic compression. Fitting (3) to creep test data allows the two parameters ψ/V and t_0 to be determined. The model has been developed in terms of effective stresses and therefore relates to the fundamental stress–strain behaviour of the soil skeleton.

2.4 Equivalent Time

"Equivalent Time" was defined by Yin and Graham [11,12] for creep behaviour under 1-D straining in an oedometer. Here it is explained for creep behaviour under the isotropic stressing shown in Fig. 1. As discussed previously, when a creep test is loaded from point 3 to point (i+1)″ in Fig. 1 and then allowed to creep to (i+1) under constant stress $\sigma'_{z(i+1)}$, the "equivalent time" t_{e} between (i + 1)″ and (i + 1) is equal to the load duration t. Differentiating (3) gives the creep rate at point (i + 1)

$$\varepsilon_z^{\mathrm{vp}} = \frac{\psi}{V}\frac{1}{t_0 + t} = \frac{\psi}{V}\frac{1}{t_0 + t_{\mathrm{e}}}. \tag{4}$$

Equation (4) indicates that constant equivalent time t_{e} lines are also lines of constant visco-plastic strain rate.

Now consider what would happen to creep rate if (i + 1) had been reached by a different path or different loading history, say an unloading and reloading sequence. The "equivalent time" concept says that the creep rate at point (i+1) for any loading path or history is the same as that obtained by creeping from (i + 1)″ on the reference time line for an "equivalent time" t_{e} as in (4). In fact, using the "equivalent time" t_{e}, the creep rate is dependent on the stress/strain rate $(\sigma'_z, \varepsilon_z)$ only. If the creep rate can be calculated using (4) for any loading path, the total creep strain can also be calculated using (3) for any loading path. In this way, creep behaviour in an over-consolidated or unloading/reloading stress range can be described by the single equation as shown in (3).

Based on these concepts, a general 1-D elastic visco-plastic (1-D EVP) constitutive model for time-dependent stress–strain behaviour of clays has been derived as follows:

$$\frac{\mathrm{d}\varepsilon_z}{\mathrm{d}t} = \frac{\kappa/V}{\sigma'_z}\frac{\mathrm{d}\sigma'_z}{\mathrm{d}t} + \frac{\psi/V}{t_0}\exp\left[-(\varepsilon_z - \varepsilon^{\mathrm{r}}_{z0})\frac{V}{\psi}\right]\left(\frac{\sigma'_z}{\sigma'_{z0}}\right)^{\lambda/\psi}. \tag{5}$$

Equation (5) is a general 1-D EVP relationship for any 1-D compression loading, including unloading and reloading. This model is called classic

1-D EVP model in this paper as simple logarithmic fitting functions are used. This model has been verified by comparing predicted results to measured results [11, 12].

3 A 1-D EVP Model Using a Non-Linear Creep Function for 1-D Straining Condition

The logarithmic function has a limitation that may cause serious error for estimation of the long-term settlement. This limitation is that, when the time is infinite, the settlement (or strain) is infinite. This is certainly incorrect. Results of long-term creep tests have showed that the relationship of creep strain (or void ratio) vs. log(time) is not a straight line [4]. The slope of creep strain vs. log(time), commonly denoted as $C_{\alpha\varepsilon}$ (coefficient of "secondary" consolidation), decreases with time. Thus, the use of logarithmic function may over-estimate the creep settlement. Overcoming the limitation of logarithmic function is of practical and academic importance to both engineers and researchers. Yin [9] suggested a new non-linear logarithmic mathematical function with a limit for fitting the non-linear creep behaviour of soils. This section presents a new 1-D EVP model using this non-linear creep function. Using the non-linear creep function with a limit, the final creep strain under a constant load reaches a limiting value in the σ'_z, ε_z-coordinate when the time is infinite. The limit time line is a line of all final creep strain and is assumed to have the same slope λ/V in the $\log \sigma'_z, \varepsilon_z$-space.

This non-linear logarithmic creep function [9] is expressed as

$$\varepsilon_z^{\mathrm{vp}} = \frac{\dfrac{\psi_0}{V} \ln \dfrac{t_0 + t_{\mathrm{e}}}{t_0}}{1 + \dfrac{\psi_0}{V\varepsilon_{zl}^{\mathrm{vp}}} \ln \frac{t_0+t_{\mathrm{e}}}{t_0}} = \frac{\dfrac{\psi_0}{V}}{1 + \dfrac{\psi_0}{V\varepsilon_{zl}^{\mathrm{vp}}} \ln \dfrac{t_0 + t_{\mathrm{e}}}{t_0}} \ln \frac{t_0 + t_{\mathrm{e}}}{t_0} = \frac{\psi}{V} \ln \frac{t_0 + t_e}{t_0}, \tag{6}$$

where

$$\frac{\psi}{V} = \frac{\psi_0/V}{1 + \frac{\psi_0}{V\varepsilon_{zl}^{\mathrm{vp}}} \ln \frac{t_0+t_{\mathrm{e}}}{t_0}}. \tag{7}$$

In (6) and (7), $\psi_0/V, t_0$ and $\varepsilon_{zl}^{\mathrm{vp}}$ are three constant parameters from oedometer creep tests. Again, t_0 has a unit of time but it is not a real time, but a parameter. If considering $\ln[(t_0 + t_{\mathrm{e}})/t_0]$ together as a variable, (6) is in fact a hyperbolic function. Consequently, a new general 1-D elastic visco-plastic model with a creep limit (denoted as 1-D EVP) is derived as

$$\begin{cases} \dot{\varepsilon}_z = \frac{\kappa \dot{\sigma}'_z}{V\sigma'_z} + g(\sigma'_z, \varepsilon_z) & \text{for } (\sigma'_z, \varepsilon_z) \text{ above the limit timeline} \\ \dot{\varepsilon}_z = \frac{\kappa \dot{\sigma}'_z}{V\sigma'_z} & \text{for } (\sigma'_z, \varepsilon_z) \text{ below the limit timeline} \end{cases}, \tag{8}$$

where

$$g(\sigma'_z, \varepsilon_z) = \frac{\psi_0}{V t_0} \left(1 + \frac{\varepsilon^{\mathrm{r}}_{z0} + \frac{\lambda}{V} \ln \frac{\sigma'_z}{\sigma'_{z0}} - \varepsilon_z}{\varepsilon^{\mathrm{vp}}_{zl}} \right)^2 \exp \left\{ \frac{V}{\psi_0} \frac{\varepsilon^{\mathrm{r}}_{z0} + \frac{\lambda}{V} \ln \frac{\sigma'_z}{\sigma'_{z0}} - \varepsilon_z}{1 + \left(\varepsilon^{\mathrm{r}}_{z0} + \frac{\lambda}{V} \ln \frac{\sigma'_z}{\sigma'_{z0}} - \varepsilon_z \right) \Big/ \varepsilon^{\mathrm{vp}}_{zl}} \right\}. \tag{9}$$

It is noted that there is a condition in (8). If the state point $(\sigma'_z, \boldsymbol{\varepsilon}_z)$ is above the limit time line, the behaviour is EVP and the first equation in (8) shall be used. If the state point $(\sigma'_z, \varepsilon_z)$is below the limit time line, the behaviour is purely elastic and the second equation in (8) shall be used.

4 A 3-D EVP Model as Extension of the Classic 1-D EVP Model and the Modified Cam-Clay Model

The above 1-D EVP models are of great significance not only for direct applications in 1-D deformation/consolidation analysis [13], but also as a basis for extension to 3-D EVP modelling of the stress–strain behaviour [14]. Yin and Graham [14] developed the classic 1-D EVP model into a classic 3-D EVP model based on the work of Perzyna [5, 6] and the Modified Cam-Clay [7].

According to the work by Perzyna [5, 6], total strain rates $\dot{\varepsilon}_{ij}$ are the sum of elastic strain rates $\dot{\varepsilon}^{\mathrm{e}}_{ij}$ and visco-plastic strain rates $\dot{\varepsilon}^{\mathrm{vp}}_{ij}$:

$$\dot{\varepsilon}_{ij} = \dot{\varepsilon}^{\mathrm{e}}_{ij} + \dot{\varepsilon}^{\mathrm{vp}}_{ij}, \tag{10}$$

where sub-indexes $i = 1, 2, 3$ and $j = 1, 2, 3$. The elastic strain rates $\dot{\varepsilon}^{\mathrm{e}}_{ij}$ in (10) are related to effective stress rates $\dot{\sigma}'_{kl}$ by

$$\dot{\varepsilon}^{\mathrm{e}}_{ij} = C_{ijkl}\ \dot{\sigma}'_{kl}, \tag{11}$$

where C_{ijkl} is a fourth order compliance tensor with sub-indexes $k = 1, 2, 3$ and $l = 1, 2, 3$. Summation is implied if two sub-indexes of two items are the same. If the elastic deformation of the soil is assumed to be isotropic there are only two constants (or moduli), for example, an elastic shear modulus G^{e} and an elastic bulk modulus K^{e}.

Similar to the flow rule by Perzyna [5, 6], Yin and Graham [14] suggested that visco-plastic strain rates $\dot{\varepsilon}^{\mathrm{vp}}_{ij}$ in (1) be calculated from the following associated flow rule:

$$\dot{\varepsilon}^{\mathrm{vp}}_{ij} = S \frac{\partial F}{\partial \sigma'_{ij}}, \tag{12}$$

where S is a scaling function. F is referred to as a "flow surface function" [14]. Yin and Graham [14] suggested a method for determination of the scaling

function S using the 1-D EVP model [11, 12] serving as an "evolution law" and an elliptic flow surface.

According to Yin and Graham [14], the EVP constitutive relationship under an isotropic stressing condition ($q = 0, p' = p'_{\mathrm{m}}$) can be expressed as

$$\dot{\varepsilon}_{\mathrm{vm}} = \dot{\varepsilon}^{\mathrm{e}}_{\mathrm{vm}} + \dot{\varepsilon}^{\mathrm{vp}}_{\mathrm{vm}} = \frac{\kappa/V}{P'_{\mathrm{m}}}\dot{p}'_{\mathrm{m}} + \frac{\psi/V}{t_0}\exp\left[-(\varepsilon_{\mathrm{vm}} - \varepsilon^{ep}_{\mathrm{vm}o})\frac{V}{\psi}\right]\left(\frac{p_{\mathrm{m}}}{p_{\mathrm{m0}}}\right)^{\lambda/\psi}, \tag{13}$$

where $\kappa/V,\ \psi/V,\ t_0,\ \lambda/V,\ p'_{\mathrm{m0}}$ and $\varepsilon^{ep}_{\mathrm{vm}o}$ are five constants, the definition and determination of which have been discussed in Yin and Graham [14]. In (13), the total strain rate $\dot{\varepsilon}_{\mathrm{vm}}$ is equal to the sum of elastic strain rate $\dot{\varepsilon}^{\mathrm{e}}_{\mathrm{vm}}$ and visco-plastic strain rate $\dot{\varepsilon}^{\mathrm{vp}}_{\mathrm{vm}}$ under isotropic effective stress p'_{m}. In (13), $\dot{p}'_{\mathrm{m}}$ is the mean effective stress rate in isotropic stress condition; and V is specific volume of soil.

In (13), the visco-plastic strain rate $\dot{\varepsilon}^{\mathrm{vp}}_{\mathrm{vm}}$ under isotropic stressing condition ($q = 0, p' = p'_{\mathrm{m}}$) is

$$\begin{aligned}\dot{\varepsilon}^{\mathrm{vp}}_{\mathrm{vm}} &= \frac{\psi/V}{t_0}\exp\left[-(\varepsilon_{\mathrm{vm}} - \varepsilon^{ep}_{\mathrm{vm0}})\frac{V}{\psi}\right]\left(\frac{p'_{\mathrm{m}}}{p'_{\mathrm{m0}}}\right)^{\lambda/\psi} \\ &= \frac{\psi/V}{t_0}\exp\left\{\left[-(\varepsilon_{\mathrm{vm}} - \varepsilon^{ep}_{\mathrm{vm0}}) + \frac{\lambda}{V}\mathrm{In}\left(\frac{p'_{\mathrm{m}}}{p'_{\mathrm{m0}}}\right)\right]\frac{V}{\psi}\right\}.\end{aligned} \tag{14}$$

In (12), the "flow surface function" F is selected to be the same as the potential function used in the modified Cam-Clay model:

$$F = p'^2 - p'p'_{\mathrm{m}} + \frac{q^2}{M_{\mathrm{c}}^2} = 0, \tag{15}$$

where the mean effective stress $p' = (\sigma'_{11}+\sigma'_{22}+\sigma'_{33})/3$ (p' is a stress invariant); M_{c} is the slope of the strength envelope in compression and $M_{\mathrm{c}} = 6\sin\phi'/(3-\sin\phi\prime)$ (ϕ' is friction angle). The value of p'_{m} is the mean effective stress value at which the flow surface locus meets the p'-axis as shown in Fig. 1a. The subscript "m" stands for a state of isotropic stressing, that is, $q = 0$. The generalised deviator stress q (a stress invariant) is defined as

$$q = \sqrt{\frac{3}{2}S_{ij}S_{ij}}, S_{ij} = \sigma'_{ij} - \delta_{ij}p', \delta_{ij} = 1 \quad \text{for} \quad i = j$$
$$\text{or} \quad \delta_{ij} = 0 \quad \text{for} \quad i \neq j.$$

It is assumed by Yin and Graham [14] that the visco-plastic volume strain rate $\dot{\varepsilon}^{\mathrm{vp}}_{\mathrm{v}}$ in (p', q)- space ($q > 0$) is equal to the visco-plastic strain rate $\dot{\varepsilon}^{\mathrm{vp}}_{\mathrm{vm}}$ under the corresponding isotropic stressing condition ($q = 0, p' = p'_{\mathrm{m}}$), that is $\dot{\varepsilon}^{\mathrm{vp}}_{\mathrm{v}} = \dot{\varepsilon}^{\mathrm{vp}}_{\mathrm{vm}}$. Thus the scaling function S can then be determined as

$$S = \frac{\psi/V}{t_0}\exp\left\{\left[-(\varepsilon_{\mathrm{vm}} - \varepsilon^{ep}_{\mathrm{vm0}}) + \frac{\lambda}{V}\mathrm{In}\left(\frac{p'_{\mathrm{m}}}{p'_{\mathrm{m0}}}\right)\right]\frac{V}{\psi}\right\}\frac{1}{|2p' - p'_{\mathrm{m}}|}. \tag{16}$$

Using S in (16) and an isotropic elastic model for the elastic strain rates $\dot{\varepsilon}^{\mathrm{e}}_{ij}$, the general 3-D EVP constitutive model is

$$\dot{\varepsilon}_{ij} = \left(\frac{1}{2G^{\mathrm{e}}}S_{ij} + \frac{1}{K^{\mathrm{e}}}p'\delta_{ij}\right) + S\frac{\partial F}{\partial \sigma'_{ij}}. \tag{17}$$

It has been approved that when the viscosity of the soil is zero, that is, let $\psi/V = 0$, the above 3-D EVP model becomes the modified Cam-Clay model. The 3-D EVP model is considered to be an extension of the modified Cam-Clay model for describing the time and strain rate effects on the stress–strain behaviour.

5 A Refined 3-D EVP Model Using More General Flow Surfaces on (q, p')-Plane

It is noted that the failure of geomaterials follows better to the Mohr-Coloumb's criterion and the shapes of the flow surfaces (or yield surfaces) in $q-p'$-plane may be different for different soils. Therefore it is necessary to refined Yin and Graham's 3-D EVP model for wide applications. Using the Mohr-Coloumb's criterion and a more general flow surface function, a refined 3-D EVP model is derived for modelling the time-dependent behaviour of clayey soils [10].

The flow surface may not be an elliptic surface passing through the original point with $q = p' = 0$. This note introduces a flow surface consisting of two parts [1], that is, f_1 and f_2, as shown in Fig. 2 for EVP modelling. This flow surface is more general than the elliptic surface, which is only a special form of the proposed flow surface. The f_1 is the part of the flow surface within the strength envelope line for normally or lightly over-consolidated behaviour and is expressed by

$$F = f_1\frac{p'^2}{\beta^2} - \frac{2p'p'_{\mathrm{m}}}{(1+\beta)\beta^2} + \frac{t^2}{M_{\mathrm{c}}^2} + \left(\frac{1}{\beta^2} - 1\right)\frac{p'^2_{\mathrm{m}}}{(1+\beta)^2} = 0. \tag{18}$$

The f_2 is the other part of the flow surface above the strength envelope line for heavily over-consolidated behaviour and is expressed by

$$F = f_2 = p'^2 - p'p'_{\mathrm{m}} + \frac{t^2}{M_{\mathrm{c}}^2} = 0. \tag{19}$$

Equation (19) is in fact an elliptic surface (part) passing through the origin. The t in (18) and (19) is

$$t = q\frac{(1+K) - (1-K)\,(r/q)^3}{2K}. \tag{20}$$

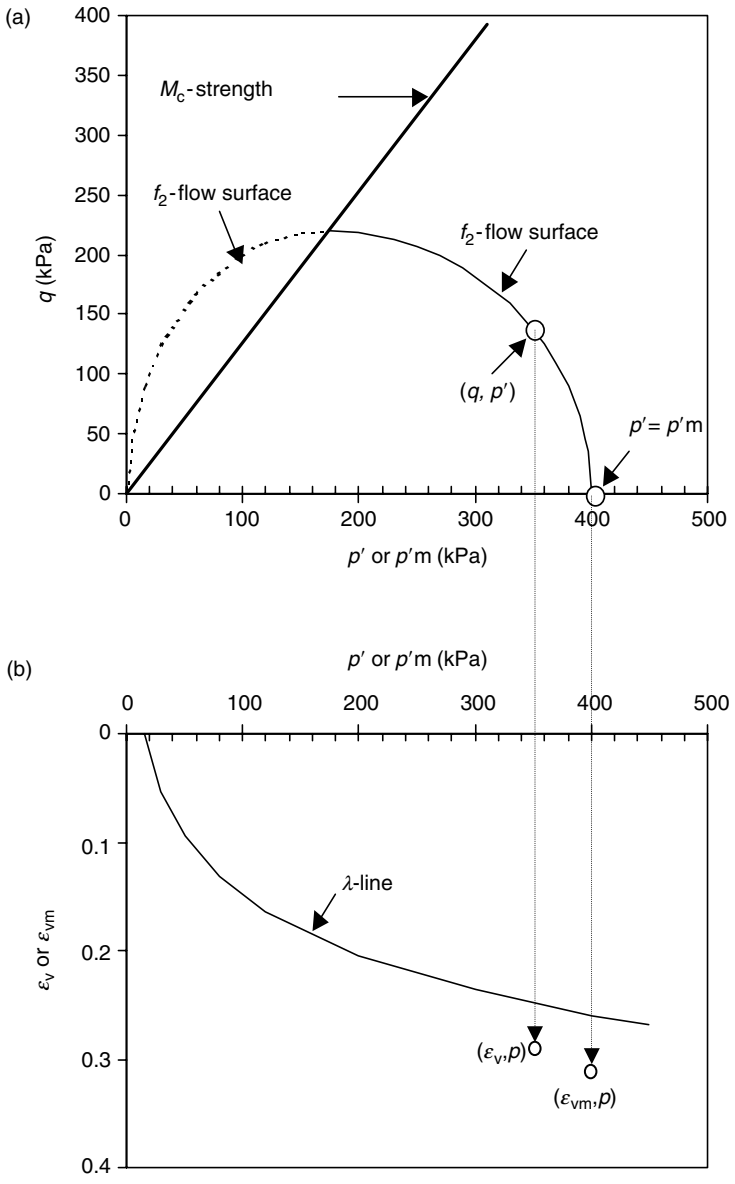

Fig. 2. (**a**) Strength line, flow surfaces f_1 and f_2, current stress point (q, p'), and p'_{m} point and (**b**) λ-line (reference time line), point $(\varepsilon_{\mathrm{v}}, p')$, and point $(\varepsilon_{\mathrm{vm}}, p'_{\mathrm{m}})$

The value of p'_{m} is the mean effective stress value at which the flow surface locus meets the p'-axis as shown in Fig. 2a. The subscript "m" stands for a state of isotropic stressing, that is, t (or q) $= 0$. The stress t in (18) and (19) is related to the generalised deviator stress q (a stress invariant) and the

third stress invariant r as expressed in (20). The deviator stress q is defined as

$$q = \sqrt{\frac{3}{2} S_{ij} S_{ij}}, \qquad S_{ij} = \sigma'_{ij} - \delta_{ij} p', \quad \delta_{ij} = 1 \quad \text{for} \quad i = j$$
$$\text{or} \quad \delta_{ij} = 0 \quad \text{for} \quad i \neq j.$$

The stress invariant r is expressed as $r = \left(\frac{9}{2} S_{ij} S_{jk} S_{kl}\right)^{1/3}$.

This note focuses on modelling normally consolidated or lightly overconsolidated clays with the flow surface $F = f_1$ in (18). Using (12), viscoplastic volume strain rate $\dot{\varepsilon}_{\mathrm{v}}^{\mathrm{vp}}$ and deviator strain rate $\dot{\varepsilon}_{\mathrm{s}}^{\mathrm{vp}}$ can be expressed as

$$\begin{cases} \dot{\varepsilon}_{\mathrm{v}}^{\mathrm{vp}} = S \frac{\partial F}{\partial p'} \\ \dot{\varepsilon}_{\mathrm{s}}^{\mathrm{vp}} = S \frac{\partial F}{\partial q} \end{cases}, \tag{21}$$

where the "dot" represents differentiation with respect to time. It is known that the total deviator strain ε_{s} is defined as $\varepsilon_{\mathrm{s}} = \sqrt{\frac{2}{3} E_{ij} E_{ij}}$, where $E_{ij} = \varepsilon_{ij} - \frac{1}{3} \boldsymbol{\delta}_{ij} \boldsymbol{\varepsilon}_{\mathrm{v}}, \delta_{ij} = 1$ for $i = j$ or $\delta_{ij} = 0$ for $i \neq j$. In the triaxial state, $\varepsilon_{\mathrm{s}} = \frac{2}{3}(\varepsilon_1 - \varepsilon_3)$. Using (18)

$$\frac{\partial F}{\partial p'} = \frac{\partial f_1}{\partial p'} = \frac{2p'}{\beta^2} - \frac{2p'_{\mathrm{m}}}{(1+\beta)\beta^2} \tag{22}$$

and

$$\frac{\partial F}{\partial q} = \frac{\partial f_1}{\partial t} \frac{\partial t}{\partial q} = \frac{2t}{M_{\mathrm{c}}^2} \frac{\partial t}{\partial q} = \frac{2t}{M_{\mathrm{c}}^2} \frac{1}{2K} [(1+K) + 2(1-K) r^3 / q^3]. \tag{23}$$

It is noted that for triaxial compression, since $r = q$, using (18), $t = q$. Thus, (23) can be written as

$$\frac{\partial F}{\partial q} = \frac{2q}{M_{\mathrm{c}}^2} \frac{3-K}{2K}. \tag{24}$$

For triaxial extension, since $r = -q$, then $t = q/K$. Thus, (23) can be written as

$$\frac{\partial F}{\partial q} = \frac{2q}{M_{\mathrm{c}}^2} \frac{3K-1}{2K^2}. \tag{25}$$

For both triaxial compression and extension shear conditions, using (21), (22), (24) and (25), (21) can be rewritten as

$$\begin{cases} \dot{\varepsilon}_{\mathrm{v}}^{\mathrm{vp}} = S \left(\frac{2p'}{\beta^2} - \frac{2p'_{\mathrm{m}}}{(1+\beta)\beta^2} \right) \\ \dot{\varepsilon}_{\mathrm{s}}^{\mathrm{vp}} = S \frac{2q}{M_{\mathrm{c}}^2} f(K) \end{cases}, \tag{26}$$

where $f(K) = (3-K)/2K$ for triaxial compression and $f(K) = (3K-1)2K^2$ for triaxial extension.

Table 1. Values of all parameters in the refined 3-D EVP model

M_c	1.265	K/V	0.018
K	0.75	ψ/V	0.0025
β	1.3	t_0 (min)	1440
$K^e = p'/(K/V)$(kPa)	55.56 p'	λ/V	0.0792
$G^e = 0.23K^e$(kPa)	12.8 p'	$p'mo$ (kPa)	15.2
		ε_{vm0}^{ep}	0

The visco-plastic strain rate $\dot{\varepsilon}_{vm}^{vp}$ under isotropic stressing condition ($q = 0$, $p' = p'_m$) is the same as that in (26) on the flow surface, that is, the condition $\dot{\varepsilon}_v^{vp} = \dot{\varepsilon}_{vm}^{vp}$. Thus, the scaling function S related the flow surface f_1 can then be determined as

$$S = \frac{\psi/V}{t_0} \exp\left\{\left[-(\varepsilon_{vm} - \varepsilon_{vm0}^{ep}) + \frac{\lambda}{V}\ln\left(\frac{p'_m}{p'_{m0}}\right)\right]\frac{V}{\psi}\right\} \frac{1}{\left(\frac{2p'}{\beta^2} - \frac{2p'_m}{(1+\beta)\beta^2}\right)}. \quad (27)$$

Using (27) for S, the refined 3-D EVP model can be written in the same format as that in (17) [10].

The above refined 3-D EVP model has been calibrated using data of tests on a Hong Kong marine clay (HKMC). A summary of the values of all parameters is given in Table 1.

The calibrated refined EVP model was used to predict the time-dependent stress–strain behaviour of the HKMC under triaxial stress conditions. Figure 3 shows the measured and predicted results for one consolidated undrained test sheared at a constant deviator stress rate $\dot{q} = 30\,\mathrm{kPa\,h^{-1}}$. It is seen from the figure that the predicted deviator stress is higher than the measured data for strain from 0 up to 8% but very close to the measured data when strain is larger than 8%. The predicted porewater pressure is closer to the measured results compared to the deviator stress. The effective stress path (ESP) is close to the measured one at initial part and the final part, but deviated from the measured one in the middle part.

From the comparative study, it is found that the refined EVP model can simulate well, in general, the time-dependent stress–strain behaviour, for example, time and strain rate effects. Some discrepancies between predicted results and measured results are observed. Generally speaking, the comparison shows that the refined model is promising, but further refinement and verification are recommended.

6 A More General 3-D EVP Model for both Normally and Over-consolidated Clayey Soils

The above two 3-D EVP models has limitations in modelling over-consolidated soil behaviour. Yin et al. [16] developed a more general 3-D EVP Model for

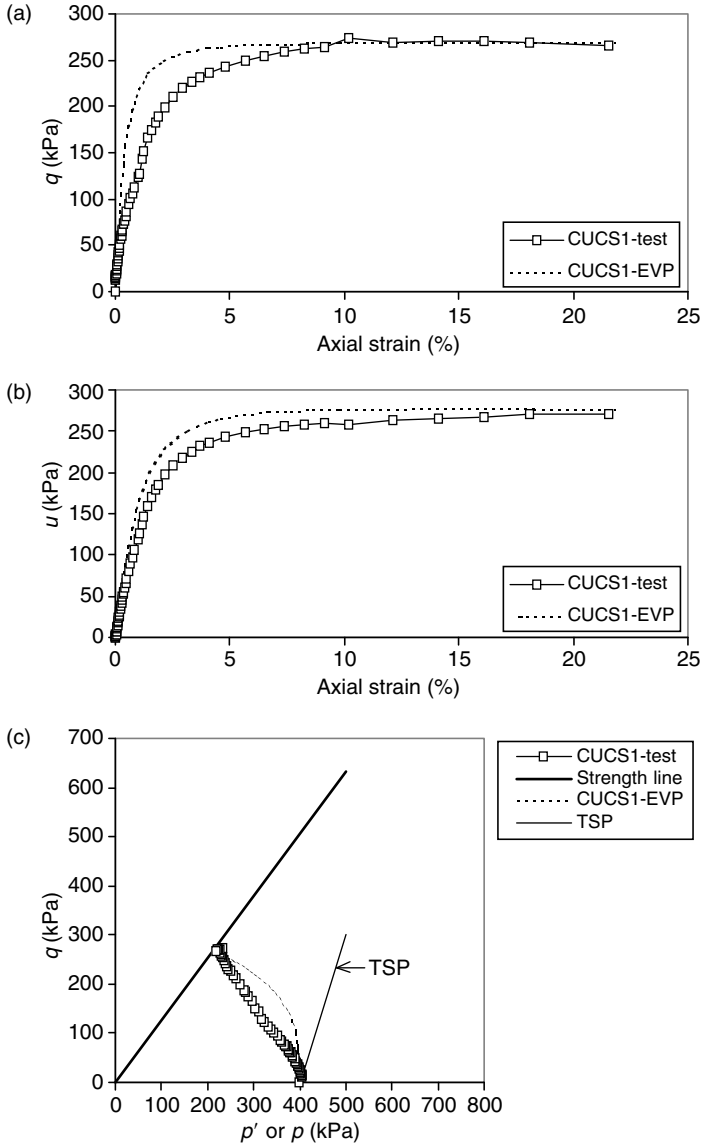

Fig. 3. Comparison of measured and predicted results, (**a**) deviator stress vs. axial strain, (**b**) porewater pressure vs. axial strain and (**c**) effective stress paths (ESP) and total stress paths (TSP) in a consolidated undrained shear test at a constant stress rate $\dot{q} = 30\,\mathrm{kPa\,h^{-1}}$ (after [15])

both normally and over-consolidated clayey soils. A new loading surface consisting of two parts of f_1 and f_2 is proposed. The f_1 is the part of the loading surface within the critical state line in $p'-q$ plane for normally or lightly overconsolidated behaviour and is expressed by

$$F = f_1 = \frac{p'^2}{\beta^2} - \frac{2p'p'_{\mathrm{m}}}{(1+\beta)\beta^2} + \frac{q^2}{M_2 g^2_{(\theta)}} + \frac{1-\beta}{(1+\beta)\beta^2} p'^2_{\mathrm{m}} = 0, \tag{28}$$

where $M = 6\sin\phi'(3-\sin\phi')$ is the slope of failure line in $p'-q$ plane, and p'_{m} is the mean effective stress value at which the loading surface in (28) intercepts the mean effective stress p'-axis in $p'-q$ plane. β in (28) is a parameter controlling shear shape in $p'-q$ plane. After investigating results of some undrained compression and extension triaxial tests, the authors have found that the stress paths for compression and extension tests are different. Therefore, the authors suggest that β is a function of stress Lode angle, and it may be empirically determined by $\beta = \frac{1}{5}[6 + \sin(3\theta - \pi/2)]$.

The f_2 is the part of the loading surface above the critical state line in $p'-q$ plane. It is for the behaviour of heavily overconsolidated soil and is expressed by

$$F = f_2 = p' \left[1 + \frac{1}{n-1}\left(\frac{q}{M g_{(\theta)} p'}\right)^n\right] - p'_0, \tag{29}$$

where p'_0 is the mean effective stress value at which the loading surface in (29) intercepts the mean effective stress p'-axis in $p'-q$ plane. The n in (29) is a parameter.

The 1-D EVP model using the non-linear creep function in (8) has been extended for the time-dependent stress–strain behaviour under isotropic stressing and is used an evolution law in the general 3-D EVP model. Thus, the general 3-D EVP constitutive relationship in a general stress state is written as

$$\begin{aligned}\dot{\varepsilon}_{ij} = {} & \frac{1}{2G}\dot{s}_{ij} + \frac{\kappa}{3V}\frac{\dot{p}'}{p'}\delta_{ij} + \frac{\psi_0}{V t_0}\left(1 + \frac{\varepsilon^{\mathrm{r}}_{\mathrm{vm}} - \varepsilon_{\mathrm{vm}}}{\varepsilon^{\mathrm{vp}}_{\mathrm{vml}}}\right)^2 \\ & \exp\left\{\frac{\varepsilon^{\mathrm{r}}_{\mathrm{vm}} - \varepsilon_{\mathrm{vm}}}{[1 + (\varepsilon^{\mathrm{r}}_{\mathrm{vm}} - \varepsilon_{\mathrm{vm}})/\varepsilon^{\mathrm{vp}}_{\mathrm{vml}}]}\frac{V}{\psi_0}\right\}\frac{1}{|\partial F/\partial p'|}\frac{\partial F}{\partial \sigma'_{ij}}.\end{aligned} \tag{30}$$

This 3-D EVP model has a total of ten parameters, i.e. κ/V, $\lambda/V, \psi_0/V, \varepsilon^{\mathrm{r}}_{\mathrm{vm0}}$, $p'_{\mathrm{m0}}, t_0, \varepsilon^{\mathrm{vp}}_{\mathrm{vml}}, M, \beta$ and n. All the ten parameters can be determined by a multi-stage isotropic consolidation test and undrained (or drained) triaxial tests (at least one in the normally consolidated range for β and one in the heavily over-consolidated range for n).

The model has been calibrated using data of tests on a HKMC. The calibrated model is then used to simulate the strain-rate dependent stress–strain behaviour of the same HKMC with different over-consolidation ratios (OCRs). A comparison of the measured and simulated results is shown in Fig. 4.

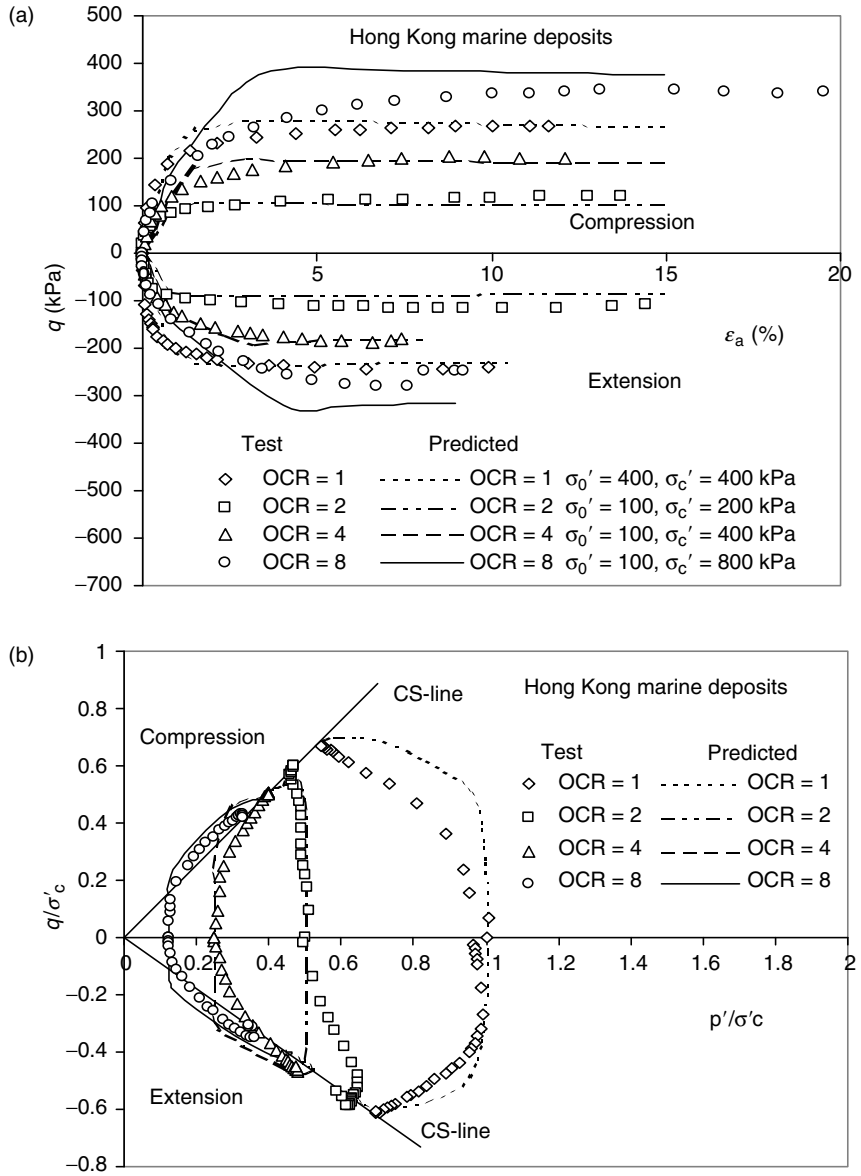

Fig. 4. Comparison between measured and predicted results of CIU tests for overconsolidated HKMC, (**a**) axial strain vs. deviator stress and (**b**) effective stress paths normalized with respected to preconsolidation pressure σ'_c

7 Summary and Conclusions

A total of five EVP models for the time for the time-dependent stress–strain behaviour of clayey soils have been introduced in the paper. The key points in the modelling approach, relations, features and applications of these EVP models are presented and discussed. Methods for determining all model parameters are briefly described. Typical measured and simulated time-dependent stress–strain relationships of clayey soils are compared and discussed.

It is found from the study that all EVP models can consider viscosity effects on the stress–strain behaviour of clayey soils under given conditions (1-D straining, 1-D stressing or 3-D stress states). These models have limitations in certain cases. Improvements are being made. The basic concepts and EVP modelling approaches provide a wide and useful framework for modelling the time-dependent stress–strain-strength of geomaterials.

Acknowledgements

Financial supports from RGC grants of the University Grants Council of the Hong Kong SAR Government of China and The Hong Kong Polytechnic University are acknowledged.

References

1. ABAQUS (2005). ABAQUS program and manuals, HIBBITT, KARLSSON & SORENSEN, INC, USA
2. Bjerrum, L. (1967). Engineering geology of Norwegian normally consolidated marine clays as related to the settlements of buildings. *Géotechnique*, 17, No. 2, pp. 83–118
3. Graham, J., Crooks, J.H.A. and Bell, A.L. (1983). Time effects on stress-strain behaviour of natural soft clays. *Geotechnique*, 33, No. 3, pp. 327–340
4. Leroueil, S., Kabbaj, M., Tavenas, F. and Bouchard, R. (1985). Stress-strain-strain rate relation for the compressibility of sensitive natural clays. *Geotechnique*, 35, No. 2, pp. 159–180
5. Perzyna, P. (1963). The constitutive equations for working hardening and rate sensitive plastic materials. *Proc. Vib. Prob.* Warsaw, 4, No. 3, pp. 281–290
6. Perzyna, P. (1966). Fundamental problems in viscoplasticity, *Advances in Applied Mechanics*, Academic, New York, No. 9, pp. 244–368
7. Roscoe, K.H. and Burland, J.B. (1968). On the generalised stress-strain behaviour of wet clay. *Engineering plasticity.* (eds. Heyman, J. and Leckie, F.P.), pp. 535–609. Cambridge University Press, Cambridge
8. Yin, J.-H. (1990). *Constitutive modelling of time-dependent stress-strain behaviour of soils.* Ph.D. thesis, University of Manitoba, Winnipeg, March, 1990, 314 pages
9. Yin, J.-H. (1999). Equivalent time and elastic visco-plastic models for geomaterials. *Chin. J. Rock Mech. Eng.* CSRME. (in Chinese), 18, No. 2, pp. 124–128

10. Yin, J.-H. (2001). A refined elastic visco-plastic model for clayey soils. *J. Geotech. Eng.* SEAGS, 32, No. 1, pp. 23–32
11. Yin, J.-H. and Graham, J. (1990). Reply to the Discussion by G.Mesri (CGJ, Vol.27, 259–261, 1990) on "Viscous-elastic-plastic modelling of one-dimensional time-dependent behaviour of clays" by J.-H. Yin and J. Graham (CGJ, Vol.26,199–209, 1989). *Can. Geotech. J.*, Vol.27, 262–265.
12. Yin, J.-H. and Graham, J. (1994). Equivalent times and one-dimensional elastic visco-plastic modelling of time-dependent stress-strain behaviour of clays. *Can. Geotech. J.* 31, pp. 42–52
13. Yin, J.-H. and Graham, J. (1996). Elastic visco-plastic modelling of one-dimensional consolidation. *Geotechnique*, 46, No. 3, pp. 515–527
14. Yin, J.-H. and Graham, J. (1999). Elastic visco-plastic modelling of the time-dependent stress-strain behaviour of soils. *Can. Geotech. J.* 36, pp. 736–745
15. Yin, J.-H. and Zhu, J.-G. (1999). Measured and predicted time-dependent stress-strain behaviour of Hong Kong marine deposits. *Can. Geotech. J.* 36, pp. 760–766
16. Yin, J-H, Zhu, JG and Graham, J. (2002). A new elastic visco-plastic model for time-dependent behaviour of normally and overconsolidated clays – theory and verification. *Can. Geotech. J.* 39, No. 1, pp. 157–173

Part III

Micromechanics

Micro-Polar Effects under Monotonic and Cyclic Shearing

E. Bauer*, J. Tejchman†, S.F. Tantono#, and W. Huang¶

* Institute of General Mechanics, Graz University of Technology, Austria
erich.bauer@tugraz.at
† Civil Engineering Department, Technical University of Gdańsk, Poland
# Institute of General Mechanics, Graz University of Technology, Austria
¶ Department of Civil, Surv. & Env. Eng., The University of Newcastle, Australia

1 Introduction

In the present paper monotonic and cyclic shearing of a cohesionless granular layer is numerically investigated using a micro-polar hypoplastic continuum approach. The constitutive equations for the stress and the couple stress are non-linear tensor-valued functions and based on the concept of hypoplasticity [17]. The model was formulated by Tejchman [18], Tejchman and Gudehus [22], who extended a non-polar hypoplastic model proposed by Gudehus [9] and Bauer [2] within a micro-polar continuum or so-called Cosserat continuum. Due to the presence of a characteristic length in the form of the mean grain diameter and by taking into account a polar parameter, the model can simulate the formation of patterns of shear zones with a certain thickness (e.g. [11, 15, 16, 19, 20]). Finite element calculations show that the thickness of the localized zones does not depend upon the mesh discretization if the size of the finite elements in the shear zone is small enough. However, the initial density, the pressure level and the boundary conditions can have a significant influence on the thickness of the localized zone [4, 10, 14, 18]. For the present study of monotonic and cyclic shearing, numerical calculations are carried out for quasi-static shear deformations of an infinite strip of a micro-polar hypoplastic material located between two parallel rigid plates with rough boundaries and a constant normal pressure. Attention is paid to the influence of the shear amplitude and the number of cycles on the evolution of the void ratio across the height of the shear layer. With respect to the boundary conditions for an infinite shear layer the results are independent of the co-ordinate in the direction of shearing.

2 Micro-Polar Hypoplastic Material Model

Following Eringen [7] a micro-polar continuum is characterized by the macro-displacement field u_i and micro-rotations or so-called Cosserat rotations ω_i^{c} $(i = 1, 2, 3)$. The rate of deformation and the rate of curvature are defined as $\dot{\varepsilon}_{ij} = \partial \dot{u}_i/\partial x_j + \epsilon_{kij}\dot{\omega}_k^{\mathrm{c}}$ and $\dot{\kappa}_{ij} = \partial \dot{\omega}_i^{\mathrm{c}}/\partial x_j$, respectively, where ϵ_{ijk} denotes the permutation tensor. The velocity gradient $\partial \dot{u}_i/\partial x_j$ can be decomposed into the symmetric part $D_{ij} = (\partial \dot{u}_i/\partial x_j + \partial \dot{u}_j/\partial x_i)/2$ and the skew-symmetric part $W_{ij} = (\partial \dot{u}_i/\partial x_j - \partial \dot{u}_j/\partial x_i)/2$. Hence the strain rate $\dot{\varepsilon}_{ij}^{\mathrm{c}}$ can alternatively be represented as $\dot{\varepsilon}_{ij}^{\mathrm{c}} = D_{ij} + W_{ij} - W_{ij}^{\mathrm{c}}$ where W_{ij} denotes the macro-spin and $W_{ij}^{\mathrm{c}} = -\epsilon_{kij}\dot{\omega}_k^{\mathrm{c}}$ denotes the micro-spin or so-called Cosserat spin. In the following, it is assumed that state of a granular body is determined by the current void ratio e, the non-symmetric stress tensor $\boldsymbol{\sigma}$ and the couple stress tensor $\boldsymbol{\mu}$. The evolution of these state quantities are described in the present paper using a hypoplastic constitutive model proposed by Tejchman and Gudehus [22], wherein the components of their objective rates have the following representations:

$$\mathring{\sigma}_{ij} = f_{\mathrm{s}}\Big[\hat{a}^2\dot{\varepsilon}_{ij} + (\hat{\sigma}_{kl}\dot{\varepsilon}_{kl} + \hat{\mu}_{kl}\dot{\bar{\kappa}}_{kl})\hat{\sigma}_{ij} + f_{\mathrm{d}}\hat{a}(\hat{\sigma}_{ij} + \hat{\sigma}_{ij}^{\mathrm{d}})\sqrt{\dot{\varepsilon}_{kl}\dot{\varepsilon}_{kl} + \dot{\bar{\kappa}}_{kl}\dot{\bar{\kappa}}_{kl}}\Big], \quad (1)$$

$$\mathring{\mu}_{ij} = f_{\mathrm{s}}d_{50}\Big[\hat{a}^2\,\dot{\bar{\kappa}}_{ij} + \hat{a}^2\hat{\mu}_{ij}\left(\hat{\sigma}_{kl}\dot{\varepsilon}_{kl} + \hat{\mu}_{kl}\dot{\bar{\kappa}}_{kl} + f_{\mathrm{d}}a_{\mathrm{c}}\sqrt{\dot{\varepsilon}_{kl}\dot{\varepsilon}_{kl} + \dot{\bar{\kappa}}_{kl}\dot{\bar{\kappa}}_{kl}}\right)\Big], \quad (2)$$

$$\dot{e} = (1 + e)\dot{\varepsilon}_{kk}. \quad (3)$$

$\hat{\sigma}_{ij}, \hat{\sigma}_{ij}^{\mathrm{d}}, \hat{\mu}_{ij}$ and $\dot{\bar{\kappa}}_{ij}$ are the components of the normalized quantities of the stress, the deviatoric part of the stress, the couple stress and the rate of curvature, respectively, which are defined as

$$\hat{\sigma}_{ij} = \frac{\sigma_{ij}}{\sigma_{kk}}, \quad \hat{\sigma}_{ij}^{\mathrm{d}} = \hat{\sigma}_{ij} - \frac{\delta_{ij}}{3}, \quad \hat{\mu}_{ij} = \frac{\mu_{ij}}{d_{50}\sigma_{kk}} \text{ and } \dot{\bar{\kappa}}_{ij} = d_{50}\,\dot{\kappa}_{ij}.$$

Herein δ_{ij} denotes the Kronecker delta and d_{50} is the mean grain diameter, which enters the constitutive model as the internal length. The influence of the mean pressure and the current void ratio on the incremental stiffness, the dilatancy behaviour and the peak stress ratio are taken into account with the stiffness factor f_{s}, i.e.

$$f_{\mathrm{s}} = \frac{h_{\mathrm{s}}}{n}\left(\frac{1}{c_1^2} + \frac{1}{3} - \frac{1}{c_1\sqrt{3}}\left(\frac{e_{\mathrm{i0}} - e_{\mathrm{d0}}}{e_{\mathrm{c0}} - e_{\mathrm{d0}}}\right)^{\alpha}\right)^{-1}\left(\frac{e_{\mathrm{i}}}{e}\right)^{\beta}\frac{(1 + e_{\mathrm{i}})}{e_{\mathrm{i}}}\left(-\frac{\sigma_{kk}}{h_{\mathrm{s}}}\right)^{1-n} \quad (4)$$

and the density factor f_{d}, i.e.

$$f_{\mathrm{d}} = \left(\frac{e - e_{\mathrm{d}}}{e_{\mathrm{c}} - e_{\mathrm{d}}}\right)^{\alpha}. \quad (5)$$

Herein α, β, n an h_{s} are constitutive constants. In (4) and (5) the current void ratio e is related to the maximum void ratio e_{i}, the minimum void ratio

e_{d} and the critical void ratio e_{c}. These limit void ratios decrease with an increase of the mean pressure σ_{kk}, i.e. $e_{\mathrm{i}}/e_{\mathrm{i0}} = e_{\mathrm{d}}/e_{\mathrm{d0}} = e_{\mathrm{c}}/e_{\mathrm{c0}} = \exp[-(-\sigma_{kk}/h_{\mathrm{s}})^n]$, where $e_{\mathrm{i0}}, e_{\mathrm{d0}}, e_{\mathrm{c0}}$ are the corresponding values for $\sigma_{kk} = 0$. Factors $\hat{a}$ and a_{c} in (1) and (2) are related to critical states, i.e. a_{c} is assumed to be $a_{\mathrm{c}} = \hat{a}^{-1}$ (Tejchman and Gudehus 2001) and $\hat{a}$ depends on the so-called angle of internal friction φ_{c} and the normalized stress deviator, $\hat{\sigma}^{\mathrm{d}}$, according to (Bauer 1995):

$$\hat{a}^{-1} = c_1 + c_2\sqrt{\hat{\sigma}^{\mathrm{d}}_{kl}\hat{\sigma}^{\mathrm{d}}_{kl}}\left[1 - \sqrt{6}\hat{\sigma}^{\mathrm{d}}_{kl}\hat{\sigma}^{\mathrm{d}}_{lm}\hat{\sigma}^{\mathrm{d}}_{mk}/(\hat{\sigma}^{\mathrm{d}}_{kl}\hat{\sigma}^{\mathrm{d}}_{kl})^{3/2}\right] \tag{6}$$

with $c_1 = \sqrt{3/8}(3 - \sin\varphi_{\mathrm{c}})/\sin\varphi_{\mathrm{c}}$ and $c_2 = (3/8)(3 + \sin\varphi_{\mathrm{c}})/\sin\varphi_{\mathrm{c}}$. It can be noted that for the special case of purely coaxial and homogeneous deformations starting from an initially symmetric stress tensor or for $d_{50} \to 0$ there are no polar effects, i.e. $\mu_{ij} = \dot{\mu}_{ij} = 0$, $W^{\mathrm{c}}_{ij} = W_{ij}$, $\dot{\varepsilon}^{\mathrm{c}}_{ij} = D_{ij}$ and $\sigma_{ij} = \sigma_{ji}$, so that the present micro-polar hypoplastic model is reduced to the non-polar one given by Gudehus [9] and Bauer [2], i.e.

$$\mathring{\sigma}_{ij} = f_{\mathrm{s}}\left[\hat{a}^2 D_{ij} + \hat{\sigma}_{ij}(\hat{\sigma}_{kl}D_{kl}) + f_{\mathrm{d}}\hat{a}(\hat{\sigma}_{ij} + \hat{\sigma}^{\mathrm{d}}_{ij})\sqrt{D_{kl}D_{kl}}\right], \tag{7}$$

$$\dot{e} = (1 + e)D_{kk}\ . \tag{8}$$

It follows from (7) that functions $f_{\mathrm{s}}, \hat{a}$ and f_{d} are the same for the micro-polar and non-polar version. Therefore, coaxial and homogeneous deformations are sufficient for the adaptation of the constants involved in these functions.

Altogether the constitutive model includes ten constants, which can be calibrated based on the data of standard element tests and simple index tests [2, 12]. For the numerical calculations presented in the present paper the following quantities are used: $\varphi_{\mathrm{c}} = 30°$, $e_{\mathrm{i}}0 = 1.3$, $e_{\mathrm{d0}} = 0.51$, $e_{\mathrm{c0}} = 0.82$, $n = 0.5$, $h_{\mathrm{s}} = 190\,\mathrm{MPa}$, $\alpha = 0.3$, $\beta = 1.0, d_{50} = 0.5\,\mathrm{mm}$, $a_{\mathrm{c}} = \hat{a}^{-1}$.

3 Plane Shearing under a Constant Vertical Pressure

For the numerical simulation of cyclic shearing of an infinite granular layer located between two parallel rigid plates under plane strain conditions the micro-polar hypoplastic model was implemented in a finite element program [13, 18]. Linear shape functions for displacements and the Cosserat rotation were used. With an updated Lagrange formulation large deformations are taken into account. The initial height of an element was chosen to be five times the mean grain diameter d_{50}, which was found to be sufficiently small to ensure that the predicted thickness of the localized zone was mesh independent. With respect to the case of plane strain only three degrees of freedom remain for each element node, i.e. u_1, u_2 and ω^{c}_3, and the non-zero static quantities within the element are $\sigma_{11}, \sigma_{22}, \sigma_{33}, \sigma_{12}, \sigma_{21}, \mu_{31}$ and μ_{32} with respect to the co-ordinate system in Fig. 1. For a micro-polar material the behaviour under

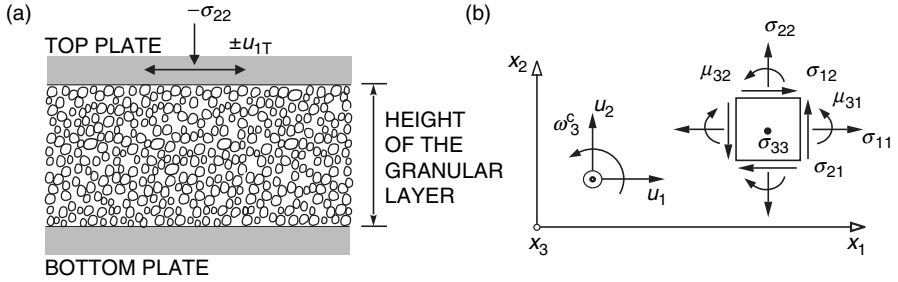

Fig. 1. Modeling of a plane infinite granular shear layer under constant vertical stress σ_{22}: (**a**) section of the granular layer between parallel plates with rough surfaces, (**b**) degrees of freedom u_1, u_2 and ω_3^c, stress components $\sigma_{11}, \sigma_{22}, \sigma_{33}, \sigma_{12}, \sigma_{21}$ and couple stress components μ_{31} and μ_{32} in a micro-polar continuum approach with respect to the Cartesian co-ordinate system

plane shearing is influenced by width of the granular layer in the direction of shearing [4]. Only in the case of an infinite shear layer the field quantities are independent of the co-ordinate in the direction of shearing, i.e. $\partial(\cdot)/\partial x_1 = 0$. In the finite element simulation this property is modeled using displacement and rotating constraints, i.e. for nodes with the same vertical co-ordinate x_2 the displacements and micro-rotations must be the same. As a consequence of the symmetry condition the width of the horizontal section of the shear layer chosen for the numerical simulation is arbitrary. In order to simulate very rough surfaces of the rigid bottom and top plates without sliding and rotating of particles against the bounding structure, relative interface displacements and micro-rotations are set equal to zero. Quasi-static shearing was initiated by horizontal node displacements prescribed along the top of the layer, while the nodes at the bottom were kept fixed. The first shear displacement is assumed to be large enough so that shear localization occurs and a stationary state is almost reached for both monotonic and cyclic shearing. The dilatancy of the top layer perpendicular to the direction of shearing is not locked, i.e. vertical displacements are a result of the constant vertical stress σ_{22} applied to the top of the layer and the dilatancy behaviour of the material under shearing.

3.1 Behaviour Under Monotonic Shearing

For an initial height of the shear layer of 20 mm, an initially homogeneously distributed void ratio of $e_0 = 0.6$ and a constant vertical pressure of $\sigma_{22} = -100\,\mathrm{kPa}$, the numerical results are shown in Fig. 2 and 3 for different horizontal shear displacements $u_{1\mathrm{T}}$ prescribed at the top of the layer. Herein the normalized quantities are defined as: $\sigma_{ij}^* = \sigma_{ij}/h_\mathrm{s}, \mu_{ij}^* = \mu_{ij}/(h_\mathrm{s} d_{50}), \dot{\kappa}_{ij}^* = \dot{\overline{\kappa}}_{ij}$.

In contrast to the classical non-polar continuum the velocity field, the stress rate field and the couple stress rate field are non-linearly distributed

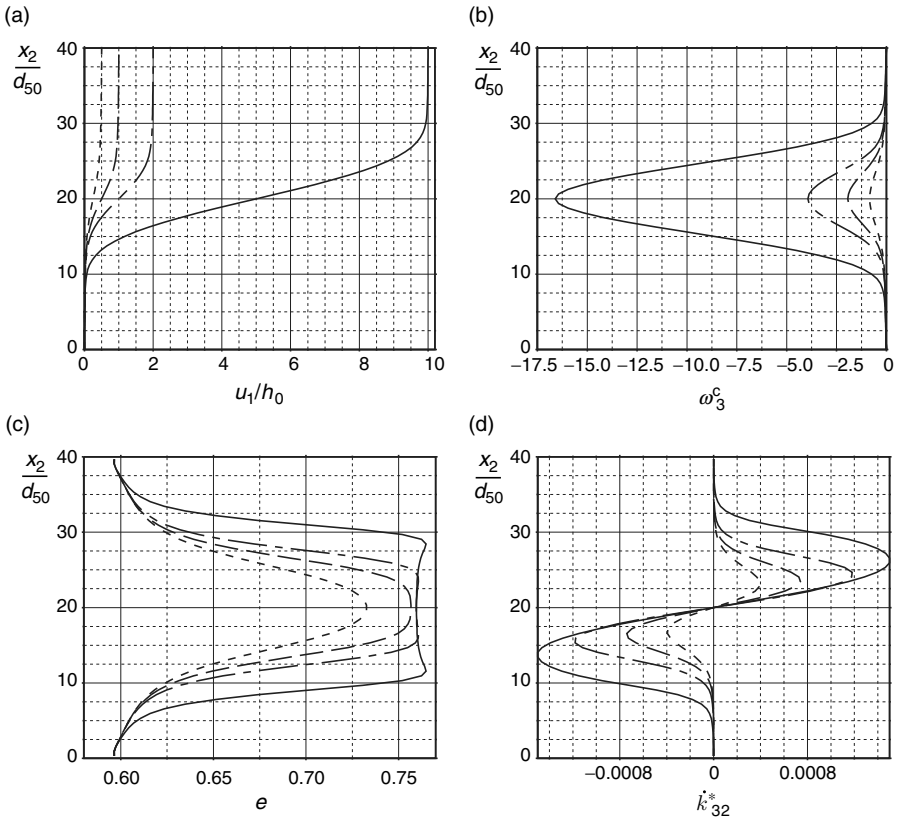

Fig. 2. Distribution of: (**a**) horizontal displacements, (**b**) Cosserat rotations, (**c**) void ratio and (**d**) rate of curvature for $u_{1\mathrm{T}} = 0.5$ *(short-dash curve)*, $u_{1\mathrm{T}} = 1.0$ *(dashed curve)*, $u_{1\mathrm{T}} = 2.0$ *(dot-dash curve)*, $u_{1\mathrm{T}} = 10.0$ *(solid curve)*

across the height of the layer. The shear stresses σ_{12} and σ_{21} are different, which means that the stress tensor is non-symmetric. It was also proved analytically by Bauer and Huang [4] that polar effects appear within the shear layer from the beginning of shearing even for the case of an initially isotropic stress state and initially zero couple stresses. For larger shearing a localization of the shear strain can be observed in the middle of the layer and leads to a displacement field with an S-shape (Fig. 2a). A similar behaviour was observed in experiments with sand specimens in a ring shear apparatus [8]. The Cosserat rotation and the rate of curvature are only significant within the localized zone (Fig. 2b,d) while the couple stress can also be pronounced outside the localized. The increase of the void ratio is experimentally evident and can be explained with the tendency of a dense granular materials to dilate under shearing. The boundaries of the localized zone are characterized

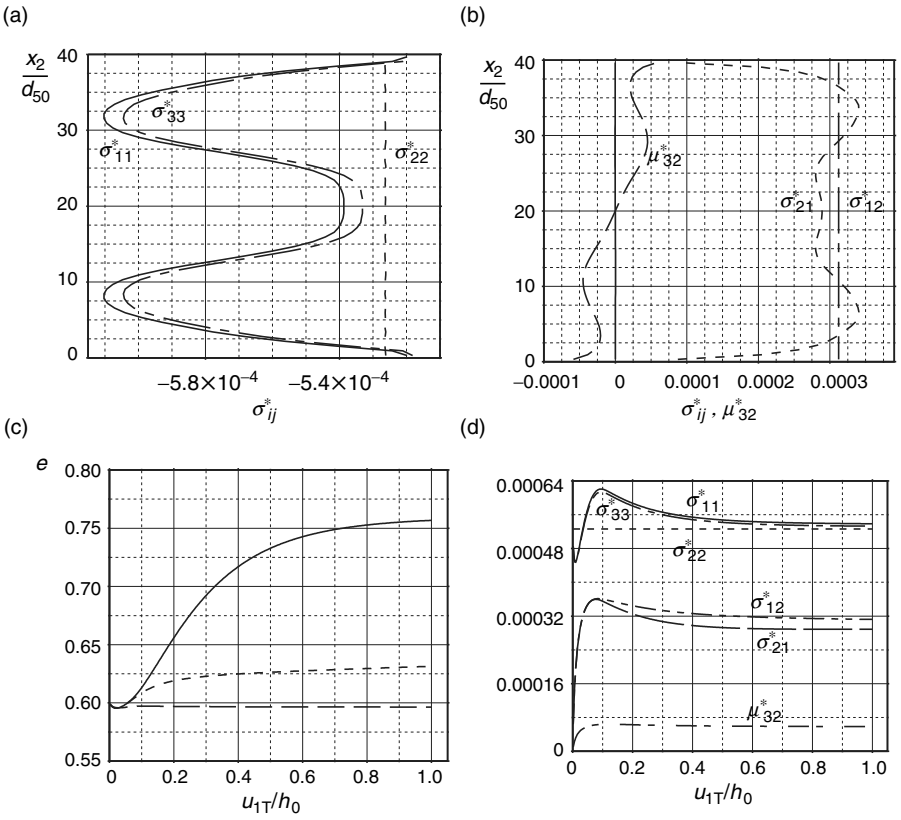

Fig. 3. Distribution of (**a**) stresses and (**b**) couple stresses across the height of the shear layer for $u_{1T}/h_0 = 1.0$. Evolution of (**c**)the void ratio in the middle of the layer, i.e. at $x_2/h_0 = 0.5$ *(solid curve)*, at $x_2/h_0 = 0.75$ *(short-dash curve)*, and at $x_2/h_0 = 1.0$ *(long-dash curve)* and (**d**) the stress components and couple stress in the middle of the layer

by high gradients of the void ratio and the rate of curvature (Fig. 2c,d). The extreme value of the Cosserat rotation occurs in the middle and it increases with an increase of shearing. With an increase of shearing the thickness of the localized zone increases as well. Thus, the thickness of the localized zone is not a material constant. In this context it should be noted that the tendency of the localized zone to increase or to decrease is influenced by the specification of the model. While the Cosserat rotation continuously increases (Fig. 2b), the increase of the void ratio (Fig. 2c) is limited. This is also shown in Fig. 3c for the evolution of the void ratio at $x_2/h = 0.5$. At the beginning of shearing the void ratio in the middle of the layer slightly decreases and then increases and tends towards a pressure dependent stationary value called critical void ratio. For large shearing the stress and couple stress components also lead to

stationary values (Fig. 3c) as it is required in the concept of critical state soil mechanics, which is embedded in the present hypoplastic model. By applying the definition of critical states, i.e. $\mathring{\sigma}_{ij} = 0, \mathring{\mu}_{ij} = 0$ and $\dot{e} = 0$, to the constitutive equations (1)–(3) the following relations for critical states can be derived (Huang 2000):

$$f_{\mathrm{d}} = \frac{\sqrt{||\dot{\boldsymbol{\varepsilon}}^{\mathrm{c}}||^2 + \lambda||\dot{\overline{\boldsymbol{\kappa}}}||^2}}{\sqrt{||\dot{\boldsymbol{\varepsilon}}^{\mathrm{c}}||^2 + ||\dot{\overline{\boldsymbol{\kappa}}}||^2}}, \tag{9}$$

$$||\hat{\boldsymbol{\sigma}}^{\mathrm{d}}|| = \frac{\hat{a}||\dot{\boldsymbol{\varepsilon}}^{\mathrm{c}}||}{\sqrt{||\dot{\boldsymbol{\varepsilon}}^{\mathrm{c}}||^2 + \lambda||\dot{\overline{\boldsymbol{\kappa}}}||^2}}, \quad ||\hat{\boldsymbol{\mu}}|| = \frac{\gamma||\dot{\overline{\boldsymbol{\kappa}}}||}{\sqrt{||\dot{\boldsymbol{\varepsilon}}^{\mathrm{c}}||^2 + \lambda||\dot{\overline{\boldsymbol{\kappa}}}||^2}}, \tag{10}$$

$$\left(\frac{||\hat{\boldsymbol{\sigma}}^{\mathrm{d}}||}{\hat{a}}\right)^2 + \left(\frac{||\hat{\boldsymbol{\mu}}||}{\lambda_2 a_{\mathrm{c}}}\right)^2 = 1 \tag{11}$$

with

$$\lambda = \frac{1}{\hat{a}(a_{\mathrm{c}} - \hat{a})}, \quad \gamma = \frac{1}{a_{\mathrm{c}} - \hat{a}}, \quad \lambda_2 = \sqrt{\frac{\hat{a}}{a_{\mathrm{c}} - \hat{a}}}.$$

It follows from (11) that the stress tensor and couple stress tensor in stationary states are coupled except for states with $\dot{\boldsymbol{\kappa}} = \mathbf{0}$. From Fig. 2d it follows that $\dot{\boldsymbol{\kappa}} = \mathbf{0}$ appears in the middle of the localized zone. Thus the relations in (9) and (10) reduce to $f_{\mathrm{d}} = 1$, and $||\hat{\boldsymbol{\sigma}}^{\mathrm{d}}|| = \hat{a}$, respectively. Herein a value of $f_{\mathrm{d}} = 1$ means that the void ratio is equal to the critical one, i.e. $e = e_{\mathrm{c}}$, as it is also obtained for the non-polar model [3]. However, for states in the neighborhood of the center of the localized zone $||\dot{\overline{\boldsymbol{\kappa}}}|| \neq 0$ and therefore $f_{\mathrm{d}} > 1$ or equivalently $e > e_{\mathrm{c}}$. In other words, for the present micro-polar model the void ratio in a stationary state can be greater than the value of the critical void ratio e_{c}, which can also be detected in Fig. 3c. In this context it can be noted that with the modified version by Huang et al. [15] the factor $f_{\mathrm{d}} = 1$ is fulfilled in critical states independent of the rate of curvature, so that the void ratio in the localized zone does not exceed the critical value.

3.2 Behaviour Under Cyclic Shearing

In order to investigate the behaviour under plane cyclic shearing calculations were performed with two different initial densities, i.e. an initially medium dense state with $e_0 = 0.6$ and an initially loose state with $e_0 = 0.9$, and two different shear amplitudes, i.e. $u_{1\mathrm{T}}/h_0 = \pm 1$ and $u_{1\mathrm{T}}/h_0 = \pm 0.01$. In all calculations an initial height of $h_0 = 20\,\mathrm{mm}$ and a constant vertical pressure is considered. The material is first compressed with the pressure $p = -500$ kPa, which is applied at the top of the layer, and then subjected to shearing in one direction up to an almost stationary stress state at $u_{1\mathrm{T}}/h_0 = -1$. Herein $u_{1\mathrm{T}}$ denotes the horizontal displacement of the top of the layer. Afterwards, the direction of shearing is repeatedly changed with a prescribed horizontal

displacement amplitude at the top. For more details about the numerical procedure used the reader is referred to Tejchman and Bauer [21].

The results obtained for an initial void ratio of $e_0 = 0.6$ ($e = 0.582$ after consolidation) and a shear amplitude of $u_{1\mathrm{T}}/h_0 = \pm 1$ are shown in Figs. 4–7. Figure 4 shows the evolution of normalized stress components $\sigma^*_{ij} = \sigma_{ij}/h_\mathrm{s}$ and the normalized couple stress $\mu^*_{32} = \mu_{32}/(h_\mathrm{s} d_{50})$ close to the middle of the layer against the normalized horizontal displacement of the top $\hat{u}_{1\mathrm{T}} = u_{1\mathrm{T}}/h$. At the beginning of shearing the amounts of the stresses increase and reach a peak value within a small horizontal shear deformation with the exception of the vertical stress σ_{22}, which is prescribed to be constant. After the peak the amounts of the shear stresses and the couple stress decrease and tend towards a stationary value for larger shearing. During reversal shearing the shear stresses and the couple stress change their sign and reach a stationary value again. The stress–displacement curves are closed where the extreme values of the stresses decrease with the number of cycles. In this context, it can be noted that the amount of the pronounced stress peak during the first loading is not reached again when cyclic shearing is continued. The normal stresses remain almost constant except right after changes of the shear direction (Fig. 4c,e).

With the exception of the horizontal shear stress σ_{12} and the vertical stress σ_{22} the stresses and the couple stress are distributed in a non-linear way across the height of the shear layer as shown in Fig. 5a for a state after the first shearing and in Fig. 5b for a state after six full shear cycles. Only the shear stress σ_{12} and the vertical stress σ_{22} are independent of the vertical coordinate x_2, which results from the requirement of equilibrium. A comparison of the state quantities after the first shearing (Fig. 5a,c,e) with those after six full shear cycles (Fig. 5b,d,f) qualitatively shows a similar distribution but quantitatively a significant increase of the width of the localized zone. In particular, the thickness of the shear zone is about 14 times the mean grain diameter d_{50} after the initial shearing and it is 18 times d_{50} after six full shear cycles. Thus, the thickness of the shear band is not a material constant and in the case of an initially dense specimen it increases with the number of cycles. The numerical investigations show that the growth in thickness is almost finished within the first three cycles.

A section of the deformed shear layer is shown for different states in Fig. 6. At the end of each shear motion (Fig. 6b,d,e) the displacement field shows an S-shape similar to the one obtained for a monotonic shearing. However, when the top plate returns to the initial position, i.e. $u_{1T} = 0$ (Fig. 6c), the horizontal displacements shows a zig-zag distribution across the height of the localized zone. Thus the memory of the preceding shearing is not completely swept out in this state. A comparison of Fig. 6b with Fig. (6e) indicates that the thickness of the localized zone grows with the number of cycles. In particular the thickness is about $14 * d_{50}$ after the initial shearing and $18 * d_{50}$ after six full shear cycles.

Figure 7 shows the evolution of the void ratio in four elements along the height of the layer from the bottom ($x_2/h_0 = 0.03$) up to the symmetry plane

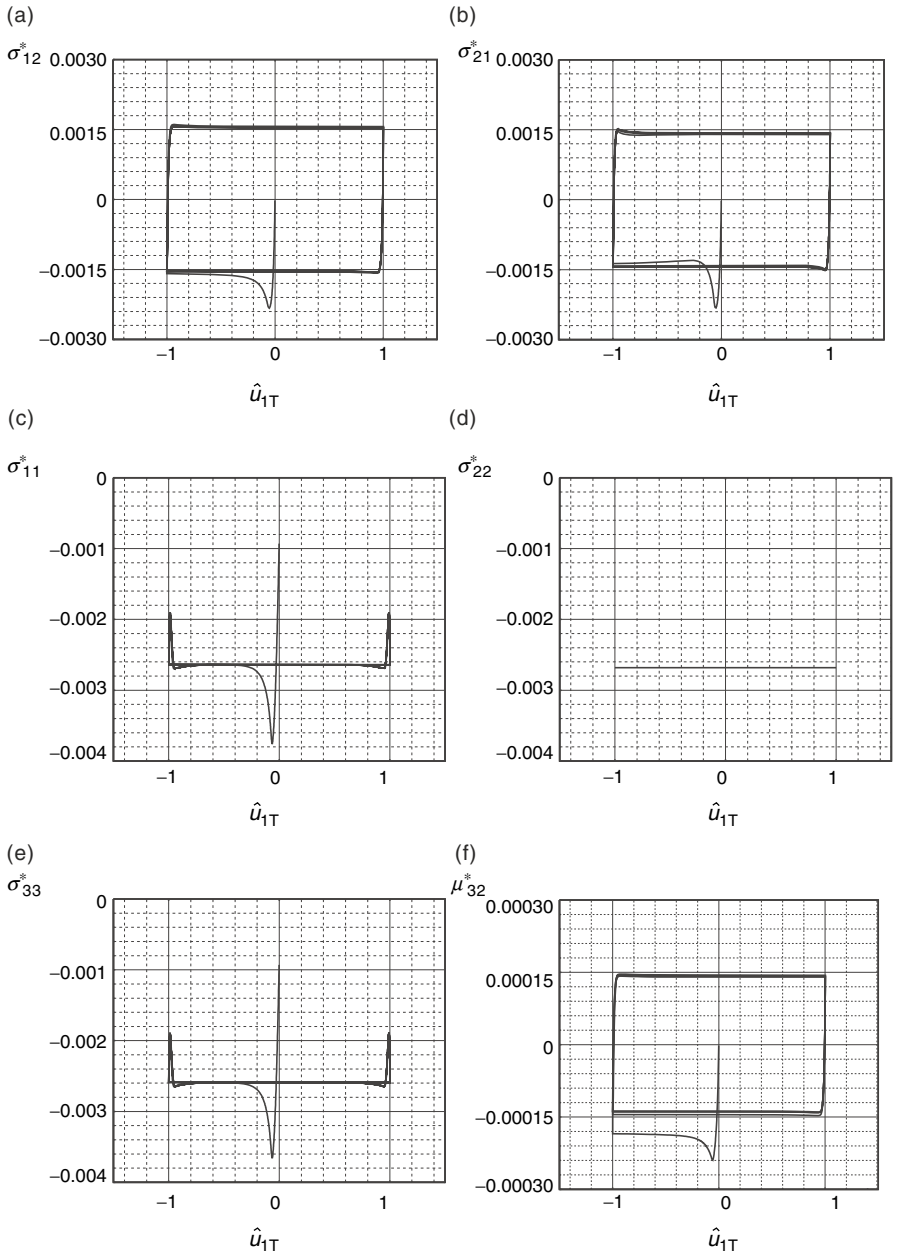

Fig. 4. Evolution of the normalized stress components σ^*_{ij} and the normalized couple stress μ^*_{32} against the normalized shear displacement $\hat{u}_{1T}$ close to the middle of the shear layer

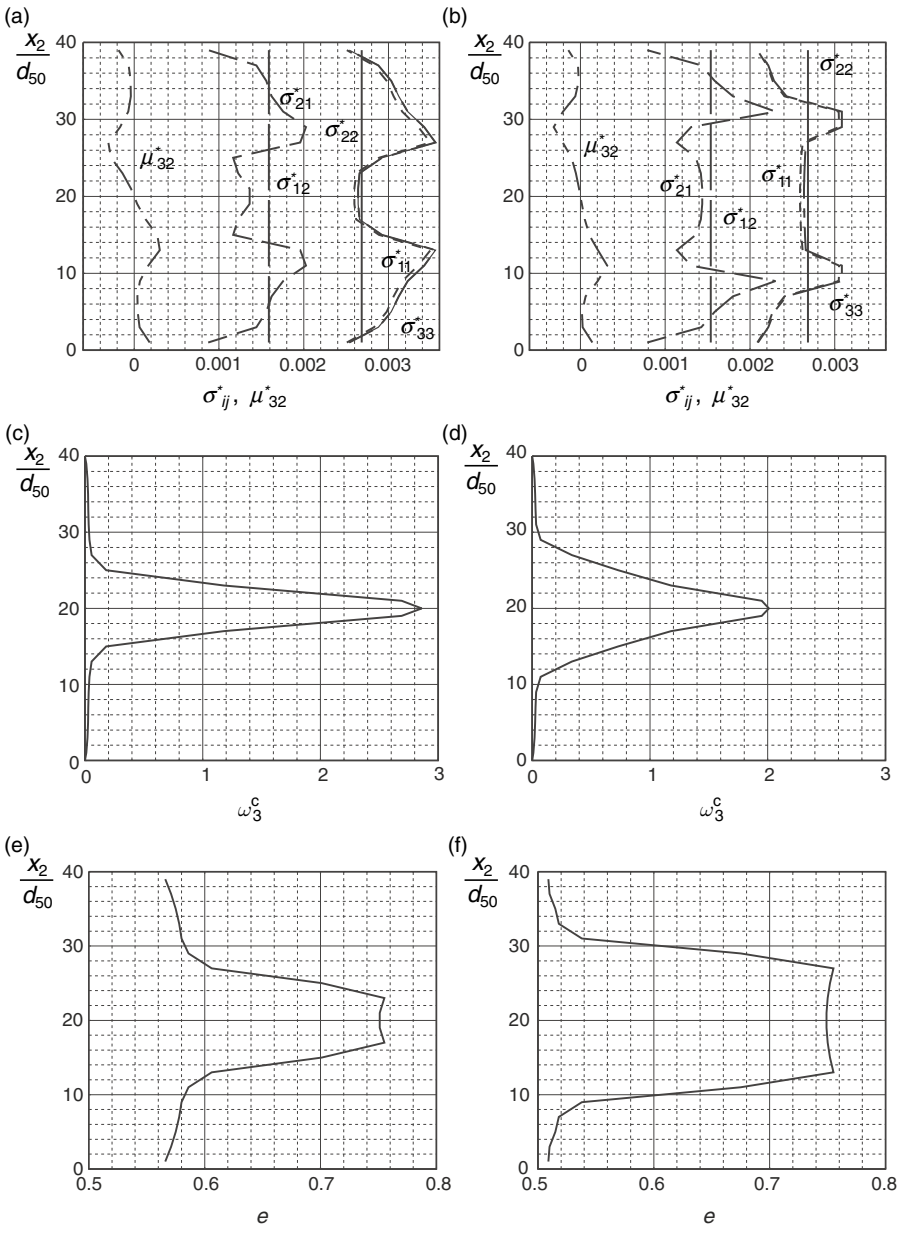

Fig. 5. Initially medium dense state ($e_0 = 0.6$): distribution of the stresses σ^*_{ij}, couple stress μ^*_{32}, Cosserat rotation ω^c_3 and void ratio e across the height of the shear layer: (**a**),(**c**),(**e**) after the first shearing and (**b**),(**d**),(**f**) after six shear cycles

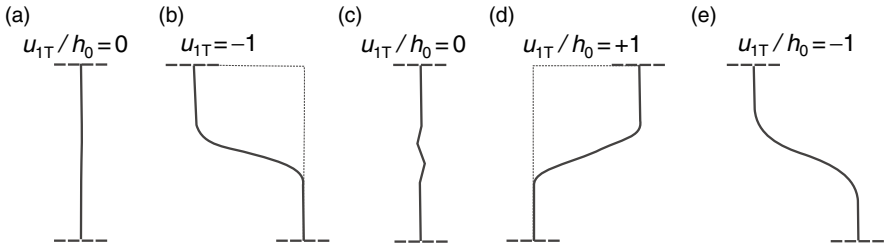

Fig. 6. Section of a plane infinite layer subjected to cyclic shearing. Deformed finite element mesh: (**a**) initial state, (**b**) after the first shearing, (**c**) in the reversed initial state, (**d**) after the first full reversed shearing, (**e**) after the sixth shear cycle

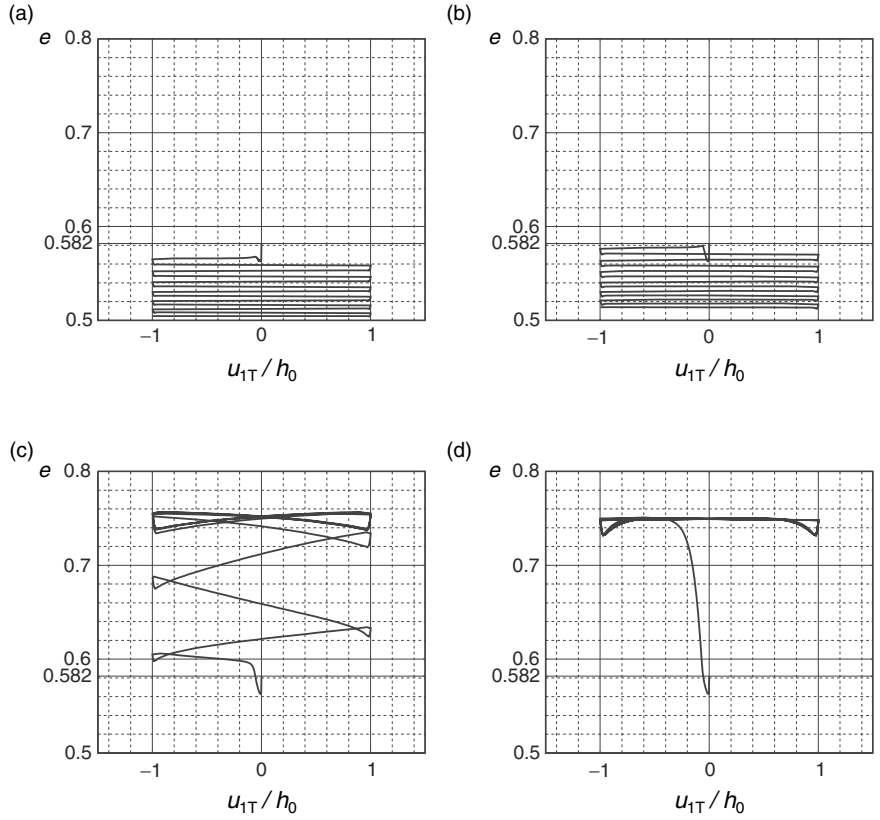

Fig. 7. Cyclic shearing for $e_0 = 0.6$ and $u_{1T}/h_0 = \pm 1$. Evolution of e in the shear layer at: (**a**) $x_2/h_0 = 0.03$, (**b**) $x_2/h_0 = 0.2$, (**c**) $x_2/h_0 = 0.3$ and (d) $x_2/h_0 = 0.5$

in the middle of the layer ($x_2/h_0 = 0.5$) versus the shear displacement u_{1T}/h_0 at the top. It is clearly visible that close to the boundaries of the shear layer the void ratio decreases with the number of cycles (Fig. 7a,b). Within the localized zone (Fig. 7c,d) the void ratio slightly decreases right after a change of the shear direction but then strongly increases as a result of dilatancy. After several cycles a closed stationary loop round the so-called critical void ratio is reached. Although the local change of the void ratio is significant, the mean value across the height of the shear layer is less pronounced. In particular the mean value after the first shearing is $\overline{e} = 0.63$ and the mean value after six shear cycles is $\overline{e} = 0.633$. Therefore the mean value of the void ratio is not a relevant quantity to represent the dilatancy in the localized zone when the shear layer is higher than the shear band thickness. This may be of importance for the evaluation of experiments and the calibration of constitutive models.

The results obtained for an initially loose state, i.e. for an initial void ratio of $e_0 = 0.9$ ($e = 0.837$ after consolidation), and a shear amplitude of $u_{1T}/h_0 = \pm 1$ are shown in Fig. 8. The void ratio globally decreases and

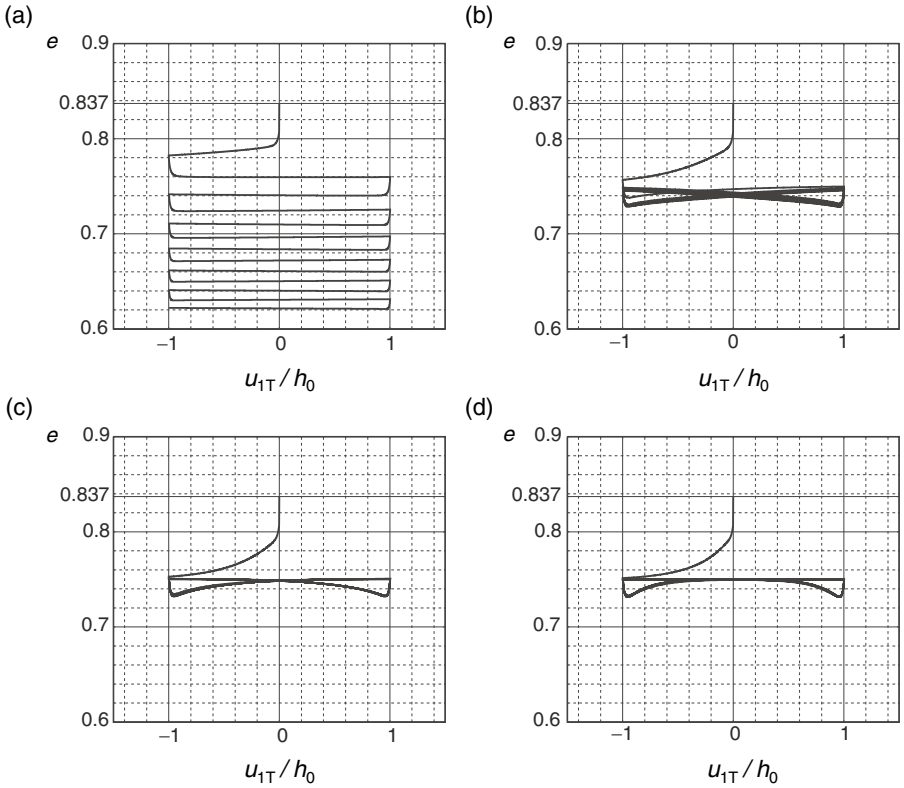

Fig. 8. Cyclic shearing for $e_0 = 0.9$ and $u_{1T}/h_0 = \pm 1$. Evolution of e in the shear layer at: (**a**) $x_2/h_0 = 0.03$, (**b**) $x_2/h_0 = 0.2$, (**c**) $x_2/h_0 = 0.3$ and (**d**) $x_2/h_0 = 0.5$

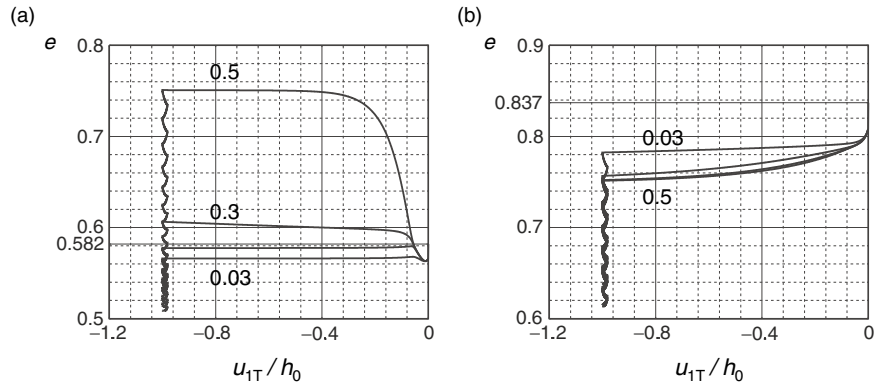

Fig. 9. Cyclic shearing for $u_{1T}/h_0 = \pm 0.01$ and (**a**) $e_0 = 0.6$, (**b**) $e_0 = 0.9$. Evolution of e in the shear layer at $x_2/h_0 = 0.03, 0.2, 0.3, 0.5$

that the contractancy is most pronounced in the first shearings. Close to the boundaries of the layer the compaction increases (Fig. 8a) with the number of cycles while in the middle the the compaction is limited (Fig. 8d). Although a small compaction also takes place at the beginning of each reversal shearing, it again disappears due to dilatancy with advanced shearing, i.e the void ratio in the middle of the layer tends towards the pressure-dependent critical value of $e_c \approx 0.75$. A comparison of Fig. 7d with Fig. 8d shows that the critical void ratio is independent of the initial void ratio as it is assumed in the concept of critical state soil mechanics.

Further investigations by Tejchman and Bauer [21] indicate that the question as to whether the mean value of the void ratio across the shear layer increases or decreases strongly depends on the magnitude of the shear amplitude. After an initial shearing of $u_{1T}/h_0 = -1$ the behaviour under a small shear amplitude of $u_{1T}/h_0 = \pm 0.01$ is demonstrated in Fig. 9a for $e_0 = 0.6$ and in Fig. 9b for $e_0 = 0.9$. Independently of the initial void ratio the material only behaves in a contractant way and with an increasing number of cycles the void ratio tends towards the pressure dependent minimum value. Thus for very small cyclic shear amplitudes the material becomes generally denser, while for larger shear amplitudes and an initially dense state the void ratio may increase.

4 Conclusions

Monotonic and cyclic shearing of an infinite granular layer located between two parallel plates was investigated using a micro-polar hypoplastic continuum approach. In contrast to a non-polar continuum the distribution of the state quantities across the height of the layer for a micro-polar hypoplastic continuum becomes nonlinear from the beginning of shearing. For larger shearing

the deformation is localized in the middle of the shear layer. As a result of dilatancy the void ratio increases and it tends towards the critical value. If the shear layer is higher than the thickness of the localized zone, the material becomes denser outside the localized zone, i.e. beyond the localized shear zone, the void ratio decreases in the granular layer with each shear cycle. The thickness of the localized zone is not a material constant. With an increase of the number of shear cycle, the thickness of the shear zone increases. It should be noted that a direct comparison of the numerical results with experiments is still outstanding because in experiments only the global volume change of the specimen is usually recorded. The experimental measuring of local volume changes is very expensive and relevant data are thus a rarity. Cyclic shearing locally leads to significant volume changes within the shear layer depending on the initial density and the magnitude of the shear amplitude. For very small cyclic shear amplitudes the material becomes generally denser, while for larger shear amplitudes and an initially dense state the void ratio may increase.

References

1. Bauer E. (1995)Constitutive modelling of critical states in hypoplasticity. In: G.N. Pande and S. Pietruszczak (eds) Proc. 5th Int. Symp. on Numerical Models in Geomechanics. Balkema
2. Bauer, E. (1996) Soils Found. 36(1): 13–26
3. Bauer, E. (2000) Mech. Cohes-Frict. Mater. 5(2): 125–148
4. Bauer, E. and Huang, W. (1999) Numerical study of polar effects in shear zone In: G.N. Pande, S. Pietruszczak and H. Schweiger (eds) Proc. 7th Int. Symp. on Numerical Models and Geomechanics. Balkema
5. Bauer, E. and Huang, W. (2001) Evolution of polar quntities in a granular Cosserat material under shearing. In: H.-B. Mühlhaus, A.V. Dyskin and E. Pasternak (eds) Proc. Int. Workshop on Bifurcation and Localization Theory in Geomechanics. Balkema
6. Bauer, E. and Huang, W. (2004) Sci. Eng. Compos Mater 11(4):239–246
7. Eringen, C. (1976) Polar and nonlocal field theories. In: Continuum Physics vol. IV. Academic, New York, San Francisco, London
8. Garga, V.K. and Infante Sedano, J.A. (2002) Geot. Testing J. 25(4): 414–421
9. Gudehus, G. (1996) Soils Found. 36(1): 1–12
10. Gudehus, G. (1998) Shear localization in simple grain skeleton with polar effect. In: T. Adachi, F. Oka and A. Yashima (eds) Proc. 4th Int. Workshop on Localization and Bifurcation Theory for Soils and Rocks. Balkema
11. Gudehus, G. and Nübel, K. (2004) Géotechnique 54(3): 187–201
12. Herle, I. and Gudehus, G. (1999) Mech. Cohes-Frict. Mater 4: 461–486
13. Huang, W. (2000) Hypoplastic modelling of shear localisation in granular materials. Doctoral Thesis, Graz University of Technology, Austria
14. Huang, W. and Bauer, E. (2003) Int. J. Numer. Anal. Meth. Geomech. 27: 325–352
15. Huang, W., Nübel, K., Bauer, E. (2002) Mech Mater 34: 563–576

16. Huang, W., Bauer, E., and Sloan, S. (2003) Struct. Eng. Mech. 15(3): 315–329
17. Kolymbas, D. (1991) Arch. Appl. Mech. 61: 143–151
18. Tejchman, J. (1997) Modelling of shear localisation and autogeneous dynamic effects in granular bodies. In: Veröffentlichungen des Institutes für Bodenmechanik und Felsmechanik der Universität Fridericiana in Karlsruhe, Heft 140
19. Tejchman, J. (2002) Acta Mech 155(1–2): 71–95
20. Tejchman, J. (2004) Comput Geotech 31(8): 595–611
21. Tejchman, J. and Bauer, E. (2004) Granul. Matter 5: 201–212
22. Tejchman, J. and Gudehus, G. (2001) Int. J. Numer. Methods Geomech. 25: 1–28

Modeling the Post-localization Regime with Local Second Gradient Models: Non-uniqueness of Solutions and Non-persistent Shear Bands

P. Bésuelle* and R. Chambon†

*Laboratoire 3S (Sols, Solides, Structures), UJF/INPG/CNRS, Grenoble, France
pierre.besuelle@hmg.inpg.fr
†Laboratoire 3S, Grenoble, France
Rene.Chambon@hmg.inpg.fr

1 Introduction

The strain localization is a classical mode of failure of geomaterials. Numerical simulations of this phenomena need a specific approach to overcome the practical problem of mesh size dependence. Several technics have been developed recently, among others, models with internal length like nonlocal models (e.g., [17]) or second gradient models (e.g., [16, 20]). Then, one restores an objectivity of computations and it becomes significant to study the postlocalization regime.

A preliminary question is the representability of such computations. What is the validity which can be given to a simulation or, in other terms, is a solution of a limit conditions problem unique, and if not, is it possible to quantify the variation between solutions? The aim of this paper is to explore this question. We use the framework of local second gradient models [6, 14]. The constitutive law (the classical part) is an elasto-plastic model initially developed for a rock [13]. We will study some key points as the onset of localization, pattern and orientation of deformation bands.

Afterward, we will explore by a simple constitutive parametric study, the kind of postlocalization responses which can be obtained, depending on the characteristics of the model used: strain hardening or strain softening. We will compare these preliminary results with some experimental observations of geomaterial behavior, and more precisely make a parallel with the brittle regime and brittle–ductile regime of failure that is observed when the mean stress level change.[1]

[1] In the following, the usual sign convention of mechanics (compression negative) is adopted throughout.

2 Local Second Gradient Model

Local second gradient models belong to a particular subclasses of models with microstructure which descend from pioneer works of [8, 12, 15, 19]. They use an enriched kinematic description of the continuum, with respect to classical continua. In addition to the displacement field u_i, a second-order tensor, the so-called microkinematic gradient v_{ij}, is introduced. Particular subclasses of enriched models introduce a constrain on the microkinematic field. For example, Cosserat models can be viewed as a microstructured model for which the microstrain is vanishing, i.e., the symmetric part of the tensor v_{ij} is zero. In the same spirit, (local) second gradient models assume that the microkinetic gradient is equal to the displacement gradient

$$v_{ij} = \partial u_i / \partial x_j, \tag{1}$$

where x_j is the spatial coordinate. Such models have been developed recently for geomaterials [5, 6, 14] and metals [10].

For local second gradient models, the virtual work principle can be summarized as follow, [12]: for every virtual displacement field u_i^* kinematically admissible

$$\int_\Omega \left(\sigma_{ij} \varepsilon_{ij}^* + \Sigma_{ijk} \frac{\partial^2 u_i^*}{\partial x_j \, \partial x_k} \right) \mathrm{d}v = \int_\Omega G_i u_i^* \, \mathrm{d}v + \int_{\partial\Omega} \left(t_i u_i^* + T_{ij} \frac{\partial u_i^*}{\partial x_j} \right) \mathrm{d}s, \tag{2}$$

where σ_{ij} is the Cauchy stress, ε_{ij}^* is the virtual macro strain, Σ_{ijk} is the dual static variable associated to the second gradient of the virtual displacement, so called *double stress*. G_i is the body force by unit volume, t_i is the traction force by unit surface and T_{ij} is the double force by unit surface. More conveniently, the virtual work of external forces can be rewritten using the normal derivative $\mathrm{D}u_i = n_k \partial u_i / \partial x_k$ on the boundary (here, assumed to be regular)

$$\int_\Omega \left(\sigma_{ij} \varepsilon_{ij}^* + \Sigma_{ijk} \frac{\partial^2 u_i^*}{\partial x_j \partial x_k} \right) \mathrm{d}v = \int_\Omega G_i u_i^* \, \mathrm{d}v + \int_{\partial\Omega} (p_i u_i^* + P_i \mathrm{D}u_i^*) \, \mathrm{d}s, \tag{3}$$

where p_i and P_i are two independent variables which can be prescribed on the boundary.

For such a class of models, the balance equations and boundaries conditions yield:

$$\frac{\partial \sigma_{ij}}{\partial x_j} - \frac{\partial^2 \Sigma_{ijk}}{\partial x_j \, \partial x_k} + G_i = 0, \tag{4}$$

$$\sigma_{ij} n_j - n_k n_j \mathrm{D}\Sigma_{ijk} - \frac{\mathrm{D}\Sigma_{ijk}}{\mathrm{D}x_k} n_j - \frac{\mathrm{D}\Sigma_{ijk}}{\mathrm{D}x_j} n_k + \frac{\mathrm{D}n_l}{\mathrm{D}x_l} \Sigma_{ijk} n_j n_k - \frac{\mathrm{D}n_j}{\mathrm{D}x_k} \Sigma_{ijk} = p_i, \tag{5}$$

$$\Sigma_{ijk} n_j n_k = P_i, \tag{6}$$

where $\mathrm{D}q/\mathrm{D}x_j$ denotes the tangential derivatives of any quantity q:

$$\frac{\mathrm{D}q}{\mathrm{D}x_j} = \frac{\partial q}{\partial x_j} - n_j \mathrm{D}q. \tag{7}$$

More details on the theoretical aspects can be found in [6]. The numerical treatments and the development of a finite element for this kind of model is detailed in [14]. The element has been implemented in the F.E.M. code *Lagamine*, initially developed in Liège, Belgium. It has been chosen to write the constitutive relation in two independent parts. A classical part links the strain rate to the rate of deformation, it is decoupled from the second gradient part which links the double stress rate to the rate of second gradient of displacement. The classical relation is detailed in Sect. 3. The second gradient part has been chosen as simple as possible, i.e., a linear elastic isotropic relation with only one parameter:

$$\begin{bmatrix} \overset{\nabla}{\Sigma}_{111} \\ \overset{\nabla}{\Sigma}_{112} \\ \overset{\nabla}{\Sigma}_{121} \\ \overset{\nabla}{\Sigma}_{122} \\ \overset{\nabla}{\Sigma}_{211} \\ \overset{\nabla}{\Sigma}_{212} \\ \overset{\nabla}{\Sigma}_{221} \\ \overset{\nabla}{\Sigma}_{222} \end{bmatrix} = \begin{bmatrix} D & 0 & 0 & 0 & 0 & D/2 & D/2 & 0 \\ 0 & D/2 & D/2 & 0 & -D/2 & 0 & 0 & D/2 \\ 0 & D/2 & D/2 & 0 & -D/2 & 0 & 0 & D/2 \\ 0 & 0 & 0 & D & 0 & -D/2 & -D/2 & 0 \\ 0 & -D/2 & -D/2 & 0 & D & 0 & 0 & 0 \\ D/2 & 0 & 0 & -D/2 & 0 & D/2 & D/2 & 0 \\ D/2 & 0 & 0 & -D/2 & 0 & D/2 & D/2 & 0 \\ 0 & D/2 & D/2 & 0 & 0 & 0 & 0 & D \end{bmatrix} \begin{bmatrix} \frac{\partial \dot{v}_{11}}{\partial x_1} \\ \frac{\partial \dot{v}_{11}}{\partial x_2} \\ \frac{\partial \dot{v}_{12}}{\partial x_1} \\ \frac{\partial \dot{v}_{12}}{\partial x_2} \\ \frac{\partial \dot{v}_{21}}{\partial x_1} \\ \frac{\partial \dot{v}_{21}}{\partial x_2} \\ \frac{\partial \dot{v}_{22}}{\partial x_1} \\ \frac{\partial \dot{v}_{22}}{\partial x_2} \end{bmatrix}, \tag{8}$$

where $\dot{v}_{ij}$ is the material time derivative of v_{ij} and $\overset{\nabla}{\Sigma}_{ijk}$ is the Jaumann double stress rate.

3 Constitutive Law

The classical part of the law used in this work is an elasto-plastic law inspired from the model published by Holcomb and Rudnicki [13] for a rock (Tennessee marble), itself issues from the constitutive framework of Rudnicki and Rice [18]. The law has been simplified a little bit in order to reduce the number of parameters, in particular, we assume a vanishing cohesion because we believe that it has not a qualitative influence for the aim of this study.

It is a nonassociated model where the yield surface and the plastic potential are smooth, depending on the first and second stress invariants, and linear with respect the first one (Drucker-Prager type surfaces). The surfaces can evolve with the accumulated plastic shear strain.

We define, from the Cauchy stress σ_{ij}, the equivalent shear stress $\overline{\tau}$ as:

$$\overline{\tau} = \sqrt{(1/2) s_{ij}\, s_{ij}}, \tag{9}$$

where the repeated subscript implies the summation and where $s_{ij} = \sigma_{ij} - \sigma\, \delta_{ij}$ is the deviatoric stress, δ_{ij} being the Kronecker delta, and $\sigma = 1/3\ \mathrm{tr}(\sigma_{ij})$ the mean stress. The accumulated plastic shear strain is defined as:

$$\overline{\gamma}^{p} = \int \sqrt{2 \mathrm{d}e^{\mathrm{p}}_{ij} \mathrm{d}e^{\mathrm{p}}_{ij}}, \tag{10}$$

where $\mathrm{d}e^{\mathrm{p}}_{ij} = \mathrm{d}\varepsilon^{\mathrm{p}}_{ij} - 1/3\ \mathrm{d}e^{\mathrm{p}} \delta_{ij}$ is the deviatoric part of the plastic strain increment and $\mathrm{d}e^{\mathrm{p}} = \mathrm{tr}(\mathrm{d}\varepsilon_{ij})$ is the plastic volumic strain increment.

The yield surface is defined by

$$F = \overline{\tau} + \sigma \mu(\overline{\gamma}^{\mathrm{p}}), \tag{11}$$

μ is a friction coefficient function of the accumulated plastic shear strain.

The consistency condition implies that

$$\mathrm{d}F = \mathrm{d}\overline{\tau} + \mu \mathrm{d}\sigma - H \mathrm{d}\overline{\gamma}^{\mathrm{p}} = 0, \tag{12}$$

where $H = -\sigma . \partial\mu / \partial\overline{\gamma}^{\mathrm{p}}$ is a hardening parameter, positive for a strain hardening and negative for a strain softening. This relation can also be wrote as:

$$\mathrm{d}\overline{\gamma}^{\mathrm{p}} = \frac{1}{H} \left(\frac{s_{ij}}{2\overline{\tau}} + \frac{1}{3} \mu\ \delta_{ij} \right)\ \mathrm{d}\sigma_{ij}. \tag{13}$$

The plastic potential is defined as:

$$G = \overline{\tau} + \sigma \beta(\overline{\gamma}^{\mathrm{p}}), \tag{14}$$

β is a dilatancy coefficient function of the accumulated plastic shear strain. The flow rule can be expressed as:

$$\mathrm{d}\varepsilon^{\mathrm{p}}_{ij} = \mathrm{d}\lambda \frac{\partial G}{\partial \sigma_{ij}}, \tag{15}$$

where $\mathrm{d}\lambda$ is a positive term, which in fact, due to the expression of $\overline{\gamma}^{\mathrm{p}}$ in (10) is equal to $\mathrm{d}\overline{\gamma}^{\mathrm{p}}$. So, the plastic strain can be expressed as:

$$\mathrm{d}\varepsilon^{\mathrm{p}}_{ij} = \frac{1}{H} \left(\frac{s_{ij}}{2\overline{\tau}} + \frac{1}{3} \beta \delta_{ij} \right) \left(\frac{s_{kl}}{2\overline{\tau}} + \frac{1}{3} \mu \delta_{kl} \right)\ \mathrm{d}\sigma_{kl} \tag{16}$$

and also decomposed in two parts:

$$\begin{cases} \mathrm{d}e^{\mathrm{p}}_{ij} = \frac{1}{2}\ \frac{s_{ij}}{\overline{\tau}} \mathrm{d}\overline{\gamma}^{\mathrm{p}} \\ \mathrm{d}e^{\mathrm{p}}\ = \beta \mathrm{d}\overline{\gamma}^{\mathrm{p}}. \end{cases} \tag{17}$$

The functions μ and β are defined by:

$$\mu(\overline{\gamma}^{\mathrm{p}}) = (h_0 - h_\infty)\gamma_0 \ \mathrm{atan}\,(\overline{\gamma}^{\mathrm{p}}/\gamma_0) + h_\infty\,\overline{\gamma}^{\mathrm{p}}, \tag{18}$$

$$\beta(\overline{\gamma}^{\mathrm{p}}) = \beta_\infty - \frac{\beta_\infty - \beta_0}{1 + (\overline{\gamma}^{\mathrm{p}}/c_0)^2}, \tag{19}$$

such that $H(\overline{\gamma}^{\mathrm{p}} = 0) = -h_0\sigma$, $H(\overline{\gamma}^{\mathrm{p}} = \infty) = -h_\infty\sigma$, $\beta(\overline{\gamma}^{\mathrm{p}} = 0) = \beta_0$ and $\beta(\overline{\gamma}^{\mathrm{p}} = \infty) = \beta_\infty$. γ_0 and c_0 are constitutive parameters. h_0 is (generally) positive in order to have a strain hardening at the beginning of the loading, but h_∞ can be either positive to have a law which is always hardening, or negative to have a softening regime. Illustration of the constitutive relation is given in Fig. 1.

The elastic part of the law is assumed to be linear and isotropic and can be written as:

$$\mathrm{d}\sigma_{ij} = [G(\delta_{ik}\delta_{jl} + \delta_{il}\delta_{jk}) + (K - 2/3G)\delta_{ij}\delta_{kl}]\ \mathrm{d}\varepsilon^{\mathrm{e}}_{kl}, \tag{20}$$

where superscript "e" denotes the elastic part of the strain and K and G are the bulk modulus and the shear modulus, respectively. That can be decomposed in two parts:

$$\begin{cases} \mathrm{d}s_{ij} = 2G\mathrm{d}e^{\mathrm{e}}_{ij} \\ \mathrm{d}\sigma \ \ = K\mathrm{d}e^{\mathrm{e}}. \end{cases} \tag{21}$$

And finally, we have assumed as usual that the total strain is the sum of the plastic strain and the elastic strain: $\mathrm{d}\varepsilon_{ij} = \mathrm{d}\varepsilon^{\mathrm{p}}_{ij} + \mathrm{d}\varepsilon^{\mathrm{e}}_{ij}$.

The law has been implemented in the finite element code *Lagamine* by an implicit backward Euler method and subtime increments. We used the Jaumann rate of the Cauchy stress tensor to compute the stress increment during a time step.

For the following computations, we have adopted the parameters given in Table 1. They do not correspond to a specific material but seem reasonable.

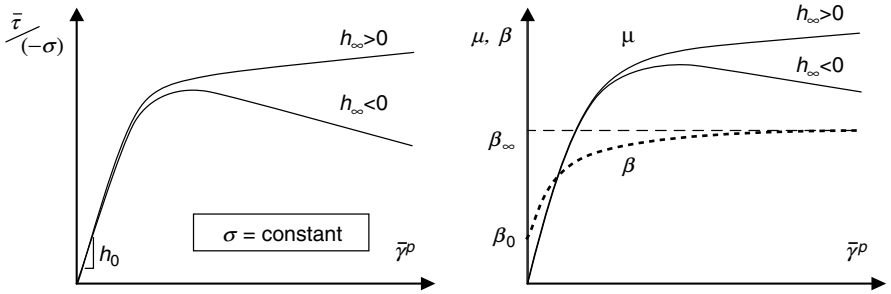

Fig. 1. Schematic illustration of the response of the law for a constant mean stress case (*left*) and illustration of the nonassociated aspect of the law: $\mu \neq \beta$ (*right*)

Table 1. Values of the constitutive parameters of the classical part of the law

parameter	value	unit
G	23.1	GPa
K	50	GPa
h_0	1,000	
h_∞	-30 or $+5$	
γ_0	5×10^{-4}	
β_0	0.01	
β_∞	0.4	
c_0	5×10^{-4}	

4 Nonunicity of Solutions

4.1 Theoretical Analysis

We focus here on the loss of uniqueness of solutions by emergence of solutions with strain localization, i.e., deformation bands. The bifurcation theory which consists to exhibit conditions for existence of a deformation band (e.g., [2,18]) can be extended to local second gradient models. It appears that bifurcation condition for such models, at least when classical law and second gradient law are decoupled, is the same than for classical models but it introduces in addition a size effect [4].

The classical law used here is a bilinear rate law, and, assuming a small strain hypothesis, the bifurcation condition can be expressed as [5]:

$$\det(K_{ijkl}\ n_j\ n_k) \leq 0, \tag{22}$$

where K_{ijkl} is the constitutive tensor which links the stress rate to the rate of deformation (for simplicity, we neglect the additional terms introduced by the Jaumann rate), and n_i is a unit normal vector to the incipient deformation band.

As there is a continuous evolution of the stiffness modulus during the accumulation of plastic strain in the model used here, the first possibility to satisfy the previous criterium corresponds to a vanishing determinant. However, the full domain where the bifurcation condition is satisfied corresponds to a negative determinant. In consequence, the orientation of the deformation band can be nonunique but belongs to a limited fan of orientations. If we call θ the angle between the normal vector to the band and the most compressive principal stress, and θ_c the critical orientation corresponding to the minimum of $\det(K_{ijkl}\ n_j\ n_k)$, then if $\det(K_{ijkl}\ n_j(\theta_\mathrm{c})\ n_k(\theta_\mathrm{c})) < 0$, there exist two ranges on each side of θ_c for which $\det(K_{ijkl}\ n_j(\theta)\ n_k(\theta)) \leq 0$.

Unlike the classical models, local second gradient models introduce an internal length. In the bifurcation theory, one searches solutions for which the additional rate of deformation inside the incipient band has the form $\Delta\dot{\varepsilon}_{ij} = (g_i n_j + g_j n_i)/2$ where g_i is an arbitrary vector which gives the kinematic

inside the band. Due to the second gradient law, this vector has an harmonic form $g_i(\alpha) = g_i^0 \sin(\alpha/\xi)$, where α is the position across the band and ξ is a specific length [4]. The latter depends on the modulus of the constitutive law and can be viewed as an indicator of the band thickness. It appears that when $\det(K_{ijkl}\ n_j(\theta)\ n_k(\theta)) = 0$, the band has an infinite thickness, and a finite thickness if the determinant is strictly negative. In consequence, theoretically, the bifurcation onset for local second gradient models is not different from one for the underlying classical models. However, there is a size effect which delays the onset of localization.

We illustrate these results on a plane strain compression path in Fig. 2. In direction 3, a stress of 10^6 Pa is imposed, the direction 2 corresponds to the plane strain direction and direction 1 to the direction of compression. Two cases are illustrated, on the left, the case $h_\infty = -30$ which means a softening regime after an initial hardening regime, and on the right, the case $h_\infty = +5$ which means a law exhibiting always strain hardening. Due to the nonassociated aspect of the law, the first onset where the bifurcation condition (22) is satisfied, is in the hardening regime (indicated by a star in Fig. 2a, c).

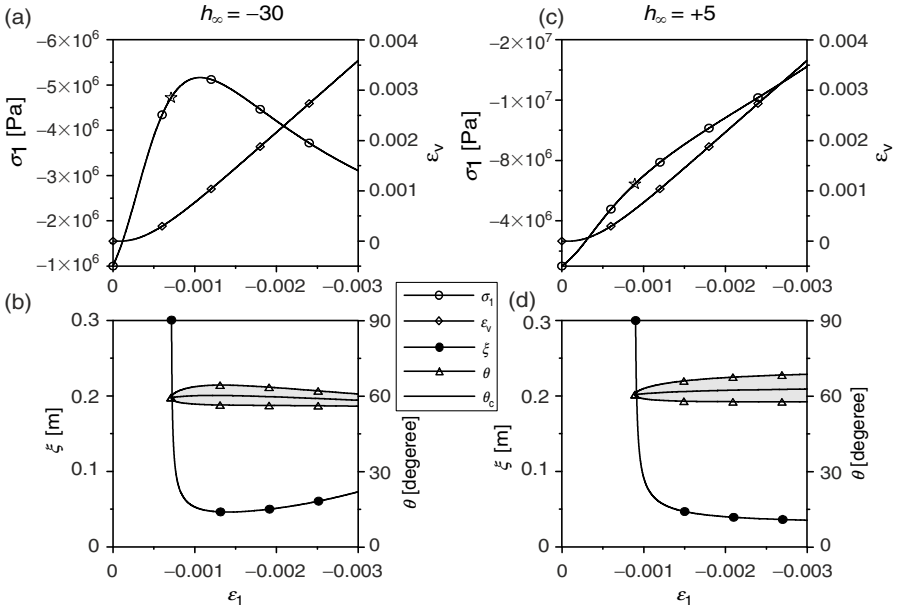

Fig. 2. Response of the law for a plane strain compression loading path (small strain assumption) with a softening regime, $h_\infty = -30$ (**a**), and no softening regime, $h_\infty = +5$ (**c**). Compression stress σ_1 and volumic strain ε_v versus the strain in direction 1, ε_1, are plotted. The characteristics of the bifurcation analysis are shown in the lower part. The range of possible orientation θ of the band and the specific length ξ corresponding to the critical angle θ_c (**b**) and (**d**) are plotted versus ε_1. The star in (**a**) and (**c**) corresponds to the first onset of possible localization

At this onset, the specific length, which should be considered as an indicator of the incipient band thickness, is infinite. This length decreases quickly during the subsequent loading and becomes more or less constant (Fig. 2b, d). This limit value is depending, among others, on the second gradient law modulus which has been choose here at $D = 5 \times 10^5$ Pa m^2, and more precisely is proportional to the square root of D. It can be adjusted, so, length values are essentially qualitative in this present work. As far as the band orientation is concerned, at the first possible onset of bifurcation, the orientation is unique, but a range of orientation is possible in the subsequent loading. The critical orientation θ_c corresponds to the middle of this range.

The specific length ξ is itself dependent on the band orientation angle θ. The specific length plotted in Fig. 2b, d corresponds to the critical angle θ_c, and is the minimum of ξ on the range of possible orientations. The evolution of ξ with respect to the band orientation angle θ is shown in Fig. 3 for three steps of loading on the previous plane strain path. On the limits of the orientation range, the length tends toward infinity. There is also here a size effect which tends to limit the range of possible orientations.

4.2 Numerical Examples

A numerical specimen has been created with a 1-m width and a 2.5-m height. It has been tested on a plane strain compression path. A normal pressure of 10^6 Pa is imposed on the lateral surfaces and an axial displacement is imposed at the top of the specimen (Fig. 4).

To illustrate the bifurcation condition (22), which indicates that the strain localization becomes possible after a first onset, some solutions of the specimen response in term of resulting force versus the relative specimen shortening are shown in Fig. 5. Three localized solutions with a unique shear band through the specimen are presented. The first one is initiated in the hardening regime (i.e., $H > 0$), the band induces a global softening and clearly the peak of

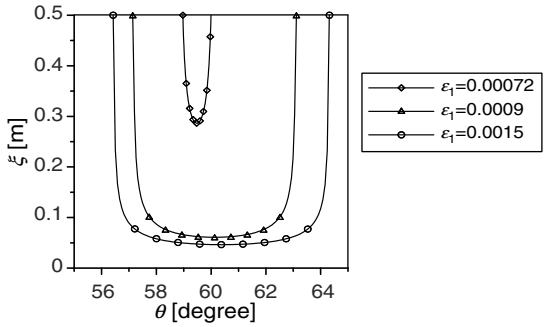

Fig. 3. Evolution of the specific length ξ with respect to the band orientation angle θ for three steps of the plane strain path (case with $h_\infty = -30$)

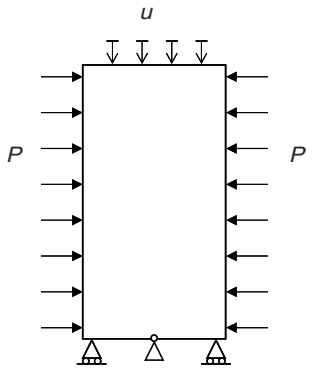

Fig. 4. Limit conditions of the plane strain compression. P is a constant normal pressure and u is a vertical imposed displacement

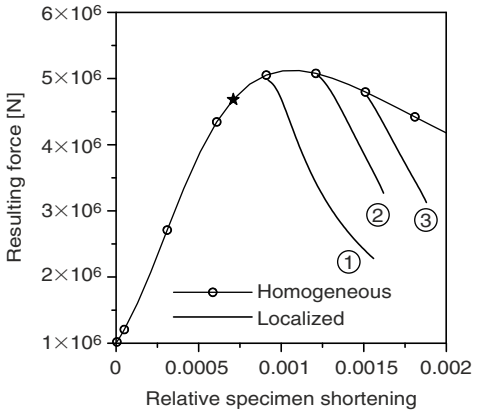

Fig. 5. Example of responses of a numerical specimen in a plane strain compression (case with $h_\infty = -30$). One solution is the homogeneous one, but localization can occur (1, 2, and 3). The first localized solution is initiated in the hardening regime ($H > 0$), whereas the two others in the softening regime. The star shows the first theoretical onset of bifurcation

this response is due to the strain localization. The two others solutions are initiated in the softening regime.

The localized solutions have been found using a so-called directional research algorithm. It consists, when in a time step of the computation, a full Newton–Raphson method is used to solve the linearized problem, to initiate the method with a random nodal values field. The algorithm has been used initially for classical models [7] and then for second gradient models [4, 5]. More details can be found in these references.

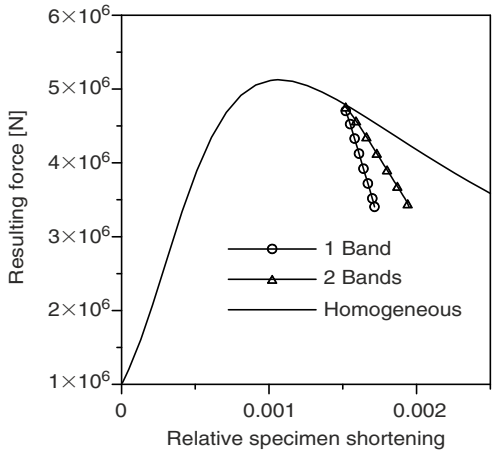

Fig. 6. Example of responses of a numerical specimen in a plane strain compression (case with $h_\infty = -30$, $D = 3 \times 10^5$ Pa m^2, and a specimen height of 3 m). One solution is the homogeneous one, but localization can occur with one or several bands. The postlocalized solution is governed by the number of bands

An other example of nonuniqueness of the solutions of the problem is illustrated in Fig. 6. The number (and also the position) of deformation bands is not imposed by the limit conditions. After the random initiation, one obtains solutions with one or two bands. The response in the postlocalized regime is governed by the number of deformation bands, the most softening solution being the one band solution.

5 Postlocalisation Responses

It seems interesting to explore the effect of the constitutive model on the postlocalization response, what kind of response we are able to obtain? We have studied here only the effect of the parameter h_∞. If this one is positive, then the law is always a strain hardening one and if it is negative, there is a softening regime after an initial strain hardening one. We did not change the other parameters of the model, in particular, we keep the parameters related to the plastic volume variation. Homogeneous and a localized solutions are shown in Fig. 7 for four values of $h_\infty : +5, 0, -10, -30$. For the four localized solutions, one observes a global decrease of the axial force at the onset of localization, even if sometimes this drop is very small. Then, for $h_\infty = +5$ and 0, one observe a global force increase in the localized solutions, and for $h_\infty = -10$ and -30, a global force decrease of the response. For these two last cases, the zone of strain localization remains the same during the loading history, but for the two first cases, one observes a nonpersistence of the zone of localization, this zones change abruptly and several times during the specimen

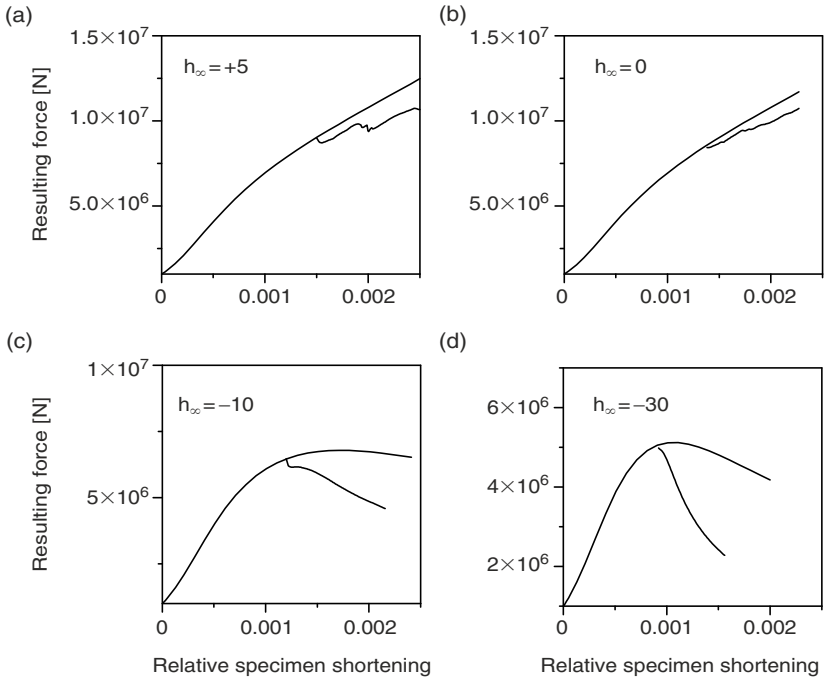

Fig. 7. Examples of responses of a numerical specimen on a plane strain compression path (the homogeneous solution and one localized solution) for several values of h_∞: (**a**) $h_\infty = +5$, (**b**) $h_\infty = 0$, (**c**) $h_\infty = -10$, (**d**) $h_\infty = -30$

loading. This volatility appears on the evolution of the resulting force as small peaks. It can be interpreted as an effect of "saturation" of the shear band and it becomes more favorable to localize elsewhere than to continue to activate the current band.

These results have a strong similitude with the experimental observations on soft porous rocks or sands. For example, in experimental axisymmetric triaxial compression tests controlled by the rate of axial shortening, which are classical tests in rock mechanics, it is well known that the porous rock behavior changes with the level of confining pressure (e.g., [1,3]). For the low confining pressure, the behavior is generally called brittle and the failure is characterized by a strong decrease of the axial force and the presence of a few deformation bands. For high confining pressure, in the brittle–ductile transitional regime, it can be observed, after the strain localization, an increase of the axial force and a large number of deformation bands. Moreover, the evolution of the axial force presents also several small peaks which are generally associated with a high level of acoustic emission events and explained by an apparition of some new deformation bands. An illustration of such a behavior is given in Fig. 8, at two levels of confining pressure on a porous sandstone. More or less similar loading force evolutions can be observed in sand specimens. For example in

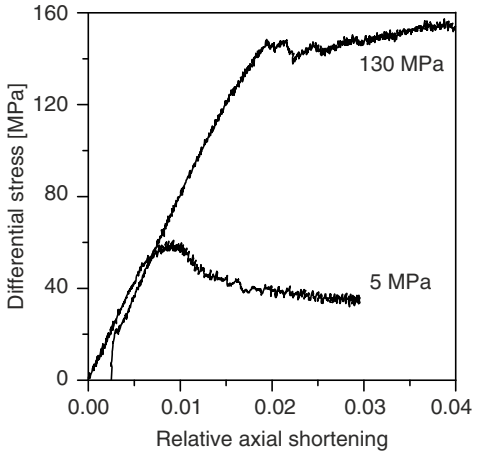

Fig. 8. Responses of two Rothbach sandstone specimens tested in compression with axisymmetric conditions at 5 and 130 MPa confining pressure, corresponding to a brittle behavior and a brittle–ductile transition, respectively (from [3])

plane strain compression on prismatic sand specimens, a brittle type response is observed for initially dense samples and a ductile type response in initially loose samples (e.g., [9]).

6 Conclusion

If models with an internal length like local second gradient models resolve the problem of mesh size dependence, the uniqueness of solution is not necessarily restored. In fact, there is no reason to restore the uniqueness. If one considers this question from the experimental point of view, it is known that the post localization regime is rarely reproducible, even with the best care as possible for preparing a specimen and performing a test. This nonrepeatability is probably induced by a large part to some microstructural details in the material which make that for a given specimen, localization will occur earlier or latter, in this zone and not elsewhere, with one shear band or several, etc. These details cannot be captured with constitutive models and it is our opinion that we have to make the comparison between the numerical nonuniqueness and the experimental nonrepeatability.

Therefore, we showed that postlocalized behaviors observed experimentally like the brittle regime or the brittle–ductile transition can be simulated. For example, the resulting axial force applied during a plane strain compression of a numerical specimen can, after localization, decrease but also increase, depending on the constitutive parameters. We showed also, and this confirms the theoretical predictions, that the localization can occur with a strain hardening model and that the softening is not necessarily for that. However, the

localization with a strain hardening model seems numerically more difficult to obtain than with a softening model. To overcome this point we had to use meshes with preferential orientations to favor the strain localization. We observed with hardening models a non persistence of the areas of strain localization, it is probably influenced by some numerical parameters (time step, mesh, etc.), but it seems significant and once again it is not so far from experimental observations. In a porous sandstone, in the brittle–ductile regime, Fortin et al. [11] have observed by location of acoustic events the deactivation of existing bands and activation of new deformation bands during axisymmetric compression tests.

References

1. Baud P, Klein E, Wong T-f (2004) J Struct Geol 26:603–624
2. Bésuelle P, Rudnicki JW (2004) Localization: Shear bands and compaction bands. In: Guéguen Y, Boutéca M (eds) Mechanics of Fluid-Saturated Rocks. Academic, Elsevier, 219–321.
3. Bésuelle P, Baud P, Wong T-f (2003) Pageoph 160:851–868
4. Bésuelle P, Chambon R, Collin F (2006) J. of Mechanics of Materials and Structures (submitted)
5. Chambon R, Moullet J-C (2004) Comput Methods Appl Mech Eng 193:2771–2796
6. Chambon R, Caillerie D, Matsushima T (2001) Int J Solids Struct 38:8503–8527
7. Chambon R, Crochepeyre S, Charlier R (2001) Int J Numer Methods Eng 51:315–332
8. Cosserat E, Cosserat F (1909), Théorie des Corps Déformables. Hermann, Paris
9. Desrues J, Viggiani G (2004) Int J Numer Anal Methods Geomech 28:279–321
10. Fleck NA, Hutchinson JW (1997) Adv Appl Mech 33:295–361
11. Fortin J, Stanchits S, Dresen G, Guéguen Y (2005) J Geophys Res, *submitted*
12. Germain P (1973) J Méc 12:235–274
13. Holcomb DJ, Rudnicki JW (2001) Int J Numer Anal Methods Geomech 25:109–129
14. Matsushima T, Chambon R, Caillerie D (2002) Int J Numer Methods Eng 54:499–521
15. Mindlin RD (1964) Arch Ratlonal Mech Anal 4:50–78
16. Mühlhaus H, Aifantis E (1991) Int J Solids Struct 28:845–857
17. Pijaudier-Cabot G, Bažant ZP (1987) J Eng Mech 113:1512–1533
18. Rudnicki JW, Rice JR (1975) J Mech Phys Solids 23:371–394
19. Toupin RA (1962) Arch Ratlonal Mech Anal 11:385–414
20. Vardoulakis I, Aifantis E (1991) Acta Mech. 87:197–217

Confined Compression and Rod Penetration of a Dense Granular Medium: Discrete Element Modelling and Validation

Y.C. Chung and J.Y. Ooi

School of Engineering and Electronics, University of Edinburgh, UK
j.ooi@ed.ac.uk

1 Introduction

Many of the materials handled by industry each year are of a granular or particulate nature. These include pharmaceutical powders, chemical pellets, agricultural grains, coals and other minerals, sands and gravels. In recent years, the discrete element method (DEM) [3] has been used extensively to investigate the behaviour of granular solids subjected to a variety of loading conditions. However, the majority of the numerical computations were often not validated or compared with experimental results and there is a question as to whether DEM is capable of producing quantitative predictions rather than only qualitative representation of a particulate assembly. It is thus useful to verify DEM calculations and to investigate the relative importance of the DEM input parameters for producing satisfactory predictions.

This paper describes two physical experiments and the corresponding DEM computations of a densely packed granular medium subjected to compression and penetration. These two loading conditions were studied because they are frequently encountered in many situations where a boundary surface from an object (such as a machine or a geotechnical structure) contacts with a granular solid. The experiments consisted of an instrumented Perspex cylinder filled with granular solids. The first experiment was to compress the solid vertically under nearly K_0 (zero lateral deformation) condition and the second was to insert a cylindrical rod into the granular medium. The mechanical response of the granular system and the load transfer to the containing walls, the bottom platen and the penetrating rod were observed. The experiments were simulated closely using DEM and a detailed comparison between experiment and computation was made.

Both spherical (glass beads) and non-spherical (corn grains) particles were studied. Spherical particles have a tendency to rotate more than non-spherical particles and can be expected to exhibit quite different behaviour from non-spherical particles, so it is important to study both systems. The required mechanical and geometrical properties for the particles were measured

carefully in laboratory tests for use in DEM computations. The sensitivity of DEM prediction to the key input parameters was also explored. The results show that DEM can produce quantitative predictions of the system studied, and that whilst it is important to use the correct particle stiffness parameter when attempting to predict the deformation response of a granular assembly, this may not be so important for producing satisfactory prediction of the force transmission in a dense quasi-static system.

2 Calibration Experiments

The confined compression test (Fig. 1) was designed to investigate the mechanical response of a granular material under vertical loading and the load transfer to the containing walls [10]. A load was applied to a granular assembly contained in the cylinder through a top platen driven by an INSTRON machine at a constant displacement rate of $1.5\,\mathrm{mm\,min^{-1}}$. The applied load and vertical displacement were measured using the INSTRON machine. The force transmitted to the walls was measured using four pairs of strain gauges equally spaced around the cylinder walls in both circumferential and axial directions. The vertical force transmitted to the bottom platen was measured by the bottom load cell. The lateral pressure ratio K and the wall friction coefficient μ can be approximately evaluated using (1) where $\overline{\sigma_{\mathrm{V}}}$ is the average vertical stress, σ_{H} is the horizontal stress and $\overline{\tau}$ is the average shear stress, as expressed in (2).

$$K = \frac{\sigma_{\mathrm{H}}}{\overline{\sigma_{\mathrm{V}}}}, \quad \mu = \frac{\overline{\tau}}{\sigma_{\mathrm{H}}}, \tag{1}$$

$$\overline{\sigma_{\mathrm{V}}} = \frac{2(F_{\mathrm{T}} + F_{\mathrm{B}})}{\pi D^2 (1+\varepsilon_\theta)^2}, \quad \sigma_{\mathrm{H}} = \frac{2tE_w(\varepsilon_\theta + \nu_w \varepsilon_{\mathrm{a}})}{D(1-\nu_w^2)}, \quad \overline{\tau} = \frac{F_{\mathrm{T}} - F_{\mathrm{B}}}{\pi\, Dh(1-\overline{\varepsilon_{\mathrm{V}}})}. \tag{2}$$

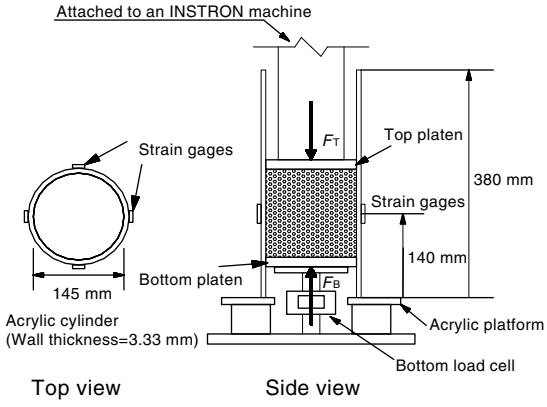

Fig. 1. Confined compression test setup

In (2) D, t, E_w and ν_w are the diameter, thickness, Young's modulus and Poisson's ratio of the cylinder, respectively; ε_θ, ε_a are the average hoop strain and axial strain of the cylinder at the measurement points, respectively; $F_\mathrm{T}, F_\mathrm{B}$ are the applied load at the top platen and the measured force at the bottom platen, respectively; $\overline{\varepsilon_\mathrm{V}}$ is the mean vertical strain and h is the height of the granular solid.

The penetration test was designed to evaluate the resistance of granular bulk to penetration of a moving object and the dynamic force transmission to a contact surface. The experimental design is depicted in Fig. 2. The force and displacement of a rod were monitored using an INSTRON machine as the rod was pushed into granular bulk at a constant displacement rate of $50\,\mathrm{mm\,min^{-1}}$.

3 Discrete Element Model

Discrete element method is an increasingly popular numerical technique for simulating moving particles [3]. It is based on the use of an explicit numerical scheme in which the interactions between a finite number of particles are monitored contact by contact and the motion of the particles is modelled particle by particle. The particles are rigid but deform locally at the contact points by means of an overleap (soft contact method). Newton's equations of motion for each particle effectively replace the equilibrium equations used in continuum mechanics, and the model of inter-particle contacts replaces the constitutive model. The essential feature of this approach is that each particle is modelled separately, so the integrated behaviour of the mass should be accurately represented, without the need for control tests to establish constitutive models for the bulk behaviour. In this paper, a Hertz–Mindlin no-slip [13] contact model with damping and a frictional slider in the tangential direction is used, as shown schematically in Fig. 3.

The DEM calculations were performed using both the EDEM code [4] and the PFC3D code [6]. The reason was to compare the outcomes of two independent DEM codes using exactly the same problem configurations. The numerical samples were prepared by filling a cylindrical container (diameter=145 mm, length=300 mm) with 3,591 glass beads and 4,608 corn

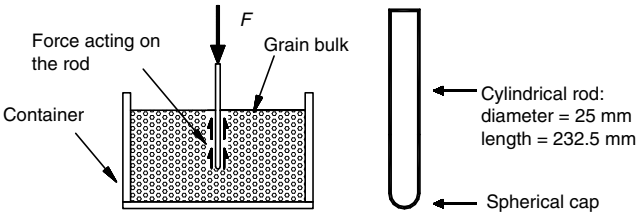

Fig. 2. Rod penetration: test setup and rod dimensions

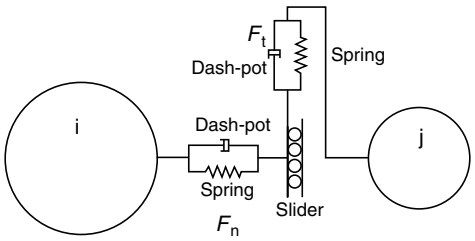

Fig. 3. Non-linear spring and dashpot contact model with a tangential slider

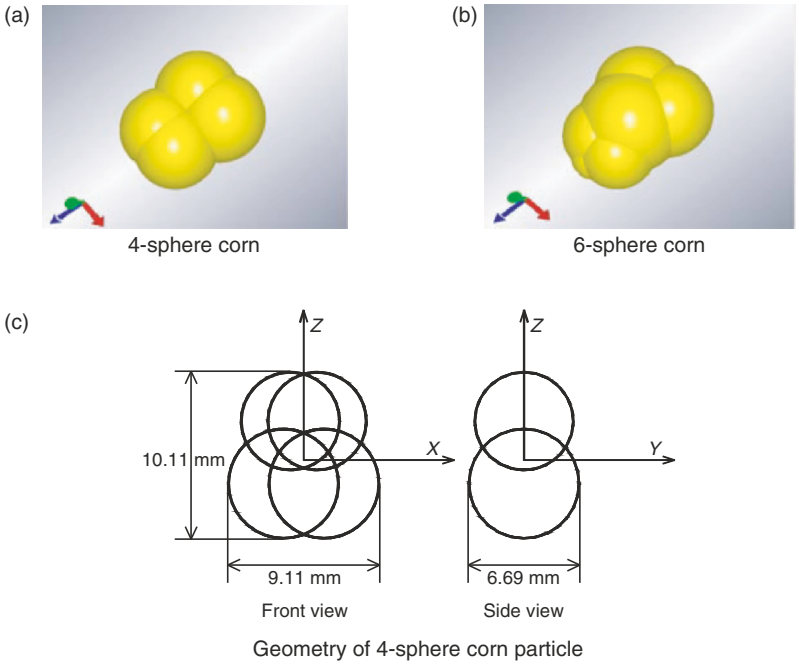

Fig. 4. Representations of corn grains using overlapping spheres

grains in each set of computations. Particle size variation was not considered in the numerical calculations. The corn particle was represented using overlapping spheres [5] to match the measured average major, intermediate and minor dimensions. A number of shape representations are possible as shown in Fig. 4 and a 4-sphere representation (Fig. 4c) was chosen mainly because using increasing number of spheres to represent each particle leads to additional computational cost. The particles were positioned in layers starting from the base, at 1.01 d centre to centre in a regular pattern with an initial velocity of $2.56\,\mathrm{m\,s^{-1}}$ (where $d =$ major diameter of the particle). They are then allowed to fall under gravity to achieve the initial filled state. The initial velocity corre-

sponds to the drop height of 335 mm used in the experiments where the particles were placed in a sieve at a height of 335 mm and allowed to "rain" through the sieve into the cylinder. This approximate particle generation scheme saves considerable computational effort, but may influence the numerical outcome since it is known that particle packing can have significant influence on bulk behaviour. The effect of this approximation was explored using different initial particle positions and will be discussed later. The particles were deemed to have settled down when the kinetic energy of the system approached zero ($<10^{-8}$ J) and the mean unbalanced force approached zero ($<10^{-5}$ N). After achieving the filled state, the confined compression was simulated by adding a top platen and the rod penetration was simulated by adding a rod, both moving at a displacement rate of 50 mm min^{-1}.

The boundary surfaces (the cylinder, the loading platen and the rod) were tessellated using triangular elements employing techniques common to finite element meshing [8,9]. This method allows any complex boundary surfaces to be represented relatively easily whilst maintaining computational efficiency in contact detection. Example snapshots for the confined compression and rod penetration DEM models are shown in Fig. 5.

Input parameters for the glass beads and the corn grains are listed in Tables 1 and 2, respectively. The elastic modulus was determined from the single particle compression test assuming Hertzian contact. For the case of non-spherical corn, the two orthogonal curvatures at the point of contact were required and these were measured using a laser scanner. The particle–surface static friction coefficient was measured from a three-particle sliding test. A drop test apparatus was devised to determine the Particle–surface resultant coefficient of restitution. For non-spherical particle, the impact results in a more complex trajectory involving particle rotation, all of which need to be determined carefully to evaluate the restitution coefficient accurately. Details of these characterisation tests can be found in Chung et al. [1,2].

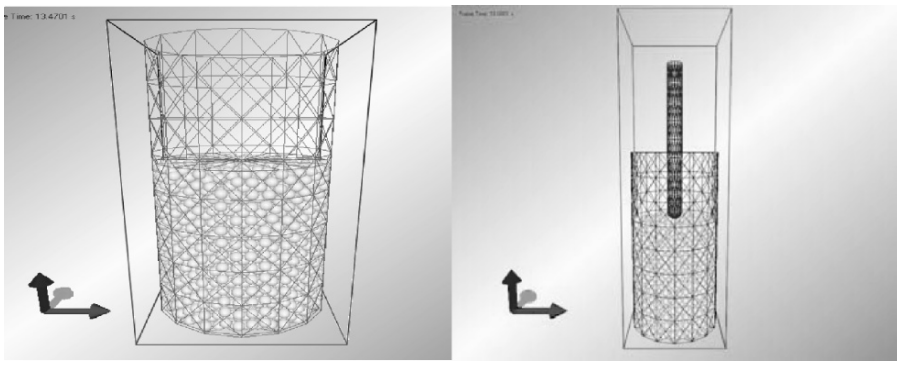

Fig. 5. Example snapshots of confined compression and rod penetration

Table 1. Input parameters for glass beads

parameter	values	unit
density	2,530	$\mathrm{kg\,m^{-3}}$
diameter	10	mm
Young's modulus	41	GPa
Poisson's ratio	0.22	
friction coefficient		
particle–particle, particle–wall	0.24	
restitution coefficient	0.79	

Table 2. Input parameters for corn grains

parameter	values	unit
density	1,220	$\mathrm{kg\,m^{-3}}$
mass	0.427	g
major dimension	10.11	mm
intermediate dimension	9.11	mm
minor dimension	6.69	mm
Young's modulus	1,660	MPa
Poisson's ratio	0.40	
friction coefficient		
particle–particle, particle–wall	0.34	
restitution coefficient	0.59	

3.1 Confined Compression: Experiment and Modelling

Figure 6a, b compare the load–displacement responses between DEM computation and four confined compression tests for glass beads and corn grains, respectively. The overall trend of increasing stiffness as vertical load increases is as expected. Although each physical test followed the same filling procedure, the results show that at the initial stage when the forces are small, the loading response can vary significantly from test to test. This suggests that the natural variation in initial packing in each experiment can give significantly different loading response at low confining pressures. After this initial confinement (say after 150 N vertical force), the loading responses were largely parallel to each other, indicating that each test assembly converged to a repeatable loading response at higher confining pressures. The DEM predicted response appears to be stiffer. This is partly because the DEM model does not take into account the flexibility of the cylindrical walls (which was necessary to achieve a measurable strain to determine the loading condition). Adjusting for the additional vertical deformation deduced from the strain gauge readings was found to account for a significant part but not all of the mismatch between experiment and computation. The stiffer numerical prediction was further explored in [2].

Figure 7 shows the force transmission onto the bottom platen during compression. Both the experimental and numerical results show the force acting

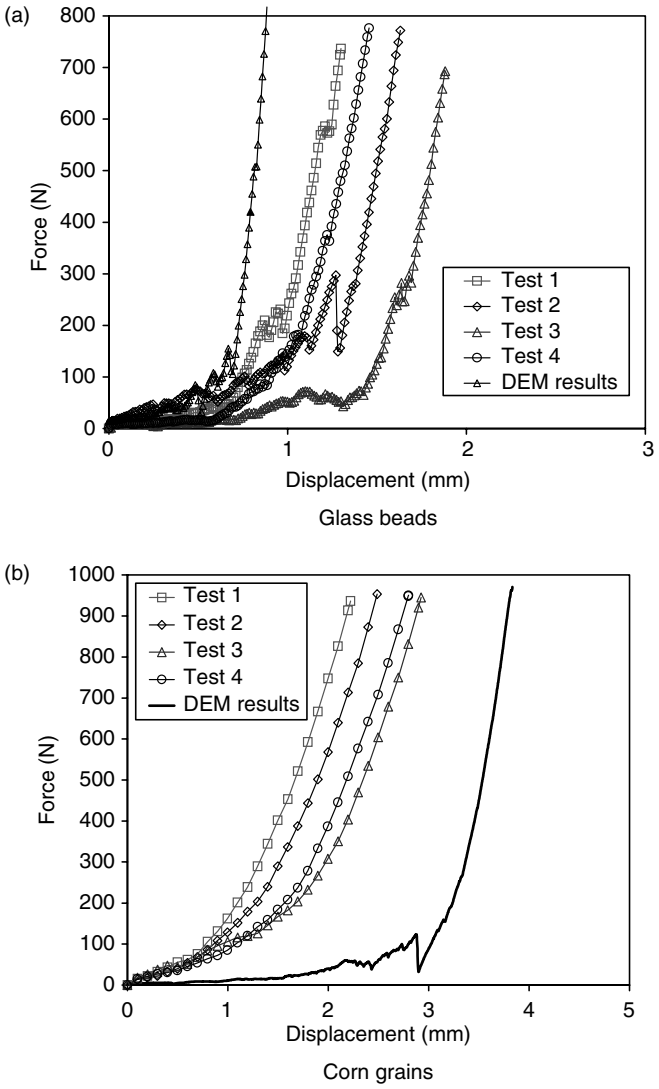

Fig. 6. Load–displacement response during confined compression

on the bottom platen increases linearly with the applied vertical force. The physical tests show that only 50% of the applied load reached the bottom platen for the glass beads compared with 65% for the corn grains. Although the wall friction coefficient μ for corn is some 40% larger than for glass beads, the lateral pressure ratio K for corn is significantly smaller, such that the product μK is smaller (1), giving a smaller share of the load acting on the cylindrical walls for the case of corn grains.

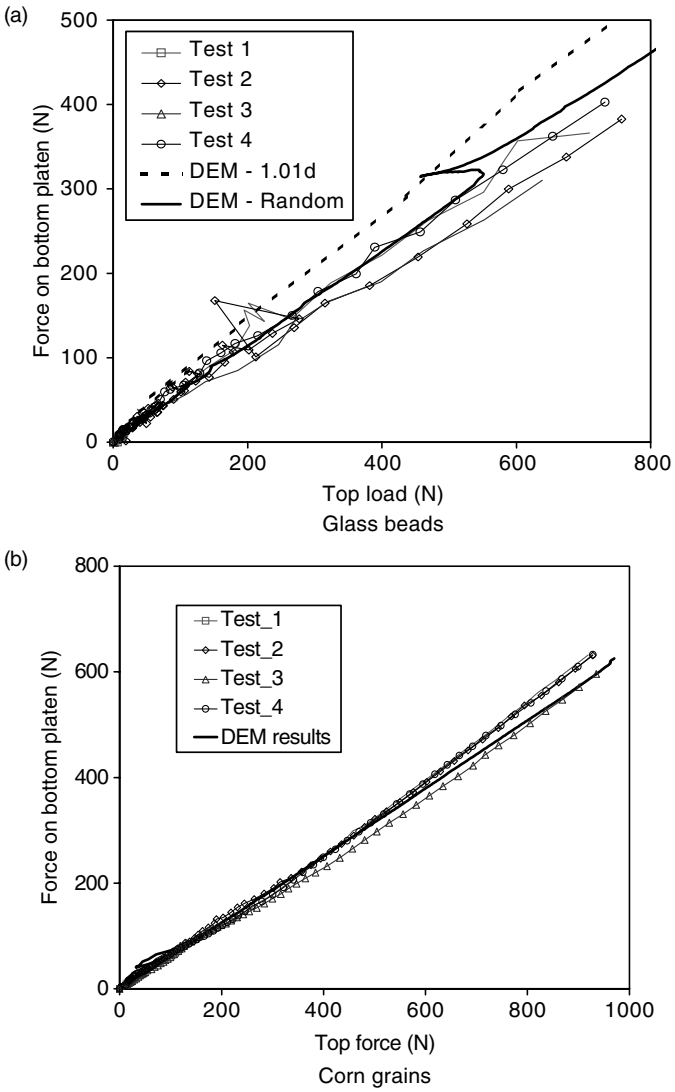

Fig. 7. Force transmission onto bottom during compression

The DEM prediction (hold case) is in excellent agreement with experiments for the corn grains but significantly overpredicts the force on the bottom platen for the glass beads. Further DEM calculations to explore the influence of initial particle generation arrangements have been conducted separately, showing that the DEM predictions are more sensitive to how the spherical glass beads are filled than non-spherical corn particles. In particular, one glass beads computation with a randomly generated initial particle positions gives a close match with the experiments, also shown in Fig. 7a. A plausi-

ble explanation is that uniform spheres have the tendency to form crystalline structure and are more sensitive to initial packing but such sensitivity is less significant for "real" particles which are predominantly non-spherical. The approximate layered initial particle positions to simulate the filling process may have contributed to this occurrence. A systematic investigation of the influence of initial packing on the loading behaviour can be found in [2].

Figure 8 shows the normal wall pressure distribution on the cylinder at the end of filling. This pressure distribution may be compared with the

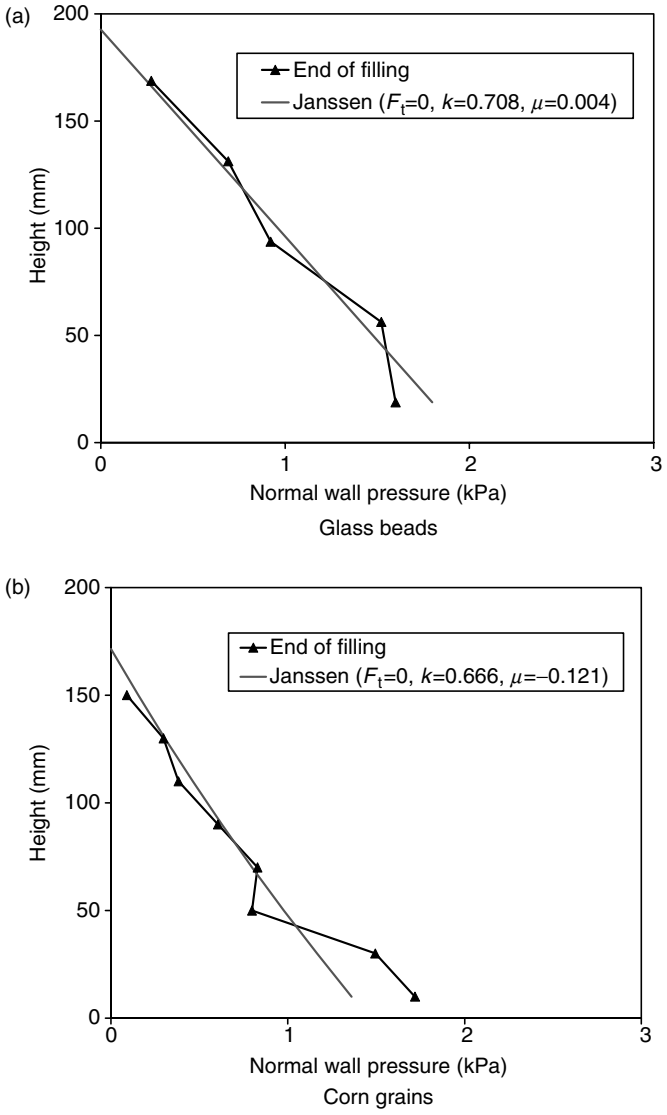

Fig. 8. Normal wall pressure distribution at the end of filling

one-dimensional theory of Janssen for silo wall pressure [7, 11]:

$$P_n = \frac{D\gamma}{4\mu}(1 - \mathrm{e}^{-z/z_0}) + Kq_{\mathrm{T}}\mathrm{e}^{-z/z_0}, \tag{3}$$

$$z_0 = \frac{D}{4\mu K},\ q_{\mathrm{T}} = \frac{4F_{\mathrm{T}}}{\pi D^2}, \tag{4}$$

where K is the lateral pressure ratio, μ is the wall friction coefficient, γ is the bulk density, z_0 is Janssen reference depth and q_{T} is the mean vertical pressure that may be applied at the top boundary ($z = 0$). The predicted K and μ can be calculated from an unbiased best fit of the boundary forces in the DEM results, the results give $K = 0.71, \mu = 0.004$ and $K = 0.67, \mu = -0.12$ for glass beads and corn grains, respectively. The friction best fit bulk differs significantly from the input values, which is probably a result of the dynamic filling process. The parameters K and μ are important in the silo design and their values under vertical compression will be explored further. Using the best fit parameters from the DEM calculation, the Janssen equation matches very well with the evaluated normal pressures from contact forces.

Figure 9 shows the development of the normal wall pressures during vertical compression for both materials. The effect of vertical compression can be evaluated from the extended Janssen equation with the inclusion of an applied vertical stress at $z = 0$ (3). These are also plotted in Fig. 9 for comparison, using K and μ derived from DEM results. The increase of normal wall pressure during vertical compression matches the Janssen equation reasonably well away from the boundaries. Since Janssen is a one-dimensional theory that does not take into account the top and bottom boundary conditions, there is significant mismatch towards the boundaries.

Dividing the vertical traction with the normal pressure at any given point on the wall gives an indication of the "mobilised friction coefficient" at that point. Figure 10a shows that the mobilised wall friction at the five calculation positions are within the range of 0.07–0.17 for the glass beads, significantly smaller than the input particle–wall friction coefficient of 0.24. This is in agreement with previous studies [12] showing significantly smaller macroscopic friction than the inter-particle microscopic friction for a spherical assembly. For the corn grains, a higher mobilised friction coefficient is achieved with values of 0.21–0.31 when the vertical force is close to 1,000 N (this compares with input friction coefficient of 0.34). One reason may be that since corn grains are much softer than glass beads, they generate sufficient slip displacement against the wall, resulting in a larger friction mobilisation. The tendency for perfect spheres to rotate more as compared to non-spherical particles may be one main reason also contribute to the much smaller macroscopic friction. Circumferential traction acting on the cylinder was also evaluated and found to be relatively small, as expected in an axisymmetric system.

The lateral pressure ratio K was evaluated from the experimental data using (1) and plotted against the DEM prediction in Fig. 11. The experimental

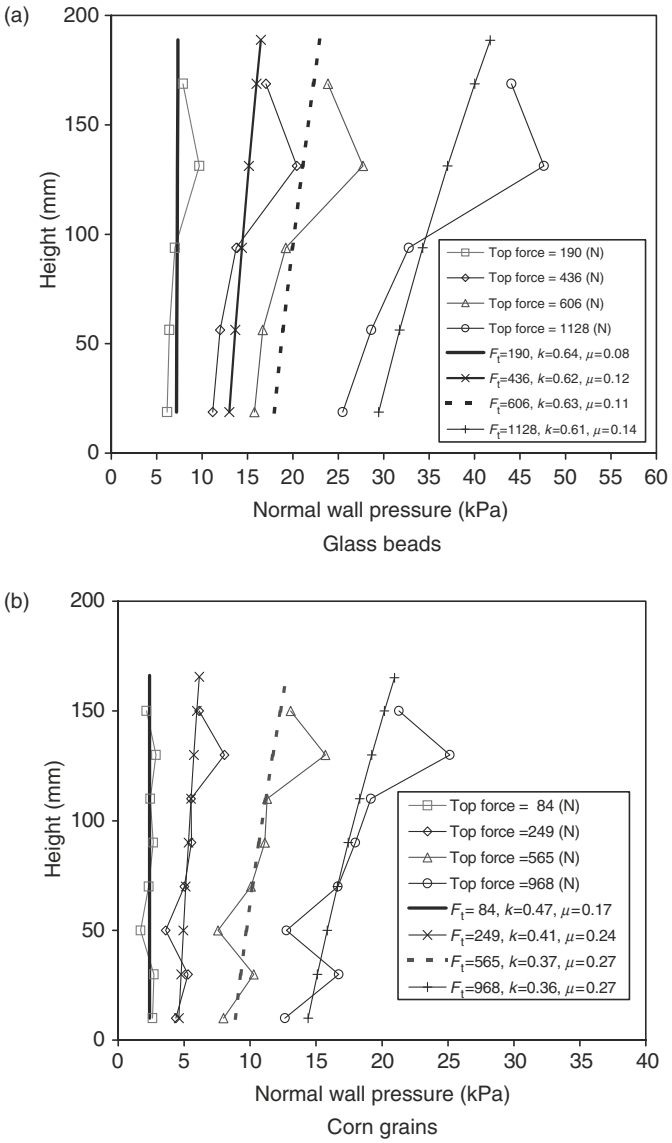

Fig. 9. Normal wall pressure distribution during compression

results are reasonably repeatable for each material, showing a trend of the K value increasing and reaching a stable value of $\sim$0.4 for glass beads and $\sim$0.35 for corn grains, with a larger scatter for the glass beads. It should be noted that the evaluation of lateral pressure ratio K is only approximate here since the mean vertical stress was calculated from the average of top and bottom

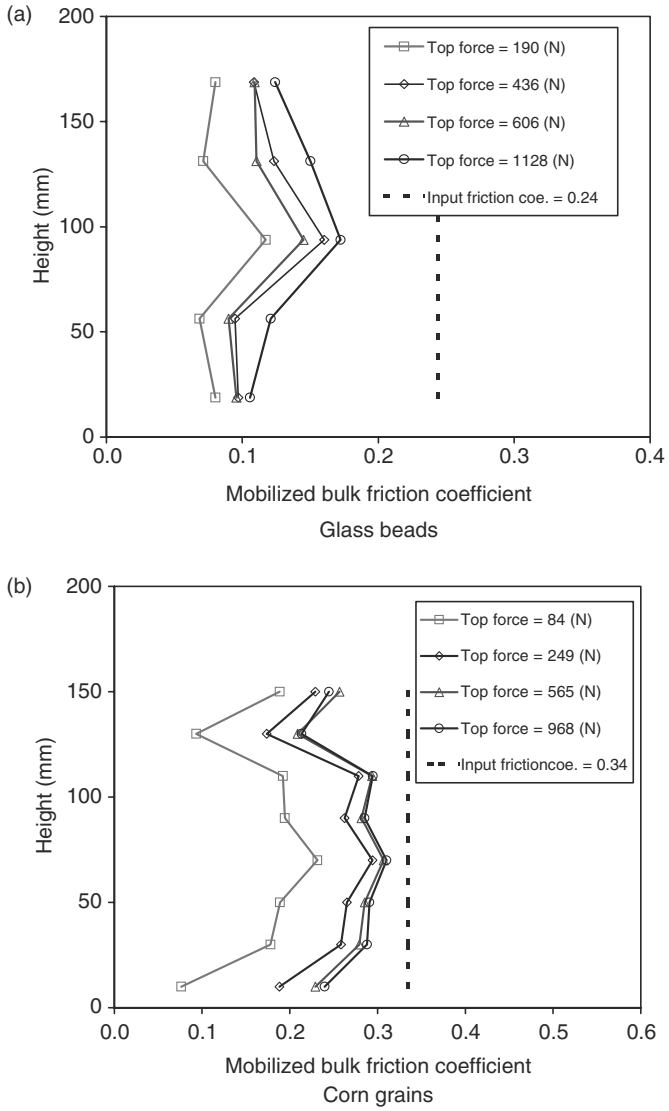

Fig. 10. Mobilised wall friction coefficient during compression

platen forces (2) and the normal pressure came from measurement at the strain gauge level in the experiment and from boundary forces in the DEM simulations. The DEM prediction for the corn computation is in excellent agreement but for the sphere assembly, DEM predicts a much larger K value of $\sim$0.62. The over-prediction of K value matches the finding from previous studies for 2D circular disks [12].

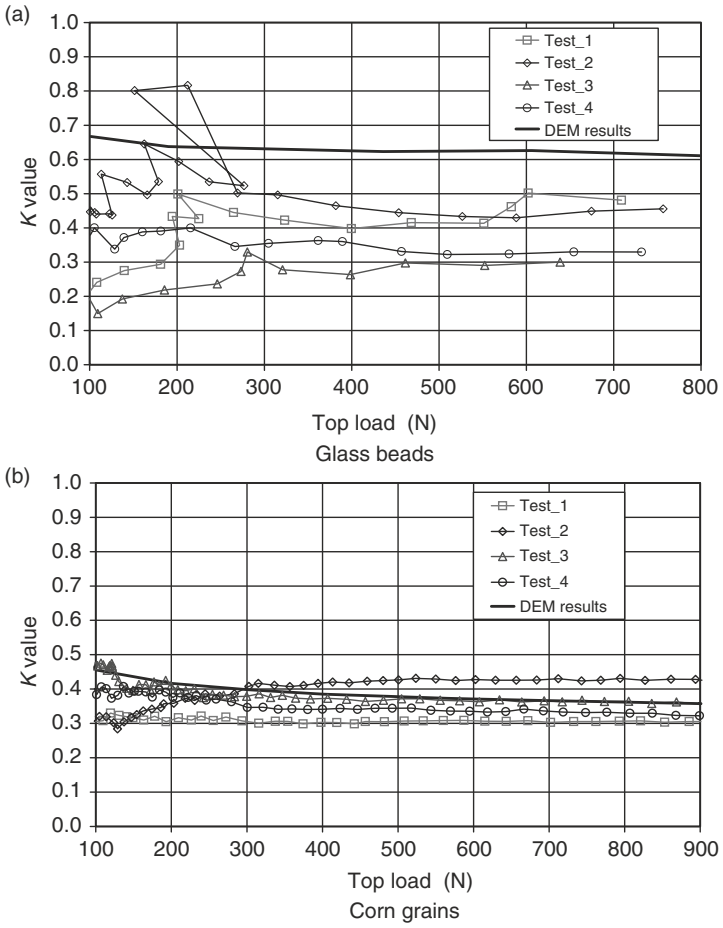

Fig. 11. Comparison of predicted lateral pressure ratio with experiments

3.2 Rod Penetration: Experiment and Modelling

The load–displacement responses for the rod penetration into glass beads and corn grains are shown in Fig. 12. These computations were performed with particle shear modulus G decreased to $0.01G$ to reduce computational effort. In addition, for the glass beads computation, a further computational advantage was gained by increasing the density ρ to $1,000\rho$. Density scaling has been used successfully in previous studies (e.g. [14]). The measured force fluctuated significantly during penetration into each material, but the average trend is repeatable with the corn grains giving a larger resistance to penetration. The DEM results also fluctuated in a seemingly similar fashion and show a good quantitative match with the experiments in each material.

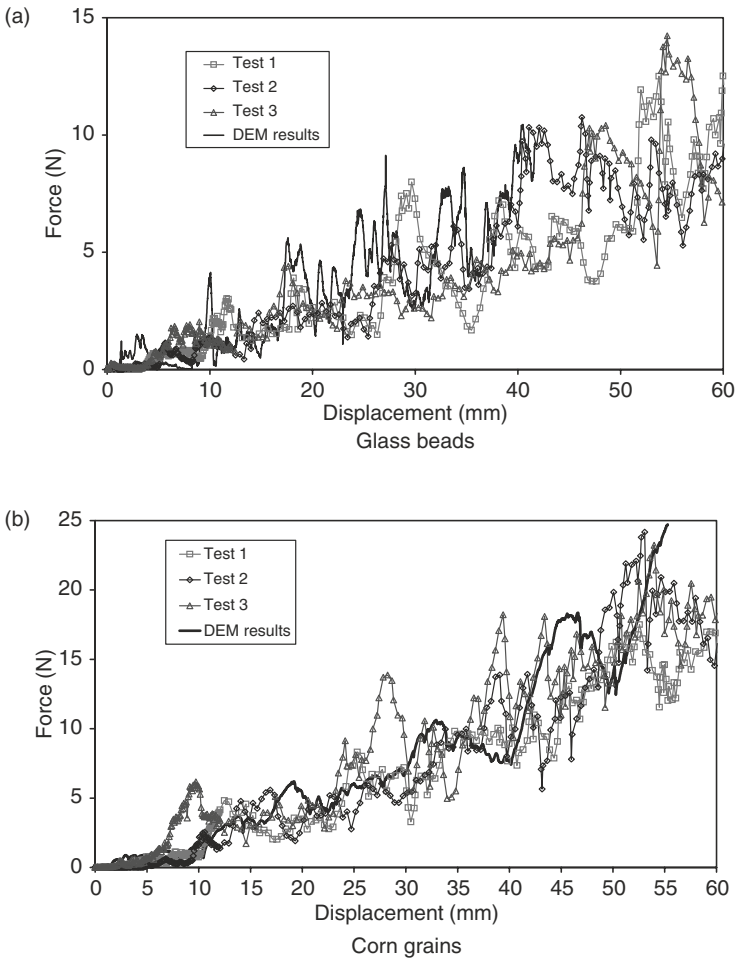

Fig. 12. Load–displacement response during rod penetration

3.3 Influence of Input Parameters

Further calculations were conducted to explore the sensitivity of the input parameters on the numerical outcomes. One other objective was to investigate the methodology for reducing DEM computational time since the calculation time step is inversely proportional to $\sqrt{G/\rho}$, where G is the shear modulus and ρ is the density of particles. Due to space constraint, only the influence of particle stiffness is discussed here. The rest can be found in [2].

DEM computations were conducted with particle shear modulus reduced to $10^{-2}G, 10^{-3}G$ and $10^{-4}G$. For the load–displacement response in confined compression which is strongly dependent on the bulk stiffness of the assembly, reduced particle stiffness results in a softer response as expected. Figure 13 shows the force acting on the bottom platen during vertical compression for

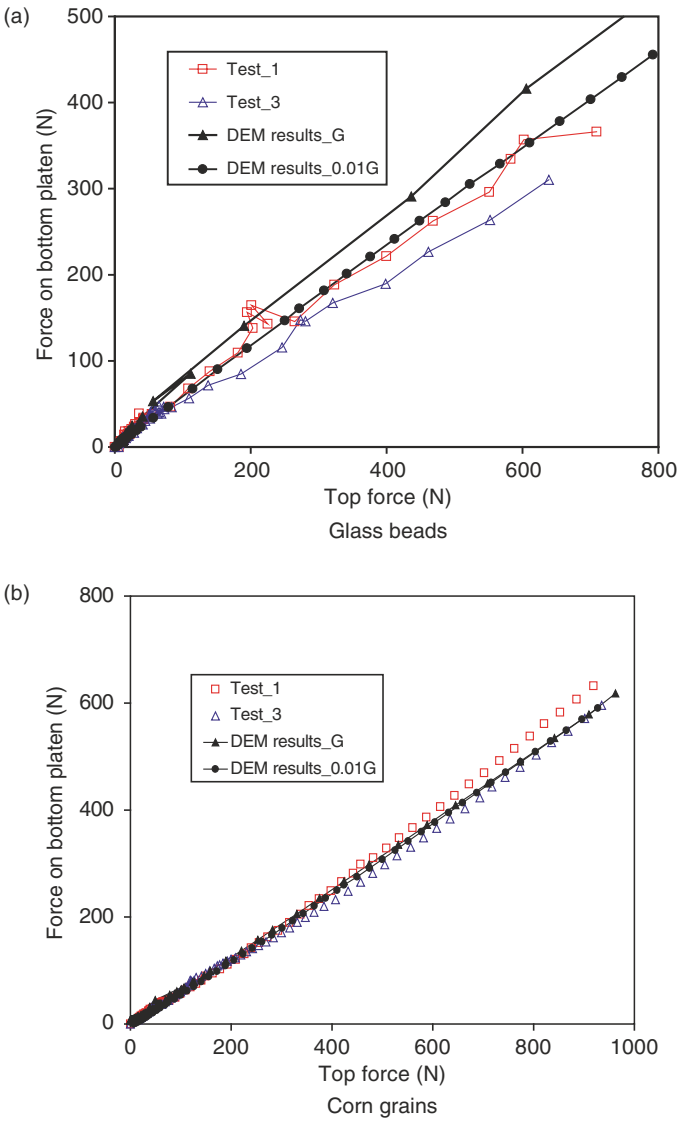

Fig. 13. Effect of shear modulus on predicted response for confined compression

the cases of full stiffness and 100 times smaller stiffness. The results show that when particle stiffness is reduced by 100 times, the proportion of the applied force transmitted to the bottom platen reduced by ∼10% for glass beads and there is no noticeable difference in the results for corn grains. The results show that for this confined quasi-static system, reducing the particle stiffness by a few orders may have only secondary effects on the load transfer mechanism.

4 Conclusions

Discrete element modelling of confined compression and rod penetration into a spherical and a non-spherical granular assemblies have been presented. The physical experiments were performed with care, including which include direct laboratory measurements of the key DEM input parameters. Comparisons have been made between the numerical results and the experiments.

The study has shown that for the corn grains, the DEM predictions are in good agreement with the experiments for all cases except the force–displacement response. This provides some verification that DEM is capable of producing quantitative predictions. The results also suggest that very accurate representation of the particle shape may not be necessary to produce satisfactory predictions and capturing the key linear dimensions of a particle may be adequate.

The DEM results for the spherical glass beads were not always in quantitative agreement with the experiments. DEM predictions have been found to be more sensitive to how the spherical glass beads are filled than non-spherical corn particles. The spherical assembly appears to be more sensitive to initial packing structure resulting from how the particles are generated initially. The sensitivity of DEM computations to initial packing structure needs further study.

The sensitivity of DEM prediction to the stiffness parameter was also explored. It has been found that reducing the particle stiffness by a few orders only has secondary effects on the load transmission in the quasi-static assembly. Since contact forces propagate through the granular assembly to transmit to the boundary surfaces, the development of the force chains and the internal states of stress and strain within the assembly is important and is being investigated.

Acknowledgements

The first author would like to acknowledge Deere & Company, DEM Solutions Ltd. and the University of Edinburgh for funding this research. The authors are very grateful to Dipl. Ing. Johannes Härtl for his assistance in the experimental work and to Drs John Favier and Carol Plouffe for their advice and discussion about this project.

References

1. Chung YC, Ooi JY, Favier JF (2004a) Measurement of mechanical properties of agricultural grains for DE models. 17th ASCE Engineering Mechanics Conference, Newark, USA, 8 pp
2. Chung YC (2006) Phd Thesis, University of Edinburgh, UK

3. Cundall P, Strack OA (1979) A discrete numerical model for granular assemblies. Geotechnique, 29: 47–65
4. DEM Solutions Ltd (2005) EDEM discrete element code. Beta Version, Edinburgh, UK (*http://www.dem-solutions.com/*)
5. Favier JF, Abbaspour-Fard MH, Raji AO, Kremmer M (1999) Shape representation of axi-symmetrical arbitrary particles in discrete element simulation using multi-element model particles. Eng. Comput., 16: 467–480
6. Itasca Consulting Group, Inc. (2003) PFC3D – Particle Flow Code in 3 Dimension. Version 3.0, Minneapolis, USA
7. Janssen HA (1895) Versuche über getreidedruck in silozellen. Z. Vereines Deutscher Ingenieure, 39: 1045–1049
8. Kremmer M, Favier JF (2001a) A method for representing boundaries in discrete element modelling: Part I – Geometry and contact detection. Int. J. Numeri. Methods Eng., 51: 1407–1421
9. Kremmer M, Favier JF (2001b) A method for representing boundaries in discrete element modelling: Part II – Kinematics. Int. J. Numer. Methods Eng., 51: 1423–1436
10. Masroor SA, Zachary LW, Lohnes RA (1987) A test apparatus for determining elastic constants of bulk solids. SEM Spring Conference on Experimental Mechanics, Houston, USA, 553–558
11. Ooi JY, Rotter JM (1990) Wall pressures in squat steel silos from finite element analysis. Comput. Struct., 37: 361–374
12. Rotter JM, Holst, JMFG, Ooi JY, Sanad AM (1998) Silo pressure predictions using discrete element and finite element analyses. Phil. Trans. R. Soc. Lond. A, 356: 2685–2712
13. Tsuji Y, Tanaka T, Ishida T (1992) Lagrangian numerical simulation of plug flow of cohesionless particles in a horizontal pipe. Powder Technol., 71: 239–250.
14. Zhang L (2003) PhD Thesis, Aston University, UK

Application of Discrete Element Method to Geomechanics

M. Jiang*,†, H.-S. Yu*

* Department of Geotechnical Engineering Tongji University, Shanghai, China
mingjing.jiang@nottingham.ac.uk
† School of Mathematics, University of Manchester, UK

Abstract. This chapter introduces recent application of the Distinct Element Method (DEM) to geomechanics. Different contact laws were introduced and used to investigate the noncoaxiality of granular materials, effective stress in unsaturated soils, bonding effect in natural soils and penetration mechanism in granular ground. The study shows that DEM is a promising tool to solve some difficult problems not only in fundamental geomechanics but also in complex boundary value problems in geotechnical engineering.

1 Introduction

Soils consist of particles, macropores, micropores, pore fluids (air, water, others), assembled possibly with interparticle bonding to form a fabric. Although soils are in essence a kind of discrete materials, they have been traditionally treated as continuum material in theoretical, constitutive modelling and numerical analyses within continuum mechanics. This method plays important role and is widely used in geotechnical engineering. However, the behaviour of soils is so complex that, although some general features are agreed upon, no particular model or theory has received universal acceptance yet.

Two types of ways have been used to consider the discrete feature of soils. The first method is to revise the available continuum models or theories by introducing additional laws which reflects the change of microstructure of soils, such as fabric [32], or by improving existing constitutive laws based on the available micromechanical studies on soils [29]. The method is usually employed by continuum constitutive modellers. In contrast, the second method treats soils as an assembly of discrete materials directly, while its macroscopic–microscopic responses under loading are obtained analytically, numerically or experimentally. This method is widely used by micromechanical researchers [5, 6, 10, 28].

In this latter method, the Distinct Element Method (DEM) becomes more and more popular, which is a numerical simulation technique originally

developed for dry granular materials by Cundall and Strack [10]. The main feature of DEM is that complex responses of an assembly of discrete materials can be controlled by very simple contact laws at interparticle contacts. For example, the Mohr–Coulomb criterion is used to control shear behaviour at contacts for dry granular materials. DEM has been used for examining several aspects of soil behaviour. Table 1 provides some application of DEM to fundamental geomechanics. Table 1 shows that DEM has been used in granular mechanics [30], creep theory [35], anisotropy of clay [33], particle crushing [7, 26], strain localization [1, 14] and dynamic behaviour or liquefaction of sands [25, 27]. To illustrate if these topics are still interesting to modern georesearchers, Table 2 presents main topics in this workshop (Modern Trends in Geomechanics workshop, 26–29 June 2005, Vienna, Austria). Table 2 shows that these topics are all discussed in this workshop. In addition, many researchers in this workshop discuss four other aspects in geomechanics: constitutive modelling, unsaturated soils, natural soils and boundary value problems. All the topics reflect the trends in geomechanics in the 21st century.

Table 1. Some application of DEM to fundamental geomechanics

topics	features of the study	investigators
granular mechanics	examining failure criteria of granular material; standard contact laws for granular material	Thornton (2000) [30]
creep theory	examining the theory of rate processes; contact laws incorporating creep theory	Kuhn and Mitchell [35]
anisotropy of clay	examining the mechanism of anisotropic behaviour of clay; contact laws incorporating repulsive force	Anandarajah (2000) [33]
particle crushing	examining the mechanism of particle fracture and crushing; contact laws for cementation incorporated in *PFC3D*	McDowell and Harireche (2002); Cheng et al. (2003) [7, 26]
strain localization	examining the mechanism of shear banding process; standard contact laws or that incorporating rolling resistance for granular material	Bardet and Proubet (1991); Iwashita and Oda (1998, 2000) [1, 14]
dynamic behaviour or liquefaction	regularly-packed disk assemblies considering motion of pore water or randomly-packed disk assemblies using the "quasi-pore pressure" method	Kiyama et al. (1994); Ng and Dobry (1994) [25, 27]

Table 2. Main topics in this workshop (Modern Trends in Geomechanics workshop, 26–29 June 2005, Vienna, Austria)

topics	presenters
granular mechanics	Bolton M, Borja R, Doanh T, Harris D, Hill J, Huang A-B, Jiang MJ, Lade P, McDowell G, Ooi J, Spencer T, Tagmanini C, Viggiani C, Wu W, Yu H-S
creep theory	Gudehus G, Yin J-H.
anisotropy	Bolton M, Doanh T, Shao J-F, Wu W
particle crushing	Bolton M, McDowell G, Vardoulakis I
strain localization	Bauer E, Bolton M, Borja R, Chambon R, Darve F
dynamic behaviour or liquefaction	Bauer E, Bolton M, Huang A-B, Niemunis A, Zhang J-M
constitutive modelling	Bolton M, Collins I, Darve F, Gens A, Gudehus G, Harris D, Herle I, Houlsby, Jiang MJ, Lade P, Niemunis A, Nova R, Puzrin AM, Selvadurai APS, Shao JF, Shen ZJ, Tagmanini C, Viggiani C, Wu W, Yin J-H, Yu H-S
unsaturated soils	Gens A, Jiang MJ, Molenkamp F, Shen ZJ, Yu H-S
natural soils	Bolton M, Huang A-B, Jiang MJ, Nova R, Shen ZJ, Yu H-S
boundary value problem	Bolton M, Harris D, Jiang MJ, Moore I, Ponter A, Salgado R, Shen ZJ, Spencer T, Yu H-S, Zhang J-M
others	Bolton M, Cristescu ND, Dafalias Y, Jiang MJ, Ooi J, Ponter A, Selvadurai APS, Shao JF, Sheng Y, Sikora Z, Triantafyllidis T, Vermeer P

The main objective of this chapter is to introduce the application of DEM to these latter four aspects in geomechanics. The introduction is limited to those related to the first author's two postdoctoral fellowships in Canada and UK. After introducing the DEM code developed by the first author, we shall present its application to noncoaxiality of granular materials, effective stress in unsaturated soils, bonding effect in natural soils and penetration mechanism in granular ground. We shall mainly introduce the target, contact models and main results in each application. The reader is referred to the references for their further detail.

2 Discrete Element Method (DEM)

The two-dimensional (2-D) DEM code used has techniques similar to those proposed by Cundall and Strack [10]. The code was first developed in Canada [19–21] and improved further in UK [16–18, 23, 24] by the first author and his co-workers, namely *NS2D* hereafter. Each particle of the soil mass is a rigid disk that is identified independently with its own mass, m, moment of inertia, I_0 and contact properties as illustrated in Figs. 1, 4 and 8 later. The total

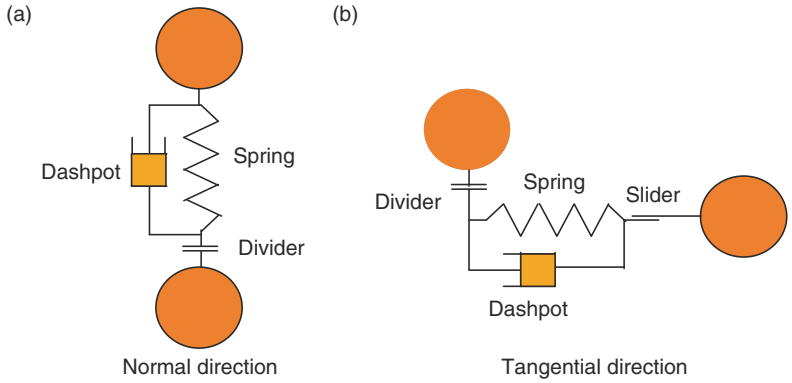

Fig. 1. Standard contact models of two rigid disks used in DEM for examining noncoaxial continuum model

unbalanced force for motion $F_i^{(m)}$ (i represents x or y direction) and moment M_0 acting on each particle are computed and then used to estimate the instantaneous acceleration of each particle, a, based on Newton's second law. The acceleration a is used to calculate velocities and then displacements in the x and y directions. This is repeated at each time increment until the simulation is stopped. For each particle, the normal and tangential contact forces for motion, denoted by $F_{\mathrm{n}}^{(m)}$ and $F_{\mathrm{s}}^{(m)}$, respectively, are summed up over the p neighbours, giving:

$$\frac{\partial^2 x_i}{\partial t^2} = \frac{1}{m}\sum_{r=1}^{p} F_i^{(m)r}; \quad \frac{\partial^2 \theta}{\partial t^2} = \frac{1}{I_0}\sum_{r=1}^{p} M_0^r. \tag{1}$$

In the *NS2D* code, $F_{\mathrm{n}}^{(m)}$ is calculated by a function f_{n}

$$F_{\mathrm{n}}^{(m)} = f_{\mathrm{n}}(F_{\mathrm{n}}, D_{\mathrm{n}}, R_{\mathrm{n}}), \tag{2}$$

where F_{n} is the normal contact force calculated from the overlaps of particles. D_{n} is the normal damping force and R_{n} is the normal bonding strength that results from capillary water (CW) for unsaturated soil or from cementatious material for natural soils. Note that R_{n} is always zero for dry granular material. A typical function in (2) for unsaturated or natural soils can be expressed as

$$F_{\mathrm{n}}^{(m)} = F_{\mathrm{n}} + D_{\mathrm{n}} - R_{\mathrm{n}}, \tag{3}$$

which is termed as "translational-axis method" for bonded material [20, 24].

$F_{\mathrm{s}}^{(m)}$ is determined by

$$F_{\mathrm{s}}^{(m)} = F_{\mathrm{s}} + D_{\mathrm{s}}, \tag{4}$$

where F_{s} is the tangential contact force and D_{s} is the tangential damping force. $D_{\mathrm{s}} = 0$ stands in the case that F_{s} exceeds the peak shear strength $F_{\mathrm{s}}^{\mathrm{peak}}$

for contacts with intact bonds or residual shear strength $F_{\mathrm{s}}^{\mathrm{resid}}$ for contacts without intact bonds.

$F_{\mathrm{s}}^{\mathrm{peak}}$ ($F_{\mathrm{s}}^{\mathrm{resid}}$) can be described by a function f_{s}^{p} (f_{s}^{r})

$$F_{\mathrm{s}}^{\mathrm{peak}} = f_{\mathrm{s}}^{p}(F_{\mathrm{n}}, \tan\varphi_{\mu}, R_t);\ F_{\mathrm{s}}^{\mathrm{resid}} = f_{\mathrm{s}}^{r}(F_{\mathrm{n}}, \tan\varphi_{\mu}), \tag{5a,b}$$

where $\tan\ \varphi_{\mu}$ is called the interparticle friction coefficient. R_{t} is the tangential bonding strength that results from CW for unsaturated soil or from cementatious material for natural soils. Typical functions in (5) for dry granular material and natural soils can be respectively expressed as

$$F_{\mathrm{s}}^{\mathrm{peak}} = F_{\mathrm{n}}\ \tan\ \varphi_{\mu} = F_{\mathrm{s}}^{\mathrm{resid}} \qquad \text{for dry granular material,} \tag{6a,b}$$

$$F_{\mathrm{s}}^{\mathrm{peak}} = F_{\mathrm{n}}\ \tan\ \varphi_{\mu} + R_t; F_{\mathrm{s}}^{\mathrm{resid}} = F_{\mathrm{n}} \tan\varphi_{\mu} \quad \text{for natural soils} \tag{6c,d}$$

Equation (6) are the Mohr–Coulomb criterion. If two particles are separated due to normal tension force in excess of R_{n}, then $F_{\mathrm{n}}^{(m)} = 0$, $F_{\mathrm{s}}^{(m)} = 0$. Damping, as well as frictional sliding, is used in DEM analyses to dissipate energy due to the dynamic formulation of the model.

The strain tensor is obtained by the position change of rigid boundaries as follows:

$$\varepsilon_{ij} = \Delta h_i / h_j, \tag{7}$$

where Δh_i is the deformation of specimen in i direction and h_j is total length of specimen in j direction at time t.

The stress tensor is defined on the rigid boundaries as follows:

$$\sigma_{ij} = (\sum f_i)/h_j, \tag{8}$$

where f_i is the contact force acting on the boundary with the normal direction as i. In addition, a unit of length (m) is implicitly included in (8) in the direction vertical to the plane.

Because *NS2D* is a 2-D DEM code, the density of specimen is described in term of planar void ratio e_{p} by

$$e_{\mathrm{p}} = (A - A_{\mathrm{g}})/A_{\mathrm{g}}, \tag{9}$$

where A and A_{g} are the total area of the specimen and the sum of the area of all grains (disks), respectively.

NS2D can form an assembly of particles according to its grain size distribution. The number of particles of each specific radius was calculated in the DEM by

$$N_{(i)} = \frac{P_{(i)}}{r_{(i)}^{s} \cdot P} \cdot N, \tag{10}$$

where $N_{(i)}$ is the total number of particle i with specific radius $r_{(i)}$ and $P_{(i)}$ is weight percentage of particle i. N is total number of particles of different

radii used in the DEM analyses. Parameter s is 2 for disk. P is a variable obtained by

$$P = \sum_{i=1}^{n_{\mathrm{p}}} \frac{P_{(i)}}{r_{(i)}^{s}}, \tag{11}$$

where n_{p} is the type number for particles.

We shall in Sect. 3 introduce the application of *NS2D* to geomechanics, which are related to the four topics in this workshop.

3 Application of DEM to Geomechanics

In this section, we shall present the application of DEM to noncoaxiality of granular materials, effective stress in unsaturated soils, bonding effect in natural soils and penetration mechanism in granular ground. We shall introduce each application by its target, contact model and main results

3.1 Noncoaxiality of Granular Materials

Noncoaxiality means the noncoincidence of the principal stress tensor and the principal plastic deformation-rate tensor, a known feature of granular material. Since granular materials are inherently *discrete* with *particle rotation* and a grain length scale, we shall examine if these features can be included in a noncoaxial continuum model. The detailed information can be found in the references [17, 18].

Given a randomly packed assembly composed of particles of different sizes, a novel kinematic variable, the "*averaged micropure rotation-rate*" (APR), denoted by ω_3^c, was proposed as follows [17]

$$\omega_3^c = \frac{1}{N}\sum_{k=1}^{N} \dot{\theta}^p = \frac{1}{N}\sum_{k=1}^{N} \left[\frac{1}{r^k} \left(\dot{\theta}_1^k r_1^k + \dot{\theta}_2^k r_2^k \right) \right], \tag{12}$$

where the summations are over the N contacts in the mass body, by counting each contact k, which is shared by two particles of radii r_1^k and r_2^k, the angular velocity $\dot{\theta}_1^k$ and $\dot{\theta}_2^k$. The common radius is $r^k = 2r_1^k r_2^k/(r_1^k + r_2^k)$. ω_3^c can also be expressed in terms of a sum over particles instead of contacts [21]. It is a kinematic variable generally related to particle rotations and particle sizes, which does not appear in classical continuum mechanics yet. But, it can be unified with kinematic variables in standard continuum mechanics, see later.

In standard continuum mechanics, the Eulerian velocity field v is considered. The deformation rate D_{ij} and the spin tensor W_{ij} are then defined by

$$D_{ij} = \frac{1}{2}\left(\frac{\partial v_i}{\partial x_j} + \frac{\partial v_j}{\partial x_i} \right); \quad W_{ij} = \frac{1}{2}\left(\frac{\partial v_i}{\partial x_j} - \frac{\partial v_j}{\partial x_i} \right), \tag{13a,b}$$

where v_i denotes the velocity components, with i or $j = 1, 2$ in the 2-D case.

We propose a tensor R_{ij} as follows:

$$R_{ij} = \frac{\partial v_i}{\partial x_j} + e_{3ij}\omega_3^c, \quad \text{where} \quad e_{3ij} = \begin{bmatrix} 0 & 1 \\ -1 & 0 \end{bmatrix}, \tag{14a,b}$$

which leads to the symmetric (skew-symmetric) tensor d_{ij} (w_{ij}) by

$$d_{ij} = \frac{1}{2}(R_{ij} + R_{ji}); \quad w_{ij} = \frac{1}{2}(R_{ij} - R_{ji}) \tag{15a,b}$$

Relationships amongst D_{ij}, W_{ij}, d_{ij} and w_{ij} can be obtained from (13)–(15)

$$d_{ij} = D_{ij}; \quad w_{ij} = W_{ij} + e_{3ij}\omega_3^c \tag{16a,b}$$

which shows that d_{ij} indeed is deformation rate tensor. w_{ij} is a frame indifferent tensor composed of both W_{ij} and ω_3^c, even though none of then is an objective continuum variable. When $\omega_3^c = 0$, the tensor w_{ij} will reduce to W_{ij}.

We shall present a new noncoaxial continuum model for granular material [17], which is based the unified double-slip plasticity model [36] and the d_{ij} and w_{ij}. The unified kinematic equations governing the velocity field proposed by Harris (1995) are

$$(D_{11} + D_{22}) \cos\left(\frac{\nu + \xi}{2}\right) = [(D_{11} - D_{22}) \cos 2\psi_\sigma + 2D_{12} \ \sin \ 2\psi_\sigma] \times \sin\left(\frac{\nu - \xi}{2}\right), \tag{17a}$$

$$2\,(\vartheta + W_{12}) \sin\left(\frac{\nu + \xi}{2}\right) = [(D_{11} - D_{22}) \sin 2\psi_\sigma - 2D_{12} \ \cos \ 2\psi_\sigma] \times \cos\left(\frac{\nu - \xi}{2}\right), \tag{17b}$$

where the quantities ν and ξ are material parameters, and ϑ is an angular velocity which may be given a number of physical interpretations. D_{ij} and W_{ij} are the deformation rate tensor and the spin tensor respectively as shown in (13). The principal stress inclination ψ_σ is defined as the angle of major principal stress axis to x-axis, in terms of Cauchy stress tensor σ_{ij}

$$\psi_\sigma = \frac{1}{2} \arctan\left(\frac{2\sigma_{12}}{\sigma_{11} - \sigma_{22}}\right). \tag{18}$$

The new continuum model was proposed in essence by identifying the quantity ϑ in (17) with ω_3^c. By further choosing $\nu = \phi$, the angle of internal friction, $\xi = \phi - 2\chi$ where χ is a dilatancy parameter, and (15), the new model

for a class of dilatant materials, becomes

$$(d_{11} + d_{22}) \cos(\phi - \chi) = [(d_{11} - d_{22}) \cos 2\psi_\sigma + 2d_{12} \sin 2\psi_\sigma] \sin \chi, \quad (19a)$$

$$2w_{12} \sin(\phi - \chi) = [(d_{11} - d_{22}) \sin 2\psi_\sigma - 2d_{12} \cos 2\psi_\sigma] \cos \chi, \quad (19b)$$

or further reduced for incompressible materials,

$$d_{11} + d_{22} = 0; \quad 2w_{12} \sin \phi = (d_{11} - d_{22}) \sin 2\psi_\sigma - 2d_{12} \cos 2\psi_\sigma \quad (20a,b)$$

Equations (19b) or (20b) show that, generally, the constitutive equations for granular materials presented here are noncoaxial due to the presence of w_{ij}. Since the original unified plasticity model is called the double-slip model and now is extended by ω_3^c, the new model may be called the "*double-slip and rotation-rate model*" (DSR^2 model).

The *NS2D* was used to carry out tests to verify the DSR^2 model, since no geolab technology is available to measure ω_3^c yet. The contact model used is a standard contact laws shown in Fig. 1. This simple contact model consists of a normal (tangential) contact model to resist traction (shear) force. They are similar in their principle: both include a spring reflecting an elastic behaviour of the contact before failure and a dashpot that allows energy dissipation and quasi-static deformations in DEM analyses. The normal contact model includes a divider to simulate the fact that no traction force is transmitted through the contact when the particles are separated. The tangential contact model includes a slider that provides the contact a shear resistance controlled by the Mohr–Coulomb criterion.

The granular material used has a distribution of particle size shown in Fig. 2a. The material is composed of discs with a maximum diameter of

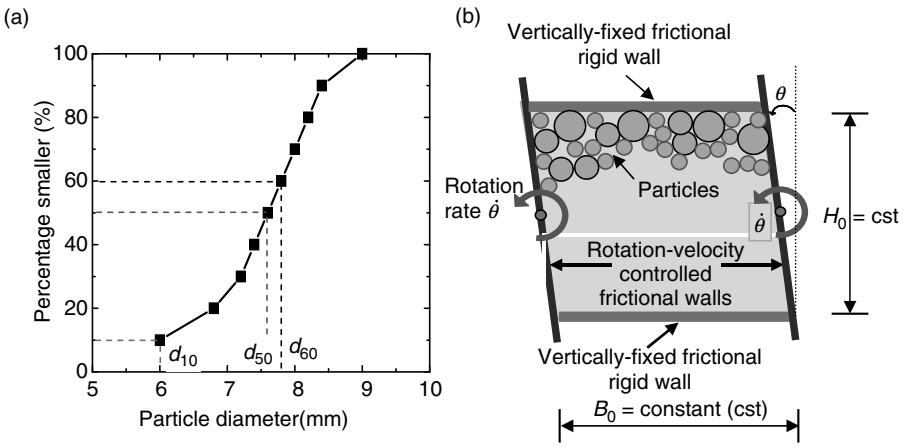

Fig. 2. Distribution of grain size used in DEM verification on noncoaxial models (**a**); boundary conditions in simple shear stage (**b**)

9.0 mm, and a minimum diameter of 6.0 mm, an average grain diameter $d_{50} = 7.6$ mm and uniformity coefficient $d_{60}/d_{10} = 1.3$. For simplicity, simple shear tests were simulated for the verifications, in which the specimens are regarded to be "incompressibile", i.e. their volume change is zero under shear. The incompressibility is targeted by (a) selecting specimens that internally tends to perfect plasticity with its dilatancy–contractancy close to zero; (b) controlling boundary condition that the volumetric strain rate is zero under shear. The samples were prepared by the under-compaction technique [19], which efficiently provided homogeneous loose/medium-dense samples ($e_{\mathrm{p}} = 0.32/0.30$). The boundary condition in the simple shear stage is shown in Fig. 2b. The particle-wall friction coefficient was set to a value of 0.5, the same value as the interparticle friction coefficient, followed by simple shear under constant volume. The top and bottom rigid walls were vertically fixed, but moved horizontally by following the side rigid walls which rotated with rotation rate $\dot{\theta}$. Monotonic and cyclic simple shear tests were carried out with different variations of $\dot{\theta}$. Using (13), (16), (20b) and theoretical description of velocity field under simple shear, the theoretical APR predicted by the DSR^2 model may be written:

$$\mathrm{APR} = \left(\frac{\cos\ 2\psi_\sigma}{2\ \sin\ \phi} + \frac{1}{2} \right) \dot{\theta}, \tag{21}$$

which, as well as ω_3^c, can be obtained in the DEM tests [18].

Figure 3a provides the APRs measured and predicted by the DSR^2 model for the medium-dense specimen in the monotonic DEM tests, and their respective average values for all specimens deduced from all the monotonic DEM tests. For the predicted values, $\phi = 30^\circ$ was used in (21), which is very close to that measured in experiments on granular materials. Figure 3a shows that although there is very slight difference between the predicted and measured APRs, a good agreement appears between these quantities during the DEM tests. Both of them are positive, and decrease slightly with the shear strain in the tests. Good agreement is also observed between the predicted and the measured APRs in the tests on all the other specimens of different density. For conciseness, the average values of the predicted and the measured APRs are provided in Fig. 3a to represent these results. Again, a good agreement is evidently observed in Fig. 3a between the predicted and the measured values.

Figure 3b presents the APRs measured and predicted by the DSR^2 model in the cyclic DEM simple shear tests on loose/medium-dense specimens. Figure 3b shows that there is also a good agreement between these predicted and measured quantities in the DEM tests. They are both periodic, varying between 0.0025 and $-0.0025\,\mathrm{rad\,s^{-1}}$ with the same period during cyclic shear tests on the different specimens. Hence, the numerical results in Fig. 3 confirm that: (a) DSR^2 model is a reasonable extension of the unified double-slip plasticity model; (b) DEM is a useful tool in examining the noncoaxiality of granular mateials.

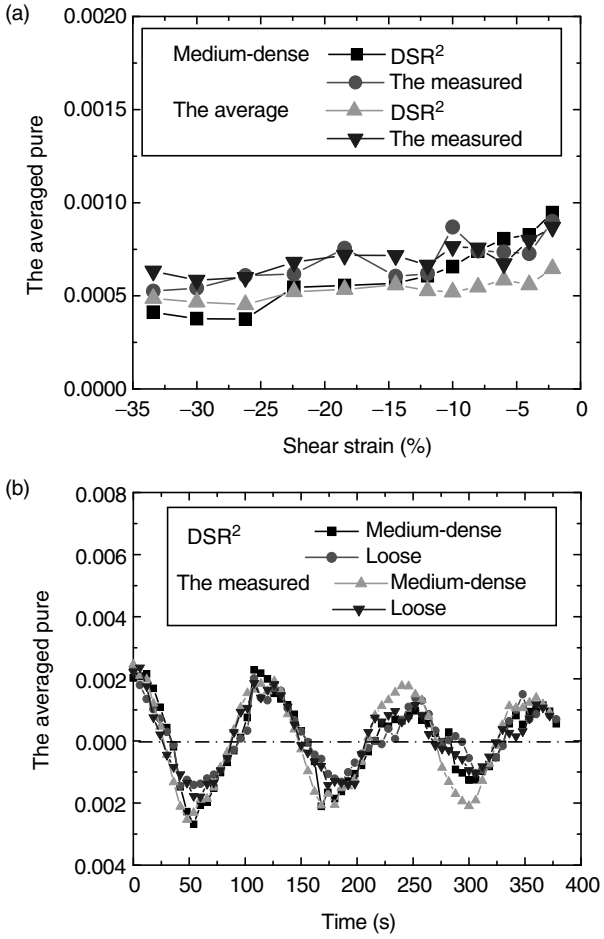

Fig. 3. The APRs measured and predicted by noncoaxial models (DSR^2 model) for the medium-dense specimen, and their respective average values for all specimens in the all monotonic DEM simple shear tests (**a**); the measured and the predicted APRs in the cyclic DEM simple shear tests on loose/medium-dense specimens (**b**)

3.2 Effective Stress in Unsaturated Soils

One of long-term arguable topics in unsaturated soils is the existence and applicability of effective stress [13, 15]. We shall here introduce micromechanically defined effective stress and its verification by DEM from the viewpoint of strength. In the definition, the interparticle force due to CW is composed of two components: one due to suction and the other due to the surface tension which is missing in unsaturated soil mechanics.

Equation (8) is widely used in geolabs to measure stresses. This stress tensor is equivalent to net stress ($\sigma_{ij} - u_{\mathrm{a}}$) used in unsaturated soil mechanics

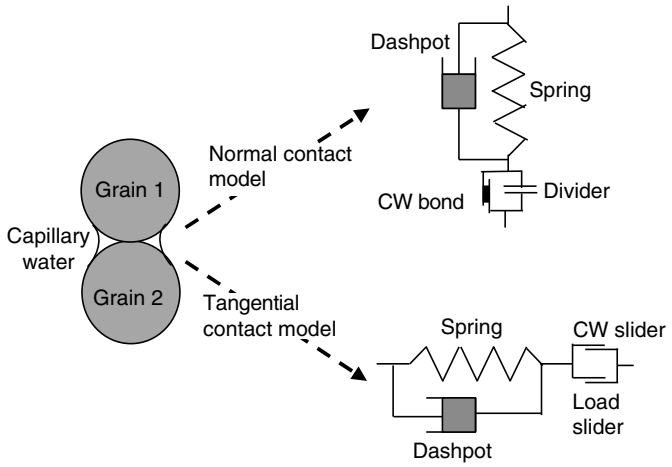

Fig. 4. Contact model for CW [20]

because the pore air pressure u_{a} is used as a reference pressure and is effectively zero in many practical problems. In contrast, in micromechanics on dry granular media, there are several expressions of the stress tensor, and controversies still exist on such topics as the asymmetry [2, 6, 11]. We consider three symmetric average stress tensors with all defined within the volume V:

$$\sigma_{ij} = \frac{1}{V}\sum_{k=1}^{N} R_k \sum_{c=1}^{p} l_i^c T_j^c; \quad \sigma_{ij} = \frac{1}{V}\sum_{a=1}^{M} T_i^a l_j^a; \quad \sigma_{ij} = \frac{1}{V}\sum_{a=1}^{2M} x_i^a T_j^a \quad (22\text{a,b,c})$$

where T_i^c and l_j^c are the contact force vector and the contact orientation vector at contact c of particle k. R_k is the radius of particle k. N is the number of particles in V and p is the number of contacts on particle k [10]. M is the number of contacts in V. T_i^a and l_j^a are the contact force vector and the contact orientation vector at contact a in V [8]. x_i^a defines the coordinates of contact a referenced to the particle centroid [31].

Nevertheless, the average stress tensors in (22) are all equivalent to that by computing the forces exerted upon the peripheral particles along the assembly's boundary S.

$$\sigma_{ij} = \frac{1}{V}\sum_{\beta\in S} T_i^\beta l_j^\beta. \quad (23)$$

Based on (22)–(23) and the concepts proposed by one of the authors [22], two new stress tensors have been defined by Jiang et al [16, 21]. The first one is defined as the stress tensor in (22) or (23) when T_i^c (T_i^a or T_i^β) is the interparticle force due to *both load and CW*, then $\sigma_{ij} = \sigma''_{ij}$. It is termed generalized effective stress (GES) and denoted by σ''_{ij} here to distinguish it from the effective stress σ'_{ij} used in saturated soil mechanics. The second one is

defined as the stress tensor in (22) or (23) when T_i^c (T_i^a or T_i^β) is equal to interparticle force *solely due to CW*, then $\sigma_{ij} = \sigma_{ij(eq)}$. It is termed the GES due to suction (GESS) here to follow the habit in geomechanics. The *GES due to suction* indeed should be referred to as the *GES due to CW* since the interparticle force component due to the surface tension is included, based on the theoretical work by Fisher [12]. The stress $\sigma_{ij(eq)}$, in principle, is similar to other terms, such as "normal stress", "equivalent effective stress", "effective boundary stress" etc. used in the literature to describe the effect of suction on shear strength. We use a subscript "eq" in $\sigma_{ij(eq)}$ to note that GESS is similar to "equivalent effective stress" in essence. Note that both GES and GESS are defined explicitly in terms of interparticle forces via (22) or (23) here. More importantly, interparticle force due to CW is a theoretical solution [12], composed of components due to both the suction and the surface tension. We shall next introduce DEM examination on the strength envelopes of unsaturated soils described in different stress tensors, since no geolab technology is available for this task yet.

The contact model used for unsaturated soils is illustrated in Fig. 4, which was proposed by Jiang et al. [21]. It also consists of a normal (tangential) contact model to resist traction (shear) force. Compared with the standard model in Fig. 1, the normal contact model introduces additionally a bond element to represent the action of CW whereas the tangential contact model includes a CW slider. No traction/repulsive force is transmitted when the CW bond is broken and the particles are separated. The tangential contact model includes two sliders that provide the contact a shear resistance controlled by the Mohr–Coulomb criterion, with one component linked to the CW and the other to the load. The introduction of the CW slider comes from the fact that the interparticle force due to CW increases the normal contact force at contact and thus consequently its shear resistance. Note that the CW bond is recoverable after its breakage, i.e. the CW bond recovers once particles contact again. The introduction of the CW bond and slider will lead to mechanical performance at the contact as elasto-brittle-plastic in normal and elasto-plastic in shear directions [21].

The particle assemblies of grain size distributions shown in Fig. 5 were used. They are fine-sized materials of the same mean diameter d_{50} as 0.0078 mm, but of different uniformity coefficients d_{60}/d_{10} as 1.3 for Distribution A and as 1.8 for Distribution B. A series of biaxial compression tests were carried out on the unsaturated granulates under different suctions and different confining stress. Note that, during the tests, the disappearance of manusci is simulated [21].

The peak shear strength envelopes described by net stresses (total stress over air pressure), i.e. the stresses defined in (8), are plotted in Fig. 6a, which are deduced from the biaxial compression tests on material A. Figure 6a shows that, for the material with zero suction (Su), the shear strength envelope almost passes through the origin, confirming that the material is cohesionless. The peak shear strength envelopes move parallel to each other with the

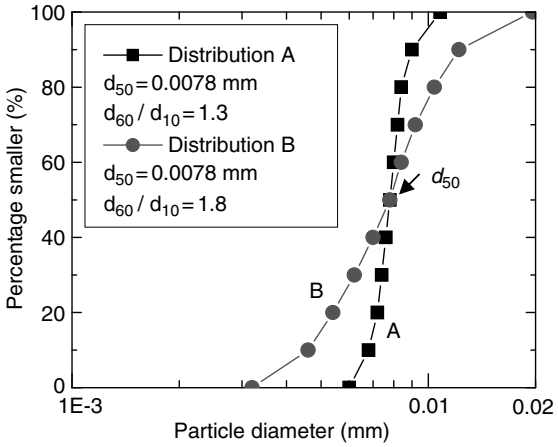

Fig. 5. Grain-size distributions used in the DEM analyses on unsaturated soils

increase of Su in the direction of increasing peak shear strength. A nonlinear relationship is observed between the deduced apparent cohesion and Su in Fig. 6b, which is in agreement with the observations from experiments.

The peak shear strength envelope described by the GES are illustrated in Fig. 7a, which are deduced from the same tests on material A as in Fig. 6. Figure 7a indicates that there appears to be a unique peak strength envelope for all the tests on the same material, even with different consolidation stress or different suction (Su). In addition, the peak friction angle deduced from this envelope is equal to 27.4°, very close to that deduced from the zero-suction envelope (26.5°) for the same material shown in Fig. 7a. In addition, Fig. 7b provides the peak strength envelope described by GES, deduced from 12 tests on material B. Figure 7b demonstrates that the results obtained from material B support the observations made for material A. Furthermore, Fig. 7 shows that there is also a unique residual shear strength envelope for each material if it is described in terms of GES. These observations seem to support the existence of "effective stress" for unsaturated soils [3] in controlling the shear strength. However, it is easy to realize that there is a difference between the original definition [3] and the definition given via (22) or (23). Since the applicability of the principle of effective stress has been debated for a long time [13, 15], it is beyond the purpose of this chapter to give any comments on the topic here. Hence, Figs. 6 and 7 show that DEM is a useful tool in examining the effective stress in unsaturated granular materials.

3.3 Bonding Effect in Natural Soils

Natural soils are sometimes named as "problematic soil", since their mechanical behaviour are evidently distinct from the reconstituted soils usually employed in laboratory. Their peculiar behaviour results from their

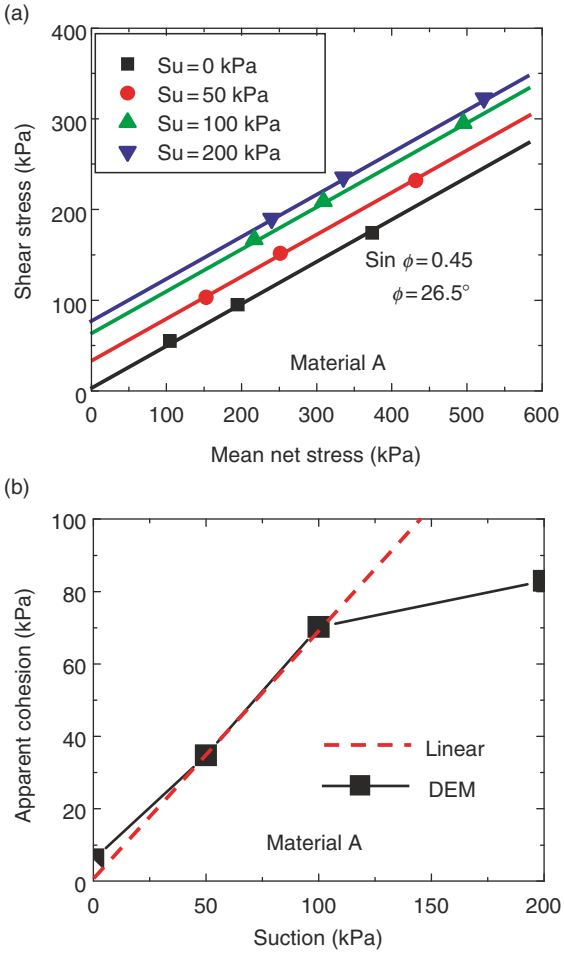

Fig. 6. Peak shear strength envelopes described by net stresses $[(\sigma_{\mathrm{v}} - \sigma_{\mathrm{h}})/2, (\sigma_{\mathrm{v}} + \sigma_h)/2 - u_{\mathrm{a}}]$ (**a**), and relationship between apparent cohesion and suction (Su) (**b**), obtained from biaxial compression tests on specimens of unsaturated material A

microstructure which is mainly characterized with bonding materials between particles or aggregates (bonds) and fabric. In this subsection, we shall present our most recent DEM application to natural sands: the link between the yielding and bond breakage; the Coop and Willson criteria on weak bonding and strong bonding [9]. The reader is referred to the reference [24] for further detail and other information. We chose DEM, because no geolab technology is available to measure bond information quantitatively and continuously yet.

The contact model used for bonds in natural soils is shown in Fig. 8, which was proposed by Jiang et al. [20, 24]. In comparison to the standard contact model in Fig. 1, the bond contact model introduces irrecoverable rigid-plastic

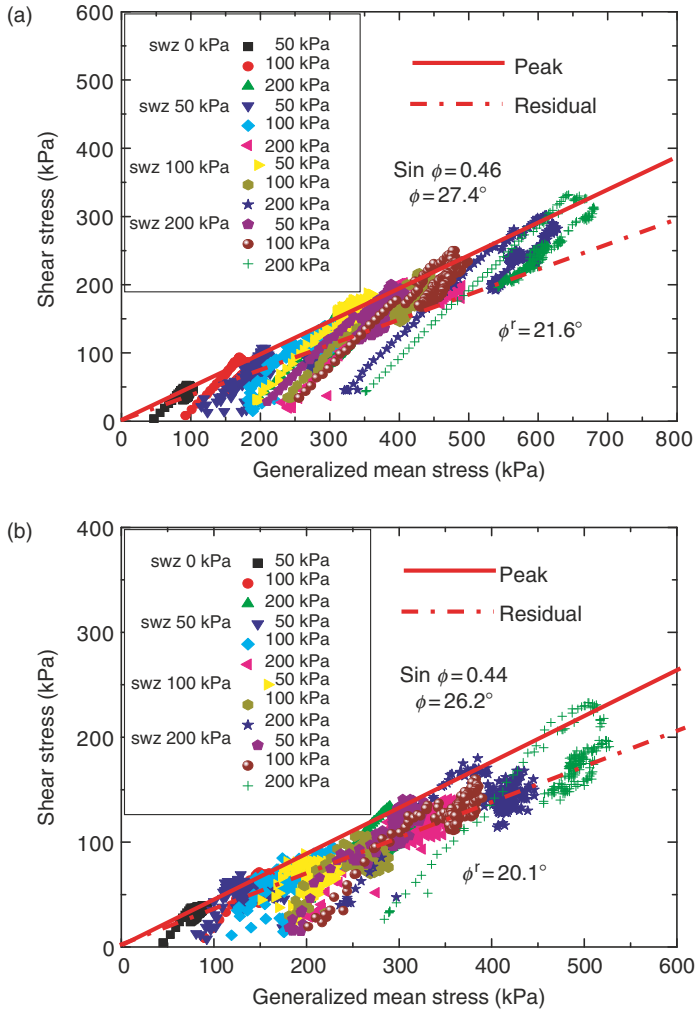

Fig. 7. Peak/residual shear strength envelopes under different suctions (Su), described by the GES $((\sigma''_v - \sigma''_h)/2, (\sigma''_v + \sigma''_h)/2)$, obtained from biaxial tests on unsaturated specimens of distribution A (**a**) and distribution B (**b**)

bond elements into the normal and tangential directions, respectively. Unlike the recoverable CW bond shown in Fig. 4, the bond here is irrecoverable, i.e. the bond will never recover its strength once the bond breaks. The rigid bond element is set to be parallel with divider (slider) in the normal (tangential) contact model to produce tension (shear) resistance, which represents the main action of bonding materials. The introduction of the bonds will lead to mechanical performance at the contact as elasto-brittle-plastic in both normal and shear directions [20, 24].

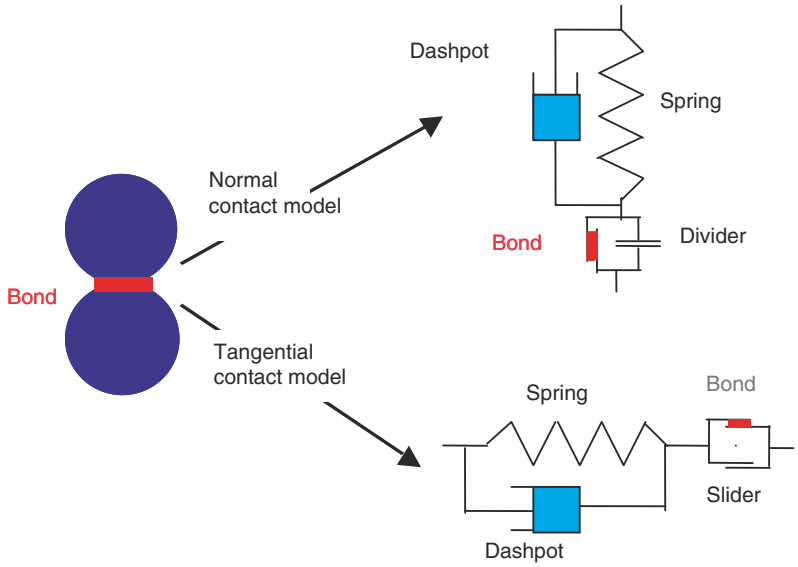

Fig. 8. Contact model proposed for bonds in natural soils [20]

The DEM material used has a distribution of particle size shown in Fig. 2a. The samples were prepared by the under-compaction technique [19] at very loose (planar void ratio $e_{\mathrm{p}} = 0.34$), loose (0.32), medium-dense (0.30) and dense (0.28) states, followed by bonding at contacts with different bonding strength. Isotropic consolidation tests were carried out on these bonded material, by following the procedure in laborotory [24].

For the first target in this subsection, Fig. 9a presents the variation of planar void ratio e_{p} with applied mean stress σ'_{m}, whereas Fig. 9b provides the broken contact ratio as a function of σ'_{m}, for the very-loose DEM materials of the bonding strength $R = 0, 1, 5, 10, 20, 30$ MN. The broken contact ratio is the proportion of the initially-bonded contacts that have been broken and can be regarded as a damage index of the bond breakage. The numerical curve obtained for the very-loose unbonded material in Fig. 9a provides a reference curve (normal compression line, NCL) for the other DEM tests. This numerical reference curve shows three features: there is a significant reduction in void ratio (e_{p}) against σ'_{m} when the pressure is relatively small (< 0.4 MPa); once σ'_{m} exceeds this value, the rate of void ratio reduction becomes smaller; this is true until the pressure is close to 10 MPa when the void ratio reduction rate increases again. The second feature in the DEM data comes from that that there is a little space for the assembly to be compacted further as it arrives at a relative dense state. The third feature of the numerical reference curve appears to be unusual. This peculiar feature is largely due to the fact that overlap between particles is excluded from calculating e_{p} by (9). Nevertheless, such ignorance does not affect the difference between bonded and unbonded materials.

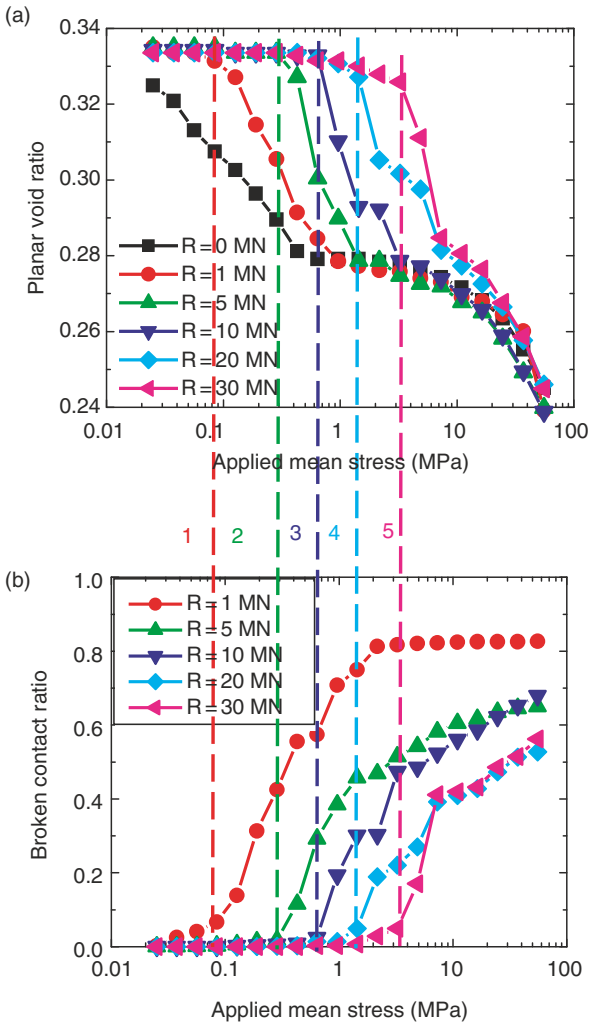

Fig. 9. The yielding observed in the DEM isotropic compression tests on very-loose materials of different bonding strengths from: (**a**) compression curves; (**b**) broken contact ratio

The bonded materials in Fig. 9a shows that the gross-yielding stress is well defined in light of volumetric strain (also known as *preconsolidated pressure* in the geotechnical community). They are able to go in part of the $e_{\mathrm{p}} - \sigma'_{\mathrm{m}}$ space that is not accessible to the unbonded material. At a given consolidation pressure, their void ratio is generally larger than unbonded counterpart. The preyield deformation is small; deformation increases abruptly if consolidation pressure is larger than the yield stress. Given a void ratio, the gross-yielding stress increases with the bonding strength. These are in agreement with the recent understanding on natural soils.

Micromechanically, Fig. 9b shows that the yielding can also be well defined for the samples in terms of breakage of bonds (the most-gradient point on the curve) for bonded specimens, which namely the microyielding hereafter. There is no or few bond breakage when σ'_{m} is smaller than the microyielding stress. Once σ'_{m} exceeds the microyielding stress, a large amount of bonds break. By comparing Fig. 9a with Fig. 9b, with the help of the dotted lines 1–5 in Fig. 9, it is observed that the microyielding stress appears to be equal to or slightly smaller than the respective gross yielding stress. Hence, the DEM results confirm that the gross yielding of natural sands must be related to bond breakage.

For the second target in this subsection, Fig. 10 provides schematic representation of the factors that might influence the effect of inter-particle cementing on the compression behaviour of a natural sand, proposed by Coop and Willson [9]. Figure 10 shows that a yield point in compression may be above (outside) or below (inside) NCL. The former one is termed as strong bonding (s), while the latter as weak bonding (w). They believe that whether the bonding is weak or strong depends on three factors, which, if regardless of particle breakage/crushing, are:

(a) The amount and strength of the cement deposited, with a smaller amount clearly being present for the weak bonding while a larger amount for the strong bonding, as indicated in Fig. 10a;
(b) The position of NCL. The same yield stress may be regarded as strong bonding if NCL is inside it, or weak bonding if NCL is outside, as shown in Fig. 10b;
(c) The initial density. A denser bonded material, even though it has the higher yield stress in compression, may show the weak mode of behaviour, whereas a looser bonded material of the lower yield stress may show the strong mode, as demonstrated in Fig. 10c.

Figure 11 presents the variation of e_{p} with σ'_{m} in the isotropic DEM compression tests, showing the three factors influencing the effect of bonds on the compression behaviour. Note that all materials are of the same coefficient of interparticle friction as $\mu = 0.5$, except specifically stated below. It can be seen:

(a) In Fig. 11a that the DEM medium-dense material predicts a weak bonding behaviour at bonding strength R =1 MN but a strong bonding behaviour at $R = 10$ MN. This confirms the first Coop and Willson criterion concerned with the amount and strength of the cement.
(b) In Fig. 11b that the response of the two unbonded very loose materials shows that NCL of $\mu = 0.5$ (NCL1 in the figure) is well above that of $\mu = 0.2$ (NCL2 in the figure), which is reasonable since larger μ produces larger resistance against compaction under a give pressure. The two bonded DEM medium-dense materials, which have $R = 1$ MN for $\mu = 0.5$ (Material 1) and $R = 1.5$ MN for $\mu = 0.2$ (Material 2), respectively, predict almost the same gross yielding stress, with the compression curves approaching their own NCL after yielding. In addition, the gross yielding

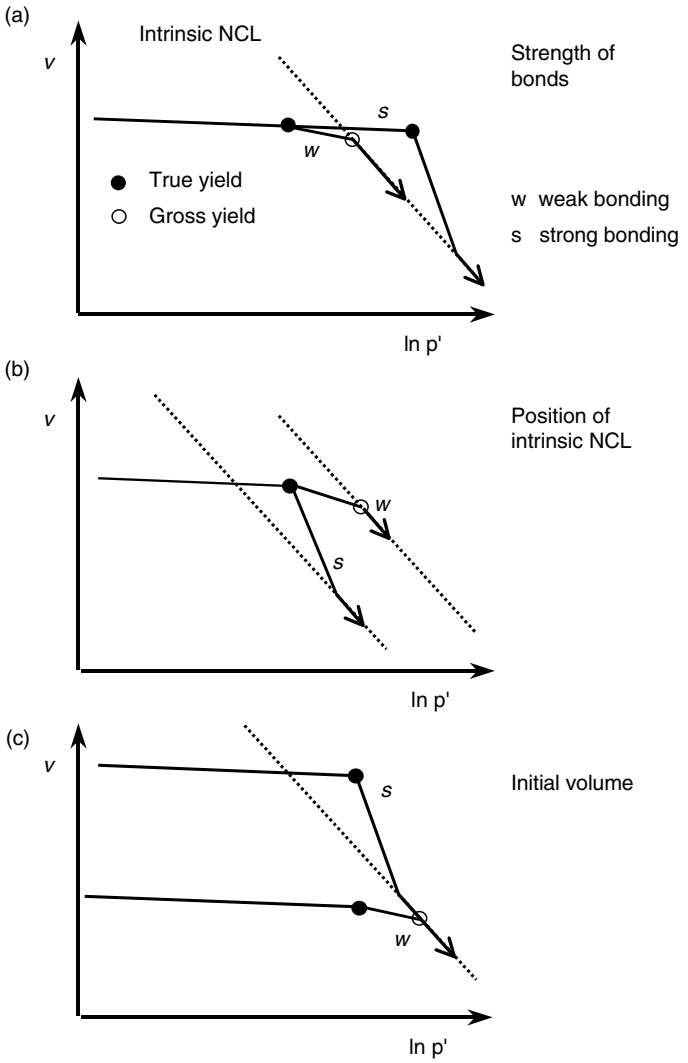

Fig. 10. Weak bonding (w) and strong bonding (s) criteria used by Coop and Willson [9] in investigating the factors might influence the effect of bonds on the compression behaviour of a sand: strength of bonds (**a**); position of NCL (**b**); initial volume (**c**). (after Coop and Willson [9])

stress of the two bonded materials lies between NCL1 and NCL2, indicating that Material 1 should be regarded as a weak bonding since NCL1 is outside it, while Material 2 a strong bonding since NCL2 is inside it. This confirms the second Coop and Willson criterion concerned with the position of the intrinsic NCL.

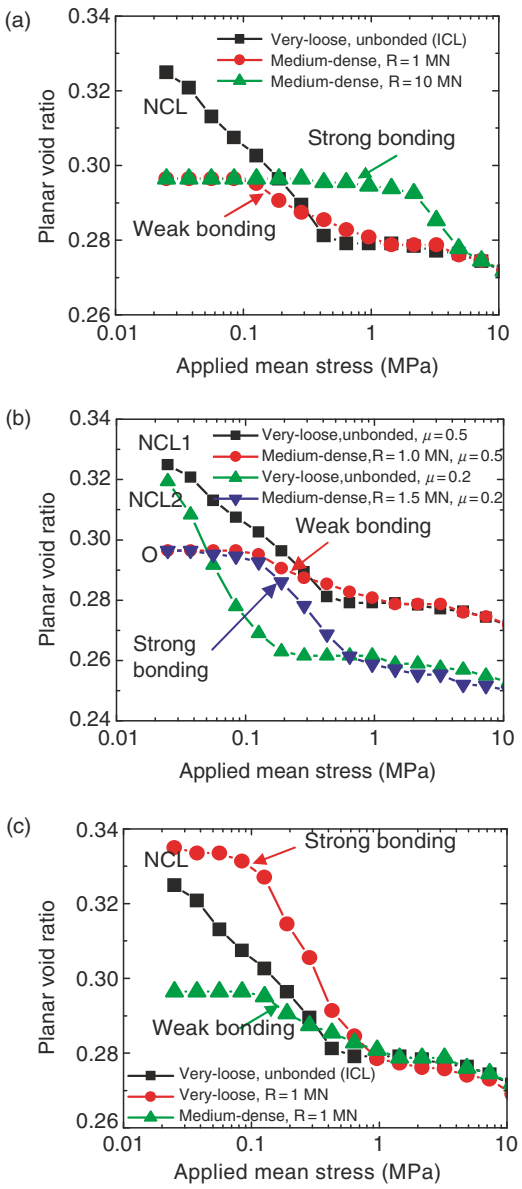

Fig. 11. The factors influencing the effect of bonds on the compression behaviour observed in the DEM tests on bonded materials: strength of bonds (**a**); position of NCL (**b**); and initial density (**c**)

(c) In Fig. 11c that the very-loose bonded DEM material, even though it has the lower yield stress in compression, shows the strong mode of behaviour, whereas the medium-dense bonded material of the higher yield stress shows the weak mode (these two bonded materials both have $R = 1$ MN). Hence, Fig. 11c confirms the third Coop and Willson criterion concerned with initial density.

Figures 10 and 11 show that DEM is a useful tool in examining the bonding effect in natural soils.

3.4 Penetration Mechanism in Granular Ground

The cone-penetration test is an insitu test in geotechnical engineering, in which a cone-shaped penetrometer is pushed into the ground at a constant rate. The resistance on the cone tip is measured and is then related to soil classification and soil properties. However, the penetration mechanism is still not very clear, due to the complex of the boundary-value problem which involves: (a) large relative sliding on the soil-penetrometer interface; (b) large deformation of the soil; (c) the high gradient of the field variables around the penetrometer, and (d) the soil involved undergoing an complex stress-path which is evidently different from that representative of the conventional laboratory tests. We shall introduce some plane-strain penetration mechanism in granular material using DEM, which is described in terms of displacement path and stress field. The detailed observation can be found in the reference [23]. We use DEM, because it can capture the aforementioned four features easily.

The contact mode used is a standard contact laws shown in Fig. 1. The material used is composed of 20 types of disks with a maximum diameter of 3.525 mm, a minimium diameter of 2.25 mm, an average grain diameter $d_{50} = 2.925$ mm and uniformity coefficient $d_{60}/d_{10} = 1.25$ [23]. Take advantage of the geometric symmetry of the problem, only half of the ground and half of the penetrometer are considered in the analyses. The target ground consists of 10,000 particles with planar void ratio of about 0.24, and has a depth and width as $16R$ and $17.5R$, respectively, where R represents the half-width of the penetrometer. The multi-layer under-compaction method [19] was used to generate the ground. After the ground is generated, half of a standard penetrometer with its radius as $R = 18$ mm and its apex angle as $60°$, is formed over the ground, as shown in Fig. 12. The penetrometer is described with three rigid walls, i.e. a frictional wall to simulate penetrometer *tip*, vertical frictional and frictionless walls to simulate penetrometer *sleeves*. The effect of tip-soil friction is to be clarified by choosing different frictional coefficient μ between the tip (or frictional sleeve) and particles. For simplicity, a perfectly-smooth (P-S) and a perfectly-rough (P-R), i.e. $\mu = 0$ and $\mu = \tan\phi_\mu$, respectively, are considered. The penetrometer is pushed downward at $2\,\mathrm{mm\,s^{-1}}$ (around $0.1\,\mathrm{R\,s^{-1}}$). The K_0 boundaries are used reduce possible boundary effects [23].

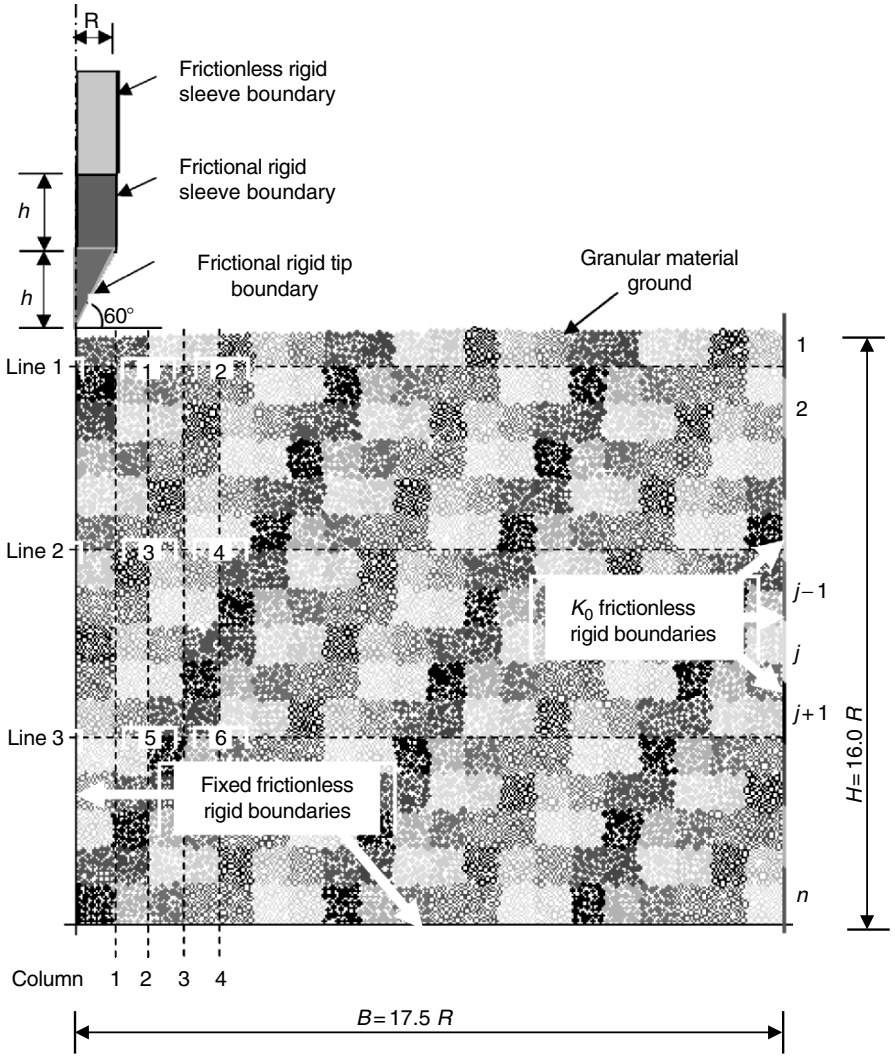

Fig. 12. Boundary conditions and observance positions in DEM penetration tests

Figure 13 provides the tip resistances (q_c) and their normalized values by the initial vertical stress (q_c/σ_{v0}), measured continually during the penetration in both P-R and P-S cases. Figure 13a shows that q_c increases with penetration depth with its initial gradient larger than the latter one in both cases. At the same depth, the P-R leads to q_c larger than the P-S as expected. Figure 13b shows that q_c/σ_{v0} initially increases, then decreases, and finally approaches a constant with depth. This is in agreement with that observed in centrifuge modelling [4].

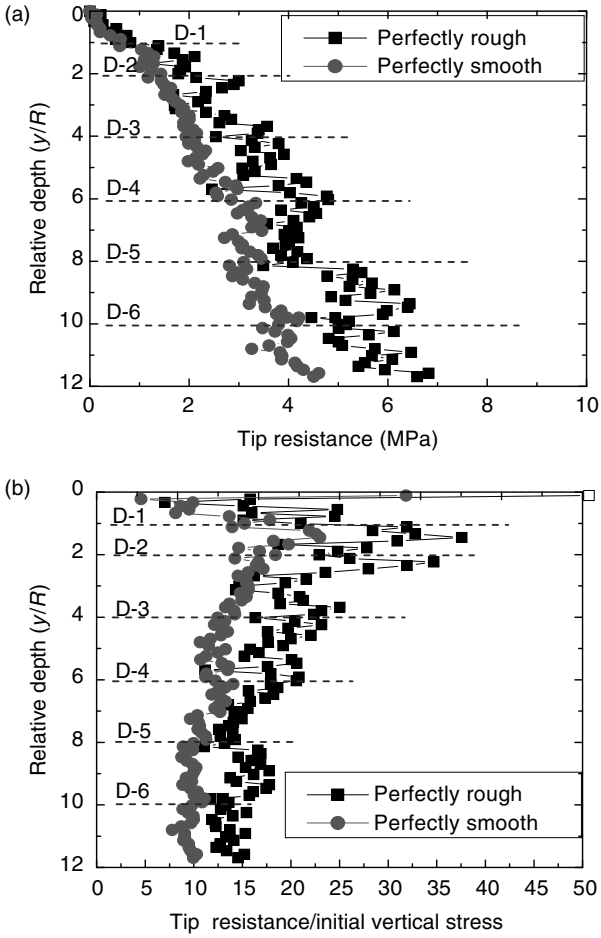

Fig. 13. Tip resistances, and their normalized values in DEM penetration tests

Figure 14 presents the displacement paths of the grid nodes on lines 1–3 (see Fig. 12). The vertical displacement is shown on an amplified scale in the figure. Figure 14 shows that:

(a) The final positions of the nodes on line 1 are all above their initial positions in both the perfectly-rough (P-R) and perfectly-smooth (P-S) cases. The nodes of $X/R > 2$ move upward and sideward, and their final position moves down with X/R. In contrast, those grid nodes of $X/R \leq 2$ initially moves downward and then upward while moving sideward ("hook" shape), and their final position moves up with X/R. The tip-soil friction shows evident influence on the displacement path of the nodes of $X/R \leq 2$, with the P-R leading to a larger downward displacement than the P-S.

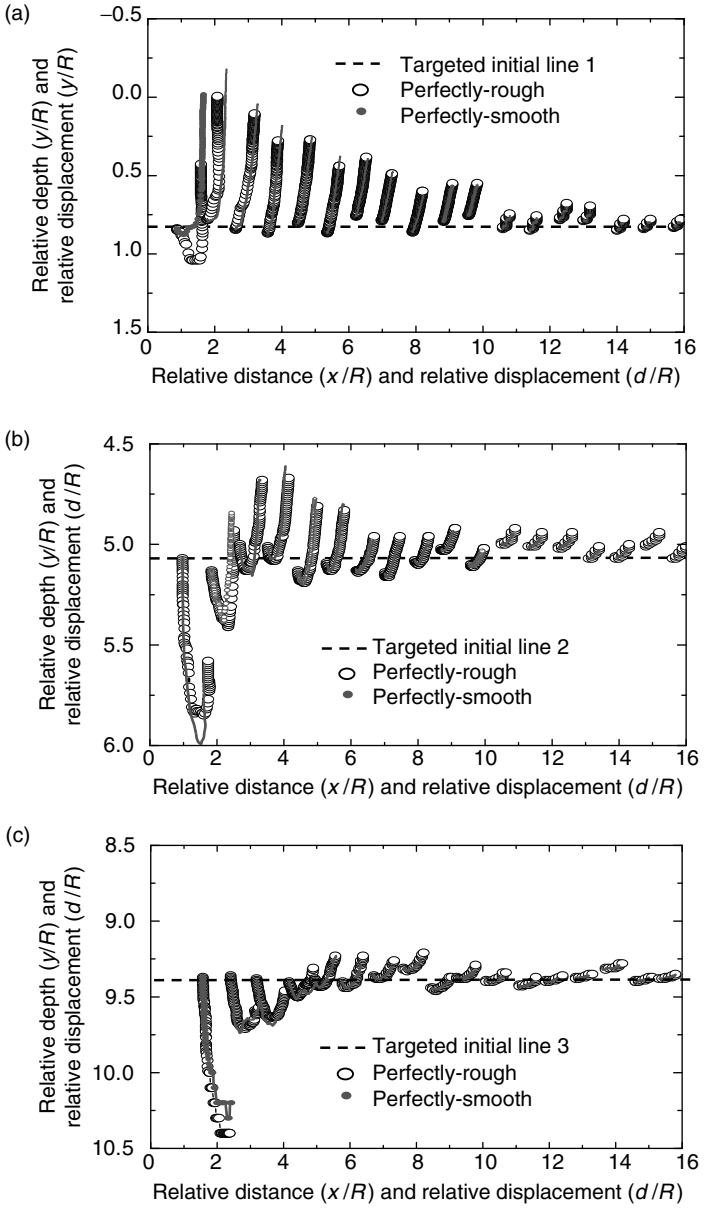

Fig. 14. Displacement paths of grid nodes on lines 1–3 (a–c) in DEM penetration tests

Furthermore, the P-R leads to a smaller upward displacement within $X/R \leq 6$ but a larger upward displacement for $X/R \geq 6$ than the P-S.

(b) On line 2, the final positions of the nodes are all above their initial positions in both P-R and P-S cases except for those nodes of $X/R \leq 1$. In addition, the final position of the nodes moves up with the increasing of X/R until $X/R = 4$, then moves down with X/R. The nodes of $X/R \leq 9$ show "hook" shape displacement path, while the grid nodes of $X/R > 9$ undergo only upward and sideward motions. The magnitude of downward motion is as large as about R for the node at $X/R = 1$, and decrease greatly with the increasing of X/R. Again, the tip-soil friction shows evident influence on the displacement path of the nodes of $X/R \leq 2$. Generally, the P-R leads to a smaller upward displacement within $X/R \leq 6$ but a larger upward displacement $X/R \geq 6$ than the P-S.

(c) The behaviour of grid nodes on line 3 is similar to that on line 2. However, all the nodes show evidently larger downward motions. The final positions of the grid nodes of $X/R \leq 3$ are all below their initial positions in both the P-R and P-S cases, while others are above the corresponding initial positions. The "hook" shape range is up to $X/R = 11$ and moreover the nodes of $X/R = 1$ move only downward and sideward.

Figure 15 provides the distributions of major and minor principal stress vectors during the tests. In the figure, the maximum major stresses are plotted by a vector of a constant length in order to illustrate the distributions clearly, although the maximum major stress differs in the perfectly-rough (P-R) and perfectly-smooth (P-S) cases and changes with penetration depth. Figure 15 shows that

(a) The penetration has great effect on the stress distribution in the area near the penetrometer, where high gradient of stresses including the values and directions is observed as expected. The maximum stresses occur near the tip, with its major principal stress nearly perpendicular to the tip;

(b) In the area close to the penetrometer, all the major principal stresses tend to be in a direction to the penetrometer centre. In the area far from the penetrometer, the penetration effect is very small, and hence the principal stresses are prodominatly controlled by the self-gravity with the major principal stress in the vertical directon as expected.

(c) The stresses beneath the tip point are larger in the P-R than in the P-S. This is consistent with the observation in Fig. 14 that the P-R leads to larger downward motion of the particles beneath the tip point than the P-S. In addition, the major principal stress near the tip has a larger inclination to Y-axis in the P-R than in the P-S, probably due to the shear force on the tip which is induced by the tip-soil friction.

Figures 13–15 show that DEM is also a useful tool to some complex boundary value problems in geotechnical engineering.

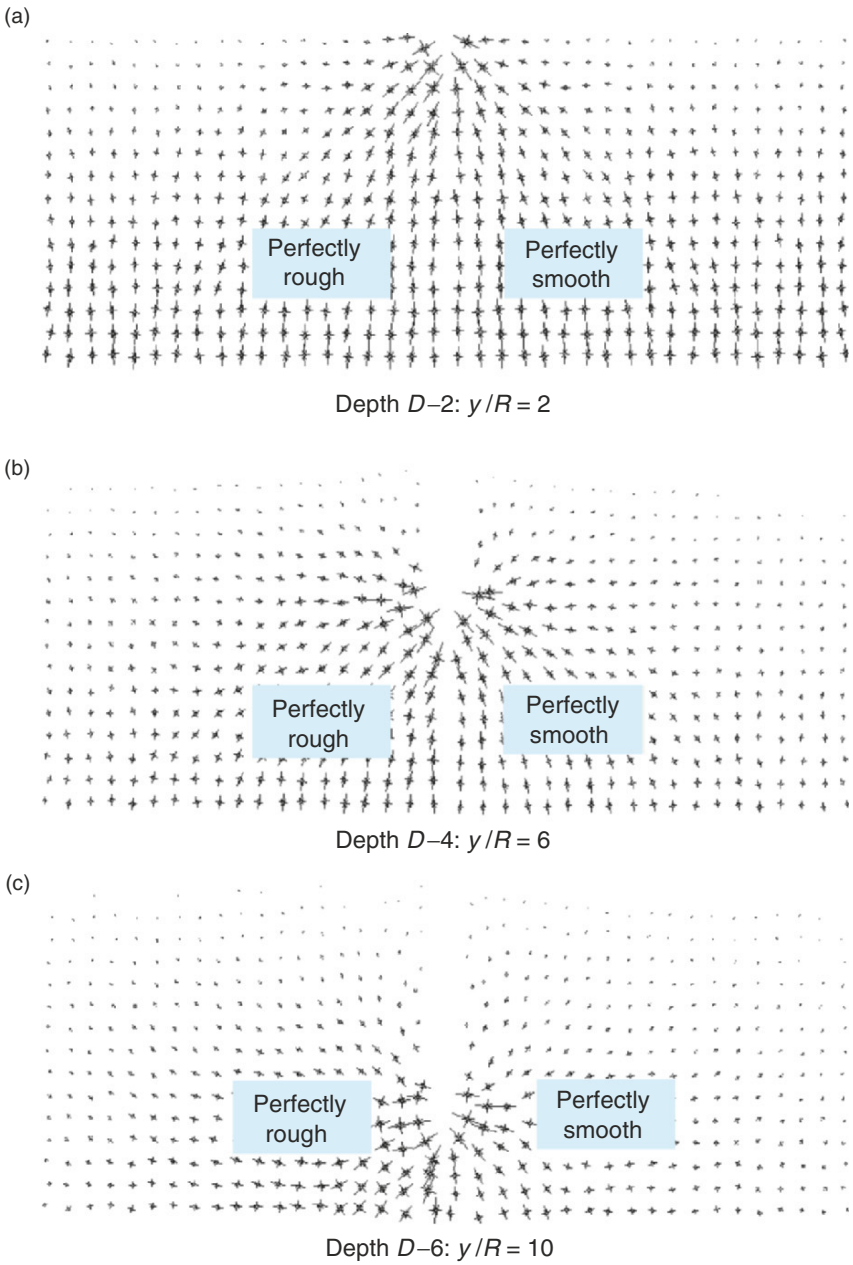

Fig. 15. Distributions of major and minor principal stress vectors in DEM penetration tests

4 Concluding Remarks

This chapter introduced recent application of the DEM to geomechanics, which is limited to the work related to the first author's two postdoctoral fellowships in Canada and UK and which are concerned with main topics in this workshop. It can be drawn from these application examples that:

(a) DEM is a numerical simulation technique that treats soils as an assembly of discrete materials, and can efficiently provide their macroscopic–microscopic responses under loading. The behaviour of assemblies can be controlled rigorously by very simple contact laws at interparticle contacts.
(b) One of the key issues on DEM is the contact laws at interparticle contacts. Different contact laws have been introduced and are found useful for investigating noncoaxiality of granular materials, effective stress in unsaturated soils, bonding effect in natural soils and penetration mechanism in granular ground.
(c) DEM is a very promising tool to solve some problems not only in fundamental geomechanics but also in complex boundary value problems in geotechnical engineering, which are difficult to solve by other geomethods.

Acknowledgements

The authors thank the EPSRC, UK with grant number GR/R85792/01; NSERC, Canada, for the financial support of the first author during his two postdoctoral fellowships. The contributions to the work in this article from Prof. Serge Leroueil and Prof. Jean-Marie Konrad, Department of Civil Engineering, Laval University, Canada; Dr. David Harris, School of Mathematics, The University of Manchester, UK are greatly appreciated.

References

1. Bardet J.P. and Proubet J. (1991). A numerical investigation of the structure of persistent shear bands in granular media. Géotechnique, 41: 599–613
2. Bardet J.P. and Vardoulakis I. (2001). The asymmetry of stress in granular media. International Journal of Solids and Structures, 38(2): 353–367
3. Bishop A.W. (1959). The principle of effective stress. Teknisk Ukeblad, 106(39): 859–863
4. Bolton M.D. and Gui M.W. (1993). The study of relative density and boundary effects for cone penetration tests in centrifuge. Research report: CUED/D-SOILS/TR256, Dept. of Engrg., Cambridge University, UK
5. Chang C.S. and Liao C.L. (1990). Constitutive relation for a particulate medium with effect of particle rotation. International Journal of Solids and Structures, 26: 437–453

6. Chang C.S. and Ma L. (1991). A micromechanically-based micropolar theory for deformation of granular solids. International Journal of Solids and Structures, 28(1): 67–86
7. Cheng Y.P., Nakata Y. and Bolton M.D. (2003). Discrete element simulation of crushable soil. Géotechnique, 53(7): 633–641
8. Christoffersen J., Mehrabadi M.M., Nemat-Nassar S. (1981). A micromechanical description on granular material behaviour. ASME, J. Appl. Mech., 48: 339–344
9. Coop M.R. and Willson S.M. (2003). On the Behavior of Hydrocarbon Reservoir Sands and Sandstones. J. Geotech. Eng. ASCE, 129(11): 1010–1019
10. Cundall P.A. and Strack O.D.L. (1979). The distinct numerical model for granular assemblies. Géotechnique, 29: 47–65
11. Ehlers W., Ramm E., Diebels S. and D'Addetta G.A. (2003). From particle ensembles to Cosserat continua: homogenization of contact forces towards stresses and couple stresses. International Journal of Solids and Structures, 40(24): 6681–6702
12. Fisher R.A. (1926). On the capillary forces in an ideal soil. Journal of Agricultural Science, 16: 492–505
13. Fredlund D.G. and Rahardjo H. (1993). Soil mechanics for unsaturated soils. Wiley Publications, New York
14. Iwashita K. and Oda M. (1998). Rolling resistance at contacts in simulation of shear band development by DEM. Journal of Engineering Mechanics, ASCE, 124(3): 285–292
15. Jennings J.E. and Burland J.B. (1962). Limitations of the use of effective stresses in partly saturated soils. Géotechnique, 2(2): 13–19
16. Jiang M.J. and Harris D. (2003). Generalized effective stress in unsaturated granulate by DEM analysis. Int. Conf.: From Experimental Evidences Towards Numerical Modelling of Unsaturated Soils, Weimar, Germany, September 18th–19th, 2003, Vol. II, pp. 201–214
17. Jiang M.J., Harris D. and Yu H.-S. (2005a). Kinematic models for non-coaxial granular materials: Part I: theories. International Journal for Numerical and Analytical Methods in Geomechanics, 29(7): 643–661
18. Jiang M.J., Harris D. and Yu H.-S. (2005b). Kinematic models for non-coaxial granular materials: Part II: evaluation. International Journal for Numerical and Analytical Methods in Geomechanics, 29(7): 663–689
19. Jiang M.J., Konrad J.M. and Leroueil S. (2003). An efficient technique to generate homogeneous specimens for DEM studies. Computers and Geotechnics, 30(5): 579–597
20. Jiang M.J., Leroueil S. and Konrad J.M. (2002). DEM study of microstructured soil. 55th CSCE-ASCE conference, Hamilton, Ontario, Canada, pp. 313–320
21. Jiang M.J., Leroueil S. and Konrad J.M. (2004). Insight into strength functions in unsaturated granulate by DEM analysis. Computers and Geotechnics, 31(6): 473–489
22. Jiang M.J. and Shen Z.J. (1996). A structural suction model for structured clays, In: 2nd International Conference on Soft Soil Engineering (eds. Z.J. Shen et al.). Nanjing, China, pp. 213–247
23. Jiang M.J., Yu H.-S. and Harris D. (2005c). Discrete Element Modelling of Deep Penetration in Granular Soils. Numerical and Analytical Methods in Geomechanics, 30(4): on-line

24. Jiang M.J., Yu H.-S. and Leroueil S. (2005d). A simple and efficient approach to capturing bonding effect in natural sands by DEM. (Submitted to Int. Journal for Numerical and Analytical Methods in Engineering for publication)
25. Kiyama H., Nishimura T. and Fujimura H. (1994). Advanced distinct element model coupling with pore water. Doboku Gakkai Rombun-Hokokushu/Proceedings of the Japan Society of Civil Engineers, 499 (III-28), pp. 31–39
26. McDowell G.R. and Harireche O. (2002). Discrete element modelling of soil particle fracture. Géotechnique, 52(2): 131–135
27. Ng T.T. and Dobry R. (1994). A nonlinear numerical model for soil mechanics. Journal of Geotechnical Engineering, ASCE, 120(2): 388–403
28. Oda M., Konishi J. and Nemat-Nasser S. (1982). Experimental micromechanical evaluation of strength of granular materials: effects of particle rolling. Mechanics of Materials, 1: 269–283
29. Shen Z.J. (1999). A granular medium model for liquefaction analysis of sands. Chinese Journal of Geotechnical Engineering, 21(5): 742–748
30. Thornton C. (2000). Numerical simulation of deviatoric shear deformation of granular media. Géotechnique, 50(1): 43–53
31. Thornton C. and Barnes D.J. (1986). Computer simulated deformation of compact granular assemblies. Acta Mechanica, 64: 45–61
32. Wan R.G. and Guo P.J. (2004). Stress dilatancy and fabric dependencies on sand behaviour. Journal of Engineering Mechanics, ASCE, 6(1): 635–645
33. Anandarajah A. (2000). On influence of fabric anisotropy on the stress-strain behaviour of clays. Computers and Geotechnics, 27: 1–17.
34. Iwashita K. and Oda M. (2000). Micro-deformation mechanism of shearbanding process based on modified distinct element. PowderTechnol, 109: 192–205.
35. Kuhn M.R. and Mitchell J.K. (1993). New perspectives on soil creep. Journal of Geotechnical Engineering, ASCE, 119(3): 507–524.
36. Harris D. (1995). A unified formulation for plasticity models of granular and other materials. Proc. R. Soc. Lond., A450: 37–49.

The Role of Particle Crushing in Granular Materials

G. R. McDowell

Nottingham Centre for Geomechanics, School of Civil Engineering, University of Nottingham, UK
glenn.mcdowell@nottingham.ac.uk

1 Introduction

This chapter presents recent developments made by the author in providing an understanding of micromechanics of yielding and plastic hardening of granular materials and the role of particle crushing in determining the constitutive behaviour. It will be shown that there is nothing "special" about soil; breakfast cereals and pasta have normal compression lines similar to soil. The role of particle crushing is demonstrated with discrete element modelling (DEM) as well as experimental data, and a theory of fractal crushing is shown to be consistent with hardening of yield surfaces for sands. A constitutive model based on micromechanics incorporating particle crushing is presented, and some deficiencies in the model are highlighted. The role of particle crushing in creep is also discussed.

2 Yielding and Normal Compression

2.1 Experimental Data

Figure 1 shows plots of voids ratio against the logarithm of vertical effective stress for sands which have been one dimensionally normally compressed. Beyond the yielding region (2) a linear normal compression line emerges over approximately one decade of stress. Yield might conveniently be taken to relate to the point of maximum curvature on the plot. Questions which arise are: Is yield the onset of particle crushing and can we learn anything about yielding and normal compression from other (non-geotechnical) materials? Figure 2 shows samples of breakfast cereals (cornflakes, rice krispies) and pasta. Samples of these materials were subjected to oedometer tests in a 150-mm diameter oedometer. The normal compression plots are shown in Fig. 3 [25] and compared with oedometer tests on silica sand [18]. The shape of the particle size distribution which emerges for pasta, for example, compares well

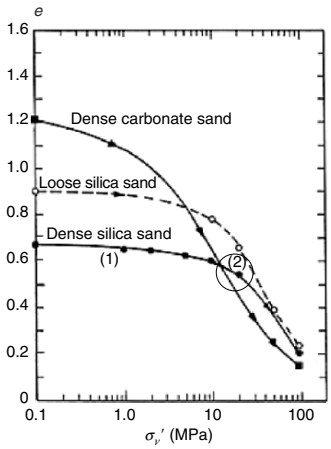

Fig. 1. One-dimensional normal compression of sand [7]

Fig. 2. (**a**) Cornflakes, (**b**) rice krispies and **(c)** pasta

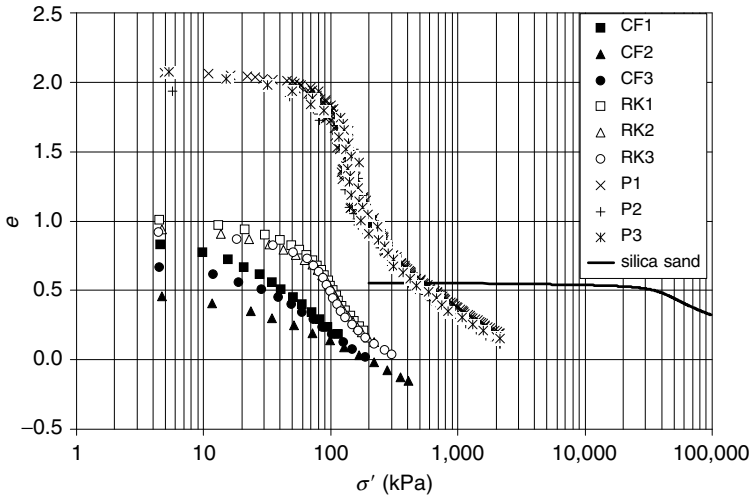

Fig. 3. Normal compression plots for cornflakes (CF), rice krispies (RK), pasta (P) and silica sand [25]

with that for silica sand, though the particle sizes and stress levels are different [25]. The question arises as to whether particle strength could be a suitable normalizing parameter for effective stress.

Particles of the materials in Fig. 2 were therefore subjected to single particle crushing tests between flat platens, in order to measure the tensile strength. The same was performed on the silica sand particles relating to Fig. 3 [18]. McDowell [17] has shown that the number of tests required to quantify strength sufficiently accurately depends on the variability of the material. For a true Weibull modulus [34] of 3, we can be 95% certain that the measured mean strength is within 13% of the true value with 30 tests. Confidence limits on the mean are obtained from Student's t-distribution, and those for the variance are obtained from the χ^2-distribution [17]. This analysis explains why some authors (e.g. [3]) found a size effect on average strength, but little variability in strength for a given size; Billam [3] only performed 10 tests, for example. If it is assumed that the particle–platen contact area is negligible and that bulk fracture occurs within the particle, it is possible to integrate maximum tensile stress over the volume of the particle, so that the probability of survival $P_\mathrm{s}(d)$ for a particle of size d under a characteristic stress $\sigma = F/d^2$ where F is the diametral force applied and d is the distance between the platens, is given by

$$P_\mathrm{s}\left(d\right) = \exp\left[-\left(d/d_0\right)\left(\sigma/\sigma_0\right)^m\right], \tag{1}$$

where σ_0 is the stress corresponding to a survival probability of 37% for particles of a reference size d_0, and is approximately equal to the average strength, and m is the Weibull modulus which decreases with increasing variability in strength. This gives a size effect on average strength such that

$$\sigma_0 \propto d^{-3/m}. \tag{2}$$

It should be noted that for some materials, such as railway ballasts [14], surface fracture rather than bulk fracture may dominate so that the size effect becomes

$$\sigma_0 \propto d^{-2/m}. \tag{3}$$

In addition, (1) is based on the assumption that the material is homogeneous and isotropic. Furthermore, (1) states that particles subjected to a very low stress have a high chance of survival. It is possible that a threshold stress may exist, below which no particles break. In this case the survival probability for a given size might be given by

$$P_\mathrm{s} = \exp\left[-\left(\frac{\sigma - \sigma_\mathrm{u}}{\sigma_0}\right)^m\right], \tag{4}$$

where σ_u is the threshold stress. Figure 4 shows the normal compression curves in Fig. 3 re-plotted with stress normalized by 37% strength σ_0. It can be seen that yielding occurs in the region $\sigma/\sigma_0 \approx 0.1$–$0.3$. This is consistent with

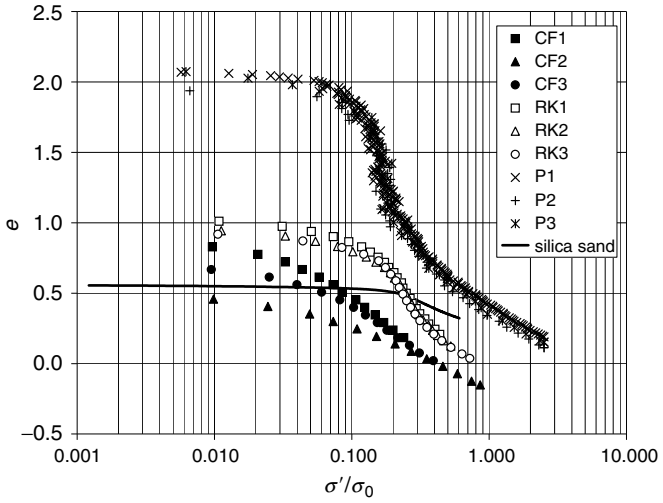

Fig. 4. Normal compression plots with stress normalized by 37% strength

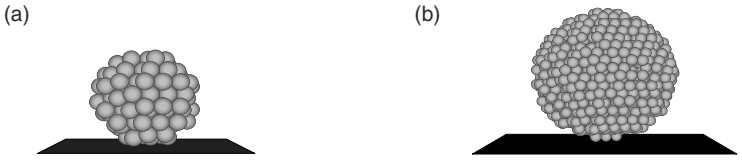

Fig. 5. (**a**) 0.5-mm agglomerate and (**b**) 1-mm agglomerate

the observation that discrete element models [4] show columns of strong force such that the macroscopic stress to cause yield should be much less than the average particle strength. Now it seems appropriate to ask whether DEM can also demonstrate whether particle crushing is the origin of yield and normal compression. McDowell [18] showed that yield stress for silica sand reduced in proportion to average particle strength, which increased with reducing particle size. Using DEM, it should be possible to show that yield corresponds to particle breakage and that normal compression arises from crushing.

2.2 Discrete Element Modelling

Figure 5 shows agglomerates of bonded balls used to model particle fracture using the software program PFC3D [10] – details of the model parameters are given in McDowell and Harireche [23]. Agglomerates are created by bonding balls in regular arrays and then removing balls to give a more random geometry and to simulate flaws. Single agglomerates were crushed between flat platens to determine model parameters which gave the correct average strength and variability in strength, comparing with experimental data by

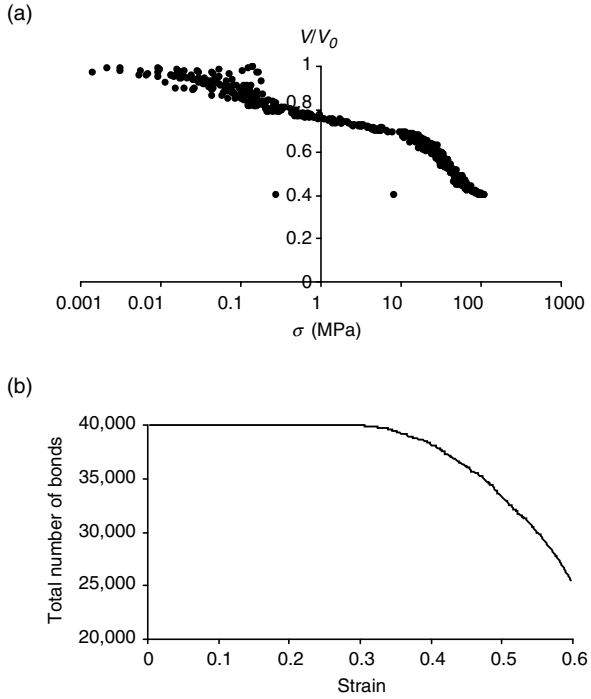

Fig. 6. (**a**) Normal compression line for 159 agglomerates 0.5-mm in diameter and (**b**) bond breakage as a function of strain (V_0 is initial sample volume)

McDowell [18] for silica sand. Figure 6 shows the result of a normal compression test on 159 agglomerates of 0.5-mm diameter. The sample was not compacted initially – which explains the stress fluctuations at low stress levels. Yielding is seen to occur at a volumetric (axial) strain of about 30%, which corresponds to the onset of bond fracture. Increasing the bond strength by a factor of 2 [24].

Figure 7 shows Fig. 6 re-plotted with stress normalized by 37% strength in addition to the equivalent plot for an aggregate of 13 agglomerates of 1-mm diameter, having a lower 37% strength. It can be seen that the yield stress is proportional to agglomerate strength. A similar normal compression curve has been obtained for DEM of an oedometer test on railway ballast [15], and it has been shown that beyond yield on the linear normal compression line, a constant value of coefficient of earth pressure at rest K_0 emerges, consistent with Jâky's [11] equation. Harireche and McDowell [9] also showed that bond breakage provides the mechanism for irrecoverable volume change under cyclic loading.

The question is now posed as to what provides the mechanism for plastic hardening under triaxial conditions.

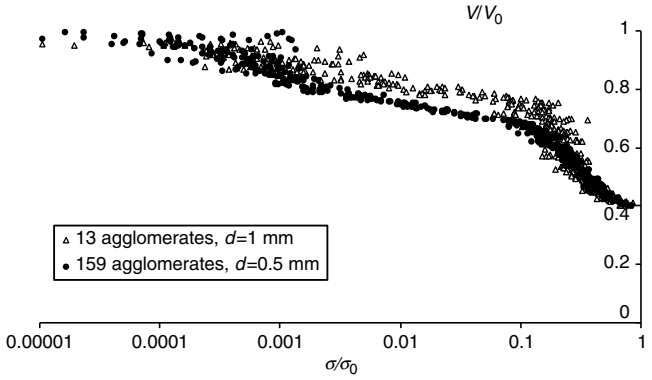

Fig. 7. Normal compression of small and large agglomerates with stress normalized by 37% strength

3 Mechanics of Plastic Hardening

McDowell and Bolton [21] proposed the following work equation for aggregates subjected to one-dimensional plastic compression (elastic terms were neglected for simplicity):

$$\sigma' \frac{\mathrm{d}e}{1+e} = -\frac{\Gamma \mathrm{d}S}{(1-\mu)\, V_\mathrm{s}\, (1+e)}, \tag{5}$$

where σ' is the applied macroscopic stress, e is voids ratio, S is surface area, V_s is volume of solids, Γ is surface energy and μ is a friction constant representing the proportion of plastic work dissipated in friction. If the plot of e against ln σ' is linear for a soil subjected to plastic compression, then

$$\mathrm{d}e = -\lambda \frac{\mathrm{d}\sigma'}{\sigma'}, \tag{6}$$

where λ is the plastic compressibility index. In this case (5) predicts

$$\mathrm{d}\sigma' \propto \mathrm{d}S_\mathrm{m}, \tag{7}$$

where S_m is the surface area per unit mass of solids or "specific surface". Since the lateral earth coefficient K_0 in one-dimensional normal compression is found to be constant according to Jâky [11], then the mean effective stress p' is proportional to σ' and if the isotropic normal compression and one-dimensional normal compression lines are parallel in $e - \ln p'$ space, then it follows from (7) that the total increase in surface area per unit mass is linearly proportional to the change in preconsolidation pressure p'_0, defined as the value of p' at the point of intersection of a standard κ-line (after [32]) with the isotropic normal compression line in $e - \log p'$ space

$$\Delta S_\mathrm{m} \propto \Delta p'_0. \tag{8}$$

An alternative approach is to consider the fractal distribution of particles which evolves during the one-dimensional compression of an initially uniformly graded aggregate of grains [21, 22]. If the smallest particle size is d_s, and the fractal dimension of the sample is 2.5, then the total surface area of the sample per unit mass S_m is given as [21]

$$S_m \propto d_s^{-1/2}. \tag{9}$$

If linear elastic fracture mechanics applies, then it is expected that the smallest particle size is related to the applied macroscopic stress according to the equation

$$\sigma' \sqrt{d_s} \propto \sigma'_0 \sqrt{d_0}, \tag{10}$$

where d_0 is the initial particle size in the uniformly graded sample and σ'_0 is the yield stress of the aggregate [21]. In this case (9) and (10) combine to give

$$S_m \propto \sigma' \propto p'_0, \tag{11}$$

assuming the isotropic normal and one-dimensional normal compression lines are parallel in e–log p' space. Equation (11) is similar to (8), but would appear to predict an initial yield stress for a compacted sample given the initial surface area, but this is not the case because the initially compacted sample will not be fractal. Nevertheless, (11) does reinforce the expectation that the change in surface area per unit mass of sample should be a linear function of the preconsolidation pressure. Equation (5) also implies a proportional relationship between increase in surface area and plastic work done on the soil sample. Thus the work of McDowell and Bolton [21] implies that suitable plastic hardening parameters are increase in surface area per unit mass, preconsolidation pressure p'_0, and plastic work per unit mass or per unit initial sample volume. Based on their work, it is expected that these hardening parameters should be linear functions of one another, and related to the plastic reduction in voids ratio. This chapter now examines whether this hypothesis is valid for samples of silica sand subjected to plastic compression under a range of stress paths in the triaxial apparatus [27]. If the hypothesis is correct, it should be possible to establish a state boundary surface inside which all strains can be assumed to be elastic and isotropic, and such that the size of a yield surface relates to the surface area per unit mass and plastic work done per unit initial sample volume.

Figure 8 shows some of the stress path tests on a silica sand described by McDowell et al. [27]. Samples have been subjected to different stress paths to points on an assumed modified clay state boundary surface with isotropic preconsolidation pressures of both 30 and 40 MPa. Figure 9 (the key for the target points refers to the figures in [27]) shows the actual obtained state boundary surface, which has an equation

$$\frac{q}{p'_0} = 0.8 \frac{p'}{p'_0} \left[2 \ln \left(p'_0/p'\right)\right]^{1/2}, \tag{12}$$

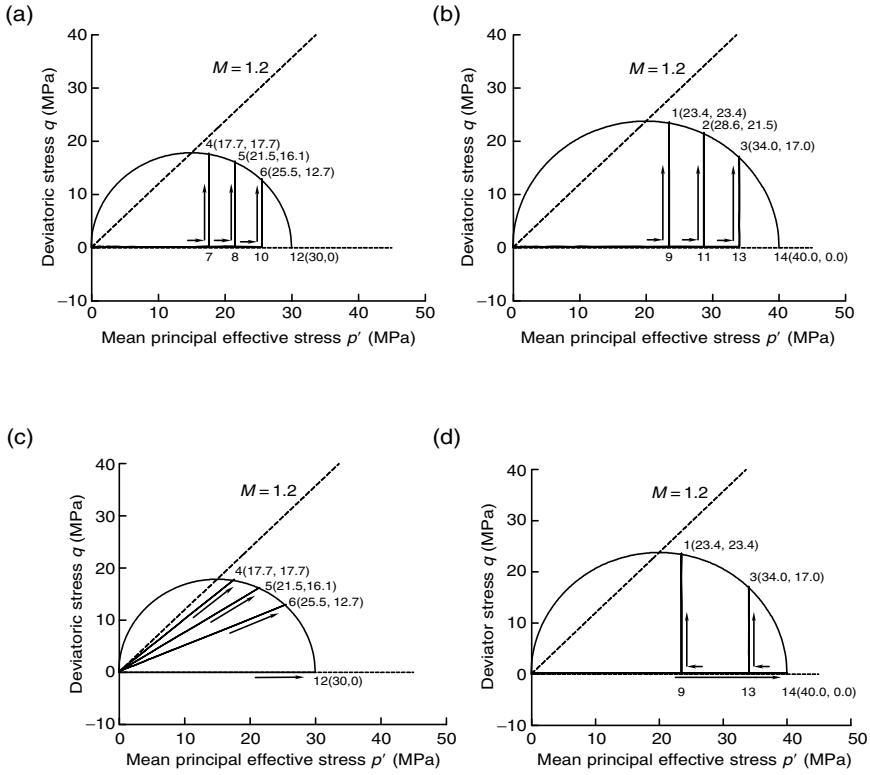

Fig. 8. Different stress path tests on a silica sand to the same points on the state boundary surface [27]

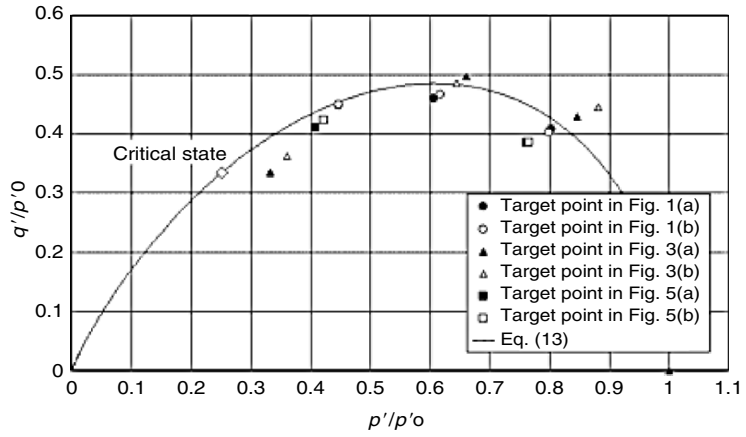

Fig. 9. Actual state boundary surface for silica sand

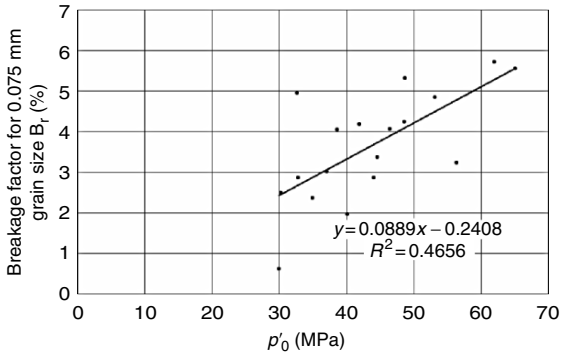

Fig. 10. Correlation of breakage factor B_r with p'_0

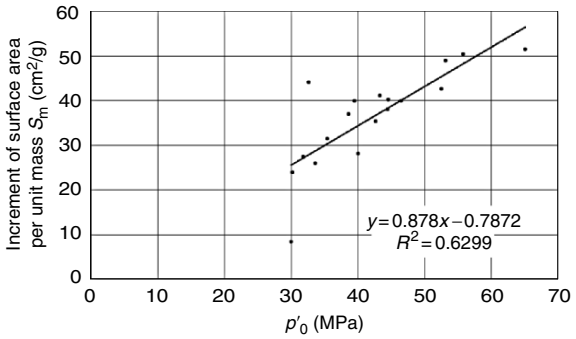

Fig. 11. Correlation of increase of surface area per unit mass with p'_0

with a critical state constant $M = 1.2$. Figure. 10 shows that a satisfactory relationship is not obtained between Hardin's breakage factor B_r [8] and the preconsolidation pressure p'_0, when plotted on linear scales. Figures 11 and 12 show that suitable hardening parameters are preconsolidation pressure p'_0, increase in surface area per unit mass S_m, and plastic work per unit volume W^p, and these can be assumed to be linear functions of one another in agreement with the theory proposed, though clearly the idea of shear hardening makes it difficult to generate models within a critical state framework. McDowell et al. [27] found that the value of the ratio of total plastic work done per unit sample volume to increase in total sample surface area per unit volume was typically $0.04\,\mathrm{J\,cm^{-2}}$ or $400\,\mathrm{J\,m^{-2}}$. The surface energy Γ of rocks is typically $25\,\mathrm{J\,m^{-2}}$ [21] so that the ratio of total plastic work to energy dissipated in fracture is typically $400/25 = 16$. This result indicates that most of the plastic work must be dissipated in friction. The result is not so surprising, since it has been pointed out by Thornton et al. [33] that discrete element simulations of the impact of agglomerates show that during the fracture of a single

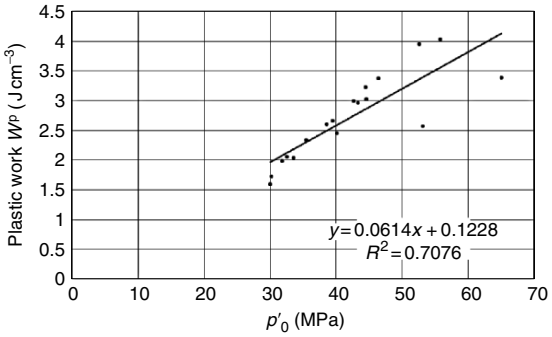

Fig. 12. Correlation of plastic work per unit volume with p'_0

agglomerate, the energy dissipated by bond rupture is only a fraction of the initial work input, and this is because of frictional dissipation at sliding particle contacts during the fracture process. The question then arises as to whether the surface area term in the work equation proposed by McDowell and Bolton [21]

$$q\delta\varepsilon_q + p'\delta\varepsilon_v = Mp'\delta\varepsilon_q + \frac{\Gamma \mathrm{d}\, S}{V_\mathrm{s}\,(1+e)} \tag{13}$$

is appropriate. The surface area term is clearly necessary, because only then is it possible to relate plastic reduction in voids ratio to the increase in surface area of the sample, which has been shown to be a suitable hardening parameter. It may be possible to improve the consistency of (13) by modifying either the frictional dissipation term or the fracture term. Macroscopic models for crushing aggregates are the subject of Sect. 4.

4 From Micromechanics to Continuum Mechanics

If the relative proportion of plastic work dissipated in fracture and friction in (13) is taken to be a function of stress ratio, i.e.

$$\frac{\text{Energy dissipated in fracture}}{\text{Energy dissipated in friction}} = F\,(\eta)\,, \tag{14}$$

then the fracture term in (13) can be written

$$\frac{\Gamma \mathrm{d}\, S}{V_\mathrm{s}\,(1+e)} = Mp'\delta\varepsilon_q\,[F\,(\eta)]\,. \tag{15}$$

The rationale for this approach is that during isotropic plastic compression, most of the plastic work might be dissipated in fracture, with little particle rearrangement occurring. At a critical state, infinite shear strains occur at constant volume. At a critical state, therefore, all plastic work is dissipated in

friction. The work equation (13) can now be re-written

$$q\delta\varepsilon_q + p'\delta\varepsilon_v = Mp'\delta\varepsilon_q \left[1 + F\left(\eta\right)\right]. \tag{16}$$

We now examine a simple set of functions $F(\eta)$ [16] which generate a convenient family of yield loci. If (16) is re-written as a stress–dilatancy rule

$$\eta + \frac{\mathrm{d}\ \varepsilon_v}{d\ \varepsilon_q} = M\left[1 + F\left(\eta\right)\right], \tag{17}$$

then for the isotropic case, we require $\delta\varepsilon_v/\delta\varepsilon_q = \infty$, hence $F(\eta) = F(0) = \infty$. At a critical state, $\eta = M, \delta\varepsilon_v/\delta\varepsilon_q = 0$, hence we require $F(\eta) = F(M) = 0$. A simple function which satisfies these requirements is

$$F\left(\eta\right) = \frac{M - \eta}{\eta}. \tag{18}$$

It can be seen that when (18) is substituted into (14), for the isotropic case $\eta = 0$ and energy is dissipated solely in fracture, whilst at a critical state $\eta = M$ and energy is dissipated solely in the frictional rearrangement of grains. Substituting (18) into (17) gives rise to the stress–dilatancy rule

$$\frac{\mathrm{d}\ \varepsilon_v}{\mathrm{d}\ \varepsilon_q} = \frac{M^2 - \eta^2}{\eta}, \tag{19}$$

which differs from the Modified Cam clay stress–dilatancy rule (Roscoe and Burland, 1968) by a factor of 2. Equation (19) can be re-cast as a work equation

$$q\delta\varepsilon_q + p'\delta\varepsilon_v = \sqrt{\left(p'\ \delta\varepsilon_v\right)^2 + \left(\mathrm{M}p'\ \delta\varepsilon_q\right)^2 + pq\delta\varepsilon_v\delta\varepsilon_q} \tag{20}$$

This work equation is similar to that quoted by Miura et al. (1984) for sands in a particle-crushing stress region. The equation of the yield surface can be found by applying the normality principle and integrating to give (McDowell, 2002b)

$$\eta = M\sqrt{2\ln\left(p'_0/p'\right)}. \tag{21}$$

Coincidentally, (21) is identical to that proposed by Murata et al. (1987), based on experimental results for sand. It is easy to see how a whole family of yield surfaces can be generated. If we choose

$$F\left(\eta\right) = \frac{M^a - \eta^a}{\eta^a}, \tag{22}$$

then by substituting (22) into (17), assuming the normality principle applies, and integrating

$$\eta = M\left[\left(a+1\right)\ln\left(p'_0/p'\right)\right]^{\frac{1}{a+1}}. \tag{23}$$

This is the same family of yield surfaces as proposed by Yu [35] for the CASM model using Rowe's [31] stress–dilatancy rule and the state parameter

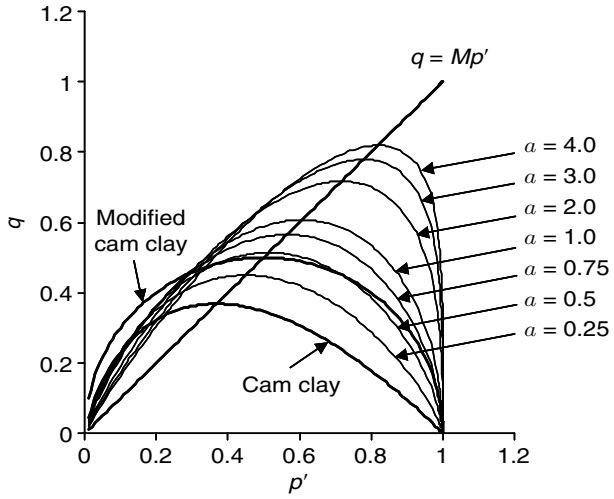

Fig. 13. A family of yield loci based on micromechanics [16]

concept [2]. The family of yield surfaces is shown in Fig. 13. All yield loci are drawn for the same preconsolidation pressure, which has been taken to be 1 MPa. The Cam clay and Modified Cam clay yield surfaces are shown in bold type for comparison. For non-associated flow models, the yield surface can be defined as [19]

$$\eta = N\left[(a+1)\ln\left(p_0'/p'\right)\right]^{\frac{1}{a+1}}, \tag{24}$$

where N is the stress ratio corresponding to the peak value of q/p_0', and the plastic potential can be defined as

$$\eta = M\left[(b+1)\ln\left(p_{\mathrm{p}}'/p'\right)\right]^{\frac{1}{b+1}}, \tag{25}$$

where p_{p}' is the value of p' at $q = 0$ for the plastic potential through the current point on the yield surface in stress space and b controls the flow rule.

Equations (24) and (25) make it easy to generate simple yield surfaces and with a versatile flow rule. Figures 14 and 15 show how the parameter b can be used to change the flow rule. This approach, based on micromechanics, is useful. However, the assumed micromechanics must be incorrect as Sect. 3 demonstrated that most of the plastic work done is dissipated in friction – even in isotropic tests. This means that it is necessary to replace the $Mp'\delta\varepsilon_q$ term in (13) or re-define surface energy so that it includes frictional dissipation which occurs during the fracture process. If the latter approach is adopted, then $Mp'\mathrm{d}\varepsilon_q$ in (13) relates to the sliding of broken fragments and $\Gamma\mathrm{d}S/V_{\mathrm{s}}(1+e)$ relates to the energy dissipated during the fracture process, which also includes frictional sliding. In this case, the micromechanical approach adopted will be useful in generating continuum models.

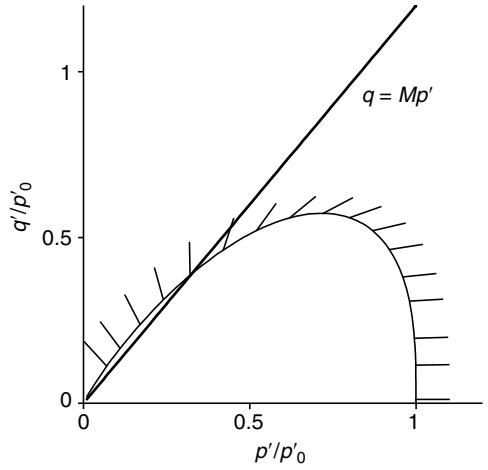

Fig. 14. Yield locus with $N = 0.8, a = 2$; flow rule with $M = 1.2, b = 2$

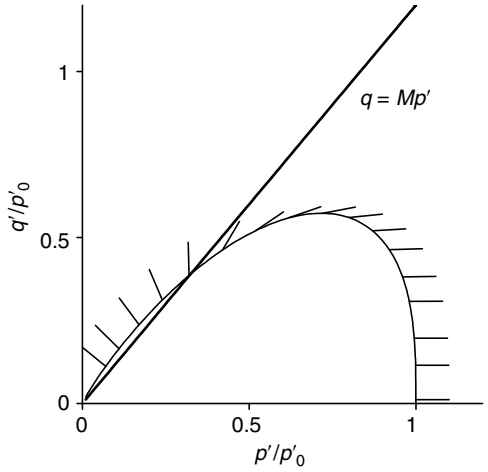

Fig. 15. Yield locus with $N = 0.8, a = 2$; flow rule with $M = 1.2, b = 4$

5 Creep

The chapter now examines whether particle crushing might be responsible for creep in granular materials. The creep of granular materials subjected to one-dimensional compression only is examined [20]. It is well known that granular materials creep under constant effective stress [12, 13] such that creep strain is proportional to log time

$$\varepsilon = C \log t/t_0, \tag{26}$$

where t_0 is the time from which creep strains are measured. The question arises as to whether the equation of a linear normal compression line

$$e = e_c - \lambda \ln (\sigma / \sigma_c) \tag{27}$$

could be consistent with (26) for a granular material subjected to creep at constant stress under one-dimensional conditions, if the micro mechanical origin of creep is particle crushing. The stress σ_c is simply a stress on the normal compression line, and voids ratio e_c is the voids ratio at that applied stress. If a sharp yield point can be defined for a compacted sand, then these values could be taken to relate to first yield. McDowell and Bolton [21] proposed that the mechanism for plastic hardening was fractal crushing, such that the current macroscopic stress should be proportional to the average strength of the smallest particles σ_s in the aggregate: These particles continue to crush under increasing stress levels, becoming statistically stronger and filling voids. Thus, an aggregate should be in equilibrium with a voids ratio e_c under an applied stress σ_c, with

$$\sigma_c = k\sigma_s. \tag{28}$$

The constant k is independent of particle size, because as the smallest particle size reduces, the smallest particles are in self-similar geometrical configurations. Further compression can only occur if the stress level increases above σ_c or if the average strength of the smallest particles σ_s decreases. It is the fracture of the smallest particles which gives the reduction in voids ratio, because even once a wide distribution of particle sizes has formed, if some large particles break, there are no available voids for the large fragments to fill. Substituting (28) into (27) gives:

$$e = e_c - \lambda \ln (\sigma / k\sigma_s) . \tag{29}$$

It is well established in the materials literature [1,5] that ceramics exhibit time-dependent strength. This is caused by slow crack growth as moisture in the environment interacts with flaws in the material. The end result is that for a tensile test on a ceramic specimen, if the standard test used to measure the tensile strength σ_{TS} takes a time t(test), then the stress which the sample will support safely for a time t is given by the equation

$$\left(\frac{\sigma}{\sigma_{TS}} \right)^n = \frac{t\,(\text{test})}{t}, \tag{30}$$

where n is the slow-crack growth exponent. Data for n are very limited, but n is 10–20 for oxides at room temperature; for carbides and nitrides, n can be as large as 100 [1]. It is now possible to examine the effect of the dependence of σ_s on time at constant stress level in (29). If σ_{s0} is the average particle strength which could be measured at time $t = t_0$, then the average strength σ_s after a time t, according to (30) would be

$$\sigma_s = \sigma_{s0} \, (t_0 / t)^{1/n} . \tag{31}$$

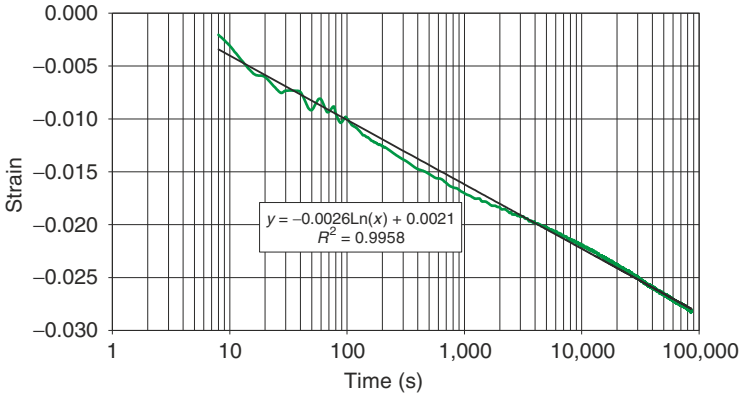

Fig. 16. Creep of pasta [26]

Substituting (31) into (29) gives

$$e = e_{\mathrm{c}} - \lambda \ln\left(\sigma / k\sigma_{\mathrm{s0}}\right) - \frac{\lambda}{n} \ln\left(t/t_0\right). \tag{32}$$

Hence the reduction in voids ratio Δe as a function of time after time t_0 is simple

$$\Delta e = \frac{\lambda}{n} \ln\left(t/t_0\right) = \frac{2.3\lambda}{n} \log_{10}\left(t/t_0\right), \tag{33}$$

so that the log time effect is observed and the creep coefficient in (26) is given as

$$C = \frac{2.3\lambda}{n} \frac{1}{1 + \boldsymbol{e}_0}, \tag{34}$$

where e_0 is the initial voids ratio. McDowell [20] showed that typical values of λ and n in (34) were consistent with data by Leung et al. [13] for one-dimensional compression of sand at high stress levels. In addition, Feng (2004) pointed out that the creep coefficient C is often found to be proportional to the compressibility index $C_{\mathrm{c}} (= 2.3\lambda)$ for a given soil, which is consistent with (34). In addition he pointed out that typical values of C/C_{c} found in the literature are consistent with (34) for typical values of n. Figure 16 shows the log-time relationship in (26) is also observed for creep of pasta subjected to one-dimensional compression [26], and that this creep is consistent with particle crushing, as shown by the change in the particle size distribution in Fig. 17.

6 Conclusions

It has been shown that the onset of particle crushing appears to be the origin of yield. Yield is a gradual process but for one-dimensional compression, the point of maximum curvature of the normal compression line in e– $\log \sigma'$ space

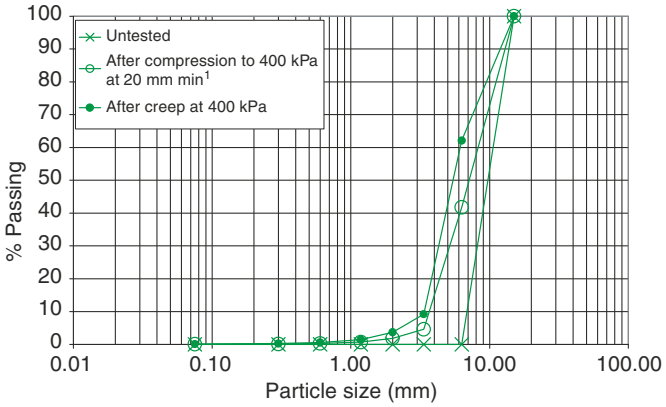

Fig. 17. Crushing which results in creep of pasta [26]

appears to be a suitable of definition of yield, and the use of e– $\log \sigma'$ space appears useful since it will give rise to bilinear plots with well–defined yield points for overconsolidated materials (the one-dimensional compression of an elastic array of spheres might give rise to what might resemble a normal compression line for a crushable aggregate in e– $\log \sigma'$ space, but the unloading curve would be the same as the loading curve, which is not observed for crushable aggregates). Particle crushing appears to be give rise to normal compression lines for non-geotechnical granular materials, so there is nothing "special" about soil.

Change in surface area of particles appears to be a suitable plastic hardening parameter for granular materials, as shown by experimental data for triaxial tests, and it appears to be a linear function of preconsolidation pressure, in agreement with a proposed theory of fractal crushing. Plastic work also seems to be a useful hardening parameter, though this makes the development of critical state models difficult, and more work is required in this area.

DEM is a useful tool for exploring the role of particle crushing in granular materials and has been shown to shed light on the micromechanics of yield and normal compression.

It has been shown to be possible to develop simple continuum models based on micromechanics incorporating particle crushing, though further work is required in defining energy terms for frictional dissipation and fracture.

The time dependence of particle strength has been shown to give rise to realistic creep behaviour and to predict the correct relationship between the plastic compressibility index and creep coefficient.

It would therefore appear that particle crushing plays a fundamental role in determining the constitutive behaviour of granular materials.

References

1. Ashby, M.F. and Jones, D.R.H. (1986) *Engineering Materials 2*. Oxford: Pergamon
2. Been, K. and Jeffries, M.G. (1985) A state parameter for sands. *Géotechnique* **35**, No. 2, 99–112
3. Billam, J. (1972) Some aspects of the behaviour of granular materials at high pressures. Stress–strain behaviour of soils. *Proceedings of the Roscoe Memorial Symposium* (ed. R.H.G. Parry), pp. 69–80
4. Cundall, P.A. and Strack, O.D.L. (1979) A discrete element model for granular assemblies. *Géotechnique* **29**, No. 1, 47–65
5. Davidge, R.W. (1979) *Mechanical behaviour of ceramics*. Cambridge: Cambridge University Press
6. Feng, T.-W. (2004) Discussion on: Micromechanics of creep of granular materials. *Géotechnique* **54**, No. 6, 427–428
7. Golightly, C.R. (1990) *Engineering properties of carbonate sands*. Ph.D. dissertation, Bradford University
8. Hardin, B.O. (1985) Crushing of soil particles. *ASCE Journal of Geotechnical Engineering* **111**, No. 10, 1177–1192
9. Harireche, O. and McDowell, G.R. (2003) Discrete element modelling of cyclic loading of crushable aggregates. *Granular matter* **5**, No. 3, 147–151
10. Itasca Consulting Group, Inc. (1999) *Particle flow code in 3 dimensions*
11. Jâky, J. (1944). A nyugalmi nyomâs tényezöje (The coefficient of earth pressure at rest). *Magyar Mérnök és Epitész-Egylet Közlönye (Journal of the Union of Hungarian Engineers and Architects)*, 355–358
12. Lade, P.V. and Liu, C-T. (1998) Experimental study of drained creep behaviour of sand. *Journal of Engineering Mechanics, ASCE* **124**, No. 8, 912–920
13. Leung, C.F., Lee, F.H and Yet, N.S. (1996) The role of particle breakage in pile creep in sand. *Canadian Geotechnical Journal* **33**, 888–898
14. Lim, W.L., McDowell, G.R. and Collop, A.C. (2004) The application of Weibull statistics to the strength of railway ballast. *Granular Matter* **6**, No. 4, 229–237
15. Lim, W.L. and McDowell, G.R. (2005) Discrete element modeling of railway ballast. *Granular Matter* **7**, No. 1, 19–29
16. McDowell, G.R. (2000) A family of yield loci based on micromechanics. *Soils and Foundations* **40**, No. 6, 133–137
17. McDowell, G.R. (2001) Statistics of soil particle strength. *Géotechnique* **51**, No. 10, 897–900
18. McDowell, G.R. (2002) On the yielding and plastic compression of sand. *Soils and Foundations* **42**, No. 1, 139–145
19. McDowell, G.R. (2002) A simple non-associated flow model for sand. *Granular Matter* **4**, No. 2, 65–69
20. McDowell, G.R. (2003) Micromechanics of creep of granular materials. *Géotechnique* **53**, No. 10, 915–916
21. McDowell, G.R. and Bolton, M.D. (1998) On the micromechanics of crushable aggregates. *Géotechnique* **48**, No. 5, 667–679
22. McDowell, G.R. and Daniell, C.M. (2001) Fractal compression of soil. *Géotechnique* **51**, No. 2, 173–176

23. McDowell, G.R. and Harireche, O. (2002a) Discrete element modelling of soil particle fracture. *Géotechnique* **52**, No. 2, 131–135
24. McDowell, G.R. and Harireche, O. (2002b) Discrete element modelling of yielding and normal compression of sand. *Géotechnique* **52**, No. 4, 299–304
25. McDowell, G.R. and Humphreys, A. (2002) Yielding of granular materials. *Granular Matter* **4**, No.1, 1–8
26. McDowell, G.R. and Khan, J.J. (2003) Creep of granular materials. *Granular Matter* **5**, No. 3, 115–120
27. McDowell, G.R., Nakata, Y. and Hyodo, M. (2002) On the plastic hardening of sand. *Géotechnique* **52**, No. 5, 349–358
28. Miura, N, Murata, H. and Yasufuku, N. (1984). Stress–strain characteristics of sand in a particle crushing region. *Soils and Foundations* **24**, No. 1, 77–89
29. Murata, H, Hyodo, M. and Yasufuku, N. (1987). Yield characteristics of dense sand under low and high pressure. *Proceeding of Japan Society of Civil Engineers* **382**, 183–192 *(in Japanese)*
30. Roscoe, K.H. and Burland, J.B. (1968). On the generalised stress–strain behaviour of 'wet' clay. In *Engineering Plasticity* (eds. J. Heyman and F.A. Leckie), pp. 535–609. Cambridge: Cambridge University Press
31. Rowe, P.W. (1962) The stress–dilatancy relation for static equilibrium of assembly of particles in contact. *Proceedings of Royal Society* **267**, 500–527
32. Schofield, A. N. and Wroth, C. P. (1968). *Critical State Soil Mechanics*. London: McGraw-Hill
33. Thornton, C., Yin, K. and Adams, M. J. (1996). Numerical simulation of the impact and fragmentation of agglomerates. *Journal of Physics D: Application Physics* **29**, 424–435
34. Weibull, W. (1951) A statistical distribution function of wide applicability. *Journal of Application Mechanics* **18**, 293–297
35. Yu, H. S. (1998) CASM: A unified state parameter model for clay and sand. *International Journal for Numerical and Analytical Methods in Geomechanics* **33**, 621–653

Micromechanical Study of Damage and Permeability Variation in Brittle Rocks

J.J. Zhou*, J.F. Shao*, and D. Lydzba†

*Laboratory of Mechanics of Lille, Polytech-Lille, France
jian-fu.shao@polytech-lille.fr
†Institute of Geotechnics and Hydrotechnics, Wroclaw University of Technology, Poland

1 Introduction

In brittle geomaterials like rocks and concrete, damage by nucleation and growth of microcracks is an essential mechanism of deformation and failure. The induced damage not only affects the mechanical properties of materials, but also the flow and conductivity properties. The variation of permeability with the growth of microcracks is one of the most significant phenomena to be taken into account in many engineering applications, for example, the storage of nuclear wastes, the stability of rock slopes, and hydraulic dams, and the long term durability of concrete structures.

A number of constitutive models have been proposed for the description of induced damage in geomaterials (we do not give an exhaustive list of these models here). They can be roughly separated into two classes: phenomenological models and micromechanical models. Generally, the advantage of the micromechanical models remains in the possibility to account for physical mechanisms involved in material damage. However, the numerical implementation of these models in view of engineering application is not easy and the associated computation procedure is usually time-consuming. On the other hand, the phenomenological models provide with simple and unified mathematical formulations. These models can be easily implemented in a computer code and then used as a powerful tool for engineering analyses. However, some assumptions and concepts used in the phenomenological models, for instance the effective stress concept, are not clearly based on physical backgrounds. On the other hand, various approaches have been proposed for the estimation of permeability in fractured media, involving empirical and statistical investigations [2–4, 7–9, 12, 14, 15, 17]. However, these investigations are generally performed for a given distribution of fractures in rocks, and they are not coupled with the evolution of mechanical behaviors of materials. There are very few studies on the coupled modeling of mechanical damage and permeability evolution.

In the first part of this work, we propose to develop a new anisotropic damage model for brittle rocks essentially subjected to compressive stresses. The proposed model will be based on the relevant micromechanics analyses, in order into take into account main physical mechanisms involved in the microstructure scale. In the second part, the mechanical model is extended to the description of variation of permeability due to growth of microcracks. The variation of permeability is then directly associated with the mechanical damage of material. Throughout the chapter, the following notations for tensorial calculations will be used:

$$(\overrightarrow{a} \otimes \overrightarrow{b})_{ij} = a_i b_j, (\underline{\underline{A}} \cdot \overrightarrow{b})_i = A_{ij} b_j, (\underline{\underline{A}} : \underline{\underline{B}}) = A_{ij} B_{ji}, (\overrightarrow{a} \cdot \overrightarrow{b}) = a_i b_i.$$

2 Formulation of the Damage Model

In this chapter, it is assumed that rocks are submitted to compression-dominated stresses. The crack density remains small and the interaction between microcracks can be neglected before the onset of coalescence of microcracks. The initial behavior of materials is isotropic and the anisotropy is fully induced by preferential distribution of microcracks.

2.1 Free Enthalpy and Constitutive Equations

In brittle materials like rocks, damage by nucleation and growth of microcracks is the essential dissipation mechanism. Plastic deformation due to dislocation-like sliding can be neglected. Macroscopic irreversible strains are developed due to residual opening and mismatch of microcracks during loading–unloading process. Consider now a representative volume element (RVE) of the cracked material. The volume of RVE is noted by Ω. The RVE is composed of an elastic solid matrix, which is weakened by a number of sets of microcracks in different directions. The RVE is submitted to a uniform stress field $\boldsymbol{\sigma}$ on its boundary. For the simplicity of mathematical formulation, we first consider a single family of N similar microcracks inside the RVE, oriented in the direction defined by the unit normal vector $\overrightarrow{n}$. In the same family, all the cracks have the same geometrical form. The vector of displacement jump on each microcrack is defined as follows:

$$\overrightarrow{b} = \overrightarrow{u}^{+} - \overrightarrow{u}^{-}, \tag{1}$$

where $\overrightarrow{u}^{+}$ and $\overrightarrow{u}^{-}$ are, respectively, the displacement vector on the two opposite faces of the crack. The macroscopic strain tensor of the REV can be determined by

$$\boldsymbol{\varepsilon} = \mathbf{S}^0 : \boldsymbol{\sigma} + \frac{1}{2}\frac{N}{\Omega} \int_{\Gamma^+} (\overrightarrow{b} \otimes \overrightarrow{n} + \overrightarrow{n} \otimes \overrightarrow{b}) \mathrm{d}s. \tag{2}$$

Γ^+ denotes the crack face with the positive normal unit vector $\overrightarrow{n}$. $\mathbf{S}^0$ is the initial elastic compliance tensor of undamaged material. In the case of penny-shaped cracks, the unit normal $\overrightarrow{n}$ is constant along the crack surface and the vector $\overrightarrow{b}$ is taken as the average displacement jump over the crack. The elastic free enthalpy can be expressed as:

$$w_{\mathrm{c}} = \frac{1}{2}\boldsymbol{\sigma} : \mathbf{S}^0 : \boldsymbol{\sigma} + \frac{N}{\Omega}(\boldsymbol{\sigma} \cdot \overrightarrow{n}) \cdot \overrightarrow{b}\,(\pi r^2). \tag{3}$$

The variable r denotes the radius of microcracks. According to the fundamental work by Kachanov [6], the displacement jump can be decomposed into a normal component and a shear component. The two components can be related respectively to the normal stress and shear stress vector applied to the crack:

$$\overrightarrow{b} = \beta(\overrightarrow{n} \cdot \boldsymbol{\sigma} \cdot \overrightarrow{n})\overrightarrow{n} + \gamma\left[\boldsymbol{\sigma} \cdot \overrightarrow{n} - (\overrightarrow{n} \cdot \boldsymbol{\sigma} \cdot \overrightarrow{n})\overrightarrow{n}\right]. \tag{4}$$

The two coefficients involved in (4) are given by Kachanov [6]:

$$\beta = \frac{16(1-\nu_0^2)}{3E_0}\frac{r}{\pi}, \qquad \gamma = \frac{2}{2-\nu_0}\beta. \tag{5}$$

E_0 and ν_0 are, respectively, the initial Young's modulus and Poisson's ratio of undamaged material. According to (4), the normal displacement jump is proportional to the normal stress applied to the crack. As the normal displacement jump must be positive (opened cracks) or zero (closed cracks), the following closure condition of crack have to be prescribed:

$$\begin{cases} (\overrightarrow{n} \cdot \boldsymbol{\sigma} \cdot \overrightarrow{n}) > 0, & \text{opened cracks} \\ (\overrightarrow{n} \cdot \boldsymbol{\sigma} \cdot \overrightarrow{n}) \leq 0, & \text{closed cracks.} \end{cases} \tag{6}$$

By introducing this closure condition and the relation (4) into (3), the free enthalpy function becomes:

$$w_{\mathrm{c}} = \frac{1}{2}\boldsymbol{\sigma} : \mathrm{S}^0 : \boldsymbol{\sigma} + \omega h \left\{ (1 - \frac{\nu_0}{2}) < \overrightarrow{n} \cdot \boldsymbol{\sigma} \cdot \overrightarrow{n} >^+ \overrightarrow{n} + \left[(\boldsymbol{\sigma} \cdot \overrightarrow{n}) - (\overrightarrow{n} \cdot \boldsymbol{\sigma} \cdot \overrightarrow{n})\overrightarrow{n}\right] \right\} \cdot (\boldsymbol{\sigma} \cdot \overrightarrow{n}). \tag{7}$$

The bracket $\langle x \rangle^+$ defines the positive cone of the normal stress. The variable ω denotes the crack density associated with the family of microcracks oriented in the direction $\overrightarrow{n}$ and h is the elastic compliance of crack, respectively defined by

$$\omega = \frac{Nr^3}{\Omega}, \qquad h = \frac{16(1-\nu_0^2)}{3E_0(2-\nu_0)}. \tag{8}$$

Let's denote $\mathbf{S}^{\mathrm{hom}}$ the fourth order effective elastic compliance tensor of cracked material, the free enthalpy function (7) can be rewritten as $w_{\mathrm{c}} = (1/2)\boldsymbol{\sigma} : \mathbf{S}^{\mathrm{hom}} : \boldsymbol{\sigma}$. The effective elastic compliance tensor is the expressed as

follows:

$$\mathbf{S}^{\text{hom}} = \mathbf{S}^0 + \omega h \left\{ (\overrightarrow{n} \otimes \overrightarrow{n}) \underline{\bar{\otimes}} \boldsymbol{\delta} + \boldsymbol{\delta} \underline{\bar{\otimes}} (\overrightarrow{n} \otimes \overrightarrow{n}) + c(\overrightarrow{n} \otimes \overrightarrow{n} \otimes \overrightarrow{n} \otimes \overrightarrow{n}) \right\}. \quad (9)$$

The coefficient c is equal to $c = -\nu_0$ for the opened crack and $c = -2$ for the closed crack. The free enthalpy function (7) and the effective elastic compliance tensor (9) are obtained for the brittle material containing one set of microcracks. This result should be extended to the material containing cracks with arbitrary distributions. This can be done using the assumption of noninteraction between microcracks. The overall free enthalpy of cracked material is obtained by the addition of the contributions from each set of microcracks. To do this, let us define a continuous crack density function, noted by $\omega(\overrightarrow{n})$, to represent an arbitrary distribution of microcracks in the space orientation. The macroscopic free enthalpy can be obtained by the integration of the function (7) over all the space orientations on the surface of unit sphere, denoted by S^2. This surface is decomposed into two complementary but nonoverlapped subdomains, respectively, the subdomain S^{2+} corresponding to the orientations of opened cracks and the subdomain S^{2-} corresponding to the orientations of closed cracks [11]. Thus, we have:

$$W_{\text{c}} = \frac{1}{2}\boldsymbol{\sigma} : \mathbf{S}^0 : \boldsymbol{\sigma} + \frac{h}{4\pi} \int\limits_{S^{2+}} \omega(\overrightarrow{n})(1 - \frac{\nu_0}{2})(\boldsymbol{\sigma} \cdot \overrightarrow{n}) < \overrightarrow{n} \cdot \boldsymbol{\sigma} \cdot \overrightarrow{n} >^+ \overrightarrow{n} \mathrm{d}S$$
$$+ \frac{h}{4\pi} \int\limits_{S^2} \omega(\overrightarrow{n}) \left\{ (\boldsymbol{\sigma} \cdot \boldsymbol{\sigma}) : (\overrightarrow{n} \otimes \overrightarrow{n}) - \boldsymbol{\sigma} : (\overrightarrow{n} \otimes \overrightarrow{n} \otimes \overrightarrow{n} \otimes \overrightarrow{n}) : \boldsymbol{\sigma} \right\} \mathrm{d}S. \quad (10)$$

In general loading condition, the integral form (10) of the free enthalpy can not be analytically evaluated. A numerical integration procedure has to be employed. In this chapter, a Gauss-type method is chosen for the numerical integration on the surface of the unit sphere [1]. Therefore, the surface of the unit sphere is discretized in a limited number of orientations P. The kth orientation is defined by the unit vector $\overrightarrow{n}^k$ and associated to the weight coefficient λ_k. The free enthalpy function (10) is then approximated by

$$W_{\text{c}} = \frac{1}{2}\boldsymbol{\sigma} : \mathbf{S}^0 : \boldsymbol{\sigma} + h \left(1 - \frac{\nu_0}{2}\right) \sum_{k=1}^{P_1} \lambda_k \omega_k (\sigma \cdot \overrightarrow{n}^k) < \overrightarrow{n}^k \cdot \boldsymbol{\sigma} \cdot \overrightarrow{n}^k >^+ \overrightarrow{n}^k$$
$$+ h \sum_{k=1}^{P} \lambda_k \omega_k \left\{ (\boldsymbol{\sigma} \cdot \boldsymbol{\sigma}) : (\overrightarrow{n}^k \otimes \overrightarrow{n}^k) - \sigma : (\overrightarrow{n}^k \otimes \overrightarrow{n}^k \otimes \overrightarrow{n}^k \otimes \overrightarrow{n}^k) : \boldsymbol{\sigma} \right\}. \quad (11)$$

In this equation, P_1 denotes the number of orientations corresponding to opened cracks. According to this approximation, the effective elastic compliance tensor (9) can be extended to an arbitrary distribution of microcracks:

$$\mathbf{S}^{\hom} = \mathbf{S}^0 + h(2-\nu_0)\sum_{k=1}^{P_1}\lambda_k\omega_k(\overrightarrow{n}^k\otimes\overrightarrow{n}^k\otimes\overrightarrow{n}^k\otimes\overrightarrow{n}^k) + h\sum_{k=1}^{P}\lambda_k\omega_k\left\{\begin{array}{l}\overrightarrow{n}^k\otimes\overrightarrow{n}^k)\underline{\bar{\otimes}}\boldsymbol{\delta}+\boldsymbol{\delta}\underline{\bar{\otimes}}(\overrightarrow{n}^k\otimes\overrightarrow{n}^k)\\ -2(\overrightarrow{n}^k\otimes\overrightarrow{n}^k\otimes\overrightarrow{n}^k\otimes\overrightarrow{n}^k)\end{array}\right\}. \tag{12}$$

2.2 Crack Propagation and Damage Evolution

In the framework of thermodynamics, the damage evolution law is determined by the formulation of a dissipation potential in the space of the conjugated force associated with the damage tensor. However, the conjugated damage force is usually a complex function of applied stresses and it is not easy to give a simple physical interpretation. This renders difficult the experimental identification of the damage law. In rock mechanics, as most laboratory tests are performed in stress-controlled or strain-controlled conditions, it appear simpler to formulate the damage evolution law directly in the stress or strain space. Therefore, in the present work, a direct approach is preferred in order to facilitate the experimental determination of the damage evolution law. The damage evolution is directly related to the crack propagation criterion which is based on the fracture mechanics. According to extensive experimental data from triaxial compression tests on brittle rocks [10,16], the crack propagation is controlled by both the normal stress and shear stress applied to the crack. The crack growth is caused by increasing shear stress while the compressive normal pressure has a role of preventing the initiation and growth of microcracks. Different crack propagation criteria can be determined from laboratory data. Based on linear fracture mechanics, the real crack is replaced by a fictive crack which is subjected to an equivalent tensile force. The fictive crack is propagating in mode I. The equivalent tensile force is a function of the normal stress and shear stress applied to the real crack. For the sake of simplicity, the following linear function is used in the present work:

$$F(\boldsymbol{\sigma},\overrightarrow{n},r) = \sqrt{r}\,[\sigma_{\mathrm{n}} + f(r)\,|\overrightarrow{\tau}|] - C_r \le 0, \tag{13}$$

$$\sigma_{\mathrm{n}} = \overrightarrow{n}\cdot\boldsymbol{\sigma}\cdot\overrightarrow{n},\ \overrightarrow{\tau} = (\sigma\cdot\overrightarrow{n})\cdot(\boldsymbol{\delta}-\overrightarrow{n}\otimes\overrightarrow{n}). \tag{14}$$

In this criterion, σ_{n} is the normal stress applied to crack surfaces and, $\overrightarrow{\tau}$ denotes the shear stress vector applied to the crack. This shear stress is generated by the macroscopic deviatoric stress and represents the driving force for the crack propagation. The term with the normal stress allows us to take into account the pressure sensitivity of frictional materials. The parameter C_r denotes the material resistance to crack propagation, which is physically equivalent to the critical toughness (K_{Ic}) in fracture mechanics. $f(r)$ is a scalar valued function controlling the kinetics of crack propagation. It plays the similar role as the hardening–softening function in plastic models. The expression of this function may be determined from relevant numerical results

of micromechanical models and from numerical fitting of experimental data. The general form of the function must, however, satisfy certain requirements. For small crack extents, it should decrease, reflecting the relaxation of local tensile stress as the crack grows away from the source; as the crack length becomes large enough to interact with the stress fields of other nearby cracks $f(r)$ increases or reaches an asymptotic value. The first effect causes initially stable growth and the second marks the onset of accelerated crack interaction producing damage localization and macroscopic failure. The following simple function having these basic features is here used:

$$\begin{cases} f(r) = \eta \left(\dfrac{r_{\mathrm{f}}}{r} \right), \ r < r_{\mathrm{f}} \\ \\ f(r) = \eta, \ r \geq r_{\mathrm{f}}. \end{cases} \tag{15}$$

The parameter r_{f} is the critical crack radius for instable propagation of microcracks, and η is a parameter of model. By putting $r = r_0$ in (13), we obtain the damage initiation surface in stress space. Similarly, by putting $r = r_{\mathrm{f}}$ in (13), the macroscopic failure surface in stress space can be determined. Therefore, the stress levels at the onset of damage growth and at the macroscopic failure state can be entirely determined for any loading paths. The values of the three parameters involved in the criterion (13) can be determined from the stress–strain curves obtained from triaxial compression tests. For example, the onset of damage initiation is identified as the point of a stress–strain curve where the linear relationship is lost. The failure state is determined as the pick stress of the stress–strain curves.

3 Determination of Permeability Variation

3.1 Damage Induced Dilatancy

According to the closure condition of microcracks (5), the crack is closed under a compressive normal stress. The normal displacement jump vanishes. However, in geomaterials like rocks and concrete, actual crack surfaces are not smooth and contain different kinds of asperities. The roughness of crack surface depends on the microstructure of material (grains and cementation). Due to these asperities, a normal aperture can take place during the relative shear sliding along the crack surfaces. This normal aperture generates a macroscopic volumetric dilatancy, which is commonly observed in brittle geomaterials. Further, in closed cracks, the shear sliding is governed by the local friction law, for instance the Mohr–Coulomb law. The friction law generally induces a hysteretic behavior during the loading–unloading process. As a consequence on the macroscopic behavior, hysteretic loops are observed during unloading–reloading cycles. However, this hysteretic phenomenon is not studied in this work.

Let's denote the normal aperture of cracks in the orientation $\overrightarrow{n}$ by $e(\overrightarrow{n})$. It is a constant (in average sense) for a penny-shaped crack. Therefore, the tensor of damage-related irreversible strains in the constitutive equations can be determined by the integration of normal aperture over all the space orientations:

$$\boldsymbol{\varepsilon} = \mathbf{S}^{\text{hom}} : \boldsymbol{\sigma} + \varepsilon^r, \quad \boldsymbol{\varepsilon}^r = \frac{1}{4\pi} \int_{S^2} \frac{N}{\Omega} e(\overrightarrow{n})(\overrightarrow{n} \otimes \overrightarrow{n})(\pi r^2) \mathrm{d}S. \tag{16}$$

The evolution of the normal aperture is associated to the rate of damage evolution. It is assumed that the normal aperture increment is proportional to the increment of average crack radius, that is, $\mathrm{d}e = \chi \ \mathrm{d}r$, with χ being a proportionality coefficient depending on the geometrical roughness of the crack faces. In general, the proportional coefficient χ should be a function of damage state. However, in the present work, only a constant value is used as a simplified case of the model.

3.2 Estimation of the Permeability Variation

The permeability of a cracked medium is composed of two parts; the initial permeability $\mathbf{k}^0$ due to initial porosity, and the crack enhanced permeability $\mathbf{k}^{\text{c}}$. The total permeability is given by $\mathbf{k} = \mathbf{k}^0 + \mathbf{k}^{\text{c}}$. In this work, a simplified case is considered. It is assumed that all cracks are embedded in a porous medium and then connected to the pore networks. In real situations, a certain number of cracks may be hydraulically isolated and do not contribute to the variation of permeability. Therefore, this assumption should lead to an overestimation of the real permeability variation. The crack permeability is essentially due to the crack aperture and evolves with crack propagation. The average crack aperture is associated to the crack radius. Therefore, the crack permeability directly depends on the microcrack distribution, which is determined using the anisotropic damage model presented in Sect. 3.1. As the microcrack distribution is orientation-dependent, the crack permeability induces an anisotropic character of fluid flow.

Consider now a RVE of rock mass, composed of a porous matrix and a random distribution of microcracks, subjected to a uniform pressure gradient on the boundary. If all the cracks are fully interconnected to make a flow network, the RVE can be assumed to be a homogeneous, anisotropic porous medium. It obeys to the Darcy's law, the apparent flow velocity $\overrightarrow{v}$ of fluid is related to the macroscopic pressure gradient ∇p through a linking symmetric tensor $\mathbf{k}$ called the permeability tensor:

$$\overrightarrow{v} = -\frac{\mathbf{k}}{\mu} \nabla p = -\frac{(\mathbf{k}^0 + \mathbf{k}^{\text{c}})}{\mu} \nabla p. \tag{17}$$

The parameter μ is the dynamic viscosity of fluid.

The present study is now focussing on the determination of crack permeability. The crack permeability tensor $\mathbf{k}^{\mathrm{c}}$ is regarded as a function of the crack orientation $\overrightarrow{n}$, average radius variation $r(\overrightarrow{n})$ and average aperture $e(\overrightarrow{n})$. For the set of cracks in the given orientation $\overrightarrow{n}$, the fluid flow velocity is assumed to be described by the Navier–Stokes equation for laminar flow between two parallel plates:

$$\overrightarrow{v}^{\mathrm{c}}(\overrightarrow{n}) = -\frac{\lambda}{12}\frac{1}{\mu}e(\overrightarrow{n})^2(\boldsymbol{\delta} - \overrightarrow{n}\otimes\overrightarrow{n})(\nabla p)^{\mathrm{c}}. \tag{18}$$

$(\nabla p)^{\mathrm{c}}$ is the local pressure gradient applied to the crack. $\boldsymbol{\delta}$ denotes the second order unit tensor. The positive scalar λ, less than the unity, is introduced to take into account the fact that every part of a crack does not work as a conduit. But some parts may be left as dead end. When $\lambda = 1$, the classic cubic law is recovered [13]. However, it is important to point out that the use of Navier–Stokes equation for flow in cracks represents a quite strong assumption. The validity of this equation for fluid flow between rough surfaces of crack is not proved. It is used here for the sake of simplicity because it provides with a first approximation to real flow regime. The local pressure gradient may be related to the macroscopic gradient by an appropriate localization law [5]. In this model, we have used a simplified law by assuming that $(\nabla p)^{\mathrm{c}} = \boldsymbol{\delta}\cdot\nabla p$. This implies that the local pressure gradient is also uniform and equals to the macroscopic one. Therefore, local deviations of pressure gradient are neglected. By analogy to the Voigt's bound of elastic compliance tensor of a cracked material, this simplification should correspond to the upper bound of crack permeability.

The macroscopic fluid velocity $\overrightarrow{v}$ is determined from the average of local crack velocity $\overrightarrow{v}^{\mathrm{c}}$ over the related volume:

$$\overrightarrow{v} = -\frac{\mathbf{k}^0}{\mu}\nabla p + \frac{1}{\Omega}\int_{\Omega}\overrightarrow{v}^{\mathrm{c}}\mathrm{d}\Omega = -\frac{\mathbf{k}^0}{\mu}\nabla p + \frac{1}{\Omega}\int_{\Omega^{\mathrm{c}}}\overrightarrow{v}^{\mathrm{c}}\mathrm{d}\Omega^{\mathrm{c}}. \tag{19}$$

Ω^{c} denotes the volume occupied by the microcracks. According to the anisotropic damage model presented in Sect. 3.1, the volume occupied by the set of cracks in the orientation $\overrightarrow{n}$ may be expressed by $\mathrm{d}\Omega^{\mathrm{c}}(\overrightarrow{n}) = N.e(\overrightarrow{n}).\pi r(\overrightarrow{n})^2$. The total crack volume can be obtained by integration over all the space orientations. Therefore, the macroscopic velocity can be rewritten as:

$$\overrightarrow{\mathbf{v}} = -\frac{\mathbf{k}^0}{\mu}\nabla p + \frac{N}{\Omega}\frac{1}{4\pi}\int_{S^2}\overrightarrow{v}^{c}(\overrightarrow{n})e(\overrightarrow{n})\pi r(\overrightarrow{n})^2\mathrm{d}S. \tag{20}$$

Introducing (18) into (20), the macroscopic flow velocity is finally expressed by

$$\overrightarrow{\mathbf{v}} = -\frac{\mathbf{k}^0}{\mu}\nabla p + \left(-\frac{1}{\mu}\right)\frac{\lambda}{12}\frac{N}{\Omega}\frac{1}{4\pi}\int_{S^2}e(\overrightarrow{n})^3\pi r(\overrightarrow{n})^2(\boldsymbol{\delta} - \overrightarrow{n}\otimes\overrightarrow{n})\mathrm{d}S\cdot\nabla p. \tag{21}$$

Comparing (21) with the macroscopic Darcy law (17), the macroscopic crack permeability tensor can be determined as follows:

$$\mathbf{k}^{\mathrm{c}} = \frac{\lambda\pi}{12}\frac{N}{\Omega}\frac{1}{4\pi}\int\limits_{S^2} e(\overrightarrow{n})^3 r(\overrightarrow{n})^2(\boldsymbol{\delta} - \overrightarrow{n}\otimes\overrightarrow{n})\mathrm{d}S. \tag{22}$$

By using the same numerical integration method as that used for the calculation of effective elastic compliance tensor, the components of the crack permeability can be approximated by

$$\mathbf{k}^{\mathrm{c}} = \frac{\lambda\pi}{12}\frac{2N}{\Omega}\sum_{k=1}^{P} w_k e(\overrightarrow{n}_k)^3 r(\overrightarrow{n}_k)^2(\boldsymbol{\delta} - \overrightarrow{n}_k\otimes\overrightarrow{n}_k). \tag{23}$$

4 Numerical Simulations

The proposed coupled model contains nine parameters, which can be determined from a series of triaxial compression tests with different confining pressures. The initial elastic constants of intact material, E_0 and ν_0, are determined from the linear part of stress–strain curves. The parameters involved in the crack propagation criterion; $r_0, r_{\mathrm{f}}, \eta$, and C_r; can be identified drawing the damage initiation surface (initial yield surface) for $r = r_0$ and the failure surface for $r = r_{\mathrm{f}}$ in the conventional $p - q$ stress plane. The damage initiation surface is determined from the stress level where the linearity is lost while the failure surface is obtained from the peak stresses. The normal dilation parameter χ and the crack number involved in the RVE can be estimated from the nonlinear responses of the axial and radial strains during a triaxial compression test. Finally, the roughness coefficient of crack faces λ can be determined from experimental data on the increase of permeability during a triaxial compression test. The proposed model is applied to a typical brittle rock, sandstone. For this material, the typical values of model's parameters are as follows: $E_0 = 20,300\,\mathrm{MPa}$, $\nu_0 = 0.26$, $r_0 = 3\times10^{-3}\,\mathrm{m}, r_{\mathrm{f}} = 9\times10^{-3}\,\mathrm{m}, C_r = 1.06\,\mathrm{MPa}a\sqrt{m}$, $\eta = 9.75\times10^{-3}$, $N = 6.3\times10^6$, $\chi = 0.0005$, $\lambda = 0.083$.

Figure 1 shows the simulation of two triaxial compression tests. There is a good agreement between the numerical simulations and experimental data. The proposed anisotropic damage describes the main features of mechanical behaviors of typical brittle rocks such as nonlinearity, volumetric dilatancy, and pressure dependency. For the determination of the variation of permeability due to crack growth, an isotropic initial permeability is assumed. Further, in each orientation, the number of microcracks remains the same but the average crack radius is different. The average radius of cracks in each orientation is explicitly determined by the propagation criterion and the average normal aperture is determined using the dilatancy coefficient. Numerical predictions of the variations of permeability in the axial direction during a

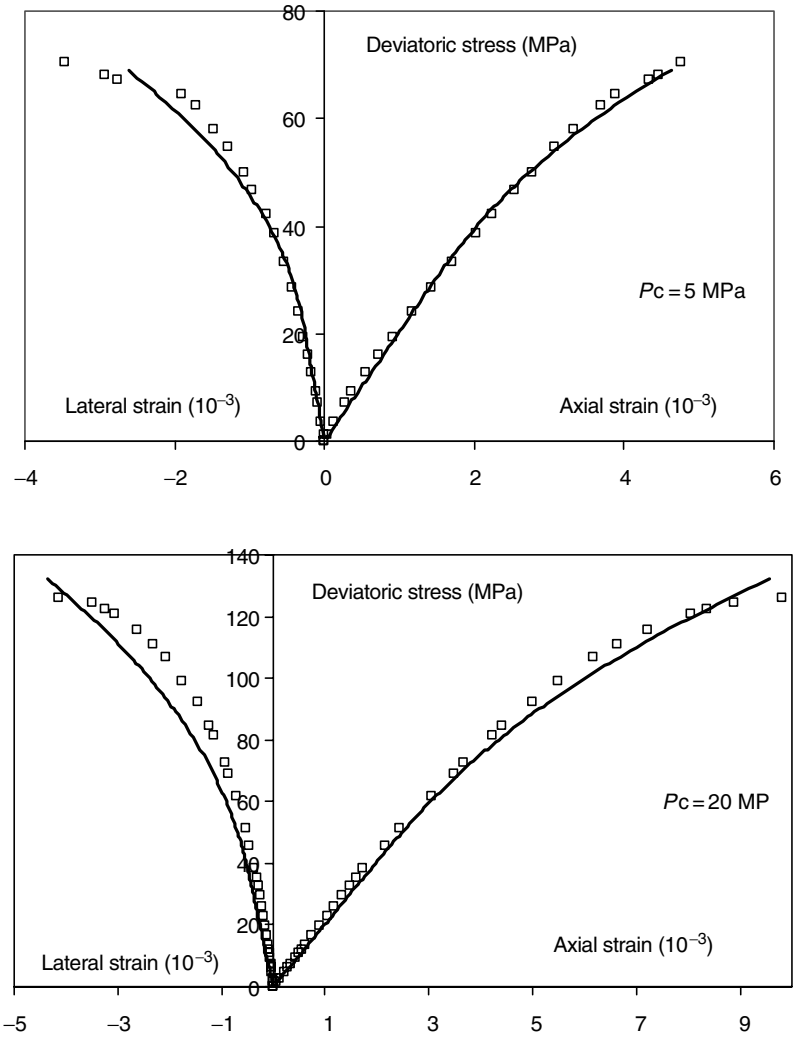

Fig. 1. Simulation of a triaxial compression test with (**a**) 5 MPa (**b**) 20 MPa confining pressure (the continuous lines are numerical simulations)

triaxial compression test are shown in Fig. 2 for different confining pressures. Unfortunately, experimental data on the permeability variation are not available for this rock under such test conditions. It is then impossible to give a quantitative comparison. However, from the qualitative point of view, these are qualitatively in agreement with experimental data obtained in brittle rock materials, mentioned in the first part of the chapter.

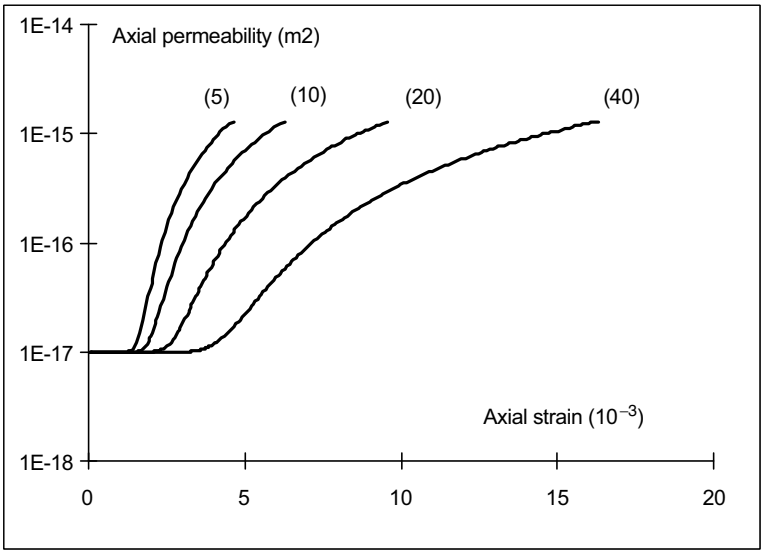

Fig. 2. Variation of the axial permeability due to crack propagation in triaxial compression tests with different confining pressures

5 Conclusions

An anisotropic damage model is proposed by taking into account the variation of permeability due to growth of microcracks. The formulation of the model is based on micromechanical analysis and experimental evidences from brittle materials like rocks and concrete. The damage evolution is determined from the crack propagation condition. By assuming fully connected microcracks, the permeability variation due to crack growth is explicitly coupled with the evolution of mechanical damage of material. The roughness of crack faces is taken into account. The proposed model is able to describe the main features of mechanical behaviors of brittle materials and the coupling with hydraulic flow. The simulations given by the proposed model are qualitatively in agreement with experimental data. However, it is a progressing but promising work, extensive experimental validation will be necessary to check the performance of the model. Some extensions could also be introduced, for example considering a partial crack connectivity, to improve the performance of the model.

References

1. Bazant Z.P. and Oh B.H. (1986). Efficient numerical integration on the surface of a sphere. *ZAMM, Z. Angew. Math. U Mech.* 66(1), 37–49
2. Berkowitz B. (2002). Characterizing flow and transport in fractured geological media: a review. *Adv. Water Resour.* 25, 861–884

3. Chen Z., Narayan S.P., Yang Z., Rahman S.S. (2000). An experimental investigation of hydraulic behaviours of fractures and joints in granitic rock. *Int. J. Rock Mech. Min. Sci.* 37, 1061–1071
4. Doolin D.M. and Mauldon M. (2001). Fracture permeability normal to bedding in layered rock masses. *Int. J. Rock Mech. Min. Sci.* 38, 199–210
5. Dormieux L. and Kondo D. (2004). Approche micromécanique du couplage perméabilité-endommagement. *C.R. Mécanique* 332, 135–140
6. Kachanov M. (1993). Elastic solids with many cracks and related problems. In *Advances in Applied Mechanics*, Vol. 30, Hutchinson J. and Wu T. (eds.), Academic, New York, 259–445
7. Lee C.H., Deng B.W. and Chang J.L. (1995). A continuum approach for estimating permeability for naturally fractured rocks. *Eng. Geol.* 39, 71–85
8. Oda M. (1985). Permeability tensor for discontinuous rock masses. *Géotecnique* 35(4), 483–495
9. Oda M., Takemura T. and Aoki T. (2002). Damage growth and permeability change in triaxial compression tests of Inada granite. *Mech. Mater.* 34, 313–331
10. Paterson S. (1978). Experimental Deformation of Rocks: The Brittle Field. Springer, Berlin Heidelberg New York
11. Pensée V., Kondo D. and Dormieux L. (2002). Micromechanical analysis of anisotropic damage in brittle materials. *J. Eng. Mech. ASCE*, 128(8), 889–897
12. Schulze O., Popp T. and Kern H. (2001). Development of damage and permeability in deforming rock salt. *Eng. Geol.* 61, 163–180
13. Snow D.T. (1969). Anisotropic permeability of fractured media. *Water Resour. Res.*, 5(6), 1273–1289.
14. Suzuki K, Oda M., Yamazaki M. and Kuwahara T. (1998). Permeability changes in granite with crack growth during immersion in hot water. *Int. J. Rock Mech. Min. Sci.* 35(7), 907–921
15. Wang J.A. and Park H.D. (2002). Fluid permeability of sedimentary rocks in a complete stress–strain process. *Eng. Geol.* 63, 291–300
16. Wong T.F. (1982). Micromechanics of faulting in Westerly granite. *Int. J. Rock Mech. Min. Sci.* 19, 49–6
17. Zhang X., Sanderson D.J., Harkness R.M. and Last N.C. (1996). Evaluation of the 2-D permeability tensor for fractured rock masses. *Int. J. Rock Mech. Min. Sci. & Geomech. Abstr.* 33(1), 17–37

Part IV

Analytical and Numerical Methods

Hydrologically Driven Slope Failure Initiation in Variably Saturated Porous Media

R.I. Borja, G. Oettl, B.A. Ebel and K. Loague

Stanford University, Stanford, USA
borja@stanford.edu

Abstract. We develop a physics-based slope failure initiation model that considers deformation and strain localization based upon three-phase continuum mixture theory for variably saturated porous media. The spatial and temporal variations in pore pressures needed to drive the slope stability model are simulated with a recently developed integrated hydrology model (InHM). To capture unsaturated soil response, the slope model has been formulated in the context of a three-phase material that explicitly accounts for the effect of the suction stress. The coupling of InHM to a rigorous slope stability model makes it possible, for the first time, to quantitatively investigate at the field-scale the nonintuitive interplay between fluid and hillslope processes that control hydrologically driven slope failure initiation.

1 Introduction

Landslides occur when earth material moves rapidly downslope after failing along a shear zone. Debris flows are differentiated from landslides by the pervasive, fluid-like deformation of the mobilized material. The formation of debris flows most often occurs as a result of a landslide partially or completely mobilizing into a debris flow. A physics-based characterization of debris flow initiation is important because of the rapid and destructive nature of these events.

A comprehensive physics-based model, known as InHM, was recently developed [5] and tested [3, 6] to simulate fully coupled near-surface hydrologic response. InHM can be employed to calculate subsurface fluid pressures in variably saturated soils. These fluid pressures can, in turn, be used to predict solid deformation and slope movement, as well as calculate several indicators of impending slope failure.

Also recently, a mechanical model for partially saturated soils has been formulated that utilizes nonlinear continuum mechanics applied to a three-phase solid–water–air material [1, 2]. This mechanical model satisfies the three

master balance laws: mass, linear momentum, and energy, and, furthermore, elucidates the role of entropy inequality on the development of specific constitutive laws for a soil skeleton exhibiting nonlinear irreversible responses. The model uses an effective Cauchy stress tensor motivated by principles of thermodynamics, as well as the Cam-Clay theory of critical state soil mechanics in which the yield function depends not only on the effective stress but also on the suction stress.

The objective of this paper is to demonstrate how these recently developed hydrologic response and solid deformation models may be integrated to study the physics of hydrologically driven slope failure initiation in variably saturated porous media. The procedure consists of sequential computational modeling in which the physics-based model InHM is first used to calculate the pore pressure response, which is then supplied to the deformation model to predict the solid deformation and stress responses. The latter responses may be used to predict slope failure initiation using different stability indicators.

2 Integrated Hydrology Model

The comprehensive InHM was designed to quantitatively simulate fully coupled near-surface hydrologic response. The important and innovative characteristics of InHM include (i) adaptive temporal weighting and time stepping, (ii) robust and efficient solution methods with the solution precision and mass-balance error stipulated by convergence tolerances, (iii) solution of one system of discrete equations with spatially variable properties and boundary conditions that requires no iteration between separate surface and subsurface models and no artificial boundary conditions, and (iv) no a priori assumption of a specific hydrologic-response mechanism. InHM is capable of simulating each of the hydrologic-response mechanisms: groundwater discharge, subsurface stormflow, Horton and Dunne overland flow. Infiltration and exfiltration rates are determined in space and time by spatially variable subsurface properties, spatially and temporally variable subsurface pressure-head gradients, and spatially and temporally variable surface water depths. The flow of water in both the surface and subsurface continua is therefore intimately coupled. The governing equations are discretized in space using the control volume FE method. Each coupled system of nonlinear equations in an InHM simulation is solved implicitly using Newton iteration. Efficient and robust iterative sparse matrix methods are used to solve the large sparse Jacobian systems. Subsurface flow, in 3D variably saturated porous medium and inside macropores, is calculated by

$$\nabla \cdot f^{\mathrm{a}} \boldsymbol{q} \pm q^{\mathrm{b}} \pm q^{\mathrm{e}} = f^{\mathrm{v}} \frac{\partial \phi S_{\mathrm{w}}}{\partial t}, \tag{1}$$

where $\boldsymbol{q}$ is the Darcy flux, q^{b} is a specified rate source/sink, q^{e} is the rate of water exchange between the subsurface and surface continua, ϕ is porosity, S_{w} is degree of saturation, t is time, f^{a} is the area fraction associated with each

continuum, and f^{v} is the volume fraction associated with each continuum. The Darcy flux is given by

$$\boldsymbol{q} = -k_{\mathrm{rw}} \frac{\rho_{\mathrm{w}} g}{\mu_{\mathrm{w}}} \boldsymbol{k} \cdot \nabla(\psi + z), \tag{2}$$

where k_{rw} is the relative permeability, ρ_{w} is the density of water, g is the gravitational acceleration, μ_{w} is the dynamic viscosity of water, $\boldsymbol{k}$ is the intrinsic permeability vector, z is the elevation head, and ψ is the pressure head (note, ψ is less than zero above the water table, zero at the water table, and greater than zero below the water table). The transient flow of water on the land surface (fully coupled to the subsurface) is estimated by the 2D diffusion wave approximation of the depth-integrated shallow water equations, with surface water velocities calculated with a 2D form of the Manning water depth/friction discharge equation. The subsurface fluid pressures [passed (x, y, z, t) to the slope stability model] are calculated by

$$p_{\mathrm{w}} = \rho_{\mathrm{w}} g \psi. \tag{3}$$

3 Solid Deformation Model

We consider a three-phase mixture of solid, water, and air phases and write balance of mass for each constituent as

$$\frac{\mathrm{d}\rho^{\alpha}}{\mathrm{d}t} + \rho^{\alpha} \mathrm{div}(\boldsymbol{\nu}) = -\mathrm{div}(\boldsymbol{w}^{\alpha}), \tag{4}$$

where $\mathrm{d}(\cdot)/\mathrm{d}t$ is a material time derivative following the solid phase motion, $\boldsymbol{\nu}$ is the solid phase velocity, ρ^{α} is the partial mass density of constituent α (= s, w, a for solid, water, and air, respectively), and $\boldsymbol{w}^{\alpha}$ is the Eulerian relative flow vector of the α constituent relative to the solid phase ($\boldsymbol{w}^{\mathrm{s}} = \boldsymbol{0}$, by definition).

Introducing K_{α} as the bulk modulus of the α constituent, then (1) can be re-written as

$$\frac{\mathrm{d}\phi^{\alpha}}{\mathrm{d}t} + \frac{\phi^{\alpha}}{K_{\alpha}} \frac{\mathrm{d}p_{\alpha}}{\mathrm{d}t} + \phi^{\alpha} \mathrm{div}(\boldsymbol{\nu}) = -\frac{1}{\rho_{\alpha}} \mathrm{div}(\boldsymbol{w}^{\alpha}), \tag{5}$$

where ϕ^{α} is the volume fraction, p_{α} is the intrinsic pressure, and ρ_{α} is the intrinsic mass density of the α constituent (note: $\rho^{\alpha} = \phi^{\alpha} \rho_{\alpha}$).

Balance of linear momentum for each constituent may be expressed as

$$\mathrm{div}(\boldsymbol{\sigma}^{\alpha}) + \rho^{\alpha} \boldsymbol{g} + \boldsymbol{h}^{\alpha} = \rho^{\alpha} \frac{\mathrm{d}^{\alpha} \boldsymbol{\nu}_{\alpha}}{\mathrm{d}t}, \tag{6}$$

where $\boldsymbol{\sigma}^{\alpha}$ is the partial Cauchy stress tensor, $\boldsymbol{g}$ is the gravity acceleration vector, $\boldsymbol{h}^{\alpha}$ is the volume–density force vector exerted by the other constituents on the α constituent, $\boldsymbol{\nu}_{\alpha}$ is the velocity of the α constituent, and $\mathrm{d}^{\alpha}(\cdot)/\mathrm{d}t$ is the material time derivative following the α constituent. Summing (6) for all

the three constituent phases gives

$$\operatorname{div}(\boldsymbol{\sigma}) + \rho \boldsymbol{g} = \sum_{\alpha=\mathrm{s,w,a}} \rho^{\alpha} \frac{\mathrm{d}^{\alpha} \boldsymbol{\nu}_{\alpha}}{\mathrm{d}t}, \tag{7}$$

where $\boldsymbol{\sigma} = \boldsymbol{\sigma}^{\mathrm{s}} + \boldsymbol{\sigma}^{\mathrm{w}} + \boldsymbol{\sigma}^{\mathrm{a}}$ is the total Cauchy stress tensor, and $\rho = \rho^{\mathrm{s}} + \rho^{\mathrm{w}} + \rho^{\mathrm{a}}$ is the total mass density of the mixture.

Let K be the kinetic energy per unit volume and I the total internal energy per unit volume of a three-phase mixture. The first law of thermodynamics may be written as

$$\dot{K} + \dot{I} = P, \tag{8}$$

where P is the mechanical power per unit volume and the superposed dot, $(\cdot)$, denotes a material time derivative relative to the mixture taken as a whole. Using balance of mass and balance of linear momentum, we obtain the following expression for the rate of change of internal energy:

$$\dot{I} = \sum_{\alpha=\mathrm{s,w,a}} \boldsymbol{\sigma}^{\alpha} : \boldsymbol{d}_{\alpha}, \tag{9}$$

where $\boldsymbol{d}_{\alpha}$ is the rate of deformation tensor for the α constituent. Assuming $K_{\mathrm{s}} = \inf$ (incompressible solid grains, which is a reasonable assumption for soils), (9) can be converted into the form

$$\dot{I} = \boldsymbol{\sigma}' : \boldsymbol{d} + \dot{I}', \tag{10}$$

where $\boldsymbol{d}$ is the solid rate of deformation tensor,

$$\boldsymbol{\sigma}' = \boldsymbol{\sigma} + [S_{\mathrm{r}} p_{\mathrm{w}} + (1 - S_{\mathrm{r}}) p_{\mathrm{a}}] \mathbf{1}, \tag{11}$$

is a Cauchy effective stress tensor conjugate to $\boldsymbol{d}$ and analogous to that proposed by Schrefler [4], and $\dot{I}'$ consists of additional terms not associated with the deformation of the solid phase. The effective Cauchy stress tensor $\boldsymbol{\sigma}'$ differs from the total Cauchy stress tensor $\boldsymbol{\sigma}$ by an isotropic pore pressure equal to the average of the intrinsic pore water and pore air pressures weighted according to the degree of saturation S_{r}. Thus, the total Cauchy stress tensor lends itself to the additive decomposition

$$\boldsymbol{\sigma} = \boldsymbol{\sigma}' - [S_{\mathrm{r}} p_{\mathrm{w}} + (1 - S_{\mathrm{r}}) p_{\mathrm{a}}] \mathbf{1}. \tag{12}$$

This form may be used to develop the matrix equation for the finite element problem.

4 Finite Element Model

The finite element matrix equation for the solid deformation model takes the form

$$\boldsymbol{F}_{\mathrm{INT}}(\boldsymbol{d}, \boldsymbol{p}_{\mathrm{a}}, \boldsymbol{p}_{\mathrm{w}}) = \boldsymbol{F}_{\mathrm{EXT}}, \tag{13}$$

where $\boldsymbol{F}_{\mathrm{EXT}}$ is the nodal external force vector induced by gravity load, and $\boldsymbol{F}_{\mathrm{INT}}$ is the internal nodal force vector induced by the solid matrix displacement vector $\boldsymbol{d}$ and the prescribed pore water and pore air pressure vectors $\boldsymbol{p}_{\mathrm{w}}$ and $\boldsymbol{p}_{\mathrm{a}}$, respectively. Specifically, the internal nodal force vector $\boldsymbol{F}_{\mathrm{INT}}$ is obtained from the total Cauchy stress tensor $\{\boldsymbol{\sigma}\}$ through an equation of the form

$$\boldsymbol{F}_{\mathrm{INT}} = \int_V \boldsymbol{B}^{\mathrm{T}}\{\boldsymbol{\sigma}\}\,\mathrm{d}V, \tag{14}$$

where $\boldsymbol{B}$ is the strain–displacement transformation matrix. From (12), the functional relationship $\boldsymbol{F}_{\mathrm{INT}} = \boldsymbol{F}_{\mathrm{INT}}(\boldsymbol{d}, \boldsymbol{p}_{\mathrm{a}}, \boldsymbol{p}_{\mathrm{w}})$ is evident.

Using an uncoupled solution strategy, the vectors $\boldsymbol{p}_{\mathrm{w}}$ and $\boldsymbol{p}_{\mathrm{a}}$ may be determined from the hydrology model (for near-surface conditions the pore air pressure is nearly atmospheric, so $\boldsymbol{p}_{\mathrm{a}} = \boldsymbol{0}$ is typically assumed in this case). The vector $\boldsymbol{F}_{\mathrm{EXT}}$ is constant for quasi-static loading; thus, the slope deformation response $\boldsymbol{d}$ is driven exclusively by the prescribed temporal variations of $\boldsymbol{p}_{\mathrm{w}}$. To better elucidate the overall global algorithm, an outline of the solution is presented in Fig. 1.

Putting (13) in residual form gives

$$\boldsymbol{R}(\boldsymbol{d}) = \boldsymbol{F}_{\mathrm{EXT}} - \boldsymbol{F}_{\mathrm{INT}}(\boldsymbol{d}, \boldsymbol{p}_{\mathrm{a}}, \boldsymbol{p}_{\mathrm{w}}). \tag{15}$$

We then want to dissipate the residual nodal force vector $\boldsymbol{R}$ by finding the response vector $\bar{\boldsymbol{d}}$ at each time instant in the solution. Here we utilize Newton's method to find the roots of the nonlinear equations, and construct the

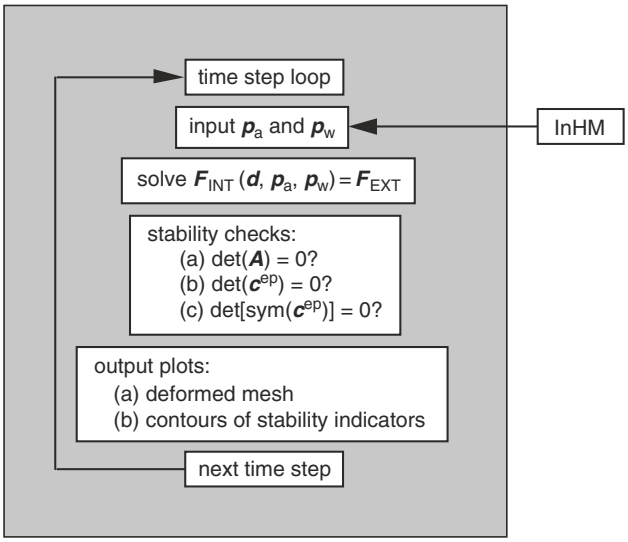

Fig. 1. Algorithm for hydrologically driven finite element deformation analysis of slopes

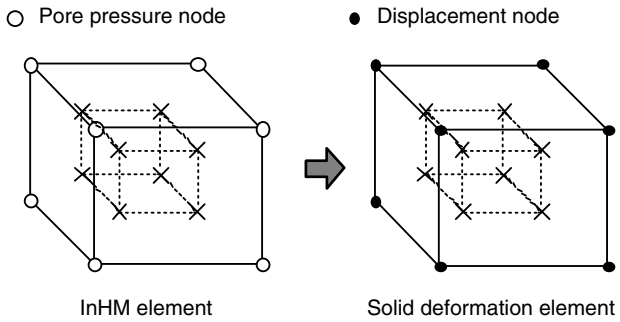

Fig. 2. Interfacing InHM with the solid deformation model

consistent tangent operator as

$$\boldsymbol{R}'(\boldsymbol{d}) = -\boldsymbol{F}'_{\mathrm{INT}}(\boldsymbol{d}, \boldsymbol{p}_{\mathrm{a}}, \boldsymbol{p}_{\mathrm{w}}) = -\partial \boldsymbol{F}_{\mathrm{INT}}/\partial \boldsymbol{d}. \tag{16}$$

Asymptotic quadratic convergence of the iterations can be expected from Newton's method provided that a consistent algorithmic tangent operator $\boldsymbol{R}'(\boldsymbol{d})$ is used.

The integrated hydrology model InHM generates spatial and temporal descriptions of calculated pore water pressures within the slope using conventional finite element approximations. Figure 2 shows a finite element used by InHM, an eight-node brick element with a trilinear interpolation of the pore water pressure field. The standard numerical integration for this element is a $2 \times 2 \times 2$-point Gauss rule in the interior of the element, denoted by the symbol $\times$. In the solid deformation model we adopt a similar level of interpolation so that the interpolated pore water pressures at the Gauss points can be used directly to evaluate the total stresses in the solid deformation model. Note that mesh locking is not engendered by the same level of interpolation for the pore water and solid displacement fields since the present approach entails an uncoupled analysis. By constraining motion in the out-of-plane direction, the brick element shown in Fig. 2 may be used for plane strain loading conditions as well.

5 Numerical Example

For preliminary numerical investigations we consider a simple example consisting of a variably saturated slope deforming in plane strain. The slope has horizontal and vertical dimensions of approximately 50 and 30 m, and is inclined at an angle of about 30°, see Fig. 3. The domain is spatially discretized using 527 constrained brick finite elements described in Sect. 4. Each element consists of nodes with horizontal and vertical displacement degrees of freedom, as well as pore water and pore air pressure degrees of freedom. The pore

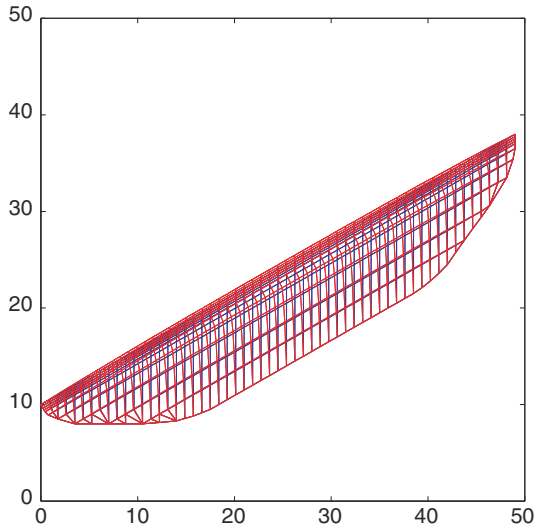

Fig. 3. Undeformed and deformed meshes (all coordinates in meters)

air pressure is assumed to remain equal to atmospheric everywhere within the slope, but the spatial distribution of the pore water pressure has been calculated by InHM and is used to drive the deformation model. For purposes of deformation analysis all nodes supporting the bottom of the slope are assumed to be pinned to the bedrock.

The soil is modeled as an elastoplastic material yielding according to the modified Cam-Clay theory and enhanced to accommodate the effect of suction on the yield condition. The mathematical framework of the constitutive model is based on a three-phase solid–water–air mixture formulation presented by Borja [1]. For the record, the material parameters used in the present analysis are the same as those used by Borja [1].

The numerical simulation of the problem consists of two steps. The first step consists of establishing the initial condition, whereas the second step consists of calculating the deformation produced by the imposed changes in the pore water pressures. The initial state is characterized by a bilinear pore water pressure distribution in the vertical direction. The ground water table marking the position of zero pore pressures is located at a depth of 2.5 m below the slope. Below the ground water level the pore water pressure increases hydrostatically; above the ground water table tensile pore water pressures (i.e., suction stresses) exist in the slope, as generated by InHM. For purposes of describing the prevailing initial yield condition, the soil is assumed to be normally consolidated everywhere.

The second step of the simulation consists of raising the ground water table elevation by about 0.9 m. This has the effect of saturating an initially unsaturated zone, as well as increasing the pore water pressures everywhere

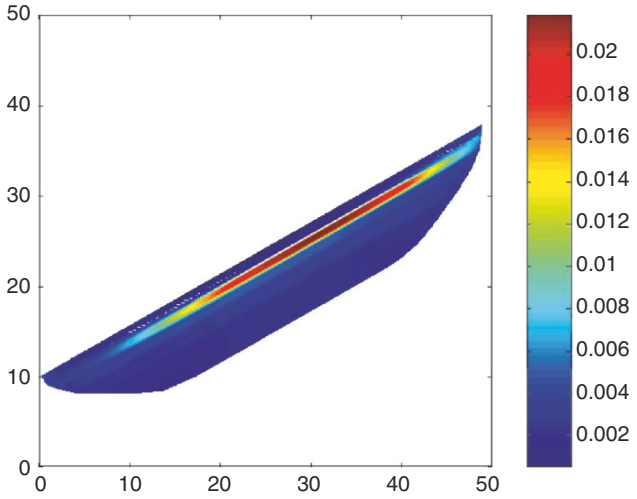

Fig. 4. Shear strain distribution (in decimals) after water table rise

in the slope. Figure 4 depicts the distribution of the shear strains in the domain after the water table rise, clearly indicating a significant shear strain concentration within a sub-region of the slope where the unsaturated zone has become saturated. This shear strain distribution agrees with a high displacement gradient forming in the vicinity of the water table rise. The vertical displacements are one order of magnitude smaller than the horizontal displacements. However, due to the imposed displacement boundary conditions where the deformations are constrained at both the top and bottom of the slope, the maximum deformations occur at about the mid-height of the slope.

6 Closure

We have developed a physics-based slope failure initiation model that considers deformation and strain localization based upon three-phase continuum mixture theory for variably saturated porous media. The spatial and temporal variations in pore pressures needed to drive the slope stability model can be simulated with a recently developed InHM. To capture unsaturated soil response, the slope model has been formulated in the context of a three-phase material that explicitly accounts for the effect of the suction stress. The coupling of a rigorous slope stability model to a hydrology model will make it possible for the first time to quantitatively investigate at the field-scale the nonintuitive interplay between fluid and hillslope processes that control hydrologically driven slope failure initiation. Work is currently in progress to apply the modeling approach to an experimental catchment that has experienced slope failure.

Acknowledgments

The first author acknowledges the support of National Science Foundation Grant No. CMS-0201317. The second author is currently supported by an Erwin-Schroedinger Fellowship provided by the Austrian Science Fund (FWF) during his visit to Stanford University. The third and fourth authors have benefited from their long and ongoing collaboration with Joel VanderKwaak and partial support from the National Science Foundation Grant No. EAR-0409133.

References

1. Borja, R.I. 2004. Cam-Clay plasticity. Part V: A mathematical framework for three-phase deformation and strain localization analyses of partially saturated porous media. *Comput. Methods Appl. Mech. Engrg.* 193, 5301–5338
2. Borja, R.I. 2006. On the mechanical energy and effective stress in saturated and unsaturated porous continua, *Int. J. Solids Struct.* 43, 1764–1786
3. Loague, K., C.S. Heppner, R.H. Abrams, J.E. VanderKwaak, A.E. Carr, and B.A. Ebel. 2005. Further testing of the Integrated Hydrology Model (InHM): Event-based simulations for a small rangeland catchment located near Chickasha, Oklahoma. *Hydrol. Process.* 19, 1373–1398
4. Schrefler, B.A. 1984. The finite element method in soil consolidation (with applications to surface subsidence), Ph.D. Thesis, University College of Swansea, C/Ph/76/84
5. VanderKwaak, J.E. 1999. Numerical simulation of flow and chemical transport in integrated surface-subsurface hydrologic systems. Ph.D. Dissertation, University of Waterloo, Waterloo, Ontario, Canada
6. VanderKwaak, J.E. and K. Loague. 2001. Hydrologic-response simulations for the R-5 catchment with a comprehensive physics-based model. *Water Resour Res* 37, 999–1013

A Survey of Some Mathematical Results for Highly Frictional Granular Materials

G.M. Cox, N. Thamwattana and J.M. Hill

University of Wollongong, Australia
gcox@uow.edu.au

Abstract. Recently the authors have exploited the notion of a highly frictional granular material to derive analytical solutions for certain problems. Generally, we use the term highly frictional granular material to refer to those materials which possess an angle of internal friction such that the trigonometric sine of the angle of internal friction is close to unity. There are many granular materials for which this is the case, such as black and brown coal and limestone powder. For such materials formal perturbation solutions can be derived for which the zeroth-order solution corresponds to an angle of internal friction precisely equal to 90°, while the full perturbation solution applies to a larger range of angles of internal friction. In this paper, we present a survey of the ideas and the theory underlying highly frictional granular materials and catalogue the major solution types which are available for such materials. We illustrate some of the recent results obtained by using these analytical solutions to model the problems of determining the stress and velocity distributions in a gravity flow hopper, and the stress profiles beneath a stockpile and within a stable rat-hole.

1 Introduction

Modelling granular materials is an area that still provides an unlimited source of interesting challenges and problems, as it has done for many years. This is due to the diversity of material properties and material behaviour that granular materials can exhibit, which often cause some surprising physical behaviour under seemingly simple conditions. In this paper, we present a survey of some recent results for those granular materials termed highly frictional granular materials. These results have been obtained by the authors for the classical Coulomb-Mohr continuum theory of granular materials, and applied to the three granular problems of determining the stress and velocity distributions in a gravity flow hopper, and the stress profiles beneath a stockpile and within a stable rat-hole.

We use the term highly frictional granular material to refer to any granular material which has the property that the value of the trigonometric sine of the

angle of internal friction is close to unity. Examples of such materials include black and brown coal and limestone powder (see, for example, Australian Standard [1], Sture [2], Perkins [3, 4] and Perkins and Gui [5]). The major issue here is not the actual magnitude of the angle of internal friction in relation to $\pi/2$, but rather the proximity of the sine of the angle in relation to unity, noting that even a value of 64 degrees gives a value close to one, namely $\sin 64^\circ = 0.9$. We emphasize that the limiting value $\phi = \pi/2$ does not necessarily correspond to the case of infinite friction, but rather inter-particle slip may still occur due to the alternative possibility of slip under zero normal traction (see, for example, the discussion given by Lynch and Mason [6]). For further discussion on highly frictional granular materials, we refer the reader to Cox et al. [7] and Thamwattana et al. [8].

In the following section, we state the basic equations governing the stress and velocity distributions for two-dimensional plane strain and axially symmetric steady quasi-static flow according to the classical Coulomb-Mohr continuum theory for granular materials for the stress distribution and the non-dilatant double-shearing theory (Spencer [9, 10]) for the velocity field. Some recently determined exact solutions of the governing equations are summarized in Sect. 3, while applications of some of these solutions are illustrated graphically in Sects. 4–6 for the three problems of determining the stress and velocity profiles for gravity flow in a hopper, and the stress profiles beneath a stockpile and within a stable rat-hole, respectively.

2 Basic Equations

In this section we state the basic equations governing the stress and velocity distributions according to the classical Coulomb-Mohr continuum theory for the stress field, and the non-dilatant double-shearing theory for the velocity field. In particular, we consider both two-dimensional plane strain and axially symmetric equations for the three problems considered, where it is only the boundary conditions that distinguish between each problem.

2.1 Two-Dimensional Plane Strain Equations

For steady quasi-static plane strain gravity flow, the equilibrium equations, in the usual rectangular Cartesian coordinates (x, y) shown in Fig. 1a, are given by

$$\frac{\partial \sigma_{xx}}{\partial x} + \frac{\partial \sigma_{xy}}{\partial y} = 0, \quad \frac{\partial \sigma_{xy}}{\partial x} + \frac{\partial \sigma_{yy}}{\partial y} = \rho g, \tag{1}$$

where g is the acceleration due to gravity and ρ is the bulk density, both assumed constant, while σ_{xx}, σ_{xy} and σ_{yy} denote the non-zero physical components of the Cauchy stress tensor. Assuming the usual stress decomposition

$$\sigma_{xx} = -p + q\cos 2\psi,\ \sigma_{yy} = -p - q\cos 2\psi,\ \sigma_{xy} = q\sin 2\psi, \tag{2}$$

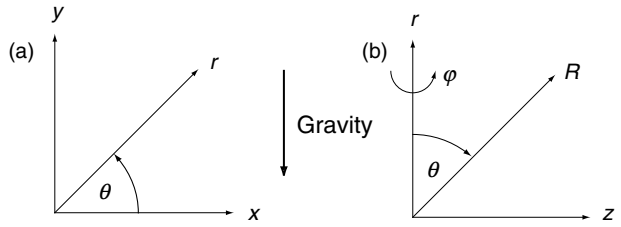

Fig. 1. Coordinates for (**a**) plane strain and (**b**) axially symmetric problems

where p and q are the stress invariants given by

$$p = -\frac{1}{2}(\sigma_{xx} + \sigma_{yy}), \quad q = \frac{1}{2}\{(\sigma_{xx} - \sigma_{yy})^2 + 4\sigma_{xy}^2\}^{1/2}, \tag{3}$$

and ψ is the angle between the direction of the maximum principal stress and the x-axis, in the direction of increasing θ, which can be expressed as

$$\tan 2\psi = \frac{2\sigma_{xy}}{\sigma_{xx} - \sigma_{yy}}, \tag{4}$$

then the Coulomb-Mohr yield condition can be written in the form

$$q = p \sin\phi + c\cos\phi, \tag{5}$$

where c is the cohesion and ϕ is the angle of internal friction of the material, both assumed constant. Thus, (1)–(5) constitute the governing equations for the stress distribution for steady quasi-static plane strain gravity flow.

To determine the associated velocity distribution, we assume the non-dilatant double-shearing theory (Spencer [9, 10]), which states that if $u(x, y)$ and $v(x, y)$ are the non-zero physical components of the velocity vector in the x and y directions, respectively, then under steady quasi-static plane strain flow the velocity components satisfy

$$\frac{\partial u}{\partial x} + \frac{\partial v}{\partial y} = 0,$$

$$\left(\frac{\partial v}{\partial x} + \frac{\partial u}{\partial y}\right)\cos 2\psi - \left(\frac{\partial u}{\partial x} - \frac{\partial v}{\partial y}\right)\sin 2\psi = \sin\phi\left(\frac{\partial v}{\partial x} - \frac{\partial u}{\partial y} - 2\Omega\right), \tag{6}$$

where Ω is defined by

$$\Omega = \dot{\psi} = u\frac{\partial \psi}{\partial x} + v\frac{\partial \psi}{\partial y}. \tag{7}$$

Thus, for a known stress distribution, the above equations constitute the governing equations for the associated velocity distribution for steady quasi-static plane strain gravity flow.

Now, in the limit of $\phi = \pi/2$, Thamwattana and Hill [11] show that the governing equations for the stress distribution reduce to the single second

order non-linear partial differential equation

$$\frac{\partial^2 h}{\partial x^2} - 2h\frac{\partial^2 h}{\partial x \partial y} + h^2\frac{\partial^2 h}{\partial y^2} = 0, \tag{8}$$

where $h = \cot\psi$. Further, if the stream-function $\chi(x, y)$ is defined by

$$u(x, y) = \frac{\partial \chi}{\partial y}, \quad v(x, y) = -\frac{\partial \chi}{\partial x}, \tag{9}$$

so that $(6)_1$ is automatically satisfied, then $(6)_2$ becomes

$$\frac{\partial^2 \chi}{\partial x^2} - 2h\frac{\partial \chi^2}{\partial x \partial y} + h^2\frac{\partial^2 \chi}{\partial y^2} = \frac{\partial h}{\partial x}\frac{\partial \chi}{\partial y} - \frac{\partial h}{\partial y}\frac{\partial \chi}{\partial x}, \tag{10}$$

which is a second-order linear partial differential equation governing the associated velocity distribution for $\phi = \pi/2$.

2.2 Three-Dimensional Axially Symmetric Equations

In terms of the cylindrical polar coordinates (r, φ, z) defined in Fig. 1b, the equilibrium equations for steady quasi-static axially symmetric gravity flow are given by

$$\frac{\partial \sigma_{rr}}{\partial r} + \frac{\partial \sigma_{rz}}{\partial z} + \frac{\sigma_{rr} - \sigma_{\varphi\varphi}}{r} = 0, \quad \frac{\partial \sigma_{rz}}{\partial r} + \frac{\partial \sigma_{zz}}{\partial z} + \frac{\sigma_{rz}}{r} = \rho g, \tag{11}$$

where $\sigma_{rr}, \sigma_{rz}, \sigma_{zz}$ and $\sigma_{\varphi\varphi}$ denote the non-zero physical components of the Cauchy stress tensor, which admit the representation

$$\sigma_{rr} = -p + q\cos 2\psi, \ \sigma_{zz} = -p - q\cos 2\psi, \ \sigma_{rz} = q\sin 2\psi, \tag{12}$$

where the invariants p and q are defined by

$$p = -\frac{1}{2}(\sigma_{rr} + \sigma_{zz}), \ q = \frac{1}{2}\{(\sigma_{rr} - \sigma_{zz})^2 + 4\sigma_{rz}^2\}^{1/2}, \tag{13}$$

and ψ is given by

$$\tan 2\psi = \frac{2\sigma_{rz}}{\sigma_{rr} - \sigma_{zz}}. \tag{14}$$

We note that physically ψ is the angle the direction of the maximum principal stress makes with the r-axis, in the direction of increasing θ, and the Coulomb-Mohr yield condition can be expressed in the form (5). We also note that in axial symmetry we need to make an additional assumption regarding the hoop stress $\sigma_{\varphi\varphi}$. Here we assume the particular Haar-von Karman regime such that the hoop stress is equal to the maximum principal stress, so that

$$\sigma_{\varphi\varphi} = -p + q. \tag{15}$$

We comment that Cox, Eason and Hopkins [12] state that the plastic regimes which agree with the Haar-von Karman hypothesis will give rise to solutions that are most likely to be of the greatest significance to axially symmetric problems. Further, the heuristic Haar-von Karman principle states that under an axially symmetric condition the hoop stress is equal to either the maximum

or the minimum principal stress, where here we assume the former. We note that this choice differs from the traditional view (see Jenike [13, 14], Spencer [15]), in which more physically realistic results for converging flow are believed to be produced by assuming the hoop stress is equal to the minimum principal stress, while (15) is believed to be more applicable for diverging flow. However, here we adopt (15) in order to make analytical progress, but we emphasize that the results produced upon assuming (15) satisfy the necessary physical condition that the rate of work is non-negative, as detailed in Cox et al. [16]. As such, we adopt (15) and we keep in mind that the results obtained may not be as physically applicable as those obtained when the hoop stress is equal to the minimum principal stress. Thus, for steady quasi-static axially symmetric gravity flow, the governing stress equations are given by (5) and (11)–(15).

Again, assuming the non-dilatant double-shearing theory as formulated by Spencer [9, 10], the associated velocity distribution for steady quasi-static axially symmetric flow is given by

$$\frac{\partial u}{\partial r} + \frac{\partial v}{\partial z} + \frac{u}{r} = 0,$$

$$\left(\frac{\partial v}{\partial r} + \frac{\partial u}{\partial z}\right)\cos 2\psi - \left(\frac{\partial u}{\partial r} - \frac{\partial v}{\partial z}\right)\sin 2\psi = \sin\phi\left(\frac{\partial v}{\partial r} - \frac{\partial u}{\partial z} - 2\Omega\right), \quad (16)$$

where $u(r, z)$ and $v(r, z)$ are the non-zero physical components of the velocity vector in the r and z directions, respectively, and Ω is defined by

$$\Omega = \dot{\psi} = u\frac{\partial \psi}{\partial r} + v\frac{\partial \psi}{\partial z}. \quad (17)$$

Thus, for given ψ, the governing equations for the associated velocity distribution for steady quasi-static axially symmetric gravity flow are given by (16) and (17).

Thamwattana and Hill [11] show that in the limit of $\phi = \pi/2$ the governing stress equations reduce to the second-order non-linear partial differential equation

$$\frac{\partial^2 h}{\partial r^2} - 2h\frac{\partial^2 h}{\partial r \partial z} + h^2\frac{\partial^2 h}{\partial z^2} - \frac{1}{r}\left(\frac{\partial h}{\partial r} - h\frac{\partial h}{\partial z}\right) = 0, \quad (18)$$

where $h = \cot\psi$, and with the stream-function $\chi(r, z)$ given by

$$u(r, z) = \frac{1}{r}\frac{\partial \chi}{\partial z}, \quad v(r, z) = -\frac{1}{r}\frac{\partial \chi}{\partial r}, \quad (19)$$

then from (16) and (17) we may deduce the second order linear partial differential equation

$$\frac{\partial^2 \chi}{\partial r^2} - 2h\frac{\partial^2 \chi}{\partial r \partial z} + h^2\frac{\partial^2 \chi}{\partial z^2} - \frac{1}{r}\left(\frac{\partial \chi}{\partial r} - h\frac{\partial \chi}{\partial z}\right) = \frac{\partial h}{\partial r}\frac{\partial \chi}{\partial z} - \frac{\partial h}{\partial z}\frac{\partial \chi}{\partial r}, \quad (20)$$

the solution of which determines the associated velocity distribution for $\phi = \pi/2$.

3 Exact Solutions

In this section we list some of the numerous exact solutions to the governing equations for plane strain flow (8) and (10) and for axially symmetric flow (18) and (20). For further details of these solutions and their derivation, we refer the reader to Thamwattana and Hill [11] and McCue, Johnpillai and Hill [17].

3.1 Plane Strain Exact Solutions

Stress Solutions

Using Lie symmetry methods, the governing stress partial differential equation (8) remains invariant under certain one-parameter groups, which in turn reduce (8) to an ordinary differential equation. The various functional forms for $h(x, y)$ are given by

$$\begin{aligned}&1.\ h = f(y), \quad 2.\ h = f(x), \quad 3.\ h = -x + f(y - x^2/2),\\ &4.\ h = yf(x - a\log y), \quad 5.\ h = f(x) - y/x, \quad 6.\ h = f(y - \log x)/x,\\ &7.\ h = -\log x + f(y/x - \log x), \quad 8.\ h = x^a f(y/x^{a+1}),\end{aligned} \tag{21}$$

where f denotes an arbitrary function to be determined by solving the resulting ordinary differential equation. Each functional form in (21) gives rise to a family of solutions, which are presented in Table 1. We note that throughout this paper, a, b, C_1, C_2, C_3 and C_4 denote arbitrary constants while $I(s), I_1(s)$ and $I_2(s)$ denote the three integrals defined, respectively, by

$$\begin{aligned}I(s) &= \int^s t^{-1/2}\mathrm{e}^{t/2}\mathrm{d}t + C_1,\\ I_1(s) &= \int^s t^{-1/3}\mathrm{e}^{t/3}\mathrm{d}t + C_1, \quad I_2(s) = \int^s t^{-2/3}\mathrm{e}^{t/3}\mathrm{d}t + C_1,\end{aligned} \tag{22}$$

and s is a parameter. We note that these integrals can be expressed in terms of error functions, gamma functions and incomplete gamma functions, but it is more convenient for our purposes to use (22).

Velocity Solutions

For each of the functional forms for $h(x, y)$ given in (21), with the corresponding solution in Table 1, there exists at least one functional form for $\chi(x, y)$ which is also invariant under the one-parameter group and in turn reduces the linear partial differential equation (10) to an ordinary differential equation. Generally this particular stream-function is easier to solve for. We present the various functional forms for $\chi(x, y)$ in Table 2, where we note that for each $h(x, y)$, there are at least two possible forms for $\chi(x, y)$. Here, we do

Table 1. Exact solutions of (8) for the eight families of (21)

$h(x,y)$ family	solution for f
1. $h = f(y)$	$f = C_1 y + C_2$
2. $h = f(x)$	$f = C_1 x + C_2$
3. $h = -x + f(\xi)$, $\xi = y - x^2/2$	$\xi = (f + \log\lvert C_1 f - 1\rvert)/C_1 + C_2$
4. $h = yf(\xi)$, $\xi = x - a\log y$	$\xi = a(\log[f^2 + C_1^2(1+af)])/2 + C_2 + \dfrac{2 - a^2C_1^2}{C_1(4 - a^2C_1^2)^{1/2}} \times \left[\arctan\left(\dfrac{2f + aC_1^2}{C_1(4 - a^2C_2^2)^{1/2}}\right) - \dfrac{\pi}{2}\right]$
5. $h = f(x) - y/x$	$f = C_1/x + C_2x^2$
6. $h = f(\xi)/x$, $\xi = y - \log x$	$f = -2 + s^{1/2}\mathrm{e}^{-s/2}I(s)/2$ $\xi = -\dfrac{1}{2}\log s + \dfrac{1}{4}\displaystyle\int^s t^{-1/2}\mathrm{e}^{-t/2}I(t)\mathrm{d}t + C_2$
7. $h = -\log x + f(\xi)$, $\xi = y/x - \log x$	$f = -\xi - 1 + s^{-1/2}\mathrm{e}^{-s/2}I(s)/2$ $\xi = -\dfrac{1}{4}\displaystyle\int^s t^{-3/2}\mathrm{e}^{-t/2}I(t)\mathrm{d}t + C_2$
8. $h = f(y)/x$ $(a = -1)$	$f = C_2 s^{1/2}\mathrm{e}^{s/2}$ $y = -C_2 I(s)/2$
8. $h = f(\xi)$, $\xi = y/x$ $(a = 0)$	$f = C_2 I(s)$ $\xi = C_2[2s^{-1/2}\mathrm{e}^{s/2} - I(s)]$
8. $h = xf(\xi)$, $\xi = y/x^2$ $(a = 1)$	$f = C_2[2s^{-1/2}\mathrm{e}^{s/2} - I(s)]$ $\xi = -C_2[2s^{-1/2}\mathrm{e}^{s/2} + (1-s)I(s)/s]/2$
8. $h = x^2 f(\xi)$, $\xi = y/x^3$ $(a = 2)$	$f = C_2[2s^{-1/2}\mathrm{e}^{s/2} + (1-s)I(s)/s]$ $\xi = -C_2[2(s-2)s^{-3/2}\mathrm{e}^{s/2} + (3-s)I(s)/s]/3$

not present all the corresponding solutions to each functional form of $\chi(x,y)$, but rather we present only the solutions for the functional form of 8 (i) (from Table 2), for the four values of $a = -1, 0, 1$ and 2, and some of these solutions are used to determine the stress and velocity distributions for the three granular problems examined in Sects. 4–6. In particular, Table 3 states the exact parametric solutions for $a = -1$, 0, 1 and 2 corresponding to the functional forms of $h(x,y) = x^a f(\xi)$ and $\chi(x,y) = x^b g(\xi)$, where $\xi(x,y) = y/x^{a+1}$.

3.2 Axially Symmetric Exact Solutions

Stress Solutions

On examining the governing partial differential equation (18) using Lie symmetry methods we may deduce the following six functional forms for $h(r,z)$

$$\begin{gathered} 1.\ h = f(r), \quad 2.\ h = zf(r), \quad 3.\ h = f(r) - z/(r+a), \\ 4.\ h = f(z + \log r)/r, \quad 5.\ h = -\log r + f(z/r - \log r), \\ 6.\ h = r^a f(z/r^{a+1}), \end{gathered} \tag{23}$$

which on substitution reduce (18) to an ordinary differential equation, and each functional form gives rise to the families of solutions presented in Table 4.

Table 2. The corresponding functional forms of $\chi(x, y)$ for the eight families of (21)

$h(x, y)$ family		corresponding $\chi(x, y)$ families
1. $h = f(y)$	(i)	$\chi = bx + g(y)$
	(ii)	$\chi = (b + f(y))x + g(y)$
	(iii)	$\chi = \mathrm{e}^x g(y)$
2. $h = f(x)$	(i)	$\chi = by + g(x)$
	(ii)	$\chi = yf(x) + g(x)$
	(iii)	$\chi = \mathrm{e}^y g(x)$
3. $h = -x + f(\xi)$	(i)	$\chi = g(\xi)$
$\xi = y - x^2/2$	(ii)	$\chi = \mathrm{e}^x g(\xi)$
	(iii)	$\chi = -x^2/2 + g(\xi) + \int f(\xi)\mathrm{d}x$
4. $h = yf(\xi)$	(i)	$\chi = y^b g(\xi)$
$\xi = x - a \log y$	(ii)	$\chi = \log y + g(\xi)$
	(iii)	$\chi = y \log[yf(\xi)] + yg(\xi)$
5. $h = f(x) - y/x$	(i)	$\chi = g(x)$
	(ii)	$\chi = \mathrm{e}^{y/x} g(x)$
	(iii)	$\chi = yf(x)/x - y^2/(2x^2) + g(x)$
6. $h = f(\xi)/x$	(i)	$\chi = x^b g(\xi)$
$\xi = y - \log x$	(ii)	$\chi = \log x + g(\xi)$
	(iii)	$\chi = g(\xi)/x$
7. $h = -\log x + f(\xi)$	(i)	$\chi = x^b g(\xi)$
$\xi = y/x - \log x$	(ii)	$\chi = -(\log^2 x)/2 + g(\xi) + \int f(\xi)/x \ \mathrm{d}x$
8. $h = x^a f(\xi)$	(i)	$\chi = x^b g(\xi)$
$\xi = y/x^{a+1}$	(ii)	$\chi = \log x + g(\xi)$
	(iii)	$\chi = x^a g(\xi), a \neq -1$
	(iv)	$\chi = (\log[xf(y)])/x + g(y)/x, a = -1$

Table 3. Exact solutions of (10), for $h(x, y) = x^a f(\xi)$, $\chi(x, y) = x^b g(\xi)$ and $a = -1, 0, 1$ and 2

a	$\xi(x, y) = y/x^{a+1}$	$g(\xi)$
-1	$-C_2 I(s)/2$	$s^{-b/2}(C_3 \mathrm{e}^{s/2} + C_4)$
0	$C_2[2s^{-1/2}\mathrm{e}^{s/2} - I(s)]$	$s^{-b/2}(C_3 I(s) + C_4)$
1	$-C_2[2s^{-1/2}\mathrm{e}^{s/2} + (1-s)I(s)/s]/2$	$s^{-b/2}(C_3[2\mathrm{e}^{s/2} - s^{1/2}I(s)] + C_4)$
2	$-C_2[2(s-2)s^{-3/2}\mathrm{e}^{s/2}$ $+(3-s)I(s)/s]/3$	$s^{-b/2}(C_3[2s^{1/2}\mathrm{e}^{s/2} + (1-s)I(s)] + C_4)$

Velocity Solutions

For each of the six functional forms in (23) for $h(r, z)$ (where the corresponding solutions are stated in Table 4) there is at least one functional form each for $\chi(r, z)$ for which (20) is left invariant by the same one-parameter group and which in turn reduces the linear partial differential equation to an ordinary differential equation. These functional forms for $\chi(r, z)$ are presented in Table 5. Again, we do not present all the corresponding solutions to each

Table 4. Exact solutions of (18) for the six families of (23)

$h(r,z)$ family	solution for f
1. $h = f(r)$	$f = C_1 r^2 + C_2$
2. $h = zf(r)$	$f = \eta'(r)/\eta(r)$
	$\eta(r) = C_2 \mathrm{Ai}(C_1 r) + \mathrm{Bi}(C_1 r)$,
	where Ai and Bi are Airy functions
3. $h = f(r) - z/(r+a)$	$f = [C_1 + C_2(3r^2 + 8ar + 6a^2)r^2]/(r+a)$
4. $h = f(\xi)/r$, $\xi = z + \log r$	$f = s^{1/3}\mathrm{e}^{-s/3} I_1(s)/3$
	$\xi = \frac{1}{3}\log s - \frac{1}{9}\int^s t^{-2/3}\mathrm{e}^{-t/2} I_1(t)\mathrm{d}t + C_2$
5. $h = -\log r + f(\xi)$,	$f = -\xi - 1 - s^{-1/3}\mathrm{e}^{-s/3} I_2(s)/3$
$\xi = z/r - \log r$	$\xi = -\frac{1}{9}\int^s t^{-4/3}\mathrm{e}^{-t/3} I_2(t)\mathrm{d}t + C_2$
6. $h = f(z)/r$	$f = C_2 s^{1/3}\mathrm{e}^{s/3}$
$(a = -1)$	$z = -C_2 I_2(s)/3$
6. $h = f(\xi)$, $\xi = z/r$	$f = C_2 I_1(s)$
$(a = 0)$	$\xi = C_2[3s^{-1/3}\mathrm{e}^{s/3} - I_1(s)]$
6. $h = r^2 f(\xi)$, $\xi = z/r^3$	$f = C_2[3s^{-2/3}\mathrm{e}^{s/3} - I_2(s)]$
$(a = 2)$	$\xi = -C_2[3s^{-2/3}\mathrm{e}^{s/3} + (2-s)I_2(s)/s]/3$
6. $h = r^3 f(\xi)$, $\xi = z/r^4$	$f = C_2[3s^{-1/3}\mathrm{e}^{s/3} + (1-s)I_1(s)/s]$
$(a = 3)$	$\xi = -C_2[3(s-3)s^{-4/3}\mathrm{e}^{s/3} + (4-s)I_1(s)/s]/4$

Table 5. The corresponding functional forms of $\chi(r,z)$ for the six families of (23)

$h(r,z)$ family	corresponding $\chi(r,z)$ families
1. $h = f(r)$	(i) $\chi = bz + g(r)$
	(ii) $\chi = zf(r) + g(r)$
	(iii) $\chi = \mathrm{e}^z g(r)$
2. $h = zf(r)$	(i) $\chi = z^b g(r)$
	(ii) $\chi = \log z + g(r)$
	(iii) $\chi = z\log[zf(r)] + zg(r)$
3. $h = f(r) - z/(a+r)$	(i) $\chi = g(r)$
	(ii) $\chi = \mathrm{e}^{z/(r+a)} g(r)$
	(iii) $\chi = zf(r)/(a+r) - z^2/[2(a+r)^2] + g(r)$
4. $h = f(\xi)/r$	(i) $\chi = r^b g(\xi)$
$\xi = z - \log r$	(ii) $\chi = \log r + g(\xi)$
	(iii) $\chi = g(\xi)/r$
5. $h = -\log r + f(\xi)$	(i) $\chi = r^b g(\xi)$
$\xi = z/r - \log r$	(ii) $\chi = -(\log^2 r)/2 + g(\xi) + \int f(\xi)/r \ \mathrm{d}r$
6. $h = r^a f(\xi)$	(i) $\chi = r^b g(\xi)$
$\xi = z/r^{a+1}$	(ii) $\chi = \log r + g(\xi)$
	(iii) $\chi = r^a g(\xi), a \neq -1$
	(iv) $\chi = (\log[rf(z)])/r + g(z)/r, a = -1$

Table 6. Exact solutions of (20), for $h(r,z) = r^a f(\xi), \chi(r,z) = r^b g(\xi)$ and $a = -1, 0, 2$ and 3

a	$\xi(r,z) = z/r^{a+1}$	$g(\xi)$
-1	$-C_2 I_2(s)/3$	$s^{-b/3}(C_3 \mathrm{e}^{s/3} + C_4)$
0	$C_2[3s^{-1/3}\mathrm{e}^{s/3} - I_1(s)]$	$s^{-b/3}(C_3 I_1(s) + C_4)$
2	$-C_2[3s^{-2/3}\mathrm{e}^{s/3}$ $+(2-s)I_2(s)/s]/3$	$s^{-b/3}(C_3[3\mathrm{e}^{s/3} - s^{2/3}I_2(s)] + C_4)$
3	$-C_2[3(s-3)s^{-4/3}\mathrm{e}^{s/3}$ $+(4-s)I_1(s)/s]/4$	$s^{-b/3}(C_3[3s^{2/3}\mathrm{e}^{s/3} + (1-s)I_1(s)] + C_4)$

functional form of $\chi(r,z)$, but rather we state in Table 6 only the exact parametric solutions corresponding to 6(i) (from Table 5) for $a = -1, 0, 2$ and 3. We note that these solutions are new, and have not been presented elsewhere.

4 Gravity Flow in Hoppers

In this section we present stress and velocity profiles according to some of the exact solutions presented in Sect. 3 for gravity flow of granular materials through two-dimensional plane strain wedge and axially symmetric cone hoppers. In particular, we utilize the solution $8(a = 0)$ in Table 1, and the corresponding velocity solution in Table 3, for the wedge hopper, while solution $6(a = 0)$ in Table 4, with corresponding velocity solution in Table 6, is applied to the cone hopper. We note that solution $8(a = 0)$ in Table 1 was the first derived exact solution of (8) with two arbitrary constants, as detailed in Hill and Cox [18].

For both wedge and cone hoppers $b = 0$, which results in C_4 being eliminated when u and v are determined according to (9) and (19), respectively. As such, we require only three boundary conditions; two for the stress (symmetry about vertical axis and Coulomb friction along the hopper walls) and one for the velocity (assigning radial velocity along vertical axis). For further details of the boundary conditions see [16, 18, 19].

Figures 2 and 3 show the variation of ψ and ru vs. θ for two-dimensional plane strain wedge and axially symmetric cone hoppers, respectively. We note each figure contains numerically determined profiles for three values of the angle of internal friction ϕ, where the numerical solution for $\phi = \pi/2$ corresponds precisely to the appropriate exact solution for $\phi = \pi/2$. For details of the numerical solutions see [16, 18, 19]. We also note that the exact solutions applying for $\phi = \pi/2$ provide reasonable estimates to the numerical solution for smaller values of ϕ.

Further, the exact parametric solutions $8(a = 0)$ in Table 1, with the corresponding velocity solution in Table 3, for a wedge hopper, and solution $6(a = 0)$ in Table 4, with corresponding velocity solution in Table 6, for a cone hopper, have been utilized as the zeroth-order terms in a perturbation

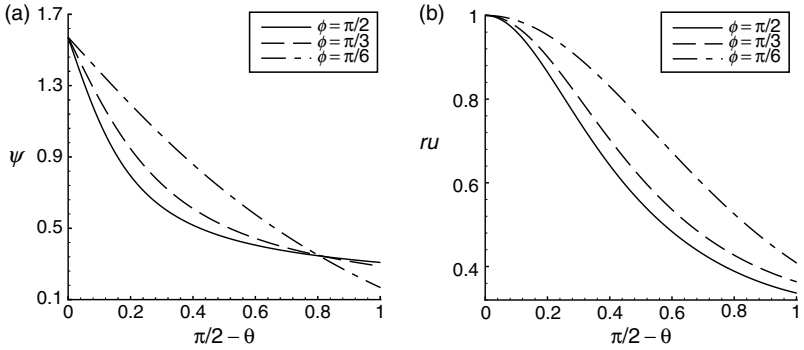

Fig. 2. Variation of $\psi(\theta)$ and $u(\theta)$ for two-dimensional plane strain wedge hopper for three values of ϕ ((**a**) ψ and (**b**) ru)

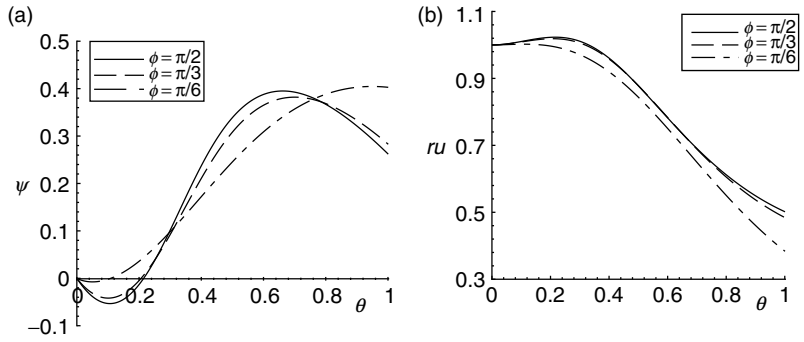

Fig. 3. Variation of $\psi(\theta)$ and $u(\theta)$ for two-dimensional axially symmetric cone hopper for three values of ϕ ((**a**) ψ and (**b**) ru)

scheme in powers of $1 - \sin\phi$, as detailed in Cox et al. [16] and Thamwattana and Hill [22]. These perturbation solutions extend the range of validity for which the solutions provide a reasonable estimate. For example, Fig. 4 shows the comparison of the solutions according to the perturbation solution, the zeroth-order solution ($\phi = \pi/2$) and a full numerical solution, where overall the perturbation solution provides a better estimate than the zeroth-order solution. We also note that these perturbation solutions becomes more accurate for steeper hopper walls.

5 Beneath Stockpiles

Here we present profiles for the stress distribution beneath two-dimensional plane strain parabolic and axially symmetric cubic stockpiles according to some of the exact solutions presented in Sect. 3. In particular, we utilize the

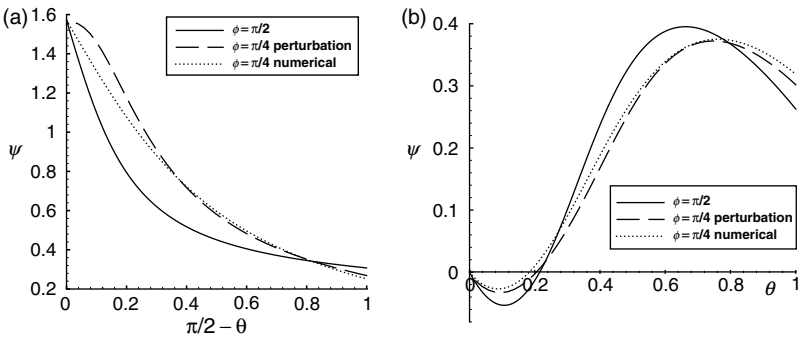

Fig. 4. Comparison of $\psi(\theta)$ for plane strain and axially symmetric hoppers according to the zeroth-order ($\phi = \pi/2$) and the full perturbation solutions and a numerical solution ((**a**) plane strain and (**b**) axial symmetry)

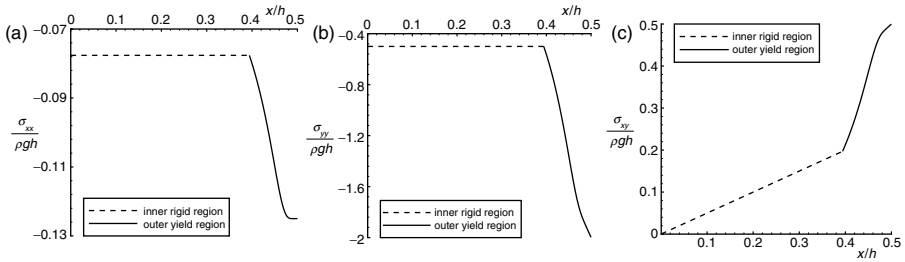

Fig. 5. The stress profile for a two-dimensional plane strain parabolic stockpile with an inner rigid region and an outer yield region ((**a**) σ_{xx}, (**b**) σ_{yy} and (**c**) σ_{xy})

solution $8(a = 1)$ in Table 1 for the parabolic stockpile, while solution $6(a = 2)$ in Table 4 is applied to the cubic stockpile. These solutions were first utilized in Thamwattana and Hill [20].

The stockpiles are assumed to contain an inner rigid region and an outer yield region, where the exact solutions hold in the outer yield region while the stresses are extended continuously into the inner rigid region in a natural manner. Further, the stress field is assumed to satisfy a free surface condition on the top surface of the outer yield region and a symmetric condition about the vertical axis. For full details see [20].

Figures 5 and 6 show the stress profiles for two-dimensional plane strain parabolic and axially symmetric cubic stockpiles, respectively. In the outer yield region the profile corresponds to the appropriate exact solution, namely $8(a = 1)$ in Table 1 or $6(a = 2)$ in Table 4, while the profile in the inner rigid region is obtained by extending the stress solution continuously inwards as detailed in [20]. We note that these profiles are non-unique.

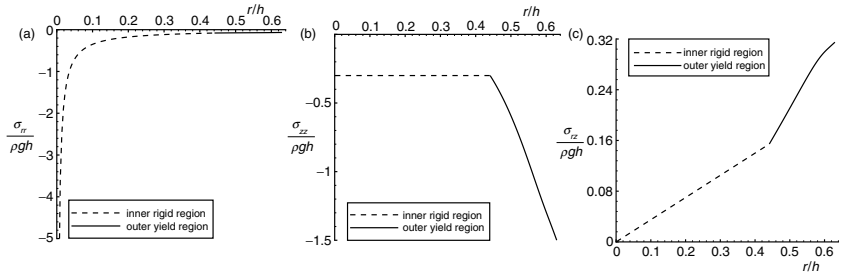

Fig. 6. The stress profile for an axially symmetric cubic stockpile with an inner rigid region and an outer yield region ((**a**) σ_{rr}, (**b**) σ_{zz} and (**c**) σ_{rz})

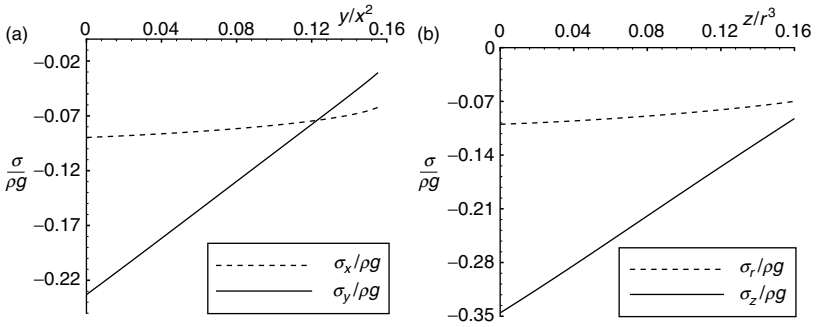

Fig. 7. The stress profiles for a two-dimensional plane strain parabolic and axially symmetric cubic rat-holes ((**a**) parabolic and (**b**) cubic).

6 Stable Rat-Holes

In this section we present profiles for the stress distribution within stable two-dimensional plane strain parabolic and axially symmetric cubic rat-holes, as given by the exact solutions $8(a = 1)$ in Table 1 and $6(a = 2)$ in Table 4, respectively. Thamwattana and Hill [21] utilize these solutions, and for full details of the rat-hole problem we refer the reader to [21].

As detailed in [21], we assume stable rat-holes have formed within a stockpile or hopper, and that the granular material is at the limiting point of yield and contained between vertical boundaries. Further, the material is assumed to be resting on a rigid base with an infinitesimal central outlet while the upper surface of the rat-hole is assumed to be stress free. We note that Coulomb friction at the boundaries is only satisfied in an average sense. Figure 7 shows the resulting stress profiles for a two-dimensional plane strain parabolic and an axially symmetric cubic rat-hole, respectively.

Acknowledgements

This work is supported by the Australian Research Council through the Discovery Project Scheme.

References

1. Australian Standard: Loads on bulk solids containers (1996) Standards Association of Australia. ISBN 0733707335, AS 3774:23
2. Sture S (1999) Constitutive issues in soil liquefaction. In: Lade PV, Yamamuro JA (eds) *Proceedings in Physics and Mechanics of Soil Liquefaction*. Balkema, Rotterdam, 133–143
3. Perkins SW (1994) Non-linear limit analysis for the bearing capacity of highly frictional soils. *2nd Congress on Computing in Civil Engineering*, ASCE, Atlanta, 4 June 1995, 1:629–636
4. Perkins SW (1995) Bearing capacity of highly frictional material. *2nd ASTM Geotech. Testing J.* 18:450–462
5. Perkins SW, Gui D (1994) Mechanical properties of lunar regolith and their effect on bearing capacity. In: Siriwardane, Zaman (eds) *Computer Methods and Advances in Geomechanics*. Balkema, Rotterdam, 1521–1526
6. Lynch KM, Mason MT (1995) Pulling by pushing, slip with infinite friction, and perfectly rough surfaces. *Int. J. Rob. Res.* 14:174–183
7. Cox GM, Hill JM, Thamwattana N (2004) A formal exact mathematical solution for a sloping rat-hole in a highly frictional granular solid. *Acta Mech.* 170:127–147
8. Thamwattana N, Cox GM, Hill JM (2004) Stress distributions in highly frictional granular heaps. *Zeitschrift für angewandte Mathematik und Physik (ZAMP)* 55:330–356
9. Spencer AJM (1964) A theory of the kinematics of ideal soils under plane strain conditions. *J. Mech. Phys. Solids* 12:337–351
10. Spencer AJM (1982) Deformation of ideal granular materials. In: Hopkins HG, Sewell MJ (eds) *Mechanics of Solids: The Rodney Hill 60th Anniversary Volume*. Pergamon, Oxford, 607–652
11. Thamwattana N, Hill JM (2003a) Analytical stress and velocity fields for gravity flow of highly frictional granular materials. *Acta Mech.* 164:91–112
12. Cox AD, Eason G, Hopkins HG (1961) Axially symmetric plastic deformations in soils. *Phil. Trans. Roy. Soc. London A* A254:1–45
13. Jenike AW (1964) Steady gravity flow of frictional-cohesive solids in converging channels. *J. Appl. Mech.* 31:5–11
14. Jenike AW (1965) Gravity flow of frictional-cohesive solids - Convergence to radial stress fields. *J. Appl. Mech.* 32:205–207
15. Spencer AJM (1997) Remarks on coaxiality in fully developed gravity flows of dry granular materials. In: Fleck NA, Cocks ACF (eds) *Mechanics of Granular and Porous Matetials*. Kluwer, Dordrecht, 227–238
16. Cox GM, McCue SW, Thamwattana N, Hill JM (2005) Perturbation solutions for flow through symmetrical hoppers with inserts and asymmetrical wedge hoppers. *J. Eng. Maths* 52:63–91

17. McCue SW, Johnpillai IK, Hill JM (2005) New stress and velocity fields for highly frictional granular materials. *IMA J. Appl. Maths* 70:92–118
18. Hill JM, Cox GM (2001) An exact parametric solution for granular flow in a converging wedge. *Zeitschrift für angewandte Mathematik und Physik (ZAMP)* 52:657–668
19. Cox GM, Hill JM (2005) Some exact velocity profiles for granular flow in converging hoppers. *Zeitschrift für angewandte Mathematik und Physik (ZAMP)* 56:92–106
20. Thamwattana N, Hill JM (2004) Stress distributions within curved highly frictional granular stockpiles. *Q. J. Mech. Appl. Maths* 57:447–466
21. Thamwattana N, Hill JM (2003b) Analytical solutions for tapering quadratic and cubic rat-holes in highly frictional granular solids. *Int. J. Solids Struc.* 40:5923–5948
22. Thamwattana N, Hill JM (2005) Perturbation solutions for highly frictional granular media. *Proc. R. Soc. A* 461:21–42

Double-Slip and Spin: Dilatant Shear in a Reduced Cosserat Model

D. Harris

School of Mathematics, University of Manchester, UK.
david.harris@manchester.ac.uk

1 Introduction

The problem of constructing constitutive equations (often called flow rules or kinematic equations in the context of plasticity models) capable of describing the deformation and flow of granular materials has proven to be one of the most intractable and controversial problems in continuum mechanics, with little consensus as to which model, or class of models, is best suited for the task. For dense packings, granular materials exhibit solid-like behaviour. Each grain is in contact with several others, each contact is non-impulsive, of finite duration and the dominant interactions are by way of slip, rolling and rotation. We shall consider two classes of model for this regime, each utilising the concept of a yield condition, namely elastic- (or rigid-) plasticity (flow rules) based upon a plastic potential and the class of so-called physically based kinematic equations. Other types of model, for example, hypo-plasticity in which there is no yield condition and in which both the elastic and irreversible parts of the deformation are combined into a single set of equations, will not be considered here.

The well known elastic–plastic model incorporating a yield condition and plastic potential is used extensively in geotechnical and civil engineering in the context of irreversible but pre-failure deformations. Physically based flow rules have been used mainly in the context of post-failure rigid-plastic flow. There is a vast literature on the elastic–plastic model and we will not attempt to review it, except to say briefly that the original suggestion that methods of metal plasticity (pressure independent yield condition), Hill [1] could be transferred to problems of soil mechanics was made by Drucker and Prager [2], by the incorporation of a pressure dependent yield condition. The extension to history dependent physical parameters (strain, work or density hardening/softening) by Drucker et al. [3], provided a sufficiently realistic framework whereby theoretical predictions could be compared with experimental results on pre-failure deformations. Using the yield function as the plastic potential (associated flow rule) allows only one parameter to model two physical quantities

(internal friction and dilatation), whereas for real soils, the magnitude of the latter is rather less than that of the former and this gave rise to the adoption of distinct yield and plastic potentials (non-associated flow rules), Mroz and Szymansk [4]. Yield conditions for granular materials may be grouped into two types, one in which yield and flow is independent of the intermediate principal stress (the so called Mohr–Coulomb type material) and those for which it depends on all three principal stresses (for want of a better name, we shall refer to these as standard materials). The model presented here is applicable to both types of material.

Physically based kinematic equations in which modes of flow, usually shear, dilatation/consolidation and rotation, are specified relative to an underlying stress field in which frictional and other resistances have been exhausted, have been considered by a number of authors, among which we may mention Mandel [5], Geniev [6], de Josselin de Jong [7, 8], Spencer [9, 10], Mehrabadi and Cowin [11] and Anand [12]. Such an approach has the advantage that the flow may be visualised as being made up of a number of distinct contributions, each contribution bearing a clear physical relationship both to the other modes and to the underlying stress field (via the Coulomb yield directions). Each model varies in the choice and nature of the modes of flow and also their relationship to the stress field. Thus, Geniev [6] considered a single shear mode aligned along one of the two Coulomb yield directions, de Josselin de Jong [7] considered two shear modes together with an undetermined spin on two slip directions which have orientations bounded by the Coulomb yield directions. Spencer considers two shear modes one in each of the Coulomb yield directions together with the spin of the principal axes of stress, Mehrabadi and Cowin [11] consider two dilatant shear modes on the Coulomb yield directions together with the spin of the principal directions of stress, while Anand [12] considers two dilatant shears in two arbitrary slip directions, together with the spin of the principal axes of stress. Various names have been associated with the modes of flow, for example, shearing, sliding and free rotation. In this paper we use the following terminology, the shearing modes are called 'slip' and the rotational modes are called 'spin'. We shall refer to a model comprising two slip modes and a spin mode as a 'double slip and spin' model.

There are theoretical difficulties associated with both types of model. Thus, if the inertia terms are retained in the equations of motion and transient flows in two space dimensions considered, both the non-associated flow rule and the double-shearing model are linearly ill-posed for the Cauchy initial value problem, see Pitman and Schaeffer [13], Schaeffer [14] and Harris [15, 16]. In fact, for transient planar deformations, any model for which the velocity characteristic directions (slip directions) do not coincide with the stress characteristic directions suffers loss of hyperbolicity for such flows and is linearly ill-posed (for example, we may cite all non-associated flow rules, de Josselin de Jong [8], Anand [12]). Any model which uses the spin of the principal axes of stress to ensure coincidence of the slip and Coulomb yield directions is also linearly

ill-posed (for example, Spencer [9], Mehrabadi and Cowin [11]). Thus, the double-shearing model is ill-posed due to the way in which the spin of the principal axes of stress is incorporated into the constitutive formulation.

The present author, Harris [17], has shown that the plastic potential model may also be considered to have a physical basis, in the case of planar flows, comprising two equal strength dilatant shear slip modes together with a spin mode. For an associated flow rule, the direction of the shear modes (slip lines) coincide with the Coulomb yield directions, for a non-associated flow rule, the slip lines are distinct from the Coulomb yield directions. For an associated flow rule, the spin is arbitrary, while for a non-associated flow rule, the spin may be identified with half the vorticity. The dilatant double-shearing model and the plastic potential model may also be combined into a single model, as demonstrated in Harris [18], governed by a common set of equations. The present paper extends this work.

It is the author's contention that the reason for the lack of success in constructing a continuum model for the flow and deformation of granular materials lies in the following explanation. The space averaged response to loading by forces of these essentially discrete systems in which the grains have finite size cannot be encompassed in a standard continuum formulation of strain, deformation rate and symmetric stress tensor. In particular, for transient flows, the averaged grain rotation fields in a standard continuum are inadequate for the description of the kinematics. Ultimately, this is the reason for the loss of hyperbolicity of post-failure rigid-plastic models and the consequent linear ill-posedness of many models of granular materials.

In this paper, we further develop a model proposed in Harris and Grekova [19], which has a domain of well-posedness (namely, isochoric flows). We postulate a general three-dimensional constitutive equation, which for planar flows comprises double slip and spin. The model allows for both non-coaxial and coaxial flow and we demonstrate that a non-coaxial dilatant shear may, under some simple assumptions, evolve into a coaxial simple shear. There is some evidence in the literature, see for example Roscoe [20], Savage and Lockner [21], that such flows are indeed initially non-coaxial, tending to coaxiality as the accumulated strain increases.

For the model presented here, non-coaxiality is closely associated with transient or unsteady flows i.e., there is some quantity associated with the flow which is time dependent. It is thus necessary to follow the history of the flow in order to determine the non-coaxiality, proceeding directly to asymptotic steady state conditions, as is common practice in plasticity theory, will lead to some indeterminacy. In particular, a completely quasi-static deformation or flow, and here is meant both translational and rotational loading, will not determine the non-coaxial behaviour. Most experiments performed in geotechnical engineering are carefully controlled to ensure both quasi-static conditions and the coincidence of the principal axes of stress and deformation-rate (although many experiments terminate with an uncontrolled transient event called 'failure' of the specimen). However, real granular materials in the

field are not subject to such careful control, and small departures from steady-state conditions may allow non-coaxiality to develop. It may also be stated that many discrete element method discrete element method (DEM) and other numerical simulations are also carried out under strictly controlled quasi-static conditions. Also, time dependent space averaging of micro-mechanical quantities to obtain bulk average quantities is a very difficult process to carry out.

2 Mathematical Model

Consider a deformation or flow of a body B comprising granular material and which at time t occupies a region of space R. Let $Ox_i, i = 1, 2, 3$, denote a set of rectangular Cartesian co-ordinate axes. We shall utilise a continuum model with an enhanced kinematic structure which will enable the modelling of the averaged rotation-rate of a representative volume element (RVE) by two distinct types of spin, namely that which is called vorticity in fluid mechanics and that which we shall call the *intrinsic spin*. The latter intuitively arises out of an equivalent rigid rotation of the RVE and the inertia associated with this additional type of spin results in a balance of angular momentum enabling the Cauchy stress to be non-symmetric. Its inclusion is effectively due to the fact that the finite grain-size prevents taking the limit of space averages of physical quantities as the magnitude of the volume tends to zero (in a standard continuum, this limit is taken, and the resulting limiting value of the inertia is zero). It should be carefully noted that we deliberately refrain from incorporating the concept of couple stress into the continuum.

Let $\mathbf{v} = (v_i)$ denote the Eulerian velocity field, $\mathbf{\Gamma} = \left(\frac{\partial v_i}{\partial x_j}\right)$ denote the velocity gradient tensor and denote the symmetric (the deformation-rate tensor) and anti-symmetric (the spin tensor, which is related to the vorticity) parts of $\mathbf{\Gamma}$ by $\mathbf{d} = (d_{ij})$ and $\mathbf{s} = (s_{ij})$, respectively. The continuum also possesses an extra kinematic variable, a vector, $\mathbf{\Omega}$, called the intrinsic spin. We shall not distinguish notationally between the vector $\mathbf{\Omega}$ and its dual representation as an anti-symmetric second-order tensor. Define the objective anti-symmetric tensor ω by

$$\omega = \mathbf{s}^{\mathrm{t}} - \mathbf{\Omega}, \tag{1}$$

which we shall call the *Cosserat spin tensor*. It is a measure of the spin of the material in the neighbourhood of a point relative to the point body spin at that point.

The continuum also possesses an extra material parameter, a second-order symmetric tensor $\mathbf{I}$, called the moment of inertia density tensor. Intuitively, the moment of inertia of a representative volume element (RVE), which may contain several grains and on which the informal continuum averaging is based, is incorporated in the continuum model because the finite size of the grains implies the volume of RVE cannot be reduced to zero and hence the rotational inertia does not reduce to zero. The intrinsic spin $\mathbf{\Omega}$ then represents the spin of

the (possibly non-unique) triad of the principal directions of inertia. Finally, let ρ denote the bulk density.

Let $\sigma = (\sigma_{ij})$ denote the (possibly non-symmetric) Cauchy stress tensor. Define the general deviatoric stress by

$$\tau = \sigma - \frac{1}{3}\left(\mathrm{tr}\sigma\right)\mathbf{I} \tag{2}$$

and the Mohr–Coulomb or planar deviatoric stress by

$$\tau = \sigma - \frac{1}{2}\left(\mathrm{tr}\sigma\right)\mathbf{I}, \tag{3}$$

where in the latter σ denotes a planar tensor, which deviatoric stress is required should be clear from the context. Denote the symmetric and anti-symmetric parts of the stress and deviatoric stress by $\sigma^{\mathrm{s}}, \sigma^{\mathrm{a}}, \tau^{\mathrm{s}}, \tau^{\mathrm{a}}$ respectively. One effect of introducing the moment of inertia and intrinsic spin is that it has been shown to regularise both the double-shearing model and the (non-associated) plastic potential model for isochoric flows, Harris and Grekova, [19]. Linear ill-posedness, in this context, is concerned with the growth of perturbations of solutions, for example the growth of large inertia from approximately quasi-static conditions, in the limit of vanishingly short wave lengths. The moment of inertia density is small when measured on a macroscopic length scale and $\sigma^{\mathrm{a}}, \mathbf{s}^{\mathrm{a}}$ may both be small. For many purposes, it may be possible to neglect them. However, given a prescribed solution of the model, these quantities play a crucial role in suppressing the growth of large perturbations, in other words they have a stabilising effect on the model. A well-posed model may, of course, still allow unstable solutions. The Cosserat spin ω itself, may not, in general be small, but its evolution is governed by the small quantities σ^{a} and I.

We now consider the form of the constitutive equations and consider a three-dimensional formulation, extending the work of Ostrowska-Maciejewska and Harris [22]. Suppose that the constitutive equation comprises two tensor valued functions, one for the symmetric part and one for the anti-symmetric part of the stress and objective kinematic tensors. The symmetric part of the constitutive equation is postulated to be of the form

$$\mathbf{d} = \lambda_{\mathrm{s}}\left[A\mathbf{I} + B\tau^{\mathrm{s}} + C\left(\tau^{\mathrm{s}}\right)^2\right] + D\left(\omega\tau^{\mathrm{s}} - \tau^{\mathrm{s}}\omega\right), \tag{4}$$

where A, B, C, D, E are functions of the invariants $I_1 = \mathrm{tr}(\sigma), J_2 = \mathrm{tr}(\tau^2)$, $J_3 = \mathrm{tr}(\tau^3)$. In particular we may take

$$\mathbf{d} = \lambda_{\mathrm{s}}\frac{\partial g}{\partial \sigma^{\mathrm{s}}} + D\left(\omega\tau^{\mathrm{s}} - \tau^{\mathrm{s}}\omega\right), \tag{5}$$

where $g = g\left(I_1, J_2, J_3\right)$ denotes an arbitrary plastic potential function. Non-coaxiality of σ_{s} and $\mathbf{d}_{\mathrm{s}}$ is provided for by the term $D\left(\omega\tau^{\mathrm{s}} - \tau^{\mathrm{s}}\omega\right)$ and the

function D may be fitted to experimental data, however, later we shall impose some mathematical restrictions on D which will, effectively, determine it. We have written the constitutive equation in a form suitable for a standard material, but it is easily seen to be applicable to a planar flow of a Mohr–Coulomb material by restricting the tensors to be planar. Equations governing three-dimensional flows of Mohr–Coulomb materials may then be generated by standard methods, see for example Cox et al. [23], Spencer [10]

We shall restrict attention to the symmetric part of the constitutive equation, and leave the anti-symmetric part to a future publication.

3 Planar Flow

Consider a planar deformation or flow to take place in the Ox_1x_2, plane. It is convenient to define, for future use, planar stress invariants by

$$p = -\frac{1}{2}\left(\sigma_{11} + \sigma_{22}\right), \qquad q = \frac{1}{2}\left[\left(\sigma_{11} - \sigma_{22}\right)^2 + \left(\sigma_{12} + \sigma_{21}\right)^2\right]^{1/2}, \tag{6}$$

$$r = \frac{1}{2}\left(\sigma_{12} - \sigma_{21}\right), \qquad s = \sigma_{33}. \tag{7}$$

The angle ψ that the greater principal direction of σ^{s} makes with the x_1-axis is given by

$$\tan 2\psi = \frac{\sigma_{12} + \sigma_{21}}{\sigma_{11} - \sigma_{22}} \tag{8}$$

and this gives the following representation for the stress components

$$\sigma_{11} = -p + q\cos 2\psi, \;\; \sigma_{22} = -p - q\cos 2\psi, \tag{9}$$

$$\sigma_{12} = r + q\sin 2\psi, \quad \sigma_{21} = -r + q\sin 2\psi. \tag{10}$$

In this section, we first specialise the symmetric part of the constitutive equation to the case of planar flow and then consider a representation of the stress tensor for such flows.

3.1 Symmetric Part of the Constitutive Equation

For planar deformation or flow, assuming that the Ox_3 is a principal direction of stress, (4) reduce to

$$d_{11} = \lambda_s\left[A + B\tau_{11} + C\left(\tau_{11}^2 + \tau_{12}^2\right)\right] + 2D\omega_{12}\tau_{21}, \tag{11}$$

$$d_{22} = \lambda_s\left[A + B\tau_{22} + C\left(\tau_{22}^2 + \tau_{12}^2\right)\right] - 2D\omega_{12}\tau_{21}, \tag{12}$$

$$d_{12} = \lambda_s B\tau_{12} - D\omega_{12}\left(\tau_{11} - \tau_{22}\right), \tag{13}$$

$$A + B\tau_{33} + C\tau_{33}^2 = 0. \tag{14}$$

The multiplier λ_s may be eliminated from the first three equations to obtain

$$(d_{11} - d_{22}) \sin 2\psi - 2d_{12} \cos 2\psi = -2\beta (s_{21} - \Omega), \tag{15}$$

$$d_{11} + d_{22} = \alpha [(d_{11} - d_{22}) \cos 2\psi + 2d_{12} \sin 2\psi], \tag{16}$$

where

$$\alpha = \frac{A - C \det \mathbf{s}}{Bq_\sigma} \tag{17}$$

and $\beta = 2Dq_\sigma$, so α, β are dimensionless and α depends only on g. Using standard methods, Harris [15], the characteristic equation for these equations may be shown to be

$$(a + \cos 2\psi_\sigma) m^2 + (2 \sin 2\psi_\sigma) m + (a - \cos 2\psi_\sigma) = 0, \tag{18}$$

where

$$a = \frac{\alpha + \beta}{1 + \alpha\beta}. \tag{19}$$

Thus, the planar equations are hyperbolic provided $-1 < a < 1$.

3.2 Yield conditions

Suppose now, that the yield condition governing the symmetric part of the stress, which may be written $f(p, q, s) <= 0$ for an isotropic material, is such that the stress equilibrium equations together with $f = 0$ form a hyperbolic set of equations, then we define the angle of internal friction by

$$\sin \phi = -\frac{f_p}{f_q}, \tag{20}$$

where the subscripts p and q denote partial differentiation with respect to the planar stress invariants p and q, respectively. We shall further suppose that the magnitude of the dilatation does not exceed that of the internal friction, from which it follows that $-1 < \alpha < 1$ and we may define the dilatancy angle ν by

$$\sin \nu = \alpha = -\frac{g_p}{g_q}. \tag{21}$$

We now make the assumption that the stress and velocity characteristics coincide, i.e. $a = \sin \phi$. In this case, it then follows necessarily that $-1 < \beta < 1$ and so we may define a non-coaxiality angle χ by $\sin \chi = \beta$. Thus, assuming coincident stress and velocity characteristics

$$\sin \chi = \frac{\sin \phi - \sin \nu}{1 - \sin \phi \sin \nu}. \tag{22}$$

There are two reasons for ensuring that the stress and velocity characteristic directions coincide, one physical, the other mathematical. In the case of the Coulomb yield criterion, the stress characteristics coincide with the

Coulomb yield directions, while the velocity characteristics coincide with the slip lines. Physically, it is appropriate for the yield and slip curves to coincide. Mathematically, it can be shown, Harris [15] that if the velocity and stress characteristics do *not* coincide then the governing equations are linearly ill-posed when the inertia terms are included in the equation of motion and in this case the Cauchy initial value problem for the model cannot be solved, i.e. the equations cease to be evolutionary.

For simplicity, in the remainder of the paper we shall assume that the components of σ^{s} satisfy the Coulomb–Mohr yield condition

$$q \leq p \sin\phi + c\cos\phi, \tag{23}$$

where ϕ denotes the angle of internal friction, c denotes the coefficient of cohesion and ϕ and c are material constants.

In addition, the components of σ^a are assumed to satisfy a yield condition of the form

$$g\left(\sigma^a, M\right) \leq 0, \tag{24}$$

where M is a material parameter which we shall call the *rotational yield strength*. We shall refer to this as the rotational yield condition. For planar deformations, the simplest such yield condition is

$$2r = \varepsilon M_0, \tag{25}$$

where

$$\varepsilon = \begin{cases} +1 \text{ if } \sigma_{12} > \sigma_{21}, \\ 0 \text{ if } \sigma_{12} = \sigma_{21}, \\ -1 \text{ if } \sigma_{12} < \sigma_{21} \end{cases} \tag{26}$$

and M_0 is a material constant. This corresponds as closely as possible to the concept of perfect plasticity in a standard continuum.

3.3 One Parameter Representation of the Stress

Consider a simple experiment in which the material is constrained to undergo a dilatant shear on planes parallel to the x_1-axis. We shall suppose, following the example worked through in detail by Spencer [24], that the value of σ_{22} is prescribed, say $\sigma_{22} = -\sigma$. We envisage the body is loaded up from a state in which $\sigma_{12} = 0$ and from which state σ_{12} is increased monotonically. σ_{11} then takes whatever value is required to maintain the stress-state at yield. Then

$$\sigma = p + q\cos 2\psi \tag{27}$$

together with the yield condition gives

$$p = \frac{\sigma - c\cos\phi\cos 2\psi}{1 + \sin\phi\cos 2\psi}, \tag{28}$$

$$q = \frac{\sigma\sin\phi + c\cos\phi}{1 + \sin\phi\cos 2\psi} \tag{29}$$

from which

$$\sigma_{11} = \frac{-\sigma\left(1 - \sin\phi\cos 2\psi\right) + 2c\cos\phi\cos 2\psi}{1 + \sin\phi\cos 2\psi}, \tag{30}$$

$$\sigma_{12} + \sigma_{21} = 2\frac{(\sigma\sin\phi + c\cos\phi)\sin 2\psi}{1 + \sin\phi\cos 2\psi}. \tag{31}$$

The last equation, together with (25) gives

$$\sigma_{12} = \frac{(\sigma\sin\phi + c\cos\phi)\sin 2\psi}{1 + \sin\phi\cos 2\psi} + \varepsilon M, \tag{32}$$

$$\sigma_{21} = \frac{(\sigma\sin\phi + c\cos\phi)\sin 2\psi}{1 + \sin\phi\cos 2\psi} - \varepsilon M, \tag{33}$$

where the ambiguity in sign is removed by consideration of the sign of the spin.

4 Non-Cosserat Models

In order to compare the new model with existing models, three types of model for a classical continuum are written here

4.1 Plastic Potential Model

$$d_{ij} = \dot{\lambda}\frac{\partial g}{\partial \sigma^s_{ij}}, \tag{34}$$

where g denotes the plastic potential function, $\dot{\lambda}$ is a scalar multiplier. For planar flows the equations may be written

(a) equation for dilatancy

$$d_{11} + d_{22} = \sin\nu\left[(d_{11} - d_{22})\cos 2\psi + 2d_{12}\sin 2\psi\right], \tag{35}$$

where the dilatancy parameter ν is defined by (21)

(b) equation for coaxiality of $\mathbf{d}, \sigma$

$$(d_{11} - d_{22})\sin 2\psi - 2d_{12}\cos 2\psi = 0. \tag{36}$$

4.2 Double-Shearing Model

(a) Equation for dilatancy

$$(d_{11} + d_{22})\cos(\phi - \chi) = \sin\chi\left[(d_{11} - d_{22})\cos 2\psi + 2d_{12}\sin 2\psi\right] \tag{37}$$

where ϕ is the angle of internal friction and χ is a dilatancy parameter.

(b) Equation for non-coaxiality of $\mathbf{d}, \sigma$

$$2\left(\dot{\psi} - s_{21}\right)\sin(\phi - \chi) = \cos\chi\left[(d_{11} - d_{22})\sin 2\psi - 2d_{12}\cos 2\psi\right], \tag{38}$$

where the superposed dot denotes the material derivative.

4.3 Double-Sliding Free-Rotating Model

The dilatancy equation is identical to the double-shearing model, and so we only state the condition of non-coaxiality,

$$2\left(\Omega - s_{21}\right)\sin\left(\phi - \nu\right) = \cos\nu\left[\left(d_{11} - d_{22}\right)\sin 2\psi - 2d_{12}\cos 2\psi\right], \tag{39}$$

where the quantity Ω is to be regarded as an undefined and indeterminable rotation-rate. This equation is a consequence of the assumptions underlying the double-sliding free-rotating model, but care must be taken in discussing it. It is not one of the equations governing the model because the unknown Ω renders it indeterminate, however, it is intended to represent the physical reality of the indeterminate nature of the response of a granular material to loading. It should be noted that for the above equation, together with the dilatancy equation, the stress and velocity characteristics would coincide. De Josselin de Jong [8] replaces the above equation with the requirement that the rate of working in the two Coulomb yield directions both be non-negative. This condition merely restricts the magnitude of the non-coaxiality between the stress and deformation-rate tensors, but does not determine it. It also has the consequence that the slip directions no longer coincide with the Coulomb yield directions, the orientation of the slip directions being arbitrary, but bounded by the Coulomb yield directions.

5 Reduced Cosserat Model

In this section, we write down the complete set of governing equations for the reduced Cosserat model.

(a) Linear momentum

$$\begin{aligned}\rho\left(\partial_t v_1 + v_1\partial_1 v_1 + v_2\partial_2 v_1\right) &= \partial_1\sigma_{11} + \partial_2\sigma_{21} + \rho F_1,\\ \rho\left(\partial_t v_2 + v_1\partial_1 v_2 + v_2\partial_2 v_2\right) &= \partial_1\sigma_{12} + \partial_2\sigma_{22} + \rho F_2,\end{aligned} \tag{40}$$

where F_1, F_2 denote the body force components.

(b) Rotational momentum

$$\rho I\left(\partial_t\Omega + v_1\partial_1\Omega + v_2\partial_2\Omega\right) - 2r - \rho G = 0, \tag{41}$$

where I denotes the moment of inertia density and G denotes the body couple.

(c) Coulomb yield condition

$$q \le p\sin\phi + c\cos\phi. \tag{42}$$

(d) Rotational yield condition

$$2r = \varepsilon M_0. \tag{43}$$

(e) Continuity

$$\partial_t \rho + v_1 \partial_1 \rho + v_2 \partial_2 \rho + \rho \partial_1 v_1 + \rho \partial_2 v_2 = 0. \tag{44}$$

(f) Dilatancy

$$(d_{11} + d_{22}) = \sin \nu \left[(d_{11} - d_{22}) \cos 2\psi + 2 d_{12} \sin 2\psi \right]. \tag{45}$$

(g) Intrinsic spin/noncoaxiality equation

$$2 (\Omega - s_{21}) \sin \chi = \left[(d_{11} - d_{22}) \sin 2\psi - 2 d_{12} \cos 2\psi \right], \tag{46}$$

where Ω denotes the intrinsic spin and s_{21} denotes the spin component.

6 Dilatant, Rotational Shear

We shall assume that the material parameters ϕ, c, I and M_0 are constant. On the other hand we shall allow the angle of dilatancy ν to vary and in this sense the model is not one of perfect plasticity. We deal with a rate independent material under quasi-static conditions of loading. We further suppose the stress components and the deformation to be homogeneous in space. There are no body forces or couples. Thus $\sigma_{ij} = \sigma_{ij}(t)$. We suppose that the flow is that of dilatant shear

$$v_1 = \alpha x_2, \qquad v_2 = \beta(t)\, x_2, \qquad \Omega = \Omega(t) \tag{47}$$

subject to the initial conditions

$$\alpha > 0, \qquad \beta(0) = \beta_0, \qquad \Omega(0) = \Omega_0. \tag{48}$$

The material cannot indefinitely dilate or densify, hence, we must assume that $|\beta(t)|$ is, in some sense a decreasing function of t, $\beta(t) \to 0$ (or at least a function which oscillates between dilatation and compaction). We note in passing that the material does not behave symmetrically with respect to these two possibilities, as the material densifies and the void fraction decreases, the limit to the elastic deformation of the grains and the constraint of non-overlap means that the maximal density at a given ambient pressure is a "hard" constraint, whereas as the material dilates, the void fraction increases and ultimately the grains separate from each other and the model ceases to be valid, in this sense dilatation is a "soft" constraint. The case $\beta = 0$ corresponds to simple shear and then $\nu = 0$. It seems reasonable to suppose that $\alpha > |\beta_0|$. In summary, there are three cases, $\beta > 0$ corresponding to dilatation, $\beta = 0$ corresponding to isochoric flow and $\beta < 0$ corresponding to consolidation. Finally, we note that whereas simple shear satisfies the equations of motion identically, dilatant shear does not, and in assuming quasi-static conditions we assume that the inertia terms are negligible.

6.1 Non-Coaxial Flow

For the dilatant, rotational shear given in (47), the deformation-rate and spin tensor components are

$$d_{11} = 0, \qquad d_{22} = \beta, \qquad 2d_{12} = \alpha, \qquad 2s_{21} = -\alpha \tag{49}$$

and the constitutive equations may be written

$$\begin{bmatrix} a_{11} & a_{12} \\ a_{21} & a_{22} \end{bmatrix} \begin{bmatrix} \beta \\ \alpha \end{bmatrix} = \begin{bmatrix} 0 \\ -2\Omega \sin\chi \end{bmatrix}, \tag{50}$$

where

$$\begin{aligned} a_{11} &= 1 + \sin\nu \cos 2\psi, \\ a_{12} &= -\sin\nu \sin 2\psi, \\ a_{21} &= \sin 2\psi, \\ a_{22} &= \sin\chi + \cos 2\psi. \end{aligned}$$

The linear algebraic equations (50) have a unique solution for α and β unless

$$\cos 2\psi = -\sin\phi. \tag{51}$$

In terms of ϕ and ν

Case 1. If $\cos 2\psi = -\sin\phi$ then the solution is

$$\Omega = 0, \qquad \frac{\beta}{\alpha} = \frac{\sin\nu\cos\phi}{1 - \sin\nu\cos\phi}. \tag{52}$$

Case 2. If $\cos 2\psi \neq -\sin\phi$ then the solution may be written as

$$\alpha = -\frac{2\Omega\,(\sin\phi - \sin\nu)}{\cos^2\nu}\,\frac{1 + \sin\nu\cos 2\psi}{\sin\phi + \cos 2\psi}, \tag{53}$$

$$\beta = -\frac{2\Omega\sin\nu\,(\sin\phi - \sin\nu)}{\cos^2\nu}\,\frac{\sin 2\psi}{\sin\phi + \cos 2\psi}. \tag{54}$$

We also note that

$$\frac{\beta}{\alpha} = \frac{\sin\nu\sin 2\psi}{1 + \sin\nu\cos 2\psi} \tag{55}$$

and so the relationship between α and β depends upon the stress as well as ν. However, we may obtain the following limiting cases

(1) Let $\cos 2\psi \to -\sin\phi$, $\sin 2\psi \to \cos\phi$ and $\Omega \to 0$, simultaneously, then cases (1) and (2) are consistent in the sense that α becomes arbitrary and that

$$\frac{\beta}{\alpha} \to \frac{\sin\nu\cos\phi}{1 - \sin\nu\cos\phi}. \tag{56}$$

(2) Let $\cos 2\psi \to -\sin\phi$, $\sin 2\psi \to \cos\phi$ and $\nu \to \phi$ then again α becomes arbitrary and in this case

$$\frac{\beta}{\alpha} \to \tan\phi. \tag{57}$$

Finally, (53) may be written

$$\frac{\Omega}{\alpha} = -\frac{\cos^2\nu}{2\left(\sin\phi - \sin\nu\right)} \frac{\sin\phi + \cos 2\psi}{1 + \sin\nu\cos 2\psi} \tag{58}$$

giving the ratio of the intrinsic spin to the spin in terms of the stress and showing clearly that $\Omega = 0$ if and only if $\sin\phi + \cos 2\psi = 0$, unless $\phi = \nu$, in which case, the intrinsic spin Ω is arbitrary.

6.2 Coaxial Flow

As stated earlier, there is some experimental evidence to suggest that pre-failure deformation of granular materials is non-coaxial, but that as the strain increases, the principal axes of stress and deformation-rate rotate into coincidence, Roscoe [20], Savage and Lockner [21]. For this reason, we now consider coaxial flow. For dilatant shear, the Cosserat spin equation (46) becomes

$$2\left(\Omega - s_{21}\right)\sin\chi = -\left(\beta\sin 2\psi + \alpha\cos 2\psi\right). \tag{59}$$

The condition of coaxiality is attained if the solution of the equations governing the model is such that the left- and right-hand sides of the above equation separately become equal to zero. It should be noted that we ascribe the property of coaxiality to the solution and not to the governing equations. There are two possibilities to consider.

Case 1. Suppose that the intrinsic spin is indeed equal to half the vorticity

$$\Omega = s_{21} = -\frac{1}{2}\alpha \tag{60}$$

then the flow is also coaxial

$$\left(d_{11} - d_{22}\right)\sin 2\psi - 2d_{12}\cos 2\psi = 0. \tag{61}$$

This is irrespective of the value of the quantity χ given in equation (22) and the case where $\phi \neq \nu$ corresponds to a non-associated flow rule. The flow rule now reduces to

$$\left(1 + \sin\nu\cos 2\psi\right)\beta - \left(\sin\nu\sin 2\psi\right)\alpha = 0, \tag{62}$$

$$\left(\sin 2\psi\right)\beta + \left(\cos 2\psi\right)\alpha = 0 \tag{63}$$

and there are non-trivial solutions provided

$$\cos 2\psi = -\sin\nu. \tag{64}$$

Hence

$$\psi = \frac{\pi}{4} + \frac{\nu}{2} \tag{65}$$

and

$$\cot 2\psi = -\frac{\beta}{\alpha} = -\tan\nu. \tag{66}$$

If $\nu = 0$ then we obtain the classical coaxial solution for incompressible materials

$$\psi = \frac{1}{4}\pi. \tag{67}$$

Case 2. Alternatively, we may consider the case of full dilatancy, i.e. $\phi = \nu$. This case corresponds to an associated flow rule and it turns out that $\Omega - s_{21}$ is arbitrary, since now $\chi = 0$. For dilatant shear, from equations (62), (63)

$$\cot 2\psi = -\frac{\beta}{\alpha} = -\tan\phi. \tag{68}$$

As a special case, we have metal plasticity ($\phi = \nu = 0$) which corresponds to omitting all internal friction, dilatation and intrinsic spin from the model.

6.3 Stress in terms of flow parameters

We summarise the above results for the stress variable ψ.

Case 1. For the incompressible case $\nu = 0$ and so necessarily, $\beta = 0$ and

$$\cos 2\psi = -\left(1 + \frac{2\Omega}{\alpha}\right)\sin\phi. \tag{69}$$

Thus the principal stress direction depends on the ratio of the intrinsic spin to the spin strength. We have the following classical stress solutions:

- In the case of non-coaxial flow with $\Omega = 0$

$$\psi = \frac{\pi}{4} + \frac{\phi}{2}. \tag{70}$$

  This solution corresponds to that of the double-shearing model and in that model it is an unstable solution. We shall see later that it is also unstable for (69).
- The case of coaxial flow $\Omega = -\frac{1}{2}\alpha$ gives

$$\psi = \frac{\pi}{4}. \tag{71}$$

  This solution corresponds to the classical plastic potential model. In the case of a pressure dependent yield condition this solution is unstable if the inertia terms are incorporated

- For (69), there is a restriction on the magnitude of the ratio of the intrinsic spin to the spin strength, given by

$$-\frac{1}{2}\left(1+\csc\phi\right) \leq \frac{\Omega}{\alpha} \leq \frac{1}{2}\left(\csc\phi - 1\right). \tag{72}$$

Case 2. In the case of contractant or dilatant flow, $\nu \neq 0$ and

$$\cos 2\psi = -\frac{\alpha \sin\phi \cos^2\nu + 2\Omega\left(\sin\phi - \sin\nu\right)}{\alpha\cos^2\nu + 2\Omega\sin\nu\left(\sin\phi - \sin\nu\right)}. \tag{73}$$

- In the case of non-coaxial flow with $\Omega = 0$ we again have

$$\psi = \frac{\pi}{4} + \frac{\phi}{2} \tag{74}$$

  and so the stress is independent of the dilatation in non-coaxial flow.
- In the case of coaxial flow $\Omega = -\frac{1}{2}\alpha$ gives

$$\cos 2\psi = -\sin\nu \tag{75}$$

  and so the stress does depend upon the dilatation in coaxial flow.
- In the case of (73), the restriction on the magnitude of the ratio of the intrinsic spin to the spin strength is

$$-\frac{1}{2}\frac{\cos^2\nu}{1-\sin\nu}\frac{1-\sin\phi}{\sin\phi-\sin\nu} \leq \frac{\Omega}{\alpha} \leq \frac{1}{2}\frac{\cos^2\nu}{1-\sin\nu}\frac{1+\sin\phi}{\sin\phi-\sin\nu}. \tag{76}$$

Regarding α as fixed and given and ϕ to be a known constant, the equations determine ψ in terms of Ω and ν.

6.4 Density

Since $\operatorname{tr}\mathbf{d}$ is constant the density ρ is homogeneous and may be considered as a function of any one of the following variables, $\rho = \rho(t), \rho(\beta), \rho(\nu)$. We shall suppose that the history of the density is a sequence of intervals in which ρ is either monotonically increasing or decreasing. In the case of dilatant shear, (44) becomes

$$\partial_t\rho + \rho\beta = 0. \tag{77}$$

Since the density cannot indefinitely decrease or increase we shall assume the existence of a critical density, denoted by ρ_c (which will in general be dependent upon the pressure p) such that $\rho \to \rho_c$ as $\beta \to 0$. If the initial density $\rho_0 > \rho_c$ then the material dilates ($\beta > 0$), while if $\rho_0 < \rho_c$, the material consolidates ($\beta < 0$). The volumetric strain may be defined as

$$e = \int_0^t \operatorname{tr}\mathbf{d}\,\mathrm{d}\tau = \int_0^t \beta\,\mathrm{d}\tau \tag{78}$$

but this integral is intractable, so consider instead

$$\int_{\rho_0}^{\rho} \frac{\mathrm{d}\rho'}{\rho'\beta} = -\int_0^t \mathrm{d}\tau. \tag{79}$$

Considering ρ as a function of β, we shall assume the inverse function exists, $\beta = \beta(\rho)$, then since $\beta = 0$ in the asymptotic simple shear, we assume the simple relation

$$\beta = k(\rho - \rho_c), \tag{80}$$

where k is a material parameter.

$$\int_{\rho_0}^{\rho} \frac{d\rho'}{\rho'(\rho' - \rho_c)} = -k\int_0^t \mathrm{d}t. \tag{81}$$

The evolution of the density is governed by the equation

$$\frac{\rho(t)}{\rho_0} = \frac{\rho_c}{\rho_0 - (\rho_0 - \rho_c)\exp(-k\rho_c t)}. \tag{82}$$

Thus, at $t = 0$, $\rho(0) = \rho_0$ and as $t \to \infty, \rho \to \rho_c$. The asymptotic simple shear is thus reached asymptotically as $t \to \infty$.

7 Anti-Symmetric part of the flow

Exact rotationally quasi-static conditions give, in the absence of body couples, that $\sigma_{12} = \sigma_{21}$ and $\Omega =$ constant. For dilatant shear, the balance of rotational momentum equation (41), in the absence of body couples, becomes

$$\rho I \frac{\mathrm{d}\Omega}{\mathrm{d}t} = \sigma_{12} - \sigma_{21} \tag{83}$$

subject to $\Omega = \Omega_0$ when $t = 0$, i.e.,

$$\Omega = \Omega_0 + \varepsilon \frac{M_0}{I}\int_0^t \frac{1}{\rho}\mathrm{d}\tau \tag{84}$$

and hence we obtain

$$\Omega(t) = \Omega_0 + \frac{\varepsilon M_0}{I\rho_c}\left[t - \frac{\rho_0 - \rho_c}{k\rho_c\rho_0}\left[1 - \exp(-k\rho_c t)\right]\right]. \tag{85}$$

This equation remains valid until the time $t = T$ at which $\omega(T) = 0$. From this time onwards, determined by the equation

$$kT - \left(\frac{1}{\rho_c} - \frac{1}{\rho_0}\right)\left[1 - \exp(-\rho_c kT)\right] + \frac{kI\rho_c}{\varepsilon M_0}\left(\Omega_0 + \frac{1}{2}\alpha\right) = 0 \tag{86}$$

Here, $\varepsilon = 0$ and the flow remains coaxial. In this simple example, the flow becomes coaxial before the critical density ρ_c is reached. If the initial data corresponds to the classical "double-shearing" type solution, $\omega = s_{21}$, then this flow is unstable, and the flow evolves to a classical "coaxial" type solution, corresponding to $\omega = 0$ at finite time. In summary, ρ evolves towards a known ρ_c and ω evolves to zero, corresponding to coaxial flow, with coaxiality being attained at finite time and the critical state density being attained asymptotically.

8 Conclusions

We have presented a three-dimensional constitutive equation in tensorial form comprising frame-indifferent quantities which is such that:

- it has, as a special case an arbitrary plastic potential model
- it has the ability to exhibit both coaxial and non-coaxial behaviour, the physical origin of the non-coaxiality being ascribed to the existence of two types of spin, the vorticity and the intrinsic spin
- for planar flows the modes of flow comprise double slip and spin, with coincident stress and velocity characteristics (i.e. coincident slip lines and Coulomb yield directions)
- in the case of a dilatant shear, some simplifying assumptions concerning the model show that it is possible to exhibit an initially non-coaxial dilatant, rotational shear which becomes coaxial after a finite time and which tends asymptotically to a critical state density. This behaviour is consistent with experimental data

References

1. Hill R (1950) The Mathematical Theory of Plasticity. The Clarendon, Oxford
2. Drucker DC, Prager W (1952) Q Appl Math 10: 157–165
3. Drucker DC, Gibson RE and Henkel DJ, (1957) ASCE Trans, 122: 338–346
4. Mroz Z, Szymansk, Cz (1979) Non-associated flow rules in description of plastic flow of granular materials, CISM Course 217 (1974), Udine. In: Olszak W, Suklje L (eds) Limit Analysis and Rheological Approach in Soil Mechanics, Springer, Vienna, New York, Berlin, Heidelberg
5. Mandel (1947) CR Acad Sci Paris 225: 1272–1273
6. Geniev GA (1958) Akad Stroit Archit SSSR, Moscow 3–121
7. de Josselin de Jong G (1959) Statics and kinematics of the failable zone of a granular material, Uitgeverij Waltmann, Delft
8. de Josselin de Jong G (1977) Archs Mech 29: 561–591
9. Spencer AJM, (1964) J Mech Phys Solids 12: 337–351
10. Spencer AJM, (1981) Deformation of ideal granular materials. In: Hopkins HG, Sewell MJ (eds) The Rodney Hill 60th. Anniversary Volume, Pergamon Oxford
11. Mehrabadi MM, Cowin SC (1978) J Mech Phys Solids 26: 269–284

12. Anand L (1983) J Mech Phys Solids 31: 105–122
13. Pitman EB and Schaeffer DG (1987) Comm Pure Appl Math: 421–447
14. Schaeffer DG (1990) Mathematical issues in the continuum formulation of slow granular flow. In: Joseph DD, Schaeffer DG (eds) Two phase waves in fluidised beds, sedimentation and granular flows. Minneapolis: Institute of Mathematics and its Applications, University of Minnesota
15. Harris D (2001) Acta Mech 146: 199–225
16. Harris D (2001) Proc R Soc Lond A 457:349–370
17. Harris D (1995) Proc Roy Soc Lond A 450: 37–49
18. Harris D (1993) J Mech Phys Solids 41: 1515–1531
19. Harris D, Grekova EF (2005) Jnl Engineering Mathematics 52:107–135.
20. Roscoe KH (1970) Geotechnique 20: 129–170
21. Savage JG, Lockner DA (1997) Jnl Geophys Res 102: 12287–12294
22. Ostrowska-Maciejewska J, Harris D (1990) Proc Camb Phil Soc 108: 153-169
23. Cox AD, Eason G, Hopkins HG (1961) Phil Trans R Soc LOndon A 254: 1–45
24. Spencer AJM (2003), J Eng Math 45: 55–74

The Linear Matching Method for Limit and Shakedown Analysis

A.R.S. Ponter and M. Boulbibane

Department of Engineering, University of Leicester, UK.
asp@le.ac.uk

1 Introduction

Strength calculations form a basic component of geotechnical design. There are essentially two versions of such calculation in current use. Classical methods based on Coulomb's method and the slip circle methods, rely upon a limited set of kinematically admissible slip surface mechanisms, the Mohr–Coulomb yield condition and an energy dissipation balance equations that makes use of overall equilibrium conditions. At yield, it is generally assumed that no volume change occurs during relative movement across the slip surface, i.e. a non-associated flow rule is implicitly assumed. With the development of limit analysis, the full power of the upper and lower bound limit theorems became available, providing general methods with a secure and well understood theoretical background. However, for such theorems to strictly apply, the material needs to satisfy the maximum work principle and, in turn, this implies convexity of the yield condition and an associated flow rule. Yield conditions for soils are usually convex and, for the instantaneous yield surface, the plastic strain rate vector may well be associated; critical state soil mechanics and many other constitutive equations adopt this assumption. But where the limit state is concerned, i.e. states of stress at which indefinite plastic flow occurs with no significant change in internal state, the plastic strain rate is associated, at best, with the yield surface and certainly not with the locus of limit states. Mohr–Coulomb and related conditions do not model the yield condition but are loci of limit states.

This problem is, of course, well known, and limits the applicability of the limit theorems to the evaluation of limit states in soil structures. In fact, the exact solution to the limit state for an associated flow rule provides the absolute maximum load that exists for which there is an equilibrium state of stress that lies within the yield surface. If, at the limit state, the flow rule is non-associated, the limit load must necessarily be less.

In recent years the emphasis has increasingly turned towards computational methods that rely upon the limit theorems. These provide, assuming

an associated flow rule, strict upper and lower bounds to the limit load using the kinematics of the displacement finite element method, Kim et al. [6], for upper bounds and stress finite elements for lower bounds, Merifield et al. [9]. The procedure is the same in both cases. The relevant limit theorem is posed as a programming problem, to which an appropriate programming method, such as linear programming, is applied.

In parallel with these developments, limit analysis and the extension to variable loading, shakedown analysis, has been applied to structural design and life assessment, particularly for severe thermal loading. For example, the methods used for the assessment of the remaining life of high temperature power plant [1], rely upon a sequence of simplified calculations, many of which have their origins in limit and shakedown analysis. The problems in this field are of a different nature. There is no difficulty over the convexity of yield or the association of the flow rule. However, the range of material behaviour that needs to be taken into account is much wider than classical plasticity; high temperature creep occurs, internal damage takes place leading to rupture, reverse cycles of plasticity are unavoidable leading to consideration of low cycle fatigue. Hence classical limit and shakedown calculations have limited use, other than for producing useful reference solutions. The type of methods that prove efficient for limit analysis are not particularly relevant for these more demanding problems.

These considerations have led to the search for methods of greater generality, particularly those that may be implemented within standard finite element codes. This has resulted in the development of the Linear Matching Methods. The basis of such methods may be understood from the following example. Simple lower bound limit state calculations can be constructed by the following procedure. First, a linear elastic solution is calculated. In regions of the structure the stress is then found to exceed yield. However, if the local Young's modulus is increases, the local stresses may be expected to decrease. By scaling of the resulting stress distribution a lower bound limit load can be found. This idea forms the basis of the Reduced Modulus Method of Marriot [8], the Elastic Compensation Method of Boyle et al. [3] and a variety of methods by Seshadri [14]. They all have in common the notion that non-linear material behaviour may be simulated by linear solutions where the linear moduli vary in space. This idea has been developed into the Linear Matching Method, a simple and powerful method for addressing a range of design related calculations involving both plasticity and creep behaviour (see, for example [4]). The method is essentially an upper bound programming method where, at each iteration, conditions of both compatibility and equilibrium are satisfied and the error in the current solution arises from inconsistencies between the linear solution and the non-linear material behaviour. For a range of yield conditions, strict convergence conditions can be derived for shakedown [11]. Linear Matching Methods have been developed for all stages of the R5 life assessment method of British Energy [1] and are currently being introduced into practice.

In this paper, the application to limit and shakedown limits for the Drucker–Prager yield condition is discussed. The nature of the matching condition needs to be adapted in this case and monotonic convergence cannot be proven. However, we find in practice that convergent solutions may still be obtained. Further, as an equilibrium stress field is generated at each iteration, the method may be applied to limit state solutions with a non-associated flow rule, allowing a direct comparison with solutions for an associated flow rule. The particular problem of primary interest is the shakedown limit for rolling contact of a semi-infinite solid, where current programming methods are difficult to apply.

In Sect. 2, a formal discussion of the Linear Matching Method for shakedown analysis is given, together with sufficient conditions for convergence for an associated flow rule. Application to the Drucker–Prager condition is then discussed. A new matching procedure is adopted that makes use of the equilibrium stress distributions generated by the linear solutions. This produces a method that generally converges in a stable manner. Numerical examples for both limit analysis and shakedown are given and compared with known analytic solutions.

2 Upper Bound Shakedown Theorem

Consider an isotropic, homogeneous elastic–perfectly plastic body, V, bounded by the surface S. In a fixed Cartesian space, let $u_i(x,t) = 0$ and $\lambda P_i(x,t)$ denote the displacements and the applied cyclic loads over S_u and S_T, complementary parts of S, respectively, where x is a position vector, t is the time and λ is a positive load parameter. The convex yield condition and associated flow rule are given by

$$f(\sigma_{ij}) \leq 0, \tag{1}$$

$$\dot{\varepsilon}^{\mathrm{p}}_{ij} = \dot{\Lambda}\frac{\partial f}{\partial \sigma_{ij}}, \qquad f(\sigma_{ij}) = 0, \tag{2}$$

where $\dot{\Lambda}$ is a plastic multiplier.

For a typical cycle, $0 \leq t \leq \Delta t$, consider a class of kinematically admissible plastic strain rate histories $\dot{\varepsilon}^{\mathrm{c}}_{ij}$ with a corresponding displacement increment fields Δu^{c}_i and associated compatible strain increment,

$$\Delta\varepsilon^{\mathrm{c}}_{ij} = \frac{1}{2}\left(\Delta u^{\mathrm{c}}_{i,j} + \Delta u^{\mathrm{c}}_{j,i}\right). \tag{3}$$

The strain rate history $\dot{\varepsilon}^{\mathrm{c}}_{ij}$, which need not be compatible, satisfies the following condition:

$$\int_0^{\Delta t} \dot{\varepsilon}^{c}_{ij}\, \mathrm{d}t = \Delta\varepsilon^{\mathrm{c}}_{ij}. \tag{4}$$

The kinematic shakedown theorem, due to Koiter [7], states that shakedown will not occur for a load parameter $\lambda_{\mathrm{UB}}^{\mathrm{c}}$ defined by any kinematically admissible plastic strain cycle as follows:

$$\lambda_{\mathrm{s}} \le \lambda_{\mathrm{UB}}^{\mathrm{c}} = \frac{\int_0^{\Delta t} \int_{\mathrm{V}} \sigma_{ij}^{\mathrm{c}}(t)\ \dot{\varepsilon}_{ij}^{\mathrm{c}}(t)\ \mathrm{d}V\ \mathrm{d}t}{\int_0^{\Delta t} \int_{V} \widehat{\sigma}_{ij}(t)\ \dot{\varepsilon}_{ij}^{\mathrm{c}}(t)\ \mathrm{d}V\ \mathrm{d}t}, \tag{5}$$

where $\widehat{\sigma}_{ij}(t)$ denotes the linear elastic solution to the problem for $\lambda = 1$ and $\lambda_{\mathrm{UB}}^{\mathrm{c}}$ is an upper bound to the value of load parameter λ_{s} at shakedown.

3 The Linear Matching Method

The linear matching method involves the derivation of a sequence of linear problems, each producing a kinematically admissible strain rate history, so that the upper bound $\lambda_{\mathrm{UB}}^{\mathrm{c}}$ monotonically reduces and converges to the least upper bound associated with the class of displacement fields under consideration. We assume that the associated flow rule (2) may be inverted, so that the stress at yield σ_{ij}^{p} corresponding to a plastic strain rate $\dot{\varepsilon}_{ij}^{\mathrm{p}}$ is uniquely defined

$$\sigma_{ij}^{\mathrm{p}} = \sigma_{ij}(\dot{\varepsilon}_{ij}^{\mathrm{p}}). \tag{6}$$

We define a suitable class of linear viscous materials expressed in terms of a quadratic potential $U(\dot{\varepsilon}_{ij}^{\mathrm{L}})$ or, equivalently, by a complementary potential $\overline{U}(\sigma_{ij}^{\mathrm{L}})$,

$$\dot{\varepsilon}_{ij}^{\mathrm{L}} = \frac{\partial \overline{U}}{\partial \sigma_{ij}^{\mathrm{L}}}, \qquad \sigma_{ij}^{\mathrm{L}} = \frac{\partial U}{\partial \dot{\varepsilon}_{ij}^{L}}, \qquad \overline{U} + U = \sigma_{ij}^{\mathrm{L}} \dot{\varepsilon}_{ij}^{\mathrm{L}}. \tag{7}$$

To describe the process we assume that an initial kinematically admissible strain rate history $\dot{\varepsilon}_{ij}^{\mathrm{i}}$ is known with a corresponding upper bound $\lambda_{\mathrm{UB}}^{i}$. We seek a new kinematically admissible strain rate history $\dot{\varepsilon}_{ij}^{\mathrm{f}}$ so that the corresponding upper bound $\lambda_{\mathrm{UB}}^{\mathrm{f}} \le \lambda_{\mathrm{UB}}^{\mathrm{i}}$ with equality only when $\dot{\varepsilon}_{ij}^{\mathrm{f}} = \dot{\varepsilon}_{ij}^{\mathrm{i}}$. This is achieved by defining a linear material so that the both the flow rule (6) and the linear material (7) give rise to same stress state for $\dot{\varepsilon}_{ij}^{\mathrm{i}}$, i.e. if

$$\dot{\varepsilon}_{ij}^{\mathrm{i}} = \dot{\varepsilon}_{ij}^{\mathrm{p}} = \dot{\varepsilon}_{ij}^{\mathrm{L}}, \qquad \text{then} \qquad \sigma_{ij}^{\mathrm{pi}} = \sigma_{ij}^{\mathrm{Li}}, \tag{8}$$

where the superscript i refers to quantities derived from $\dot{\varepsilon}_{ij}^{\mathrm{i}}$ and superscript L refers to quantities related by the linear relationship (7). This may be achieved by suitable choice of the linear material coefficients, which become functions of both space and time. With constants so chosen, a linear problem may be defined for strain rate history $\dot{\varepsilon}_{ij}^{\mathrm{f}}$ and stress history

$$\sigma_{ij}^{\mathrm{f}} = \lambda_{\mathrm{UB}}^{\mathrm{i}} \widehat{\sigma}_{ij} + \overline{\rho}_{ij}^{\mathrm{f}}, \qquad \dot{\varepsilon}_{ij}^{\mathrm{f}} = \frac{\partial \overline{U}}{\partial \sigma_{ij}^{\mathrm{f}}}, \tag{9}$$

where $\overline{\rho}^{\mathrm{f}}_{ij}$ is a constant residual stress field. Imposition of the conditions that the accumulated strain $\Delta\varepsilon^{\mathrm{f}}_{ij} = \int_0^{\Delta t} \dot{\varepsilon}^{\mathrm{f}}_{ij}\,\mathrm{d}t$ be compatible and that $\overline{\rho}^{\mathrm{f}}_{ij}$ is in equilibrium with zero loads on S_T, results in a linear problem that yields $\Delta\varepsilon^{\mathrm{f}}_{ij}$ and $\overline{\rho}^{\mathrm{f}}_{ij}$, and hence $\dot{\varepsilon}^{\mathrm{f}}_{ij}$ from (9). With suitable restrictions on the linear material, discussed later, then $\lambda^{\mathrm{f}}_{\mathrm{UB}} \leq \lambda^{\mathrm{i}}_{\mathrm{UB}}$. An initial solution may be found by choosing arbitrary values for the linear material constants, usually constants in time and space, so that an initial kinematically admissible strain rate history may be found to begin the process. Repeated application of the procedure then produces a sequence of monotonically reducing upper bounds that converge to the exact solution, if all the linear problems may be evaluated exactly. When the linear solutions are provided by the minimum of the rate form of the potential energy for a chosen class of displacement fields, the upper bound converges to the least upper bound. Hence a finite element method can be derived so that the upper bound converges to the minimum upper bound corresponding to the class of displacement fields defined by a finite element mesh geometry.

The sufficient condition for convergence may be expressed either as a restriction on $U(\dot{\varepsilon}^{\mathrm{L}}_{ij})$ or $\overline{U}(\sigma^{\mathrm{L}}_{ij})$. In terms of strain rates, the following extended inequality must be satisfied [11];

$$U(\dot{\varepsilon}^{\mathrm{f}}_{ij}) - U(\dot{\varepsilon}^{\mathrm{i}}_{ij}) - \frac{\partial U}{\partial \dot{\varepsilon}^{i}_{ij}}(\dot{\varepsilon}^{\mathrm{f}}_{ij} - \dot{\varepsilon}^{\mathrm{i}}_{ij}) \geq (\sigma^{\mathrm{pf}}_{ij} - \sigma^{\mathrm{pi}}_{ij})\dot{\varepsilon}^{\mathrm{f}}_{ij} \geq 0, \tag{10}$$

where the second inequality is the maximum work principle. In this inequality $\dot{\varepsilon}^{\mathrm{i}}_{ij}$ is the matching strain rate and $\dot{\varepsilon}^{\mathrm{f}}_{ij}$ is any other strain rate. This inequality is equivalent to the statement that the surface described by $\overline{U} = \text{Constant}$, that forms a tangent to the yield surface at the matching point, otherwise coincides with or surrounds the yield surface in stress space. This later condition provides a simple graphical understanding of the restriction that is generally easier to apply.

Hence the application of the linear matching method relies upon the following assumptions:

(A) A class of linear materials may be found that are capable of being matched to any point on the yield surface. Hence the class of strain rates that are described by the linear material must at least include all strain rates given by the associated flow rule. Conversely, the strain rates generated by the linear solutions must correspond to the plastic strain rates associated with some point on the yield surface.

(B) The matching condition must be achievable, i.e. when the linear strain rate is matched to the plastic strains, the range of material constants must be such that the stresses may also be matched.

(C) The sufficient condition for convergence must also be satisfied.

For a given yield condition the choice of a suitable class of linear materials is usually straightforward. For example, for the von Mises yield condition, all the conditions are satisfied by an incompressible linear material.

In this case contours of constant $\overline{U}$ coincide with the yield surface. For yield conditions that depend upon both the von Mises effective stress $\overline{\sigma}$ and the hydrostatic pressure p the position becomes more complicated. Parrinello and Ponter [10] investigated a class of Drucker–Prager yield conditions with a cap where continuous curvature of the yields surface is allowed so that the strain rate uniquely defines the stress at yield. However, convergence was slow and the method is inapplicable to the Drucker–Prager yield condition.

$$f(\overline{\sigma}, p) = (\overline{\sigma} + p \tan \phi' - c') = 0. \tag{11}$$

The solution to this problem is discussed in Sects. 4 and 5.

4 Shakedown Limits for the Drucker–Prager Yield Condition

The associated flow rule for yield condition (11) yields the constraint

$$\frac{\dot{\varepsilon}_{\mathrm{v}}^{\mathrm{p}}}{\overline{\dot{\varepsilon}}^{\mathrm{p}}} = \tan \psi, \quad \psi = \phi'. \tag{12}$$

Consider the class of linear isotropic materials given by

$$\overline{U} = \frac{1}{2} \frac{1}{3\mu} \left\{ \overline{\sigma}^2 + \frac{(p - p_{\mathrm{L}})^2}{g(\nu_{\mathrm{L}})} \right\}, \tag{13}$$

where

$$\overline{\dot{\varepsilon}}^{\mathrm{L}} = \frac{\partial \overline{U}}{\partial \overline{\sigma}} = \frac{1}{3\mu} \overline{\sigma} \quad \text{and} \quad \dot{\varepsilon}_{\mathrm{v}}^{\mathrm{L}} = \frac{\partial \overline{U}}{\partial p} = \frac{(p - p_{\mathrm{L}})}{K}. \tag{14}$$

Here $(\overline{\sigma}, \overline{\dot{\varepsilon}})$ denote the von Mises effective stress and strain rate and $(p, \dot{\varepsilon}_{\mathrm{v}})$ are the hydrostatic stress and rate of volume change. The linear moduli are given by the shear modulus μ, bulk modulus K and Poison's ratio ν_{L}.

In this situation neither condition A nor B is satisfied. Solution to the linear problem generally will yield strain rates that do not satisfy (12). The sufficient condition for convergence is not satisfied except for the special case of $\phi' = 0$ and $\nu_{\mathrm{L}} \cong 0.5$. In the following, we describe an alternative iterative process that overcome these problems [2].

5 Linear Matching Method for the Drucker–Prager Yield Condition and a Non-Associated Flow Rule

In this case, zero volume change at yield is assumed, so that $\psi = 0$ in (12). The class of linear materials are chosen as in (13) and (14). As before, suppose an initial kinematically admissible strain rate history $\dot{\varepsilon}_{ij}^{\mathrm{i}}$ is assumed known. As such histories will be generated by solutions of linear problem

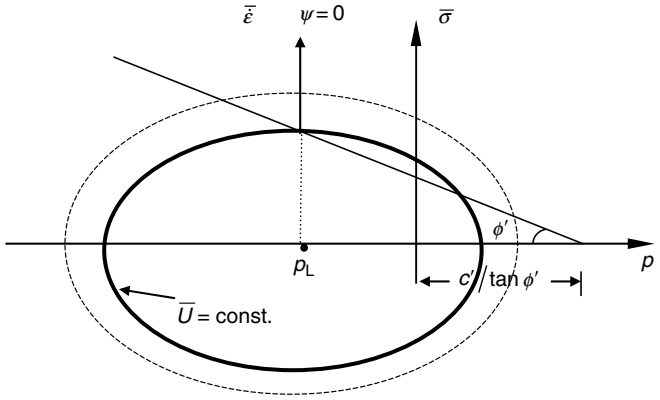

Fig. 1. Linear matching for Drucker–Prager yield condition and non-associated flow rule

where compressibility may occur we assume $\dot{\varepsilon}^{\mathrm{i}}_{\mathrm{v}} = \dot{\varepsilon}^{\mathrm{i}}_{kk} \neq 0$. However, the converged solution must satisfy the condition $\dot{\varepsilon}_{\mathrm{v}} = 0$ and this implies from (14) that $p = p_{\mathrm{L}}$. This suggests the inclusion in the iterative process of p^{i}, the hydrostatic pressure corresponding to the current linear solution. Consider therefore an iterative process where the matching conditions are given by

$$\bar{\dot{\varepsilon}}^{\mathrm{L}} = \bar{\dot{\varepsilon}}^{\mathrm{i}} = \frac{\partial \overline{U}}{\partial \overline{\sigma}} = \frac{1}{3\mu}\overline{\sigma} = \frac{1}{3\mu}\overline{\sigma}^{\mathrm{p}},$$

$$\text{i.e.} \quad \mu = \frac{\overline{\sigma}^{\mathrm{p}}}{3\bar{\dot{\varepsilon}}^{\mathrm{i}}} \tag{15}$$

and

$$p_{\mathrm{L}} = p_i = (\lambda \widehat{\sigma}^i_{kk} + \overline{\rho}^i_{kk})/3, \tag{16}$$

where now $\overline{\sigma}^{\mathrm{p}} = c' - p_i \tan\phi'$. This matching condition is shown in Fig. 1.

6 Linear Matching Method for the Drucker–Prager Yield Condition and an Associated Flow Rule

The method may now be extended to the Drucker–Prager yield condition with an associated flow rule

$$\frac{\dot{\varepsilon}^{\mathrm{p}}_{\mathrm{v}}}{\bar{\dot{\varepsilon}}^{\mathrm{p}}} = \tan\phi'. \tag{17}$$

In this case we identify p_i with the pressure at yield. Hence, the matching point on the yield surface is given by

$$\overline{\sigma}^{\mathrm{p}} = c' - p_i \tan\phi', \quad p^{\mathrm{p}} = p_i = (\lambda \widehat{\sigma}^{\mathrm{i}}_{kk} + \overline{\rho}^{\mathrm{i}}_{kk})/3 \tag{18}$$

and the associated plastic strains are given by

$$\dot{\overline{\varepsilon}}^{\mathrm{p}} = \dot{\overline{\varepsilon}}^{\mathrm{i}}, \quad \dot{\varepsilon}_{\mathrm{v}}^{\mathrm{p}} = \dot{\overline{\varepsilon}}^{\mathrm{i}} \tan\phi'. \tag{19}$$

This yields the following equations for μ and p_{L}:

$$\dot{\overline{\varepsilon}}^{\mathrm{p}} = \frac{1}{3\mu}\overline{\sigma}^{\mathrm{p}}, \quad \dot{\varepsilon}_{\mathrm{v}}^{\mathrm{p}} = \frac{1}{3\mu g(v_{\mathrm{L}})}(p^{\mathrm{p}} - p_{\mathrm{L}}). \tag{20}$$

Hence, by substituting (18) and (19) into (20)
$\mu = \frac{(c' - p_i \tan\phi')}{3\dot{\overline{\varepsilon}}^{\mathrm{i}}}$ and

$$p_{\mathrm{L}} = p_i\left(1 + \frac{2(1+v_{\mathrm{L}})\tan^2\phi'}{9(1-2v_{\mathrm{L}})}\right) - \frac{2}{9(1-2v_{\mathrm{L}})}c'\tan\phi'. \tag{21}$$

This matching condition is shown schematically in Fig. 2. Note that ν_{L} may be chosen arbitrarily. The value of $\nu_{\mathrm{L}} = 0.35$ was chosen for the calculations described later.

The upper bound (5), in the case when the strain rate history consists of a sequence of m discrete strains $\Delta\varepsilon_{ij}^{\mathrm{r}}$ at times t_{r}, is given by,

$$\int_V \sum_{r=1}^{m} \sigma_y^r \overline{\varepsilon}(\Delta\varepsilon_{ij}^r)\,\mathrm{d}V + \int_V \sum_{r=1}^{m} p_y^{\mathrm{r}} \varepsilon_{\mathrm{v}}(\Delta\varepsilon_{ij}^{\mathrm{r}})\,\mathrm{d}V = \lambda_{\mathrm{UB}}^{\mathrm{c}} \int_V \sum_{r=1}^{m} \widehat{\sigma}_{ij}(t_r)\,\Delta\varepsilon_{ij}^r\,\mathrm{d}V, \tag{22}$$

where $\overline{\sigma} = \overline{\sigma}^{\mathrm{p}} = \sigma_y^{\mathrm{r}}$ and $p = p^{\mathrm{p}} = p_y^{\mathrm{r}}$, given by (18). For consistency with the flow rule (17), $\dot{\varepsilon}_v^{\mathrm{p}} = \dot{\overline{\varepsilon}}^{\mathrm{p}} \tan\phi'$ is treated as a derived quantity. Hence (22) ceases to be a strict upper bound, except at convergence when (17) is satisfied exactly.

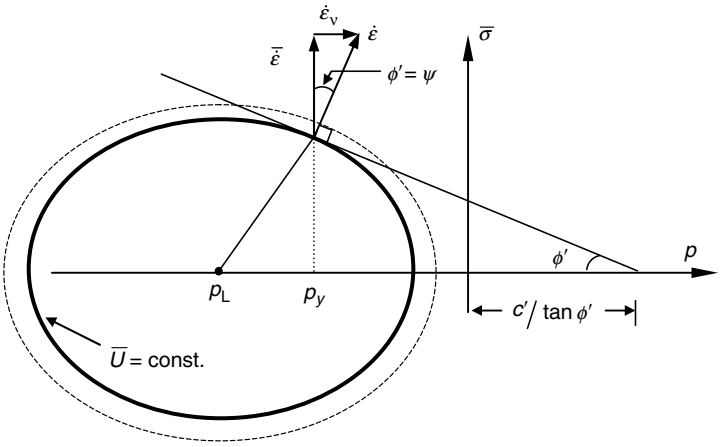

Fig. 2. Linear matching for the Drucker–Prager yield condition and the associated flow rule

7 Examples

All the solutions given here were generated by an implementation of the method into the commercial finite element code ABAQUS.

7.1 Limit Analysis

Consider the two-dimensional indentation problem shown in Fig. 3 for which a slip line solution for the Mohr–Coulomb solution is known [13]. The Drucker–Prager yield condition and the Mohr–Coulomb condition are identical for two dimensional plane strain problems, once account has been taken of the flow rule. The following solutions are given for the corresponding Mohr–Coulomb values (c, ϕ).

The converged solutions for the limit pressure $\lambda P/c$ are shown in Fig. 4 in the two cases. The Prandtl solution is included for comparison. The solution for the non-associated flow rule gives a lower value, as expected, although significant differences only occur for $\phi > 35°$.

For a non-associated flow rule there is a question of whether the solution is unique. Figure 5 shows the convergence of $\lambda P/c'$ with the number of iterations for a range of values of the linear Poisson's ratio ν_{L}. In each case, the progress to convergence varies significantly, but all solutions converge to the same value, indicating, for this problem at least, a unique solution is defined by the method. The same phenomenon was shown by all other solutions discussed here.

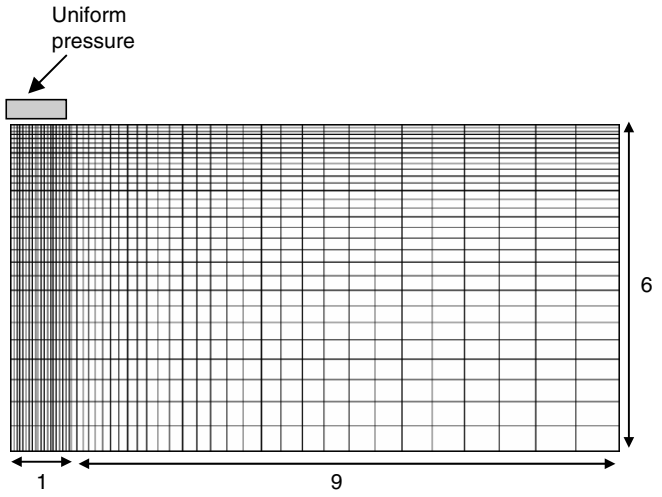

Fig. 3. Finite element mesh for indentation problem, eight-noded quadrilateral elements

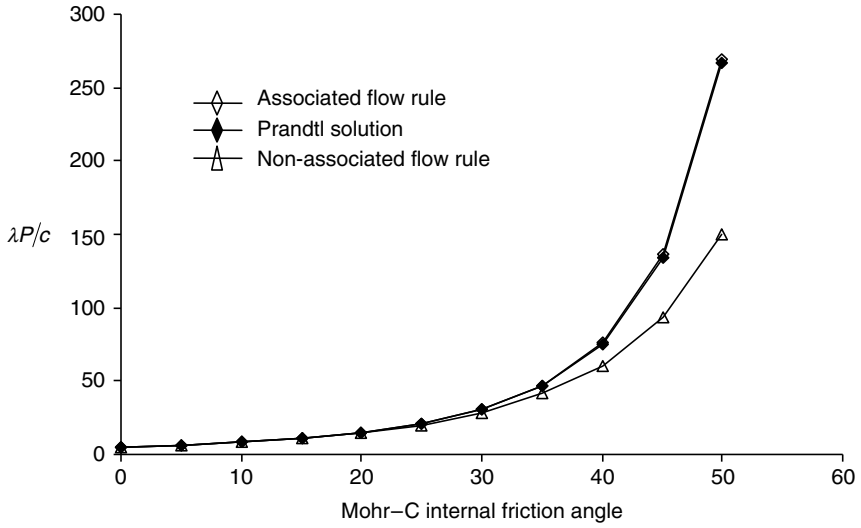

Fig. 4. Comparison of limit load solutions for the indentation problem of Fig. 3

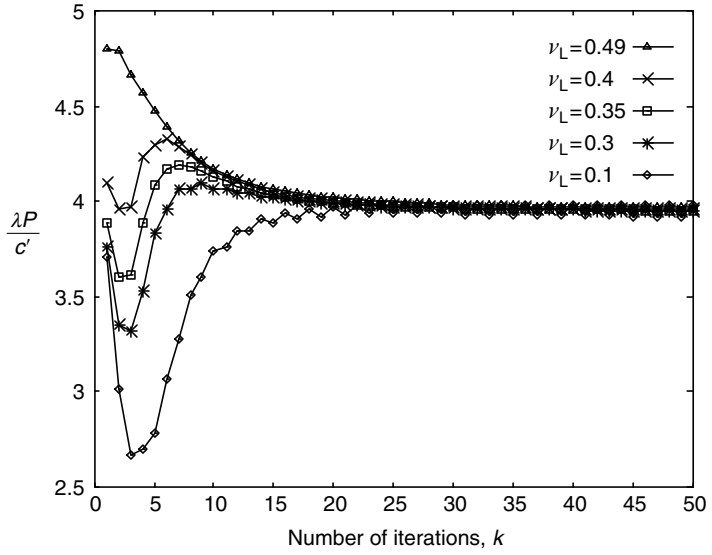

Fig. 5. Convergence for a range of ν_L for a non-associated flow rule and $\phi' = 10^0$. Indentation problem of Figs. 3 and 5

7.2 Shakedown Solutions for Rolling Contact

Consider the problem shown in Fig. 6 where a circular region of radius a on a half space is subjected a Hertzian distribution of normal pressure of $P/2\pi a^2$. The loaded area passes, repeatedly along a straight line, the x axis, and a

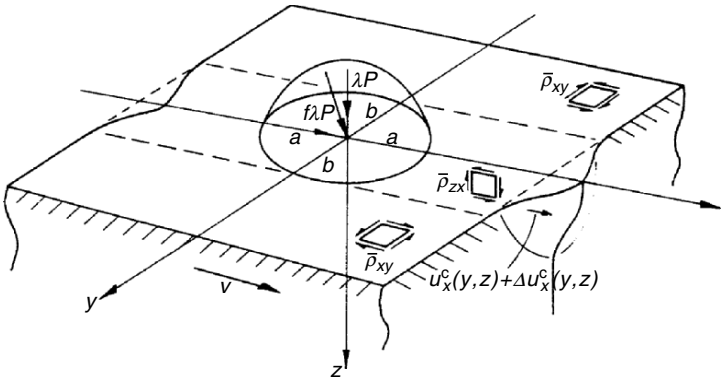

Fig. 6. Rolling and sliding contact problem

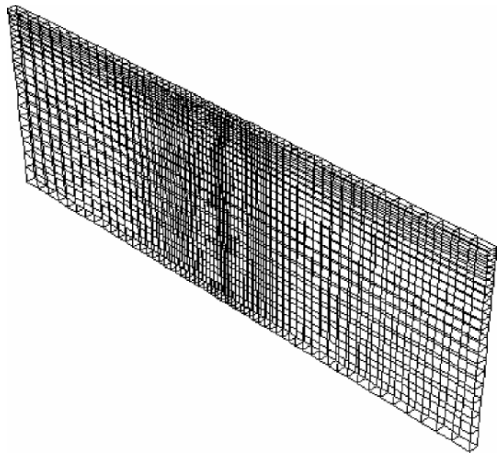

Fig. 7. Finite element mesh for problem of Fig. 6: 1,200 eight-noded brick elements, 42 time instants.

frictional traction is generated in the direction of travel with a coefficient of friction f, as shown. In this case all surfaces perpendicular to the direction of travel suffer the same deformation modes; the finite element mesh consists of a single layer of elements in the (y, z) plane, as shown in Fig. 7, where the displacement on the front and back surface are constrained to be identical, a facility available in ABAQUS. The history of elastic stresses experienced by Gauss points within the finite element mesh corresponds to a sequence of positions of the centre of the pressure region relative to the mesh. The elastic problem has a known analytic solution, Hamilton [5], and the number and positions of the load instants were increased until there were no change in the converged solution.

The variation of the shakedown limit with friction co-efficient for both an associated and non-associated flow rule are shown in Fig. 8. The solution for

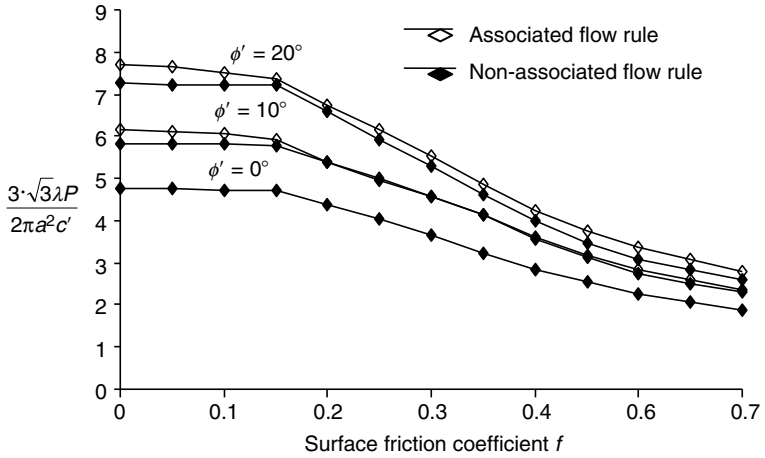

Fig. 8. Comparison of the shakedown limits for the problem of Fig. 6 for the Drucker–Prager yield condition and for associated and non-associated flow rules

$\phi' = 0$, the von Mises yield condition, corresponds closely to the semi analytic solution by Ponter et al. [12]. Again, the solution for the non-associated flow rule is slightly less than for the associated flow rule.

8 Conclusions

The linear matching method is a simple and flexible method for the solution of complex shakedown problems. For the Drucker–Prager yield condition, the method derived by Ponter and Engelhardt [11] needs to be adapted by including the hydrostatic pressure generated by the linear solutions into the matching condition. A sufficient condition for convergence is no longer available, but fully convergent solutions were obtained for the problems discussed in this paper.

9 Acknowledgements

The authors acknowledge the support of the Science and Engineering Research Council during the course of the work reported in this paper. They also wish to express their appreciation of useful discussions with Professor Hai-Sui Yu and his colleagues at the University of Nottingham.

References

1. Ainsworth R.A. (Ed) (2003), R5: Assessment Procedure for the High Temperature Response of Structures. Issue 3. British Energy Generation Ltd, Barnwood, Gloucester, UK
2. Boulbibane M. and Ponter A.R.S. (2005), Extension of the linear matching method to geotechnical problems, Comput. Methods Eng Appl Mech, 194, 4633–4650
3. Boyle J.T., Hamilton R., Shi J., Mackenzie D. (1997), Simple method of calculating lower-bound limit loads for axisymmetric thin shells, J. Pressure Vessel Tech, 119, 236–24
4. Chen H.F. and Ponter A.R.S., Integrity assessment of a 3D tube-plate using the linear matching method, Int. J. Pressure Vessels Piping, 82, Part 1: Shakedown, reverse plasticity and ratchetting, 85–94, Part 2: Creep relaxation and reverse plasticity, 95–104
5. Hamilton G.M. (1983), Explicit equations for the stresses beneath a sliding spherical contact, Proc. Inst. Mech. Eng., 197C, 53–59
6. Kim, J., Salgado, R. Yu, H.S. (1999), Limit analysis of soil slopes subjected to pore–water pressures J Geotechn. Geoenviron. Eng., ASCE, 125, 49–58
7. Koiter W.T., (1960) General theorems of elastic–plastic solids, In: Sneddon J. N., Hill R. (Eds.), Progress in Solid Mechanics, 1, 167–221
8. Marriott D.L. (1998), Evaluation of deformation or load control of stresses under inelastic condition using elastic finite element stress analysis. Proceedings of the ASME Pressure vessel and Piping Conference, Pittsburg, PA, PVP-136, 3–9, 1998
9. Merifield R.S., Sloan S.W., Y, S.H. (1999), Rigorous plasticity solutions for the bearing capacity of two-layered clays. Géotechnique, 49, 4, 471–490
10. Parrinello F., Ponter A.R.S. (2001). Shakedown limits based on linear solutions, for a hydrostatic pressure dependent material, Proceedings of the 2nd European Conference on Computational Mechanics, Cracow, University of Technology, Poland
11. Ponter A.R.S. Engelhardt M. (2000), Shakedown limits for a general yield condition: implementation and examples for a von Mises yield condition, Eur. J. Mech., A/Solids, 19, 423–446, 2000
12. Ponter A.R.S., Hearle A.D., Johnson K.L. (1985), Application of the kinematical shakedown theorem to rolling and sliding point contacts, J. Mech. Phys. Solids, 33, 339–362, 1985
13. Prandtl, L. (1921), Über die eindringungs-festigkeit (Härte) plastischer baustoffe und die festigkeit von schneiden, Z. Angew. Math. Mech., 1 (1), 15–20
14. Seshadri R., Mangalaramanan S.P. (1997), Lower bound limit loads using variational concepts: the m_α-method, Int. J. Pressure Vessels Piping, 71, 93–106, 1997

On Recent Analytical Results for Advective Transport in Fluid-Saturated Porous Media

A.P.S. Selvadurai*

Department of Civil Engineering and Applied Mechanics, McGill University, Montréal, Canada
patrick.selvadurai@mcgill.ca

Abstract. This paper reviews analytical solutions that have been developed recently for the theoretical modelling of the classical problem dealing with advective transport of a chemical species in a fluid-saturated porous medium. The advective Darcy flow results from a hydraulic potential, which is responsible for the transport process. The analytical solutions play an important role in providing benchmarks against which the accuracy of computational developments can be assessed. The paper provides a catalogue of solutions that involve advective transport dealing with initial boundary value problems and certain advective–diffusive transport problems that can be formulated as one-dimensional initial value problems.

1 Introduction

The topic of groundwater-borne transport of hazardous materials, contaminants and other chemical substances including fertilizers and pesticides is of considerable interest to geoenvironmental engineering. Invariably the discussions concerning these topics ultimately reduce to the assessment of the risk to human health and the environment, although the means of assessing such risks eventually centers round the estimation of the levels of concentration of the chemicals and hazardous materials that will be encountered at a particular location at a particular time. The basic mechanisms of waterborne transport of either a chemical or a hazardous substance in a porous geologic medium are complex, and the processes responsible for the transport are governed by the physico-chemical characteristics of the porous medium, the chemical composition of the species that is being transported, the variability of the fluid transport properties of the porous medium, the capacity for natural attenuation and the complete coupling between chemical, hydraulic, mechanical and thermal characteristics of the system. The literature dealing with the topic of contaminant transport in fluid-saturated porous media is extensive and no attempt will be made to provide a comprehensive bibliography of the subject. Important developments concerning this topic can be found in the articles and

* *William Scott Professor* and *James McGill Professor*

volumes by Lindstrom et al. [16], Barenblatt et al. [3], Philips [20], Bear and Bachmat [4], Appelo and Postma [1], Banks [2], Lichtner et al. [15], Sun [28], Bedient et al. [5], Ingham and Pop [14], Domenico and Schwartz [8], Massel [17], Charbeneau [6], Ingebritsen and Sanford [13], Zheng and Bennett [34] and Selvadurai [23].

The basic transport process governing transport of a chemical species through a non-deformable porous medium under isothermal conditions can be described in terms of the idealizations that can be attributed to advective and diffusive phenomena. In the advective process, the chemical species is transported through the pore space of the non-deformable medium through the velocity of the fluid saturating the pore space. The flow velocity is characterized by a Dupuit-Forchheimer-type hydraulic conductivity that is related to average velocity in the pore space. This in turn can be related to the area averaged hydraulic conductivity as expressed by a Darcy-type hydraulic conductivity. The velocities in the porous medium are assumed to be such that the hydraulic potential consists of only the pressure and datum components of the Bernoulli potential. The process of diffusion of the chemical species within the pore space of the porous medium is dependent on the gradient of the concentration of the species and is governed by Fick's law. In addition to these basic transport processes, the movement of the chemical can also take place as a result of hydrodynamic dispersion that is governed by the fluid velocities in the pore space. All three processes can occur simultaneously during the transport of the chemical and the dominancy of any single process is usually related to the velocities within the pore space of the porous medium. For example, when the flow velocities are zero, the chemical movement must take place through diffusion and similarly, when the flow velocities are large, the advection processes and hydrodynamic dispersion effects can dominate. The extent to which the separate processes can influence the transport process can be estimated by appeal to the non-dimensional Peclet Number ($Pe = \|\mathbf{v}\|\, h/D$, where $\|\mathbf{v}\|$ is a flow velocity norm within the region, h is a characteristic length associated with the region and D is the diffusion coefficient. When the Peclet number is generally greater than unity, the advective phenomena will be dominant. Under such circumstances, the movement of the chemical species within the porous medium can be adequately described by the classical advection equation. Even under the simplifications offered, the classical model for advective transport does not take into consideration the influences that could take place as a result of chemically-induced alteration of the fluid transport characteristics of the porous medium. The basic formulation can account for processes such as natural attenuation that can exert a considerable influence on the decay of the concentration of chemicals and contaminants as they migrate through a porous medium [10, 33].

The solution of any practical problem dealing with the migration of chemicals and contaminants in fluid-saturated porous media has to use an approach that involves computational schemes. The development of computational schemes for the solution of transport processes that include both advective and diffusive processes has been the subject of extensive research

during the past three decades. The computational approaches to the class of problems involving diffusion-dominated transport processes in porous media is relatively well established [7, 19, 34, 35]. The computational treatment of the class of problems where the advective transport processes dominate are less routine. Specially in situations that involve advective transport processes with sharp discontinuous fronts in the concentration profile, the computational approaches give rise to phenomena such as numerically induced diffusion, oscillations in the solution that propagate in directions opposite to the migration of the front, negative concentrations in the solution and other undesirable effects. Some aspects of the inaccuracies present in the computational approaches are given by Gresho and Lee [11], Hughes and Brooks [12], Vichnevetsky and Bowles [29], Noorishad et al. [18], Wendland and Schmid [32], Wang and Hutter [30], Selvadurai and Dong [27] and Dong and Selvadurai [9]. While unconditional stability and accuracy of the computational schemes such as the *Streamline Upwind Petrov–Galerkin*, *Least-Squares*, *Taylor–Galerkin*, *Modified Least Squares* and other variations of these methods cannot be assured, they can be combined with suitable mesh- and time adaptive schemes to produce reliable computational results for advection-dominated transport processes that contain even discontinuous concentration fronts. The accuracy of these computational schemes should be continually assessed by appeal to comparisons with known analytical solutions. The traditional approach for achieving this objective is through the use of relatively straightforward solutions applicable to one-dimensional problems. The analytical results that involve multi-dimensional problems of both fluid flow and advective transport are rare and are continually being developed. This paper presents certain analytical results that provide useful benchmarks for the calibration of computational schemes for advection-dominated transport of a chemical or contaminant species in a fluid-saturated porous medium. In particular attention is focused on (i) the advective transport in a plane sector region subjected to a constant hydraulic potential and constant chemical concentration on the same surface, (ii) advective transport from a prolate spheroidal cavity, the boundary of which is subjected to a constant hydraulic potential and chemical concentration and (iii) the advective-diffusive transport of a plug of chemical in a one-dimensional element which is considered to be of finite length with respect to the advective flow but of infinite length with respect to the advective-diffusive transport processes. In all these cases, the analytical solution is developed in *exact closed form*. This presents a considerable advantage in exercises that involve calibration of the accuracy of the currently available computational approaches for the solution of advection-dominated transport of chemicals and other contaminants in the fluid-saturated geosphere.

2 Governing Equations

We consider a fluid-saturated porous medium in which steady flow is established under a reduced Bernoulli hydraulic potential $\varphi(\mathbf{x})$. The average velocity of the fluid in the pore space is defined by $\mathbf{v}(\mathbf{x})$. The average flow velocity in

the pore space is related to the gradient of the flow potential through Darcy's law. Assuming that the porous medium exhibits hydraulic isotropy we have

$$\mathbf{v}(\mathbf{x}) = -k\,\nabla\varphi, \tag{1}$$

where k is the Dupuit-Forchheimer hydraulic conductivity measure, which is related to the conventional Darcy hydraulic conductivity $\tilde{k}$ through the porosity n^* (i.e. $k = \tilde{k}/n^*$). We consider pore fluids that are incompressible for which

$$\nabla \cdot \mathbf{v} = 0 \tag{2}$$

and assuming spatial homogeneity of the porous medium, the partial differential equation governing the flow potential is Laplace's equation

$$\nabla^2\varphi(\mathbf{x}) = 0. \tag{3}$$

The partial differential equation (3) is subject to the conventional Dirichlet, Neumann or Robin type boundary conditions applicable to partial differential equations of the elliptic type. The uniqueness of solutions of the resulting boundary value problems is well established [21, 31]. We now consider the transport of the chemical (or the contaminant) that moves with the fluid in the pore space without affecting either the permeability characteristic of the porous medium or the physical and flow characteristics of the fluid that transports the chemical (or the contaminant). This is an important idealization that permits the development of the classical advective transport equation. We define $C(\mathbf{x}, t)$ as the concentration of the chemical measured per unit volume of the pore space. Alternatively, the concentration $\tilde{C}$ measured per unit volume of the entire porous medium is given by $\tilde{C} = C\,n^*$. We consider the presence of both advective and diffusive transport processes in the porous medium with the advective flux defined in terms of an advective flux and a diffusive flux, the latter dependent on a Fickian law of diffusion. Considering conservation of mass of the chemical species it can be shown that the advection-diffusion equation is given by

$$\frac{\partial C}{\partial t} + \nabla \cdot (\mathbf{v}C) - D\nabla^2 C = -\zeta C, \tag{4}$$

where ζ accounts for the attenuation of the chemical, through natural or other means, as it migrates through the porous medium. The partial differential equation (4) governing advective-diffusive transport is subject to an appropriate boundary conditions and an initial condition. The uniqueness of solution of the resulting initial boundary value problem can also be proved [23–26]. Equations (3) and (4) form the *weakly coupled* set of partial differential equations that govern the advective-diffusive transport problem. In this sense, the potential problem can be solved completely independent of the advective-diffusive transport problem. While development of generalized results for the governing partial differential equations is certainly possible, it is more prudent

to examine specific solutions that will be of benefit to the assessment of the accuracy of computational schemes that have been proposed for the solution, in particular of advection-dominated transport problems.

3 Advective Transport from a Plane Crack

We consider a porous medium occupying the two-dimensional plane annular domain $a \leq r < b, 0 < \theta < 2\pi$, where r and θ refer to the plane polar coordinate system. Potential flow is induced in the medium by subjecting the region to the boundary conditions

$$\phi(r,0) = \phi_0; \qquad \phi(r,2\pi) = 0 \tag{5}$$

$$\left[\frac{\partial \phi}{\partial r}\right]_{r=a} = 0; \qquad \left[\frac{\partial \phi}{\partial r}\right]_{r=b} = 0. \tag{6}$$

The advective transport in the porous medium is induced by subjecting the region to the following boundary and initial conditions:

$$C(r,0,t) = C_0 H(t); \quad C(r,\theta,0) = 0, \tag{7}$$

where $H(t)$ is the Heaviside step function of time and C_0 is the boundary concentration. The solution of the potential problem is sought from the general solution for Laplace's equation (3) subject to the boundary conditions (5) and (6). The general solution of (3) takes the form [21]

$$\phi(r,\theta) = A \ln r + B\theta \ln r + C\theta + D + \sum_{n=1,2}^{\infty} \left[A_n r^n + \frac{B_n}{r^n}\right] [C_n \sin n\theta + D_n \cos n\theta], \tag{8}$$

where $A, B, \ldots, A_n, B_n ..$, etc., are arbitrary constants. The required solution, however, reduces to the simplified result [21, 22]

$$\phi(r,\theta) = \phi_0 \left(1 - \frac{\theta}{2\pi}\right). \tag{9}$$

Correspondingly, the advective transport equation takes the form

$$\frac{\partial C}{\partial t} + \frac{k\phi_0}{2\pi r^2} \frac{\partial C}{\partial \theta} = -\zeta C. \tag{10}$$

The solution of (10) can be obtained quite conveniently by employing a Laplace transform approach; this gives

$$C(r,\theta,t) = C_0 \exp\left(-\zeta \tau(\eta)\right) \mathrm{H}\left[t - \tau(\eta)\right], \tag{11}$$

where

$$\tau(\eta) = 2\pi a^2 \eta^2 \theta / k\phi_0; \quad \eta = r/a. \tag{12}$$

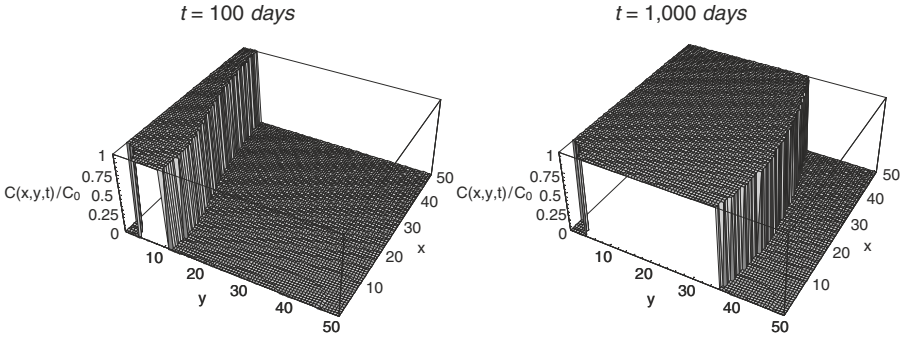

Fig. 1. Advective transport from the boundary of a plane crack in the absence of attenuation

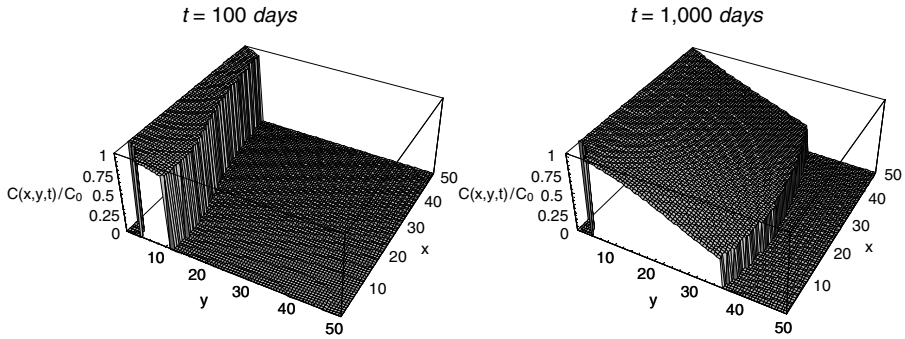

Fig. 2. Advective transport from the boundary of a plane crack-in the presence of attenuation

We illustrate the results for the concentration distribution derived from this solution by considering a quadrant of the domain of interest. The radius of the obstacle $a = 4\,\mathrm{m}$, the domain is defined by $x \in [0, 50\,\mathrm{m})$ and $y \in [0, 50\,\mathrm{m})$ and the transport and decay parameters chosen for the computations include the following: $k\varphi_0\ a^2 \approx 4\pi(\mathrm{days})^{-1}; \zeta = 0.0005(\mathrm{day})^{-1}$. The Fig. 1 illustrates the chemical distribution within the region of interest when there is no natural attenuation present and the results in Fig. 2 consider the effects of the attenuation parameter.

4 Advective Transport from a Spheroidal Cavity

Analytical solutions that deal with three-dimensional advective transport in porous media are important to the validation of computational schemes that can ultimately be used for the solution of practical three-dimensional problems in contaminant and chemical transport in fluid-saturated porous media. Such solutions are, however, rare and can be developed only for a very limited

number of cases. The advective transport from a spheroidal cavity, either oblate or prolate, is one such example. We consider a porous medium of infinite extent that is bounded internally by a prolate spheroidal cavity. The formulation is referred to the prolate spheroidal coordinate system (α, β, γ), where parametric surfaces $\alpha = \text{const.}$, say $\alpha_0, \beta = \beta_0$, and $\gamma = \gamma_0$, form a triple orthogonal confocal family of prolate spheroids, hyperboloids of two sheets and meridional half-planes, respectively. The prolate spheroidal cavity, which corresponds to $\alpha = \alpha_0$, is subjected to a constant hydraulic potential φ_0 and the far field potential is assumed to be zero. The potential equation (3) takes the form

$$\nabla^2 \varphi(\alpha, \beta) = \left(\frac{\partial^2}{\partial \alpha^2} + \frac{\partial^2}{\partial \beta^2} + \coth \alpha \frac{\partial}{\partial \alpha} + \cot \beta \frac{\partial}{\partial \beta} \right) \varphi(\alpha, \beta) = 0 \tag{13}$$

which is subject to the boundary condition

$$\varphi(\alpha_0, \beta) = \varphi_0 \tag{14}$$

and the regularity condition, $\varphi(\alpha, \beta) \to 0$, as $\alpha \to \infty$. This allows for the development of an exact closed form result for the potential distribution within the porous medium:

$$\varphi(\alpha) = \frac{\varphi_0}{\ln \xi_0} \ln \xi; \quad \xi = \left(\frac{\cosh \alpha + 1}{\cosh \alpha - 1} \right); \quad \xi_0 = \xi(\alpha_0). \tag{15}$$

This simplified form of the hydraulic potential results in an advective transport equation of the form

$$\frac{\partial C}{\partial t} + \frac{2\, k \phi_0}{c_p^2 \, \sinh \alpha (\sinh^2 \alpha + \sin^2 \beta) \, \ln \xi_0} \frac{\partial C}{\partial \alpha} = -\zeta C. \tag{16}$$

The solution of the advective transport equation is subject to the boundary and initial conditions

$$C(\alpha, \beta, t) = C_0 \mathrm{H}(t); \quad C(\alpha, \beta, 0) = 0, \tag{17}$$

where $\mathrm{H}(t)$ is the Heaviside step function of time. The solution of (16) can be obtained by applying Laplace transform techniques and the exact closed form solution for the time-dependent distribution of chemical concentration within the porous medium is given by

$$\frac{C(\alpha, \beta, t)}{C_0} = \exp \left[-\zeta \, \Omega_p \left(\alpha, \beta, \lambda \right) \right] \mathrm{H} \left[\, t - \Omega_p \left(\alpha, \beta, \lambda \right) \right], \tag{18}$$

where

$$\Omega_p(\alpha, \beta, \lambda) = \frac{c_p^2 \ln \xi_0}{6 k \varphi_0} \left[\cosh^3 \alpha - \cosh^3 \alpha_0 \right. \\ \left. -3 \cos^2 \beta \, \left\{ \cosh \alpha - \cosh \alpha_0 \right\} \right]. \tag{19}$$

In (19)

$$c_p = \sqrt{a_p^2 - b_p^2}; \quad \xi = \left(\frac{\cosh\alpha + 1}{\cosh\alpha - 1}\right); \quad \xi_0 = \xi(\alpha_0) \tag{20}$$

and the trigonometric and hyperbolic functions can be expressed in terms of the normalized cylindrical coordinates $\rho_p = r/a_p$ and $\eta_p = z/a_p$. The availability of an exact closed-form solution for the initial boundary value posed by (16) and (17) is a considerable advantage for the calibration of computational developments. The solution is also versatile to the extent that sharp fronts can be encountered in the chemical transport profile regardless of the value of ζ, the attenuation parameter. As an example consider the case where the initial condition for the advective transport problem is changed from the first equation of (17) to the following:

$$C(\alpha, \beta, t) = C_0\{\,\mathrm{H}(t) - \mathrm{H}(t - t^*)\} \tag{21}$$

implying that the boundary of the prolate spheroidal cavity is subjected to chemical concentration only for a finite period $0 \le t \le t^*$. The exact analytical solution for the chemical concentration distribution within the porous medium is given by

$$\begin{aligned}\frac{C(\alpha,\beta,t)}{C_0} &= \exp\left[-\zeta\,\Omega_p\,(\alpha,\beta,\lambda)\right] \\ &\quad \times \left\{\mathrm{H}\left[\,t - \Omega_p\,(\alpha,\beta,\lambda)\right] - \,\mathrm{H}\left[t - t^* - \Omega_p\,(\alpha,\beta,\lambda)\right]\right\}.\end{aligned} \tag{22}$$

Figure 3 illustrates the migration of the chemical front at different time intervals, and calculated for the following spatial variables $\eta_p = z/a_p$; $\rho_p = r/a_p$ and for the system parameters chosen such that, $6k\varphi_0/(a_p^2 - b_p^2) \approx 4(\text{days})^{-1}$, $\zeta \approx 0.005(\text{days})^{-1}, t^* = 200\text{days}, a_p = 8\,\text{m}$ and $b_p = 1\,\text{m}$. The results of the chemical migration patterns indicate that the effect of advective transport and the natural attenuation is to decrease the spatial distribution of chemical concentration as the front migrates from the original source. The chemical concentration profiles also display the characteristic sharp front associated with the transport problem with boundary conditions of the type (17) and (20) involving the Heaviside step function of the time-dependent concentration. It should also be noted that the result (18) can be regarded as a fundamental solution that can be used in conjunction with a superposition technique to determine the chemical concentration profiles corresponding to any arbitrary time-dependency in the concentration that is uniformly applied to the *entire boundary* of the prolate spheroidal cavity.

The basic approach can also be applied to determine the chemical concentration in the porous medium that is internally bounded by an oblate spheroidal cavity. When the boundary of the cavity is subjected to a constant potential φ_0 and a chemical concentration with strength C_0 and a time dependency in the form of a Heaviside step function

$$\frac{C(\alpha,\beta,t)}{C_0} = \exp\left[-\zeta\Omega_0\,(\alpha,\beta,\mu)\right]\mathrm{H}\left[\,t - \Omega_0\,(\alpha,\beta,\mu)\right], \tag{23}$$

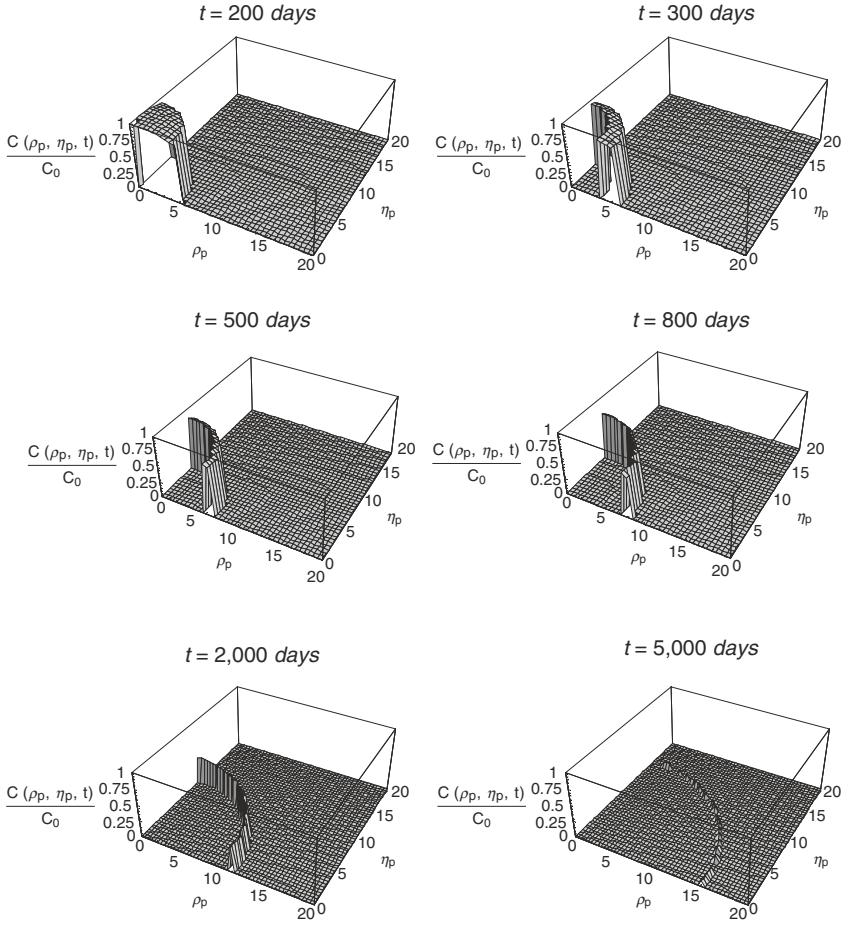

Fig. 3. Advective transport from the boundary of a prolate spheroidal cavity due to a boundary chemical dosing of finite duration and constant attenuation

where

$$\Omega_0(\alpha,\beta,\mu) = \frac{b_0^2(1-\mu^2)\cot^{-1}(\sinh\alpha_0)}{3k\varphi_0} \times[\sinh^3\alpha - \sinh^3\alpha_0 + 3\cos^2\beta)(\sinh\alpha - \sinh\alpha_0)], \quad (24)$$

$$\sinh\alpha_0 = \frac{\mu}{\sqrt{1-\mu^2}}; \quad \mu = \frac{a_0}{b_0} < 1. \quad (25)$$

For details of these developments the reader is referred to Selvadurai [23, 25].

5 Advective-Diffusive Transport with Time-Dependent Flow Velocity

In almost all developments dealing with the classical advective transport equation, it is assumed that the advective velocities can be functions of the spatial coordinates as determined by the solution of Laplace's equation (3). In general, the flow velocities can exhibit time-dependency due to a variety of effects including hydraulic potentials that can vary with time, compressibility of either the pore fluid or the porous skeleton and poroelastic effects in the system. When there is no compressibility in the system, time-dependency in the flow velocities can result from time dependency in the boundary potential. A simple instance of such a situation is the conventional one-dimensional falling head test that is used to determine the hydraulic conductivity characteristics of porous media. In such a test, the velocity is uniform over the length of the sample but the velocity will decay exponentially with time. Here we consider the advective-diffusive transport problem applicable to a one-dimensional problem resulting from the movement of a plug of chemical that is located within a porous column of finite length, which is subjected to flow velocity that is uniform but varies exponentially with time. In terms of the advective flow problem, the porous column is assumed to be a finite domain, whereas in terms of the advective-diffusive transport problem the region is assumed to be infinite. We consider the problem of a porous column of length l that is subjected to an initial hydraulic head H_0 as shown in Fig. 4. The chemical is located within the porous column and occupies the region $x \in (-a, a)$. As the hydraulic head diminishes, the velocity in the porous column will vary exponentially with time. We can formulate an initial value problem defined by the partial differential equation

$$\frac{\partial C}{\partial t} + v_0 \exp(-\lambda t)\frac{\partial C}{\partial x} = D\frac{\partial^2 C}{\partial x^2}; x \in (-\infty, \infty); \quad t > 0, \tag{26}$$

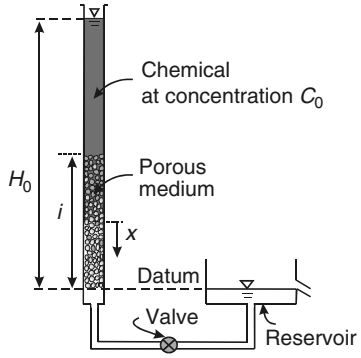

Fig. 4. Advective diffusive transport in a porous column

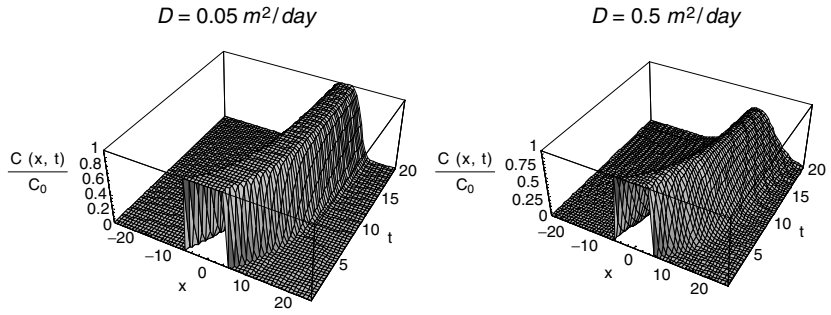

Fig. 5. Advective-diffusive transport in a porous column

where

$$v_0 = kH_0/l; \quad \lambda = k/l. \tag{27}$$

The PDE (26) is solved subject to the initial condition

$$C(x,0) = C_0\left[\mathrm{H}(x+a) - \mathrm{H}(x-a)\right]; \quad x \in (-\infty, \infty). \tag{28}$$

The solution to the problem can be obtained [26] in exact closed form as follows:

$$\frac{C(x,t)}{C_0} = \frac{1}{2}\mathrm{erf}\left(\frac{-x+a+v_0\frac{\{1-\exp(-\lambda t)\}}{\lambda}}{2\sqrt{Dt}}\right) - \frac{1}{2}\mathrm{erf}\left(\frac{-x-a+v_0\frac{\{1-\exp(-\lambda t)\}}{\lambda}}{2\sqrt{Dt}}\right); \quad x < v_0 t, \tag{29a}$$

$$\frac{C(x,t)}{C_0} = \frac{1}{2}\,\mathrm{erfc}\left(\frac{x-a-v_0\frac{\{1-\exp(-\lambda t)\}}{\lambda}}{2\sqrt{Dt}}\right) - \frac{1}{2}\mathrm{erfc}\left(\frac{x+a-v_0\frac{\{1-\exp(-\lambda t)\}}{\lambda}}{2\sqrt{Dt}}\right); \quad x < v_0 t. \tag{29b}$$

Figure 5 illustrates the time dependent advective-diffusive transport of the plug of chemical located within the porous column. The analogous initial boundary value problem where the chemical dosage takes place at the surface of the porous column can only be solved using a computational approach. In the calculations we set $v_0 \approx 2\,\mathrm{m\,day}^{-1}; \lambda \approx 0.2\,(\mathrm{days})^{-1}$ and $a = 5\,\mathrm{m}$, and the diffusivity parameter is altered to examine its influence on the chemical profile.

6 Concluding Remarks

The computational modelling of the advective transport of chemicals and contaminants in porous media presents a challenge particularly in instances

where the concentration distribution has a discontinuous profile. The accuracy of computational methods such as the *Streamline Upwind Petrov–Galerkin*, *Taylor–Galerkin*, *Least Squares*, *Modified Least Squares*, etc., needs to be tested against analytical results that will involve spatial-and time-dependent advective velocity distributions. To date many of the calibration exercises are restricted to the one-dimensional problem involving constant velocity. This paper outlines certain analytical solutions that have been recently developed for the plane and axisymmetric problems of advective transport and one-dimensional problems involving time-dependent advective velocities. These solutions have been recently applied to test the accuracy of a Modified Least Squares technique for the study of the advective transport problem that also includes time- and mesh-refining algorithms. The analytical results provided the benchmarks that were necessary for the validation of the computational scheme. The results of these investigations will be presented in future work.

Acknowledgements

The work described in this paper was initiated through a Discovery Research Grant awarded by the Natural Sciences and Engineering Research Council of Canada and completed with the assistance of the *2003 Max Planck Research Prize in the Engineering Sciences* awarded by the *Max Planck Gesellschaft* of Germany.

References

1. Appelo, C.A.J. and Postma, D. (1993) *Geochemistry, Groundwater and Pollution*, A.A. Balkema, Rotterdam, The Netherlands.
2. Banks, R.B. (1994) *Growth and Diffusion Phenomena: Mathematical Frameworks and Applications*, Springer-Verlag, Berlin Heidelberg New York.
3. Barenblatt, G.I., Entov, V.M. and Ryzhik, V.M. (1990) *Theory of Fluid Flows through Natural Rocks*, Kluwer Academic Publishers, Dordrecht, The Netherlands.
4. Bear, J. and Bachmat, Y. (1992) *Introduction to the Modelling of Transport Phenomena in Porous Media*, Reidel, Dordrecht, The Netherlands.
5. Bedient, P.B., Rifai, H.S. and Newell, C.J. (1997) *Groundwater Contamination, Transport and Remediation*, Prentice-Hall, Upper Saddle River, NJ.
6. Charbeneau, R.J. (1999) *Groundwater Hydraulics and Pollutant Transport*, Prentice Hall PTR, Upper Saddle River, NJ.
7. Codina, R. (1998) Comparison of some finite element methods for solving the diffusion-convection-reaction equation, *Comput. Methods Appl. Mech. Engrg.* Vol. 156: 185–210.
8. Domenico, P.A. and Schwartz, F.W. (1998) *Physical and Chemical Hydrogeology*, John Wiley, New York.

9. Dong, W. and Selvadurai, A.P.S. (2006) The numerical modelling of advective transport in the presence of fluid pressure transients, *Int. J. Numer. Anal. Meth. Geomech.*, doi: 10.1002/nag. 494 (In Press)
10. Grathwohl, P. (1998) *Diffusion in Natural Porous Media:Contaminant Transport, Sorption/Desorption and Dissolution Kinetics*, Kluwer Academic Publishers, Boston.
11. Gresho, P.M. and Lee, R.L. (1979) Don't suppress the wiggles-They are telling you something! In. *Finite Element Methods for Convection Dominated Flows* (T.J.R. Hughes, ed.) AMD 34 ASME, New york, 37–61.
12. Hughes, T.J.R. and Brooks, A. (1979) A multi-dimensional upwind scheme with no cross-wind diffusion, In. *Finite Element Methods for Convection Dominated Flows* (T.J.R. Hughes, ed.), AMD 34 ASME, New York, 19–36.
13. Ingebritsen, S.E and Sanford, W.E. (1998) *Groundwater and Geologic Processes*, Cambridge University Press, Cambridge.
14. Ingham, D.B. and Pop, I. (Eds.) (1998) *Transport Phenomena in Porous Media*, Pergamon, Elsevier, The Netherlands.
15. Lichtner, P.C., Steefel, C.I. and Oelkers, E.H. (Eds.) (1996) *Reactive Transport in Porous Media*, Reviews in Mineralogy, Vol. 34, The Mineralogical Socity of America, Washington DC.
16. Lindstrom, F.T., Haque, R., Freed, V.H. and Boersma, L. (1967) Theory on the movement of some herbicides in soils. Linear diffusion and convection of chemicals in soils, *Environ. Sci. Tech. Vol.* 1: 561–565.
17. Massel, S.R. (1999) *Fluid Mechanics for Marine Ecologists*, Springer Verlag, Berlin Heidelberg New York.
18. Noorishad, J., Tsang, C.-F., Perrochet, P. and Musy, A. (1992) A perspective on the numerical solution of convection dominated transport problems: A price to pay for the easy way out, *Water Resour. Res.*, Vol. 28: 551–561.
19. Oñate, E. (1998) Derivation of stabilized equations for numerical solution of advective-diffusive transport and fluid flow problems, *Comput. Methods Appl. Mech. Engrg.* Vol. 151: 233–265.
20. Philips, O.M. (1991) *Flow and Reactions in Permeable Rocks*, Cambridge University Press, Cambridge.
21. Selvadurai, A.P.S. (2000) *Partial Differential Equations in Mechanics: Vol. 1. Fundamentals, Laplace's Equation, Diffusion Equation, Wave Equation*, Springer-Verlag, Berlin Heidelberg New York.
22. Selvadurai, A.P.S. (2002) Advective transport of a chemical from a cavity in a porous medium, *Comput. Geotech.*, Vol. 29: 525–546.
23. Selvadurai, A.P.S. (2003) Contaminant migration from an axisymmetric source in a porous medium, *Water Resour. Res.* Vol. 39: No. 8, 1204, WRR 001742.
24. Selvadurai, A.P.S. (2004) On the uniqueness theorem for advective-diffusive transport in porous media: A canonical proof, *Trans. Porous Media*, Vol. 56: 51–60.
25. Selvadurai, A.P.S. (2004) Advective transport from a penny-shaped crack and an associated uniqueness theorem, *Int. J. Numer. Anal. Methods Geomech.* Vol. 28: 191–208.
26. Selvadurai, A.P.S. (2004) On the advective-diffusive transport in porous media in the presence of time-dependent velocities, *Geophys. Res. Lett.* Vol. 31: L13505, doi: 10.1029/2004GL019646.

27. Selvadurai, A.P.S. and Dong, W. (2006) Modelling of advection-dominated transport in a porous column with a time-decaying flow field, *Transport in Porous Media* (In Press).
28. Sun, N.-Z. (1996) *Mathematical Modelling of Groundwater Pollution*, Springer-Verlag, Berlin Heidelberg New York.
29. Vichnevetsky, R. and Bowles J.B. (1982) *Fourier Analysis of Numerical Approximations of Hyperbolic Equations*, SIAM Philadelphia, PA.
30. Wang, Y. and Hutter, K. (2001) Comparisons of numerical methods with respect to convectively dominated problems, *Int. J. Numer. Methods Fluids*, Vol. 37: 721–745.
31. Weinberger, H.F. (1965) *A First Course in Partial Differential Equations*, Dover, New York.
32. Wendland, E. and Schmid, G.A. (2000) Symmetrical streamline stabilization scheme for high advective transport, *Int. J. Numer. Anal. Methods Geomech.* Vol. 24: 29–45.
33. Werner, P. (2003) The contribution of natural attenuation processes for the remediation of contaminated sites, *Groundwater Engineering-Recent Advances, Proceedings of International Symposium on Groundwater Problems Related to the Geo-environment*, Okayama, (I. Kono, M. Nishigaki and M. Komatsu, eds.), A.A. Balkema, Lisse, 37–40.
34. Zheng, C. and Bennett, G.D. (2002) *Applied Contaminant Transport Modeling*, Wiley-Interscience, New York.
35. Zienkiewicz, O.C. and Taylor, R.L. (2000) *The Finite Element Method Vols. 1–3*, Butterworth-Heinemann, Massachusetts.

Part V

Granular Materials: Theory and Experiment

Unusual Soil Behaviour and its Challenge to Constitutive Modelling

J. Chu

Nanyang Technological University, Singapore, Singapore
CJCHU@ntu.edu.sg

1 Introduction

Geomechanics is a challenging discipline mainly because the formation of geomaterials and their engineering behaviour are so diversified and complex. As such, there is really nothing unusual when different soil behaviours are observed. From this point of view, the word "unusual" used in the title only means unconventional in the context of this paper. It is for the same reason that we can state that no single constitutive model can capture all the different types of behaviour of one type of soil, not saying the behaviour of different soils. The objectives of this paper are to illustrate using laboratory testing data some of the unconventional types of behaviour observed and to point out the difficulties in modelling these behaviours using the existing constitutive models. The types of behaviours to be discussed include liquefaction of dense sand, pre-failure strain softening in strain path testing and strain softening and hardening in the post-failure region, instability of sand under drained conditions, the path dependent undrained behaviour and the reversed strain rate effect on loose sand. Some of the behaviours have not been reported in the literature before and therefore, may have not been considered in the existing constitutive models. There are two issues that need to be addressed on the fundamental level. (1) Whether these unusual behaviours are the true characteristics of geomaterials. The validation can be done by conducting further experimental studies and by using constitutive models. If the so-called unusual behaviours can be modelled by constitutive models, it will not only support the validity of the data, but also help in understanding the physical meanings and mechanisms that govern the behaviours. (2) The unusual behaviours are the true characteristics of geomaterials. However, the existing constitutive models cannot be used to model these behaviours properly. In this case, the data will pose a challenge to the existing constitutive models and help in the development and verification of constitutive models for geomaterials.

2 Liquefaction of Dense Sand

Static liquefaction of sand is often associated with the undrained behaviour of loose sand, as shown in Fig. 1. As the behaviour shown in Fig. 1 is affected by both the void ratio of the soil and the confining stress, the state parameter, ψ, has been proposed by Been and Jefferies [3] to describe the effect of both factors. For liquefaction to occur under undrained conditions, ψ has to be positive. Within the normal stress range, ψ can only be positive for very loose sand. However, the void ratio of the sand that can liquefy in an undrained triaxial test is often larger than the in- situ void ratio of the soil encountered in most projects and in practice flow slide can take place in soils that will not liquefy in the laboratory [4]. Apparently, liquefaction under undrained conditions does not offer the interpretation to all the failure mechanisms. There should be other mechanisms that can explain the flow slide or liquefaction of relatively dense sand, or in other words, whether soil that have negative ψ value could possibly liquefy [10, 18].

It should be noted that "undrained" specifies only a special drainage condition at the boundary. In general, the boundary condition can either be partially drained by allowing the specimen to have either volumetric contraction or dilation. Both conditions can be modelled by strain path testing as $\mathrm{d}\varepsilon_\mathrm{v}/\mathrm{d}\varepsilon_1 > 0$ for contraction and $\mathrm{d}\varepsilon_\mathrm{v}/\mathrm{d}\varepsilon_1 < 0$ for dilation. An undrained condition is a special case when $\mathrm{d}\varepsilon_\mathrm{v}/\mathrm{d}\varepsilon_1 = 0$. When we take the general drainage condition into consideration, liquefaction of sand depends not only on the void ratio of the soil and the stress level applied, but also on the drainage conditions, or in other words, the strain path imposed.

Under the general strain path-controlled conditions, even dense sand can liquefy in the same way as loose sand does under the undrained condition. One example is shown in Fig. 2 where strain softening has occurred for a dense sand

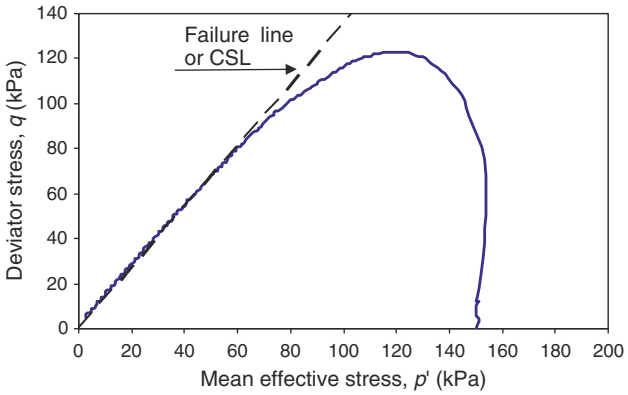

Fig. 1. Typical strain softening behaviour of very loose sand in an undrained (i.e. $\mathrm{d}\varepsilon_\mathrm{v}/\mathrm{d}\varepsilon_1 = 0$) test

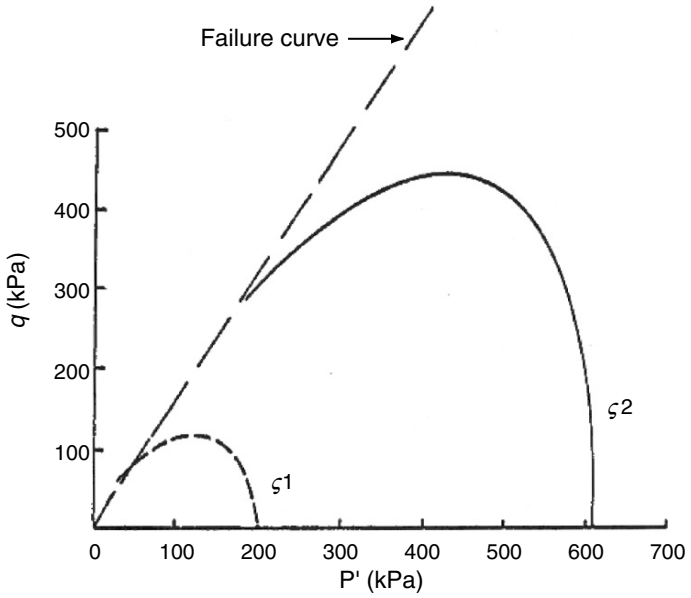

Fig. 2. Strain softening of dense sand along strain path with $d\varepsilon_v/d\varepsilon_1 = -0.67$

when it is sheared along a $d\varepsilon_v/d\varepsilon_1 = -0.67$ path. In this case, the state parameter cannot be used to describe the liquefaction behaviour of the sand anymore. To model the liquefaction (or strain softening) behaviour under general conditions, one more parameter is required to specify the drainage condition. The strain increment ratio, $(d\varepsilon_v/d\varepsilon_1)_i$ or $(d\varepsilon_v/d\varepsilon_s)_i$ can be used as such a parameter. A subscript "i" is used to specifically indicate that it is the strain increment ratio imposed, not the strain increment ratio or the dilatancy ratio manifested during a drained test, which can be denoted as $(d\varepsilon_v/d\varepsilon_s)_d$. It should be pointed out that whether liquefaction or strain softening can occur or not depends on the difference between $(d\varepsilon_v/d\varepsilon_s)_i$ and $(d\varepsilon_v/d\varepsilon_s)_d$, not on the absolute value of $(d\varepsilon_v/d\varepsilon_s)_i$ or $(d\varepsilon_v/d\varepsilon_s)_d$ as discussed by Chu et al. [15, 16] in details. Therefore, liquefaction or strain softening is not dependent on whether the soil is contractive or dilative. This is an important mechanism that has yet to be fully understood. Without reflecting this mechanism in a constitutive model, the model may not be able to describe the strain softening behaviour as shown in Fig. 2 properly.

One would argue whether a condition with an imposed $(d\varepsilon_v/d\varepsilon_s)_i$ exists in practice. In fact, some slope failure mechanisms relating to $d\varepsilon_v/d\varepsilon_1 < 0$ or the non-undrained conditions have been identified by the National Research Council [32]. Two failure mechanisms are reproduced in Fig. 3. In Mechanism B (Fig. 3a), the void ratio of the sand in a slope can redistribute within a globally undrained sand layer. In this case, some soil elements along the slope will become looser, that is, undergoing volumetric dilation. It is the soil that

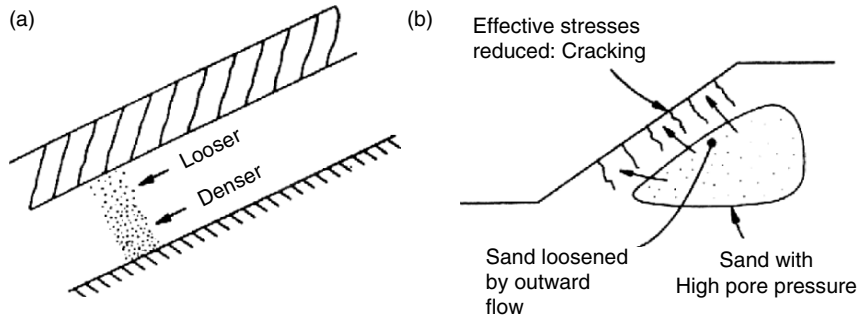

Fig. 3. (**a**) Mechanism B by NRC [32]: Situation for void redistribution within a globally undrained sand layer; (**b**) Mechanism C by NRC [32]: Situation for failure by spreading of excess pore pressure with global volume changes

undergoing dilation would fail first. It has been observed in the laboratory and the field that the water contents in the soils along a slip surface are higher than the adjacent areas [21]. In Mechanism C (Fig. 3b), some portions of the slope can be loosened, i.e. undergoing dilation, due to the spreading of the excess pore water pressure. The above two mechanisms are supported by some centrifuge testing results and case studies presented by Boulanger and Truman [7], Adalier and Elgmal [1] and Sento et al. [36]. The possibility of flow slide occurring in medium loose or dense soil or in other word, dilating soil, is also observed in several case studies. Been et al. [4] argued that the Nerlerk berm failure case might have occurred for dilating sand, as the state of the sand lies below the critical state line, that is, the state paraments is negative. Several other cases of flow slide failure in dilating sand have also been presented by Been et al. [5]. Casagrande [8] has also described one case that prior to liquefaction and flow of large masses of rather dense granular talus in the Alps, brooks emerging from the toe of the talus deposits stop flowing. Based on Casagrande's suggestion, Fleming et al. [21] have classified flow failure into contractive and dilative types. The Salmon Creek landslide in Marin Country, California, which exhibited dominantly dilative transformation from solid landslide to liquid debris flow, was used by Fleming et al. [21] to illustrate the different criteria that can be used in the field to distinguish contractive and dilative behaviour.

3 Post-Failure Strain Softening and Hardening of Sand

Before we discuss strain softening behaviour, it is important to distinguish different types of strain softening. Strain softening behaviour in sand can be classified into three different types [17]. The first type is the strain softening observed in a conventional drained triaxial test on dense sand. This type of strain softening is often used to explain the effect of dilation on the behaviour of dense sand [28]. However, the studies of Hettler and Vardoulakis [23] and

Chu et al. [15] have shown that this type of strain softening is merely a result of non-homogeneous deformation caused by the end constraints, not a true material behaviour.

The second type of strain softening is the so-called banding softening [17]. It occurs under plane-strain or three-dimensional loading conditions as a result of shear bands. However, unlike the shear bands that occur under axisymmetric conditions, the shear bands observed under plane-strain or three-dimensional conditions is a material response, not a result of imperfect boundary conditions.

The third type of strain softening is what is shown in Fig. 1 or Fig. 2. This type of strain softening is a real material behaviour. As the strain softening occurs before the stress state reaches the failure line, it has been called the pre-failure strain softening [15].

It should be pointed out that an undrained test is a strain path controlled test with $\mathrm{d}\varepsilon_\mathrm{v}/\mathrm{d}\varepsilon_1 = 0$. A drained triaxial test is a stress path test with $\mathrm{d}\sigma_3' = 0$. Strain softening is a behaviour that is likely to manifest along a strain path rather than stress path. This is because strain softening is defined as a behaviour where the shear stress (or resistance) starts to reduce with further shearing (for discussion on the definition of strain softening, see [15]). When a stress path is controlled, the stress components cannot change freely. Thus the strain softening tendency, if any, cannot develop freely. This explains why it is rare to observe strain softening behaviour in stress path controlled tests within the homogeneous deformation region (or without the presence of shear bands). In a strain path test, it is the strains, not the stresses that are controlled. Hence, strain softening, if any, can develop freely. For this reason, Chu et al. [15] have proposed the use of strain path testing method to study the strain softening behaviour. Under strain path control, strain softening as a material behaviour can occur even for dense sand as shown in Fig. 3.

If the strain softening observed in a drained test for dense sand is not a material behaviour, then will strain softening occur as a material behaviour in the post-peak, i.e. post-failure region? The answer is yes. Post-failure strain softening can occur if certain strain paths are imposed.

Figure 4 shows the stress–strain curves obtained from two triaxial tests conducted on dense sand. In conducting the two tests, the laboratory reconstituted specimens were first sheared to failure along a drained path with an effective consolidation stress of 300 kPa. Once failure was attained, a strain path in the form of $\mathrm{d}\varepsilon_\mathrm{v}/\mathrm{d}\varepsilon_1$ was imposed. At failure, the $(\mathrm{d}\varepsilon_\mathrm{v}/\mathrm{d}\varepsilon_1)_\mathrm{f}$ obtained was -0.54. When $\mathrm{d}\varepsilon_\mathrm{v}/\mathrm{d}\varepsilon_1 = -0.25$ was imposed, strain hardening behaviour was manifested in the post-failure region, as shown in Fig. 4. On the other hand, when $\mathrm{d}\varepsilon_\mathrm{v}/\mathrm{d}\varepsilon_1 = -0.67$ was imposed, strain softening occurred in the post-failure region. It needs to be pointed out that the occurrence of strain hardening or softening is not related to whether a soil is in dilation or contraction. The soil specimens in both tests were in dilation. The studies of Chu et al. [15, 17] have shown that the occurrence of post-failure strain softening

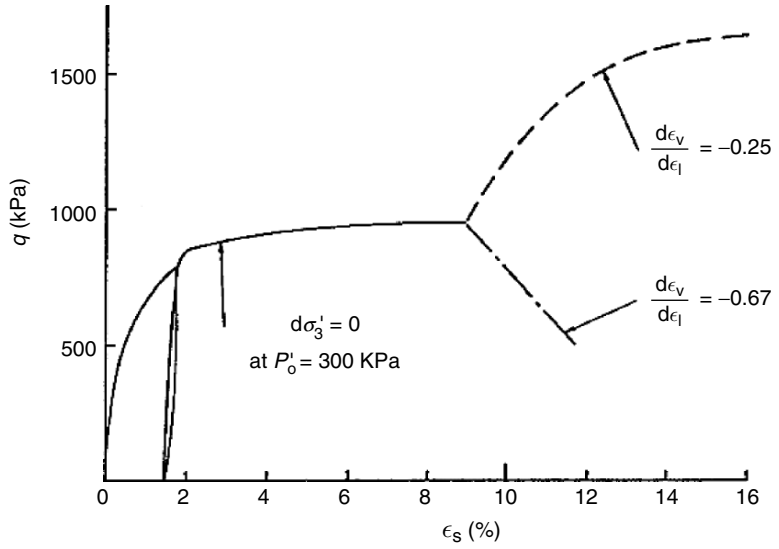

Fig. 4. Post-failure strain hardening and softening behaviour of dense sand

or hardening is controlled by the following condition:

$$\left(\frac{d\varepsilon_v}{d\varepsilon_1}\right)_i - \left(\frac{d\varepsilon_v}{d\varepsilon_1}\right)_f < 0, \quad \text{Softening} \tag{1a}$$

$$\left(\frac{d\varepsilon_v}{d\varepsilon_1}\right)_i - \left(\frac{d\varepsilon_v}{d\varepsilon_1}\right)_f < 0, \quad \text{Perfectly plastic} \tag{1b}$$

$$\left(\frac{d\varepsilon_v}{d\varepsilon_1}\right)_i - \left(\frac{d\varepsilon_v}{d\varepsilon_1}\right)_f < 0, \quad \text{Hardening} \tag{1c}$$

where $(d\varepsilon_v/d\varepsilon_1)_i$ is the strain increment ratio imposed, $(d\varepsilon_v/d\varepsilon_1)_f$ is the failure strain increment ratio the soil would manifest under a completely drained condition. The condition of perfectly plastic response, in fact, corresponds to the response of a drained triaxial test (with free-end), in which both q and $(d\varepsilon_v/d\varepsilon_1)_f$ remain constant at the failure values with continuous shearing [13]. Therefore, strain softening behaviour is controlled by the difference between $(d\varepsilon_v/d\varepsilon_1)_i$ and $(d\varepsilon_v/d\varepsilon_1)_f$, not $(d\varepsilon_v/d\varepsilon_1)_i$ or $(d\varepsilon_v/d\varepsilon_1)_f$ alone.

The effective stress paths of the above two tests together with other similar tests are also plotted in Fig. 5. It can be seen that when strain softening occurs, the effective stress path travels down along the failure line, whereas when strain hardening occurs, the effective stress path moves away from the failure line. As can be seen from Fig. 4, the stress–strain curve reached a new peak during the strain hardening process under $d\varepsilon_v/d\varepsilon_1 = -0.25$. The stress–dilatancy relationship during the post-failure strain hardening behaviour can be modelled as [15]:

$$\frac{\sigma_1'}{\sigma_3'} = K\left(1 - \left(\frac{d\varepsilon_v}{d\varepsilon_1}\right)_i\right) + \frac{m}{-\left(\frac{d\varepsilon_v}{d\varepsilon_1}\right)_f}\left[\left(\frac{d\varepsilon_v}{d\varepsilon_1}\right)_i - \left(\frac{d\varepsilon_v}{d\varepsilon_1}\right)_f\right], \tag{2}$$

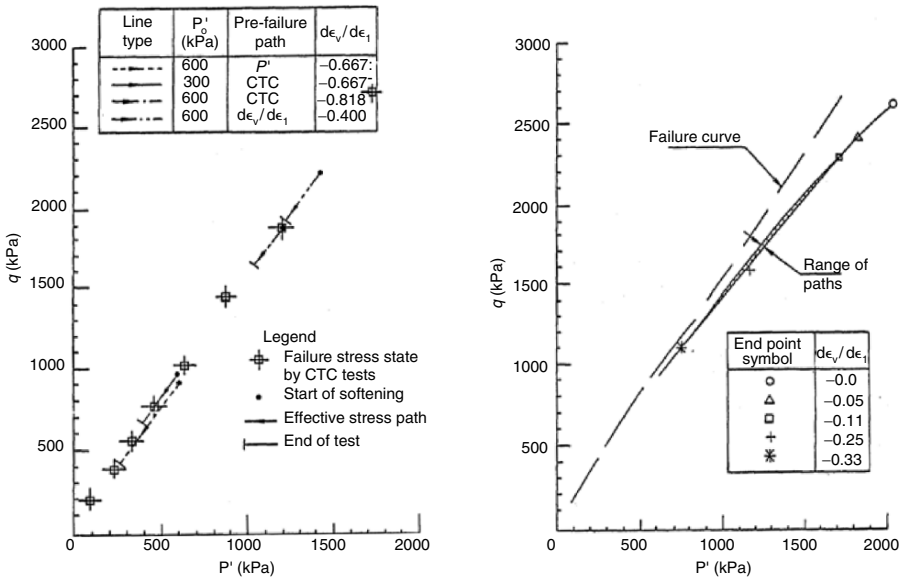

Fig. 5. Effective stress paths resulting from (**a**) post-failure strain softening; (**b**) post-failure strain hardening

where K and m are experimentally determined constants. For the soil tested, $K = 2.9$ and $m = 0.42$. The first term of (2) is the Rowe's stress dilatancy equation [34]. Therefore, (2) can be considered as an extension of Rowe's stress dilatancy theory.

The post-failure strain softening has distinct physical meanings. The post-failure strain softening causes irrecoverable loss in shear strength. After strain softening, the failure line shrinks or becomes lower than the original failure line [15]. In other words, the effective friction angle or the effective cohesion of the strain softened soil will reduce. It should be pointed out that the stress state of soil after post-failure strain softening does not approach the critical state. This is different from what is assumed in the critical state soil mechanics. For this very reason, the critical state soil mechanics framework will no longer be adequate to be used to describe the stress–strain behaviour manifested under strain path testing. In this case, a more general state, the so-called asymptotic state [14], can be used instead. The asymptotic state is defined as a state where both the mobilised stress level (q/p') and the dilatancy ratio of the soil ($-\mathrm{d}\varepsilon_\mathrm{v}/\mathrm{d}\varepsilon_1$) become constant. The critical state is a special case of asymptotic state.

For some conventional constitutive models, the compliant matrix will be set to infinity when the failure state is reached so that large plastic strain will develop. However, the above test data indicate that after the conventionally defined failure state is reached, it is still possible for soil to manifest strain hardening or softening behaviour in the post-failure region depending on the

drainage conditions or strain paths imposed in the post-failure region. How to model the post-failure strain hardening and softening behaviour of soil is another challenge to constitutive modelling.

4 Instability under Drained Conditions

The failure of loose granular soil slopes is often considered to be triggered by instability or static liquefaction occurring under undrained conditions. The term instability refers to a phenomenon where plastic strain develops rapidly under a given load or stress. Liquefaction is one type of instability. According to Chu [10,11], Chu and Leong [12], instability and strain softening are closely related. Strain softening and instability are the different magnifications of the same mechanism. Take the undrained test shown in Fig. 1 as an example. This test was conducted on loose sand under a deformation-controlled loading condition and strain softening occurred in this test. If the test were conducted under a load-controlled loading condition with other conditions remain the same, the specimen would become unstable at about the same point where strain softening has occurred. The test data of such a test are shown in Fig. 6. The test was conducted under a load-controlled deformation model. When the stress state reached point B (Fig. 6a), the specimen physically collapsed. This is also indicated by the sudden increases in the axial strain and the pore water pressure as shown in Fig. 6b, c. Therefore, instability has occurred at point B in this undrained test for loose sand. It needs to be pointed out that the test conditions for the test shown in Fig. 1 are different from those for the test shown in Fig. 6. Therefore, a direct comparison may not be made. Nevertheless, the comparison of the two tests has clearly indicated that the same soil may exhibit different stress–strain behaviours by merely changing the loading conditions without changing the stress paths and other testing conditions. When a soil is sheared in a deformation-controlled loading mode, progressive type of failure, i.e. strain softening may develop. However, when a soil is sheared in a load-controlled loading mode, the soil element can collapse suddenly, i.e. instability will occur. For more discussions on the differences between tests conducted in a deformation-controlled and a load-controlled loading mode, see Chu [10, 11] and Chu and Leong [12].

So far, instability has been studied almost exclusively under undrained conditions. However, there are cases where instability occurred under essentially drained conditions. In a recent reanalysis of the Wachusett Dam failure in 1907, Olson et al. [33] concluded that the failure was mainly triggered by static liquefaction that occurred under completely drained conditions. Through laboratory model tests, Eckersley [20] observed that the pore water pressure increase observed during failure of a gentle granular soil slope is a result, rather than the cause of flow slide. In other words, the flow slide took place under an essentially drained condition.

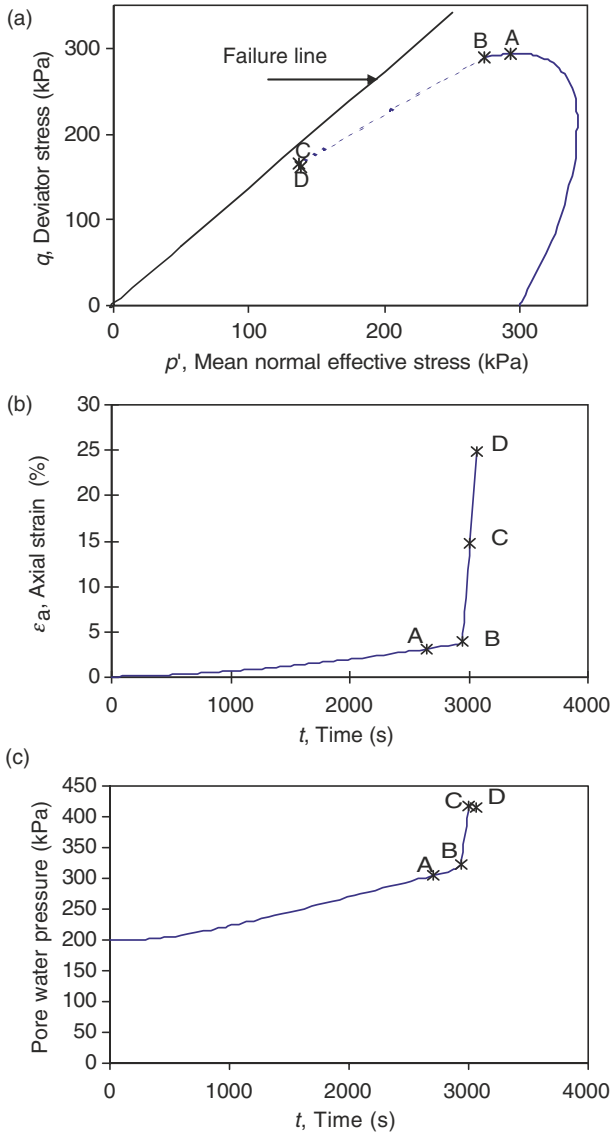

Fig. 6. Instability observed in undrained test on loose sand

Instability behaviour of sand along a drained, constant shear stress path, or the so-called CSD path [2], has been observed experimentally. The results of a typical CSD test, DR7, are shown in Fig. 7. The loose sand specimen (with a void ratio $e_c = 0.945$) was firstly sheared to point A along a drained path (Fig. 7a). The deviator stress at point A is $q = 150\,\text{kPa}$. On the constant q path, the confining stress was reduced at a rate of $1\,\text{kPa min}^{-1}$, which results

in a stress path moving from point A to point B (Fig. 7a). There were little axial and volumetric strain developments until point B where both axial and volumetric strains started to develop at a faster rate, as shown in Fig. 7b, c. This can be seen more obviously from Fig. 7d which shows that the axial strain rate shot up at point B, indicating an unstable behaviour. Using point B, the instability line can be determined as shown in Fig. 7a. With further

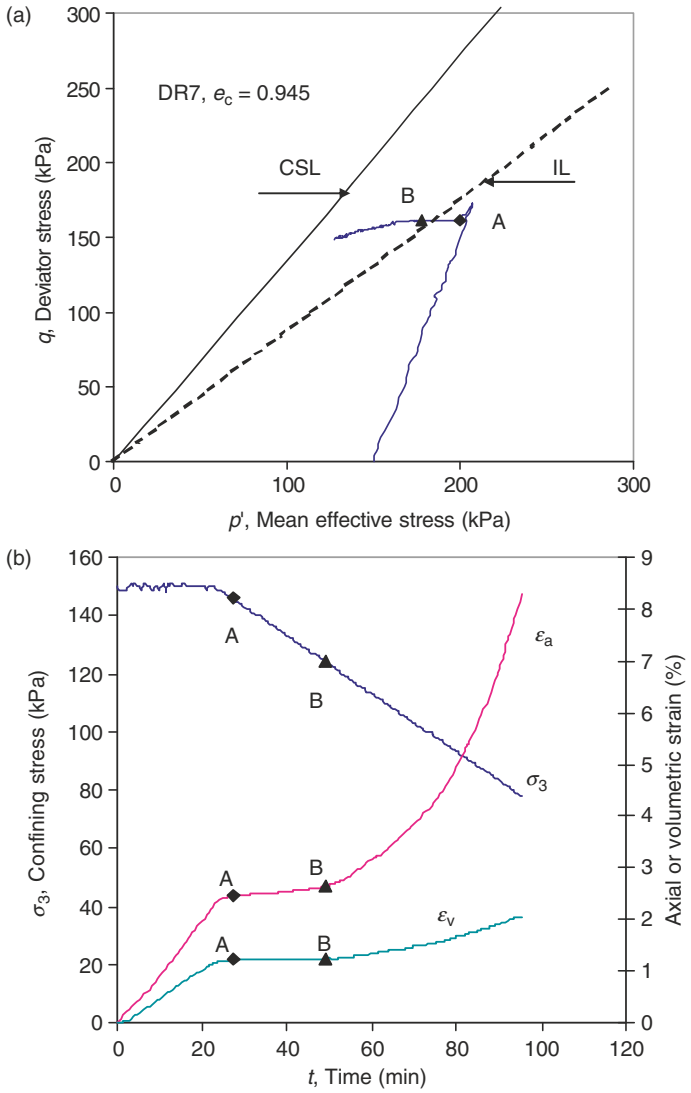

Fig. 7. Instability of loose sand under a drained condition with reduction in confining stress

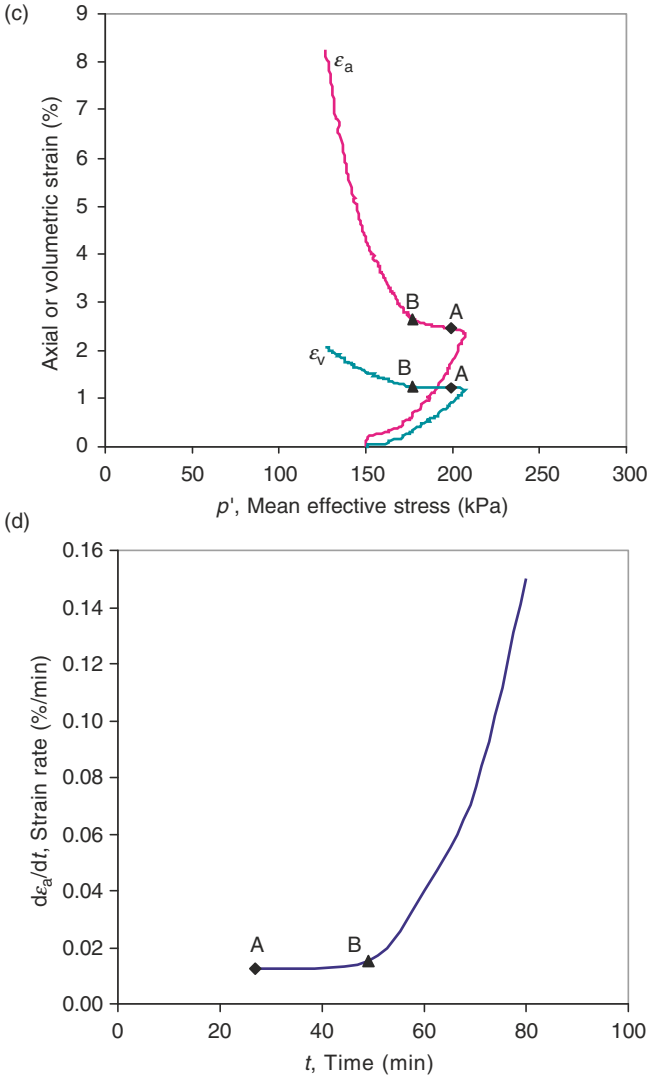

Fig. 7. *Continued*

reduction in the confining stress, the stress path moved further towards the CSL. However, at this stage the axial and volumetric strain rates had increased to such an extent that the testing system could not catch up to maintain q to be constant. It needs to be pointed out that the pore water pressure did not change during the whole test. Therefore, the instability in the form of a rapid increase in plastic strains is observed under a fully drained condition.

Although under undrained conditions, instability will not occur for dilative sand, under drained conditions the similar type of instability behaviour has

been observed to occur for dilative sand. In this case, instability occurs at a higher sress ratio, i.e. a higher instability line. The gradient of the instability line increases with density. See Chu et al. [18] for detail.

When we describe a slope as unstable, we mean either the slope is collapsing or its movement is accelerating rapidly. Therefore, in the geotechnical context, the word instability should be defined to include both a runaway type and a jump in the strain rate type of behaviour. For this purpose, instability has been defined in this paper to refer to a behaviour in which large plastic strains are generated *rapidly*. For large plastic strain to develop, the soil must be in a yielding state. Therefore, yielding is the necessary condition for instability. This has been explained by Lade [27] for the instability occurring for loose sand under undrained conditions. The instability line, in fact, is defined based on the yielding conditions [16, 27]. As such, the zone of instability is defined regardless of the drainage condition. This explains why instability can occur under both undrained and drained conditions as long as the stress path leads the stress state into the zone of instability.

Although yielding is a necessary condition for instability to occur, it is not sufficient. In other words, plastic yielding does not necessarily cause a soil specimen to become unstable. Yielding means the development of a large strain for a small change in stress. It does not imply that the specimen will become unstable which is characterised by a sudden increase in the strain increment rate, $\mathrm{d}\varepsilon_1/\mathrm{d}t$ (see Fig. 7d). Therefore, we cannot assume that yielding is automatically the condition for instability. Whether instability can occur along a given stress path needs to be established separately.

As instability is characterised by a time-rate behaviour and cannot be judged by yielding alone, it may therefore be necessary for the constitutive models that will be used to model instability to consider time effect. Furthermore, the occurrence of instability is related to a load-controlled loading condition. Hence, instability may have to be modelled as a boundary value problem, rather than a pure element behaviour. The experimental data presented above can also serve to show that plastic yielding, especially instability, can occur along an "unloading" path. As this could not be predicted by conventional plasticity as explained by Jefferies [25], the data could be useful in verifying the predictive ability of some constitutive models.

5 Non-Unique Undrained Behaviour

Triaxial tests have often been used to simulate the stress paths encountered by soil elements in the field. Four typical types of stress paths, as shown in Fig. 8, have been identified and modelled in triaxial tests [6, 24, 29]. The changes in the axial and lateral stresses that are required in modelling the four typical stress paths in triaxial tests are explained in Table 1. Paths AC and LE are for compression load with the principal stress in the vertical direction and paths AE and LC are for extension load with the principal stress

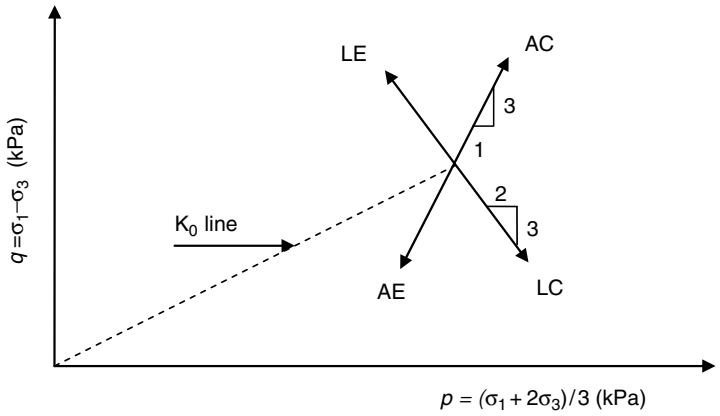

Fig. 8. Four typical types of total stress paths

Table 1. Four typical total stress paths

type	axial stress, σ_a	lateral stress, σ_r	dq/dp	α
axial compression (AC)	$\mathrm{d}\sigma_\mathrm{a} > 0$	$\mathrm{d}\sigma_\mathrm{r} = 0$	3	0
lateral extension (LE)	$\mathrm{d}\sigma_\mathrm{a} = 0$	$\mathrm{d}\sigma_\mathrm{r} < 0$	$-3/2$	0
axial extension (AE)	$\mathrm{d}\sigma_\mathrm{a} < 0$	$\mathrm{d}\sigma_\mathrm{r} = 0$	3	90
lateral compression (LC)	$\mathrm{d}\sigma_\mathrm{a} = 0$	$\mathrm{d}\sigma_\mathrm{r} > 0$	$-3/2$	90

in the horizontal direction. The geotechnical problems that can be simulated by the above stress paths are discussed in Holtz and Kovacs [24]. For geotechnical design involving soils with a very low permeability such as soft clay, an undrained condition is often assumed. In this case, the stress paths shown in Fig. 8 represent the total stress paths. One fundamental question which needs to be addressed is whether the undrained behaviour is affected by the total stress paths. The answer to this question will have important practical implications. If the undrained behaviour of soil is total stress path dependent, it will mean that the undrained shear strength determined along one type of total stress path may not be applicable to problems involving other types of total stress paths. Bishop and Wesley [6] and Law and Holtz [29] studied this problem for normally consolidated (NC) natural clay by conducting a series of triaxial K_0 consolidated undrained compression ($\mathrm{CK}_0\mathrm{UC}$) and extension ($\mathrm{CK}_0\mathrm{UE}$) tests along different total stress paths. Based on the results, they concluded that the undrained behaviour of NC clay did not seem to be affected by the total stress paths as long as the principal stress direction is the same [6, 24, 29]. Their studies, however, showed that the results obtained from the $\mathrm{CK}_0\mathrm{UC}$ and $\mathrm{CK}_0\mathrm{UE}$ tests were different. This is expected as the principal stress directions, α, in the two tests were different. The value of α was 0^o for the $\mathrm{CK}_0\mathrm{UC}$ tests and 90° for the $\mathrm{CK}_0\mathrm{UE}$ tests.

As part of a study on the undrained behaviour of loose sand, some undrained tests on laboratory reconstituted sand were conducted by following different total stress paths. Surprisingly, the results show that the total stress path *does* affect the undrained behaviour of sand. This is different from the studies of Bishop and Wesley [6] and Law and Holtz [29] for clay.

A series of CK_0UC and CK_0UE tests were conducted on loose MT specimens by following two different types of total stress paths: AC and LE for CK_0UC tests and AE and LC for CK_0UE tests, respectively [22]. The results of one pair of tests, Tests KoMT6 and KoMT9, are presented in Fig. 9. The specimens used for the two tests had the same initial void ratio of 0.852 and the consolidated void ratios were 0.826 for KoMT6 and 0.824 for Test KoMT9. The effective stress paths obtained from the two tests are shown in Fig. 9a, which are obviously different. Nevertheless, both effective stress paths approach the same CSL at the end of the tests. The slope of the CSL on the extension side is $M_{cs} = 0.97$. The stress–strain curves and the pore pressure changes obtained from the two tests are shown in Fig. 9b, c, respectively. The pore pressure generated and the maximum deviator stress obtained in the test along the LC path (KoMT9) are higher than that in the test along the AE path (KoMT6).

Similar behaviour was obtained from the series of CK_0UE tests conducted along both the AE and LC paths over a range of void ratios [22]. The test

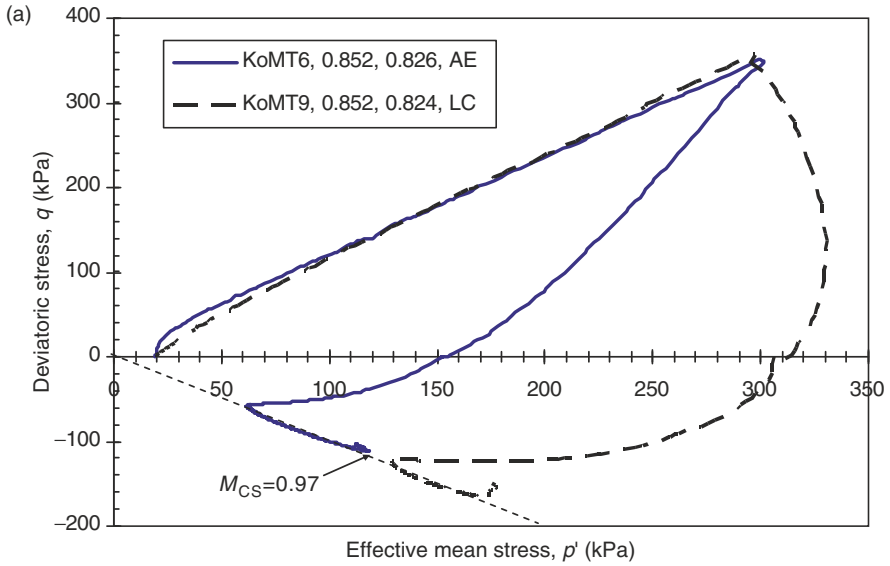

Fig. 9. Comparison of two CK_0UE tests conducted on moist tamped specimens along two total stress paths, AE and LC: (**a**) effective stress paths; (**b**) deviatoric stress versus axial strain curves; and (**c**) pore water pressure changes versus axial strain curves

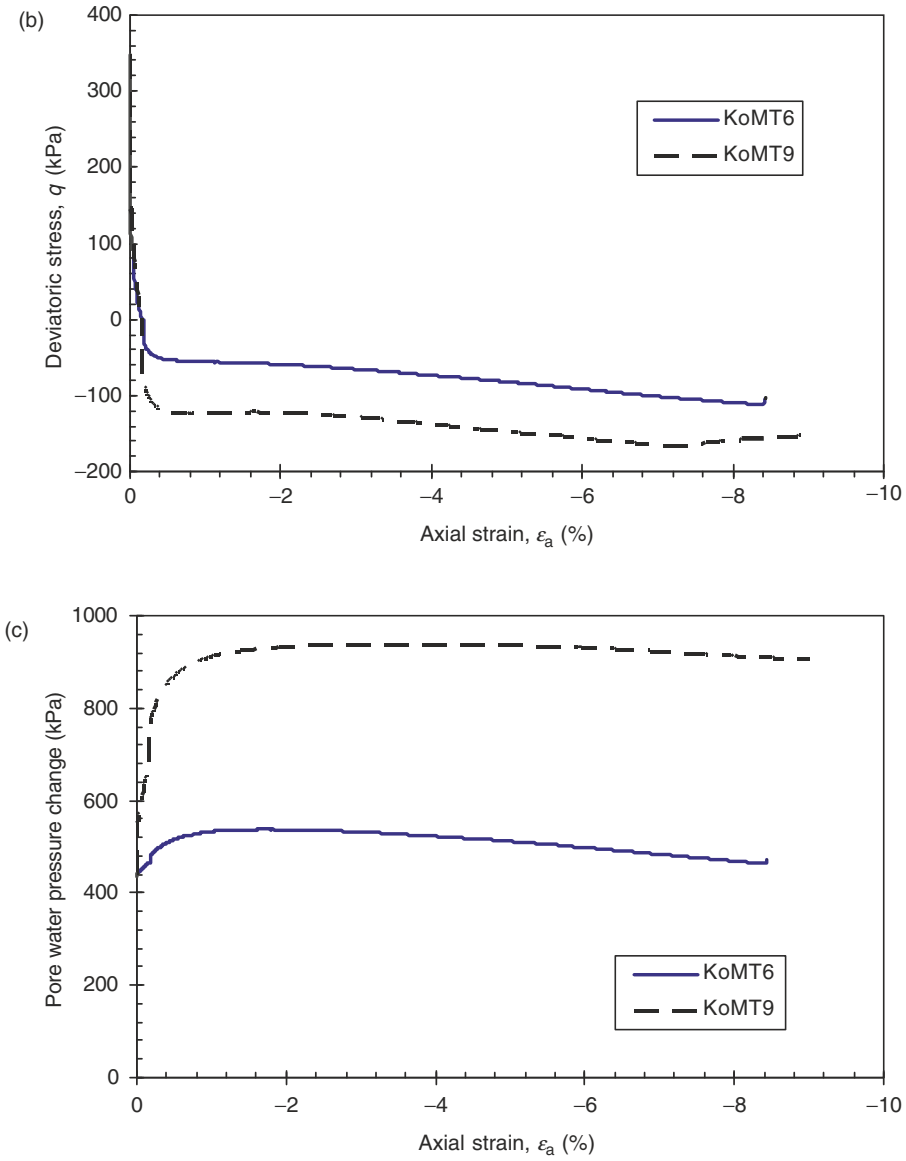

Fig. 9. *Continued*

data unambiguously indicate that the effective stress path obtained from an undrained test is affected by the total stress paths used for the undrained test even when the principal stress direction is fixed.

It needs to be pointed out that the differences in the undrained behaviour shown in Fig. 9 are not due to the testing errors such as membrane

penetrations. In fact, by assuming the soil to be a cross-anisotropic media, it can be shown analytically that the effective stress paths resulting from undrained tests conducted along different total stress paths are different.

If we assume a soil to be a cross-anisotropic elastic material, then the stress–strain relationship under the trixial condition can be written as [26]:

$$\begin{pmatrix} \Delta\varepsilon_{\mathrm{a}} \\ \Delta\varepsilon_{\mathrm{h}} \end{pmatrix} = \begin{pmatrix} \frac{1}{E_{\mathrm{a}}} & \frac{-2\nu_{\mathrm{ha}}}{E_{\mathrm{h}}} \\ \frac{-\nu_{\mathrm{ah}}}{E_{\mathrm{a}}} & \frac{1-\nu_{\mathrm{hh}}}{E_{\mathrm{h}}} \end{pmatrix} \begin{pmatrix} \Delta\sigma'_{\mathrm{a}} \\ \Delta\sigma'_{\mathrm{h}} \end{pmatrix}, \tag{3}$$

where ε_{a} is axial strain; ε_{h} is horizontal strain; σ'_{a} is effective vertical stress; σ'_{h} is effective horizontal stress, $E_{\mathrm{a}}, E_{\mathrm{h}}$ is Young's modulus in the axial and horizontal directions, respectively; $\nu_{\mathrm{ah}}, \nu_{\mathrm{ha}}$ is Poisson's ratio for the effect of axial strain on horizontal strain and Poisson's ratio for the effect of horizontal strain on vertical strain, and ν_{hh} is Poisson's ratio for the effect of horizontal strain on complementary horizontal strain. Under undrained conditions, $\Delta\varepsilon_{\mathrm{v}} = \Delta\varepsilon_{\mathrm{a}} + 2\Delta\varepsilon_{\mathrm{h}} = 0$. Using (3) we have:

$$\Delta\sigma'_{\mathrm{h}} = \frac{E_{\mathrm{h}}}{2E_{\mathrm{a}}} \frac{(2\nu_{\mathrm{ah}} - 1)\Delta\sigma'_{\mathrm{a}}}{1 - \nu_{\mathrm{ha}} - v_{\mathrm{hh}}}, \tag{4}$$

when $1 - \nu_{\mathrm{ha}} - \nu_{\mathrm{hh}} \neq 0$. As $\Delta q = \Delta\sigma'_{\mathrm{a}} - \Delta\sigma'_{\mathrm{h}}$, (4) can be re-written as:

$$\Delta\sigma'_{\mathrm{h}} = \frac{E_{\mathrm{h}}(2\nu_{\mathrm{ah}} - 1)}{2E_{\mathrm{a}}(1 - \nu_{\mathrm{ha}} - \nu_{\mathrm{hh}}) - E_{\mathrm{h}}(2\nu_{\mathrm{ah}} - 1)} \Delta q = A\Delta q, \tag{5}$$

where

$$A = \frac{E_{\mathrm{h}}(2\nu_{\mathrm{ah}} - 1)}{2E_{\mathrm{a}}(1 - \nu_{\mathrm{ha}} - \nu_{\mathrm{hh}}) - E_{\mathrm{h}}(2\nu_{\mathrm{ah}} - 1)}.$$

For undrained triaxial tests along AC (or AE) paths, $\mathrm{d}\sigma_{\mathrm{h}} = 0$. Hence:

$$\Delta u = -\Delta\sigma'_{\mathrm{h}} = -A\Delta q. \tag{6a}$$

For undrained triaxial tests along LE (or LE) paths, $\mathrm{d}\sigma_{\mathrm{a}} = 0$. Hence,

$$\Delta u = -\Delta\sigma'_{\mathrm{a}} = -(1 + A)\Delta q. \tag{6b}$$

The total stress paths followed in AC (or AE) and LE (or LC) tests are

$$\text{LE (or LC) path}: \quad \Delta p = -\frac{2}{3}\Delta q, \tag{7a}$$

$$\text{AC (or AE) path}: \quad \Delta p = \frac{1}{3}\Delta q. \tag{7b}$$

Using (6) and (7), the change in effective mean stress can thus be calculated as:

$$\text{LE (or LC) path}: \quad \Delta p'_{\mathrm{LC}} = \Delta p - \Delta u = \left(\frac{1}{3} + A\right)\Delta q, \tag{8a}$$

$$\text{AC (or AE) path}: \quad \Delta p'_{\mathrm{AE}} = \Delta p - \Delta u = \left(\frac{1}{3} - A\right)\Delta q. \tag{8b}$$

Equation (8) indicates clearly that the effective stress paths followed in the undrained tests conducted along different total stress paths are different. This is derived by merely assuming the soil is a cross-anisotropic elastic material. The differences in the effective stress paths may be more pronounced for cross-anisotropic plastic materials. Therefore, the differences in the stress–strain behaviour and the effective stress paths between undrained tests conducted along different total stress paths are a result of anisotropic soil behaviour. This anisotropic behaviour is observed for both sand and clay [6, 29] when the principal stress direction rotates from 0° (i.e. compression) to 90° (i.e. extension). However, the anisotropic behaviour due to the change in total stress paths for a fixed principal stress direction is obvious only for the sand tested in this paper, but is not obvious for the undisturbed NC clay tested by Bishop and Wesley [6] and Law and Holtz [29]. In fact, the difference in the stress–strain curves and the effective stress paths can also be seen in Bishop and Wesley's [6] data, and the difference follows the same trend as that observed in this paper. It is only because the difference is small that Bishop and Wesley [6] considered that the stress–strain curves and the effective stress paths were "almost identical" for the NC clay tested. In general, the stress–strain behaviour and the effective stress paths obtained in undrained tests can be affected by the total stress paths used in conducting the undrained tests.

6 Reversed Strain Rate Effect on Loose Sand

Unlike for clay, the effect of strain rate on the stress–strain behaviour of sand has not been well studied. This is reflected by the small number of papers that can be found in the literature, e.g. Casagrande and Shannon [9], Seed and Lundgren [35], Whitman and Healy [37] and Yamamuro and Lade [38]. There are even fewer studies on the effect of strain rate on loose sand. One reason for the luck of study on the effect of strain rate on sand is probably because of the perception that strain rate does not affect granular soil as much as it does on cohesive soils. Most of the studies on the strain rate effect of sand appear to indicate that the trend of influence for sand is similar to that for clay, i.e. the higher the strain rate, the higher the peak deviator stress in both drained and undrained tests. However, there are a few exceptions. Nash and Dixon [31] have presented some undrained test results on sand to show that the magnitudes of deviator stress and deformation moduli decrease with increasing strain rate. Similar observations have also been made by Whitman and Healy [37].

The strain rate effect on the Changi sand in Singapore has been studied. The results of four undrained tests on loose sand are shown in Fig. 10. The four specimens were prepared using the moist tamping method with void ratios in the narrow range of 0.880–0.882. Therefore, the specimens can be considered identical. The four tests were conducted using four different strain rates of 0.002, 0.02, 0.2 and 2.0 mm min^{-1}. It can be seen from Fig. 10 that the stress–strain curve is strongly affected by the strain rate and the higher the rate,

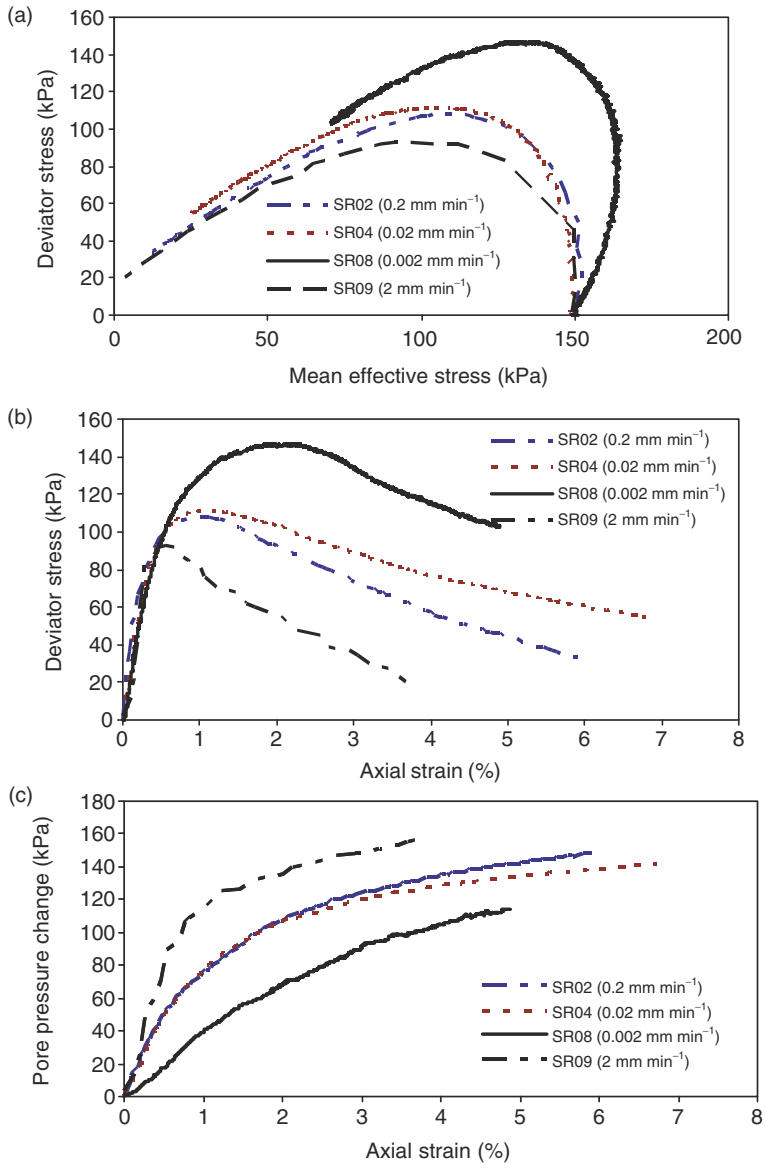

Fig. 10. Results of undrained tests on loose sand at four different strain rates

the lower the deviator stress and the higher the pore pressure generation. Therefore, a reversed strain rate effect has been observed. As the results are rather unusual, the repeatability has been check. A series of drained tests on the same loose sand were also conducted using the four different strain rates [30]. The strain rate effect on the drained behaviour is consistent with that on undrained. Therefore, the reserved strain rate effect shown in Fig. 10 is a true material behaviour.

How should the reversed strain rate effect be explained? Whitman and Healy [37] speculated that it could be due to membrane penetration errors. However, we have checked this not to be the case. One plausible explanation may be offered as follows. As the slower the strain rate, the higher the peak deviator stress, it suggests that the ageing effect in sand may be even larger than the rate effect. One contribution to the ageing effect is the formation of silicic acid gel at the surface of the sand particles as a result of chemical interaction between water and silica, as suggested by Denisov and Reltov [19]. Further studies are required on this topic.

7 Concluding Remarks

Owing to the complexity and diversity in the formation and stress–strain behaviour of geomaterials, some unusual soil behaviour has been observed and presented in this paper. These include: liquefaction of dense sand, pre-failure strain softening along strain path and strain softening and hardening in the post-failure region, instability under drained conditions, the path dependent undrained behaviour and the reversed strain rate effect on loose sand. Some of those unusual behaviours cannot be properly modelled by the existing constitutive models yet. In this case, the data pose a challenging to the existing constitutive models and help in the development and verification of constitutive models for geomaterials. On the other hand, if the unusual behaviours can be modelled by constitutive models, it will not only support the validity of the data, but also help in understanding the physical meanings and mechanisms that govern the behaviours. Only by achieving a thorough understanding of the general behaviour of soil, can we be able to model the soil behaviour properly and use it in the prediction of the performance of geotechnical facilities and structures.

8 Acknowledgements

The contributions of my research students, Wing-Kai Leong, Chin-Liang Gan and Wai-Lay Loke, in conducting the laboratory tests are gratefully acknowledged.

References

1. Adalier K, Elgamal AW 2002 Seismic response of adjacent dense and loose sand columns. Soil Dynamics and Earthquake Engineering, 22: 115–127
2. Anderson SA, Riemer MF 1995 Collapse of saturated soil due to reduction in confinement. Journal of Geotechnical Engineering, ASCE, 121(2): 216–220
3. Been K, Jefferies MG 1985 A state parameter for sands. Géotechnique, 35(2): 99–112

4. Been K, Conlin BH, Crooks JHA, Fitzpatrick SW, Jefferies MG, Rogers BT, Shinde S 1987 Back analysis of the Nerlerk berm liquefaction slides: Discussion. Canadian Geotechnical Journal, 24(1): 170–179
5. Been K, Crooks JHA, Conlin BH, Horsfield D 1988 Liquefaction of hydraulically placed sand fills. Hydraulic Fill Structures, Geotechnical Special Publication 21, DJA Van Zyl and SG Vick eds, 573–591
6. Bishop AW, Wesley LD 1975 A hydraulic triaxial apparatus for controlled stress path testing. Geotechnique, 25(4): 657–670
7. Boulanger RW, Truman SP 1996 Void redistribution in sand under post-earthquake loading. Canadian Geotechnical Journal, 33: 829–833
8. Casagrande A 1975 Liquefaction and cyclic deformation of sands – a critical review. Proceedings of the 5th Pan American Conference on Soil Mechanics And Foundation Engineering, Buenos Aires; also published as Harvard Soil Mechanics Series No. 88, Cambridge, MA
9. Casagrande A, Shannon WL 1948. Strength of soil under dynamic loads. Proceedings of ASCE, 749(4): 591–632
10. Chu J 1991 Liquefaction of sands under undrained and non-undrained conditions. Soil Dynamics and Earthquake Engineering. V, Elsevier, 277–291
11. Chu J 1998 Pre-failure strain softening and pre-failure instability of a granular soil. Pre-failure Deformation Behaviour of Geomaterials, Thomas Telford, The Institution of Civil Engineers, 337–344
12. Chu J, Leong WK 2001 Pre-failure strain softening and pre-failure instability of sand: a comparative study. Géotechnique, **51**(4): 311–321
13. Chu J, Lo S-CR 1993 On the measurement of critical state parameters of dense granular soils. Geotechnical Testing Journal, ASTM, 16(1): 27–35
14. Chu J, Lo S-CR 1994 Asymptotic behaviour of a granular soil in strain path testing. Geotechnique, 44(1): 65–82
15. Chu J, Lo S-CR, Lee IK 1992 Strain softening behaviour of a granular soil in strain path testing. Journal of Geotechnical Engineering, ASCE, 118(2): 191–208
16. Chu J, Lo S-CR, Lee IK 1993 Instability of granular soils under strain path testing. Journal of Geotechnical Engineering, ASCE, 119(5): 874–892
17. Chu J, Lo S-CR, Lee IK 1996 Strain softening and shear band formation of sand in multi-axial testing. Géotechnique, 46(1): 63–82
18. Chu J, Leroueil S, Leong WK 2003 Unstable behaviour of sand and its implications for slope instability. Canadian Geotechnical Journal, 40: 873–885
19. Denisov NY, Reltov BF 1961. The influence of certain processes on the strength of soils. Proceedings of the 5th International Conference on Soil Mechanics and Foundation Engineering, 1: 75–78
20. Eckersley JD 1990 Instrumented laboratory flowslides. Geotechnique, 40: 489–502
21. Fleming RW, Ellen SD, Algus MA 1989 Transformation of dilative and contractive landslide debris into debris flows – an example from Marin County, California. Engineering Geology, 27: 201–223
22. Gan CL 2002 Instability of granular soil under general stress conditions. MEng Thesis, Nanyang Technological University, Singapore
23. Hettler A, Vardoulakis I 1984 Behaviour of dry sand tested in a large triaxial apparatus. Geotechnique, 34(2): 183–198
24. Holtz RD, Kovacs WD 1981 An Introduction to Geotechnical Engineering, Prentice-Hall, New Jersey

25. Jefferies MG 1997 Plastic work and isotropic softening in unloading. Geotechnique, 43(1): 91–103
26. Kuwano R, Jardine RJ 2002 On the applicability of cross-anisotropic elasticity to granular materials at very small strains. Geotechnique, 52(10): 727–749
27. Lade PV 1993 Initiation of static instability in the submarine Nerlerk berm. Canadian Geotechnical Journal, 30(6): 895–904
28. Lambe TW, Whitman RV 1969 Soil Mechanics, Wiley, New York, 553 p
29. Law KT, Holtz RD 1978 A note on Skempton's A parameter with rotation of principal stresses. Geotechnique, 28(1): 57–64
30. Loke WL 2003 Failure mechanisms of gentle granular soil slopes. MEng thesis, Nanyang Technological University, Singapore
31. Nash KL, Dixon RK 1961 The measurement of pore pressure in sand under rapid triaxial tests. Proceedings of the Conference on the Pore Pressure and Suction in Soils, Butterworths, London, 21–25
32. NRC (National Research Council) 1985 Liquefaction of soils during earthquakes. National Academy Press, Washington, DC
33. Olson SM, Stark TD, Walton WH, Castro G 2000 1907 static liquefaction flow failure of the north dike of Wachusett dam. Journal of Geotechnical and Geoenvironmental Engineering, ASCE, 126(12): 1184–1193
34. Rowe PW 1962 The stress dilatancy relationship for static equilibrium of an assembly of particles in contact. Proceedings of the Royal Society, A267, 500–529
35. Seed HB, Lundgren R 1954 Investigation of the effects of transient loading on the strength and deformation characteristics of saturated sands, Proceedings of the ASCE, 54:1288–1306
36. Sento N, Kazama M, Uzuoka R, Ohmura H, Ishimaru M. 2004 Possibility of postliquefaction flow failure due to seepage. Journal of Geotechnical and Geoenviromental Engineering, ASCE, 130(7): 707–716
37. Whitman RV, Healy KA 1962 Shear strength of sands during raid loadings. Journal of Soil Mechanics and Foundations Divisions, ASCE, 88(SM2): 99–132
38. Yamamuro JA, Lade PV 1993 Effect of strain rate on instability of granular soils Geotechnical Testing Journal, 16(3): 304–313

Histotropy of Hostun RF Loose Sand

T. Doanh, Z. Finge, S. Boucq*, and Ph. Dubujet†

* Ecole Nationale des Travaux Publics de l'Etat, Laboratoire Géomatériaux, Vaulx en Velin Cedex, France
thiep.doanh@entpe.fr
† ENISE. Laboratoire de Tribologie et Dynamique des systèmes, Saint-Etienne Cedex, France

Abstract. This paper explores the histotropic effects of loosely compacted and K-overconsolidated Hostun RF sand in the triaxial plane. Several series of compression and extension undrained tests are performed on samples subjected to anisotropically K-overconsolidation with constant effective stress ratio paths from different initial stress states. The analysis is focused on the observed effective stress paths. To minimize the effect of variation of density on the observed undrained behaviour, nearly identical void ratios before the final monotonic undrained shearing are required for all tested samples.

Experimental results show some effects of histotropy : A large pseudo-elastic domain, a unique and strongly inclined pseudo-elastic response, the directional dependency of the initial inclination of the effective stress paths, the progressive appearance of dilatancy and the evolution of the undrained behaviour from the partial static liquefaction of loose sand to the completely stable state typical of dense sands, while being relatively loose at the beginning of undrained shearing. This paper offers some new insights into the mechanism of the histotropy created by simple linear stress paths in the classical triaxial plane. The effectiveness of using hyperelasticity to simulate the pseudo-elastic response of presheared sand is highlighted.

1 Introduction

Since the early date of soil mechanics, the two forms of anisotropy, inherent and induced, have been recognized as difficult challenges to the geotechnical community. Much experimental and theoretical research has been devoted to these problems, trying to capture the essential features, since natural soil, under the vertical action of gravity during sedimentation, possesses these two components.

Concerning induced anisotropy, the first past experimental studies are often restricted to isotropically consolidated materials and standard compression triaxial preshear, due to experimental difficulties, Poorooshasb et al. [29, 30], Tatsuoka et al. [33], Ishihara et al. [17–19], Vaid et al. [35] among

others. Newly designed machines are constructed to better simulate the gravitational direction of natural soil: The simple shear device, Arthur et al. [1], the hollow cylinder apparatus, Hight et al. [14], the plane strain machine, Tatsuoka et al. [34] and the true triaxial machine, Lanier [25], etc. to cite a few. New experiments showed the key role of the direction of the consolidation and the subsequent alteration of the mechanical properties of the soil by the first stress loading. The previous strain histories seem to be related to the induced anisotropy.

Despite decades of relevant experimental research, many aspects of the induced anisotropy are still elusive, many questions are still open: how to quantify the effects of induced anisotropy? how to characterize the evolution of material properties? can one have a clear-cut explanation on the role of previous preloading histories?

The purpose of this paper is to study the effects of the induced anisotropy created by simple linear stress paths from different initial stress states in the classical triaxial plane. New experimental observations from an extensive programme on loosely compacted and anisotropically overconsolidated Hostun RF sand are presented, leading to histotropy, a specialized form of induced anisotropy.

2 Normally Consolidated Behaviour

Standard Hostun RF sand is used in this experimental program. Its physical properties can be found in Flavigny [11]. Very loose and contractive sand samples were prepared with a modified moist tamping and undercompaction method. This preparation technique was inspired by the early works of Bjerrum et al. [2] and Ladd [22]. The details of the experimental procedure are given in [7, 9, 16].

The triaxial test results were interpreted in terms of the deviatoric stress $q = \sigma'_a - \sigma'_r$ and the effective mean pressure $p' = (\sigma'_a + 2\sigma'_r)/3$, where σ'_a and σ'_r are the effective axial and radial stresses. The attention of this paper is focused on the stress paths, examined in the classical $q - p'$ plane.

The undrained behaviour of very loose and normally consolidated Hostun RF sand was previously studied mainly by Canou [3], Meghachou [28], Konrad [20], Ibraim [16]. Isotropic consolidation procedure is conducted in all studies, and anisotropic consolidation along constant stress ratio paths, noted anisotropic K-consolidated paths with $K = \sigma'_r/\sigma'_a$, is rarely performed.

Figure 1 gives a fairly accurate image of the undrained behaviour of virgin isotropic consolidated (a) and anisotropic consolidated (b) sand in compression and in extension. Within the range of studied initial confining pressures, partial static liquefaction is systematically observed for all normally consolidated samples even for the largest explored $K = 0.35$ values. This partial static liquefaction is characterized by a progressive drop from the deviatoric stress peak q_{peak} and a large loss of effective mean pressure resulting from a

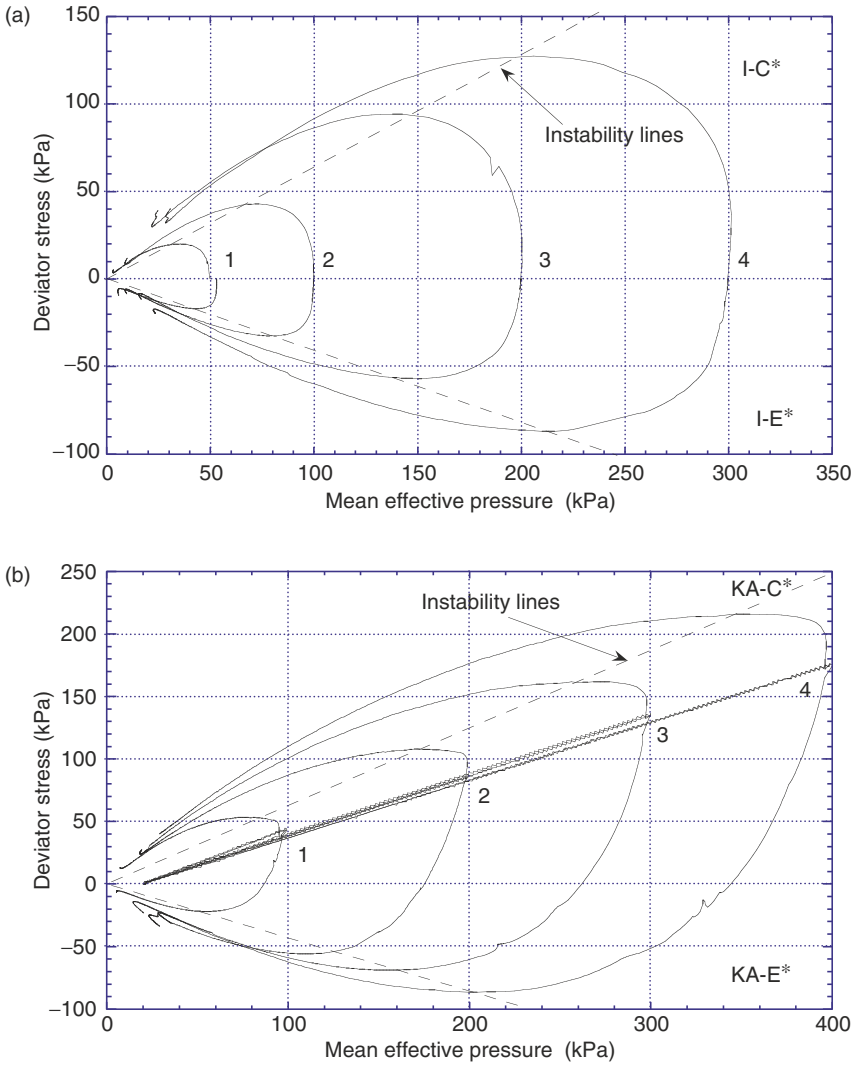

Fig. 1. Effective stress paths for normally consolidated Hostun RF loose sand. (**a**) Isotropically (**b**) anisotropically consolidated

continuous rising of pore pressure under undrained shearing. Complete static liquefaction can be observed only in compression for smaller values of initial confining pressure or a stress reversal at large strains will always liquefy the samples. The perpendicular intersection of the effective stress paths with the hydrostatic axis indicates initial isotropic sand samples.

The stress–strain undrained behaviour exhibits a pronounced peak at relatively low to very low axial strain, depending on the value of K, and a post-peak stress reduction to a small residual value at large strains corresponding

to the steady state of deformation [6,21]. The static liquefaction is essentially an instability phenomenon of very loose and normally consolidated sand, in the sense of Hill [15]. In the case of monotonic solicitation in the triaxial plane, it is equivalent to a decrease of deviatoric stress.

These studies show that the Lade's instability concept [24], defined initially for isotropically consolidated sand in compression, is corroborated in triaxial extension and even generalized to sand subjected to an initial positive anisotropic stress state. Nevertheless, this concept is strongly influenced by the monotonic consolidation history.

It should be noted that the shapes of the effective stress paths are geometrically similar, when normalized by the initial effective mean pressure. The normalized behaviour suggests the use of these shapes as the yield surface in the elastoplasticity framework [24]. Recently, several analytical equations for the yield surface of sand have been proposed and verified against experimental responses of isotropic and anisotropic consolidated sand, Imam et al. [31].

3 Overconsolidated Behaviour

The undrained behaviour of very loose and K-overconsolidated Hostun RF sand is reported recently in [10]. It tends to corroborate the compression behaviour of lightly overconsolidated Hostun sand investigated by Di Prisco et al. [4], Matiotti [27], Gajo et al. [12], and on Toyoura sand by Ishihara et al. [18]. To clarify the effects of induced anisotropy generated by constant effective stress ratio paths, two main ideas are behind the experimental works of [10]:

1. To facilitate the study of the effects of previous preloading strain histories, all anisotropic K-overconsolidated histories must lead to a same anisotropic stress state before undrained shearing. One scalar parameter, the usual overconsolidation ratio $\mathrm{OCR} = p'_{\max}/p'_{\mathrm{c}}$, characterizes the overconsolidated state.
2. To highlight only the effects of previous deviatoric strain histories, nearly similar void ratio is required before the final undrained loading. This extra requirement is needed to minimize the well-known effects of density on the observed undrained behaviour.

To aid the visual interpretation, typical effective stress paths of the undrained tests following an anisotropic K-overconsolidation history is portrayed in Fig. 2. The experimental results on isotropically (anisotropically) overconsolidated samples in compression and in extension are given in Fig. 3a, b. The numbers near q_{peak} (hollow circle) in these figures indicate the OCR values. Concerning isotropically overconsolidated sand, partial static liquefaction is still observed, in compression and extension, even for the largest explored

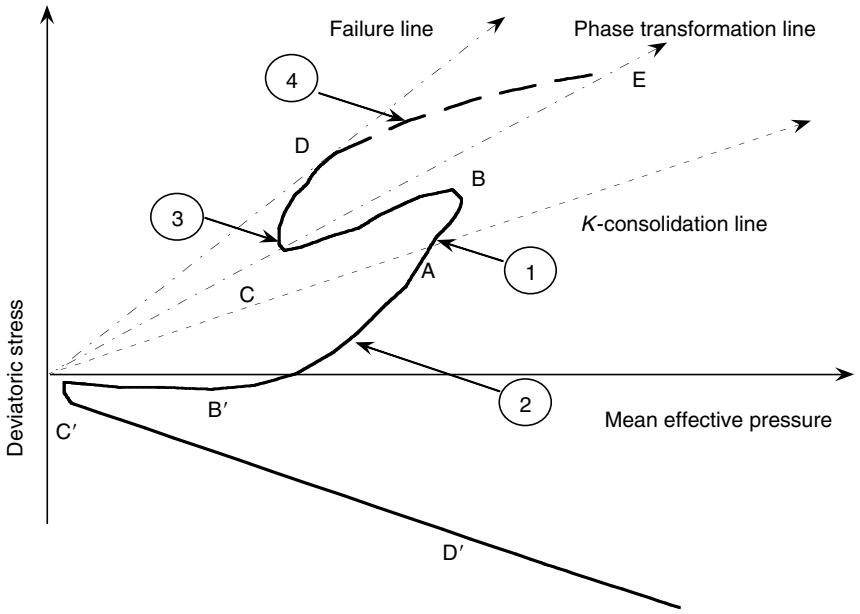

Fig. 2. Schematic illustration of the histotropic effects on anisotropically K-overconsolidated sand

OCR values of 8. Globally, isotropic overconsolidation enhances markedly the undrained shear strength with a deviatoric stress peak in compression considerably larger than that in extension. As the OCR increases, the effective stress paths of isotropic overconsolidated samples move outward with an asymmetric enlargement with respect to the isotropic axis.

New experimental findings emerge in Fig. 2 and 3b as the histotropic effects for anisotropically K-overconsolidated sand:

3.1 Directional Dependency of the Initial Gradient

From the initial anisotropic stress state A, a unique non-vertical initial gradient of the effective stress paths for each K-overconsolidation history is obtained. This initial gradient seems to relate solely to the direction of the previous stress history. The strong inclination towards the positive p' axis indicates an induced anisotropy created by the previous K-overconsolidation history, with a greater stiffness in the vertical direction, Graham et al. [13].

3.2 Pseudo-Elastic Response

All effective stress paths are strongly inclined towards the positive p' axis and follow a common highly non linear curve up to deviatoric stress peak,

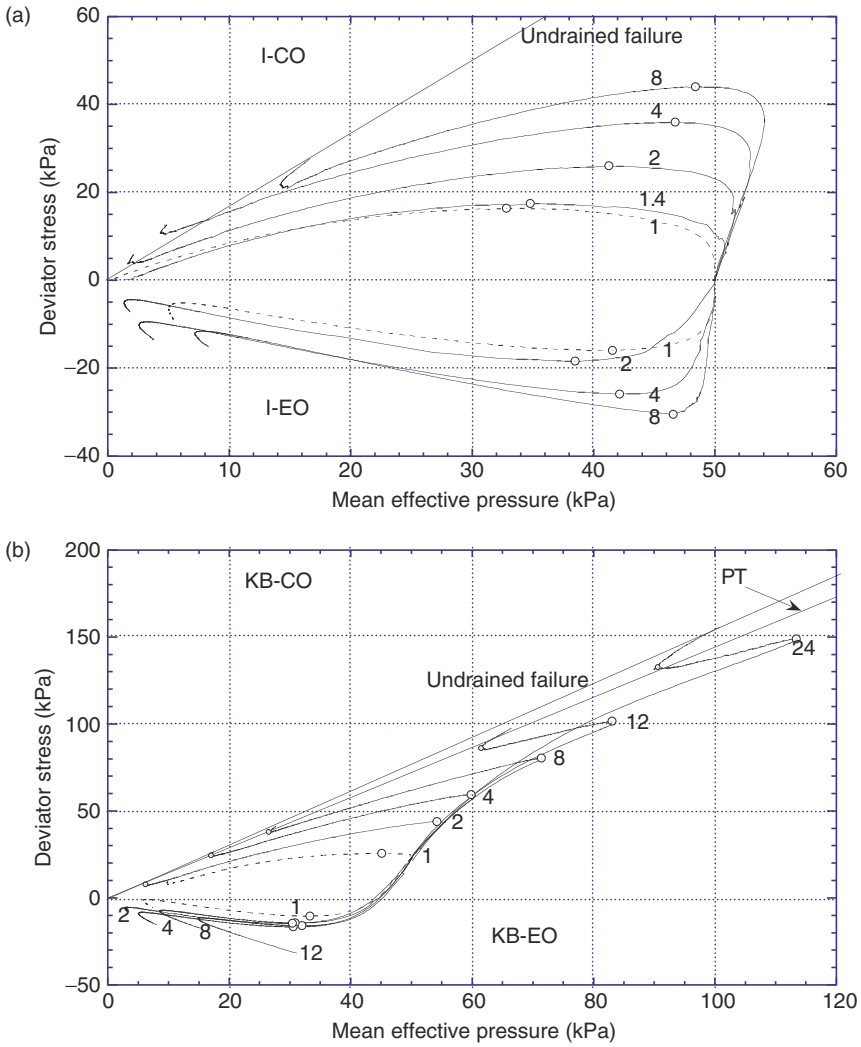

Fig. 3. Effective stress paths for overconsolidated Hostun RF loose sand. (**a**) Isotropically (**b**) anisotropically consolidated

in compression as well as in extension, independent of OCR attained during the K-overconsolidation process before the final undrained shearing. This common boundary is observed for two anisotropic K-overconsolidation histories, KB and KC ($K = 0.50$ and 0.35). Since the initial anisotropic stress state A is situated inside the past maximum yield surface generated by the K-overconsolidation history, the first section AB or AB′ is the pseudo-elastic response of the overconsolidated and loose sand. This pseudo-elastic domain has a very large size, nearly up to q_{peak}, from B to B′.

3.3 Progressive Appearance of Dilatancy

A pronounced protuberance of the effective stress path with a very sharp bend is observed in compression (the direction of consolidation) while that in extension is left nearly unchanged. The descending part BC or B′C′ after the sharp bend moves equally upwards with increasing OCR. This part characterizes the undrained instability behaviour of loose sand. The length of this descending part seems to link with the OCR or the induced anisotropy. The smaller the OCR, the longer the softening part of the stress path. As the OCR increases, the onset of the undrained instability is initiated at a stress state closer to the phase transformation (PT) line [26], [33] where dilatancy appears even if the relative density before undrained shearing indicates a relatively loose state. The effective stress paths move up again, CD or C′ D′, after the appearance of the dilatancy.

3.4 Evolution of the Undrained Behaviour

Depending on the anisotropic consolidation ratio K and on the OCR reached during K-overconsolidation, the undrained compression behaviour of samples evolves from instability for low OCR and high K ratio to complete stability for high OCR and low K, via a behaviour of temporary instability for intermediate preshearing levels for medium OCR and K. This evolution of the soil behaviour as a function of the K-overconsolidation history is similar to that due to the variation of the isotropic consolidation pressure (barotropy), where the behaviour of dense sand evolves from stable behaviour at low confining pressures to instability at very high pressures through temporary instability at medium confining pressures, [24, 36]; or that due to the well-known variation of the void ratio (pyknotropy). Static liquefaction, usually associated to loose sands, occurred for all isotropic overconsolidation levels in compression and extension in this study.

Note that for practical purposes, a linear correlation between q_{peak} and OCR in a logarithmic scale was found with different coefficients for each anisotropic consolidation level K. This correlation may be used to estimate roughly the undrained strength. The Lade's instability lines [24], and the Sladen's collapse surface [32], based on the deviatoric stress peak, clearly depend on the previous preloading history. These concepts are not intrinsic like the failure envelope.

4 Drained Presheared Behaviour

To uncouple the observed behaviour of deviatoric and isotropic stresses, a particular preloading history is extensively explored. It consists simply of a standard drained deviatoric preshear cycle, either in compression or in extension,

from an initial isotropic stress state A in Fig. 2. This series is designed to highlight only the effects of previous preloading deviatoric strain histories, since the same returning stress state remains isotropic. A detailed analysis of the experimental works is already reported in [7]. The experimental results of compressive and extensive drained presheared series are shown in Fig. 4a, b. Cross symbols give the magnitude of the drained preshear cycle in triaxial compression.

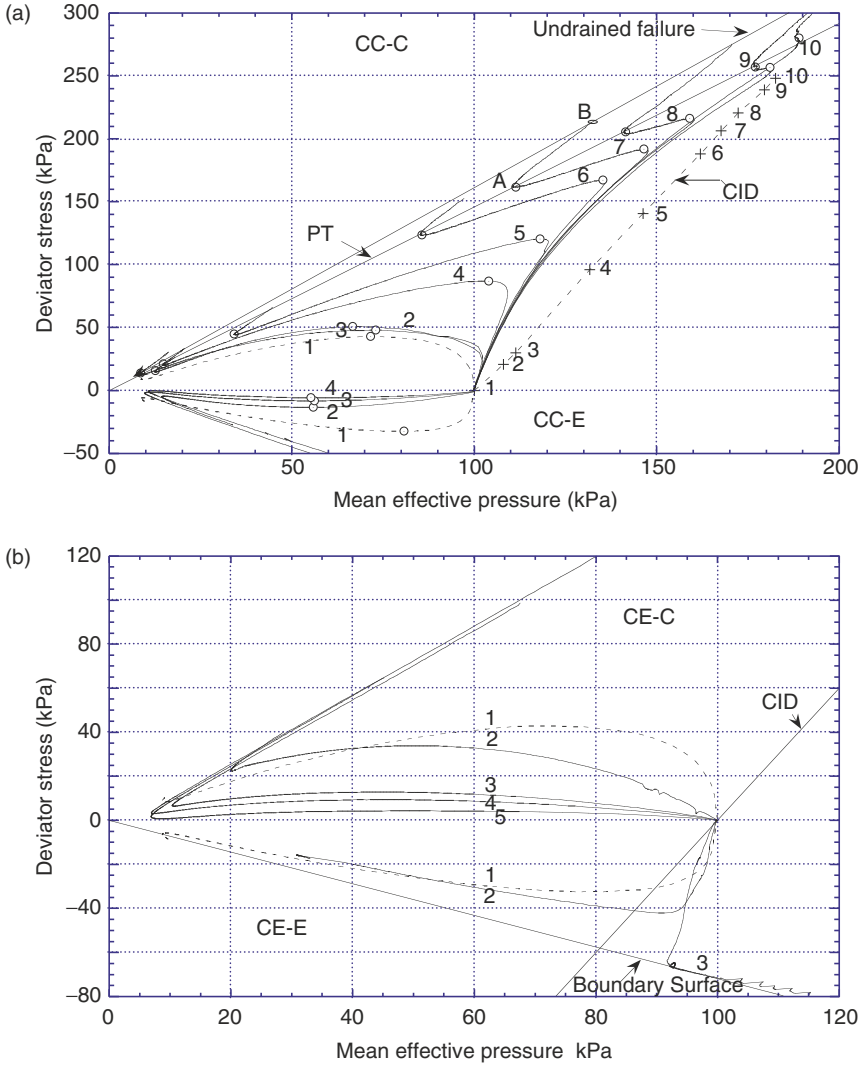

Fig. 4. Effective stress paths for drained **(a)** compression **(b)** extension presheared Hostun RF loose sand

The newly observed experimental hints of the histotropy effects in Sect. 3 are still valid, driven now by previous deviatoric strain histories: a unique initial inclination of the effective stress paths assessing its dependency only on the direction of previous history; a unique and strongly inclined pseudo-elastic response towards the positive p' axis; the progressive appearance of dilatancy in a single PT line as a function of the magnitude of axial prestraining; the concept of the PT line developed for dense sand seems to apply for loose presheared or overconsolidated sand; and finally, the evolution of the undrained behaviour from the classic partial static liquefaction of loose sand to the completely stable state typical of dense sands, while being relatively loose at the beginning of undrained shearing.

This linear preshear series assesses the well-known importance of the direction of the preloading and the subsequent loading: a same (opposite) subsequent direction always gives a stiffer (softer) behaviour. Moreover, a continuous evolution of the soil behaviour is obtained.

5 Pseudo-Elastic Response of Presheared Sand

Experimental investigations on K-overconsolidation series suggest a very large pseudo-elastic domain which can comprise the whole past maximum yield surface of the previous K-overconsolidation history. Letting aside the directional dependency of the initial gradient of the effective stress paths, the curved pseudo-elastic response seems to be an interesting challenge. Inside the current mainstream of the non-associated elastoplasticity framework, the usual incremental isotropic hypoelasticity cannot be used to describe the observed behaviour. The elastic strain increment is expressed as :

$$\dot{\varepsilon}_{ij} = \frac{\dot{I}_1}{9K}\delta_{ij} + \frac{\dot{s}_{ij}}{2G}, \tag{1}$$

where $I_1 = \sigma_{kk}, s_{ij} = \sigma_{ij} - (I_1/3)\delta_{ij}$ is the deviatoric stress, K the elastic volumetric modulus and G the elastic shear modulus depending on the first and/or the second stress invariant. The effective mean pressure increment remains unchanged during the undrained loading since the volumetric strain increment $\dot{\varepsilon}_{\mathrm{v}}$ is :

$$\dot{\varepsilon}_{\mathrm{v}} = \dot{\varepsilon}_{kk} = \frac{\dot{p}}{K} = 0. \tag{2}$$

If the elastic component depends now on I_1 and s_{ij}:

$$\varepsilon_{ij} = \frac{I_1}{9K}\delta_{ij} + \frac{s_{ij}}{2G}, \tag{3}$$

then the volumetric strain increment is written as:

$$\dot{\varepsilon}_{\mathrm{v}} = \frac{1}{K^2}(\dot{p}K - \dot{K}p) \tag{4}$$

and the effective mean pressure increment can change during the undrained loading, since the elastic volumetric modulus K is not infinite:

$$\dot{p} = \frac{p}{K}\dot{K}. \tag{5}$$

For the sake of simplicity, we choose a classical isotropic hyperelastic component, proposed by Lade and Nelson [23]. It has the form of (3) with the Young modulus defined as:

$$E = Mp_{\mathrm{a}}\left[\left(\frac{I_1}{p_{\mathrm{a}}}\right)^2 + R\frac{J_2}{p_{\mathrm{a}}^2}\right]^m \tag{6}$$

with $J_2 = s_{ij}s_{ij}/2, R = 6(1+\nu)/(1-2\nu), K = E/3(1-2\nu)$ and p_{a} is the reference atmospheric pressure. A constant Poisson's ratio ν is assumed. M and m are dimensionless constitutive parameters. The analytical equation of the pseudo-elastic response as the effective stress paths can be found in [7] using the incompressibility condition:

$$p = p_0\left[\frac{\left(\frac{3p}{p_{\mathrm{a}}}\right)^2 + \frac{R}{3}\left(\frac{q}{p_{\mathrm{a}}}\right)^2}{\left(\frac{3p_0}{p_{\mathrm{a}}}\right)^2 + \frac{R}{3}\left(\frac{q_0}{p_{\mathrm{a}}}\right)^2}\right]^m. \tag{7}$$

This equation represents a symmetric conical surface with respect to the hydrostatic axis, and gives the initial gradient of the effective stress paths under undrained conditions in the pseudo-elastic domain. As expected, this isotropic hyperelastic model always gives a vertical initial slope independently of the OCR level during the K-overconsolidation and a common curved elastic response for all effective stress paths. This hyperelasticity component associated with a transverse elasticity can capture the inclined initial gradient of the observed effective stress.

This simple isotropic hyperelastic component is used within the existing non-associated elastoplasticity framework with mixed kinematic hardening mechanism. This model with isotropic elasticity is described in [8]. An isotropic mechanism having a large range of the pseudo-elastic domain is associated to a kinematic deviatoric mechanism taking into account the presheared history. Figure 5 gives an example of the theoretical response in the case of compressive drained preshear. While a simple hyperelastic model without any reference to anisotropy gives a correct pseudo-elastic response when comparing to experimental data, many other experimental features are currently not supported in this model.

Table 1 summarizes the relevant experimental effects of the histotropy on the undrained behaviour of loosely compacted and presheared sand into a comprehensive checklist to facilitate the comparison between the theoretical simulations and the experimental observations.

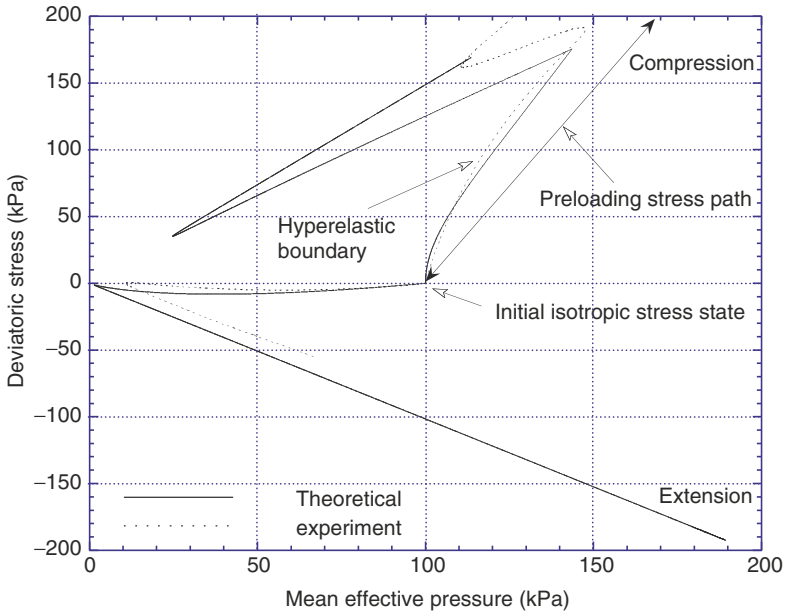

Fig. 5. Undrained behaviour of compressive presheared samples: theoretical and experiments

Table 1. Checklist for histotropic effects on loose and presheared sand

features
directional dependency of the initial gradient of stress paths
highly curved pseudo-elastic response
evolution of undrained behaviour
progressive appearance of dilatancy phenomenon
asymptotical stabilization of undrained strength

6 Conclusions

This paper has presented new experimental evidence of histotropy on loosely compacted and anisotropically K-overconsolidated Hostun RF sand. Several simple linear stress paths are used to explore the effects of histotropy. From an initial stress state in the triaxial plane, induced anisotropy is generated by K-overconsolidation with different overconsolidation ratios, or by isotropic consolidation followed by standard drained triaxial preshear, either in compression or in extension, up to a desired value of axial strain or deviatoric stress. Subsequent undrained compression and extension triaxial tests with nearly identical void ratios at the beginning of the undrained shearing were conducted to better clarify the effects of previous deviatoric strain histories on the mechanical behaviour.

The observed highly curved pseudo-elastic response, which is one of the main features of this experimental work, can be analytically expressed using simple hyperelasticity without any reference to anisotropy. The progressive appearance of the dilatancy phenomenon due to the previous deviatoric strain histories and the directional dependency of the initial gradient of the effective stress paths constitute a difficult challenge, in our opinion, in constitutive modelling.

References

1. Arthur, J.R.F., Menzies, B. Inherent anisotropy in a sand. *Geotechnique*, 22(2):115–128, 1972.
2. Bjerrum, L., Krimgstad, S., Kummeneje, O. The shear strength of a fine sand. In *Proc. 5th Int. Conf. Soil. Mech. Found. Eng.*, volume 1, pages 29–37, 1961.
3. Canou, J., Thorel, L., De Laure, E. Influence d'un déviateur de contrainte initial sur les caractéristiques de liquéfaction statique du sable. In *Proc. X ECSMFE, Firenze*, volume 1, pages 49–52, 1991.
4. Di Prisco, C., Matiotti, R., Nova, R. Theorical investigation of the undrained stability of shallow submerged slopes. *Geotechnique*, 45(3):479–496, 1995.
5. Doanh, T., Ibraim, E. Minimum undrained strength of Hostun RF. *Geotechnique*, 50(4):377–392, 2000.
6. Doanh, T., Ibraim, E., Matiotti, R. Undrained instability of very loose Hostun sand in triaxial compression and extension. Part 1: Experimental observations. *Mechanics of Cohesive-Frictional Materials*, 2(1):47–70, 1997.
7. Doanh, T., Finge, Z., Boucq, S., Dubujet, Ph. Induced anisotropy of Hostun RF loose sand: Another missing parameter. *Submitted*.
8. Dubujet, Ph., Doanh, T. Undrained instability of very loose Hostun sand in triaxial compression and extension. Part 2: Theoretical analysis using an elasto-plasticity model. *Mechanics of Cohesive-Frictional Materials*, 2(1):71–92, 1997.
9. Finge, Z *Contribution à l'étude du comportement non drainé des sables lâches surconsolidés et anisotropes*. Thèse de doctorat, Institut National des Sciences Appliquées de Lyon, 2004.
10. Finge, Z., Doanh, T., Dubujet, Ph. Undrained anisotropy of Hostun RF loose sand: New experimental hints. *Submitted*.
11. Flavigny, E., Desrues, J., Palayer, B. Le sable Hostun RF. *Revue Française de Géotechnique*, 53:67–69, 1990.
12. Gajo, A., Piffer, L. The effects of preloading history on the undrained behaviour of saturated loose sand. *Soils and Foundations*, 39(6):43–54, 1999.
13. Graham, J., Houlsby, G.T. Anisotropic elasticity of a natural clay. *Geotechnique*, 33(2):165–180, 1983.
14. Hight, D.W., Gens, A., Symes, M.J. The development of a new hollow cylinder for investigating the effects of principal stress rotation in soils. *Geotechnique*, 33(4):355–384, 1983.
15. Hill, R. A general theory of uniqueness and stability in elastic plastic solids. *J. Mech. Phys. Solids*, 6:236–249, 1958.
16. Ibraim, E. *Différents aspects du comportement des sables à partir des essais triaxiaux: des petites déformations à la liquéfaction statique*. Thèse de doctorat, Institut National des Sciences Appliquées de Lyon, 1998.

17. Ishihara, K., Okada, S. Effects of stress history on cyclic behaviour of sand. *Soils and Foundations*, 18(4):31–45, 1978.
18. Ishihara, K., Okada, S. Yielding of overconsolidated sand and liquefaction model under cyclic stresses. *Soils and Foundations*, 18(1):57–72, 1978.
19. Ishihara, K., Okada, S. Effects of large preshearing on cyclic behaviour of sand. *Soils and Foundations*, 22(3):109–125, 1982.
20. Konrad, J.M. Undrained response of loosely compacted sands during monotonic and cyclic compression tests. *Geotechnique*, 43(1):69–89, 1993.
21. Konrad, J.M., Flavigny, E., Megachou, M. Comportement non drainé du sable d'Hostun lâche. *Revue Franqise de Géotechnique*, 54:53–63, 1991.
22. Ladd, R.S. Preparing test specimens using undercompaction. *Geotechnical Testing Journal*, 1(1):16–23, 1978.
23. Lade, P.V., Nelson, R.B. Modelling of elastic behaviour of granular materials. *International Journal of Numerical and Analytical Methods in Geomechanics*, 11(5):521–542, 1987.
24. Lade, P.V., Nelson, R.B., Ito, Y.M. Instability of granular materials with nonassociated flow. *Journal of Engineering Mechanics, ASCE*, 114(12):2173–2191, 1988.
25. Lanier, J., Di Prisco, C., Nova, R. Etude expérimentale et analyse théorique de l'anisotropie induite du sable Hostun. *Revue Française de Géotechnique*, (57):59–74, 1993.
26. Luong, M.P. Etat caractéristiques du sol. *C.R.A.S. B*, 287:305–307, 1978.
27. Matiotti, R. *Analisi sperimentale del fenomeno della liquefazione statica delle sabbie sciolte e sue applicazioni numeriche*. PhD Thesis, Politechnico di Milano, 1996.
28. Meghachou, M. *Stabilité des sables lâches : essais et modélisation*. Thèse de doctorat, Université scientifique et médicale de Grenoble, 1992.
29. Poorooshasb, H.B., Holubec, I., Sherbourne, A.N. Yielding and flow of sand in triaxial compression: Part 1. *Canadian Geotechnique Journal*, 3(4):179–190, 1966.
30. Poorooshasb, H.B., Holubec, I., Sherbourne, A.N. Yielding and flow of sand in triaxial compression: Part 2 and 3. *Canadian Geotechnique Journal*, 4(4):376–397, 1967.
31. Reza Imam, S.M., Mordenstern, N.R., Robertson, P.K., Chan, D.H. Yielding and flow liquefaction of loose sand. *Soils and Foundations*, 42(3):19–31, 2002.
32. Sladen, J.A., D'Hollander, R.D., Krahn, J. The liquefaction of sands, a collapse surface approach. *Canadian Geotechnique Journal*, 22(4):564–578, 1985.
33. Tatsuoka, F., Ishihara, K. Yielding of sand in triaxial compression. *Soils and Foundations*, 14(2):63–76, 1974.
34. Tatsuoka, F., Sonoda, S., Hara, K., Fukushima, S., Pradhan, T.B.S. Failure and deformation of sand in torsional shear. *Soils and Foundations*, 26(4):79–97, 1986.
35. Vaid, Y.P., Chung, E.K.F., Kuerbis, R.H. Preshearing and undrained response of sands. *Soils and Foundations*, 29(4):49–61, 1989.
36. Yamamuro, J.A., Lade P.V. Static liquefaction of very loose sands. *Canadian Geotechnical Journal*, 34(6):905–917, 1997.

Incremental Nonlinearity in Phenomenological and Multiscale Constitutive Relations

F. Nicot* and F. Darve†

*Cemagref, Unité de Recherche Erosion Torrentielle Neige et Avalanches, Grenoble, France
francois.nicot@cemagref.fr
†Laboratoire Sols Solides Structures, UJF-INPG-CNRS, Grenoble, France

1 Introduction

The emergence of numerical methods such as the finite element method in the 1970s pointed out the paramount importance of developing proper constitutive relations that could be used to describe the mechanical behavior of the materials involved and thus provide more realistic computations. During this period, many phenomenological constitutive relations were proposed. A general view can be obtained from the international workshops providing an objective comparison of the major models, in use at the time, based on a benchmarking procedure: one held in Grenoble in 1984 (see [18]) and one in Cleveland in 1987 (see [39]). Roughly speaking, very few of these models were able to predict the response paths to nonproportional loading paths, and all of them required a refined calibration procedure with many (i.e., more than 15) constitutive parameters to be determined. It was concluded that micromechanical considerations were needed to obtain more physically based models.

In order to successfully build such multiscale models, it was necessary to develop new statistical tools that were properly adapted to granular media. Many papers were devoted to this essential step [26, 28, 30, 31, 35, 36, 40, 41]. Today it is possible to geometrically characterize a granular assembly through a statistical description of contacts (see, for example, [6–9]. The averaging procedure necessary to go from the local intergranular forces to the stress tensor has been widely discussed [4,10,25,27,42]. The localization method for deducing a local displacement field from the strain tensor is more controversial and the solution, as a rule, is not unique. Finally the local force–displacement relation can be stated as a simple elastic–plastic interaction. The complex macroscopic behavior comes from the multiplicity of intergranular contacts in various mechanical states (from elasticity to plasticity).

Thus, these micromechanical investigations now provide clear arguments that shed light on various basic points underlying the phenomenological relations such as incremental nonlinearity, singular flow rules, yield surfaces, hardening, instabilities, etc. The question of incremental nonlinearity has

been widely discussed, for example by Darve [13, 16]. Briefly, as soon as there are plastic irreversibilities, the relation between the incremental strain and the incremental stress is nonlinear and homogeneous of degree one for rate-independent materials. The existence of an elastoplastic tensor – which is the gradient of the incremental tensorial constitutive function and depends on state variables (and memory parameters) and on the direction of the incremental stress – can be deduced. This directional variation of theelastoplastic tensor characterizes incremental nonlinearity, raising an essential question: is the incremental nonlinearity continuous or discontinuous? For classical elastoplastic relations with a single plastic potential, the constitutive model is simply bilinear and characterized by one elastic tensor (in "unloading") and one elastoplastic tensor (in "loading"). In the case of multiple plastic mechanisms, the relation becomes incrementally piecewise linear with "tensorial zones" [13, 14]. Finally, for thoroughly incrementally nonlinear relations, the incremental nonlinearity can be considered as "continuous" with respect to the incremental stress direction. In this chapter, after recalling the phenomenological description of incremental nonlinearity, a multiscale model [32–34] is carefully checked with respect to its possible incrementally nonlinear character, forming the microscopic basis of the discussion on incremental nonlinearity.

2 Brief Presentation of the Phenomenological and Multiscale Models

2.1 The Incrementally Nonlinear Relation

The incremental constitutive equation for rate-independent media relates $\mathrm{d}\overline{\overline{\sigma}}$ and $\mathrm{d}\overline{\overline{\varepsilon}}$ by a tensorial function F_h, which depends on the previous stress–strain history through state variables and memory parameters h

$$\mathrm{d}\overline{\overline{\varepsilon}} = F_h\left(\mathrm{d}\overline{\overline{\sigma}}\right) \text{ or } \mathrm{d}\overline{\overline{\sigma}} = F_h^{-1}\left(\mathrm{d}\overline{\overline{\varepsilon}}\right). \tag{1}$$

Because of the rate-independence condition, F_h and F_h^{-1} are homogeneous functions of degree 1 (for positive values of the multiplicative parameter). Euler's identity for homogeneous functions implies $\mathrm{d}\overline{\overline{\varepsilon}} = \frac{\partial F_h}{\partial\left(\mathrm{d}\overline{\overline{\sigma}}\right)}\mathrm{d}\overline{\overline{\sigma}}$ or $\mathrm{d}\overline{\overline{\sigma}} = \frac{\partial F_h^{-1}}{\partial\left(\mathrm{d}\overline{\overline{\varepsilon}}\right)}\mathrm{d}\overline{\overline{\varepsilon}}$. Thus

$$\mathrm{d}\overline{\overline{\varepsilon}} = \overline{\overline{\overline{\overline{M}}}}_h\left(\mathrm{d}\overline{\overline{\sigma}}\right)\mathrm{d}\overline{\overline{\sigma}} \text{ or } \mathrm{d}\overline{\overline{\sigma}} = \overline{\overline{\overline{\overline{N}}}}_h\left(\mathrm{d}\overline{\overline{\varepsilon}}\right)\mathrm{d}\overline{\overline{\varepsilon}}, \tag{2}$$

where both four-order tensors $\overline{\overline{\overline{\overline{M}}}}_h$ and $\overline{\overline{\overline{\overline{N}}}}_h$ are homogeneous functions of degree 0. Finally:

$$\mathrm{d}\overline{\overline{\varepsilon}} = \overline{\overline{\overline{\overline{M}}}}_h\left(\overline{\overline{u}}\right)\mathrm{d}\overline{\overline{\sigma}} \text{ or } \mathrm{d}\overline{\overline{\sigma}} = \overline{\overline{\overline{\overline{N}}}}_h\left(\overline{\overline{\nu}}\right)\mathrm{d}\overline{\overline{\varepsilon}} \tag{3}$$

with $\overline{\overline{u}} = \mathrm{d}\overline{\overline{\sigma}}/\left\|\mathrm{d}\overline{\overline{\sigma}}\right\|$ and $\overline{\overline{\nu}} = \mathrm{d}\overline{\overline{\varepsilon}}/\left\|\mathrm{d}\overline{\overline{\varepsilon}}\right\|$. Let us consider Taylor's series expansions for M_{ijkl}

$$M_{ijkl}\left(\overline{\overline{u}}\right) = M^1_{ijkl} + M^2_{ijklmn}u_{mn} + M^3_{ijklmnpq}\,u_{mn}\,u_{pq} + \cdots \tag{4}$$

and restrict the study to the first two terms. The general expression of the incrementally nonlinear second-order constitutive relations is thus given by

$$\mathrm{d}\varepsilon_{ij} = M^1_{ijkl}\mathrm{d}\sigma_{kl} + \frac{1}{\left\|\mathrm{d}\overline{\overline{\sigma}}\right\|} M^2_{ijklmn}\ \mathrm{d}\sigma_{kl}\ \mathrm{d}\sigma_{mn} \tag{5}$$

Taking into account three other assumptions:

- relation (5) is orthotropic
- the shear moduli are incrementally linear
- there are not any "crossed" terms in relation (5)

we obtain in the orthotropic axes

$$\begin{cases} \begin{bmatrix} \mathrm{d}\varepsilon_{11} \\ \mathrm{d}\varepsilon_{22} \\ \mathrm{d}\varepsilon_{33} \end{bmatrix} = \overline{\overline{A}}_h \begin{bmatrix} \mathrm{d}\sigma_{11} \\ \mathrm{d}\sigma_{22} \\ \mathrm{d}\sigma_{33} \end{bmatrix} + \frac{1}{\|d\overline{\overline{\sigma}}\|} \overline{\overline{B}}_h \begin{bmatrix} (\mathrm{d}\sigma_{11})^2 \\ (\mathrm{d}\sigma_{22})^2 \\ (\mathrm{d}\sigma_{33})^2 \end{bmatrix}, \\ \mathrm{d}\varepsilon_{23} = 2G_1\ \mathrm{d}\sigma_{23}, \\ \mathrm{d}\varepsilon_{31} = 2G_2\ \mathrm{d}\sigma_{31}, \\ \mathrm{d}\varepsilon_{12} = 2G_3\ \mathrm{d}\sigma_{12}. \end{cases} \tag{6}$$

Let us introduce now "generalized" triaxial paths (two constant lateral stresses in fixed principal axes), "generalized" Young's moduli and "generalized" Poisson's ratios along these paths

$$E_i = \left(\frac{\partial \sigma_i}{\partial \varepsilon_i}\right)_{\sigma_j,\sigma_h} \quad (\sigma_j, \sigma_k \text{ constant lateral stresses}),$$
$$V_i^j = -\left(\frac{\partial \varepsilon_j}{\partial \varepsilon_i}\right)_{\sigma_j,\sigma_k}.$$

By distinguishing triaxial compressions ($\mathrm{d}\sigma_i > 0$, index "+") from triaxial extensions ($\mathrm{d}\sigma_i < 0$, index "−") in axial direction i, one can introduce both matrices $\overline{\overline{H}}^+$ and $\overline{\overline{H}}^-$ defined by

$$\overline{\overline{H}}^+ = \begin{bmatrix} \frac{1}{E_1^+} & -\frac{V_2^{1+}}{E_2^+} & -\frac{V_3^{1+}}{E_3^+} \\ -\frac{V_1^{2+}}{E_1^+} & \frac{1}{E_2^+} & -\frac{V_3^{2+}}{E_3^+} \\ -\frac{V_1^{3+}}{E_1^+} & -\frac{V_2^{3+}}{E_2^+} & \frac{1}{E_3^+} \end{bmatrix} \tag{7a}$$

and

$$\overline{\overline{H}}^- = \begin{bmatrix} \frac{1}{E_1^-} & -\frac{V_2^{1-}}{E_2^-} & -\frac{V_3^{1-}}{E_3^-} \\ -\frac{V_1^{2-}}{E_1^-} & \frac{1}{E_2^-} & -\frac{V_3^{2-}}{E_3^-} \\ -\frac{V_1^{3-}}{E_1^-} & -\frac{V_2^{3-}}{E_2^-} & \frac{1}{E_3^-} \end{bmatrix}. \tag{7b}$$

Finally by an identification procedure, we obtain

$$\overline{\overline{A}} = \frac{1}{2}\left(\overline{\overline{H}}^{+} + \overline{\overline{H}}^{-}\right) \quad \text{and} \quad \overline{\overline{B}} = \frac{1}{2}\left(\overline{\overline{H}}^{+} - \overline{\overline{H}}^{-}\right). \tag{8}$$

Relations (6)–(8) define the incrementally nonlinear model considered throughout this chapter.

For analytical calculus, the "octo-linear" model is extensively used. It is defined by

$$\begin{bmatrix} \mathrm{d}\varepsilon_{11} \\ \mathrm{d}\varepsilon_{22} \\ \mathrm{d}\varepsilon_{33} \end{bmatrix} = \overline{\overline{A}}_h \begin{bmatrix} \mathrm{d}\sigma_{11} \\ \mathrm{d}\sigma_{22} \\ \mathrm{d}\sigma_{33} \end{bmatrix} + \overline{\overline{B}}_h \begin{bmatrix} |\mathrm{d}\sigma_{11}| \\ |\mathrm{d}\sigma_{22}| \\ |\mathrm{d}\sigma_{33}| \end{bmatrix} \tag{9}$$

all other relations in (6)–(8) being the same. The octo-linear constitutive relation is incrementally piecewise linear in eight "tensorial zones". It can be viewed as the linear interpolation between the responses to the generalized triaxial paths, while the incrementally nonlinear relation is a quadratic interpolation. More details can be found in [13, 14, 16].

2.2 The MicroDirectional Model

Phenomenological approaches aim to directly formulate the observed phenomena in an appropriate and sometimes sophisticated mathematical formalism. They differ basically from multiscale approaches, which attempt to analyze and derive macroscopic properties from a local description of the medium. Such approaches can make use of homogenization techniques; an abundant literature deals with this subject, see for instance [29] for a thorough review. Other methods take advantage of numerical modeling such as the Discrete Element Method [1, 3, 11, 12, 23], and more recently [5, 24]. The term "multiscale" means that this range of methods was developed to account for the microstructure of granular media.

The microdirectional model belongs to the class of multiscale approaches and was initially developed to describe the behavior of snow, modeled as an assembly of ice particles [32, 33]. Fundamentally, this model is based on a homogenization procedure within a representative volume element (RVE), which is assumed to contain a "sufficient" number of spherical grains (or contacts). In this approach, the location of each grain is ignored and only contact directions are accounted for; the probability that some contacts exist in a given direction is investigated and local variables are averaged in each direction of the physical space, so that directional local variables are introduced. The homogenization procedure can be resolved in three stages: first, a kinematical localization procedure assesses the directional average displacement field $\mathrm{d}\overset{\widehat{\rightarrow}}{u}$ in terms of the macroscopic strain tensor $\mathrm{d}\overline{\overline{\varepsilon}}$; then, local constitutive equations are introduced to relate both kinematic and static directional average variables; and finally a static averaging procedure is built to infer the macroscopic stress tensor $\mathrm{d}\overline{\overline{\sigma}}$ from the distribution of directional average forces $\mathrm{d}\overset{\widehat{\rightarrow}}{F}$

between neighboring particles in contact. The complex macroscopic behavior comes from the multiplicity of intergranular contacts in various mechanical states (from elasticity to plasticity).

2.3 The Macroscopic Stress Tensor

Considering a representative volume element located around a given point M, the macroscopic stress tensor $\overline{\overline{\sigma}}$ is computed from the local contact forces $\overrightarrow{F^{\mathrm{c}}}$ between each pair of particles in contact in the RVE. The averaging procedure necessary to go from the local intergranular forces to the stress tensor has been largely discussed [10, 27, 42], and now it seems well established that $\overline{\overline{\sigma}}$ and $\overrightarrow{F^{\mathrm{c}}}$ can be related by the Love formula of homogenization:

$$\sigma_{ij} = \frac{1}{\nu_e} \sum_c F_i^{\mathrm{c}} \; l_j^{\mathrm{c}}, \tag{10}$$

where F_i^{c} is the ith component of the contact force $\overrightarrow{F^{\mathrm{c}}}$, l_j^{c} is the jth component of the branch vector $\overrightarrow{l^{\mathrm{c}}}$ joining the centers of particles in contact on contact c, and the sum is extended to all the contacts occurring in volume ν_e.

Equation (10) is expressed under a discrete formalism, but it can be extended to a continuum one by integrating over all the contact directions $\overrightarrow{n}(\theta, \varphi) = \cos\varphi \, \overrightarrow{x}_1 + \sin\varphi \cos\theta \, \overrightarrow{x}_2 + \sin\varphi \sin\theta \, \overrightarrow{x}_3$, where $(\overrightarrow{x}_1, \overrightarrow{x}_2, \overrightarrow{x}_3)$ constitutes a direct Cartesian frame of the physical space. Defining $\omega_e(\theta, \varphi) = \omega(\theta, \varphi) \, \nu_e$ the number of contacts oriented along a given direction, it follows [34]:

$$\sigma_{ij} = \int\limits_{[o;\pi]^2} 2 r_{\mathrm{g}} \; \omega(\theta, \varphi) \hat{F}_i(\theta, \varphi) n_j(\theta, \varphi) \sin\varphi \; \mathrm{d}\theta \; \mathrm{d}\varphi, \tag{11}$$

where r_{g} denotes the mean radius of the sphere-shaped grains and $\overrightarrow{\hat{F}}$ is the average of all contact forces $\overrightarrow{F^{\mathrm{c}}}$ associated with contacts oriented in the direction $\overrightarrow{n}$.

2.4 The Strain Localization Relation

The strain localization relation is inferred from the assessment of the strain energy increment on the one hand from macroscopic variables $(\overline{\overline{\sigma}}, \mathrm{d}\overline{\overline{\varepsilon}})$, and on the other hand from the average local variables $(\overrightarrow{\hat{F}}(\theta, \varphi), \mathrm{d}\overrightarrow{\hat{u}}(\theta, \varphi))$, where $\overrightarrow{\hat{u}}(\theta, \varphi)$ is the directional kinematic variable linked to $\overrightarrow{\hat{F}}(\theta, \varphi)$. Thus, if the representative volume element is macrohomogeneous [21] it can be shown that the kinematic average local field can be deduced from the macroscopic strain tensor as follows [34]:

$$\mathrm{d}\hat{u}_i(\theta, \varphi) = 2 r_{\mathrm{g}} \; \mathrm{d}\varepsilon_{ij} \; n_j(\theta, \varphi). \tag{12}$$

2.5 Local Constitutive Relations

The local behavior is described properly using a contact mechanical model relating both the local normal force $F_{\mathrm{c}}^{\mathrm{n}}$ and the local tangential force $F_{\mathrm{c}}^{\mathrm{t}}$ to both the local normal relative displacement $u_{\mathrm{c}}^{\mathrm{n}}$ and the local tangential relative displacement $u_{\mathrm{c}}^{\mathrm{t}}$. Many models have been proposed in the literature [2], the simplest one being the elastic–plastic model, which introduces a normal elastic stiffness k_{n} and a tangential elastic stiffness k_{t}, both constant, and a local friction angle φ_{g}. The following local constitutive incremental relations can be inferred:

$$\mathrm{d}F_{\mathrm{c}}^{\mathrm{n}} = k_{\mathrm{n}}\ \mathrm{d}u_{\mathrm{c}}^{\mathrm{n}}, \tag{13a}$$

$$\mathrm{d}\overrightarrow{F}_{\mathrm{c}}^{t} = \min\left\{\left\|\overrightarrow{F}_{c}^{t} + k_t\ \mathrm{d}\overrightarrow{u}_{c}^{t}\right\|, \tan\varphi_g\,(F_{\mathrm{c}}^{n} + k_{\mathrm{n}}\ \mathrm{d}u_{\mathrm{c}}^{n})\right\}\cdots\cdots \times \frac{\overrightarrow{F}_{\mathrm{c}}^{t} + k_{\mathrm{t}}\ \mathrm{d}\overrightarrow{u}_{\mathrm{c}}^{t}}{\left\|\overrightarrow{F}_{\mathrm{c}}^{t} + k_{\mathrm{t}}\ \mathrm{d}\overrightarrow{u}_{\mathrm{c}}^{t}\right\|} - \overrightarrow{F}_{\mathrm{c}}^{t}. \tag{13b}$$

Furthermore, granular assemblies are not able to sustain local tensile stress. This is a fundamental feature of this type of material. The following condition is therefore added

$$F_{\mathrm{c}}^{n} > 0. \tag{14}$$

It will be assumed hereafter that (13)–(14) also apply to the directional average variables $\hat{\overrightarrow{u}}(\theta,\varphi)$ and $\hat{\overrightarrow{F}}(\theta,\varphi)$.

3 Physical Bases of Incremental Nonlinearity

3.1 Phenomenological Description of Incremental Nonlinearity

As recalled in the introduction and formalized by (3), the question of incremental nonlinearity corresponds to the directional variation of the constitutive tensor $\overline{\overline{M}}$ (or respectively $\overline{\overline{N}}$) with the direction of the incremental stress (or respectively the incremental strain). The existence of constitutive tensors $\overline{\overline{M}}$ and $\overline{\overline{N}}$ and their variations only with the directions of $\mathrm{d}\overline{\overline{\sigma}}$ and $\mathrm{d}\overline{\overline{\varepsilon}}$ are direct consequences of the rate-independence assumption. Relations (3) can be viewed as general canonical expressions of elastoplastic relations. Then specific assumptions were proposed to express this directional variation of $\overline{\overline{M}}$ with $\overline{\overline{u}}(\overline{\overline{u}} = \mathrm{d}\overline{\overline{\sigma}}/||\mathrm{d}\overline{\overline{\sigma}}||)$, either continuously (i.e., thoroughly incrementally nonlinear relations) or discontinuously (i.e., incrementally piecewise linear relations). In this last case, the constitutive relation is linear inside a finite number of hypercones in the six-dimensional $\mathrm{d}\overline{\overline{\sigma}}$ space. These adjacent hyper-cones have the origin of $\mathrm{d}\overline{\overline{\sigma}}$ space as a common apex. They have been called "tensorial

zones" [13,14]. From a physical point of view, Hill has shown that monocrystals with a finite number of sliding planes exhibit an incrementally piecewise linear mechanical behavior [19,20,22]. If one wishes to roughly generalize this reasoning to granular media with a very high number of intergranular sliding directions, one obtains an incrementally nonlinear behavior. This is essentially the reason why we developed incrementally nonlinear constitutive relations for geomaterials in the 1980s. However, in this chapter we will see that a proper micromechanical investigation sheds new light on this question.

It is difficult to find discriminating experiments to clarify this point of incremental nonlinearity. One way is to try to determine the response-envelopes (in Gudehus's sense [17]). At a given stress–strain state, incremental probing stresses with the same norm ($||\mathrm{d}\overline{\overline{\sigma}}|| = \text{const}$) are applied in all stress directions. The extremities of the incremental strain responses form a diagram which is called the "response-envelope" [17]. If the behavior is incrementally piecewise linear, the response-envelopes are constituted by arcs of ellipses (whose centers are the incremental strain origin), while in the incremental nonlinear case the diagrams have no simple analytical equation. The experimental results in Fig. 1 were obtained by Royis and Doanh [38], who compared their results with those given by the octo-linear model and the nonlinear model. After an initial isotropic compression, a drained triaxial loading test is simulated in axisymmetric conditions, and then a stress probe test is performed. A stress increment $\mathrm{d}\overrightarrow{\sigma}$ in all directions with the same norm is imposed, and the strain response $\mathrm{d}\overrightarrow{\varepsilon}$ is computed. Even if the agreement is good, the only proper conclusion is that a classical elastoplastic relation (incrementally bilinear) would describe such diagrams with difficulty since it considers only two arcs of centered ellipses.

In conclusion, while experiments have shown the behavior of geomaterials to be incrementally nonlinear, the phenomenological description of such

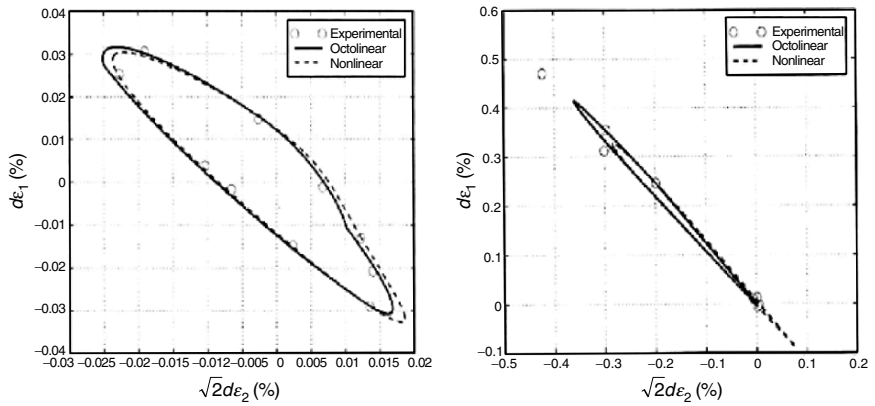

Fig. 1. Experimental response-envelopes compared to those given by the octo-linear constitutive relation and the incrementally nonlinear relation [38]

a behavior is quite natural when using a proper directional variation of the constitutive tensor with respect to the incremental stress (or strain) direction. The ultimate reason for this type of behavior remains hidden, as do its essential parameters, in this phenomenological modeling scheme. Both these questions are now considered through a micromechanical investigation.

4 MicroMechanical Description of Incremental Nonlinearity

4.1 Incremental Formulation of the Microdirectional Model

Let us restrict our analysis to axisymmetric conditions. Denoting (x_1) the axial axis of the cylinder-like specimen and ignoring as a first approximation the change in the microstructure, it can be shown that constitutive relations can be expressed in the following incremental form [16]:

$$\mathrm{d}\sigma_1 = A_{11}\ \mathrm{d}\varepsilon_1 + A_{12}\ \mathrm{d}\varepsilon_2, \tag{15}$$

$$\mathrm{d}\sigma_2 = A_{21}\mathrm{d}\varepsilon_1 + A_{22}\ \mathrm{d}\varepsilon_2. \tag{16}$$

We only detail the first term A_{11}

$$A_{11} = \frac{3}{2N_\mathrm{g} r_\mathrm{g}^2}\frac{\rho_o}{\rho_\mathrm{g}}\int_0^\pi \left\{ \frac{2r_\mathrm{g}\left(k_\mathrm{n}\cos^3\varphi + k_\mathrm{tn}\cos^2\varphi\sin\varphi + k_\mathrm{tt}\cos\varphi\sin^2\varphi\right)\omega_e(\varphi)}{1-\varepsilon_1-2\varepsilon_2} + \frac{\left(\hat{F}_\mathrm{n}(\varphi)\cos\varphi + \hat{F}_\mathrm{t}(\varphi)\sin\varphi\right)\omega_e(\varphi)}{\left(1-\varepsilon_1-2\varepsilon_2\right)^2} \right\} \cos\varphi\sin\varphi\ \mathrm{d}\varphi \tag{17}$$

with $k_\mathrm{tt} = k_\mathrm{t}, k_\mathrm{tn} = 0$ in the elastic regime, and $k_\mathrm{tt} = 0, k_\mathrm{tn} = \tan\varphi_\mathrm{g}\ k_\mathrm{n}$ in the plastic regime.

4.2 Micro-Mechanical Discussion

In its fundamentals, the microdirectional model can be regarded as an association of multiple elastic–plastic bodies; each body, related to a given contact direction, takes into account the behavior of contacts in this direction. As described by (13a) and (13b), the frictional contact model shows full incremental linearity, in respectively the elastic and plastic domains. However, at a given stress state, after a given loading history, contacts will not be in the same state: some of them are in a plastic state (plastic contacts), and the other contacts are in an elastic state (elastic contacts). Within a directional approach, it is advantageous to conventionally extend the notion of the elastic or plastic state to the contact directions. Equation (17) reveals that the unique source of nonlinearity comes from the terms k_tt and k_tn, the value of

which depends on the mechanical state of contacts in direction $\overrightarrow{n}(\varphi)$. Nonlinearity may therefore only occur during transition from the elastic regime to the plastic regime, and conversely. The state of the directions is likely to change as a function of the direction of the loading. Only a few directions are likely to evolve from an elastic state toward a plastic state, because the mechanical state of such directions must be near the plastic limit. On the contrary, as a function of the direction of the local incremental force, several plastic directions may recover an elastic state. This can thoroughly be investigated from an analytical point of view. For this purpose, let us define the elastic index r_{el} of plastic directions which recover an elastic state after a strain probe; if N_{pl} denotes the initial number of plastic directions and $N_{\mathrm{pl}}(\alpha)$ denotes the number of plastic directions just after an incremental loading of direction α, r_{el} is expressed as

$$r_{\mathrm{el}} = \frac{N_{\mathrm{pl}} - N_{\mathrm{pl}}(\alpha)}{N_{\mathrm{pl}}}. \tag{18}$$

To go further, let us particularize the loading path. After an axisymmetric drained triaxial loading, a strain probe of direction α_ε and of norm $\mathrm{d}e$ is imposed: $\mathrm{d}\varepsilon_1 = \mathrm{d}e \sin\alpha_\varepsilon$ and $\mathrm{d}\varepsilon_2 = \frac{\sqrt{2}}{2}\mathrm{d}e\cos\alpha_\varepsilon$. Let us consider a plastic direction $\overrightarrow{n}(\varphi)$. For this direction, $\left|\hat{F}_{\mathrm{t}}\right| = \tan\varphi_{\mathrm{g}}\hat{F}_{\mathrm{n}}$, and this plastic direction recovers an elastic state if

$$\left|\tilde{F}_{\mathrm{t}} + k_{\mathrm{t}}\ \mathrm{d}\tilde{u}_{\mathrm{t}}\right| < \tan\varphi_{\mathrm{g}}\left(\tilde{F}_{\mathrm{n}} + k_{\mathrm{n}}\ \mathrm{d}\tilde{u}_{\mathrm{n}}\right). \tag{19}$$

If we denote s_ε the sign of $\cos\varphi\sin\varphi\,(\varepsilon_1 - \varepsilon_2)$ and s_α the sign of $\sqrt{2}\sin\alpha_\varepsilon - \cos\alpha_\varepsilon$, it can be shown [16] that (19) gives

$$\begin{aligned} s_\alpha\left(s_\varepsilon\left|\cos\varphi\sin\varphi\right| - \frac{k_{\mathrm{n}}\tan\varphi_{\mathrm{g}}}{k_{\mathrm{t}}}\cos^2\varphi\right) < \cdots \\ \frac{k_{\mathrm{n}}\tan\varphi_{\mathrm{g}}}{k_{\mathrm{t}}}\frac{\cos\alpha_\varepsilon}{\left|\sqrt{2}\sin\alpha_\varepsilon - \cos\alpha_\varepsilon\right|}. \end{aligned} \tag{20}$$

As a consequence, the plastic direction defined by the angle φ recovers an elastic state after a strain probe defined by the angle α_ε if we have: $s_\alpha s_\varepsilon\left|\cos\varphi\sin\varphi\right| - \frac{k_{\mathrm{n}}\tan\varphi_{\mathrm{g}}}{k_{\mathrm{t}}}\cos^2\varphi < \frac{k_{\mathrm{n}}\tan\varphi_{\mathrm{g}}}{k_{\mathrm{t}}}\frac{\cos\alpha_\varepsilon}{\left|\sqrt{2}\sin\alpha_\varepsilon - \cos\alpha_\varepsilon\right|}$. Let us now consider the function χ defined by

$$\chi\left(\alpha_\varepsilon\right) = \frac{k_{\mathrm{n}}\tan\varphi_{\mathrm{g}}}{k_{\mathrm{t}}}\frac{s_\alpha\cos\alpha_\varepsilon}{\left|\sqrt{2}\sin\alpha_\varepsilon - \cos\alpha_\varepsilon\right|}.$$

It can be shown that the function $\psi(\varphi) = s_\varepsilon\left|\cos\varphi\sin\varphi\right| - \frac{k_{\mathrm{n}}\tan\varphi_{\mathrm{g}}}{k_{\mathrm{t}}}\cos^2\varphi$, which is continuous over the range $[0;\pi]$, has a minimum (denoted Min) and a maximum (denoted Max) over the range of plastic directions. Thus, if, when $s_\alpha = 1, \chi\left(\alpha_\varepsilon\right) >$ Max or when $s_\alpha = -1, \chi\left(\alpha_\varepsilon\right) <$ Min, the index r_{el} is equal to 1.

if Min $< \chi(\alpha_\varepsilon) <$ Max whatever s_α, then $0 < r_{\mathrm{el}} < 1$;
if, when $s_\alpha = 1, \chi(\alpha_\varepsilon) <$ Min or when $s_\alpha = -1, \chi(\alpha_\varepsilon) >$ Max,

then $r_{\mathrm{el}} = 0$; the strain probe does not affect the state of the plastic directions.

In light of this analysis, it can be concluded that the change in the number of plastic directions, characterized by the index of elasticity, depends explicitly on the loading direction. This makes it possible to conclude that globally the tangent stiffness matrix depends on the strain probe direction. The incremental nonlinear character is all the more pronounced since the domain containing plastic directions is extended. The purpose of the following section is to confirm these results from numerical investigations.

4.3 Numerical Investigation

The previous axisymmetric loading path was simulated and then Gudehus response-envelopes [17] were built. At a given loading state defined by $\eta = \frac{q}{p} = 3\frac{\sigma_1 - \sigma_2}{\sigma_1 + 2\sigma_2} = 0.705$, a strain probe test is performed. A strain increment $\mathrm{d}\overrightarrow{\varepsilon}$ in all directions with the same norm is imposed, and the stress response $\mathrm{d}\overrightarrow{\sigma}$ is computed. Constitutive parameters used in this simulation are reported in Table 1.

We analyze how tangent stiffness matrix $\overline{\overline{A}}$ evolves as a function of strain probe direction α_ε. Without altering the generality of the investigation, only term A_{11} is considered. Over the range $[0; 2\pi]$, the tangent stiffness matrix depends on the direction of strain increments, which is clear evidence of incrementally nonlinear behavior (Fig. 2). In addition, a strong correlation between the elasticity index and A_{11} can be pointed out in Fig. 2. It is worth noting the outstanding analogy between the incrementally nonlinear model [13] and the microdirectional model. Even though both these models differ in their basic assumptions, they are within the continuity of Hill's multislip theory [19,20,22]; for a certain class of materials such as metals, which can be considered as a set of element crystals, preferential sliding directions exist. For the incrementally nonlinear model, this character is contained in the canonical constitutive equations written on the macroscopic scale [13]. For the multiscale model this character comes from an idealized description of granular assemblies based on the distribution of contact directions. The directional character can be regarded as a straightforward physical consequence of the micromechanical

Table 1. Axisymmetric triaxial test: constitutive parameters and initial conditions

initial isotropic stress (MPa)	initial void ratio	k_{n} (kN m)	k_{t} (kN m)	φ_{g} (°)
0.125	0.66	15,708	6830	15

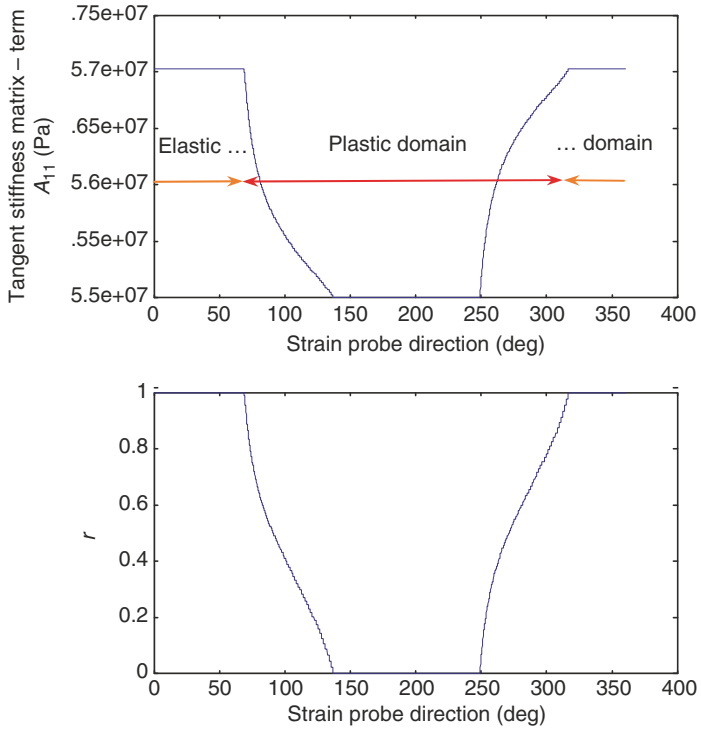

Fig. 2. Correlation between the elastic index r_{el} and the tangent stiffness matrix

description at the local level. This is an outstanding aspect of the microdirectional model, which brings a microstructural basis for the incremental nonlinearity of granular material behavior.

5 Concluding Remarks

Throughout this chapter we have attempted to discuss one outstanding feature of the constitutive behavior of granular materials, namely their incrementally nonlinear character. For this purpose, two types of models were considered: the first one is the incrementally nonlinear model, which is essentially a phenomenological model; the second one is the microdirectional model, built from a multiscale approach. These two models have clearly pointed out the incrementally nonlinear character of granular materials. It is quite remarkable that these two models, which are basically different in their approaches, highlight both this outstanding aspect of granular masses. In addition, the microdirectional model, which is micromechanically based, gives rise to an interpretation of the origin of this property; it appears that this feature (as far as the rolling motion of particles can be omitted) is related to the dependence of the

mechanical state of each contact (in the elastic or plastic regime) with respect to the direction of local loading. We should emphasize that the rolling of particles, responsible to a large extent for the so-called "buckling" effect [37], could constitute another microstructural source of incremental nonlinearity. If this property can be finally regarded as a basic ingredient of the incrementally nonlinear model, it stands rather as a consequence of the description of contacts in the case of the microdirectional model.

References

1. Bardet, J.P. (1994): Numerical simulations of the incremental responses of idealized Granular Materials. Int. J. Plast., Vol. 10, no. 8, pp. 879–908
2. Bardet, J.P. (1998): Introduction to computational granular mechanics. *In* Behaviour of Granular Materials, Edited by B. Cambou, Springer, New York, pp. 99–169
3. Bardet, J.P., and Proubet, J. (1989): Application of micro-mechanics to incrementally nonlinear constitutive equations for granular media. *In* Powders and Grains, Edited by J. Biarez and R. Gourvès, pp. 265–273
4. Caillerie, D. (1995): Evolution quasistatique d'un milieu granulaire, loi incrémentale par homogénéisation. *In* Des matériaux aux ouvrages, Hermès Publications, pp. 53–80
5. Calvetti, F., Viggiani, C., and Tamagnini, C. (2003): A numerical investigation of the incremental behavior of granular soils. Ital. Geotechn. J., no. 3, pp. 11–29
6. Cambou, B. (1993): From global to local variables in granular materials. *In* Powders and Grains, Thorton Ed., Balkema, Rotterdam, pp. 73–86
7. Cambou, B., Dubujet, P., Emeriault, F., and Sidoroff, F. (1995): Homogenization for granular materials. Eur. J. Mech. A/Solids, Vol. 14, no. 2, pp. 255–276
8. Chang, C.S. (1992): Micromechanical modelling of deformation and failure for granulates with frictional contacts. Mech. Mater., Vol. 16, pp. 13–24
9. Chang, C.S., and Liao, C.L. (1994): Estimates of elastic modulus for media of randomly packed granulates. Appl. Mech. Rev., Vol. 47, pp. 197–206
10. Christoffersen, J., Mehrabadi, M.M., and Nemat-Nasser, S. (1981): A micromechanical description of granular material behavior. J. Appl. Mech., Vol. 48, pp. 339–344
11. Cundall, P.A. and Roger, D.H. (1992): Numerical modelling of discontinua, Eng Computat, Vol. 9, pp. 101–113
12. Cundall, P.A., and Strack, O.D.L. (1979): A discrete numerical model for granular assemblies. Géotechnique, Vol. 29, pp. 47–65
13. Darve, F. (1990): The expression of rheological laws in incremental form and the main classes of constitutive equations. *In* Geomaterials Constitutive Equations and Modelling, F. Darve ed., Taylor and Francis Books, pp. 123–148
14. Darve, F., and Labanieh, S. (1982): Incremental constitutive law for sands and clays, simulations of monotonic and cyclic tests. Int. J. Numer. Anal. Methods in Geomech., Vol. 6, pp. 243–275
15. Darve, F., and Nicot, F. (2005): On incremental non linearity in granular media: phenomenological and multi-scale views (Part I). Int. J. Num. Anal. Methods in Geomechanics. Vol. 29, pp. 1387–1409.

16. Darve, F., Flavigny, E., and Meghachou, M. (1995): Yield surfaces and principle of superposition revisited by incrementally non-linear constitutive relations. Int. J. Plast., Vol. 11, no. 8, pp. 927–948
17. Gudehus, G. (1979): A comparison of some constitutive laws for soils under radially symmetric loading and unloading. *In* 3rd Int. Conference on Numerical Methods in Geomechanics, Aachen and Wittke Eds., Balkema, Vol. 4, pp. 1309–1324
18. Gudehus, G., Darve, F., and Vardoulakis, I. (1984): Constitutive relations for soils, A.A. Balkema
19. Hill, R. (1965): Continuum micro-mechanics of elastoplastic polycrystals. J. Mech. Phys. Solids, Vol. 13, pp. 89–101
20. Hill, R. (1966): Generalized relations for incremental deformation of metal crystals by multislip. J. Mech. Phys. Solids, Vol. 14, no. 2, pp. 95–102
21. Hill, R. (1967a): The essential structure of constitutive laws for metal composites and polycrystals. J Mech. Phys. Solids, Vol. 15, no. 2, pp. 79–95
22. Hill, R. (1967b): Eigenmodal deformations in elastic-plastic continua. J. Mech. Phys. Solids, Vol. 15, pp. 371–386
23. Kishino, Y. (1988): Disc model analysis of granular media. *In* Micromechanics of Granular Materials, 2nd US–Japan Seminar on Mechanical. Granular Materials, M. Satake and J.T. Jenkins Eds., Elsevier, pp. 143–152
24. Kishino, Y. (2003): On the incremental nonlinearity observed in a numerical model for granular media. Ital. Geotech. J., no. 3, pp. 30–38.
25. Love, A.E.H. (1927): A Treatise of Mathematical Theory of Elasticity. Cambridge University Press, Cambridge.
26. Mehrabadi, M.M., and Cowin, S.C. (1978): Initial planar deformation of dilatant granular materials. J. Mech. Phys. Solids, Vol. 26, pp. 269–284
27. Mehrabadi, M.M., Oda, M., and Nemat-Nasser, S. (1982): On statistical description of stress and fabric in granular materials. Int. J. Numer. Anal. Methods Geomech., Vol. 6, pp. 95–108
28. Mehrabadi, M.M., Loret, B., and Nemat-Nasser, S. (1993): Incremental constitutive relations for granular materials based on micromechanics. *In* Proceedings of Royal Society London, Vol. 441, pp. 433–463
29. Nemat-Nasser, S. (2004): Plasticity, A Treatise on the Finite Deformation of Heterogeneous Inelastic Materials. Cambridge University Press, Cambridge
30. Nemat-Nasser, S., and Mehrabadi, M.M. (1983): Stress and fabric in granular masses. *In* Mechanics of Granular Materials, New Models and Constitutive Relations, J.T. Jenkins and M. Satake, Eds., Elsevier Science, pp. 1–8
31. Nemat-Nasser, S., Mehrabadi, M.M., and Iwakuma, T. (1981): On certain macroscopic and microscopic aspects of plastic flow of ductile materials. *In* Three-dimensional Constitutive Relations and Ductile Fracture, S. Nemat-Nasser, Ed., North Holland, pp. 157–172
32. Nicot, F. (2003): Constitutive modelling of a snowcover with a change in scale. Eur. J. Mech. (A/Solids), Vol. 22–3, pp. 325–340
33. Nicot, F. (2004): From a constitutive modelling of a snowcover to the design of flexible structures. Part I, Mechanical modelling. Int. J. Solids. Struct. Vol. 41/11–12, pp. 3317–3337
34. Nicot, F., and Darve, F. (2005): A multiscale approach to granular materials. Mech. Mater., *In press.*
35. Oda, M. (1972): The mechanism of fabric changes during compressional deformation of sand. Soils Found., Vol. 12, pp. 1–23

36. Oda, M., and Konishi, J. (1974) : Microscopic deformation mechanism of granular material in simple shear. Soils Found., Vol. 14, no. 4, pp. 15–32
37. Oda, M., Konishi, J., and Nemat-Nasser, S. (1982) : Experimental evaluation of strength of granular materials, effects of particle rolling. Mech. Mater., Vol. 1, pp. 269–283
38. Royis, P., and Doanh, T. (1998): Theoretical analysis of strain response envelopes using incrementally non-linear constitutive equations. Int. J. Numer Analy. Methods in Geomech., Vol. 22, pp. 97–132
39. Saada, A., and Bianchini, G. (1987): Constitutive Equations for Granular Noncohesive Soils. Proceedings of the International Workshop, Cleveland, Ohio, 22–24 July 1987. *Edited by* A.S. Saada and G.F. Bianchini. A.A. Balkema, Rotterdam, The Netherlands
40. Satake, M. (1978): Constitution of mechanics of granular materials through graph representation. *In* Theoretical and Applied Mechanics, Vol. 26, University of Tokyo Press, pp. 257–266
41. Satake, M. (1982): Fabric tensor in granular materials. *In* IUTAM Conference on Deformation and Failure of Granular Materials, Delft, pp. 63–68
42. Weber, J. (1966): Recherches concernant les contraintes intergranulaires dans les milieux pulvérulents. Bull. Liaison P. Ch., no. 20, pp. 1–20

Long-term Deformations in Soils due to Cyclic Loading

A. Niemunis, T. Wichtmann, and T. Triantafyllidis

Institute of Soil Mechanics and Foundation Engineering, Ruhr-University Bochum, Germany
Andrzej.Niemunis@rub.de

1 Introduction

A substantial accumulation of irreversible strains in soils may appear due to cyclic loading even at relatively small amplitudes. After a large number of cycles the long-term serviceability of structures may be endangered. Under poorly drained conditions, in place of the usual densification, excessive pore pressure is generated. It may lead to soil liquefaction and eventually to a loss of the overall stability. The accumulation effects described by high cycle models refer to a large number ($>10^3$) of small to moderate total strain amplitudes ($<10^{-3}$). The phenomenon of accumulation has been described by a high-cycle explicit model. Laboratory testing of high cyclic behaviour is very laborious and therefore most explicit models in the literature are focussed on a very specific practical application only. Compared to them the presented high-cycle model of sand is attempted to be more comprehensive. The performance of the model in calculations of (differential) settlements of shallow foundations is demonstrated.

A cycle (=loop) can be conveniently decomposed into a cumulative part and a resilient part using a hodograph, Fig. 1. We usually speak of strain and stress cycles but the term cycle can be generalized to any state variable (scalar or tensorial) $\sqcup$. Having plotted the path $\sqcup(t)$ we define the *average* value $\sqcup^{\rm av}$ to be the centre of the smallest hypersphere that encompasses all $\sqcup(t)$ within a single period T. Alternatively, $\sqcup^{\rm av}$ can be defined as the middle point between the two most distant states (much easier numerical implementation). The amplitude of a scalar variable is defined as $\sqcup^{\rm ampl} = \max|\sqcup - \sqcup^{\rm av}|$. A more elegant concept of the *tensorial strain amplitude* is introduced in Sect. 3. It describes not only the size but also the polarization and the ovality of a cycle.

It turns out that (See notation in Appendix A) $\mathbf{D}^{\rm acc}$ depends strongly on several subtle properties of soil and not on stress and void ratio only. Two new state variables are therefore proposed: the cyclic preloading g^A which memorizes the amount of fatigue preloading and the back polarization $\boldsymbol{\pi}$ memorizing the recent orientation of cycles (weighted by their size), see Sects. 2.3 and 3.2.

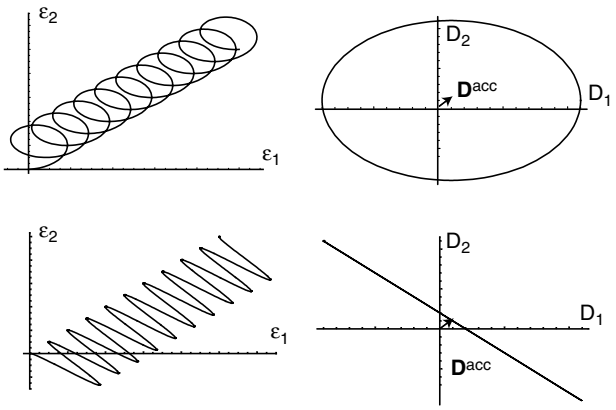

Fig. 1. A hodograph is a trajectory of $\mathbf{D}(t) \approx \dot{\boldsymbol{\epsilon}}$ parametrized with time t, analogously to the strain path $\boldsymbol{\epsilon}(t)$. The rate of accumulation can be easily identified as a drift rate (denoted with *arrow*) of the average strain upon a cycle. Note that the strain rate is an exactly periodic function $\mathbf{D}(t) = \mathbf{D}(t+NT)$ whereas the strain $\boldsymbol{\epsilon}(t)$ is not. The distinction between the cycles encompassing some area (out-of-phase cycles (=OOP) , *above*) and the open-curve cycles(in-phase cycles (=IP), *below*) will be of importance

Displacements of structures due to cyclic loading of subsoil are often predicted using *settlement formulas*, e.g. [11, 28]. The settlement $s(N)$ after N cycles is extrapolated from the residual settlement s_1 after the first cycle. Various empirical functions, e.g. $s(N) = s_1 N^C$ or $s(N) = s_1(1 + C \ln N)$ with a material constant C, were proposed in the literature. In this paper, we argue that the accumulation depends on numerous factors, see Sect. 2, which are too complicated to be lumped together into a single parameter s_1. Moreover, most of the popular settlement formulas are self-contradictory (inconsistent), as demonstrated in Appendix B.

1.1 Accumulation as a Phenomenon

The phenomenon of *accumulation* manifests itself as a summation of small residual strains (pseudo-creep) or residual stresses (pseudo-relaxation). For the two-dimensional case it is shown schematically in Fig. 2. If stress cycles are applied, Fig. 2a, we observe cyclic pseudo-creep and if strain cycles are applied, Fig. 2b, we obtain cyclic pseudo-relaxation. Many laboratory tests are mixed-controlled, so both, pseudo-relaxation and pseudo-creep, may occur simultaneously, Fig. 2c. The unspecified term *accumulation* seems, therefore, to be a convenient notion covering the cyclic pseudo-relaxation as well as the cyclic pseudo-creep. In order to understand accumulation in this general sense (independently of the technical aspect how an experiment is controlled) we have to introduce a constitutive relation (at this place let it be slightly

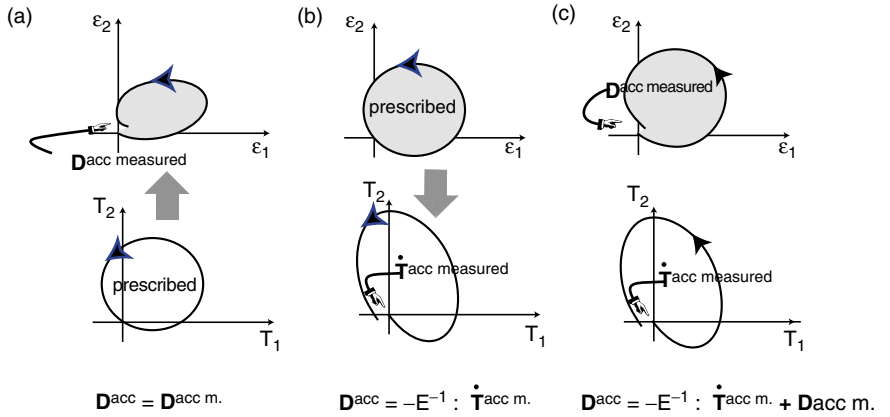

Fig. 2. (**a**) Stress cycles (= all stress components are prescribed and the stress loop is perfectly closed) leave residual strains. (**b**) Strain cycles leave residual stresses. (**c**) Mixed control tests leave both residual stresses and residual strains. Pure accumulation (not superposed by monotonic loading) is considered and therefore $\mathbf{D}^{\mathrm{pl}}$ can be disregarded. The superscript ⊔m. stands for 'measured'

simplified compared to (2))

$$\mathring{\mathbf{T}} = \mathtt{E} : (\mathbf{D} - \mathbf{D}^{\mathrm{acc}}), \tag{1}$$

wherein $\mathring{\mathbf{T}}$ is the Zaremba-Jaumann rate of the Cauchy stress, $\mathbf{D}$ denotes the total stretching, $\mathtt{E}$ is a pressure-dependent (hypo)elastic stiffness and $\mathbf{D}^{\mathrm{acc}}$ *would be* the rate of strain accumulation cyclic loading if the experiment were fully stress-controlled. The notation is explained in Appendix A. We have good reasons to express both the intensity of cyclic loading and the accumulation in terms of strain (i.e. of strain amplitude and of strain accumulation rate, respectively). Note, however, that imposing strain (amplitude) we preclude direct observation of strain (accumulation) as a material response. Therefore (1) is indispensable already for the evaluation of laboratory tests, Fig. 2. The actually measured response of the material is denoted by superscript m.

1.2 The High-Cycle Approach

Two computational strategies are usually followed for dealing with the cyclic loading:

- An *implicit calculation* of accumulation
- An *explicit calculation* (or a high-cycle) of accumulation.

The conventional (= implicit) constitutive models describe each loop proceeding by small strain increments. The accumulation of stress or strain appears as a by-product resulting from the fact that the strain or stress loops are

not perfectly closed (accumulation is "implied"). Quite sophisticated (e.g. endochronic [39] or multi-surface constitutive models [3, 4, 21]) are usually required. However, their practical applicability is limited by the number of cycles, say $N = 1,000$, because inevitable cumulative errors (inaccuracies in the constitutive model and numerical problems resulting form its implementation) become dominant. The high-cycle model proposed in this paper follows the other strategy (known also as *N-type* formulation). Explicit models [1,2,8,12,14,16–18,30,32,34–37,40,44] are similar to the viscoplastic ones in which in place of time t the number N of cycles is used. The accumulation of strain due to a package of ΔN cycles of a given amplitude is predicted directly. For example, an increment of $\Delta N = 25$ cycles with the amplitude $\epsilon^{\mathrm{ampl}} = 10^{-4}$ results in an irreversible strain $\mathbf{D}^{\mathrm{acc}}\Delta N$ wherein $\mathbf{D}^{\mathrm{acc}}$ is given by the explicit formula (5). As we shall see, this is the essential equation of the presented model. The explicit strategy is explained in the following flowchart and by Fig. 3:

1. Calculate the initial stress field (from self weight and all monotonic loads) in soil. To obtain a realistic initial stress one should use a good model for monotonic loads (not an elastic one)
2. Calculate implicitly two first load cycles (for reasons discussed further in text) recording the strain path $\boldsymbol{\epsilon}(t)$ in the second one (=first regular cycle) at each integration point. The size of the amplitude is of great importance so one should use a good model for hysteretic behaviour and small-strain nonlinearity (e.g. multi-surface plasticity or, as we do, the extended hypoplasticity [25])
3. Evaluate the *strain amplitude*. In general case it is a fourth-order tensor $\mathtt{A}_\epsilon$ discussed in Sect. 3. The size of the amplitude is assumed constant over subsequent cycles until it is recalculated in a control cycle. In fresh pluviated samples a clear (up to 15%, [42]) stiffening is of soil is observed during the first 100-1,000 cycles. Such *conditioning phase* should be considered in the hysteretic model and in this phase the amplitude should be reevaluated more frequently than afterwards.

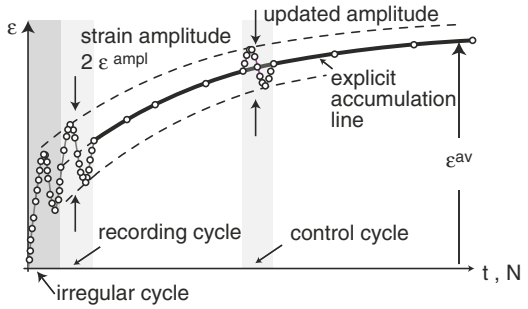

Fig. 3. The basic idea of explicit calculation of the cumulative deformation

4. Find the accumulation rate $\mathbf{D}^{\mathrm{acc}}$ of strain using the explicit formula (5). In the subsequent cycles only the general trend of the accumulation is calculated. This trend is depicted with the thick line in Fig. 3.
5. Find the Zaremba-Jaumann stress rate from the constitutive equation

$$\mathring{\mathbf{T}} = \mathtt{E} : (\mathbf{D} - \mathbf{D}^{\mathrm{acc}} - \mathbf{D}^{\mathrm{pl}}) \tag{2}$$

and the stress increment $\Delta\mathbf{T} = \mathring{\mathbf{T}}\Delta N$ caused by a package of ΔN cycles (= a single increment of the fatigue load). The number of cycles N is treated as a *continuous* time-like variable so the material "rate" of $\sqcup$ is understood as its increase "per cycle"

$$\dot{\sqcup} = \mathrm{d}\sqcup/\mathrm{d}N \tag{3}$$

in the explicit-model context. The Zaremba-Jaumann rate should also be understood "per-cycle". The presence of the conventional plastic strain rate $\mathbf{D}^{\mathrm{pl}}$ in (2) and the advantage of (2) over (1) is explained in Sect. 1.3.

The FE program redistributes stress in the course of equilibrium iteration, in effect of which $\mathbf{D}^{\mathrm{acc}}$ leads to settlements or to pseudo-relaxation, depending on the boundary conditions.

1.3 Need for Plastic Strain Rate $\mathbf{D}^{\mathrm{pl}}$

At first it might seem surprising that the plastic stretching $\mathbf{D}^{\mathrm{pl}}$ caused by monotonic loading and the cumulative stretching $\mathbf{D}^{\mathrm{acc}}$ are treated separately in (2). Indeed, from the physical point of view they cannot be distinguished. The decomposition of the irreversible strain rate into $\mathbf{D}^{\mathrm{pl}}$ and $\mathbf{D}^{\mathrm{acc}}$ is forced by the explicit strategy of calculation. Implicit models need not such separation.

To understand the usefulness of $\mathbf{D}^{\mathrm{pl}}$ it is instructive to consider a simple 1-dimensional rod made of a tension cut-off material and fixed at both ends. During a cooling process (=thermic shrinkage) tensile stress may occur. However, since no tension is allowed for, the plastic strains are indispensable. In other words, a constitutive model of the form $\dot{T} = E(D - D^{\mathrm{thermic}} - D^{\mathrm{pl}})$ is required because $\dot{T} = E(D - D^{\mathrm{thermic}})$ would lead to contradiction with the tension cut-off assumption. At first, one could expect that unlike the thermic deformation, the fatigue loading does not require plastic strains because pseudo-relaxation nudges the stress inward the yield surface. Inferring from element tests, the stress paths could not surpass e.g. the Matsuoka and Nakai [19] yield surface in the process of pseudo-relaxation because the flow rule $\mathbf{m}$ points to the outside of the yield surface, Fig. 7, and therefore the relaxation $\mathring{\mathbf{T}}^{\mathrm{acc}} = -\mathtt{E} : \mathbf{D}^{\mathrm{acc}}$ tends inwards. However, the absence of $\mathbf{D}^{\mathrm{pl}}$ does lead to severe problems in FE calculations! Tension or excessive stress ratios may appear if cyclic loading is superposed by a simultaneous monotonic loading which enforces a plastification. Even in boundary value problems under a

purely fatigue loading but with a strongly *inhomogeneous spatial distribution* of the accumulation rate (1) can inflict excessive shear or tensile stresses. For example, it is the case if an element that experiences little or no direct fatigue loading itself had a strongly loaded neighbour. The plastic rate $\mathbf{D}^{\mathrm{pl}}$ would be indispensable in the weakly loaded element to ensure the compliance with the large deformation outside.

The Matsuoka and Nakai [19] yield condition (M–N) with the associated flow rule is used to calculate $\mathbf{D}^{\mathrm{pl}}$. First the accumulation rate $\mathbf{D}^{\mathrm{acc}}$ and the elasto-cumulative predictor

$$\mathbf{T} + \mathtt{E} : (\mathbf{D} - \mathbf{D}^{\mathrm{acc}})\Delta N, \tag{4}$$

should be determined. If a return mapping onto the yield surface is necessary then it must be accompanied by a plastic deformation. The procedure is identical as in elasto-plastic algorithms. The isotropic hypoelastic stiffness $\mathtt{E}$ with a constant Poisson's ratio ($\approx$0.2) and with a pressure dependent Young modulus ($\sim(p/p_{\mathrm{atm}})^{2/3}$) is used in (2) and in (4). The *hyperelasticity* is not obligatory in the explicit formulations but it is of great importance, e.g. [24], for implicit models.

1.4 Strain Amplitude vs. Stress Amplitude

We have chosen to express the magnitude of a cycle in terms of strain ϵ^{ampl} rather than of stress T^{ampl} for three reasons. First, T^{ampl} does not provide precise information about very large amplitudes. From T^{ampl} alone one cannot distinguish between the cycles that are just touching the yield surface and those which penetrate the plastic region, Fig. 4. They have the same stress amplitude but very different strain amplitudes and cause different accumulations. Second, a usage of T^{ampl} would require a reformulation of f_p

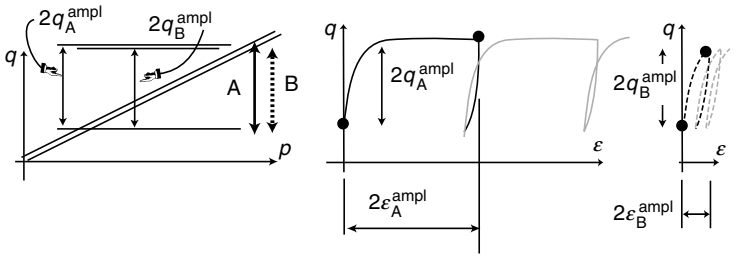

Fig. 4. Unsymmetric stress-controlled cycles. The large cycles A (*solid line*) which encounter the yield surface (*double line*) are poorly described by the stress amplitude $q_{\mathrm{A}}^{\mathrm{ampl}}$ alone. The stress path B (*dotted line*) which approaches only the yield surface without touching it has almost the same stress amplitude $q_{\mathrm{B}}^{\mathrm{ampl}} \approx q_{\mathrm{A}}^{\mathrm{ampl}}$ but the respective strain amplitudes are quite different and so are the rates of accumulation

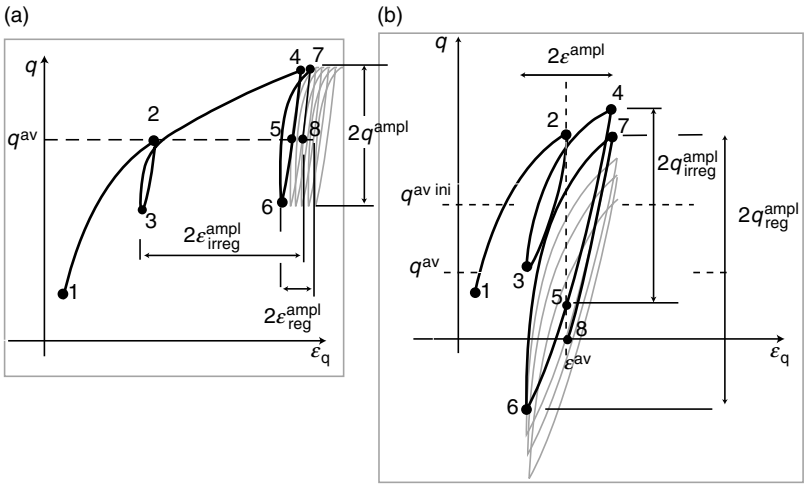

Fig. 5. (**a**) Unsymmetric stress-controlled cycles. (**b**) Unsymmetric strain-controlled cycles. Monotonic loading 1–2 is followed by the irregular cycle (2–3–4–5) and the regular cycle (5–6–7–8). In the irregular stress-controlled cycle the strain amplitude $\epsilon^{\mathrm{ampl}}_{\mathrm{irreg}}$ is too large. In the irregular strain-controlled cycle the stress amplitude is too small and, which is more important, the average stress changes from $q^{\mathrm{av\ ini}}$ to q^{av}

(Sect. 2.5) making it stronger barotropic (p-dependent). This would be numerically disadvantageous. Third, T^{ampl} vanishes at the limit $\mathbf{T}^{\mathrm{av}} = \mathbf{0}$, hence the phenomenon presented in Fig. 6 could not be described.

The amplitude evaluated from the first, so-called *irregular cycle* may be untypical. As illustrated in Fig. 5a, the strain amplitude obtained from the irregular stress-controlled cycle is too large. Moreover irregular strain-controlled cycles, Fig. 5b, commenced at $q^{\mathrm{av\ ini}}$ may strongly affect the average stress, $q^{\mathrm{av\ ini}} \to q^{\mathrm{av}}$. The subsequent pseudo-relaxation is much slower.

As already mentioned, the high-cycle models are dedicated to problems with a large number of relatively small amplitudes, $\epsilon^{\mathrm{ampl}} < 5 \times 10^{-3}$. For large amplitudes alternating plasticity may occur and the rate of strain accumulation $\mathbf{D}^{\mathrm{acc}}$ (including direction $\mathbf{m}$) depends essentially on the asymmetry of the strain loop. In such case the description given by (6) and (7) becomes inaccurate. Similarly, for stresses in the vicinity of the yield surface, even relatively small strain cycles may cause the progressive failure which is an accumulation much faster than the one described by (7). For these reasons the FE routine should control whether the yield surface is encountered during the implicit calculation (item 2 in the flowchart in Sect. 1.2) or not. If so, (7) is not applicable and the residual strain $\mathbf{D}^{\mathrm{acc}}$ should be found from *direct extrapolation*. This means that the estimation (5) is replaced by $\mathbf{D}^{\mathrm{acc}} = \mathbf{D}^{\mathrm{acc\,m}} - \mathbb{E}^{-1} : \mathring{\mathbf{T}}^{\mathrm{acc\,m}}$, wherein the recorded residuals are denoted with superscript $\sqcup^{\mathrm{m}}$, cf. Fig. 2c.

2 Explicit Formula for $\mathbf{D}^{\mathrm{acc}}$

The essential element of the presented model is the explicit formula (5). Before presenting details of this semi-empirical equation let us consider the advantage of expressing the general notion of accumulation with $\mathbf{D}^{\mathrm{acc}}$ and not with the stress rate $\overset{\circ}{\mathbf{T}}{}^{\mathrm{acc}}$, let alone the accumulated pore pressure. Our argument for $\mathbf{D}^{\mathrm{acc}}$ is based on an experiment. Fig. 6 shows that $\mathbf{D}^{\mathrm{acc}}$ need *not* vanish with the effective stress, i.e. for $\mathbf{T} = \mathbf{0}$. The pore pressure build-up would be even a worse choice because it describes merely the isotropic pseudo-relaxation.

Experiments [27,38,41–43] show that $\mathbf{D}^{\mathrm{acc}}$ depends on a number of factors which can be treated independently and which can be combined into the following multiplicative form

$$\mathbf{D}^{\mathrm{acc}} = \mathbf{m}\ f_{\mathrm{ampl}}\ \ \dot{f}_N\ f_p\ f_Y\ f_e\ f_{\boldsymbol{\pi}}. \tag{5}$$

The scalar functions $f_{\mathrm{ampl}}, \dot{f}_N, f_p, f_Y, f_e$ and $f_{\boldsymbol{\pi}}$ describe the influence of the strain amplitude ϵ^{ampl}, the number of cycles N, the average mean pressure p^{av}, the average stress ratio, the void ratio e, and the change of the polarization of the strain loop, respectively. The unit tensor $\mathbf{m}$ expresses the flow rule. The validity of the above empirical formula has been checked within the range of all performed tests. The amplitudes were varied within the range $5 \times 10^{-5} < \epsilon^{\mathrm{ampl}} < 5 \times 10^{-3}$ and the average stresses between $50 \le p^{\mathrm{av}} \le 300\,\mathrm{kPa}$ for triaxial compression as well as for triaxial extension. The components of (5) are discussed in the following sections.

2.1 Direction of Accumulation m

The accumulation $\mathbf{D}^{\mathrm{acc}}$ has a volumetric portion but also a significant deviatoric component [35,42]. Since the ratio between the deviatoric and the volumetric accumulation has been observed to be almost constant for a given stress $\mathbf{T}^{\mathrm{av}}$, Fig. 7, it seems reasonable to define a kind of flow rule $\mathbf{m}(\mathbf{T}^{\mathrm{av}}) = \mathbf{D}^{\mathrm{acc}}$. The unit tensor $\mathbf{m}$ points in the direction of accumulation in the strain space. The coaxiality between $\mathbf{D}^{\mathrm{acc}}$ and $\mathbf{T}$ is analogous to the coaxiality of $\mathbf{D}^{\mathrm{pl}}$ and $\mathbf{T}^{\mathrm{av}}$ in the plasticity theory. The direction $\mathbf{m}$ has been found independent of the void ratio e, of the amplitude ϵ^{ampl} and of the polarization $\mathtt{A}_\epsilon$, etc. The flow rule may slightly vary with increasing number of cycles N, Fig. 7, but this fact has been disregarded in the present version of the model. Judging by the triaxial tests presented in Fig. 7, the direction of accumulation $\mathbf{m}$ is well approximated by the associated flow rule

$$\mathbf{m} \sim -\frac{1}{3}(p - \frac{q^2}{M^2 p})\mathbf{1} + \frac{3}{M^2}\mathbf{T}^* \tag{6}$$

from the modified Cam-clay model [31] with the Roscoe's invariants p, q and the critical state line inclined at $M = \frac{6\sin\varphi_c}{3\pm\sin\varphi_c}$. The experiments [42] show that the accumulation is dilative beyond the critical state line, $|q/p| > M$, which is in accordance with (6).

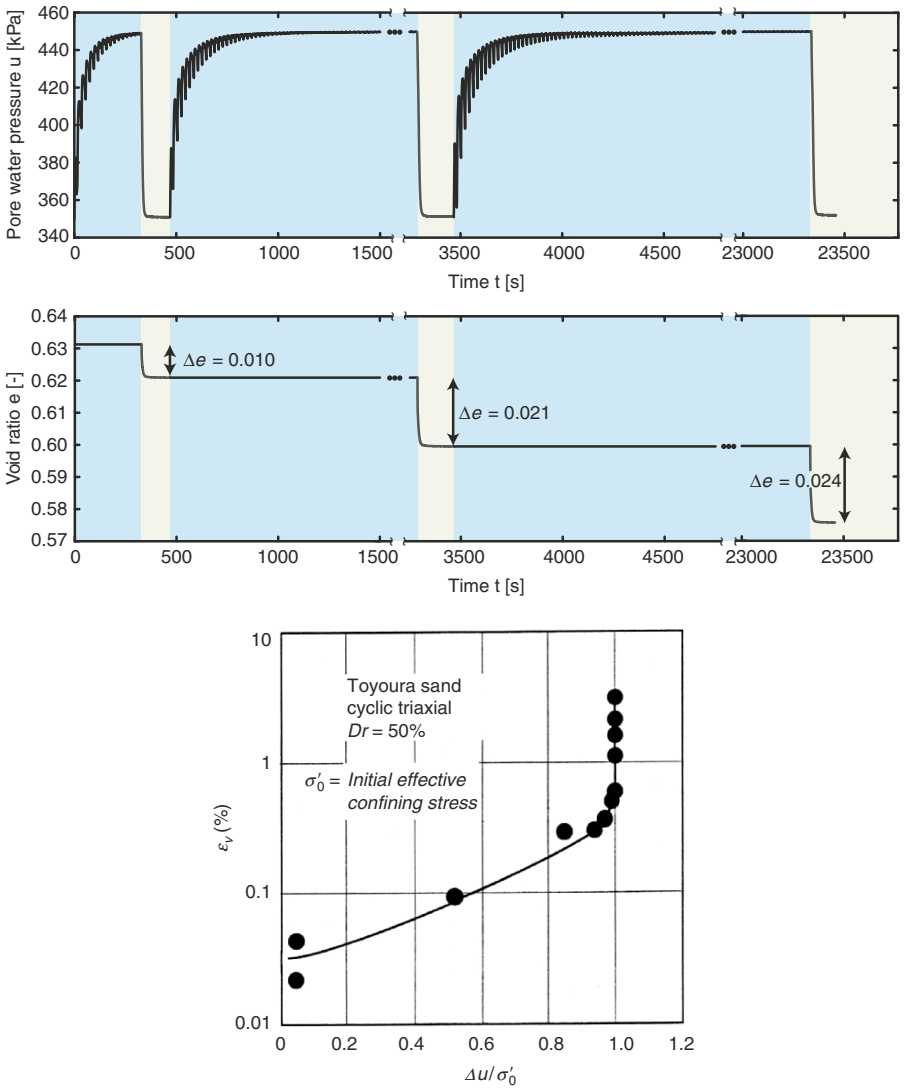

Fig. 6. Experimental evidence that the accumulation of strain continues also at vanishing effective stress $\mathbf{T} = \mathbf{0}$. *Left*: the pore pressure build up and dissipation and the corresponding change of the void ratio. *Right*: an analogous effect can be concluded from the experiments by Shamoto [33]. During cyclic loading under undrained conditions the excess pore pressure Δu increases up to the initial effective stress σ_0. Then all components of the effective stress must vanish (the soil is liquefied). The additional increase of volumetric strain from $\epsilon_v = 0.5\%$ to $\epsilon_v = 4\%$, measured during the subsequent isotropic reconsolidation, indicates that the soil skeleton must undergo a latent densification in the liquefied stage, i.e. for $\mathbf{T} = \mathbf{0}$

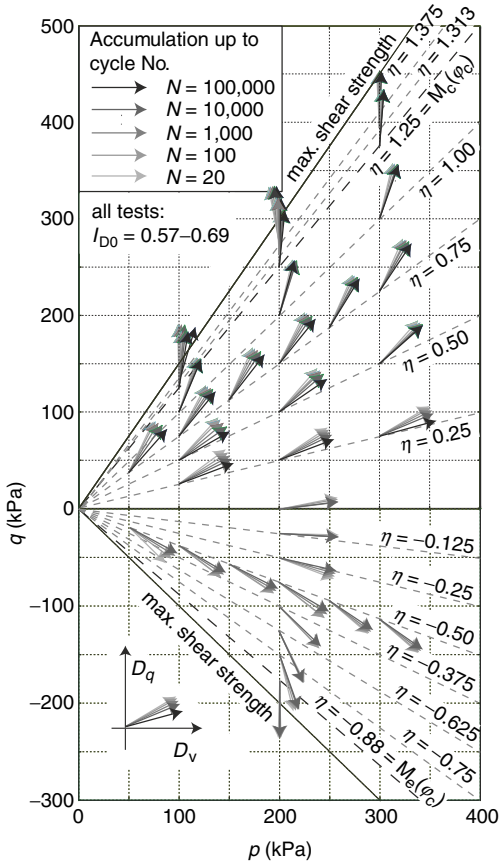

Fig. 7. Directions $\mathbf{m}$ of strain accumulation were determined from numerous cyclic triaxial tests for various stress ratios $\eta^{\mathrm{av}} = q^{\mathrm{av}}/p^{\mathrm{av}}$. The initial index of density of a sample is denoted by I_{D0}

2.2 Influence Factor $f_{\mathbf{ampl}}$ of the Amplitude

The rate of accumulation depends essentially on the amplitude which enters (5) via f_{ampl}. The factor f_{ampl} describes the influence of the *size* ϵ^{ampl} of the amplitude (= scalar value). For IP-cycles $\epsilon^{\mathrm{ampl}} = \|\boldsymbol{\epsilon}^{\mathrm{ampl}}\|$ and for OOP-cycles $\epsilon^{\mathrm{ampl}} = \|\mathtt{A}_\epsilon\|$, see Sect. 3. Fig. 8 shows that the accumulation rate is proportional to the square of the strain amplitude. This proportionality is valid up to $\epsilon^{\mathrm{ampl}} = 10^{-3}$. A few tests with very large amplitudes show that the accumulation rate remains almost constant above this limit. Therefore we propose

$$f_{\mathrm{ampl}} = \begin{cases} \left(\frac{\epsilon^{\mathrm{ampl}}}{\epsilon^{\mathrm{ampl}}_{\mathrm{ref}}}\right)^2 & \text{for } \epsilon^{\mathrm{ampl}} \le 10^{-3}, \\ 100 & \text{otherwise,} \end{cases} \tag{7}$$

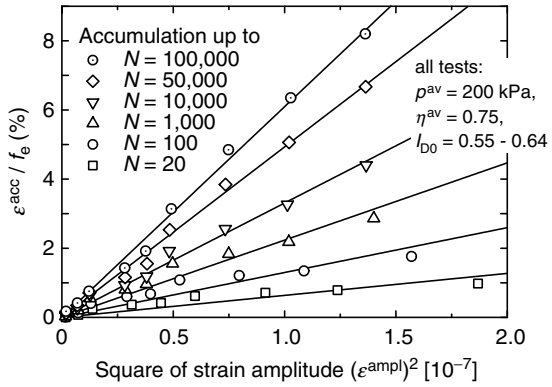

Fig. 8. The rate of accumulation is proportional to the square of the strain amplitude. The diagram has been purified from the variability of f_e

wherein the reference amplitude is $\epsilon_{\mathrm{ref}}^{\mathrm{ampl}} = 10^{-4}$. Equation (7) has been found valid for the range $5 \times 10^{-5} < \epsilon^{\mathrm{ampl}} < 5 \times 10^{-3}$.

According to some literature [15,32,41] the volumetric portion $\epsilon_P^{\mathrm{ampl}}$ of the amplitude has less influence on the rate of accumulation than the deviatoric one $\epsilon_Q^{\mathrm{ampl}}$ (see Appendix A for definition of isomorphic components). However, reinterpretation of our earlier tests with the careful consideration of the membrane penetration effect [22] has revealed that $\epsilon_P^{\mathrm{ampl}}$ and $\epsilon_Q^{\mathrm{ampl}}$ contribute equally(!) to the accumulation and need not be treated separately. Hence, $\epsilon^{\mathrm{ampl}} = \sqrt{\left(\epsilon_Q^{\mathrm{ampl}}\right)^2 + \left(\epsilon_P^{\mathrm{ampl}}\right)^2}$ can be directly substituted into (7).

2.3 Cyclic History Factor f_N

The rate of accumulation depends strongly on the *cyclic preloading*, i.e. on the number of cycles applied in the past, on their polarization and the size. Figure 9 shows the compaction curves of three triaxial samples which have different densification rates $\dot{e}$ (rates of change of the void ratio e) passing through the same void ratio $e = 0.629$. The average stress and the amplitude are identical so that the only reason for the observed difference can be the cyclic preloading which renders the accumulation slower.

In order to consider the cyclic preloading two additional state variables have been introduced: the scalar g^A for the number of cycles N and their size ϵ^{ampl} and the tensor $\boldsymbol{\pi}$ for the recent polarization. Both state variables are phenomenological, i.e. we do not investigate whether they are related to the number of grain contacts and their directional distribution, the spatial fluctuation of stress, internal systems of shear bands etc. The major disadvantage of non-physical state variables is that they cannot be directly measured. They must be estimated by their effects. In particular, the initial in situ value of g^A can be correlated [28] to the liquefaction potential [38]. The discussion of $\boldsymbol{\pi}$ is deferred until Sect. 3 and we continue with the scalar state variable g^A here.

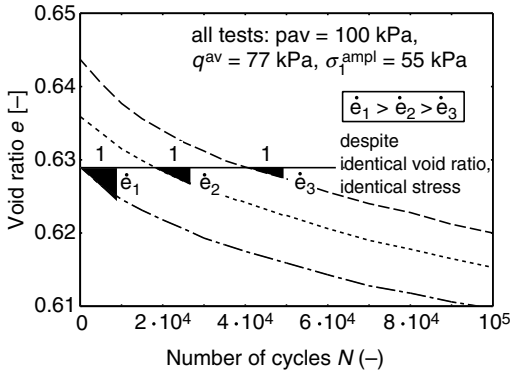

Fig. 9. The effect of cyclic loading history on the rate of densification $\dot{e} = \mathrm{d}e/\mathrm{d}N$ measured during cyclic drained triaxial test

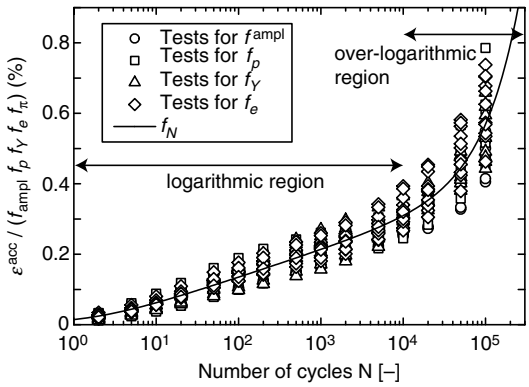

Fig. 10. Accumulated strain ϵ^{acc} divided by the functions f_{ampl}, f_p, f_Y, f_e and f_π as a function of the number of cycles

In tests on freshly pluviated samples, the cyclic history (number and size of all applied cycles) is known and one can determine exactly how the number of cycles slows down the accumulation rate. For strain cycles of constant amplitude, the increase of the total strain accumulated after N cycles see, Fig. 10, can be well approximated by the empirical formula

$$f_N = C_{N1}\left[\ln\left(1 + C_{N2}N\right) + C_{N3}N\right] \text{or in rates} \tag{8}$$

$$\dot{f}_N = C_{N1}\left[\frac{C_{N2}}{1 + C_{N2}N} + C_{N3}\right] \tag{9}$$

with three material constants C_{N1}, C_{N2} and C_{N3} (the latter is important for a large number of cycles only). Equation (8) is an already purified curve without the concurrent effects due to changes in the void ratio, stress, etc.

2.4 Miner's Rule and the State Variable g^A

Although the rate of accumulation depends strongly on the number N of cycles in the past it is not a good idea to treat N as a new state variable. Doing so the product of f_{ampl} and $\dot{f_N}$ given by (7) and (9) would severely contradict the Miner's rule [20].

Originally the Miner's rule pertains to the fatigue of metals and generalizes the Wöhler's curve. The Wöhler's SN-curve shows the number N_f of uniaxial cycles with a stress amplitude $S = T_1^{\text{ampl}} = \text{const}$ that causes failure. The Palmgren–Miner's rule describes an analogous condition for several blocks of cycles with constant amplitudes within each block. Suppose we have n blocks of cycles. In the i th block the number of actually applied cycles is N_i and their amplitude A_i is constant. Suppose also that we know the numbers N_{fi} of cycles to failure for each amplitude A_i. The Miner's rule excludes failure if inequality

$$\sum_{i=1}^{n} \frac{N_i}{N_{fi}} < 1 \tag{10}$$

is satisfied. The Miner's rule implies that:

- the sequence of application of constant-amplitude blocks is of no importance,
- the periodic strain loop can be decomposed into several *convex* loops (e.g., using the so-called rainflow algorithm). These convex loops can be applied sequentially as separate blocks with constant amplitudes.

It is controversial whether sands obey the Miner's rule very rigorously. However, in one case the inconsistency between (9) and the Miner's rule is unacceptable, namely for a combination of a package of N_1 cycles with $\epsilon_{(1)}^{\text{ampl}}$ and a package of N_2 cycles with almost vanishing amplitude $\epsilon_{(2)}^{\text{ampl}} \approx 0$. The total accumulation should be independent of the sequence of application of these packages because it does not matter whether we *do nothing* after or before the actual loading with $\epsilon_{(1)}^{\text{ampl}} > 0$. The vanishingly small cycles should have no effect at all. However, (9) unwisely disregards the sizes of amplitudes *in the past*.

A state variable memorizing the number of cycles together with their amplitudes is therefore required. Though a simple concept [32] of using the product $\left(\epsilon^{\text{ampl}}\right)^2 N$ instead of N in (9) obeys the Miner's rule, it is in conflict with (7), cf. [27]. The variable g^A, proposed in the following, is a compromise solution. We consider the product of f_{ampl} and $\dot{f}_N$ denoting it as $\dot{g} = f_{\text{ampl}}\, \dot{f}_N$. Functions f_{ampl} and $\dot{f}_N$ are further on given by (7) and (9). Note that only a part of $\dot{g}$ depends on N namely $\dot{g}^A = f_{\text{ampl}} C_{N1} C_{N2} / (1 + C_{N2} N)$. Integrating $\dot{g}$ with respect to N one obtains

$$g = \overbrace{f_{\text{ampl}} C_{N1} \ln\left(1 + C_{N2} N\right)}^{=g^A} + \overbrace{f_{\text{ampl}} C_{N1} C_{N3} N}^{=g^B}. \tag{11}$$

The idea is to reformulate (9) replacing N by g^A. For this purpose we solve $g^A = g^A(N)$ for N and substitute the result into the expression for $\dot{g}$, viz.,

$$\dot{g} = f_{\mathrm{ampl}} C_{N1} C_{N2} \exp\left(-\frac{g^A}{C_{N1} f_{\mathrm{ampl}}}\right) + f_{\mathrm{ampl}} C_{N1} C_{N3}, \tag{12}$$

wherein f_{ampl} refers to the current amplitude and g^A contains the information about the amplitudes in the past and the respective numbers of cycles. By this expedient the Miner's rule is satisfied at the limit of very small amplitudes and (9) remains valid for the special case of $\epsilon^{\mathrm{ampl}} = \mathrm{const}$.

A numerical simulation of the accumulation caused by two blocks of cycles with different amplitudes and applied in different sequences gives almost the same total accumulation, so it is in agreement with the Miner's rule and with the experiment, see Fig. 11.

Presumably apart from the cyclic preloading the static preloading [6] is also of importance and should be investigated in future.

2.5 Empirical Factors f_p and f_Y for Stress and Factor f_e for Void Ratio

The rate of accumulation depends on the average stress ratio $\widehat{\mathbf{T}}^{\mathrm{av}} = \mathbf{T}^{\mathrm{av}}/(\mathbf{T}^{\mathrm{av}})$, on the average mean stress p^{av} and the void ratio e. It turns out that one can treat these effects separately and use the product $f_Y\ f_p\ f_e$ of the respective functions. As it might be expected, the rate of accumulation increases with the stress obliquity $\mathbf{T}/\mathbf{T}$, especially if the yield surface is approached. This dependence, Fig. 12, can be approximated by

$$f_Y = \exp(C_Y \bar{Y}^{\mathrm{av}}) \mathrm{with} C_Y \approx 2, \tag{13}$$

wherein

$$\bar{Y} = \frac{Y - 9}{Y_{\mathrm{c}} - 9}, \quad Y = -\frac{I_1 I_2}{I_3} \quad \text{and} \quad Y_{\mathrm{c}} = \frac{9 - \sin^2 \varphi_{\mathrm{c}}}{1 - \sin^2 \varphi_{\mathrm{c}}}. \tag{14}$$

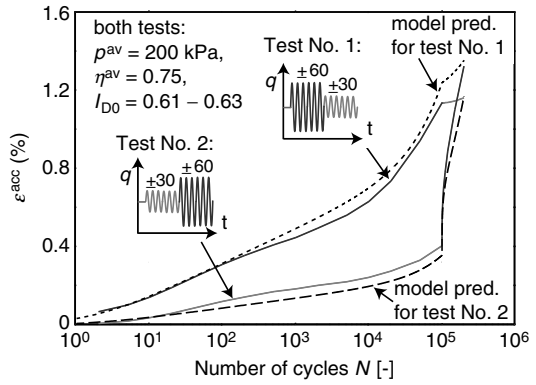

Fig. 11. Numerical calculation and experimental verification of the Miner's rule

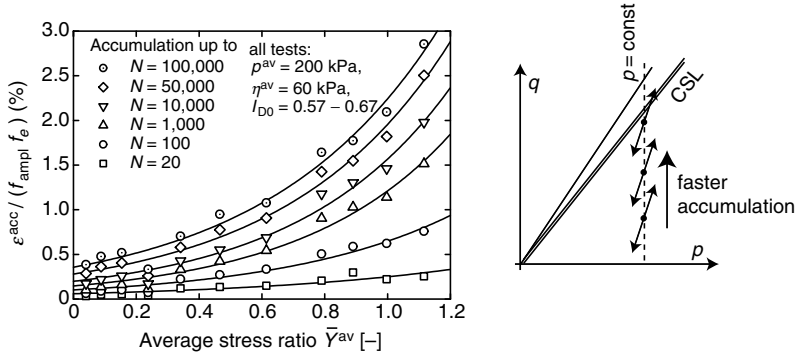

Fig. 12. Accumulated strain ϵ^{acc} as a function of the average stress ratio $\bar{Y}^{\mathrm{av}}$ for different numbers of cycles. These purified diagrams do not contain the variability due to f_{ampl} and f_e

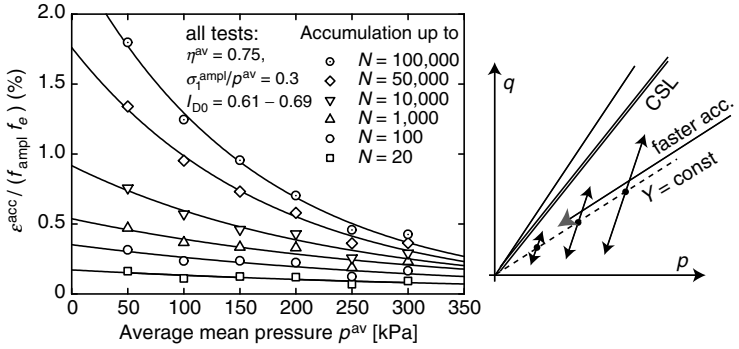

Fig. 13. Accumulated strain ϵ^{acc} in dependence on the average mean pressure p^{av} for different numbers of cycles. The diagrams have been purified from the variability of f_{ampl} and f_e

is based on the function by Matsuoka and Nakai. The stress invariants I_1, I_2, I_3 are functions of $\widehat{\mathbf{T}}^{\mathrm{av}}$ defined in Appendix A and the critical friction angle is denoted by φ_{c}.

The accumulation rate becomes smaller(!) with p^{av}. The experimental results, Fig. 13, can be approximated by

$$f_p = \exp\left[-C_p \left(\frac{p^{\mathrm{av}}}{p_{\mathrm{atm}}} - 1\right)\right], \tag{15}$$

wherein $p_{\mathrm{atm}} = 100\,\mathrm{kPa}$ and the material constant is $C_p \approx 0.43$. The validity of (13) and (15) has been tested for $50 \le p^{\mathrm{av}} \le 300\,\mathrm{kPa}$. Of course, loose sands can be easier compacted than dense ones. This is confirmed by experimental results, Fig. 14, which can be approximated by

$$f_e = \frac{(C_e - e)^2}{1 + e} \frac{1 + e_{\mathrm{ref}}}{(C_e - e_{\mathrm{ref}})^2} \tag{16}$$

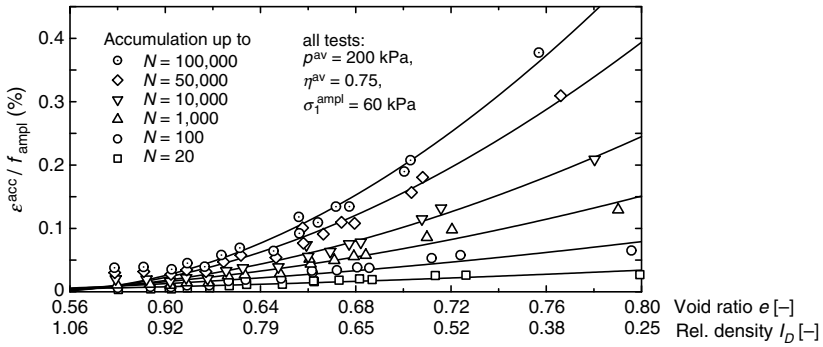

Fig. 14. Accumulated strain $\varepsilon^{\mathrm{acc}}$ in dependence on the void ratio e for different numbers of cycles. The f_{ampl}-variability has been removed here

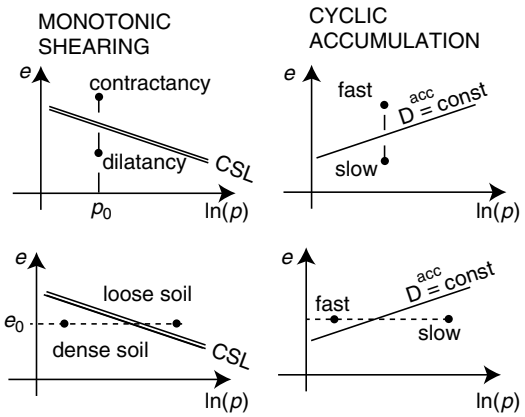

Fig. 15. Lines of constant rate of accumulation in the $e - \ln p$ diagram are differently inclined than the CSL. The notions loose sand and dense sand are pressure-dependent in the critical state soil mechanics. For cyclic accumulation this dependence is not analogous

with the material constants $e_{\mathrm{ref}} = 0.874$ and $C_e = 0.54$. The factors f_p and f_e cannot [27] be described using the 'distance to the critical state line' in the $e - \ln p$ diagram. For a given void ratio e, sand contracts faster under monotonic shearing when p is larger. Under cyclic loading it is vice versa, see Fig 15.

2.6 Sensitivity of $\mathbf{D^{acc}}$

In the previous sections we have presented various factors that influence the rate of accumulation. They have been examined in the laboratory and, one by one, approximated by simple formulas. A legitimate question is whether all these factors are really necessary in the model, because the determination

Table 1. Summary of the factors f_i and a list of the material constants C_i for the tested sand

function	Mat. constants		typical range of response	remarks
$f_{\text{ampl}} = \left(\frac{\epsilon^{\text{ampl}}}{\epsilon^{\text{ampl}}_{\text{ref}}}\right)^2$ or (7)	$\epsilon^{\text{ampl}}_{\text{ref}}$	10^{-4}	$0 \ldots 100$	
$\dot{f}_N = \frac{C_{N1}C_{N2}}{1+C_{N2}\ N} + C_{N1}C_{N3}$	C_{N1}	3.4×10^{-4}	$(0.1 \ldots 0.2)\ 10^{-3}$	$0 < N < \infty$
	C_{N2}	0.55		
	C_{N3}	6.0×10^{-5}		
$f_p = \exp\left[-C_p\ \left(\frac{p^{\text{av}}}{p_{\text{atm}}} - 1\right)\right]$	C_p	0.43	$1.5 \ldots 0.02$	$50 \le p \le 300$ kPa
	p_{atm}	100 kPa		
$f_Y = \exp\left(C_Y\ \bar{Y}^{\text{av}}\right)$	C_Y	2.0	$1 \ldots 7.4$	$0 < \bar{Y} < 1.1$
$f_e = \frac{(C_e-e)^2}{1+e}\ \frac{1+e_{\text{ref}}}{(C_e-e_{\text{ref}})^2}$	C_e	0.54	$1 \ldots 0$	
	e_{ref}	0.874		
$f_\pi = 1 + C_{\pi 1}\left[1 - \left(\overrightarrow{\mathbf{A}}_\varepsilon :: \boldsymbol{\pi}\right)\right]$	$C_{\pi 1}$	4.0	$1 \ldots 4$	quickly declines
$\boldsymbol{\pi} + \Delta\boldsymbol{\pi} = R : \boldsymbol{\pi}$ with (24)	$C_{\pi 2}$	200		

of the material constants requires a considerable effort.[1] Table 1 summarizes the presented results showing the expected variability of the functions $f_{\text{ampl}}, \dot{f}_N, f_p, f_Y, f_e$ and f_π for the typical range of input parameters.

Evidently, all presented factors may strongly influence the rate of accumulation and therefore their incorporation into the model seems justified.

3 Out-of-Phase Cycles and Polarization

We distinguish between in-phase (=IP) strain cycles and *out-of-phase* (=OOP) cycles. The IP-cycles can be defined by the equation

$$\boldsymbol{\epsilon} = \boldsymbol{\epsilon}^{\text{av}} + \boldsymbol{\epsilon}^{\text{ampl}} f(t), \tag{17}$$

wherein $\boldsymbol{\epsilon}^{\text{ampl}}$ contains the amplitudes of the individual components, i.e. $(\boldsymbol{\epsilon}^{\text{ampl}})_{ij} = (\epsilon_{ij})^{\text{ampl}}$. All components of $\boldsymbol{\epsilon}$ given by (17) oscillate together according to the same scalar periodic function, e.g. $f(t) = \sin(t)$ which is varying between -1 and 1. IP-cycles that have only one non-zero eigenvalue of $\boldsymbol{\epsilon}^{\text{ampl}}$ are termed *uniaxial*, otherwise they are *multiaxial*.

The out-of-phase (=OOP) cycles cannot be expressed by (17), e.g.

$$\boldsymbol{\epsilon}(t) = \boldsymbol{\epsilon}^{\text{av}} + \begin{pmatrix} \epsilon^{\text{ampl}}_{11}\sin(t) & 0 & 0 \\ 0 & \epsilon^{\text{ampl}}_{22}\sin(t+\theta) & 0 \\ 0 & 0 & 0 \end{pmatrix}. \tag{18}$$

[1] In the continuation of this work we intend to facilitate the determination of the material constants giving correlations to the angularity, asperity and to the grain size distribution.

Due to the phase shift $\theta \neq n\pi$, the OOP strain loop (18) encloses some area in the strain space (the shadowed area(s) in Fig. 2). The shape of a strain cycle is of importance for the accumulation (similar effect is known in the fatigue analysis of metals [7, 29]).

The rate of accumulation depends on the orientation of the strain loop (=polarization) and its ovality (=shape). It is also important how many dimensions of the strain space are penetrated by the OOP strain cycle.

Practical cases involving OOP cycles are not rare, e.g. Rayleigh waves, moving vehicles, etc. Even during conventional cyclic triaxial tests with a constant cell pressure OOP cycles may (unintentionally) occur due to the variable dilatancy. Unfortunately, OOP cycles cannot be performed easily in the laboratory and they are rarely addressed to in the literature [5, 41].

Our goal is to incorporate the information about the shape and the polarization of the strain loop into the novel *tensorial definition* of the strain amplitude $\mathtt{A}_\epsilon$. It is based on tests performed in the triaxial cell with periodic changes of both, lateral and axial stress. Moreover, several special tests have been done using an extended direct simple shear (DSS) device [41].

3.1 Tensorial Amplitude $\mathbf{A}_{\boldsymbol{\epsilon}}$

The OOP cycles produce more accumulation than the IP cycles of the same size, e.g. the accumulation caused by the loop (18) with the phase shift $\theta = 90°$ is larger than the accumulation due to an IP loop of the size $\max(\epsilon_{11}^{\mathrm{ampl}}, \epsilon_{22}^{\mathrm{ampl}})$, see Fig. 16. According to several DSS and triaxial tests [41], the accumulation caused by two-dimensional harmonic OOP cycles is equivalent to the total effect of the orthogonal IP cycles into which the strain loop could be decomposed. In particular, the accumulation caused by two-dimensional cycles (18) could be estimated using $f_{\mathrm{ampl}} \sim (\epsilon_{11}^{\mathrm{ampl}})^2 + (\epsilon_{22}^{\mathrm{ampl}})^2$. Analogously, for an

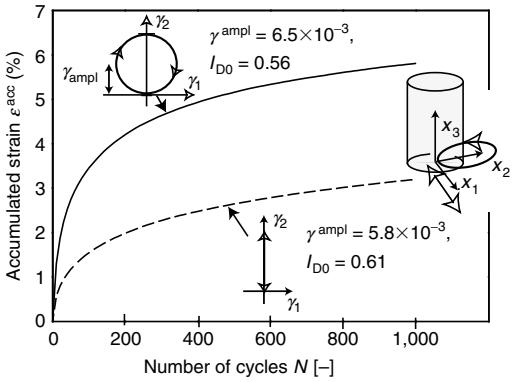

Fig. 16. Circular strain loops generate approximately twice faster accumulation than the in-phase ones

OOP cycle

$$\boldsymbol{\epsilon}(t) = \boldsymbol{\epsilon}^{\mathrm{av}} + \begin{pmatrix} \epsilon_{11}^{\mathrm{ampl}} f_{11}(t) & \epsilon_{12}^{\mathrm{ampl}} f_{12}(t) & \epsilon_{13}^{\mathrm{ampl}} f_{13}(t) \\ \epsilon_{21}^{\mathrm{ampl}} f_{21}(t) & \epsilon_{22}^{\mathrm{ampl}} f_{22}(t) & \epsilon_{23}^{\mathrm{ampl}} f_{23}(t) \\ \epsilon_{31}^{\mathrm{ampl}} f_{31}(t) & \epsilon_{32}^{\mathrm{ampl}} f_{32}(t) & \epsilon_{33}^{\mathrm{ampl}} f_{33}(t) \end{pmatrix} \tag{19}$$

with six harmonic functions $f_{ij}(t) = \sin(\omega t + \theta_{ij})$, i.e. with a common period $2\pi/\omega$ but with various phase shifts θ_{ij}, the size of the amplitude can be evaluated from the norm of the matrix composed of the amplitudes, i.e.

$$\epsilon^{\mathrm{ampl}} = \sqrt{\epsilon_{ij}^{\mathrm{ampl}} \epsilon_{ij}^{\mathrm{ampl}}}. \tag{20}$$

Note that $\epsilon_{ij}^{\mathrm{ampl}}$ denotes the amplitude of the ijth component of strain, $\epsilon_{ij}^{\mathrm{ampl}} = \max |\epsilon_{ij}(t) - \epsilon_{ij}^{\mathrm{av}}|$ and not the ijth component of a "tensorial amplitude".

Now, a generalization of (20) for arbitrary periodic functions f_{ij} is proposed, i.e. the oscillations need not be harmonic. Moreover, if the accumulation is investigated using the FE method then the analytical form (19) is not known. Suppose, we are given a strain loop in form of a sequence of discrete strains $\boldsymbol{\epsilon}(t_k), k = 1, \ldots, M$ recorded by an FE program at a Gauss point. In order to formulate a suitable definition of the tensorial amplitude $\mathbf{A}_\epsilon$ we keep in mind the following observations:

- The shape of the strain cycle, Fig. 16, influences the accumulation rate.
- The orientation (= polarization) of the cycle in the strain space is of importance, Fig. 17. A sudden change of the polarization may increase the rate of accumulation [41].
- The strain states upon a cycle need not be coaxial and therefore the paths $\boldsymbol{\epsilon}(t)$ are six-dimensional.
- The size of the six-dimensional strain path must be described by six extents (further called *spans*).

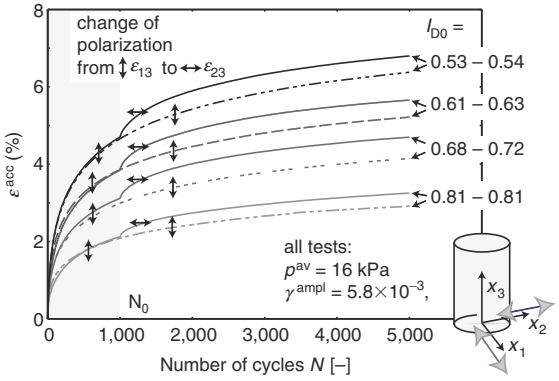

Fig. 17. After a sudden change of polarization $\mathbf{A}_\epsilon$ the rate of accumulation leaps

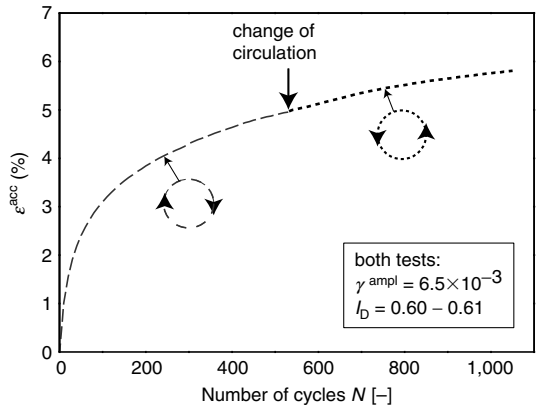

Fig. 18. A change of the circulation of the cyclic strain path does not affect the accumulation

– Polarization cannot have a sign, i.e. it has a direction but no *sense of the direction.*
– A change of circulation has no effect. Figure 18 does not show any change of the accumulation rate after the circulation was changed from the clockwise ↻ to the counterclockwise ↺,

From a recorded cycle $\boldsymbol{\epsilon}(t_k)$ with $k = 1, \ldots, M$ we may determine the pair of the two most distant points, say $\boldsymbol{\epsilon}(t_a)$ and $\boldsymbol{\epsilon}(t_b)$. The span of the cycle is quantified by its size $2R^{(6)} = ||\boldsymbol{\epsilon}(t_a) - \boldsymbol{\epsilon}(t_b)||$ and its orientation $\mathbf{r}^{(6)} = (\boldsymbol{\epsilon}(t_a) - \boldsymbol{\epsilon}(t_b))$. The upper index $\sqcup^{(i)}$ corresponds to the maximum possible number of dimensions of the loop, e.g. the original strain path (before flattening) can be at most six-dimensional, $\boldsymbol{\epsilon}^{(6)} = \boldsymbol{\epsilon}$. In order to find the second longest span the strain loop is *projected* onto the hyperplane perpendicular to $\mathbf{r}^{(6)}$. It results in the flattened strain trajectory $\boldsymbol{\epsilon}^{(5)} = \boldsymbol{\epsilon}^{(6)} - \mathbf{r}^{(6)} : \boldsymbol{\epsilon}^{(6)} \otimes \mathbf{r}^{(6)}$ which has at most five dimensions. The span of the flattened trajectory can be determined analogously and described by $R^{(5)}$ and $\mathbf{r}^{(5)}$. The flattened loop is subject to the subsequent projection, this time along $\mathbf{r}^{(5)}$, etc. Of course $R^{(6)} \geq R^{(5)} \geq \ldots \geq R^{(1)}$ holds.

The tensorial amplitude A_ϵ is proposed to be defined as the following sum:

$$\mathbf{A}_\epsilon = \sum_{i=1}^{6} R^{(i)} \quad \mathbf{r}^{(i)} \otimes \mathbf{r}^{(i)} \tag{21}$$

collecting all spans.[2] Briefly speaking, the described method consists in a gradual degeneration of the strain path in order to determine its spans. The sense of the direction of $\mathbf{r}^{(i)}$ is of no importance, which is obvious from (21). For numerical efficiency the calculation can be aborted if the size of the subsequent

[2] An analogous definition using the one-four-th of the perimeters $P^{(i)}$ of the loops instead of the radii $R^{(i)}$ lead to a worse approximation of the experiments.

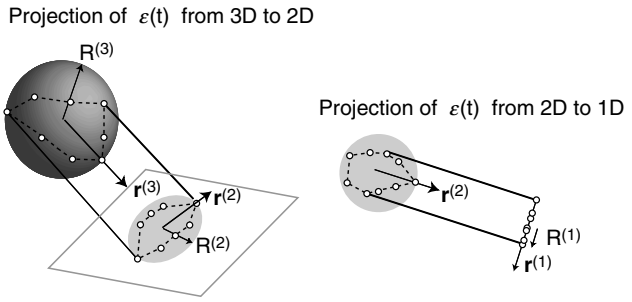

Fig. 19. The directions $\mathbf{r}_i$ and the sizes $R^{(i)}$ of the strain loop

span is negligible (say less than 10% of the largest span). Projections from a three-dimensional path to the one-dimensional path are shown in Fig. 19.

From the above algorithm a list of radii $R^{(6)} \geq R^{(5)} \geq \cdots \geq R^{(1)}$ and a list of mutually orthogonal orientations: $\mathbf{r}^{(6)}, \mathbf{r}^{(5)}, \ldots, \mathbf{r}^{(1)}$ are obtained. Substituted into (21) they constitute the tensorial amplitude. The amplitude $\mathbf{A}_\epsilon$ is a four-th order tensor which has the eigenvalues $R^{(i)}$ and the corresponding eigentensors $\mathbf{r}^{(i)}$.

The normalized amplitude

$$\mathbf{A}_{\boldsymbol{\epsilon}} = \mathbf{A}_{\boldsymbol{\epsilon}} / ||\mathbf{A}_\epsilon|| \tag{22}$$

is called *polarization* and the norm

$$\epsilon^{\text{ampl}} = ||\mathbf{A}_\epsilon|| = \sqrt{\left(R^{(6)}\right)^2 + \left(R^{(5)}\right)^2 + \cdots + \left(R^{(1)}\right)^2} \tag{23}$$

is the scalar amplitude. For harmonic cycles of type (19), definition (23) simplifies to (20). This has been demonstrated in [26].

3.2 Back Polarization $\boldsymbol{\pi}$ and Function f_π

If a package of cycles with the amplitude $\mathrm{A}_\epsilon^{(1)}$ is directly followed by another package with the amplitude $\mathrm{A}_\epsilon^{(2)}$ with the same polarization, i.e. $\mathbf{A}_{\boldsymbol{\epsilon}}^{(1)} :: \mathbf{A}_{\boldsymbol{\epsilon}}^{(2)} = 1$, no correction of the accumulation rate is needed ($f_\pi = 1$) except for f_{ampl}. However, if the polarization has changed then the above product may become significantly smaller (in the extreme case $\mathbf{A}_{\boldsymbol{\epsilon}}^{(1)} :: \mathbf{A}_{\boldsymbol{\epsilon}}^{(2)} = 0$) and then the rate of accumulation is increased ($f_\pi > 1$), Fig. 17. The function f_π which enters (5) takes this effect into account.

Let us introduce the four-th rank back polarization tensor $\boldsymbol{\pi}$ which represents the polarization in the recent history of cyclic deformation. The rate of accumulation is proposed to be a function of the angle $\alpha = \arccos(\mathbf{A}_\epsilon :: \boldsymbol{\pi})$ between the current polarization $\mathbf{A}_\epsilon$ and $\boldsymbol{\pi}$, Fig. 20.

The product $0 \leq \boldsymbol{\pi} :: \mathbf{A}_{\boldsymbol{\epsilon}} \leq 1$ reflects the degree of adaptation of the soil structure to the current polarization. During cycles with $\mathbf{A}_\epsilon = \text{const}$ the tensor $\boldsymbol{\pi}$ is evolving, asymptotically approaching the current polarization, $\boldsymbol{\pi} \to \mathbf{A}_\epsilon$.

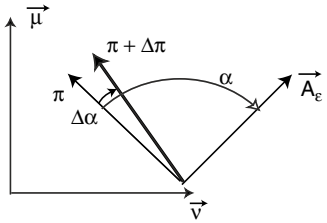

Fig. 20. Evolution of $\boldsymbol{\pi}$ can be seen as a rotation in six-dimensional space

Since both $\boldsymbol{\pi}$ and $\mathbf{A}_\epsilon$ are unit tensors the evolution of $\boldsymbol{\pi}$ is a kind of *rotation* diminishing the angle α, Fig. 20.

The angle α is proposed to evolve according to

$$\dot{\alpha} = -C_{\pi 2}\ \alpha\ (\epsilon^{\mathrm{ampl}})^2 \tag{24}$$

meaning that the rate of change of α is proportional to $-\alpha$ and to the square of the amplitude. The constant $C_{\pi 2}$ is positive so the back polarization indeed tends towards the current polarization, $\boldsymbol{\pi} \to \mathbf{A}_\epsilon$. In order to update $\boldsymbol{\pi}$ we rotate it,

$$\boldsymbol{\pi} + \Delta\boldsymbol{\pi} = R :: \boldsymbol{\pi}, \tag{25}$$

by the angle $\Delta\alpha = \dot{\alpha}\Delta N$, wherein the rotation operator is defined by

$$R = (\cos\Delta\alpha - 1)(\boldsymbol{\mu}\otimes\boldsymbol{\mu} + \boldsymbol{\nu}\otimes\boldsymbol{\nu}) + \sin\Delta\alpha(\boldsymbol{\nu}\otimes\boldsymbol{\mu} - \boldsymbol{\mu}\otimes\boldsymbol{\nu}) + \mathtt{J} \tag{26}$$

and where $\boldsymbol{\mu} = \mathbf{A}_\epsilon + \boldsymbol{\pi}$ and $\boldsymbol{\nu} = \mathbf{A}_\epsilon - \boldsymbol{\pi}$ denote mutually orthogonal tensors constructed on the hyperplane perpendicular to the rotation axis. $\mathtt{J}$ denotes the eigth-th rank identity tensor.

An increase in the rate of accumulation can be described by the factor

$$f_\pi = 1 + C_{\pi 1}(1 - \cos\alpha). \tag{27}$$

The material constants $C_{\pi 1}$ and $C_{\pi 2}$ can be determined from an increased accumulation rate due to a rapid change of polarization, Fig. 17. The presented tests have been carried out in our multiaxial direct simple shear (DSS) device. Its novelty lies in a possibility of the lower end plate to move (cyclically) along an arbitrary horizontal trajectory, [41].

Let us begin a DSS test applying a large number of ϵ_{13}-cycles, Figure 17. At first the back polarization tensor $\boldsymbol{\pi}$ is undetermined but according to (24) it must tend asymptotically (with N) to the stationary value $\boldsymbol{\pi} = \mathbf{A}_\epsilon$ corresponding to $f_\pi \approx 1$. After several hundred cycles $\boldsymbol{\pi}$ may be expected to have reached this asymptotic value. Then the polarization $\mathbf{A}_\epsilon$ of the applied loading is rapidly rotated, whereas $\boldsymbol{\pi}$ is left unchanged. In Fig. 17 the ϵ_{13}-shearing is followed by the orthogonally polarized ϵ_{23}-shearing. This change of polarization corresponds to $\alpha = 90°$. According to (27) the

rate of accumulation of the axial strain recorded during the test must increase $f_\pi = (1 + C_{\pi 1})$-times with respect to the rate of accumulation under the previous ϵ_{13}-cycles. Knowing this increase one can determine $C_{\pi 1}$. Further, it can be seen from Fig. 17 that the additional rate of accumulation declines with N vanishing completely after several hundred cycles. The solid curve corresponding to ϵ_{23}-cycles becomes parallel to the dashed curve of ϵ_{13}-cycles. The constant $C_{\pi 2}$ can be found fitting the measured curve $f_\pi(N)$ with $f_\pi(N) = 1 + C_{\pi 1}\left[1 - \cos\left(\alpha_0 \exp\left[-C_{\pi 2}(\epsilon^{\mathrm{ampl}})^2(N - N_0)\right]\right)\right]$ for $N \geq N_0$, wherein N_0 is the number of cycles prior to the rapid change of polarization. This formula can be easily derived integrating $\dot{\alpha}$ from (24) with respect to N and substituting the result (i.e. α) into (27).

For in situ soils subject to a vertical cyclic preloading $\boldsymbol{\pi}$ may be initiated with

$$\boldsymbol{\pi} = \mathbf{A}_\epsilon = \mathbf{r} \otimes \mathbf{r}, \tag{28}$$

wherein $\mathbf{r}$ corresponds to the vertical compression. The spectrum of $\boldsymbol{\pi}$ is $\{0, 0, 0, 0, 0, 0, 0, 0, 1\}$ and the non-zero eigenvalue corresponds to the prescribed eigenvector $\mathbf{r}$. Another extreme example could be a fresh sand fill with a perfectly *isotropic structure*, i.e. with no privileged direction of cyclic strain. The corresponding back polarization

$$\boldsymbol{\pi}^{\mathrm{iso}} = \frac{1}{3}\mathsf{J} \tag{29}$$

can be obtained integrating the dyadic product $\mathbf{r} \otimes \mathbf{r}$ over all directions in the strain space and dividing the result by the surface of the six-dimensional hypersphere.

4 Deformations Delayed by Pore Water

Let us consider a saturated soil stratum of height H in an axisymmetric average state subject to fast cyclic shearing (due to a shear wave caused by an earthquake). Our constitutive relation can be simplified to

$$\begin{Bmatrix} \dot{T}_{\mathrm{v}} \\ \dot{T}_{\mathrm{h}} \end{Bmatrix} = \begin{bmatrix} E_{\mathrm{vv}} & E_{\mathrm{vh}} \\ E_{\mathrm{hv}} & E_{\mathrm{hh}} \end{bmatrix} \cdot \begin{Bmatrix} D_{\mathrm{v}} - D_{\mathrm{v}}^{\mathrm{acc}} - D_{\mathrm{v}}^{\mathrm{pl}} \\ D_{\mathrm{h}} - D_{\mathrm{h}}^{\mathrm{acc}} - D_{\mathrm{h}}^{\mathrm{pl}} \end{Bmatrix}, \tag{30}$$

wherein the indices $\sqcup_{\mathrm{h}}$ and $\sqcup_{\mathrm{v}}$ denote the horizontal and the vertical components, respectively. Large H and high frequency of cyclic loading may hamper the dissipation of the excess pore water pressures u_{gen} generated by pseudo-relaxation of the effective stress $\mathbf{T}$. For simplicity we treat soil as if it were practically undrained. Assuming homogeneity in the horizontal direction we have $D_{\mathrm{h}} = 0$ and due to the equilibrium condition in the vertical direction the total vertical stress must remain constant, i.e.

$$\dot{T}_{\mathrm{v}} - \dot{u} = 0 \tag{31}$$

Let us subdivide the whole volume of soil into thin horizontal layers $I = 1, \dots M$ of equal heights. The accumulation rate of pore water pressure compensates the pseudo relaxation to keep the total stress constant

$$\dot{u}_{\mathrm{gen}I} = \dot{T}_{\mathrm{v}I} = E_{\mathrm{vv}I}(0 - D^{\mathrm{acc}}_{\mathrm{v}I}) + E_{\mathrm{vh}I}(0 - D^{\mathrm{acc}}_{\mathrm{h}I}). \tag{32}$$

This process is isochoric and therefore using $D_{\mathrm{h}} = 0$ we can conclude that $D_{\mathrm{v}} = 0$ which is already set in the above equation. Note that generation of pore pressure as such occurs immediately because no water transport is necessary. It may give a false impression that the excess pore pressure may also *spread* immediately. Actually, spreading of the excess pore pressure is similar to consolidation. This is not instantaneous because the volumetric deformations (=transport of pore water) do take place. The pore pressure requires volume changes in order to spread because it causes a *monotonic* change in the effective mean stress which involves change in volume (and flow of water).

The bulk stiffness K_{w} of water does not appear in the solution for the strain rate $\dot{\epsilon}$. Admittedly, the strain rate D_{v} depends also on K_{w} i.e. on the deformation of water and soil grains but this is a purely reversible portion of settlement which disappears during the dissipation of the excess pore pressure. Therefore it has been neglected.

4.1 Stress and Strain Rates During Reconsolidation

Although the pore pressure build up and dissipation occur simultaneously we consider them as if they acted sequentially, in each period of cyclic excitation. The rate of pore pressure dissipation (usually negative) is denoted as $\dot{u}_{\mathrm{diss}}$. During the (re)consolidation the stress is transferred from water to the soil skeleton while satisfying equilibrium condition (31). This process is governed by the well known dissipation equation

$$\frac{\partial u_{\mathrm{diss}}}{\partial t} = c_{\mathrm{v}} \frac{\partial^2 u_{\mathrm{diss}}}{\partial^2 x} \qquad \text{wherein} \quad c_{\mathrm{v}} = \frac{k E_{\mathrm{vv}}}{\rho_{\mathrm{w}} g}. \tag{33}$$

The reconsolidation results in a pore pressure rate $\dot{u} = \dot{T}_{\mathrm{v}}$, a vertical strain rate D_{v} and an effective horizontal stress increment $\dot{T}_{\mathrm{h}}$ (seepage forces are neglected). They can be easily found from the following equation system:

$$\begin{Bmatrix} \dot{T}_{\mathrm{v}} = \dot{u}_{\mathrm{diss}} \\ \dot{T}_{\mathrm{h}} \end{Bmatrix} = \begin{bmatrix} E_{\mathrm{vv}} & E_{\mathrm{vh}} \\ E_{\mathrm{hv}} & E_{\mathrm{hh}} \end{bmatrix} \cdot \begin{Bmatrix} D_{\mathrm{v}} \\ 0 \end{Bmatrix}. \tag{34}$$

Again we have assumed that the reconsolidation is elastic and the problem is homogeneous in the horizontal direction, $D_{\mathrm{h}} = 0$. As the solution one obtains

$$\dot{T}_{\mathrm{h}} = \frac{E_{\mathrm{hv}} \dot{u}_{\mathrm{diss}}}{E_{\mathrm{vv}}} \quad \text{and} \quad D_{\mathrm{v}} = \frac{\dot{u}_{\mathrm{diss}}}{E_{\mathrm{vv}}}. \tag{35}$$

4.2 Corrections for Stress and Plastic Strain

Numerically, after a fast application of a large package of cycles the resulting effective stress may lie outside the elastic range (despite concurrent consolidation). In such case a return mapping of stress onto the yield surface is necessary. Not only a correction of stress but also a correction of strain must accompany this mapping. The plastic strain rate $\mathbf{D}^{\mathrm{pl}} \neq \mathbf{0}$ cannot be neglected.

Assuming $\mathbf{D}^{\mathrm{pl}} = \mathbf{0}$ we actually compute an elasto-cumulative predictor $\mathbf{T}^{\mathrm{e}}$ of stress $\mathbf{T}$. If our predictor lies outside the yield surface, say Coulomb pyramid, say $T^{\mathrm{e}}_{\mathrm{v}}/T^{\mathrm{e}}_{\mathrm{h}} < K_a$ or $T^{\mathrm{e}}_{\mathrm{v}}/T^{\mathrm{e}}_{\mathrm{h}} > K_p$, we have to calculate the correction $\mathbf{c}_T = \dot{\mathbf{T}} - \dot{\mathbf{T}}^{\mathrm{e}}$ of the stress rate and the correction $\mathbf{c}_D = \mathbf{D} - \mathbf{D}^{e}$ of the strain rate. Due to the homogeneity in x_{h} we have $c_{\epsilon \mathrm{h}} = 0$. It is convenient to assume correction $c_{T\mathrm{v}} = 0$ because the pore pressure need not be corrected, $c_{\mathrm{u}} = 0$. Therefore $c_{T\mathrm{h}} = K_a T^{\mathrm{e}}_{\mathrm{v}} - T^{\mathrm{e}}_{\mathrm{h}}$.

Let us subtract by sides

$$\dot{\mathbf{T}} = \mathtt{E} : (\mathbf{D} - \mathbf{D}^{\mathrm{acc}} - \mathbf{D}^{\mathrm{pl}}), \tag{36}$$

$$\dot{\mathbf{T}}^{\mathrm{e}} = \mathtt{E} : (\mathbf{D}^{\mathrm{e}} - \mathbf{D}^{\mathrm{acc}}) \tag{37}$$

and express the plastic strain rate by $\mathbf{D}^{\mathrm{pl}} = \dot{\lambda}\mathbf{m}$, wherein the flow rule $\mathbf{m}$ is known. The unknown plastic multiplier $\dot{\lambda}$ has to be determined. The resulting system of equations

$$\begin{Bmatrix} 0 \\ c_{T\mathrm{h}} \end{Bmatrix} = \begin{bmatrix} E_{\mathrm{vv}} & E_{\mathrm{vh}} \\ E_{\mathrm{hv}} & E_{\mathrm{hh}} \end{bmatrix} \cdot \begin{Bmatrix} c_{\epsilon \mathrm{v}} - \dot{\lambda} m_{\mathrm{v}} \\ 0 - \dot{\lambda} m_{\mathrm{h}} \end{Bmatrix} \tag{38}$$

for soil can be easily solved and the corrections can be added to $T^{\mathrm{e}}_{\mathrm{h}}$ and to $\mathbf{D}^{\mathrm{e}}$.

If a soil layer is liquefied (the effective stress vanishes, $\mathbf{T} = \mathbf{0}$) then the accumulation term $\mathbf{D}^{\mathrm{acc}}$ cannot generate an additional pore pressure $\dot{u}_{\mathrm{gen}}$ because according to (31) the effective stress would be positive (tension). The pressure dependent stiffness vanishes so the effective stress rate $\dot{\mathbf{T}} = \mathbf{0}$ is uncoupled from the deformation rate. However, assuming a small residual stiffness and performing computing the necessary corrections mapping the tensile effective stress to the vertex of the Coulomb pyramid a latent accumulation of deformation can be calculated, as discussed in Fig. 6.

5 Examples of FE-Calculation

The presented model has been implemented into an FE program ABAQUS as a user material subroutine. Remarks on this implementation can be found in [26]. Two boundary value problems will be presented here: settlement of a strip foundation under a pulsating vertical load and differential settlement of a pair of strip foundations on a non-uniform subsoil.

5.1 Settlement of a Strip Foundation

We simulate a centrifuge model test (under increased gravity of 20 g), Fig. 21. In this test [9] a strip foundation (with a prototype width $b = 1\,\mathrm{m}$) was placed without embedment on a freshly pluviated dense fine sand ($\varrho_\mathrm{s} = 2,66\mathrm{g/cm}^3$, $e_\mathrm{min} = 0.575$, $e_\mathrm{max} = 0.908$, $d_{50} = 0.21\,\mathrm{mm}$, $U = d_{60}/d_{10} = 1.95$, $I_D \approx 0.90$) and cyclically loaded between 4% and 47% of the static bearing capacity of 345 kN. The vertical load was chosen as $Q^\mathrm{av} = 88.7\,\mathrm{kN}, Q^\mathrm{ampl} = 75.1\,\mathrm{kN}$ and the frequency was 0.44 Hz. Several load–settlement curves generated by the cycles 1–100, as well as the cycle 500, ... are plotted in Fig. 22 (prototype scale). The vertical displacement amplitude was $s^\mathrm{ampl} = 0.8\,\mathrm{mm}$ and the accumulated settlement after $N = 10^5$ cycles was $s = 7.3\,\mathrm{cm}$.

The sand used in the centrifuge test was similar (but not identical) to the laboratory sand described in this paper. Therefore several material constants $C_{N1} = 1.21 \cdot 10^{-3}, C_{N2} = 0.39, C_{N3} = 5.7 \cdot 10^{-5}, C_\mathrm{e} = 0.52$ and $e_\mathrm{ref} = 0.908$ have been determined in additional tests. The remaining constants are assumed equal to the ones of the laboratory sand, see Table 2. The hypoplasticity constants in Table 3 have been determined from standard laboratory tests except for m_T, m_R and β_R which had been taken from the literature [10,23,25] and then slightly adjusted to improve the simulation of the second cycle of the centrifuge test (estimation of amplitude).

The FE-calculation was commenced from the geostatic stress with $K_0 = 0.43$. The initial cyclic history has been assumed $g^A = 0$ because the centrifuge test was performed on freshly pluviated sand. Only a half of the 18.10×7.70 m subsoil (prototype dimensions) has been discretized taking advantage of the symmetry. Quadrilateral eight-nodal elements have been used with reduced integration and an hourglass mode control.

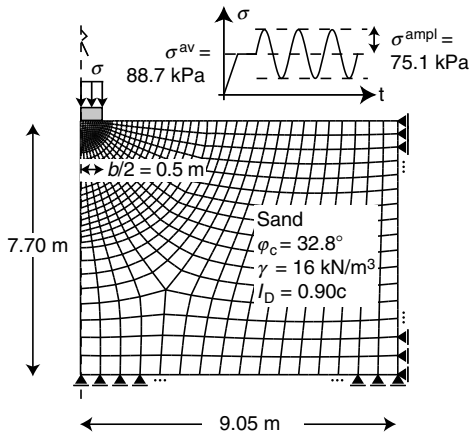

Fig. 21. Geometry of the prototype and soil parameters of the centrifuge test

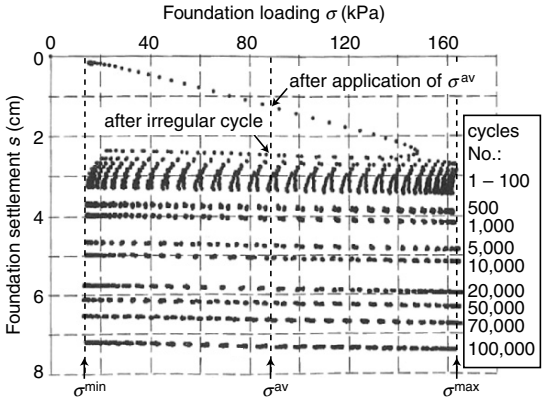

Fig. 22. Settlement of the foundation in the centrifuge test as a function of the number of cycles

Table 2. Material constants of the accumulation model for the 'centrifuge sand'

$\varepsilon_{\mathrm{ref}}^{\mathrm{ampl}}$ (–)	C_{N1} (–)	C_{N2} (–)	C_{N3} (–)	C_p (–)	p_{ref} (kPa)	C_Y (–)	C_e (–)	e_{ref} (–)
10^{-4}	1.21×10^{-3}	0.39	5.7×10^{-5}	0.43	100	2.0	0.52	0.908

Table 3. Material constants of the hypoplastic model used in the implicit steps

φ_{c} (°)	h_{s} (MPa)	ν (–)	n (–)	e_{d0} (–)	e_{c0} (–)	e_{i0} (–)	α (–)	β (–)	R (–)	m_R (–)	m_T (–)	χ (–)	β_R (–)
32.8	150	0.2	0.40	0.575	0.908	1.044	0.12	1.0	10^{-4}	6.5	3	6	0.1

Figure 23a presents the resulting field of the strain amplitude $\varepsilon^{\mathrm{ampl}}$. The field of the numerically obtained settlements s after 100,000 cycles is presented in Fig. 23b, in particular the settlement of the foundation is $s = 7.5\,\mathrm{cm}$. The calculated settlement $s(N)$ is compared to the measured test values in Fig. 24. The calculated and measured curves are in a fairly good agreement At the beginning of the simulation some discrepancy between measured and calculated data was caused by an inaccurate prediction of the residual settlement after the irregular cycle. Discussion of this discrepancy is irrelevant in this paper because the implicit model is responsible for it.

The numerical performance of the presented model is satisfactory. The mesh dependence becomes noticeable only for relative coarse discretizations (less than 100 elements). In order to allow for the utomatic time incrementation the number of cycles N has been set to be identical to the 'step-time' in the *pseudo-creep* mode. It is recommended to begin calculations in the *pseudo-creep* mode from a small increment (we have started with $\Delta N = 0.01$). The time step is promptly increased to $\Delta N = 500$ cycles or more.

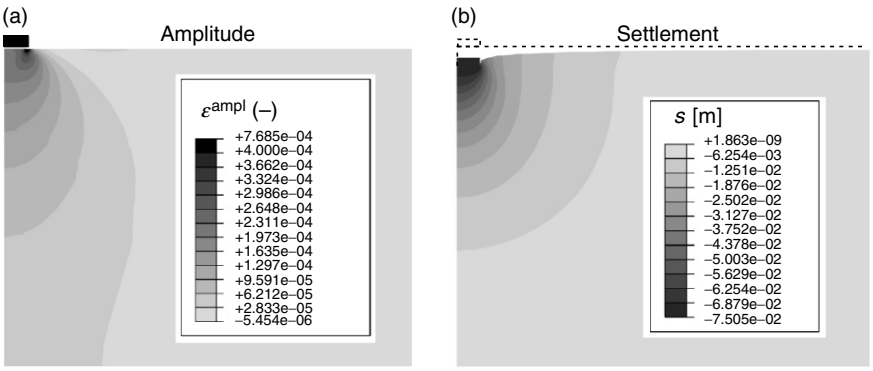

Fig. 23. (**a**) Field of strain amplitude $\varepsilon^{\mathrm{ampl}}$, (**b**) Field of accumulated settlement s^{acc} after $N = 100,000$ cycles

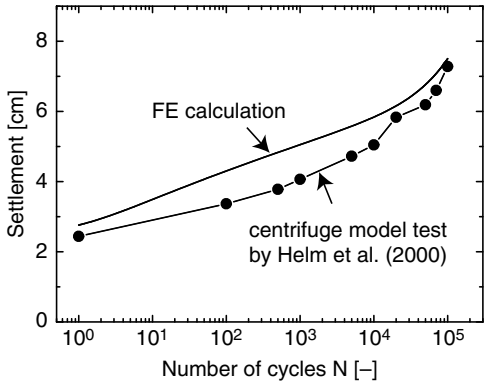

Fig. 24. Accumulation of foundation settlement during the regular cycles: FE calculation versus model test

5.2 Differential Settlement of a Pair of Strip Foundations

In this section we investigated a problem of differential settlement of two strip foundations of the width 1 m each subject to identical loading. The axial distance between the foundations is 6m, Fig. 25. In order to obtain differential settlements the generation of the initial fields of stress and void ratio involves statistics, i.e. a random (but spatially correlated) subsoil is generated and subject to monotonous and cyclic loading (plane strain). Only the void ratio is assumed inhomogeneous. The spatial variability of the void ratio field $e(\mathbf{x})$ has been described by the following isotropic autocorrelation function:

$$C_{ij} = \sigma^2 \exp\left(-\frac{||\mathbf{x}_i - \mathbf{x}_j||}{\theta}\right) \quad \text{with} \quad \sigma = \frac{1}{2}(e_{\max} - e_{\min}). \tag{39}$$

We assume $e_{\max} = 1.0$, $e_{\min} = 0.6$, the average void ratio is $\bar{e} = 0.8$. Three correlation lengths have been tried out $\theta = 0.5\,\mathrm{m}, 2.0\,\mathrm{m}$ and $20\,\mathrm{m}$. We are

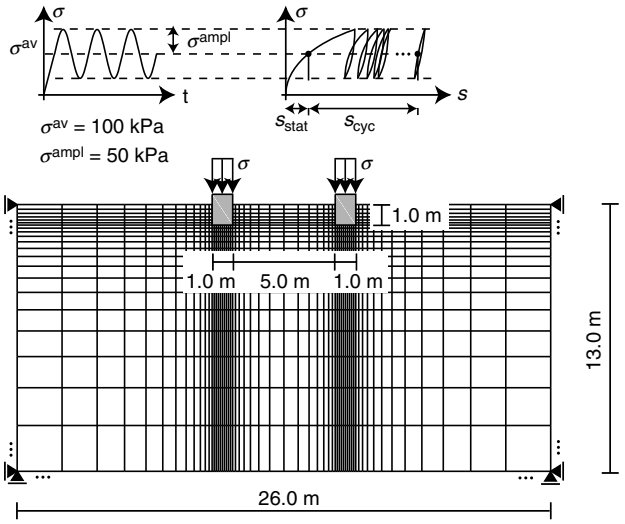

Fig. 25. BVP and FE mesh for two strip foundations

using 1,098 elements with four Gauss points per element, which results in a $(4,392 \times 4,392)$ covariance matrix. In order to obtain an autocorrelated void ratio field the matrix $\mathbf{C}$ is subject to spectral decomposition

$$\mathbf{C} = \boldsymbol{\Phi} \cdot \boldsymbol{\Lambda} \cdot \boldsymbol{\Phi}^{\mathrm{T}} \tag{40}$$

with n eigenvalues collected in $\boldsymbol{\Lambda} = \mathrm{diag}\{\lambda_1, \ldots, \lambda_n\}$ and with an orthogonal matrix $\boldsymbol{\Phi}$ composed of eigenvectors (in columns). Finally, the field $e(\mathbf{x})$ is generated with

$$e'(\mathbf{x}) = \bar{e} + \sum_{i=1}^{n} r_i^{[-1,1]} \frac{1}{2} \sqrt{\lambda_i} \boldsymbol{\Phi}_i, \tag{41}$$

wherein $r^{[-1,1]} = 2r^{[0,1]} - 1$ is a uniform variate (random real number with constant probability density function) from the range $[-1, 1]$.

The void ratio fields have been generated using the user initial stress and the user initial state routines of ABAQUS. More than 30 stochastic fields $e(\mathbf{x})$ with corresponding stress fields $\mathbf{T}(\mathbf{x})$ have been generated using (41). Examples of void ratio fields are presented in Fig. 26. Although equally loaded (at first monotonically and then cyclically) the foundations exhibit a differential settlement Δs which for each calculation is normalized by the mean settlement $\bar{s}$.

The calculation reveals that the autocorrelated fields $e(\mathbf{x})$ imply an almost linear relation between $\Delta s/\bar{s}$ calculated after monotonic loading on one hand and $\Delta s/\bar{s}$ obtained in the process of cyclic accumulation (after 10^5 cycles) on the other hand, Fig. 27.

It can be seen from Fig. 27 that the settlement $\bar{s}$ due to cyclic loading is accompanied by a three times larger differential settlement Δs than in the static

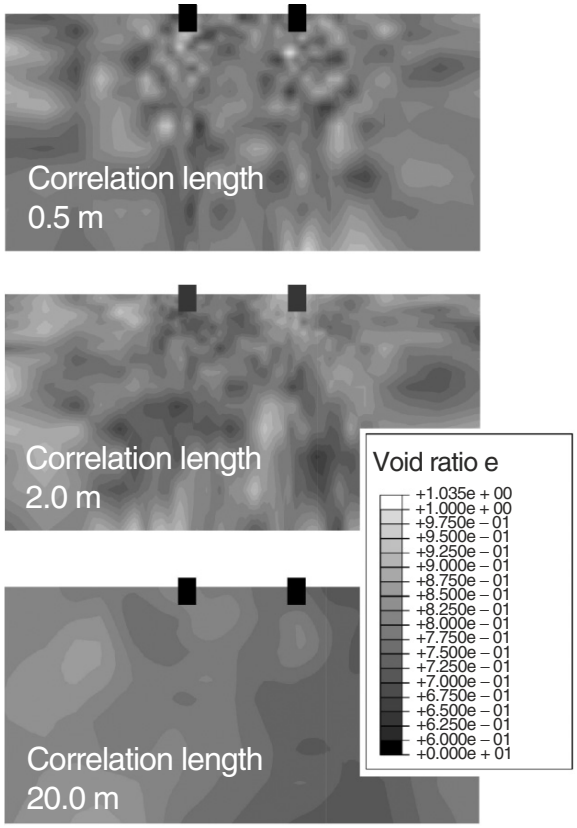

Fig. 26. Void ratio distributions generated using different correlation lengths θ

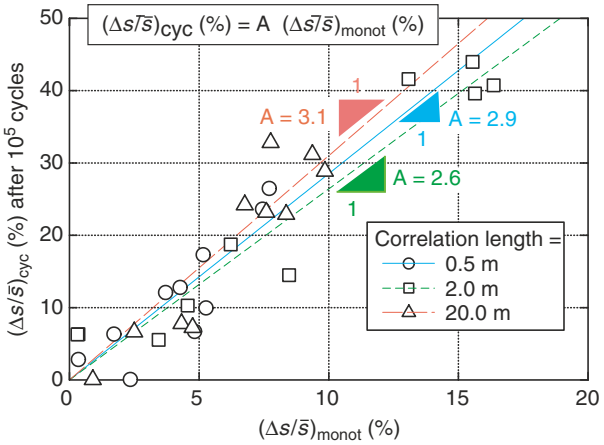

Fig. 27. Indirect limitation of differential settlement via total settlement should be three times more restrictive in case of cyclic loads. This result seems to be independent of the correlation length θ within the tested range

case. An explanation of this effect is the fact that the cyclic accumulation is proportional to the square of the strain amplitude, see Eq. 7, whereas the static settlement is approximately proportional to the load i.e. to the amplitude. Therefore cyclic accumulation is a short-range phenomenon (involves the soil volume only in the vicinity of the foundation). The probability of finding an extreme dense zone of sand under one foundation and an extreme loose zone under the other one is therefore higher in the case of cyclic loading.

Acknowledgments

The authors are grateful to DFG (German Research Council) for the financial support. This study is a part of the subproject A8 "Influence of the fabric change in soil on the lifetime of structures" of SFB 398 "Lifetime oriented design concepts".

Appendix A

Vectors and tensors are distinguished by bold typeface, for example $\mathbf{T}, \mathbf{v}$ or in sans serif font (e.g. $\mathtt{E}$). The symbol $\cdot$ denotes multiplication with one dummy index (single contraction), e.g. the scalar product of two vectors can be written as $\mathbf{a} \cdot \mathbf{b} = a_k b_k$. Multiplication with two dummy indices (double contraction) is denoted with a colon, e.g. $\mathbf{A} : \mathbf{B} = \mathrm{tr}(\mathbf{A} \cdot \mathbf{B}^{\mathrm{T}}) = A_{ij} B_{ij}$, wherein $\mathrm{tr}\,\mathbf{X} = X_{kk}$ reads trace of a tensor. The superscript $\sqcup^{\mathrm{T}}$ denotes transposition.

Analogously we may define double colon :: to quadruple contraction with four dummy indices. Two fourth order identity tensors with symmetrization $I_{ijkl} = \frac{1}{2}(\delta_{ik}\delta_{jl} + \delta_{il}\delta_{jk})$ and without symmetrization $J_{ijkl} = \delta_{ik}\delta_{jl}$ are used. The brackets $||\ \ ||$ denote the Euclidean norm. The deviatoric part of a tensor is denoted by an asterisk, e.g. $\mathbf{T}^* = \mathbf{T} - \frac{1}{3}\mathbf{1}\mathrm{tr}\mathbf{T}$, wherein $(\mathbf{1})_{ij} = \delta_{ij}$ stands for the Kronecker's symbol. The operator $()_{ij}$ extracts the ij-th component from the tensor in brackets. Permutation symbol is denoted by e_{ijk}. Dyadic multiplication is written with $\otimes$, e.g. $(\mathbf{a} \otimes \mathbf{b})_{ij} = a_i b_j$ or $(\mathbf{T} \otimes \mathbf{1})_{ijkl} = T_{ij}\delta_{kl}$. Positively proportional quantities are denoted by a tilde, e.g. $\mathbf{T} \sim \mathbf{D}$. Normalized quantities are denoted by an arrow and tensors divided by their traces are denoted with a hat, for example $\overrightarrow{\mathbf{D}} = \mathbf{D}/||\mathbf{D}||$ and $\hat{\mathbf{T}} = \mathbf{T}/\mathrm{tr}\mathbf{T}$. The sign convention of general mechanics with *tension positive* is obeyed. The superposed dot, $\dot{\sqcup}$, denotes the material rate (with respect to N) and the superposed circle $\mathring{\sqcup}$ denotes the Zaremba-Jaumann rate (finite rotations are accounted for).

The effective Cauchy stress $\mathbf{T}$, the stretching $\mathbf{D}$ and the total deformation is expressed by the logarithmic strain $\boldsymbol{\epsilon} = \ln \mathbf{U}$ is used throughout the text ($\mathbf{b}$ denotes the right stretch tensor). Generally, it would be inaccurate to interpret $\mathbf{D}$ as a time derivative of the strain $\boldsymbol{\epsilon}$ given by (48). In the axisymmetric case,

alternatively to the popular Roscoe's variables:

$$p = -(T_1 + T_2 + T_3)/3; q = -T_1 + (T_2 + T_3)/2, \tag{42}$$

$$\epsilon_{\mathrm{v}} = -(\epsilon_1 + \epsilon_2 + \epsilon_3); \quad \epsilon_q = -\frac{2}{3}(\epsilon_1 - \frac{1}{2}(\epsilon_2 + \epsilon_3)), \tag{43}$$

$$D_{\mathrm{v}} = -(D_1 + D_2 + D_3); \quad D_q = -(2D_1 - D_2 - D_3)/3, \tag{44}$$

the 'normalized', or isomorphic variables [23]

$$P = \sqrt{3}p, \quad Q = \sqrt{\frac{2}{3}}q, \tag{45}$$

$$\epsilon_P = \frac{1}{\sqrt{3}}\epsilon_{\mathrm{v}} \quad \epsilon_Q = \sqrt{\frac{3}{2}}\epsilon_q, \tag{46}$$

$$D_P = \frac{1}{\sqrt{3}}D_{\mathrm{v}} \quad D_Q = \sqrt{\frac{3}{2}}D_q \tag{47}$$

are used. The isomorphic variables preserve orthogonality and distance. Note that $P^2 = ||\frac{1}{3}\mathbf{1}\mathrm{tr}\mathbf{T}||^2$; $Q^2 = ||\mathbf{T}^*||^2$ and $D_P^2 = ||\frac{1}{3}\mathbf{1}\mathrm{tr}\mathbf{D}||^2$; $D_Q^2 = ||\mathbf{D}^*||^2$ hold. In the six-dimensional space the isomorphic components of strain are

$$\{\epsilon_{11}, \epsilon_{22}, \epsilon_{33}, \sqrt{2}\epsilon_{12}, \sqrt{2}\epsilon_{13}, \sqrt{2}\epsilon_{23}\} \text{ and}$$
$$\{T_{11}, T_{22}, T_{33}, \sqrt{2}T_{12}, \sqrt{2}T_{13}, \sqrt{2}T_{23}\}.$$

The Matsuoka-Nakai [19] inequality $-I_1I_2/I_3 - (9 - \sin^2\varphi_{\mathrm{c}})/(1 - \sin^2\varphi_{\mathrm{c}}) \leq 0$ with the critical friction angle φ_{c} is used throughout this paper as the yield criterion. It is formulated using the basic invariants of the stress tensor: $I_1 = \mathrm{tr}\mathbf{T}$, $I_2 = [\mathbf{T} : \mathbf{T} - (\mathrm{tr}\mathbf{T})^2]/2$ and $I_3 = \det \mathbf{T}$.

Quantifying the OOP-cycles (Sect. 3) one should account for the rotation of the principal strain axes within a cycle but disregard the rigid body rotation. This is done if the strain $\boldsymbol{\epsilon}$ is calculated with respect to the material frame of reference. In the presented model the logarithmic strain is defined with respect to the initial material configuration (usually K_0-state) as

$$\boldsymbol{\epsilon} = \ln \mathbf{U} = \mathbf{R}^{\mathbf{T}} \cdot \ln \mathbf{V} \cdot \mathbf{R}, \tag{48}$$

wherein $\mathbf{V}$ and $\mathbf{U}$ denote the left and the right stretch tensor and $\mathbf{R}$ is the rotation tensor appearing in the polar decomposition of the deformation gradient. We had to 'unrotate' the total strain because it is defined as $\ln \mathbf{V}$ in the FE program ABAQUS.

Appendix B

Working with a typical settlement formula

$$s(N) = s_1 f(N), \tag{49}$$

one assumes that the information about the cyclic history can be obtained from the residual settlement after a single cycle, usually from s_1 after the first one. The derivative of $s(N)$ with respect to N describes the settlement per cycle, e.g. the settlement due to the Kth cycle is

$$s_K = \left.\frac{\mathrm{d}s(N)}{\mathrm{d}N}\right|_{N=K} = s_1 f'(K). \tag{50}$$

Of course, in order to be objective, the predicted settlement due to a given cycle should not depend on how we count cycles (i.e., which cycle we call "the first"). Therefore, beside fitting the experimental observation, the function $f(N)$ must satisfy the objectivity criterion:

$$s'(N) = s_1 f'(N) = s_M f'(N - M) \tag{51}$$

in which s_M is the settlement due to an arbitrarily chosen cycle No. M (because someone may consider M as the 'first' cycle). Substituting s_M from (50) into (51) the objectivity condition takes the form

$$f'(N) \equiv f'(M) f'(N - M) \tag{52}$$

it can be shown that the widely used functions $f(N) = N^C$ or $f(N) = 1 + C\log(N)$, cf. [11,28], do not satisfy this condition. An objective (consistent) settlement formula is

$$s(N) = s_1 \frac{1}{C}\left[1 - \exp(-CN)\right], \tag{53}$$

wherein C is a positive material constant. Indeed, one can conclude from (52) that $f'(N)$ has the form

$$f'(N) = \exp(-CN). \tag{54}$$

After integration of $f'(N)$ with respect to N with the initial condition $f(0) = 0$ we arrive at (53).

References

1. R.D. Barksdale. Laboratory evaluation of rutting in base course materials. In *Third International Conference on Structural Design of Asphalt Pavements*, vol. 3, pp. 161–174, 1972
2. G. Bouckovalas, R.V. Whitman, and W.A. Marr. Permanent displacement of sand with cyclic loading. *Journal of Geotechnical Engineering*, 110(11):1606–1623, 1984
3. J.L. Chaboche. Constitutive equations for cyclic plasticity and cyclic viscoplasticity. *International Journal of Plasticity*, 5:247–302, 1989
4. J.L. Chaboche. Modelling of ratchetting: evaluation of various approaches. *European Journal of Mechanics*, 13(4):501–518, 1994

5. C. Chopi and P. Arduino. Behavioral characteristics of gravelly soils under general cyclic loading conditions. In T. Triantafyllidis, editor, *Cyclic Behaviour of Soils and Liquefaction Phenomena*, pp. 115–122. Balkema, March/April 2004. International Conference in Bochum, 31 March – 02 April 2004
6. M.R. Coop. On the mechanics of reconstituted and natural sands. In H. Di Benedetto, T. Doanh, H. Geoffroy, and Sauzéat C., editors, *Deformation characteristics of geomaterials. Recent investigations and prospects.*, pp. 29–58, Balkema, 2005
7. A. Ekberg. *Rolling contact fatigue of railway wheels*. PhD thesis, Chalmers University of Technology, 2000. Solid Mechanics
8. A. Gotschol. *Veränderlich elastisches und plastisches Verhalten nichtbindiger Böden und Schotter unter zyklisch-dynamischer Beanspruchung*. PhD thesis, Universität Gh Kassel, April 2002
9. J. Helm, J. Laue, and Th. Triantafydillis. Untersuchungen an der RUB zur Verformungsentwicklung von Böden unter zyklischen Beanspruchungen. In Th. Triantafyllidis, editor, *Böden unter fast zyklischer Belastung: Erfahrungen und Forschungsergebnisse*, pp. 109–133. Lehrstuhl für Grundbau und Bodenmechanik, Ruhr-Universität Bochum, 2000
10. I. Herle. *Hypoplastizität und Granulometrie einfacher Korngerüste*. PhD thesis, Institut für Boden- und Felsmechanik der Universität Karlsruhe, 1997. No. 142
11. A. Hettler. *Verschiebungen starrer und elastischer Gründungskörper in Sand bei monotoner und zyklischer Belastung*. PhD thesis, Institut für Boden- und Felsmechanik der Universität Karlsruhe, 1981. Heft No. 90
12. P. Hornych, J.F. Corte, and J.L. Paute. Étude des déformations permanentes sous chargements répétés de trois graves non traitées. *Bulletin de Liaison des Laboratoires des Ponts et Chaussées*, 184:77–84, 1993
13. K. Ishihara. Liquefaction and flow failure during earthquakes. *Géotechnique*, 43(3):351–415, 1993
14. S. Khedr. Deformation characteristics of granular base course in flexible pavements. In *Transportation Research Record*, vol. 1043, pp. 131–138, 1985
15. H.Y. Ko and R.F. Scott. Deformation of sand in hydrostatic compression. *Journal of Soil Mechanics and Foundations Division ASCE*, 93(SM3):137–156, 1967
16. R.W. Lentz and G.Y. Baladi. Constitutive equation for permanent strain of sand subjected to cyclic loading. In *Transportation Research Record*, vol. 810, pp. 50–54, 1981
17. W.A. Marr and J.T. Christian. Permanent displacements due to cyclic wave loading. *Journal of the Geotechnical Engineering Division ASCE*, 107(GT8):1129–1149, 1981
18. G.R. Martin, W.D.L. Finn, and H.B. Seed. Fundamentals of liquefaction under cyclic loading. *Journal of the Geotechnical Engineering Division ASCE*, 101(GT5):423–439, 1975
19. H. Matsuoka and T. Nakai. A new failure for soils in three-dimensional stresses. In *Deformation and Failure of Granular Materials*, pp. 253–263, 1982. Proceedings of IUTAM Symposium. in Delft
20. M.A. Miner. Cumulative damage in fatigue. *Transactions of the American Society of Mechanical Engineering*, 67:A159–A164, 1945
21. Z. Mróz, V.A. Norris, and O.C. Zienkiewicz. An anisotropic hardening model for soils and its application to cyclic loading. *International Journal for Numerical and Analytical Methods in Geomechanics*, 2:203–221, 1978

22. P.G. Nicholson, R.B. Seed, and H.A. Anwar. Elimination of membrane compliance in undrained triaxial testing. 1. measurement and evaluation. *Canadian Geotechnical Journal*, 30:727–738, 1993
23. A. Niemunis. *Extended hypoplastic models for soils*. Ruhr-University Bochum, Institute of Soil Mechanics and Foundation Engineering, 2003. 34, available from `www.pg.gda.pl/~aniem/an-liter.html`
24. A. Niemunis and M. Cudny. On hyperplasticity for clays. *Computers and Geotechnics*, 23:221–236, 1998
25. A. Niemunis and I. Herle. Hypoplastic model for cohesionless soils with elastic strain range. *Mechanics of Cohesive-Frictional Materials*, 2:279–299, 1997
26. A. Niemunis, T. Wichtmann, and T. Triantafyllidis. A high-cycle accumulation model for sand. *Computers and Geotechnics*, 32(4):223–315, 2005
27. A. Niemunis, T. Wichtmann, and Th. Triantafyllidis. Compaction of freshly pluviated granulates under uniaxial and multiaxial cyclic loading. In J. Vanicek et al., editor, *Geotechnical problems with man-made and man-influenced grounds*, vol. 1, pp. 855–860, August 2003. XIIIth European Conference On Soil Mechanics and Geotechnical Engineering, Prague
28. N.J. O'Riordan. Effects of cyclic loading on the long term settlements of structures. In M.P. O'Reilly and S.F. Brown, editors, *Cyclic Loading of Soils*, pp. 411–433. Blackie Glasgow, 1992
29. I.V. Papadopoulos. A new criterion of fatigue strength for out-of-phase bending and torsion of hard metals. *International Journal of Fatigue*, 16:377–384, 1994
30. J.L. Paute, P. Jouve, and E. Ragneau. Modéle de calcul pour le dimensionnement des chaussées souples. *Bulletin de Liaison des Laboratoires des Ponts et Chaussées*, 156:21–36, 1988
31. K.H. Roscoe and J.B. Burland. On the generalized stress-strain behaviour of wet clays. In J. Heyman and F.A. Leckie, editors, *Engineering plasticity*, pp. 535–609. Cambridge University Press, 1968
32. A. Sawicki. An engineering model for compaction of sand under cyclic loading. *Engineering Transactions*, 35:677–693, 1987
33. Y. Shamoto, M. Sato, and J-M. Zhang. Simplified estimation of earthquake-induced settlements in saturated sand deposits. *Soils and Foundations*, 36(1):39–50, 1996
34. A.S.J. Suiker. Fatigue behaviour of granular materials. Technical Report 7-98-119-3, Delft University of Technology, Faculty of Civil Engineering, 1998
35. A.S.J. Suiker. Static and cyclic loading experiments on non-cohesive granular materials. Technical Report 1-99-DUT-1, Delft University of Technology, Faculty of Civil Engineering, 1999
36. A.S.J. Suiker and R. de Borst. A numerical model for cyclic deterioration of railway tracks. *International Journal for Numerical Methods in Engineering*, 57:441–470, 2003
37. G.T.H. Sweere. *Unbound granular bases for roads*. PhD thesis, Delft University of Technology, Netherlands, 1990
38. T. Triantafyllidis, T. Wichtmann, and A. Niemunis. On the determination of cyclic strain history. In T. Triantafyllidis, editor, *Cyclic Behaviour of Soils and Liquefaction Phenomena*, pp. 321–334. Balkema, March/April 2004. International Conference in Bochum, 31 March–02 April 2004
39. K.C. Valanis and C.F. Lee. Endochronic theory of cyclic plasticity with applications. *Journal of Applied Mechanics*, 51:367–374, 1984

40. B. Vuong. Evaluation of back-calculation and performance models using a full scale granular pavement tested with the accelerated loading facility (alf). In *Proceedings 4th International Conference on the Bearing Capacity of Roads and Airfields, Minneapolis*, pp. 183–197, 1994
41. T. Wichtmann, A. Niemunis, and T. Triantafyllidis. The effect of volumetric and out-of-phase cyclic loading on strain accumulation. In T. Triantafyllidis, editor, *Cyclic Behaviour of Soils and Liquefaction Phenomena*, pp. 247–256. Balkema, March/April 2004. International Conference in Bochum, 31 March–02 April 2004
42. T. Wichtmann, A. Niemunis, and T. Triantafyllidis. Strain accumulation in sand due to drained uniaxial cyclic loading. In T. Triantafyllidis, editor, *Cyclic Behaviour of Soils and Liquefaction Phenomena*, pp. 233–246. Balkema, March/April 2004. International Conference in Bochum, 31 March–02 April 2004
43. T. Wichtmann, A. Niemunis, and T. Triantafyllidis. Strain accumulation in sand due to cyclic loading: drained triaxial tests. *Soil Dynamics and Earthquake Engineering*, 2005 vol. 25, No 12, pp. 967–979
44. H. Wolff and A.T. Visser. Incorporating elasto-plasticity in granular layer pavement design. In *Proceedings of Institution of Civil Engineers Transport*, vol. 105, pp. 259–272, 1994

On the Factors Affecting the Formation of Shear Band Systems in Non-Cohesive Soils Under Extensional Strain

T. Triantafyllidis, H. Wolf, and D. König

Institute for Foundation Engineering and Soil Mechanics, Faculty of Civil Engineering, Ruhr-University Bochum, Germany
office@gub.rub.de

1 Introduction

The occurrence of parallel and conjugated shear bands is frequently observed and well documented in several papers in the field of geotechnical engineering (retaining walls, slopes) and in the field of geology (faults, plate boundaries). Referring to geotechnical engineering the development of shear band systems is linked with the theory of plastic limit state in a half space which was introduced by Rankine in 1856 [39]. A loosening due to an extension of the granular material evokes shear stresses inside the soil mass and thus leads to a reduction of the horizontal stresses. The ratio of the horizontal and the vertical stress decreases from the value K_0 at rest

$$K_0 = \frac{\sigma_{h_0}}{\sigma_v} \tag{1}$$

to the value K_a

$$K_a = \frac{\sigma_{h_a}}{\sigma_v}, \tag{2}$$

where K_a is the active earth pressure coefficient. This appears in case where the loosening is increased until the active plastic limit state is reached the soil mass fails and a system of conjugated shear bands develops. The shear bands are inclined to the direction of minor principle stress with the angle of Coulomb [7]:

$$\vartheta_{\mathrm{C}} = \pm(45^\circ + \varphi/2), \tag{3}$$

where φ denotes the friction angle of the soil. Equation (3) satisfies the Coulomb hypothesis that the direction of the shear band coincides with the direction of the plane, where the ratio of shear stress and normal stress reaches a maximum. Roscoe [41] shows for dilative material that the orientation of a shear band against the direction of minor compressive stress as:

$$\vartheta_R = \pm(45^\circ + \psi/2), \tag{4}$$

where ψ denotes the dilatancy angle of the soil. A significant number of researches have investigated theoretically and experimentally the appearance of a single shear band [1,7,10,16,31,33,37,41,44,46,49,56] descriptions of systems with shear bands are rare. Valdoulakis [21] mentioned that for the orientation of the shear bands every angle between the solution of Roscoe (4) and Coulomb (3) is possible while Vermeer [22] summarized results of direct shear tests and biaxial tests [2,3,8,12] with respect to the dependence of the inclination of shear bands on particle sizes of sand, pointing out that Coulomb-type shear bands, with the angle of inclination ϑ_{C} appear in experiments with fine grained sand and Roscoe-type shear bands, with the angle of inclination ϑ_{R}, develop in experiments with coarse sand. Referring to the inclination of the shear bands Vermeer [49] summarized experimental results of Arthur et al. [3] whereupon shear bands in biaxial test are inclined to the direction of minor compressive stress by an angle which averages the inclinations proposed by Coulomb and Roscoe and which reads as follows:

$$\vartheta_{\mathrm{A}} = \pm(45^\circ + (\varphi + \psi)/4). \tag{5}$$

It is clear that the granulometry of the material plays a crucial role for the development of the shear bands, but how is the distance between the shear bands influenced? Bransby and Milligan [5] performed model tests on the deformation of soil behind flexible and rigid retaining walls. By means of radiography it was found that the failure of the soil behind the wall is accompanied by the development of a system of parallel shear bands which are inclined to the direction of minor principle stress by the angle proposed by Roscoe [41]. Based on the experimental data of Bransby and Milligan, Lesnièwska and Mróz [21, 22] calculated analytically the spacing of parallel shear bands behind flexible retaining walls. The results of their calculation agree with the magnitudes of the shear band spacing that has been extracted from the radiographs taken by Bransby and Milligan. Further examples of shear banding can be found in the research on numerical simulation of shear band patterns as done by Mühlhaus and Aifantis [32], Tejchman and Wu [45] or Nübel and Karcher [35]. Poliakov et al. [38] investigated the dependence of shear band formation on dynamic soil parameters. They simulated systems of shear bands numerically by the finite difference method, applying pure shear on a square sample of an elasto-plastic material. They introduced a non-dimensional parameter B, defined as follows:

$$B = \frac{\sigma v_{\mathrm{p}}}{G_{\mathrm{dyn}} v_{bc}} \tag{6}$$

where σ denotes the confining pressure, G_{dyn} the dynamic shear modulus and $v_{\mathrm{P}}/v_{\mathrm{bc}}$ is the ratio of the p-wave velocity v_{p} and the loading velocity v_{bc}. They postulated that the factor B controls the behavior of the shear band system. In particular, changing the various parameters does not affect the results as long as B is kept unchanged: both the evolution and the spacing of the shear

bands depend on this parameter. An increase in B leads to an increase in shear band spacing and vice versa. The latter is explained by Poliakov et al. as follows: when a shear band forms, this process is accompanied by a decrease in stress inside and an increase in stress outside the band. This increase in stress inhibits the formation of a new shear band adjacent to the former one. The stress difference propagates through the material with the p-wave velocity. Hence a large value of B, synonymous with a large p-wave velocity, leads to widely separated shear bands.

Additional information in literature with reference to a specific shear band spacing is rare although patterns of localization zones have been observed in further geotechnical experiments [4, 13, 24, 26, 42] and as a result of numerical modelling of the localization phenomena [27, 30, 35, 36, 38, 45].

In the field of geology the mechanical behavior of the earth's crust and the interaction between the brittle crust and the ductile substratum have been investigated intensively by means of experiments and numerical simulations [18,31,33,47,48]. In a series of experiments in a sand-box McClay [26–28,34,36] and McClay and Ellis [29, 30] studied the deformation of the earth's crust under various strains and compared the results with the geometry of shear band patterns that have developed in situ under similar boundary conditions. In all experiments the ductile lower crust of the earth was simulated by the use of a rubber membrane whereas the brittle crust was modelled by a layer of granular material as, e.g. sand.

All mentioned investigations have in common that the general deformation of the soil mass has been investigated but the influence of specific material properties or boundary conditions on the geometry of the developing shear band systems has not been determined yet. In the geotechnical literature the theoretical and experimental investigation of shear banding in granular materials is mainly concentrated on the description of the localization phenomena in dense specimens. This limitation is based on findings whereupon a concentration of shear strains in narrow bands can solely be observed in dense materials that show hardening followed by softening whereas in loose granular media the sand mass deforms homogeneously until the residual strength of the material is reached. Han and Vardoulakis [17] performed biaxial tests on saturated fine grained sand with different initial densities in order to study the stress–strain behavior of the material. They observed the development of shear bands that were inclined by the Coulomb angle ϑ_C in sand specimen with a medium density between $D = 0.76$ and $D = 0.52$ whereas only a homogeneous deformation of the sample could be detected in samples with a loose density of $D = 0.19$. Contrary to these experiments Desrues et al. [11] show that strain localizes in loose specimen that have been loaded in a triaxial cell.

An comprehensive study with series of sand-box extension experiments has been carried by the authors [52, 53] where the influence of the granulometric properties, the dynamic soil parameters, the stress level and the geometry of the specimens on the spacing and the inclination of the localization zones was studied. The following parameters have been varied: (a) the height and

width of the specimen (the length was kept constant, i.e. 50 cm), (b) the stress level (using centrifuge testing up to $15\,g$), (c) the velocity of loading, (d) the dynamic shear modulus of the material, (e) the initial relative density, (f) the grain size distribution (uniformity U, d_{50}, max. grain size, etc.) For further details on the investigated parameter variations the interesting reader is referred to Wolf [51].

2 Experimental Set-Up and Data Acquisition Methods

2.1 Experimental Set-Up and Model Preparation

Figure 1 shows a schematic picture of the experimental set-up. A sample of granular material is placed on a rubber membrane that is linked to a fixed wall on the one side and a movable wall on the other side. By displacing the movable wall the rubber membrane is stretched and, neglecting friction between the rubber and the bottom plate, a linear displacement distribution and thus a constant strain inside the membrane can be assumed. Consequently, the strain is applied to the granular sample by the rubber membrane.

Results of similar experiments [18, 19] suggest that special attention has to be paid in order to achieve a uniform strain distribution inside the rubber membrane. In order to achieve this requirement and with respect to a good reproducibility of the experiments, a special mechanism has been designed that provides a linear displacement of the rubber membrane during any state of the experiment. The satisfaction of the uniform strain in the rubber has to be proven also in model tests under increased gravity where friction between rubber membrane and bottom plate is significantly increased. A sketch and a photograph of the device including this mechanism are shown in Fig. 1. The mechanism consists of metal bars (1) which are connected by a scissors mechanism (2) and which slide on steel rods (3) parallel to the displacement direction

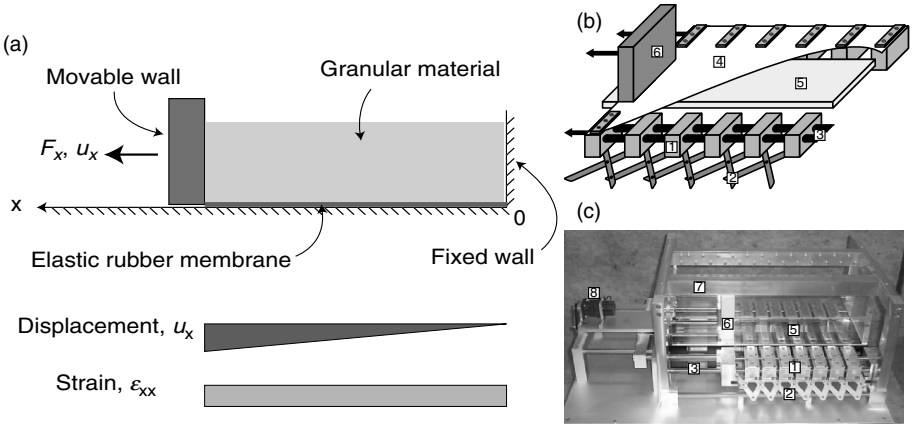

Fig. 1. (**a**) Simplified model of the experiment, (**b**) schematic view, (**c**) photograph

of the movable wall. The rubber membrane (4) lies on a glass bottom plate (5) and is fastened at the fixed wall (in the right of the figure), the movable wall (6) and the metal bars (1). The specimen is surrounded by plexiglass walls which are fixed at a frame (7), providing a small gap for the membrane to be fixed at the bars. The movable wall and the scissors mechanism are displaced by a step motor (8). The strain distribution inside the rubber membrane can be controlled during the experiments by observing a mesh that is drawn on the bottom side of the membrane through the glass plate.

Geometrical Constrains

The length of the specimen in its initial state is 50 cm, a displacement of 20 cm can be applied by the device resulting to a cumulative horizontal strain of the entire specimen of 40%. The maximum height of the sample is 30 cm. The width of the device has been chosen to 20 cm in order to minimize the influence of friction between the sample material and the side walls while providing the possibility of evaluating the experiments with X-ray technique by the available X-ray source. This choice was met after variations of the specimens width between 10 and 30 cm and observation of the arch shape of the shear bands at the top of the specimen as well as the quality of the X-ray photos taken during the tests.

Homogeneity of the Applied Strain

As already mentioned special attention has to be paid in order to ensure a homogenous distribution of the strain inside the rubber membrane during the sand-box experiments. The evaluation of the rectangular meshes that are drawn on the bottom sides of the rubber membranes confirms that the application of the scissors mechanism provides constant strain conditions along the displacement direction of the movable wall. Furthermore the elongation of the membrane perpendicular to the stretching direction is inhibited. These findings are supported by the Digital Image Correlation (DIC) evaluation of the digital pictures taken of the bottom side of the rubber membrane during the stretching process. In order to reduce friction between the rubber sheet and the glass plate, which mainly causes irregularities with respect to the strain distribution, the contact surface is prepared with talcum powder in natural gravity and with silicone oil during ng-experiments. In addition the thickness of the rubber membrane is increased from $d = 1\,\text{mm}$ to $d = 2\,\text{mm}$ during the experiments in increased gravity. Possible assumptions whereupon the spacing of the developing shear bands my be influenced by the distance of the metal bars which fix the rubber membrane have been disproved by additional experiments in which the rubber membrane has been fixed not at any but at every second steel bar. These experiments show corresponding results with respect to the spacing and the inclination of the shear bands (for further details the interesting reader is referred to Wolf [51]).

Method of Specimen Preparation

As detected by several researchers [6, 20, 24, 43, 47, 50] the density of the prepared specimen, and thus the mechanical properties of the material, are heavily dependent on the sample preparing method and on the composition of the material. In our experiments, the material is pluviated into the device with a hopper and different sieves. The sieves and the distance between them and the actual surface of the specimen are chosen with respect to the desired density, the spacing varies between 10 and 30 cm, respectively. Using this method, we obtain a density inside the quartz sand specimen for values of D (relative density) between $D = 0.4$ and $D = 1.0$.

2.2 Data Acquisition and Measurement Technique

Two different measurement techniques have been used for the determination of the distance between shear bands and their inclination. Due to difficulties of analyzing processes inside the sample with simple optical measurements, a mobile X-ray system is used to portray differences in density of the investigated granular material and thus to identify zones of shear localization within the entire sample width. By evaluating single pictures that are taken at defined stages of the experiment with a specific software, the shear band spacing as well as the shear band inclination can be determined with a high accuracy of 0.1 mm and 0.1°, respectively. In order to analyze the deformation of the soil mass on the sides of the specimen an additional technique of optical image analysis called "DIC" has been used. During the last years, DIC has been applied to the evaluation of displacements and strains of granular materials by several researchers [34, 40, 50, 51, 53]. The working principle of DIC is illustrated in Fig. 2. The method requires a series of digital pictures of the object, each taken from the same position within a certain time or displacement increment (Fig. 2a). By means of DIC the displacement of small areas of the soil mass (interrogation windows) are determined and displayed in a vector plot (Fig. 2b). On the basis of the vector field strains can be calculated (Fig. 2c). For a detailed description of the method see [53]. The experiments under natural gravity are recorded with a charge-coupled device (CCD)-camera providing a maximum image rate of 12 frames per second, the CCD matrix has a resolution of 1280 × 1024 pixel. We recorded images with a frequency of 0.5 Hz, taking into account the displacement velocities of the movable wall of 2.87 mm min^{-1} in natural gravity the displacement increment between two images is equivalent to 0.096 mm per image. The centrifuge experiments are recorded with a simple compact CCD camera with a CCD resolution of 1152 × 864 pixel. The size of the interrogation window has been chosen under the specific requirement of the size of the area of interest, the required precision and the required number of vectors (resolution).

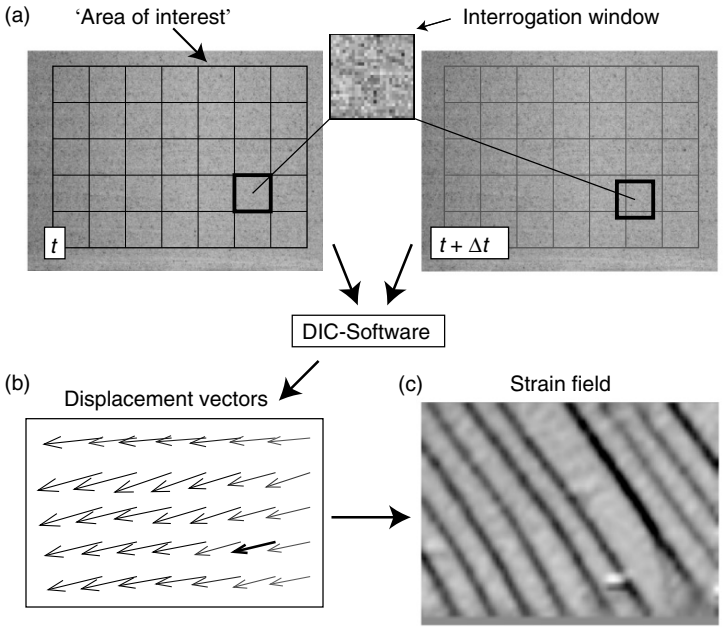

Fig. 2. Working principle of DIC

3 Experimental Programme and Results

3.1 First Series of Experiments

The experimental investigation comprises several steps. In the first series of experiments the material, the geometry of the specimen and the granulometry of the materials has been varied in order to obtain an idea of the significant parameters affecting the shear band spacing under extensional load. In this paper only the summary of the results of this series will be given. For more details the interesting reader is referred to [52, 53].

Investigated Materials and Their Parameters

For the variation of the material quartz sand, artificial particles (urea resin) chilled iron grid and glass beats have been used in our experiments. The investigated materials and their properties are summarized in Table 1.

The localization of deformation develops spontaneously with uniformly distributed shear bands over the entire length of the specimen at amounts of strain between 2 and 6% depending on the material. The failure zones remain

Table 1. Material parameters

Material	d^{a}(mm)	$d_{50}{}^{b}$(mm)	U^{c}(–)	φ^{d}(deg)	ψ^{e}(deg)	γ^{f}(D = 1.0) (kN m^3)	$\rho_s{}^{g}$(g cm^3)	$G_{\mathrm{dyn}}{}^{h}$(N mm^{-2})	$c_{\mathrm{P}}{}^{i}$(m s^{-1})
quartz sand	0.1–0.71	0.35	1.5	45.0	15.0	17.30	2.64	178	590
quartz sand	1.0–2.0	1.58	1.5	47.0	20.0	16.05	2.64	–	–
quartz sand	0.06–2.0	0.85	5.1	44.5	16.5	18.30	2.64	–	–
quartz sand	0.5–1.2	0.89	1.5	45.0	–	16.40	2.64	–	–
artificial particles	0.1–0.4	0.35	1.5	37.0	8.0	7.95	1.55	32	395
glass beads	0.06–1.0	0.32	1.4	33.0	12.0	15.90	2.50	170	618
iron grit	0.06–0.5	0.24	1.7	47.0	13.50	37.30	7.27	95	288

[a]grain size [b]average grain size [c] coefficient of uniformity [d] friction angle at peak [e] angle of dilatancy [f] specific weight [g] grain density [h] dynamic shear modulus [i] compressional wave velocity

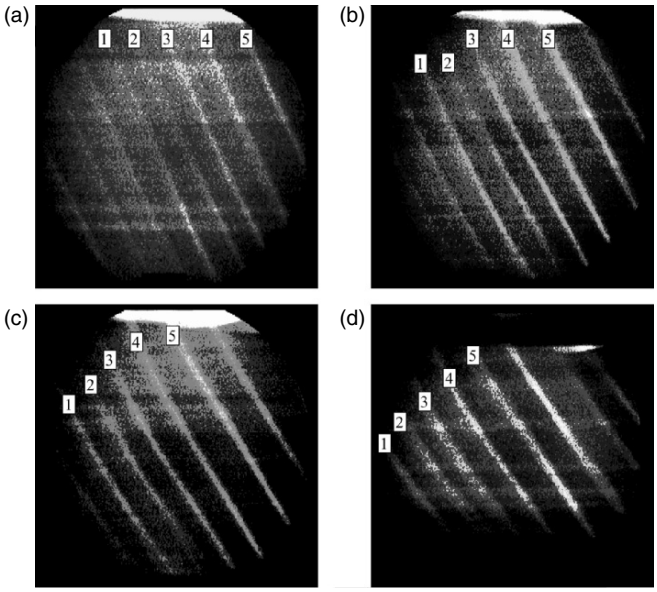

Fig. 3. Radiographs of four stages in the development of the shear band system with increasing horizontal strain: (**a**) $\epsilon_{xx} = 10\%$; (**b**) $\epsilon_{xx} = 20\%$; (**c**) $\epsilon_{xx} = 30\%$; (**d**) $\epsilon_{xx} = 40\%$. Identical shear bands are numbered

active and planar during the entire process of straining. Additional shear zones do not develop, not even at high amounts of strain (up to 40%, see Fig. 3). Supplementary strain after the localization is accumulated predominantly in the existing failure zones. In all experiments the inclination of the shear zones decreases with increasing strain while the distance between shear bands remains almost constant throughout the tests. The blocks rotate towards the moving wall ("bookshelf mechanism").

Influence of Granulometric Parameters

The average grain size diameter d_{50} hardly influences the spacing between the localization zones. Its influence on the thickness d_{SB} of the shear band is verified and amounts at the beginning of the formation between 7 and 13 times the size of d_{50}. Furthermore the maximum grain size diameter is corresponding to a larger distance between the shear bands independent on the ratio of uniformity.

In a granular material with a high coefficient of uniformity the mechanical behavior and the material parameters related to the maximum grain size govern the shape of the developing shear bands A very interesting point is the appearance of conjugate shear band systems in tests with coarse material and with a highly non-uniform sand (Fig. 4). Whereas the sand with higher

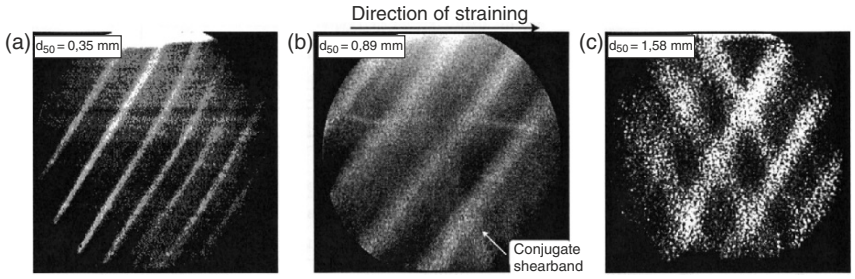

Fig. 4. Radiographs for two quartz sands with three different average grain sizes in the development of the shear band system: (**a**) $d_{50} = 0.35\,\mathrm{mm}$; (**b**) $d_{50} = 0.89$ and (**c**) $d_{50} = 1.58\,\mathrm{mm}$

non-uniformity produces only a few less distinctive conjugate shear bands, the ones in coarse sand are clear and make the same angle to either side of the vertical. The size of the d_{50} grain diameter seems to be very decisive for the appearance or not of the conjugated shear bands.

Influence of the Initial Height

The spacing of the shear zones is linearly dependent on the initial height of the specimens [39, 41, 51–53].

Influence of the Dynamic Parameters

The shape of the shear band system is independent of the rate of loading. The strong dependency of the shear band pattern on dynamic material parameters as proposed by Poliakov et al. [38] in the form the dimensionless parameter B has not been confirmed by our experimental investigations [51].

3.2 Second Series of Experiments

The second series of experiments was performed in order to investigate the influence of the stress level on the spacing between the shear bands. All experiments have been performed with quartz sand (Siligran®), owning an average grain size of $d_{50} = 0.35\,\mathrm{mm}$ and a coefficient of uniformity of $U = d_{60}/d_{10} = 1.5$. The grain size was in the range of 0.1–0.71 mm, the friction angle $\varphi = 39.8°$, the angle of dilatancy, $\psi = 14.5°$ and the grain density $\rho_s = 2.64\,\mathrm{g\,cm^3}$. Sand-box experiments on quartz sand with varying densities and geometry were performed. Some specimens are tested in increased gravity in the Bochum Geotechnical Centrifuge. While keeping all geometrical dimensions and soil properties constant, the magnitude of the gravity level has been varied up to 15 g in order to investigate the influence of the g-level and thus

the magnitude of the bulk density on the shape of the developing shear band pattern. For comparison reasons experiments with both heights of 10 and 15 cm have been performed.

Influence of Stress Level

In the increased stress field it is also observed that the shear band inclination ϑ decreases linearly with increasing horizontal strain, the spacing a between the shear bands remains almost equal compared to the amount of straining. With respect to the shear band inclination it is of particular importance that the principal stresses remain vertical and horizontal as numerical calculations have shown. The diagram shows that independent of the gravity level all experiments owning the same height in initial state have almost the same spacing and the same inclination. The proportionality between initial height and shear band spacing is also verified with the centrifuge tests (Fig. 5). The optical evaluation of the radiographs in Fig. 3 leads to the conclusion that the determining deformation mechanism is "bookshelf-deformation" as described for example by Mandl [23]. Following this model, at the initial state all localization zones are inclined to the horizontal by the angle ϑ, two adjacent shear zones surround a block and are spaced at the distance a (Fig. 5a). With increasing horizontal strain the blocks rotate towards the direction of stretching, the angle ϑ decreases while the spacing a remains constant.

3.3 Third Series of Experiments

Sand-box experiments on quartz sand with varying initial densities and a constant geometry were performed. The stress–strain behavior of the model

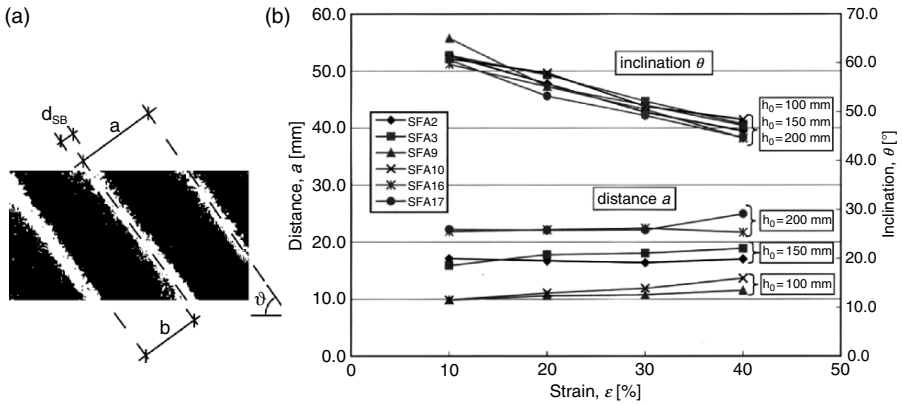

Fig. 5. (**a**) Definition of the distance a between two adjacent shear bands, the inclination ϑ, the width of the block b and d_{SB} the thickness of a shear band; (**b**) experimental results referring to shear band inclination ϑ and shear band spacing a

material is determined by performing triaxial extension tests with initial densities corresponding to those of the sand-box experiments.

Triaxial Extension Tests

The stress–strain behavior of granular materials is mainly influenced by the prevailing stress level and the density of the material. Results of pre-tests as well as experimental results in literature suggest that not only the density but also the applied stress path affects the stress–strain response of the material. In case of triaxial extension the vertical stress can be decreased while keeping the confining stress constant or the radial stress is increased whereas the axial stress remains unchanged. As the measurement of stresses is not possible during the sand-box tests the experiment has been modelled numerically by means of a hypoplastic constitutive law [55] in order to determine the development of the stresses inside the specimen and thus to find out which of the two stress paths described earlier fits best to the stress state during the sand-box experiments [53]. The results of the modelling show that the stress along the stretching direction of the rubber membrane σ_1 decreases immediately after the displacement of the movable wall has been started and reaches a constant value corresponding to an active horizontal stress as described by Rankine (cf. (2)). The horizontal stress perpendicular to the displacement direction σ_2 remains constant, the vertical stress σ_3 shows only a slight decrease due to the small reduction of the height of the sample with the beginning of the material loosening, which can be neglected at a first stage. The fact that two principle stresses σ_2 and σ_3 remain almost constant whereas one stress σ_1 decreases indicates that the stress state in the sand-box experiments can be described most suitably in triaxial extension test by keeping the cell pressure constant and decreasing the axial load. (For the behavior of the material in the sand box case is more suitable to use biaxial rather than triaxial test results.)

Figure 6 displays the results of the triaxial extension tests that have been performed on dry quartz sand. Each curve in Fig. 6 represents a specific relative density between $D_{\min} = 0.40$ and $D_{\max} = 1.05$ which is similar to the relative density of a group of sand-box experiments. The results in Fig. 6 with respect to the mobilized friction angle show that higher initial densities lead to a more brittle material behavior close to the peak and a sand sample of lower relative density shows a drawn-out plateau around the peak. The magnitude of the peak friction angle decreases with falling relative density whereas the magnitude of the shear strain at the peak of the stress–stress-curve increases (see Table 2). The composition of the volumetric strain versus the shear strain in Fig. 6b reveals a dependence of the volumetric response of the material on the relative density. All curves show dilative behavior after a certain amount of shearing where the volumetric strain rate increases with increasing density. This dependence is reflected in the angle of dilatancy ψ which is defined as the gradient of the volumetric strain versus the shear strain and which can be

Table 2. Friction angle, dilatancy angle, shear strain and theoretical shear band inclinations at the peak in dependence of the specimen's relative density

relative density D [−]	friction angle φ_{peak} [deg]	dilatancy angle ψ_{peak} [deg]	shear strain $\gamma_{\mathrm{Peak}}^{\mathrm{Triax}}$ [%]
1.05	39.8	14.5	5.67
0.84	36.6	10.6	6.87
0.69	35.0	7.8	8.24
0.55	33.3	5.3	8.96
0.40	31.1	2.8	9.70

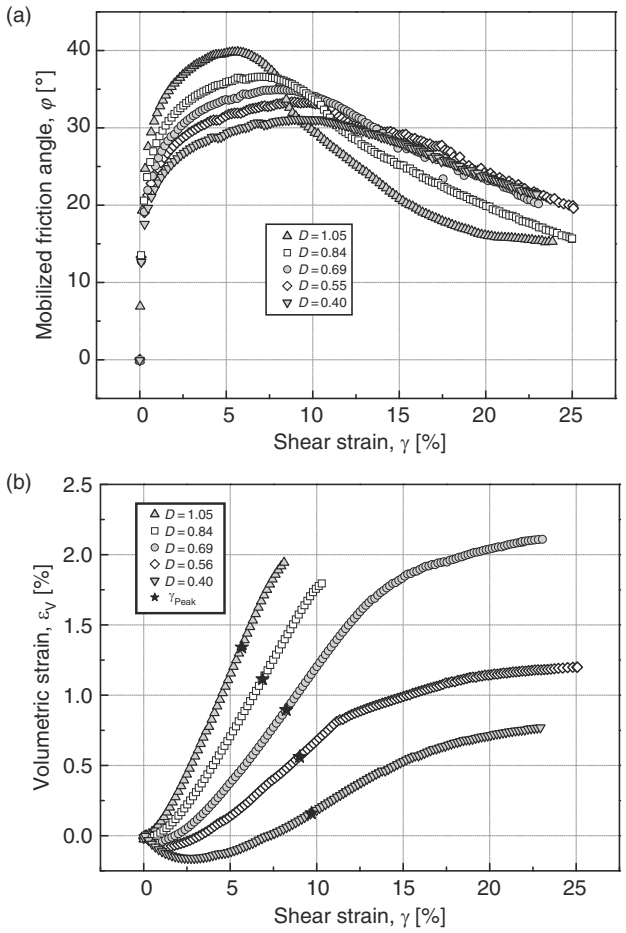

Fig. 6. (**a**) Mobilized friction angle φ and (**b**) volumetric strain ε_{V}, both versus shear strain γ

calculated as follows [15]:

$$\psi = \arctan\left[\frac{\varepsilon_{\mathrm{vol}}}{\gamma}\right] = \arctan\left[\frac{\varepsilon_1 + 2\varepsilon_3}{\varepsilon_1 - \varepsilon_3}\right]. \tag{7}$$

Around the peak of the stress–strain curve the volume of the specimen increases uniformly and thus the dilatancy angle reaches a constant value. The volumetric strain at the peak of the stress–strain curve is marked with a star in Fig. 6b. The corresponding dilatancy angles at the peaks of the stress-strain curves in dependence of the specimens' relative density are summarized in Table 2.

Sand-box Experiments with Different Densities

As the influence of the stress level has already been investigated [53] it was of interest to perform sand-box experiments with varying initial densities. The work is mainly concentrated on the performance of experiments in natural gravity but some experiments were carried out under increased gravity. By means of these tests it shall be explored whether possible changes in the granular packing of samples with a lower density due to the increasing of the stress-level influence the spacing and the inclination of the developing shear bands. If a certain amount of horizontal strain is applied to the specimen a system of shear bands develops, which is uniformly distributed over the entire length of the specimen. It is important to mention that all shear bands develop simultaneously. Figure 7 shows the results of the performed sand-box experiments with varying initial relative densities of the specimens in natural as well as in increased gravity. In both diagrams the shear band spacing a and the shear band inclination ϑ are displayed versus the applied horizontal strain ε_{xx}. Different symbols characterize different initial densities. It can be concluded from Fig. 7a and b that independent of the initial density of the specimen the spacing of the shear bands remains almost constant throughout the whole straining process. As far as the experiments in natural gravity are concerned distinct differences in the shear band spacing with respect to the density of the specimens can be detected although it is clearly visible that the deviation from the average value increases with decreasing density. A noticeable tendency whereas the shear band inclination decreases with decreasing relative density of the specimen can be recognized.

3.4 Determination of the Localization Strain

In order to determine the horizontal strain and shear strain at the time when the shear bands appear, a method is used which was presented by the authors [53] and is based on the DIC-evaluation of the digital photographs of the granular structure at the sides of the specimens. By means of DIC the shear strain on side of the specimens is calculated for different amounts of applied

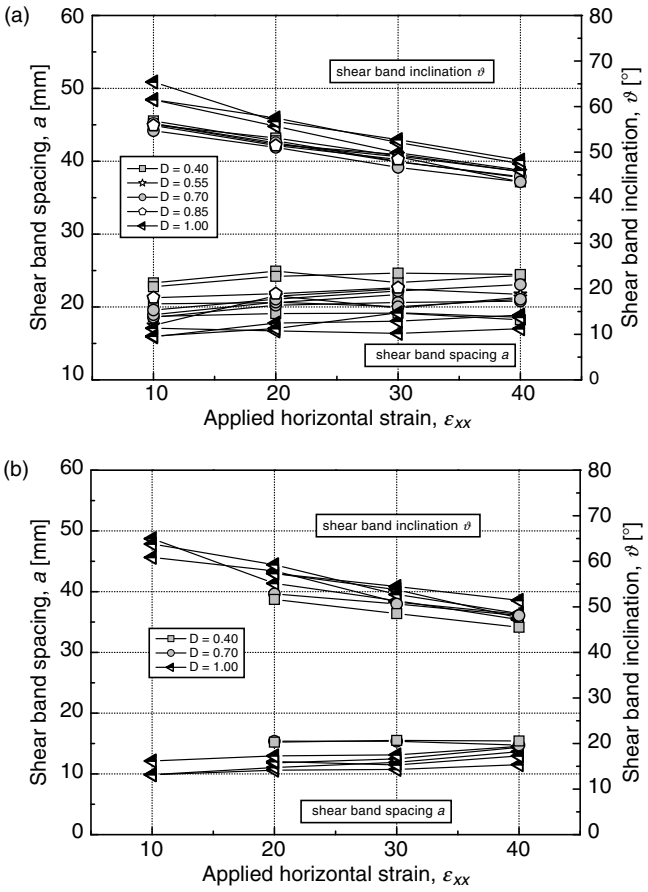

Fig. 7. Shear band spacing and shear band inclination in dependence of the relative density (**a**) in natural gravity (**b**) in increased gravity

horizontal strain, subsequently a path is defined perpendicular to the developing shear bands. The calculated magnitudes of shear strain are extracted along this path for different quantities of applied horizontal strain and are displayed versus the corresponding horizontal strain in a diagram as exemplarily shown in Fig. 8. The point of localization can be determined exactly if the shear strain γ is plotted versus the corresponding horizontal strain ε_{xx} at different positions inside and between the developing shear bands as displayed in Fig. 8a. The positions are marked in Fig. 8a with respective symbols. Both groups of curves show an observable kink, before and behind the kink the relationship between shear strain and horizontal strain is linear. The kinks denote the transition from a homogenous deformation of the specimen to the accumulation of the strains inside the shear bands and the reduction of the accumulation between the localization zones, respectively. Both segments of the

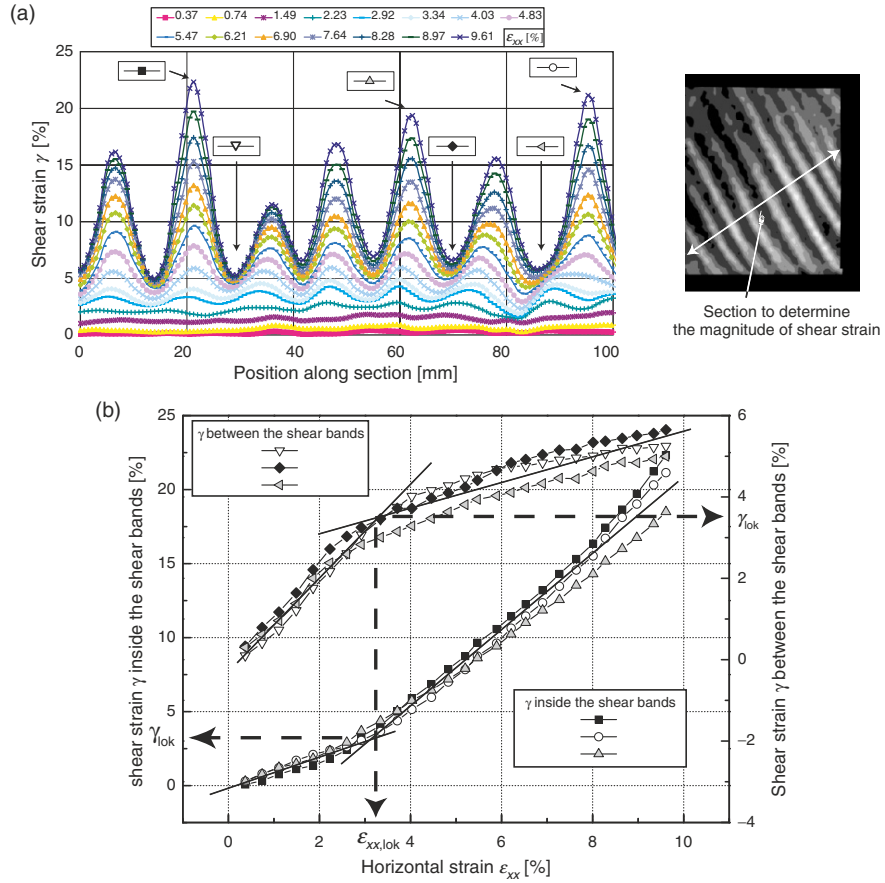

Fig. 8. (**a**) Development of the shear strain along a section defined perpendicular to the developing shear bands at different amounts of applied horizontal strain ε_{xx}, (**b**) Exact determination of the localization point

curves can be approximated by straight lines, the intersections of the lines correlate with the horizontal strain $\varepsilon_{xx,\mathrm{loc}}$ and the shear strain γ_{loc} at the point of localization. The evaluation of the curves in Fig. 8b results in $\varepsilon_{xx,\mathrm{loc}} = 3.20\%$ and $\gamma_{\mathrm{loc}} = 3.40\%$, respectively. This method of evaluation of the digital images is first introduced by Wolf [51, 53] where the evaluation of the digital images for all the experiments has been carried out and given in tables.

Influence of the Density on the Shear Band Spacing

The results with respect to the determination of the localization strains from the sand-box model tests indicate clearly that the applied horizontal localization strain $\varepsilon_{xx,\mathrm{loc}}$ as well as the shear strain at the point of localization γ_{loc} are dependent on the initial density of the specimen. The localization strain $\varepsilon_{xx,\mathrm{loc}}$ increases from $\varepsilon_{xx,\mathrm{loc}} = 3.30\%$ for a relative density of $D = 1.04$

up to a magnitude of $\varepsilon_{xx,\mathrm{loc}} = 7.42\%$ for $D = 0.55$. The magnitude of the shear strain at the localization point for $D = 1.05$ amounts to $\gamma_{\mathrm{loc}} = 3.40\%$ which is in the same order of magnitude as $\varepsilon_{xx,\mathrm{loc}}$. The localization shear strain increases up to $\gamma_{\mathrm{loc}} = 11.17\%$ for a relative density of $D = 0.55$. The dependence of the localization strains on the density of the model material indicates that higher amounts of shear strain have to be evoked inside a looser sample in order to make a localization of deformation in a shear band possible. Furthermore it can be concluded from the experimental results that the deviation from the average localization strains increases with decreasing density of the model material. It has been shown that significant differences can be identified in Fig. 7a,b whereup on the shear band spacing increases with decreasing relative density of the specimen. The change of the spacing comes along with an increasing deviation of the shear band spacing from the average value when a specimen with a low density is tested. The growing deviation with decreasing density results in the situation that some experiments with a relatively low density show smaller distances than specimens that have been prepared with a comparatively high density. The change of the deviation is attended by observations during the performance of the sand-box experiments whereupon the distribution of the shear band spacing is much more irregular if specimens with relatively low densities are tested than during experiments with dense specimens. With respect to the results of the triaxial extension tests these findings lead to the conclusion, that the deviation of the spacing of the localization zones from the average value increases the more the distinct softening and hardening behavior of a dense soil vanishes. Table 3 summarizes the shear band spacing $a_{\varnothing}$ in dependence of the relative density averaged over all experiments associated with one density and averaged over the applied horizontal strain. If the average distance is plotted versus the relative density, a linear relationship between both variables can be identified and therefore the change of the shear band spacing a can be correlated to change of the relative density of the specimen. As far as the influence of the stress–strain behavior of the material is concerned a change of the relative density causes a change of a variety of parameters as, e.g. the magnitude of the friction angle φ, the dilatancy angle ψ or the shear strain γ_{peak} at the peak of the stress–strain curve. For this reason it is not possible to correlate a change of the shear band spacing or the shear band inclination with a single parameter but with

Table 3. Average values of the shear band spacing in dependence of the relative density D

relative density, D [–]	average shear band spacing, $a_{\varnothing}$ [mm]
1.00	17.39
0.85	21.91
0.70	20.12
0.55	20.98
0.40	21.93

the "global" property density. By means of radiography it has been shown that the shear band spacing increases linearly with decreasing relative density within the investigation range, hence the change of the shear band spacing is directly correlated with the change of the density.

4 Summary of the Parameters Affecting the Shear Banding

It has been shown that the shear band formation in the sand-box extension experiment depends linearly on the height of the specimen but the stress level does not influence the spacing of the shear bands. The softening behavior of the non-cohesive material after reaching the peak friction angle depends from the initial density. The softening gradient with respect to the shear strain seems to be one of the important parameters governing the spacing between the shear bands [21,22,51]. This gradient depends on the stress ratio in a real three dimensional regime (stresses σ_1, σ_2, σ_3). which can be formulated with the factor b, determined as:

$$b = \frac{\sigma_2 - \sigma_3}{\sigma_1 - \sigma_3} \tag{8}$$

with σ_1 being the highest, σ_3 the lowest and σ_2 the medium principal stress resp. The post peak behavior of the mobilized angle of friction with respect to the shear strain shows a strong dependency on the factor b. The triaxial compression is corresponding to the value of $b = 0$ and the triaxial extension to the value $b = 1$, respectively. The biaxial experiment shows values of b between 0 and 1. The stress–strain behavior of the material under biaxial conditions shows a stronger degradation of the mobilized angle of friction than under triaxial conditions [9, 14]. In Fig. 9b the comparison of the mobilized angle of friction between biaxial experiments on sand and the theoretical approaches using non-local theories is presented [25] where in Fig. 9a the schematic view of the degradation of the angle of friction in the post peak domain is presented.

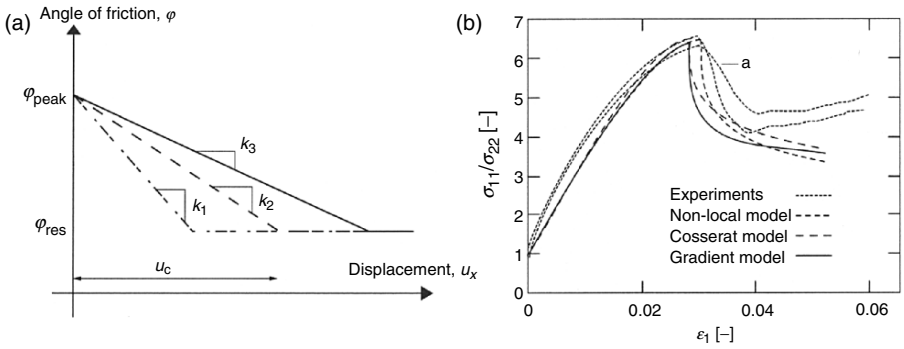

Fig. 9. (**a**) Degradation scheme for the angle of friction in the post peak regime, (**b**) experimental results and simulations of biaxial tests [25]

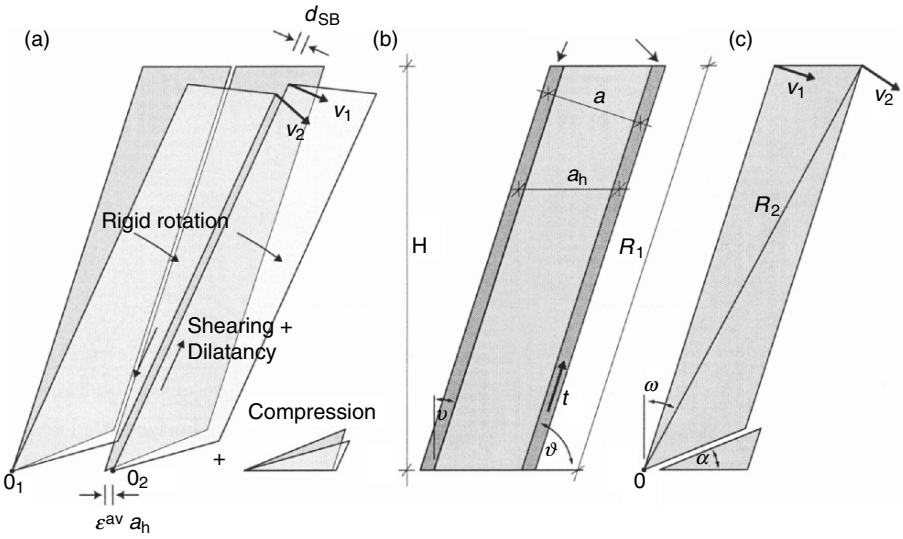

Fig. 10. Geometry of the kinetics of the shear band system

From the observations and from the experimental results (X- ray and DIC) of the deformation mechanisms after the appearance of the shear bands in the sand specimen was the "bookshelf"- mechanism, where the shear bands are dilating and the sand blocks between them compressed [51]. A first approach on the kinematics is given in [51] and the scheme of this mechanism is presented in Fig. 10. The applied energy in the system due to the rubber stretching is transferred to the movement of the rotating blocks, which deform also elastically and to the shear band dilation as well as to the deformation of the wedges at the bottom corner of the rotating blocks (see Fig. 10) where energy is dissipated. It can be shown that the application of energetic approaches (i.e. max. dissipation energy, etc.) lead to the determination of the shear band spacing. For further details the interesting reader is referred to Wolf [51] but further approaches are still needed for the correct problem description.

5 Acknowledgment

This chapter is based on the results of the up to day research work carried out within the collaborative research center (SFB 526: Rheology of the Earth, Subproject A1) and the financial support of the DFG (German Research Council) is greatfully acknowledged herewith.

References

1. Alshibli, A., Sture, S. (2000): Shear band formation in plane strain experiments on sand. Journal of Geotechnical and Geoenvironmental Engineering, **126**(6), 495–503

2. Arthur, J.R.F., Dunstan, T. (1982): Rupture layers in granular media. In: Vermeer, P.A., Luger, H.J. (Eds), *Proceedings of the UITAM Symposium. Deformation and Failure of Granular Materials, Delft*, 453–459
3. Arthur, J.R.F., Dunstan, T., Al-Ani, Q.A.J.L. (1977): Assadi A. Plastic deformation and failure in granular media. Géotechnique **27**(1), 53–74
4. Bolton, M.D., Stewart, D.I., Powrie, W. (1988): The design of deep in-situ walls. In: *Proceedings of the International conference on Centrifuge 88,* Corte JF (Ed). Balkema: Rotterdam, 405–414
5. Bransby, P.L., Milligan, G.W.E. (1998): Soil deformations near cantilever sheet pile walls. Géotechnique **48**(4), 465–481
6. Cobbold, P.R., Durand, S., Mourges, R. (2001): Sandbox modelling of thrust wedges with fluid-assisted detachments. Tectonophysics **334**, 245–258
7. Coulomb, C.A. (1773): Sur l'application des règles des maximis et minimis à quèlques problèmes de statique relatifs à l'architecture. Mémoires de Mathématique et de Physique, Académie Royale des Sciences **7**, 343–382
8. Desrue, J. (1984): La localisation de la déformation dans les matériaux granulaires. PhD dissertation, *Institute National Polytechnique de Grenoble*, Grenoble, 1–283
9. Desrues, J., Hammad, W. (1989): Shear banding on mean stress level in sand. In: Numerical Methods for Localization and Bifurcation of Granular Bodies, Danzig, 57–67
10. Desrues, J., Lanier, J., Stutz, P. (1985): Localization of the deformation in tests on sand sample. Engineering Fracture Mechanics **21**(4), 909–921
11. Desrues, J., Chambon, R., Mokni, M., Mazerolli, F. (1996): Void ratio evolution inside shear bands in triaxial sand specimens studied by computed tomography. Géotechnique **46**(3), 529–546
12. Duthilleul, B. (1982): Rupture progressive: simulation physique et numérique. PhD dissertation, *Institute National Polytechnique de Grenoble*, Grenoble, 1–260
13. Finno, R.J., Harris, W.W., Mooney, M.A., Viggiani, G. (1997): Shear bands in plane strain compression of loose sand. Géotechnique **47**(1), 149–165
14. Green, G.E., (1971): Strength and deformation of sand measured in an independent stress control cell, In stress–Strain Behaviour of Soils (Ed. R.H.G. Parry), 285–323
15. Gudehus, G. (1981): *Bodenmechanik*, Ferdinand Enke Verlag,
16. Han, C., Drescher, A. (1991): Shear bands in biaxial tests on dry coarse sand. Soils and Foundations **33**(1), 118–132
17. Han, C., Vardoulakis, I. (1991): Plane-strain compression experiments on water-saturated fine-grained sand. Géotechnique **41**(1), 49–78
18. Harper, T., Fossen, H., Nesthammer, J. (2001): Influence of uniform basement extension on faulting in cover sediments. Journal of Structural Geology **23**, 593–600
19. Jeng, F.S., Lu, C.Y., Lee, C.L. (1998): Major scale effects influencing model simulation of neotectonics. In: *Proceedings of International Conference on Centrifuge 98,* Balkema, Rotterdam, 817–823
20. Krantz, R.W. (1991): Measurements of friction coefficients and cohesion for faulting and fault reactivation in laboratory models using sand and sand mixtures. Tectonophysics **188**, 203–207
21. Leśniewska, D., Mróz, Z. (2000): Limit equilibrium approach to study the evolution of shear band systems in soil. Géotechnique **50**(5), 521–536

22. Leśniewska, D., Mróz, Z. (2001): Study of evolution of shear band systems in sand retained by flexible wall. International Journal for Numerical and Analytical Methods in Geomechanics **25**, 909–932
23. Mandl, G. (2000): *Faulting in brittle rocks*. Springer, Berlin New york Heidelberg,
24. Mandl, G., de Jong, L.N.J., Maltha, A. (1977): Shear zones in granular material. Rock Mechanics **9**, 95–144
25. Mayer Th. (2002): Numerische Modellierung der Entfestigung im rahmen der hypoplastizität *Schriftenreihe des Lehrstuhls Baugrund - Grundbau der Universität Dortmund*, Heft 24
26. McClay, K.R. (1989): Analogue models of inversion tectonics. In: *Inversion Tectonics,* Cooper, M.A., Williams, G.D. (eds). Geological Society Special Publication, 41–59
27. McClay, K.R. (1990): Deformation mechanics in analogue models of extensional fault systems. In: *Deformation Mechanisms, Rheology and Tectonics, Geological Society Special Publication,* Knipe, R.J., Rutter, E.H. (Eds). 445–453
28. McClay, K.R. (1995): The geometries of inverted fault systems: a review of analogue model studies. In: *Basin Inversion,* Buchanan, J.G., Buchanan, P.G. (Eds.), 97–118
29. McClay, K.R., Ellis, P.G. (1987): Analogue models of extensional fault geometries. In: *Continental Extensional Tectonics,* Coward, M.P., Dewey, J.F., Hancock, P.L. (Eds). Geological Society Special Publication, 109–125
30. McClay, K.R., Ellis, P.G. (1987): Geometries of extensional fault systems developed in model experiments. Geology **15**(4), 341–344
31. Mokni, M., Desrues, J. (1998): Strain localisation measurements in undrained plane-strain biaxial tests on Houston RF Sand. Mechanics of Cohesive Frictional Materials **4**(4), 419–441
32. Mühlhaus H.-B., Aifantis E.G. (1989): Strain localization in viscoplastic materials with microstructure. *Proceedings of the Second International Workshop on Numerical Methods for Localization and Bifurcation of Granular Bodies*, Gdansk, 105–116
33. Mühlhaus, H.-B., Vardoulakis, I. (1987): The thickness of shear bands in granular materials. Géotechnique **37**(3), 271–283
34. Nübel, K. (2003): Experimental and numerical investigation of shear localization in granular material. *Veröffentlichung des Instituts für Boden- und Felsmechanik, Universität Fridericiana zu Karlsruhe,* Heft 159
35. Nübel, K., Karcher, C. (1998): FE simulations of granular material with a given frequency distribution of voids as initial condition. Granular Matter **1**, 101–112
36. Nübel, K., Gudehus, G. (2001): Evolution of localized shearing: dilation and polarization in grain skeletons. In: *Proceedings: Powder and Grains*, Balkema, Rotterdam
37. Oda, M., Kazama, H. (1998): Microstructure of shear bands and its relation to the mechanisms of dilatancy and failure of dense granular soils. Géotechnique **48**(4), 465–481
38. Poliakov, A.N.B., Herrmann, H.J. (1994): Fractal plastic shear bands. Fractals **2**(4), 567–581
39. Rankine, W.J.M. (1856): On the stability of loose earth. Philosophical Transactions of the Royal Society of London **147**(1), 9–27
40. Rechenmacher, A.L., Finno, R.J. (2004): Digital image correlation to evaluate shear banding in dilative sands. Geotechnical Testing Journal **27**(1), 1–10

41. Roscoe, K.H. (1975): The influence of strains in soil mechanics. Géotechnique **25**(2), 175–195
42. Saada, A.S., Liang, L., Figueroa, J.L., Cope, C.T. (1999): Bifurcation and shear band propogation in sands. Géotechnique **49**(3), 367–385
43. Schellart, W.P. (2000): Shear test results for cohesion and friction coefficients for different granular materials: scaling implications for their usage in analogue modelling. Tectonophysics **324**, 1–16
44. Tatsuoka, F., Nakamura, S., Huang, C.C., Tani, K. (1990): Strength anisotropy and shear band direction in plane strain tests of sand. Soils and Foundations **30**(1), 35–564
45. Tejchman, J., Wu, W. (1993): Numerical study on patterning of shear bands in a Cosserat Continuum. Zeitschrift für angewandte Mathematik und Mechanik **99**, 61–74
46. Vardoulakis, I. (1980): Shear band inclination and shear modulus of sand in biaxial tests. International Journal for Numerical and Analytical Methods in Geomechanics **4**, 103–119
47. Vendeville, B., Cobbold, P.R. (1988): How normal faulting and sedimentation interact to produce listric fault profiles and statigraphic wedges. Journal of Structural Geology **10**(7), 649–659
48. Vendeville, B., Cobbold, P.R., Davy, P., Brun, J.P., Choukroune, P. (1987): Physical models of extensional tectonics at various scales. In: *Continental Extensional Tectonics, Geological Society Special Publications*, 95–107
49. Vermeer, P.A. (1990): The orientation of shear bands in biaxial tests. Géotechnique **40**(2), 223–236
50. White, D.J., Take, W.A., Bolton, M.D. (2003): Soil deformation measurement using particle image velocimetry (PIV) and photogrammetry. Géotechnique **53**(7), 619–631
51. Wolf, H. (2005): Zur Scherfugenbänderung granularer Materilien unter Extensionsbeanspruchung, *Schriftenreihe des Institutes für Grundbau und Bodenmechanik der Ruhr-Universität Bochum*, Heft Nr. 37
52. Wolf, H., König, D., Triantafyllidis, Th. (2003): Experimental investigation of shear band patterns in granular material. Journal of Structural Geology **25**(8), 1229–1240
53. Wolf, H., König, D., Triantafyllidis, Th. (2005): Centrifuge model tests on sand specimen under extensional load. International Journal for Numerical and Analytical Methods in Geomechanics **29**(1), 25–47
54. Wolf, H., König, D., Triantafyllidis, Th. (2005): The influence of the stress–strain behavior of non-cohesive soils on the geometry of shear band systems under extensional strain, *Engineering Structures* (accepted)
55. von Wolffersdorff, P.A. (1997): Verformungsprognosen für Stützkonstruktionen. Ph.D. thesis, Institut für Bodenmechanik und Felsmechanik der Universitfät Fridericiana Karlsruhe, Heft 141
56. Yoshida, T., Tatsuoka, F. (1997): Deformation property of shear band in sand subjected to plane strain compression and its relation to particle characteristics. In: *Proceedings of the Fourteenth International Conference on Soil Mechanics and Foundation Engineering,* 237–240

Acceleration Waves in Hypoplasticity - 2D Analysis

B. Weingartner, V.A. Osinov and W. Wu

Institute of Geotechnical Engineering, University of Natural Resources and Applied Life Sciences, Vienna, Austria
bernhard.weingartner@boku.ac.at

1 Introduction

Acceleration waves play an important role in the theoretical analysis of solids as their existence and properties are closely related to well-posedness, stability, bifurcation and shear band formation. These issues have been studied mainly under the assumption of incremental linearity of the constitutive equation [1,8,11–13,21]. Under this assumption, the acceleration wave analysis and the method of characteristics lead to the same equation for the wave speeds, which allows us to apply the acceleration wave approach to such issues as well-posedness and stability. Little is known for incrementally nonlinear constitutive equations. As it may entail qualitative changes in the analysis, theoretical studies with incrementally nonlinear models attract more attention in recent years [2, 4, 5, 10, 16–18, 25].

The main feature of an incrementally nonlinear solid compared to a linear one is that the spectrum of the speeds of acceleration waves is continuous. The spectrum of the characteristic wave speeds is continuous as well but is described by different equations. Thus, the connection between the existence of acceleration waves and hyperbolicity of the dynamic equations is no longer valid. The question therefore arises as to whether these two spectra are identical and whether this connection can be re-established.

In the present paper, we study acceleration waves with a fairly general hypoplastic constitutive equation. We consider plane acceleration waves, calculate wave speeds and investigate their dependence on the stress state. The aim of this study is, on the one hand, to generalize the nonlinear shear band analysis by Wu [25] to the dynamic case, i.e. to the acceleration wave propagation, and, on the other hand, to perform the wave speed analysis by the characteristic method along the lines of Osinov [14], and then to compare the results.

2 Constitutive Equation

Hypoplastic constitutive relations constitute a class of incrementally nonlinear tensorial relations between the stress rate and the strain rate developed for the description of the plastic behaviour of granular materials. The hypoplasticity theory may be viewed as an alternative to elasto-plasticity theories as it was devised without the introduction of yield surface, flow rule and without the decomposition of the deformation into an elastic and a plastic part.

A review of hypoplastic constitutive equations can be found in the recent paper by Wu and Kolymbas [24]. Some advanced versions of hypoplastic constitutive models have been proposed to describe different behaviour, e.g. critical state [6] and viscosity [7]. In the present paper, however, a simple constitutive equation is used. This has some merits in that the wave analysis is largely simplified and the outcome can be easily extended to other refined models.

Consider the following constitutive equation proposed by Wu and Kolymbas [22]:

$$\mathring{\mathbf{T}} = \mathsf{L}(\mathbf{T}) : \mathbf{D} + \mathbf{N}(\mathbf{T})\|\mathbf{D}\|. \tag{1}$$

Here $\mathring{\mathbf{T}}$ is the Jaumann derivative of the stress tensor defined as

$$\mathring{\mathbf{T}} = \frac{\mathrm{d}\mathbf{T}}{\mathrm{d}t} + \mathbf{T}\mathbf{W} - \mathbf{W}\mathbf{T}, \tag{2}$$

where $\mathrm{d}/\mathrm{d}t$ stands for the material time derivative. $\mathbf{D}$ and $\mathbf{W}$ are the rate of deformation tensor and the spin tensor, respectively,

$$\mathbf{D} = \frac{1}{2}\left[\frac{\partial \mathbf{v}}{\partial \mathbf{x}} + \left(\frac{\partial \mathbf{v}}{\partial \mathbf{x}}\right)^{\mathrm{T}}\right], \quad \mathbf{W} = \frac{1}{2}\left[\frac{\partial \mathbf{v}}{\partial \mathbf{x}} - \left(\frac{\partial \mathbf{v}}{\partial \mathbf{x}}\right)^{\mathrm{T}}\right] \tag{3}$$

and $\mathbf{v}(\mathbf{x})$ is the velocity field. $\mathsf{L}(\mathbf{T}) : \mathbf{D}$ and $\mathbf{N}(\mathbf{T})$ in (1) are isotropic tensor-valued functions. L is a fourth-order tensor and the colon ':' denotes the inner product between two tensors, $\|\cdot\|$ stands for a norm and is defined by $\|\mathbf{D}\| = \sqrt{\mathbf{D} : \mathbf{D}}$.

The wave analysis will be carried out for constitutive equation (1). For numerical calculations the following constitutive equation is used [23]:

$$\mathring{\mathbf{T}} = C_1(\mathrm{tr}\mathbf{T})\mathbf{D} + C_2\frac{(\mathbf{T} : \mathbf{D})\mathbf{T}}{\mathrm{tr}\mathbf{T}} + \left(C_3\frac{\mathbf{T}^2}{\mathrm{tr}\mathbf{T}} + C_4\frac{\mathbf{T}^{*2}}{\mathrm{tr}\mathbf{T}}\right)\|\mathbf{D}\|, \tag{4}$$

where $C_1, \ldots, C_4$ are material constants, and $\mathbf{T}^* = \mathbf{T} - \mathbf{I}\,\mathrm{tr}\mathbf{T}/3$. The following material constants typical of Karlsruhe dense sand are used in the numerical calculations: $C_1 = -106.5, C_2 = -801.5, C_3 = -797.1, C_4 = 1077.7$.

In the further analysis we will use the notion of failure surface defined in the framework of hypoplasticity as follows. A material element with a stress $\mathbf{T}$ is said to be at failure if there exists a strain rate $\mathbf{D} \neq 0$ such that $\mathring{\mathbf{T}} = 0$, that is

$$\mathsf{L}(\mathbf{T}) : \mathbf{D} + \mathbf{N}(\mathbf{T})\|\mathbf{D}\| = 0. \tag{5}$$

Dividing (5) by $\|\mathbf{D}\|$ and equating the norm of $\mathbf{D}/\|\mathbf{D}\|$ to unity, we arrive at the equation

$$\mathrm{tr}\left(\mathsf{L}^{-1}(\mathbf{T}) : \mathbf{N}(\mathbf{T})\right)^2 = 1. \tag{6}$$

Stress states satisfying (6) form a surface in the stress space called failure surface [23].

3 Acceleration Waves

An acceleration wave is defined as a propagating surface $S(\mathbf{x}, t) = 0$ of weak discontinuity [8]. This means that a field variable (in our case the velocity and the stress field) is continuous across the surface S, but the spatial and temporal derivatives exhibit a jump, as schematically shown in Fig. 1. Using brackets $[\![\ ]\!]$ to denote a jump of a function across a surface, we thus have

$$\begin{aligned} \left[\!\left[\frac{\partial \mathbf{v}}{\partial \mathbf{x}}\right]\!\right] &= \left(\frac{\partial \mathbf{v}}{\partial \mathbf{x}}\right)^{+} - \left(\frac{\partial \mathbf{v}}{\partial \mathbf{x}}\right)^{-} \neq 0, \\ \left[\!\left[\frac{\partial \mathbf{v}}{\partial t}\right]\!\right] &= \left(\frac{\partial \mathbf{v}}{\partial t}\right)^{+} - \left(\frac{\partial \mathbf{v}}{\partial t}\right)^{-} \neq 0, \end{aligned} \tag{7}$$

$$[\![\mathbf{v}]\!] = \mathbf{v}^{+} - \mathbf{v}^{-} = 0, \tag{8}$$

where the superscripts $+$ and $-$ stand for $\mathbf{v}$ immediately before and behind S.

To simplify the matter we restrict our analysis to plane waves. The velocity and stresses in such waves depend on only one spatial Cartesian component, say x_1, and time. We consider initial stress states with $T_{13} = T_{23} = 0$ in order to allow for the existence of waves with only two nonzero components of velocity

$$v_1 = v_1(x_1, t), \quad v_2 = v_2(x_1, t), \quad v_3 = 0. \tag{9}$$

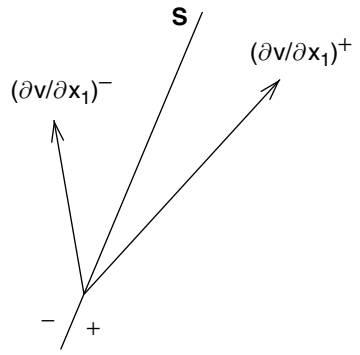

Fig. 1. Discontinuity of the velocity gradient across the surface S

With the above assumptions, constitutive equation (1) can be written out for the components T_{11} and T_{12} as (cf. [14])

$$\begin{aligned} \frac{\mathrm{d}T_{11}}{\mathrm{d}t} &= \eta_1 \frac{\partial v_1}{\partial x_1} + \eta_2 \frac{\partial v_2}{\partial x_1} + \eta_3 \|\mathbf{D}\|, \\ \frac{\mathrm{d}T_{12}}{\mathrm{d}t} &= \eta_4 \frac{\partial v_1}{\partial x_1} + \eta_5 \frac{\partial v_2}{\partial x_1} + \eta_6 \|\mathbf{D}\|, \end{aligned} \tag{10}$$

where the coefficients $\eta_1, \ldots, \eta_6$ depend on the material constants $C_1, \ldots, C_4$ and the stress state $\mathbf{T}$, and

$$\|\mathbf{D}\| = \sqrt{\left(\frac{\partial v_1}{\partial x_1}\right)^2 + \frac{1}{2}\left(\frac{\partial v_2}{\partial x_1}\right)^2}. \tag{11}$$

The constitutive equations for the components T_{22} and T_{33} are not given here because they will not appear in the subsequent analysis.
It is convenient to specify the direction of wave propagation with respect to the principal axes of the instantaneous stress tensor. For this purpose, an angle α is introduced as shown in Fig. 2. The components of the stress tensor in the coordinate system (x_1, x_2, x_3) and therefore the coefficients η_i are then functions of the principal stresses T_1, T_2, T_3 and the angle α

$$\eta_i = \eta_i \left(T_1, T_2, T_3, \alpha\right), \quad i = 1, \ldots, 6 \tag{12}$$

and are continuous across the surface S. Constitutive equations (10) written for the jumps across the surface S read

$$\begin{aligned} \left[\!\left[\frac{\mathrm{d}T_{11}}{\mathrm{d}t}\right]\!\right] &= \eta_1 \left[\!\left[\frac{\partial v_1}{\partial x_1}\right]\!\right] + \eta_2 \left[\!\left[\frac{\partial v_2}{\partial x_1}\right]\!\right] + \eta_3 [\![\|\mathbf{D}\|]\!], \\ \left[\!\left[\frac{\mathrm{d}T_{12}}{\mathrm{d}t}\right]\!\right] &= \eta_4 \left[\!\left[\frac{\partial v_1}{\partial x_1}\right]\!\right] + \eta_5 \left[\!\left[\frac{\partial v_2}{\partial x_1}\right]\!\right] + \eta_6 [\![\|\mathbf{D}\|]\!]. \end{aligned} \tag{13}$$

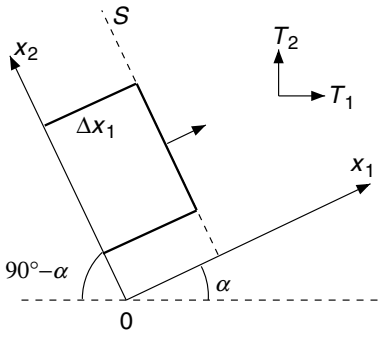

Fig. 2. Definition of the angle α of the wave propagation direction. T_1 and T_2 are the principal stresses. The inclination angle of the surface S is given by the complementary angle $90^\circ - \alpha$

Besides the constitutive relations, the equation of motion is needed

$$\operatorname{div}\mathbf{T}+\mathbf{f}=\varrho\,\frac{\mathrm{d}\mathbf{v}}{\mathrm{d}t}, \tag{14}$$

where ϱ is density, and $\mathbf{f}$ is mass force, both of which are continuous across S. For the plane waves considered here, the equations of motion for the jumps are written as

$$\begin{aligned}\left[\!\left[\frac{\partial T_{11}}{\partial x_1}\right]\!\right]&=\varrho\left[\!\left[\frac{\mathrm{d}v_1}{\mathrm{d}t}\right]\!\right],\\ \left[\!\left[\frac{\partial T_{12}}{\partial x_1}\right]\!\right]&=\varrho\left[\!\left[\frac{\mathrm{d}v_2}{\mathrm{d}t}\right]\!\right].\end{aligned} \tag{15}$$

Making use of the fact that the stresses and velocity are continuous across S, that is,

$$\left[\!\left[\frac{\partial}{\partial t}+(c+v_1)\frac{\partial}{\partial x}\right]\!\right]=0, \tag{16}$$

where c is the propagation speed of an acceleration wave relative to the material, we obtain

$$\left[\!\left[\frac{\mathrm{d}}{\mathrm{d}t}\right]\!\right]=-c\left[\!\left[\frac{\partial}{\partial x}\right]\!\right]. \tag{17}$$

From (17) and (15) we have

$$\left[\!\left[\frac{\mathrm{d}T_{11}}{\mathrm{d}t}\right]\!\right]=c^2\varrho\left[\!\left[\frac{\partial v_1}{\partial x_1}\right]\!\right],\quad \left[\!\left[\frac{\mathrm{d}T_{12}}{\mathrm{d}t}\right]\!\right]=c^2\varrho\left[\!\left[\frac{\partial v_2}{\partial x_1}\right]\!\right]. \tag{18}$$

The combination of (13) and (18) leads to the following equations for the wave speed c:

$$\begin{aligned}\eta_1\left[\!\left[\frac{\partial v_1}{\partial x_1}\right]\!\right]+\eta_2\left[\!\left[\frac{\partial v_2}{\partial x_1}\right]\!\right]+\eta_3[\![\|\mathbf{D}\|]\!]&=c^2\varrho\left[\!\left[\frac{\partial v_1}{\partial x_1}\right]\!\right],\\ \eta_4\left[\!\left[\frac{\partial v_1}{\partial x_1}\right]\!\right]+\eta_5\left[\!\left[\frac{\partial v_2}{\partial x_1}\right]\!\right]+\eta_6[\![\|\mathbf{D}\|]\!]&=c^2\varrho\left[\!\left[\frac{\partial v_2}{\partial x_1}\right]\!\right].\end{aligned} \tag{19}$$

To gain perspectives, the above equations can be recast in the following matrix notation:

$$(\mathbf{A}-c^2\varrho\mathbf{I})\,\mathbf{B}\,[\![\mathbf{g}]\!]=\mathbf{b}\,(\|\mathbf{g}^+\|-\|\mathbf{g}^-\|) \tag{20}$$

with

$$\mathbf{A}=\begin{pmatrix}\eta_1 & \eta_2\\ \eta_4 & \eta_5\end{pmatrix},\ \mathbf{B}=\begin{pmatrix}1 & 0\\ 0 & \sqrt{2}\end{pmatrix},\ \mathbf{b}=\begin{pmatrix}-\eta_3\\ -\eta_6\end{pmatrix}. \tag{21}$$

The vector $\mathbf{g}$ with components

$$g_1=\frac{\partial v_1}{\partial x_1},\quad g_2=\frac{1}{\sqrt{2}}\,\frac{\partial v_2}{\partial x_1} \tag{22}$$

represents the components of the strain tensor $\mathbf{D}$, and its length $\|\mathbf{g}\|=(g_1^2+g_2^2)^{1/2}$ is equal to the norm of $\mathbf{D}$, see (11). The matrix $\mathbf{A}$ contains the

coefficients of the linear terms in (19) and can be related to the acoustic tensor in linear constitutive models, while the vector $\mathbf{b}$ comprises the coefficients of the nonlinear terms.

The analysis of acceleration waves is equivalent to finding nontrivial solutions, i.e. $[\![\mathbf{g}]\!] \neq 0$, of the system of linear equations (20). Assuming a certain value for the difference $\|\mathbf{g}^+\| - \|\mathbf{g}^-\|$ on the rhs of (20), a solution $[\![\mathbf{g}]\!]$ can always be found provided that the matrix $(\mathbf{A} - c^2\varrho\mathbf{I})\,\mathbf{B}$ is nonsingular. This, however, does not necessarily mean that the chosen c is a possible wave speed: the solution $[\![\mathbf{g}]\!]$ must satisfy an additional geometrical condition (the triangle condition)

$$\|[\![\mathbf{g}]\!]\| \geq \big|\|\mathbf{g}^+\| - \|\mathbf{g}^-\|\big|. \tag{23}$$

In other words, in the (g_1, g_2)-plane it must be possible for the solution vector $[\![\mathbf{g}]\!]$ to connect in some way two concentric circles whose radii differ by the prescribed value $\|\mathbf{g}^+\| - \|\mathbf{g}^-\|$. This condition is illustrated in Fig. 3.

Recapitulating the findings in the investigation of the shear band formation problem [25], we introduce a ratio

$$\xi = \frac{\|[\![\mathbf{g}]\!]\|}{\|\mathbf{g}^+\| - \|\mathbf{g}^-\|}. \tag{24}$$

In order to avoid a negative denominator, in the following we consider ξ^2. The above condition (23) can be rewritten as

$$\xi^2 \geq 1. \tag{25}$$

We plot ξ^2 versus c in Fig. 4 for different stress states, starting close to the center of the octahedral plane (for reference see Fig. 5) and moving towards the failure surface. Figure 4a corresponds to a stress state close to the hydrostatic state with $\mathrm{tr}\mathbf{T} = -1{,}000$ kPa. The quantity ξ^2 is finite for all values of c except for two poles where $\xi^2 \to \infty$. Checking the condition $\xi^2 \geq 1$ graphically in Fig. 4a, we see that the spectrum of possible wave speeds is continuous and

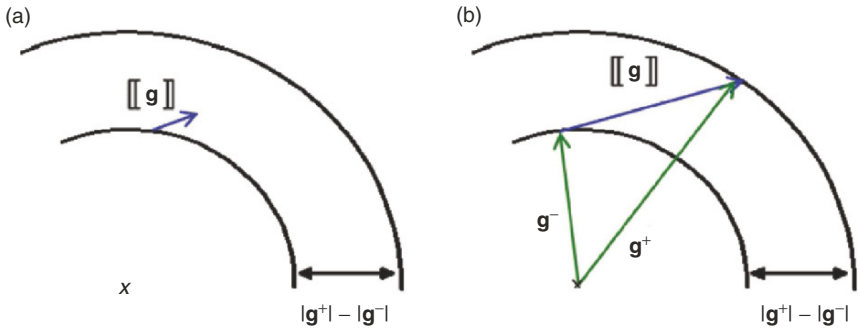

Fig. 3. The triangle condition (23) is fulfilled in **(b)** and violated in **(a)**: the length of the solution vector, $\|[\![\mathbf{g}]\!]\|$, in (a) is too small to connect the concentric circles with radii $\|\mathbf{g}^-\|$ and $\|\mathbf{g}^+\|$

consists of two intervals $[c_1, c_2]$ and $[c_3, c_4]$ situated around the poles. The boundary values $c_1, \ldots, c_4$ of the two intervals can be found by solving the equation

$$\xi^2(c^2) = 1. \tag{26}$$

This is a fourth-order algebraic equation in c^2, which in the generic case gives four real non-negative solutions.

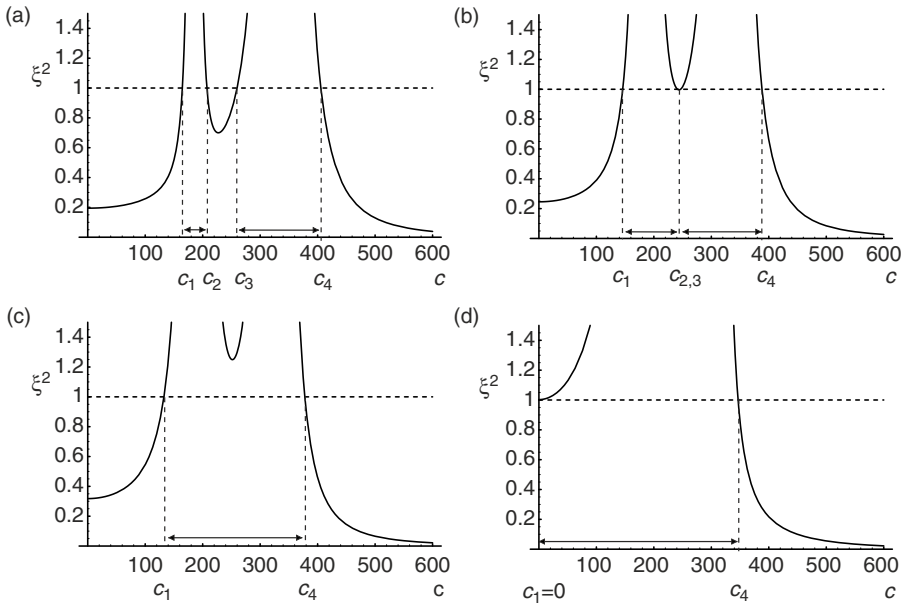

Fig. 4. Ratio ξ^2 versus c for various stress states (see Fig. 5 for reference). (**a**) Four real roots and two separate intervals. (**b**) A double real root, the transition to flutter ill-posedness. (**c**) Two real roots, flutter ill-posedness. (**d**) One zero root, shear banding

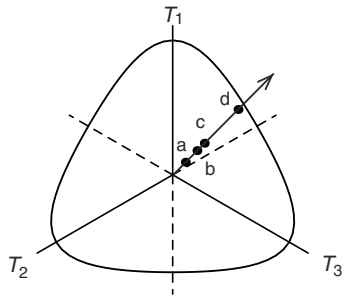

Fig. 5. Stress states from Figs. 4 and 10 on the octahedral plane $\mathrm{tr}\mathbf{T} = -1,000$ kPa. The closed curve shows the failure surface described by (6)

The condition $\xi^2 \to \infty$ or, equivalently, $\|\mathbf{g}^+\| - \|\mathbf{g}^-\| = 0$ leads to a linear system

$$(\mathbf{A} - c^2 \varrho \mathbf{I})\, \mathbf{B}\, [\![\mathbf{g}]\!] = 0 \tag{27}$$

instead of (20). This system is also obtained with $\mathbf{b} = 0$, that is, if the nonlinear term in constitutive equation (1) is dropped. Thus, the two wave speeds corresponding to the singularities of ξ^2 are found from the equation

$$\det \left[(\mathbf{A} - c^2 \varrho \mathbf{I})\, \mathbf{B}\right] = 0. \tag{28}$$

4 Flutter Ill-Posedness and Shear Banding

The investigation of the dependence of admissible wave speeds c on the stress state reveals interesting features. As the stress state changes from a nearly hydrostatic state in Fig. 4a towards the failure surface in Fig. 4b–d, the central branch of the curve $\xi^2(c)$ moves upward. In Fig. 4b the local minimum reaches the border $\xi^2 = 1$, resulting in the merging of the two intervals ($c_2 = c_3$). This stress state corresponds to the onset of what is called flutter ill-posedness (or flutter instability [1, 19]) when two wave speeds become complex-conjugate. Note that the notion of flutter instability or ill-posedness has been used for incrementally linear constitutive equations, where an initially finite perturbation grows exponentially with time [9, 20]. In case of incremental nonlinearity, however, the existence of complex conjugate wave speeds does not necessarily mean instability or ill-posednesss. The relation between them will be investigated in the next sections.

As the stress state moves further away from the hydrostatic axis, Fig. 4c, the solutions c_2, c_3 to (26) become complex and disappear from the real axis leading to one large interval of wave speeds between the remaining real solutions c_1, c_4. For a stress state near the failure surface, Fig. 4d, the left branch of the curve eventually crosses the border $\xi^2 = 1$. The lower boundary c_1 of the admissible wave speeds becomes zero, corresponding to a nonpropagating discontinuity, or shear banding.

Real solutions c to (26) are presented in Fig. 6 in polar plots, in which the distance to the origin corresponds to the value of the wave speed and the angle α shows the direction of wave propagation, see Fig. 2. The wave speeds for which the triangle condition (25) is fulfilled are gray-shaded. The plots (a),(b),(d),(f) correspond to the stress states marked in Fig. 5. Two additional plots (c) and (e) are inserted in between to illustrate particular features that arise on a stress path from nearly hydrostatic state towards the failure surface. In Fig. 6a we observe two separate spectra for all values of α. In the principal stress directions ($\alpha = 0°$ and $90°$) the left interval shrinks to one single (real) number and, correspondingly, the curve $\xi^2(c)$ in the vicinity of this pole shrinks to a Dirac-like function. Flutter ill-posedness is reached in (b), where the boundaries c_2 and c_3 coalesce. This happens for a wave propagation direction α lying close to 45°. The angle range of flutter ill-posedness increases with the further deviation towards the failure

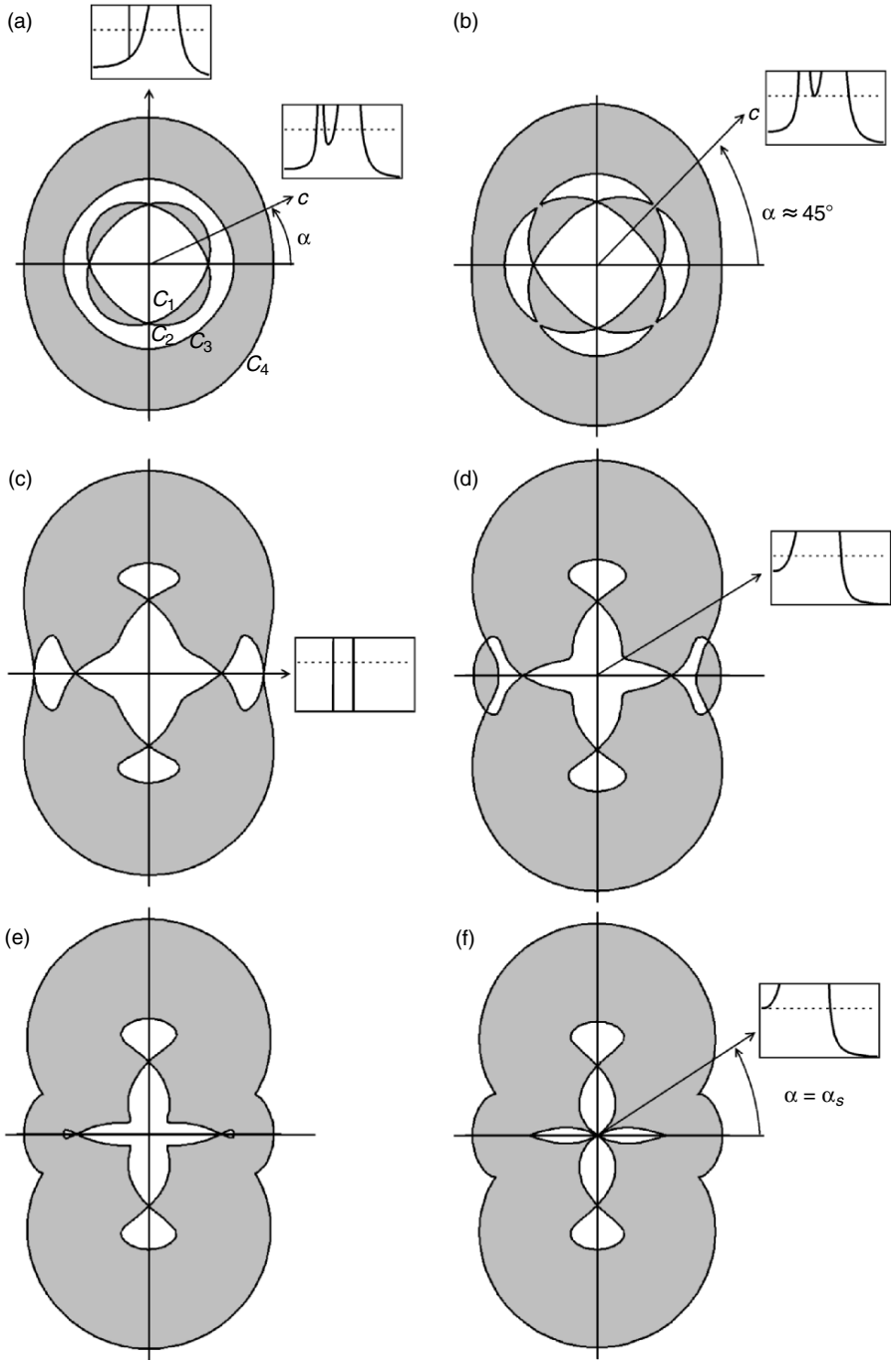

Fig. 6. Polar representation of the wave speeds for various stress states

surface, see (b–d). In (c) we observe a degenerate case for $\alpha = 0$, where both intervals shrink to single values, thus resembling two discrete solutions that are obtained in the linear case (27).

In Fig. 6e one can already anticipate the reduction of c_1 to zero, giving rise to shear banding in Fig. 6f. This occurs at an angle α_s which lies in the vicinity of 30° and depends slightly on stress. The inclination angle of a shear band, $90° - \alpha_s$, is shown in Fig. 7 on the octahedral plane, which is identical with the results obtained by Wu [25].

In order to find the regions in the stress space where flutter ill-posedness and shear banding take place, we scan all possible propagation directions α at each stress state inside the failure surface on the octahedral plane, and calculate the wave speeds. In Fig. 8, we plot the surfaces of first occurrence of flutter instability and shear banding and compare them to the failure surface. The surface of shear banding coincides with the one obtained in a previous work by Wu [25] for the same constitutive equation. Flutter instability occurs much

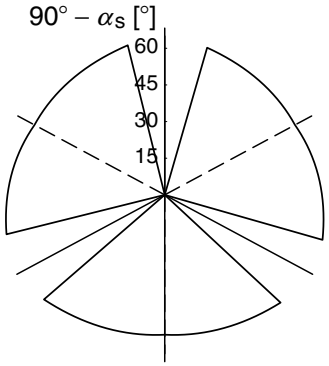

Fig. 7. Inclination of a shear band, $90° - \alpha_s$, versus Lode angle [26]

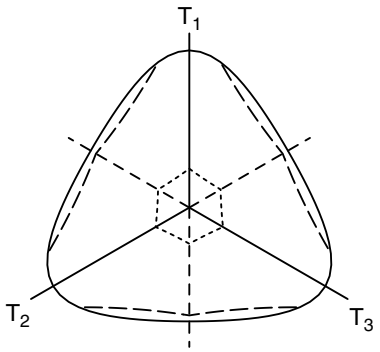

Fig. 8. Surfaces of flutter ill-posedness (*dotted*), shear banding (*dashed*) and failure surface (*solid*)

earlier than shear banding. The latter generally occurs prior to homogeneous failure. Note that the failure surface is valid for the general three-dimensional case, while flutter ill-posedness and shear banding are obtained here for a special case of two-component waves (9).

5 Characteristic Wave Speeds

A different way to evaluate wave speeds is to find the characteristics of the governing system of equations [14,15]. Since the constitutive relation is incrementally nonlinear, we should first linearize the term $\|\mathbf{D}\|$ in (10) to obtain a locally linearized quasi-linear system. This can be done by taking the linear terms in the Taylor expansion of $\|\mathbf{D}\|$ in the vicinity of $\mathbf{D}^0 \neq \mathbf{0}$. For the two-component waves defined by (9), the linearization gives

$$\|\mathbf{D}\| = \frac{g_1^0}{\|\mathbf{D}^0\|}\frac{\partial v_1}{\partial x_1} + \frac{g_2^0}{\sqrt{2}\,\|\mathbf{D}^0\|}\frac{\partial v_2}{\partial x_1} + \dots \tag{29}$$

with

$$\|\mathbf{D}^0\| = \sqrt{(g_1^0)^2 + (g_2^0)^2}, \tag{30}$$

where the components g_1, g_2 are defined by (22).

The linearized constitutive equations together with the equations of motion can be written in the matrix form

$$\frac{\partial U}{\partial t} + C\frac{\partial U}{\partial x_1} = 0, \tag{31}$$

where

$$U = (v_1, v_2, T_{11}, T_{12}) \tag{32}$$

is the column vector of the unknown functions and

$$C = \begin{pmatrix} v_1 & 0 & -1/\varrho & 0 \\ 0 & v_1 & 0 & -1/\varrho \\ -\kappa_1 & -\kappa_2 & v_1 & 0 \\ -\kappa_3 & -\kappa_4 & 0 & v_1 \end{pmatrix} \tag{33}$$

is the matrix of the system. In this system, the coefficients $\kappa_1, \dots, \kappa_4$ depend not only on the current stress state but also on the point of linearization $\mathbf{D}^0$. The slopes $\lambda = \mathrm{d}x_1/\mathrm{d}t$ of the characteristic curves are found from the equation

$$\det(C - \lambda I) = 0, \tag{34}$$

where I is the unit matrix. Expansion of the determinant (34) shows that the four roots λ are determined by the expression

$$(\lambda - v_1)^2 = c^2, \tag{35}$$

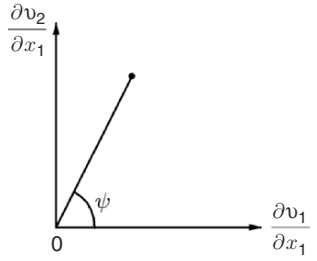

Fig. 9. Definition of the angle ψ

where

$$c^2 = \frac{1}{2\varrho}\left[(\kappa_1 + \kappa_4) \pm \sqrt{(\kappa_1 - \kappa_4)^2 + 4\kappa_2\kappa_3}\right]. \tag{36}$$

The difference $\lambda - v_1$ gives the wave speed relative to the material.

As mentioned earlier, the coefficients $\kappa_1, \ldots, \kappa_4$ depend on the point of linearization $\mathbf{D}^0$. As is evident from (29), these coefficients do not depend on $\|\mathbf{D}^0\|$ but only on the 'direction' $\mathbf{D}^0/\|\mathbf{D}^0\|$, which can be specified by an angle ψ shown in Fig. 9. This angle determines the instantaneous deformation of an infinitesimally thin layer in a plane wave. The direction of the wave propagation with respect to the principal axes of the stress tensor is determined by the angle α as defined earlier in Fig. 2. Given the principal stresses T_1, T_2, T_3, we can write $\kappa_i = \kappa_i(\alpha, \psi)$ and examine the wave speeds c in (36) as functions of the angles α and ψ (cf. [14,15]). For a given α, the wave speed spectrum is continuous through the dependence on ψ.

For stress states close to the hydrostatic axis, the squared wave speed in (36) is real and positive for both plus and minus signs in front of the square root, so that there exist four characteristic curves and, correspondingly, two real positive wave speeds. This situation is shown in Fig. 10a. With the deviation from the hydrostatic axis towards the failure surface, there exist ψ's such that (36) gives two pairs of complex-conjugate values and thus no characteristics, Fig. 10b,c. This signifies the local loss of hyperbolicity of the system of dynamic equations and is conventionally referred to as flutter instability [19]. In the vicinity of the failure surface, the lowest wave speed vanishes and then becomes imaginary, Fig. 10d. This also results in the loss of hyperbolicity and in ill-posedness of the dynamic problem. Since the wave speed vanishes before it becomes imaginary, this type of ill-posedness is referred to as stationary discontinuity [8,19].

6 Identity of the Two Wave Speed Spectra

As is well-known, for incrementally linear constitutive equations the speeds of acceleration waves coincide with the speeds calculated as the slopes of

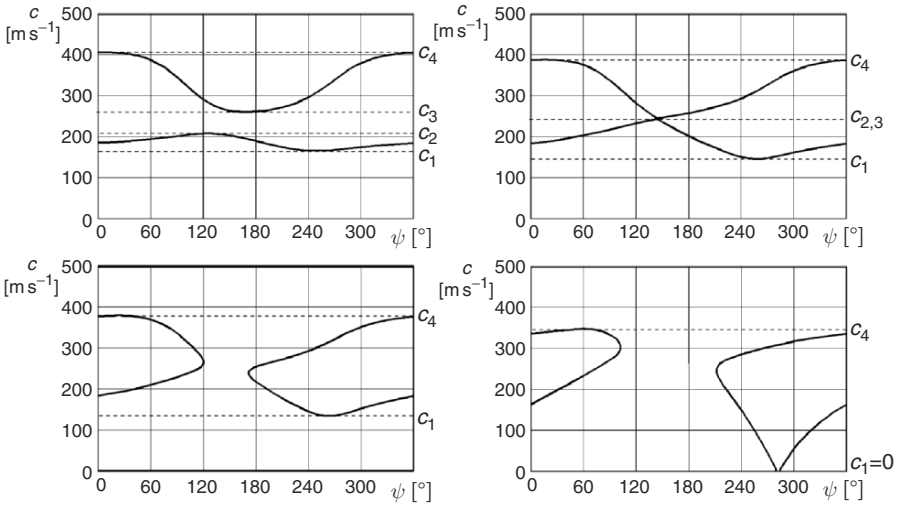

Fig. 10. Wave speeds versus angle ψ obtained from the evaluation of characteristic curves for the same stress states as in Figs. 4, 5

the characteristic curves (surfaces). In the present case, the wave speed spectra obtained with these two approaches are continuous and determined by different equations: by (19) together with the triangle condition (23) for acceleration waves, and by (36) for the characteristic wave speeds. In Fig. 10 the minima and maxima of each speed curve are marked by dotted lines. These values bound the speed intervals, and it turns out that they coincide with the maxima and minima $c_1, \ldots, c_4$ in Fig. 4. In this section, we prove that for a constitutive equation in the form (1) the two wave speed spectra – for acceleration waves and for the characteristics – are identical.

Consider system (19) for the wave speed c in the acceleration waves approach. Assume the values of $\|\mathbf{D}\|$ and c to be prescribed, whereas c is such that the matrix $(\mathbf{A} - c^2\varrho\,\mathbf{I})\,\mathbf{B}$ is nonsingular. Solving the system for $[\![\mathbf{g}]\!]$ and substituting the solution into the triangle condition (25), we obtain

$$\Lambda_1^2(c) + \Lambda_2^2(c) \geq \Lambda_0^2(c), \tag{37}$$

where

$$\begin{aligned}
\Lambda_1(c) &= \det \begin{pmatrix} -\eta_3 & \sqrt{2}\,\eta_2 \\ -\eta_6 & \sqrt{2}\,(\eta_5 - c^2\varrho) \end{pmatrix}, \\
\Lambda_2(c) &= \det \begin{pmatrix} \eta_1 - c^2\varrho & -\eta_3 \\ \eta_4 & -\eta_6 \end{pmatrix}, \\
\Lambda_0(c) &= \det \begin{pmatrix} \eta_1 - c^2\varrho & \sqrt{2}\,\eta_2 \\ \eta_4 & \sqrt{2}\,(\eta_5 - c^2\varrho) \end{pmatrix}.
\end{aligned} \tag{38}$$

Inequality (37) expresses the triangle condition in terms of c only and thus allows us to verify immediately whether a given value of c is the speed of an acceleration wave. If the matrix $(\mathbf{A} - c^2\varrho\,\mathbf{I})\,\mathbf{B}$ is singular, the corresponding c is obtained from the condition

$$\Lambda_0(c) = 0. \tag{39}$$

For the proof of the identity of the speed spectra we need the connection between the coefficients $\eta_1, \ldots, \eta_6$ in (19) and $\kappa_1, \ldots, \kappa_4$ in (33). Taking into account the linearization (29), this connection can easily be found

$$\begin{aligned} \kappa_1 &= \eta_1 + s_1\eta_3, \quad \kappa_2 = \eta_2 + \frac{1}{\sqrt{2}}\, s_2\eta_3, \\ \kappa_3 &= \eta_4 + s_1\eta_6, \quad \kappa_4 = \eta_5 + \frac{1}{\sqrt{2}}\, s_2\eta_6, \end{aligned} \tag{40}$$

where

$$s_1 = \frac{g_1^0}{\|\mathbf{D}^0\|}, \quad s_2 = \frac{g_2^0}{\|\mathbf{D}^0\|} \tag{41}$$

are components of a unit vector $\mathbf{s} : s_1^2 + s_2^2 = 1$. Simple calculations show that the characteristic equation (34) viewed as an equation in $c = \lambda - v_1$ can be reduced to

$$s_1\Lambda_1(c) + s_2\Lambda_2(c) = \Lambda_0(c). \tag{42}$$

Now we can proceed to the proof. Assume that for a given point of linearization determined by s_1, s_2, the characteristic wave speed is c, that is, c obeys (42). With the use of this equation we obtain

$$\Lambda_1^2 + \Lambda_2^2 - \Lambda_0^2 = \Lambda_1^2 + \Lambda_2^2 - (s_1\Lambda_1 + s_2\Lambda_2)^2 = (s_2\Lambda_1 - s_1\Lambda_2)^2 \geq 0. \tag{43}$$

This shows that (37) is satisfied, and therefore c is also the speed of an acceleration wave.

Now assume that c is the speed of an acceleration wave and satisfies (37). This inequality means that the length of the vector $\boldsymbol{\Lambda} = (\Lambda_1, \Lambda_2)$ is greater than or equal to $|\Lambda_0|$. Obviously, one can alway find a unit vector $\mathbf{s} = (s_1, s_2)$ such that the scalar product of $\boldsymbol{\Lambda}$ and $\mathbf{s}$ is equal to Λ_0. The characteristic equation (42) is then satisfied, and therefore c is also the characteristic wave speed. The components of $\mathbf{s}$ give the linearization point corresponding to this wave speed.

It remains to consider the special case (39). If an acceleration wave speed satisfies (39), one should merely take $\mathbf{s}$ normal to $\boldsymbol{\Lambda}$, and the characteristic equation (42) reduces to (39). Conversely, if for a given point of linearization $\mathbf{s}$ it turns out that the characteristic wave speed c is such that (39) is true, the acceleration wave criterion (37) is satisfied. This completes the proof.

7 Conclusion

The difference in the propagation of acceleration waves in incrementally linear models (such as elasto-plastic models) and nonlinear ones (such as the hypoplastic model considered here) is that in the former case the spectrum of the wave speeds is discrete, while in the latter case it is continuous. Moreover, for incrementally nonlinear constitutive equations the speeds of acceleration waves and the characteristic wave speeds are described by different equations. In contrast to incremental linearity, the correspondence between the two spectra is not readily available. It is proved that for a constitutive relation in the form (1) the two spectra of the wave speeds turn out to be identical. The equivalence of the two analyses – the acceleration waves approach and the characteristics method – in the sense of wave speeds is thus re-established.

Acknowledgements. We thank S. McCue from Griffith University, Brisbane, Australia for helpful discussions. The first author gratefully acknowledges support by the Otto Pregl Foundation.

References

1. An, L., Schaeffer, D.G. (1992) The flutter instability in granular flow. *J. Mech. Phys. Solids*, **40**, 683–698
2. Bauer, E., Wu, W., Huang, W. (2003) Influence of initially transverse isotropy on shear banding in granular materials. In: *Bifurcations & Instabilities in Geomechanics*, J.F. Labuz and A. Drescher (eds.), Balkema, Lisse, pp. 161–172
3. Bigoni, D., Zaccaria, D. (1994) On the eigenvalues of the acoustic tensor in elastoplasticity. *Eur. J. Mech., A/Solids*, **13**(5), 621–638
4. Chambon, R., Caillerie, D. (1999) Existence and uniqueness theorems for boundary value problems involving incrementally non linear models. *Int. J. Solids Struct.*, **36**, 5089–5099
5. Chambon, R., Crochepeyre, S., Desrues, J. (2000) Localization criteria for nonlinear constitutive equations of geomaterials. *Mech. Cohes.-Frict. Mater.*, **5**, 61–82
6. Gudehus, G. (1996) A comprehensive constitutive equation for granular materials. *Soils*, **36**, 1–12
7. Gudehus, G. (2004) A visco-hypoplastic constitutive relation for soft soils. *Soils Found.*, **44**(4), 11–25
8. Hill, R. (1962) Acceleration waves in solids. *J. Mech. Phys. Solids*, **10**, 1–16
9. Joseph, D.D., Saut, J. C. (1990) Short-Wave Instabilities and Ill-Posed Initial-Value Problems. *Theoret. Comput. Fluid Dyn.*, **1**, 191–227
10. Kolymbas, D., Rombach, G. (1989) Shear band formation in generalized hypoelasticity. *Ing.-Arch.*, **59**, 177–186
11. Loret, B., Harireche, O. (1991) Acceleration waves, flutter instabilities and stationary discontinuities in inelastic porous media. *J. Mech. Phys. Solids*, **39**(5), 569–606

12. Mandel, J. (1964) Propagation des surfaces de discontinuité dans un milieu élastoplastique. In: *Stress Waves in Anelastic Solids*, H. Kolsky and W. Prager (eds.), Springer, Berlin Heidelberg New York, pp. 331–340
13. Molenkamp, F. (1991) Material instability for drained and undrained behaviour. Parts 1, 2. *Int. J. Num. Anal. Methods Geomech.*, **15**, 147–180
14. Osinov, V.A. (1998) Theoretical investigation of large-amplitude waves in granular soils. *Soil Dyn. Earthquake Eng.*, **17**(1), 13–28
15. Osinov, V.A., Gudehus, G. (2003) Dynamics of hypoplastic materials: theory and numerical implementation. In: *Dynamic Response of Granular and Porous Materials under Large and Catastrophic Deformations*, K. Hutter and N. Kirchner (eds.), Springer, Berlin, pp. 265–284
16. Osinov, V.A., Wu, W. (2005) Instability and ill-posedness in the deformation of plastic solids: some correlations through simple examples. In: *Trends in Applications of Mathematics to Mechanics*, Y. Wang and K. Hutter (eds.), Shaker Verlag, Aachen, pp. 361–370
17. Petryk, H. (1992) Material instability and strain-rate discontinuities in incrementally nonlinear continua. *J. Mech. Phys. Solids*, **40**(6), 1227–1250
18. Petryk, H. (2000) Theory of material instability in incrementally nonlinear plasticity. In: *Material Instabilities in Elastic and Plastic Solids*, H. Petryk (ed.), Springer, Wien Berlin Heidelberg New York, pp. 261-331
19. Rice, J.R. (1976) The localization of plastic deformation. In: *Theoretical and Applied Mechanics*, Proceedings. 14th IUTAM Congress, W.T. Koiter (ed.), North-Holland, Amsterdam, pp. 207–220
20. Schaeffer, D.G. (1990) Instability and ill-posedness in the deformation of granular materials, *Int. J. Numer. Anal. Methods Geomech.*, **14**(4), 253–278
21. Vardoulakis, I., Sulem, J. (1995) *Bifurcation Analysis in Geomechanics*, Chapman & Hall, London
22. Wu, W., Kolymbas, D. (1990) Numerical testing of the stability criterion for hypoplastic constitutive equations. *Mech. Mater.*, **9**, 245–253
23. Wu, W., Bauer, E. (1994) A simple hypoplastic constitutive model for sand. *Int. J. Numer. Anal. Methods Geomech.*, **18**, 833–862
24. Wu, W., Kolymbas, D. (2000) Hypoplasticity then and now. In: *Constitutive Modelling of Granular Materials*, D. Kolymbas (ed.), Springer, Berlin Heidelberg New York, pp. 57–105
25. Wu, W. (2000) Non-linear analysis of shear band formation in sand. *Int. J. Numer. Anal. Meth. Geomech.*, **24**, 245–263
26. Zienkiewicz, O.C., Pande G.N. (1977) Some useful forms of isotropic yield surfaces for soil and rock mechanics. In: *Finite Elements in Geomechanics*, G. Gudehus (ed.), Wiley, Chichester, pp. 179–190

Part VI

Engineering Applications

Static and Cyclic Behavior of a Silty Sand According to Tests on Undisturbed Samples

A.B. Huang and Y.T. Huang

Department of Civil Engineering National Chiao Tung University, Hsin Chu, Taiwan
abhuang@mail.nctu.edu.tw

Abstract. The effects of plastic or nonplastic fines on the static and cyclic strength of sand have been a subject of laboratory studies for many decades. These studies have not lead to a consensus as to how fines can affect the behavior of sand. Earlier studies have mostly been limited to tests on reconstituted specimens. Some of the controversies stem from the concerns that reconstituted specimens may not be able to duplicate the soil fabric in the field. The authors used Laval sampler to retrieve high quality samples in silty sand in Central Western Taiwan, following the procedures reported earlier. A test site was developed in Yuan Lin County where standard penetration test (SPT), seismic piezocone (SCPTU) and field V_s measurements were performed in addition to Laval sampling. A series of monotonic and cyclic triaxial tests were conducted on natural and reconstituted Sand specimens. Laboratory V_s measurements were taken on the triaxial specimens using bender elements. With these data, the authors were able to evaluate the static and cyclic characteristics of YLS. This paper describes the results from Yuan Lin test site studies and discusses their implications in the assessment of liquefaction potential for the silty sand in this region.

1 Introduction

Field test results such as the N value from standard penetration test (SPT), cone tip resistance (q_c) from cone penetration test (CPT) or shear wave velocity (V_s) have been used to assess the liquefaction potential for sand under the framework of simplified procedure [13]. The simplified procedure uses an empirical correlation between the cyclic resistance ratio (CRR) and the field test results as the principal criterion to determine if the soil is potentially liquefiable. The available CRR correlation curves have been developed through field observations. These CRR correlations basically provide a clean sand base curve and a suggested procedure to account for fines (soil particles passing #200 sieve) content. There appears to be a general consensus that, for a given field test value, the corresponding CRR increases with fines content, regardless of what field test method is chosen. Whether this increase is caused by an increase of liquefaction resistance or a decrease of field test value is not clear.

Natural sand often contains fines. The effects of plastic or non-plastic fines on the behavior of sand have been a subject of geotechnical research for many decades. These research activities however, have mostly been limited to cyclic shearing tests on soil samples in laboratory. The laboratory studies have not lead to a consensus as to whether fines can increase or decrease the undrained strength or cyclic resistance of sand as described by Polito [11]. Serious questions have been raised as to the validity of laboratory tests on reconstituted silty sand samples due to the differences in soil fabric [5]. On the other hand, systematic studies on the effects of fines on N, q_c or V_s have rarely been reported. With these drawbacks, Youd et al. [13] emphasized that the CRR corrections based on fines contents should be used with engineering judgment and caution.

The Chi Chi earthquake ($M_L = 7.3, M_W = 7.6$) of September 21, 1999 triggered extensive soil liquefaction in Central Western Taiwan. The majority of the sand deposit in this region had significant amounts of fines. When performing back analysis of sand liquefaction potential in this region, the selection of field test method, its CRR correlation and the associated fines content corrections could lead to significantly different results. The factor of safety (FS) against liquefaction from SPT was consistent higher than that from CPT, which in term was higher than that according to shear wave velocities [6, 10]. The research work described herein represents part of the efforts in an attempt to resolve some of the controversies and to provide analysis procedures that reflect the characteristics of local soils.

Sand is a typical silty fine sand commonly found in Central Western Taiwan. A geotechnical test site was established as part of the postearthquake research efforts to improve our understanding of the engineering properties of the silty sand in this region. Laval and conventional piston samples along with a series of in situ tests that included SPT, seismic piezocone penetration test (SCPTU), and borehole suspension compression and shear wave logging (P–S logging) were performed at the test site. With the undisturbed samples and field test data from the same test site, it was possible to evaluate the static and cyclic behavior of the silty sand from this region, in its natural state.

2 The Yuan Lin Test Site

Yuan Lin township (see Fig. 1) which was part of Chang-hua County located at approximately 20 km north west of the epicenter of Chi Chi earthquake. Extensive soil liquefaction occurred in Yuan Lin during Chi Chi earthquake. The boreholes and test locations were distributed within a circle of 10 m diameter as shown in Fig. 2. The ground water table was at 2.6 m deep at the time of field testing/sampling. Figures 3 and 4 describe the soil profiles according to SPT and SCPTU obtained at the test site. Sieve analyses on the split-spoon samples showed that the fines (particles passing #200 sieve) content of the soil at Yuan Lin test site could range from 5% to as much as 100%.

Fig. 1. Location of Yuan Lin test site

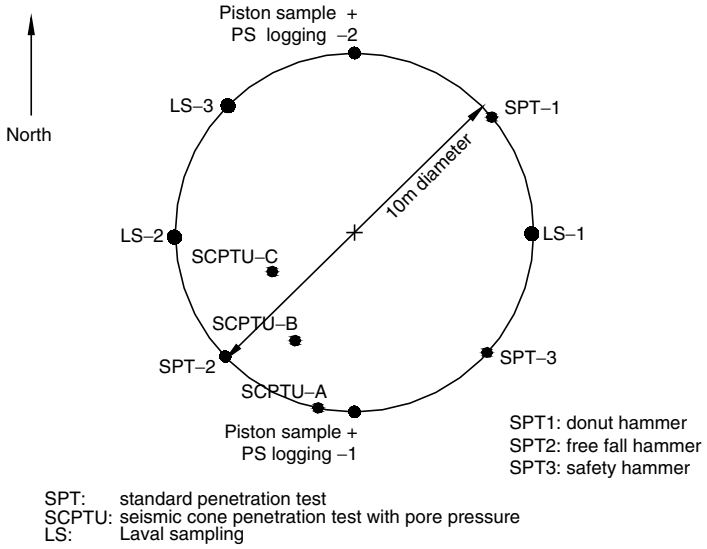

Fig. 2. Distribution of boreholes and test locations at Yuan Lin test site

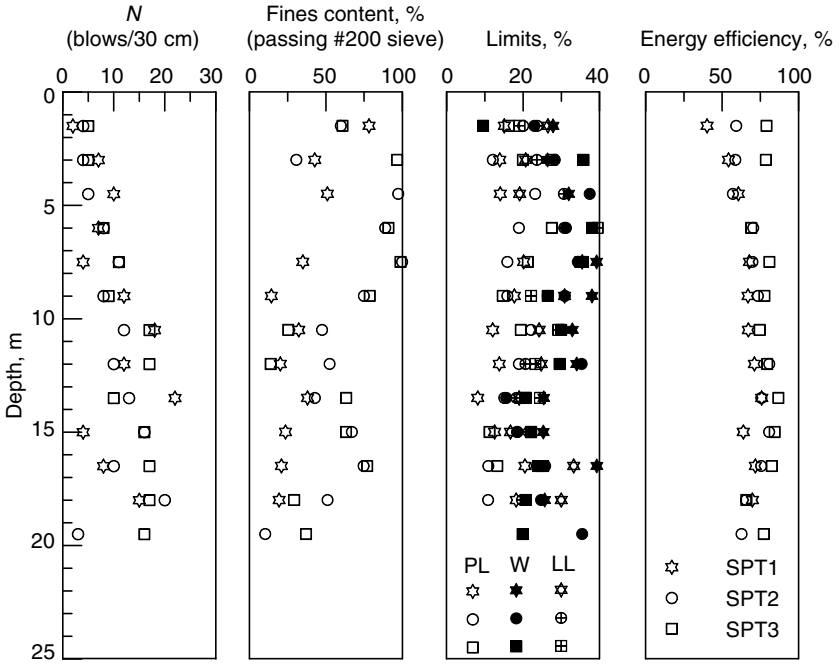

Fig. 3. SPT profiles at the Yuan Lin test site

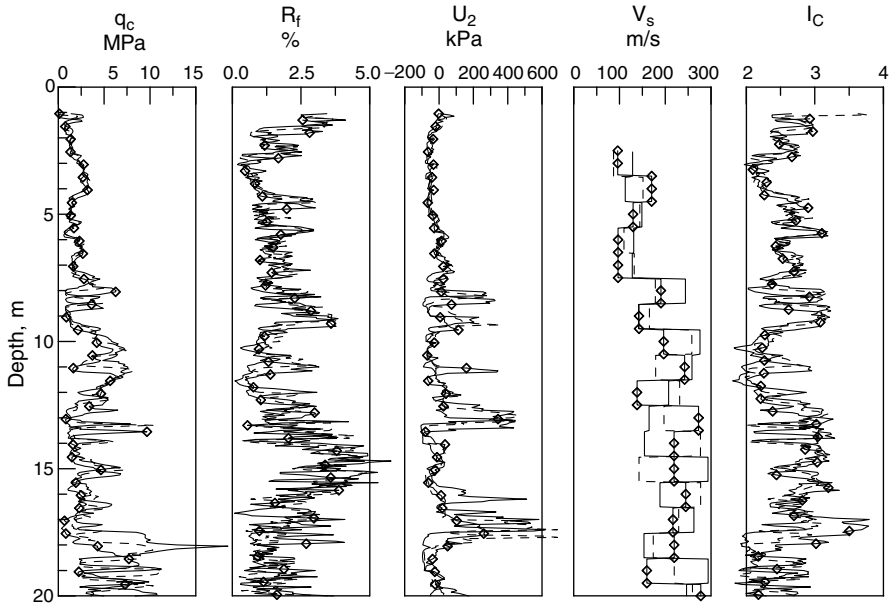

Fig. 4. SCPTU profiles at the Yuan Lin test site

The natural water contents of the split-spoon samples were often higher than their corresponding liquid limits, indicating that the soil was rather sensitive.

3 Laval Sampling and Field Packaging

Taking undisturbed or high quality samples in cohesionless soils has always been a difficult if not impossible task. The available reports on the undisturbed sampling in sand have mostly been limited to the ground freezing method. By freezing the ground water, the sand particles and their matrix were fixed in the frozen ground. The sand samples were taken by coring and remained frozen until laboratory shearing test. The process of ground freezing is time consuming and prohibitively expensive. Konrad et al. [8] reported their success in obtaining undisturbed silty sand samples form below the ground water table without freezing. The Laval sampler was developed at Laval University [9], originally for taking high quality samples in sensitive clay. A 200 mm diameter and 500 mm high sample could be obtained with the Laval sampler. Figure 5

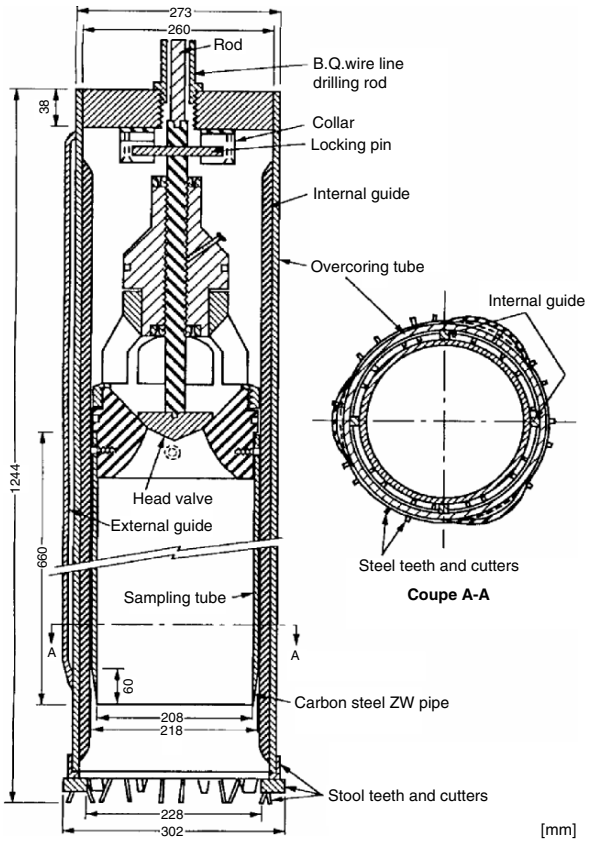

Fig. 5. Schematic view of the Laval sampler [9]

shows a schematic view of the Laval sampler. In order to prevent soil structure damage during transportation for low cohesion sand (sand with low fines content), Konrad et al. [8] developed a method to freeze the Laval sample above ground. The soil, while it is still in the sampling tube, is gradually frozen from top of the sample by dry ice. Bottom drainage is provided to allow excess pore water to be drained due to water volume expansion during freezing. Figure 6 depicts a record of time versus expelled water volume and temperature measured at the bottom of a soil sample taken at the Yuan Lin test site. For this particular sample, complete frozen was accomplished within 24 h.

A total of nine Laval samples were taken in three boreholes at the test site. In each borehole, the Laval samples were taken at 3.5–4.0, 6.0–6.5 and 11.0–11.5 m. Laval samples taken at 11m, with fines contents less than 20% were frozen on the ground surface before shipping. The rest of the Laval samples had fines contents well in excess of 40%, there was no risk of significant disturbance and thus were not frozen. The nonfrozen Laval samples were covered by a layer of wax and plastic wrap. Upon arrival in the laboratory, the nonfrozen Laval samples were stored in a sealed moisturized container.

4 Physical Properties of Yuan Lin Sand

The origin of YLS was the central mountain range that lied on the east side of Taiwan. Weathered sedimentary and metamorphic rocks on steep slopes

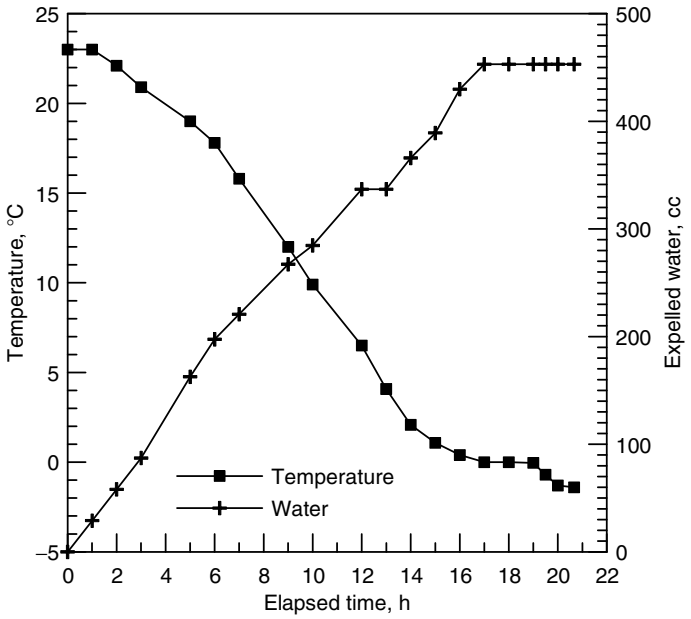

Fig. 6. Water volume expelled and temperature variation with time

were eroded by rainfall and transported by rapidly flowing streams before deposition on the west plain, to a thickness of several hundred meters.

The physical properties of soil samples taken from different boreholes at the same depth range were rather uniform in terms of water content, plasticity and gradation. Representative physical properties taken from three of the Laval samples are shown in Table 1. The corresponding grain size distribution curves are depicted in Fig. 7. The reference void ratios of YLS with three

Table 1. Physical properties of Laval samples

depth, m	borehole	FC, %	PL, %	LL, %	sample	e_{min}	e_{max}	e
					LS			0.94
3.32–3.80	LS1	43	14	21	WS	0.86	1.27	0.87
					MT			0.86
					LS			0.97
5.90–6.41	LS2	89	19	31	WS	1.01	1.69	0.78
					MT			0.81
					LS			0.93
10.98–11.40	LS3	18	14	25	WS	0.85	1.29	0.91
					MT			0.93

LS: Undisturbed Laval sample
MT: Reconstituted specimen by moist tamping
WS: Reconstituted specimen by water sedimentation

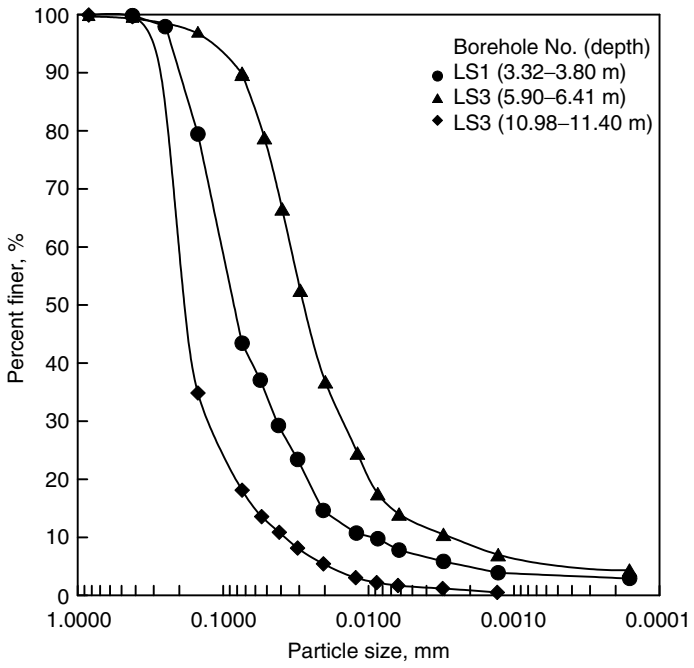

Fig. 7. Gain size distribution of Laval samples

different fines contents (FC) were determined following the related ASTM standards. The $e_{\min}$ (maximum density) was determined according to ASTM D4253 method 1 A using a standard 152.4 mm inside diameter compaction mold (total volume = $2,830\,\text{cm}^3$). The dry sand placed in the compaction mold was subjected to a surcharge of 14 kPa, and then electromagnetically vibrated under a 60 Hz frequency for 8 min. The $e_{\max}$ (minimum density) was obtained according to ASTM D4254 method C, using a 2,000 glass graduated cylinder. Approximately 1,000 g of dry sand was placed in the glass cylinder and then plugged with a stopper. The total volume under the loosest state was determined according to the height of the sand after swiftly tipping the cylinder upside down twice. It should be noted that none of the above ASTM standards were applicable for sand with fines in excess of 15%. The values of $e_{\min}$ and $e_{\max}$ are included in Table 1.

A series of X-ray refraction tests were performed on the same samples described in Table 1. The results as shown in Table 2 had distinct differences in mineral contents between coarse (retained on #200 sieve) and fine (passing #200 sieve) particles. The coarse particles had much higher contents of quartz. The fines were predominantly muscovite and clinochlore. The scanning electron microscope (SEM) photos depicted in Fig. 8 show that YLS particles were mostly subangular, and the fines were flaky.

4.1 Triaxial Specimen Preparation

A series of static and cyclic triaxial tests were performed on YLS soil samples retrieved from the Yuan Lin test site. All triaxial tests started with the Laval samples (LS). For the frozen LS, the 500 mm high Laval samples were first cut into three sections using a band saw, each with a height of 170 mm. Four, 70 mm diameter specimens were then cored from the section. Upon coring the specimen height was trimmed down to 140 mm by hand. A small slot of 1.5 mm wide, 12 mm long and 5 mm deep was cut at the top and bottom of the trimmed specimen to give room for the insertion of bender elements. The specimen was kept frozen during this preparation stage. Thawing of the specimen took place after the specimen was seated in the triaxial cell, under a confining stress of 20 kPa and a cell water temperature of 5°C. The pore water under a controlled temperature of 8–10°C was forced to enter the specimen

Table 2. Mineral contents of YLS

mineral	FC = 18%		FC = 43%		FC = 89%	
	Coarse, %	Fine, %	Coarse, %	Fine, %	Coarse, %	Fine, %
quartz	62.28	19.15	69.83	27.93	66.38	11.78
clinochlore	15.76	37.98	14.65	27.90	13.01	36.38
muscovite	14.43	39.28	12.09	39.98	12.06	50.77
feldspar	7.52	3.59	3.43	4.19	8.55	1.06

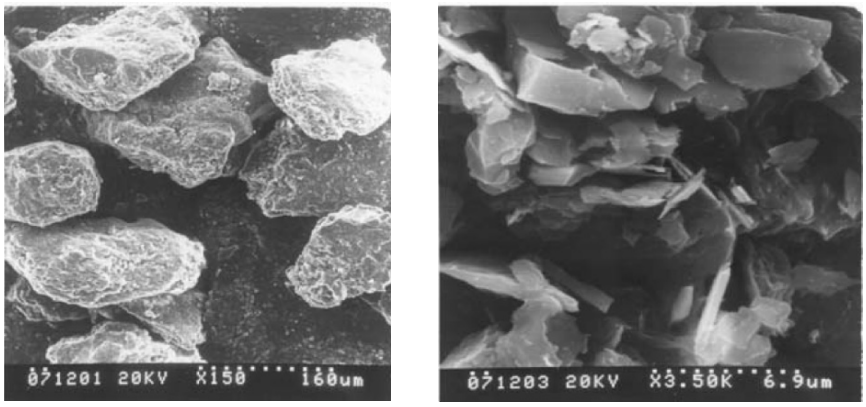

Fig. 8. SEM photos of the YLS

from the bottom under a back pressure of 10 kPa. The thawing process lasted approximately 1 h. The amount of water absorbed by the specimen and the change of specimen height were monitored during the thawing process.

For the nonfrozen LS, the 170 mm sections were cut by a wire saw. Four, 70 mm diameter and 140 mm high triaxial specimens were trimmed by hand using a wire saw and a knife, from each section. Slots on top and bottom of the specimens were cut to give room for the bender elements.

The triaxial specimen taken from Laval samples was saturated under the back pressure overnight. B values obtained after saturation had a minimum value of 0.99. Upon saturation, the specimens were isotropically consolidated under an effective confining stress (σ'_c) of 100 kPa. Because of the relatively high compressibility of the soil specimens and absorption of water in the thawing process (for the frozen specimens), the amounts of pore fluid coming in and out of the specimens were recorded. At the end of triaxial test, the whole specimen was used to determine the water content. The postconsolidation water content or void ratio (e), to be used in the following analysis of test data, was back calculated from the end-of-the-test water content measurement. Upon the triaxial tests on undisturbed specimens, soil specimens cut from the same Laval sample (i.e., same borehole and depth) were dismantled and mixed together to make the reconstituted specimens.

The triaxial tests were performed on the YLS specimens with three types of fines contents shown in Table 1. These included the LS and specimens reconstituted specimens made by MT and WS methods. The MT and WS specimens were made in an attempt to match the void ratio of the corresponding LS. In most cases, however, the reconstituted specimens had void ratios lower than those of the Laval samples.

5 Monotonic Triaxial Shearing Tests

A Wykeham–Farrance triaxial apparatus was used in the monotonic consolidation and triaxial shearing tests. An internal load cell was used to monitor the axial force imposed on the specimen and an externally mounted LVDT was used to measure the axial deformation. All specimens were isotropically consolidated under 100 kPa effective confining stress. The specimens were sheared monotonically in an undrained condition by axial compression to strains well in excess of 20% to reach or be close to critical state [2]. For the tests performed, all specimens developed positive excess pore pressure during shearing. The LS specimens had the highest peak deviator stress even when their void ratios were higher than those of MT and WS specimens. The peak deviator stress of the LS specimen with 18% FC was 64% and 37% higher than those LS specimens with 43% and 89% FC, respectively. Among the reconstituted specimens, the MT specimens generally had lower peak deviator stress. This is consistent with earlier findings (e.g., [5]).

The relationships among deviator stress, excess pore pressure and axial strain, as well as the effective stress paths in terms of $q(=(\sigma'_{\mathrm{v}}-\sigma'_{\mathrm{h}})$ and $p'(=(\sigma'_{\mathrm{v}}+2\sigma'_{\mathrm{h}})/3)$ from all the consolidated undrained triaxial tests are depicted in Figs. 9 and 10. A straight line was fitted to the data set of (p', q) that corresponded to the critical state of each triaxial test as shown in Fig. 10. The slope of this fitted line referred to as M_{s} was approximately 1.36. The $M_{\mathrm{s}}(=6\sin\phi'_{\mathrm{s}}/(3-\sin\phi'_{\mathrm{s}}))$ should correspond to interparticle friction angles (ϕ'_{s}) of 34°.

6 Shear Wave Velocity Measurements and Cyclic Triaxial Tests

Bender elements of the type described by Dyvik and Madshus [3] were installed in the top and bottom platens of the cyclic triaxial cell, each projecting 3 mm into the soil specimen. The shear wave velocity, V_{s} was measured using the bender elements after the specimen was consolidated, prior to the cyclic triaxial test. A single sinusoidal pulse with a frequency of 7–10 kHz and amplitude of ±10 V was applied in the bender element tests. The determination of the shear wave travel time followed a procedure suggested by Kawaguchi et al. [7].

Figure 11 plots the relationship between fines content and V_{s} according to bender element measurements. The results in Fig. 11 show that for the specimens from Laval samples, V_{s} decreases by no more than 20% as the fines contents change from 18% to 89%. It is likely that the fine grains of YLS are softer under small strains. The reconstituted specimens had lower V_{s} than those of the Laval samples, in spite of the fact that the reconstituted specimens had lower void ratios than those corresponding Laval samples. Among the reconstitute specimens, those made by MT had the lowest V_{s}. The V_{s} of YLS was at least 30% lower than that of angular Ottawa sand with similar void ratio and under 100 kPa confining stress, as reported by Hardin and Richart [4].

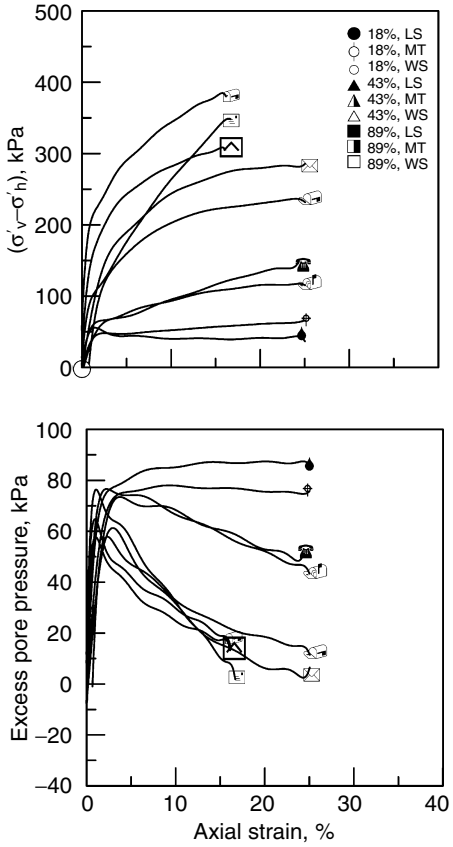

Fig. 9. Stress–strain and excess pore pressure relationship

Upon V_s measurement, the soil specimen was then subjected to a cyclic deviator stress, σ_d in axial direction at 0.1 Hz. Three to five cyclic triaxial tests were performed with various $\sigma_d/2\sigma'_c$ values. Fig. 12 depicts the cyclic triaxial test results on YLS in terms of deviator stress ratio ($\sigma_d/2\sigma'_c$) versus number of cycles. The cyclic strength of LS specimens decreased by approximately 20% as the fines content increased from 18% to 89%, under similar postconsolidation void ratio, e.

Following the cyclic triaxial test, the drainage valves were open to release the excess pore pressure. The amount of pore fluid expelled from the specimen and duration of pore fluid drainage were recorded. The results are plotted in Fig. 13 in terms of expelled water volume versus square root of time. The coefficient of consolidation (c_v) inferred from these drainage curves showed that for fines contents of 18% and 43%, c_v was on the order of $10^{-4}\,m^2\,sec^{-1}$. The c_v was lowered by one order of magnitude as the fines content increased to 89%.

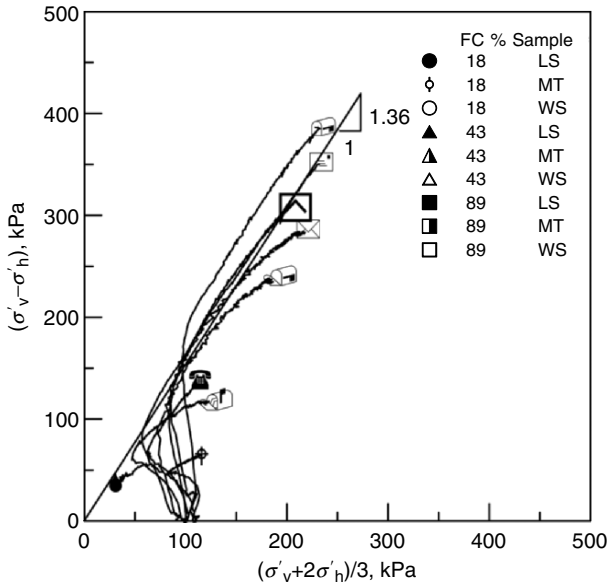

Fig. 10. Effective stress paths

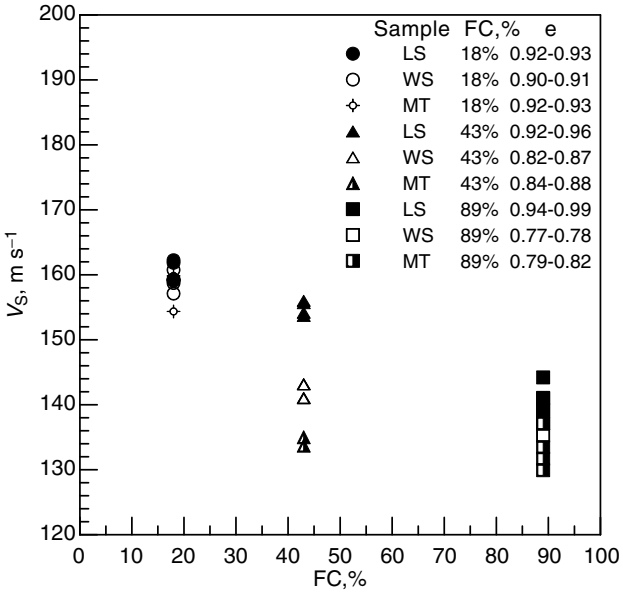

Fig. 11. Relationship between fines content and V_s

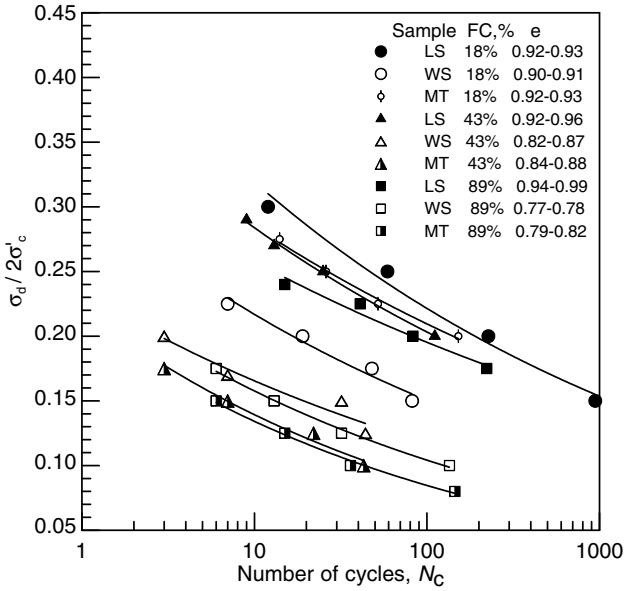

Fig. 12. Cyclic resistance of YLS

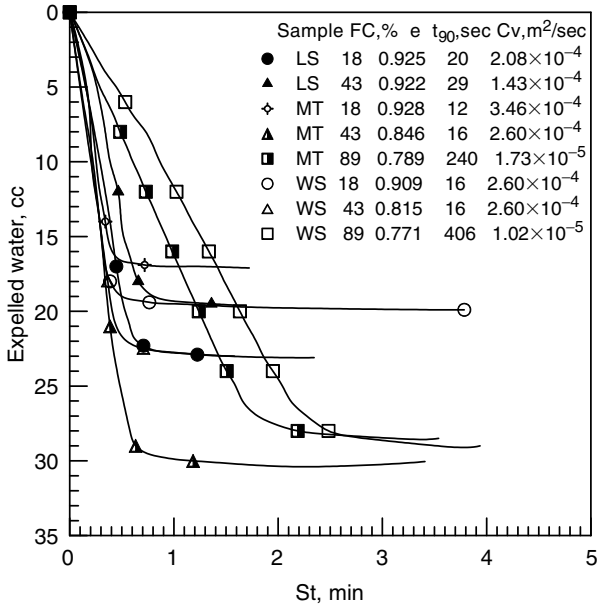

Fig. 13. Rate of drainage after cyclic shearing

7 Implications in Liquefaction Potential Assessments

The laboratory and field test data described above offered an opportunity to evaluate some of the commonly used simplified procedures in soil liquefaction assessment. The cyclic resistance ratio from triaxial test ($(\mathrm{CRR})_{\mathrm{tx}}$) was defined as the $\sigma_{\mathrm{d}}/2\sigma'_{\mathrm{c}}$ that produced an axial strain of 5% in double amplitude in 20 cycles (N_{c}) of uniform load application. A reduction factor of 0.9 was applied to infer the field cyclic resistance ratio (CRR) or $\mathrm{CRR} = 0.9(\mathrm{CRR})_{\mathrm{tx}}$. The correlation between CRR from cyclic triaxial tests on Laval samples and normalized cone tip resistance ($q_{\mathrm{c}1N}$) was compared with that proposed by Stark and Olson [12]. This comparison is shown in Fig. 14. The $q_{\mathrm{c}1N}$ was determined according to cone tip resistance (q_{c}) from the test site (shown in Fig. 4) at the same depth level as the Laval samples and normalized with respect to the atmospheric pressure based on the effective overburden stress. The limited test data did show that for similar CRR, the corresponding $q_{\mathrm{c}1N}$ decreased with fines content. The CRR-$q_{\mathrm{c}1N}$ correlations from the Laval samples generally fell to the left of those proposed by Stark and Olson [12] for comparable fines contents. In the case of YLS, the above described laboratory tests showed that the c_{v} values were similar for fines contents of 18% and 43%. Thus, the decrease of $q_{\mathrm{c}1N}$ as FC changed from 18% to 43% should be attributed to the lower strength of YLS as the FC increased to 43%. As the FC further increased to 89%, the difference in c_{v} and thus partial drainage should also be responsible for the lower $q_{\mathrm{c}1N}$. For the range of FC, the $q_{\mathrm{c}1N}$ values varied by more than 300% whereas the CRR differed by no more than 20%.

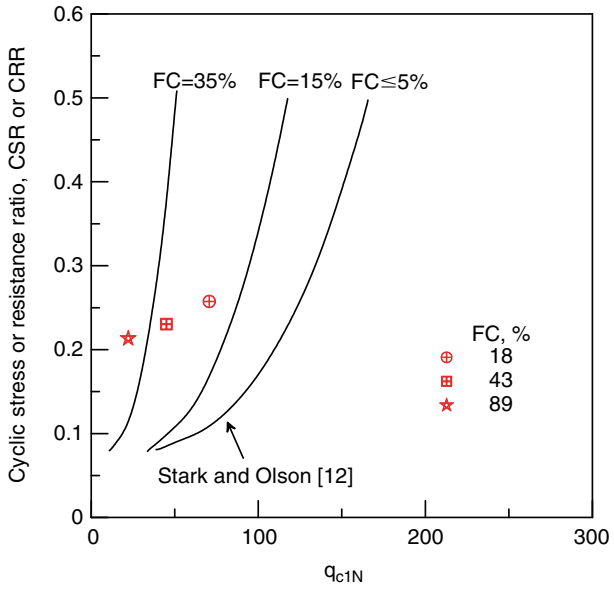

Fig. 14. Correlation between CRR and cone tip resistance

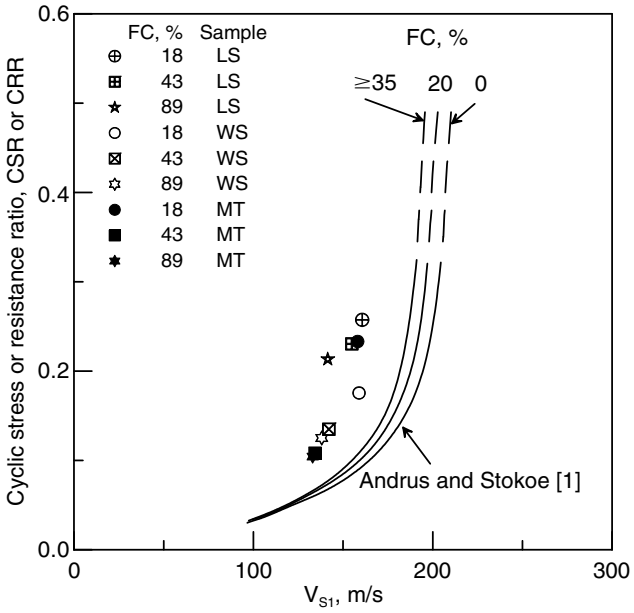

Fig. 15. Correlation between CRR and shear waver velocity

The establishment of the relationship between CRR and V_s was based on the cyclic triaxial tests and measurements using the bender element on the same soil specimen. The V_{s1} is the same as V_s for the data presented herein since all tests were performed with $\sigma'_h = \sigma'_v = 100\,\text{kPa}$. Fig. 15 shows a plot of CRR versus V_{s1} from tests on Laval samples and reconstituted specimens, and their comparison with the correlations proposed by Andrus and Stokoe [1]. For a given CRR, the V_{s1} values were generally smaller than those suggested by Andrus and Stokoe [1]. Unlike CPT however, there was no significant differences in the CRR-V_{s1} correlation as FC increased from 18% to 89%. This is consistent with the fact that the amounts of decrease in cyclic strength and V_s were both on the order of 20% as FC increased from 18% to 89%.

8 Concluding Remarks

The experience gained in this study indicates that it is practical to retrieve high quality silty sand samples. For low cohesion silty sand, the sample can be effectively frozen above ground to minimize disturbance during transportation. The laboratory cyclic and monotonic triaxial tests did show that the shear strengths of undisturbed samples were significantly higher than those of reconstituted specimens.

For YLS, the commonly used CRR-q_{c1N} and CRR-V_s correlations may be conservative in assessing the soil liquefaction potential, especially in the case

of fines content adjustment. Because of the uncertainties involved in the use of the simplified procedures, and feasibility of taking good quality samples, it may be advisable to follow the sampling and laboratory testing method in assessing the soil liquefaction potential for silty sands.

References

1. Andrus, R.D., and Stokoe, K.H., II, 2000, Liquefaction resistance of soils from shear-wave velocity, Journal of Geotechnical and Geoenvironmental Engineering, ASCE, Vol. 126, No. 11, pp. 1015–1025
2. Been, K., Jefferies, M.G., and Hachey, J., 1991, A critical state of sand, Geotechnique, Vol. 41, No. 3, pp. 365–381
3. Dyvik, R. and Madshus, C., 1985, Laboratory measurement of $G_{\max}$ using bender element, Proceedings ASCE Annual Convention: Advance in the Art of Testing Soils Under Cyclic Conditions, Detroit, pp. 186–196
4. Hardin, B.O., and Richart, F.E., 1963, Elastic wave velocities in granular soils, Journal of Soil Mechanics and Foundation Engineering Division, ASCE, Vol. 89, No. SM1, pp. 33–65
5. Høeg, K., Dyvik, R., and Sandbaekken, G., 2000, Strength of undisturbed versus reconstituted silt and silty sand specimens, Journal of Geotechnical and Geoenvironmental Engineering, Vol. 126, No. 7, pp. 606–617
6. Huang, A.B., Lee, D.H., Lin, P.S., Tsai, J.S., Lin, C.P., Chi, Y.Y., Ku, C.S., Chen, J.W., Juang C.H. and Liou, Y.J., 2003, Lessons learned from the post Chi Chi EQ geotechnical explorations in Central Western Taiwan, Proceedings, 12th Pan American Conference on Soil Mechanics and Geotechnical Engineering, Cambridge, Massachusetts, edited by Culligan et al., Vol. 1, pp. 245–252
7. Kawaguchi, T., Mitachi, T., and Shibuya, S., 2001, Evaluation of shear wave travel time in laboratory bender element test, Proceedings of the 15th International Conference on Soil Mechanics and Geotechnical Engineering, Istanbul, Vol. 1 pp. 155–158
8. Konrad ,J. M., St-Laurent, S. Gilbert, F., and Leroueil, S., 1995, Sand sampling below the water table using the 200 mm diameter Laval sampler. Canadian Geotechnical Journal, Vol. 32, pp. 1079–1086
9. La Rochelle, P., Sarrailh, J., Tavenas, F., Roy, and Laroueil, S., 1981, Causes of sampling disturbance and design of a new sampler for sensitive soils, Canadian Geotechnical Journal, Vol. 18, No. 1, pp. 52–66
10. Moh and Associates, 2000, Soil liquefaction and treatment policy evaluations, phase I (Yuan Lin, Ta Tzuen and Tou She Townships, (in Chinese), Moh and Associates, Taipei, Taiwan
11. Polito, C.P., 1999, The effects of nonplastic and plastic fines on the liquefaction of sandy soils, Ph.D. Thesis, Virginia Polytechnic Institute and State University, Blacksburg, Virginia
12. Stark, T.D., and Olson, S.M., 1995, Liquefaction resistance using CPT and field case histories. Journal of Geotechnical Engineering Division, ASCE, Vol. 121, No. 12, pp. 856–869
13. Youd, T.L., Idriss, I.M., Andrus, R.D., Arango, I., Castro, G., Christian, J.T., Dobry, R., Liam Finn, W.D., Harder Jr., L.F., Hynes, M.E., Ishihara, K.,

Koester, J.P., Liao, S.S.C., Marcuson III, W.F., Martin, G.R., Mitchell, J.K., Moriwaki, Y., Power, M.S., Robertson, P.K., Seed, R.B., and Stokoe II, K.H., 2001, Liquefaction Resistance of Soils: Summary Report from the 1996 NCEER and 1998 NCEER/NSF Workshops on Evaluation of Liquefaction Resistance of Soils, Journal of Geotechnical and Geoenvironmental Engineering, ASCE, Vol. 127, No. 10, pp. 817–833

The Role of Analysis in Non-Displacement Pile Design

R. Salgado

Department of Civil Engineering, Purdue University, West Lafayette, USA
rodrigo@ecn.purdue.edu

Abstract. Pile foundations have been used in construction for thousands of years but only in the last few decades has there been significant progress in the technology of pile installation. This progress on construction has not been matched by progress in the analysis and design of these foundation elements. This is in large part due to considerable difficulties in analyzing both pile installation and the response of piles to various types of loadings rigorously. Given these difficulties, the profession has in general used relatively crude design approaches. This is likely to change due to pressures from different directions, particularly the progress in code design (the push toward load and resistance factor design in geotechnical engineering requires a much better grip on all the factors that need to be considered in calculating pile resistances and what the uncertainties in quantities and analyses are, requiring sounder analytical frameworks) and economics (materials costs have started to rise, a trend that, if continued, would make it more economically interesting to have optimal designs). In this paper, we examine the design process for axially loaded nondisplacement piles with a focus on assessing the strength of the underlying analysis. We will show that, for these types of piles, design can be placed on a theoretical basis.

1 Introduction

While piles have been used literally for millennia, many aspects of piling are not to this day modeled with much rigor. Pile installation, particularly in the case of driven piles, cannot yet be simulated accurately. Laterally loaded piles are designed using a semiempirical technique – the p–y method – which is used almost universally. While more meaningful advances have taken place in axially loaded pile analysis, these advances have not been sufficiently integrated with current knowledge of soil mechanics or tied in a fundamental way with the process by which the tens of pile types in existence are installed in the ground. In this paper, we examine the analytical basis for calculating the base and shaft resistances of nondisplacement piles.

The analysis of axially loaded piles appears on first examination to be one of the simplest in geomechanics. The total load carried at the pile head, we

learn as undergraduate students, is simply the summation of base and shaft resistances:

$$Q = Q_{\mathrm{b}} + Q_{\mathrm{s}}. \tag{1}$$

The base and shaft resistances, in turn, are simply the multiplication of shaft and base areas, A_{s} and A_{b}, by the respective unit resistances q_{b} and q_{s}:

$$Q_{\mathrm{b}} = A_{\mathrm{b}} q_{\mathrm{b}} \tag{2}$$

and

$$Q_{\mathrm{s}} = \sum_{l=1}^{n} q_{\mathrm{si}} A_{\mathrm{si}}, \tag{3}$$

where i is a soil layer index, and the summation is over the number n of layers crossed by the pile.

The separation of pile resistance in shaft and base resistance is a simplification of the problem, albeit a perfectly acceptable one in most cases. So, up to this point, we would be justified in thinking that this is indeed an easy problem. All we would need to do to proceed is to determine these unit resistances and the problem would be solved. However, the processes used to determine pile unit resistances are far from well developed.

As load on the pile head is gradually increased, the pile settlement increases. This proceeds until a load is reached at which the pile would tend to plunge. This load is known as the plunging or limit load. Given this, a question that arises is how to define the pile base and shaft resistances. Are they the values corresponding to the limit load or those associated with a particular value of pile settlement? There is uncertainty among both practitioners and academics as to how to define pile resistance.

If resistance is used in the classical sense of the word, then it must be associated with an ultimate limit state (ULS), one associated with potentially severe consequences for the supported structure. The plunging of the pile is clearly an ULS but pile settlements beyond a certain limit would also lead to ULSs. So a resistance defined based on a certain level of settlement is also possible. Since there is some confusion in the literature regarding this, the practice we follow is to use the term limit resistance for the maximum resistance that can be reached; i.e., the limit shaft resistance is the maximum shaft resistance and the limit base resistance is the maximum base resistance. When both the limit shaft and limit base resistance are reached, the pile reaches its limit resistance and plunges. Ultimate resistance, on the other hand, is a conventional load associated with an ultimate limit state, but not necessarily a maximum resistance. The most obvious example of an ultimate resistance is the load leading to a pile settlement equal to 10% of the pile diameter, which is favored internationally as an ultimate load criterion. This load has the added advantage that, for the factors of safety typically used in practice, it both separates safe designs from potentially unsafe designs and avoids serviceability limit states.

Now that we have defined precisely what is meant by resistance, we can address its estimation or determination. We will separate soils in sands, clays

and transitional soils. In sands, pile resistances can be calculated using drained analysis with soil represented as a frictional material. In clays, pile resistances have typically been estimated using undrained analysis, with the soil modeled as a frictionless, Tresca-like material. Transitional soils, which appear often enough in piling practice, are materials with intermediate behavior, in which partial drainage may be an issue either at the site investigation stage (such as in the interpretation of cone penetration tests) or the pile design stage. Fabric or structure may play a significant role in partially drained soil response. Although extremely interesting and important, we will not discuss transitional soils in this paper.

Piles are typically grouped in two main categories: displacement and nondisplacement piles. An ideal nondisplacement pile is installed in the soil such that a volume of soil is replaced by the pile (which is in mechanics terms an equal volume of a much stronger, stiffer material, typically concrete) without causing disturbances or changes in the stress or deformation states at any point of the surrounding soil. The classical example of a nondisplacement soil is a drilled shaft (bored pile). Drilled shaft installation does cause changes in the surrounding soil; however, these changes are fairly small if installation is done with proper care. Additionally, it is possible to model, even if simply, the effects of the installation on the soil. Displacement piles, in contrast, are piles installed in the ground without any soil removal. This type of pile acquires its space by displacing soil from space it originally occupied, a large deformation process that is challenging to model.

2 Base Resistance

2.1 Sand

Limit Base Resistance

Ideally, the limit base resistance of piles in sand would be calculated from a large deformation analysis that would accurately compute the compressive stresses on the pile base as the pile is pushed through the soil. These analyses have become viable but are still challenging, and more so in the case of sands.

Limit base resistance may also be estimated using cavity expansion analysis. The analysis of Salgado and Prezzi [30] assumes a simplified mechanism to relate the pile base resistance to cylindrical cavity limit pressure. As argued by Salgado et al. [32], the existence of this relationship is intuitive in that a cylindrical pile, when pushed through the soil, does expand a cylindrical cavity in it, and is backed up by experimental evidence from calibration chamber tests (e.g., Houlsby and Hitchmann [11]) that show a clear dependence of cone tip resistance q_c, a proxy for pile limit base resistance, on lateral effective stress. Figure 1 shows the mechanism used to calculate limit base resistance, which is obtained by considering the rotation of major principal stresses from the horizontal direction associated with cylindrical cavity expansion outside the transition zone T to a subvertical direction on the cone face. The cylindrical

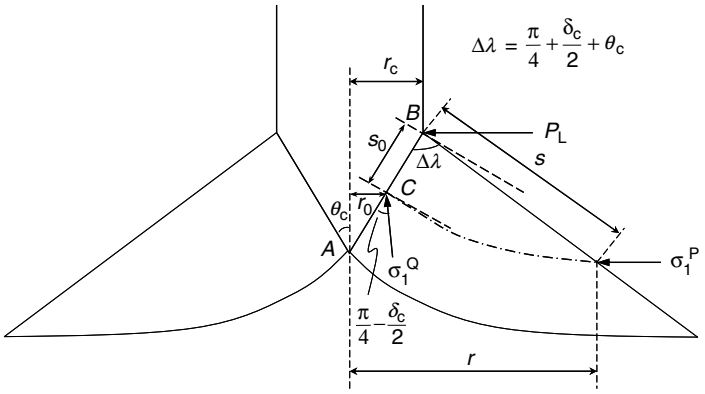

Fig. 1. Mechanism of pile base plunge

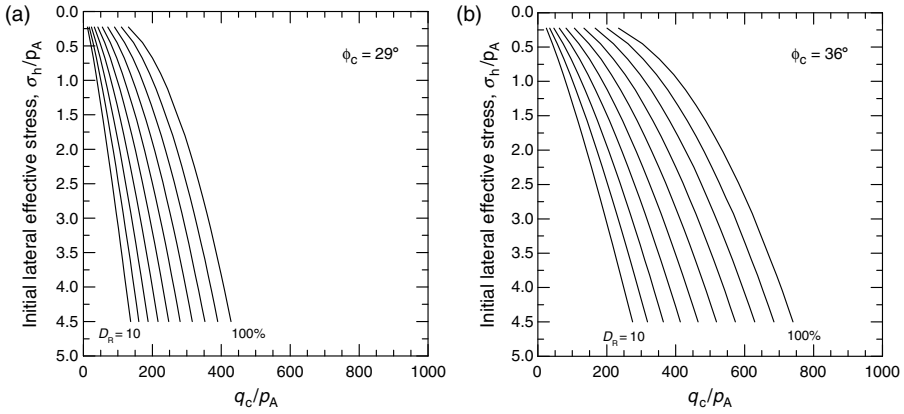

Fig. 2. Cone resistance (a proxy for q_{bL}) versus effective lateral stress and relative density for sand with critical-state friction angle equal to 29° and 36°; p_A = reference stress (= 100 kPa = 0.1 MPa ≈ 1 tsf).

cavity expansion analysis and the stress rotation analysis used to compute q_{bL} are detailed in Salgado and Prezzi [30] and Salgado and Randolph [31].[1] An illustration of the values this analysis produces is provided in Fig. 2 for two extreme values of the critical-state friction angle.

Ultimate Base Resistance

Lee and Salgado [16] performed finite element analyses using ABAQUS to obtain the base resistances of nondisplacement piles in sand. They analyzed piles with three different lengths – 5, 10, and 20 m – and a fixed radius of 60 cm, embedded in normally consolidated sand with relative densities of

[1] The program CONPOINT can be used to perform this analysis.

30, 50, 70, and 90%. Sand parameters were those in Table 1, considered fairly representative of silica sands commonly found in the field. The axisymmetric problem was modeled using eight-noded quadrilateral elements, with interface element of zero thickness at the pile–soil boundary following the Coulomb friction law. The boundaries of the domains were placed far from the pile to minimize boundary effects. The pile was elastic, and the soil, elastic–plastic following a stress–strain model modified after Fahey and Carter [6] with a nonlinear form of Drucker–Prager criterion to model failure and postfailure response.

Unit pile base resistance q_b, normalized with respect to q_c (which is approximately the same as the limit unit base resistance q_{bL}), is shown in Fig. 3 as a function of relative settlement s/B (s = settlement, B = pile diameter) for different pile lengths and for the relative densities of 30% and 90%. Cone resistance q_c was estimated using CONPOINT for various values of relative density (D_R) and stress state. The s/B versus q_b/q_c curves for 90% relative density lie noticeably below those for very loose sand because limit base resistance, which depends mostly on shear strength, increases at a higher rate with increases in relative density than the load associated with a given settlement, which depends on stiffness.

Table 2 shows q_b/q_c for $s/B = 5\%$ and 10% obtained from the analysis. Values of q_b/q_c fall within the 0.07–0.13 range for $s/B = 5\%$ and within the

Table 1. Basic properties of Ticino Sand (after [10]), the sand used in the base resistance analysis of Lee and Salgado [16]

D_{10} (mm)	D_{50} (mm)	G_s	U	ϕ_c (°)	e_{max}	e_{min}	γ_{max} (kN m^{-3})	γ_{min} (kN m^{-3})
0.36	0.54	2.623	1.5	34.8	0.922	0.573	16.68	13.65

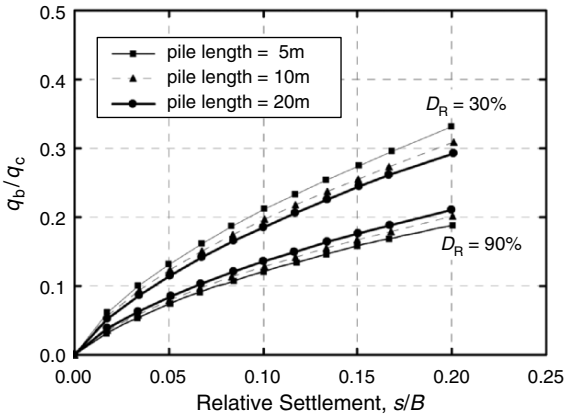

Fig. 3. Normalized base load–settlement curves in terms of q_b/q_c and s/B for nondisplacement piles

Table 2. Values of q_b/q_c for nondisplacement piles obtained from FEM analysis

pile length (m)	D_R (%)	q_b/q_c ($s/B = 5\%$)	q_b/q_c ($s/B = 10\%$)
5	30	0.13	0.21
	50	0.10	0.17
	70	0.09	0.14
	90	0.07	0.12
10	30	0.12	0.20
	50	0.10	0.16
	70	0.09	0.14
	90	0.08	0.13
20	30	0.11	0.19
	50	0.10	0.16
	70	0.09	0.15
	90	0.08	0.13

Table 3. Observed and recommended values of q_b/q_c for nondisplacement piles

author(s)	D_R (%)	q_b/q_c for $s/B = 5\%$	q_b/q_c for $s/B = 10\%$
Franke [8]	–	–	0.2
Jamiolkowski and Lancellotta [14]	–	0.2	–
Ghionna et al. [10]	50	0.09–0.14	0.11–0.19
	90	0.07–0.10	0.10–0.14
Salgado [29]	–	–	0.15
Mayne and Harris [19]	–	–	0.26
Teixeira and Albiero [42]	–	0.18	0.20
Simonini [36]	–	0.09	0.17

0.12–0.21 range for $s/B = 10\%$. The values are in general agreement with those observed in the field and laboratory (Table 3).

Figure 4 illustrates the influence of relative density on the normalized base resistance q_b/q_c. The effect is substantial, with q_b/q_c decreasing with increasing relative density. This justifies the presentation of q_b/q_c values for different relative densities in Table 2. The value of q_b/q_c at $s/B = 10\%$ is 0.19–0.21 for $D_R = 30\%$, whereas it is 0.12–0.13 for $D_R = 90\%$. The q_b/q_c ratio can be approximated reasonably well by the following equation:

$$\frac{q_{b,10\%}}{q_c} = 0.23 \exp\left(-0.0066 D_R\right). \tag{4}$$

Equation (4) indicates that the q_b/q_c ratio decreases with increasing D_R. Alternatively, it expresses the fact that larger settlements are required for soils with higher relative densities to reach a unit base resistance equal to a set percentage of q_c. The results also offer some insight into why most pile design methods that calculate q_b by multiplying q_c by a certain constant (e.g., 0.2 for 10% relative settlement, according to Franke 1989) also place an upper limit (usually in the 4.5–5 MPa range) on possible values of q_b. The results of the present analysis indicate that when piles are embedded in very dense

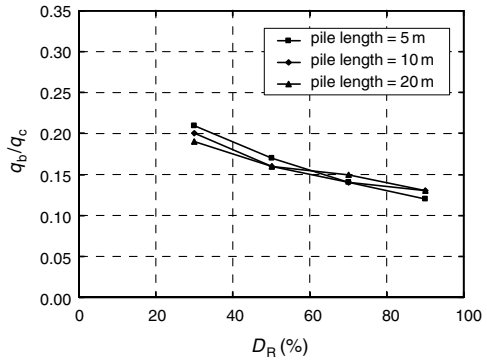

Fig. 4. Normalized unit base resistance versus relative density

sand layers, a value of q_b, chosen irrespective of relative density (for example, $q_b = 0.2\,q_c$, as proposed by Franke [10]) would yield an excessively large base resistance. Placing a limit on q_b (e.g., 5 MPa) serves a purpose in that case, but if the q_b/q_c values of Table 2 are used for design, there is no need for setting an upper limit on q_b.

The effect of pile length (i.e., confinement at pile base level) and overconsolidation on q_b/q_c was also studied. The effect of pile length on q_b/q_c was found to be small because q_b and q_c depend on initial confining stress in a similar way. The effect of K_0 on q_b/q_c was found to be inconsequential.

2.2 Clay

Limit Base Resistance

The ratio of net unit pile base resistance to undrained shear strength in clay has traditionally been taken as 9. This follows from early versions of the bearing capacity equation,

$$q_{bL}^{gross} = s_{s_u} d_{s_u} N_c s_u + q_0 \tag{5}$$

with shape and depth factors s_{s_u} and d_{s_u} proposed by Skempton [37] and Meyerhof [20, 21]; for foundations with $D/B \geq 2.5$, (5) was taken as:

$$q_{bL}^{gross} = 9 s_u + q_0 \tag{6}$$

It is common in pile design in clay to work with net limit unit bearing capacity q_{bL}^{net}. With the assumption that the pile self-weight divided by its cross-sectional area approximately balances q_0, we arrive at the value of 9 for the ratio q_{bL}^{net}/s_u. Recent research, however, suggests that 9 may be too low. Martin [18] found a value of approximately 9.3 for this ratio from lower bound analysis. He also determined that this number is essentially the same regardless of the rate of undrained shear strength increase with depth. Salgado et al. [34] showed, using limit analysis of circular foundations ranging in

depth from zero to depths typical of piles, that the unit base capacity keeps increasing with depth beyond the D/B value of 2.5 used to obtain the earlier estimates of 9 for q_{bL}/s_u. Their lower bound values for unit base resistance in clays is as high as 11 for $D/B = 5$, with upper bound as high as 13.75 for the same relative depth. It should be noted that the boundary conditions utilized did not account for the constraining effect of shaft resistance on base resistance (by which the soil on the sides of the pile, in order to move up with respect to the pile as the pile is pushed down, must overcome friction with the pile), suggesting the actual values could be higher. On the other hand, limit analysis may not capture well the confined flow mechanism that is operative for deep foundations (which, incidentally, justifies the use of cavity expansion analysis to analyze such problems). A different approach, by Yu et al. [46], arrives also at higher values for q_{bL}^{net}/s_u (typically in the 10–12 range for realistic conditions). Hu et al. [13] conducted a large strain finite element analysis that produced a net limit unit base resistance equal to $12.7s_u$ for a pre-embedded circular foundation with length to diameter ratio of 2 at a displacement of over four pile diameters. This evidence suggests that q_{bL}^{net}/s_u is at least equal to 10 and potentially as high as 12–13.7.

Ultimate Base Resistance

While in the calculation of collapse loads associated with unrestrained mechanisms the soil stiffness does not matter, in contained plastic flow, the soil stiffness plays an important role. Randolph et al. [25] argue that, for piles (i.e., for large foundation embedment), a cavity expansion mechanism is in force for the pile base. Even if unrestrained collapse mechanisms can be achieved in clay, the argument can be made that we are not necessarily interested in design in the limit resistance but rather in the value of base load at a specific value of settlement. For 10% relative settlement, Hu and Randolph [12] obtained q_{bL}^{net}/s_u values ranging from 9.3 to 9.9. In design, their average value of 9.6 could be used.

3 Shaft Resistance

3.1 Sand

The unit shaft resistance is the product of the normal effective stress on the soil–pile interface ($\sigma'_h = K\sigma'_{v0}$) by an appropriate interface friction coefficient ($\mu = \tan\delta$). Except in the case of floating piles, shaft resistance is fully mobilized along most of the pile length (except very near the base) for a pile subjected to its ultimate load defined according to the 10% relative settlement criterion. It is probably fully mobilized along most of the pile length under service conditions for well-designed piles as well.

Mathematically, the unit limit shaft resistance q_{sL} is written as:

$$q_{sL} = K\sigma'_{v0} \tan\ \delta \tag{7}$$

where K is the coefficient of lateral earth pressure (a function of soil state), δ is the interface friction angle, and σ'_{v0} is the initial vertical effective stress. We use the notation σ'_{v0} to stress that even if there may be vertical effective stress changes at very close distances from the pile shaft, our reference for calculating σ'_h is always the initial vertical effective stress.

Equation (7) is deceptively simple. Finding appropriate values for K and δ is not trivial, hence the vagueness with which the subject is typically treated in the literature. Values of δ should be expressed in terms of the critical-state friction angle ϕ_c. The argument for using ϕ_c is based on the development of large shear strains near the pile shaft at ultimate load levels. These strains are sufficiently large to cause a certain volume of soil near the pile to reach critical state.[2] At the ultimate load, critical state will be reached along the pile shaft for both stiff and compressible (slender) piles.

For nondisplacement piles, given the high degree of roughness of the concrete placed in situ, the interlocking of the shaft with the soil is such that shearing will take place within the soil immediately adjacent to the pile. It is therefore appropriate to take $\delta = \phi_c$ for nondisplacement piles. This is also illustrated experimentally by the data of Uesugi et al. [44].

The installation of nondisplacement piles preserves to a large extent the pre-existing stress state in the ground. Any limited unloading that may take place is corrected by the placement of the concrete, which has enough fluidity before setting to apply a normal stress on the soil sufficient to reestablish the original lateral stress (in fact, Fleming et al. [9] argue that the placement of concrete with high fluidity would even lead to an initial K slightly greater than K_0). When the pile is loaded, constant volume shearing will eventually develop between the pile and the sand. On the way there, the sand, if dilative, will attempt to expand but is constrained from doing so by the presence of the pile shaft; as a result, the normal stress between the pile and sand will increase. The result is that, for loose sands, K is close in value to K_0, but, for dense sands, K may be significantly greater than K_0. The literature does not appear to contain any analysis seeking to quantify K as a function of relative density and stress. A relatively simple analysis is possible to illustrate how we currently have the tools to obtain very good relationships for K.

A simple finite-element simulation of what happens in the soil as the pile is pushed down and shearing develops along the pile soil interface can be done by considering a disk of soil around the pile (Fig. 5), similarly to what was done by Gens and Potts [9]. Where the pile–soil interface would be, a vertical displacement is applied in increments until very large shear strains develop. The soil is modeled using 250 eight-noded quadrilateral, axisymmetric elements. Nodes lying in the same vertical are tied together with respect to both vertical and horizontal movement. This means the distortion of the soil disk as the pile is pushed down is captured by vertical shearing of the elements, which cannot rotate nor contract or stretch in the vertical direction. The elements are able to contract or dilate by contracting or stretching in the radial direction. The

[2] Geometrically, for a circular pile, this volume would be a hollow cylinder of soil with a thickness of barely a few times the D_{50} of the soil, as we will discuss later.

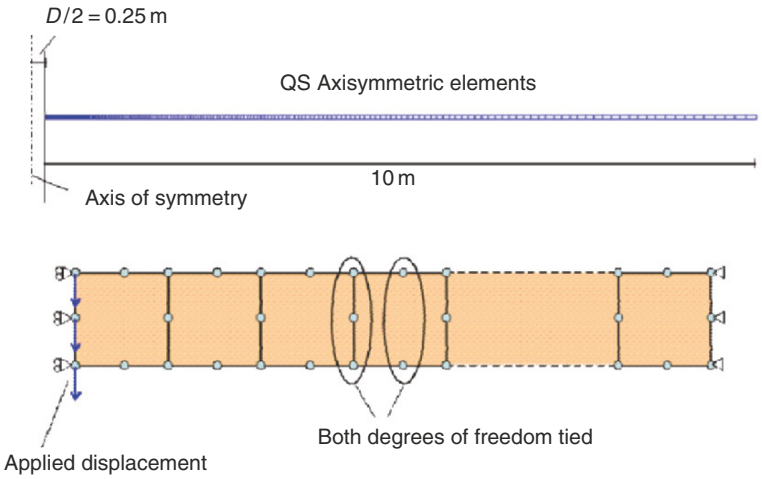

Fig. 5. Finite element representation of the application of a displacement to the side of a disc of soil representing a layer of soil around a pile

pile diameter for these analyses was 0.5 m. The sand was modeled using a constitutive model based on work of Papadimitriou and Boukovalas [23] and Dafalias and Manzari [5] calibrated with data for Ottawa sand from Salgado et al. [33] and Carraro et al. [4]. The finite element program SNAC [1] was used in all analyses.

Shear strain is highly localized next to the pile shaft. Considering the dependence of the results on the level of discretization when a strain-softening material is involved, the size (width) of the leftmost element was set to be no less than the shear band thickness that would be observed in reality. Various experimental studies (e.g., [22, 43, 45]) on shear strain localization in sand have shown that the shear band thickness is usually in the range of 5 to $20 \times D_{50}$. Most of the analyses were done for a minimum element size of $10 \times D_{50}$, corresponding to ∼4 mm for Ottawa sand, and for $K_0 = 0.4$. Sensitivity studies have shown that K/K_0 decreases slightly as the element size drops from 10 to $5 \times D_{50}$ and as K_0 increases.

Figure 6 shows the evolution of the shear stress that develops with increasing vertical pile displacement. The value of pile movement required for mobilization of q_{sL} is of the order of 4 mm (or about 0.8% of the pile diameter). Note also that for loose sand (in the case analyzed here less than about 40% relative density), the final normal stress acting on the pile shaft actually drops due to the contractive nature of the sand. From the ratio of the normal stress at the end of shearing to σ'_{v0} we can obtain K, which is given as a function of D_R in Fig. 7. K is less than K_0 for sands looser than about 40% relative density but then exceeds K_0, reaching a high just shy of $2.4K_0$, for $D_R = 90\%$ and $\sigma'_v = 50$ kPa.

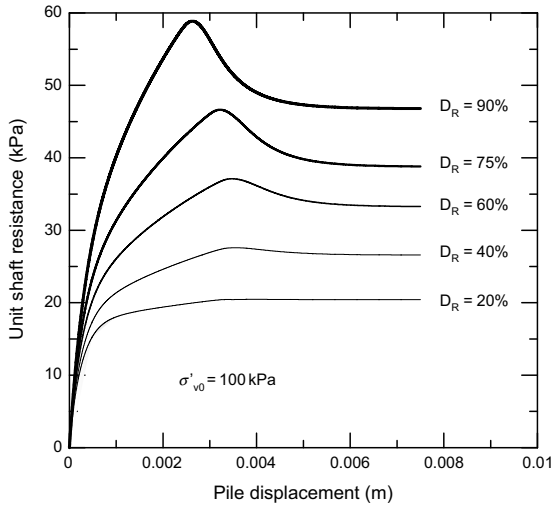

Fig. 6. Shear stress versus pile displacement for various D_R values

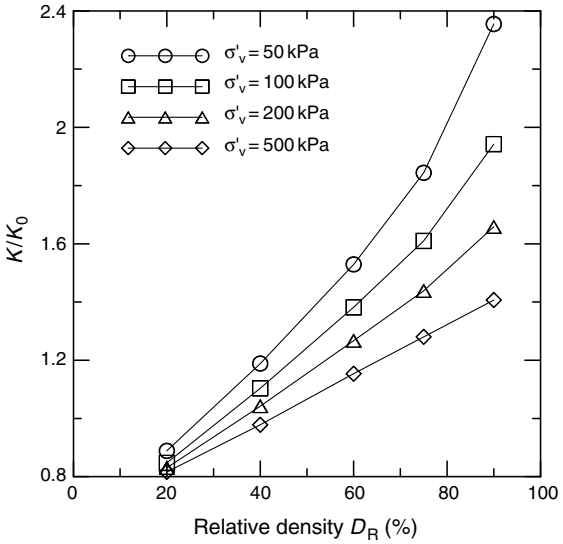

Fig. 7. Values of K/K_0 versus D_R for $\sigma'_\mathrm{v} = 50\,\mathrm{kPa}$, 100 kPa, 200 kPa, and 500 kPa

3.2 Clay

Both an effective stress analysis, using (7), and a total stress analysis can be done of the shaft resistance of a pile in clay. In the more commonly used total stress analysis, q_sL is expressed in terms of the undrained shear strength s_u of the soil as:

$$q_\mathrm{sL} = \alpha s_\mathrm{u}. \tag{8}$$

There has been little research done on the value of α for drilled shafts. Skempton [39] argued that α for stiff London clay was lower than 1 due to unloading of the clay at the walls of the shaft and remolding due to drilling operations. He proposed at the time an average $\alpha = 0.45$ for typical sizes of drilled shafts. Reese and O'Neill [27], based on their own research on drilled shafts installed in stiff clay in Texas, proposed $\alpha = 0.55$. Most publications simply refer to one of these values with little discussion. There is also no clear agreement as to what s_{u} should be in (8). We will assume s_{u} in (8) to refer to triaxial-compression, peak undrained shear strength, which may be estimated from the Skempton [38] correlation:

$$\frac{s_{\mathrm{u}}}{\sigma'_{\mathrm{v}}} = [0.11 + 0.0037(\mathrm{PI})]\,\mathrm{OCR}^{0.8}. \tag{9}$$

We can establish a simple analytical basis for determining α by examining the problem in a conceptual way. The starting point is to recognize that clay is weaker than the relatively rough concrete interface created by drilled shaft installation, and so it is reasonable to assume (as did Fleming et al. [9]) that the shearing takes place within the clay in a direction roughly parallel to the pile shaft, so that interface effects are not a significant factor in determining the value of α. This leaves the process of pile installation as the determining factor for the value of α.

The coefficient α may be expressed quite generally as:

$$\alpha = \frac{s_{\mathrm{u,\ r}}}{s_{\mathrm{u}}} = \frac{\sigma'_{\mathrm{hds}} \tan \phi_{\mathrm{r}}}{\sigma'_{\mathrm{v}}\,[0.11 + 0.0037(\mathrm{PI})]\,\mathrm{OCR}^{0.8}}, \tag{10}$$

where $s_{\mathrm{u,\ r}}$ is the residual shear strength of the clay along the shaft–soil interface that develops upon loading of the pile; ϕ_{r} is the residual friction angle of the clay (which is operative because the clay particles are aligned with the direction of shearing as a result of auger action during drilling); and σ'_{hds} is the lateral effective stress between the pile shaft and the disturbed soil during axial loading.

It is important to note that ϕ_{r} decreases with increasing effective normal stress σ' on the plane of shearing (because a larger normal stress forces greater alignment of particles as they are sheared). Figure 8 illustrates schematically the decrease in ϕ_{r} with increasing normal stress on the plane of shearing. At very large stresses, ϕ_{r} reaches an absolute minimum, denoted by $\phi_{\mathrm{r,\ min}}$. For very small stresses, ϕ_{r} approaches the critical-state friction angle ϕ_{c}. The assumption that, at σ' equal to zero, $\phi_{\mathrm{r}} = \phi_{\mathrm{c}}$ is based on the expectation that there would be negligible reorientation of particles in the absence of a normal stress forcing this reorientation to happen.

Following Maksimovic [17], ϕ_{r} can be expressed as:

$$\phi_{\mathrm{r}} = \phi_{\mathrm{r,\ min}} + \frac{\phi_{\mathrm{c}} - \phi_{\mathrm{r,\ min}}}{1 + \frac{\sigma'}{\sigma'_{\mathrm{median}}}}, \tag{11}$$

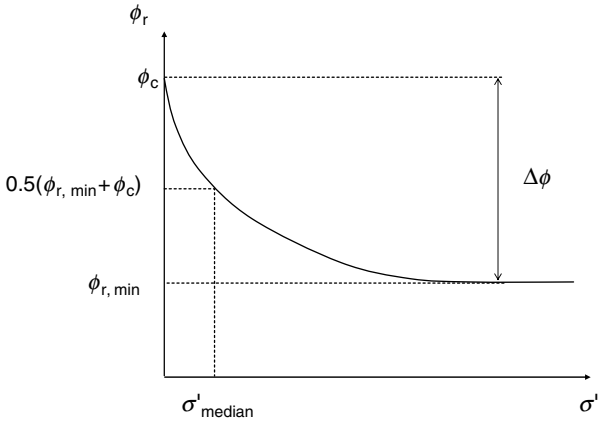

Fig. 8. Variation of ϕ_r with normal stress perpendicular to the plane of shearing

where σ' is the normal stress on the plane of shearing, and σ'_{median} is the value of σ' at which the friction angle is exactly equal to the average of the minimum residual friction angle $\phi_{\text{res, min}}$ and ϕ_c. From a practical standpoint, for clays containing a large smectite content, such as London clay, ϕ_c might have to be replaced by a lower ϕ value in order for (11) to produce acceptable results. The values from Maksimovic [17] used in (11) are not necessarily true ϕ_c values. Figure 9, for example, shows data for London clay based on both laboratory and field data. Note that the maximum value of ϕ_{res} at $\sigma' = 0$ extrapolated by Maksimovic [17] from the data is of the order of 12.5–16°, while this clay has ϕ_c in the 20–23° range. For piles, the normal effective stress on the plane of shearing to calculate ϕ_r is the lateral effective stress during pile loading.

According to Skempton [40], the residual friction angles of kaolinite, illite, and montmorillonite are approximately equal to 15°, 10°, and 5°, respectively. Values of the critical-state friction angle for London Clay and kaolinite are given as 23° and 25° by Atkinson [2]. These data are combined with data from Maksimovic [17] and Kenney [15], as reported by Maksimovic [17] in Table 4.

We must now tackle the question of how to determine σ'_{hds}. It is difficult to reduce the loading imposed on the soil during excavation and augering to a simple stress path. Naturally, there will be an induced shear stress associated with the excavation and another with the augering. On the way to critical state, we can estimate the pore pressure generated by using the Skempton concept of a pore pressure coefficient. For simple shear loading, this can be expressed as a ratio a of the pore pressure generated to the applied shear stress τ. If we assume that any changes in volume (under drained conditions) or pore pressure (under undrained conditions) beyond the critical state, towards a residual state, would happen only along the slip surface and would thus be very small, we could neglect additional pore pressure changes to obtain

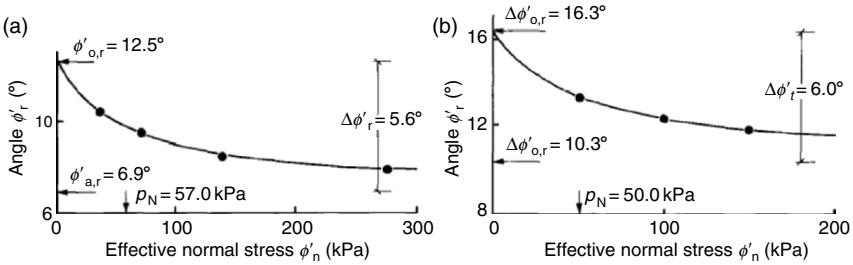

Fig. 9. Drop in residual friction angle of London clay with normal stress based on **(a)** ring shear test data from Bishop [3] and **(b)** back-calculation of landslides, after Maksimovic [17]

Table 4. Values of parameters needed to calculate α obtained from Maksimovic [17], Atkinson [2] and Skempton [40]

clay type	LL(%)	PI (%)	ϕ_c [a]	$\phi_{res,min}$	$\Delta\phi$	σ'_{median} (kPa)
london clay	75	45	16.3°	10°	13°	50
kaolinite	65	30	24[b]	13.4°[c]	10.6°	55

[a] Not true ϕ_c but rather extrapolated ϕ_r for zero normal stress (see Fig. 9b).
[b] This compares well with $\phi_c = 25°$ given by Atkinson [2].
[c] This compares well with $\phi_c = 15°$ given by Skempton [40].

a first-order estimate of σ'_h at the end of installation. The concrete would then be poured, the excess pore pressure dissipated, and σ'_h would (ideally) return to its initial value. Finally, loading of the pile would subject the soil around the pile to a simple shear loading. Having been presheared, its pore pressure generation capability would now be different from that of undisturbed soil (and represented by a pore pressure coefficient a_r). Additionally, the stress path would be capped by the residual strength envelope. The value of σ'_{hds} can now be calculated as:

$$\sigma'_{hds} = \sigma'_{h0} - 2a_r\tau_r = K_0\sigma'_v - 2a_r\sigma'_{hds}\tan\phi_r \tag{12}$$

from which σ'_{hds} can be extracted:

$$\sigma'_{hds} = \frac{K_0\sigma'_v}{1 + 2a_r\tan\phi_r}. \tag{13}$$

The value of K_0 may be estimated from the often-used Jaky's equation:

$$K_0 = (0.95 - \sin\phi)\,\mathrm{OCR}^{\sin\phi}. \tag{14}$$

We can now calculate α using, in succession, (14), (13), (11)[3], and (10). The value of a_r can be obtained either by analytical integration of a suitable constitutive model or from simple shear testing. A simple illustration of this

[3] Note the iteration between (11) and (13).

analysis can be done here for a stiff clay, for which the stress paths during installation and reloading of the remolded soil would be nearly vertical, such that we may assume for simplicity that $a_r = 0$ and $\sigma'_{hds} = \sigma'_{h0}$.

The values of α were calculated in this manner for kaolinite for σ'_v ranging from 0 to 500 kPa. Kaolinite was chosen because its fundamental parameters are reasonably well established. Table 4 has values for the parameters required in the calculations. For comparison, we have also included the parameters of London clay; although not done here, calculations of α for London clay lead to values slightly lower than for kaolinite. As it is customary in practice to plot α versus s_u, we also need to calculate the corresponding value of s_u to develop such plots, which is again done using (9). For anisotropically consolidated clay loaded in simple shear, the value of OCR associated with zero a_r is likely to be in the 3–5 range. The corresponding α values are plotted as two lines versus s_u in Fig. 10. The value of α will be in this range. We also show in Fig. 10 the α values obtained from the relatively few data cases in the literature for which reasonably accurate shaft resistance and s_u values are available and for which OCR can be estimated. The theoretical curves compare well with the data, most of which are for OCR values in the 3–9 range; however, the values associated with low s_u values in the figure are associated with either NC or lightly OC clays, and the theoretical curves are not applicable for those conditions; hence the large difference between the theoretical and field values.

One further consideration regards the clay content or clay fraction CF. Skempton [40] observed that ϕ_r varies with clay content. For clay content (clay fraction) CF less than approximately 25%, ϕ_{res} coincides with ϕ_c (note,

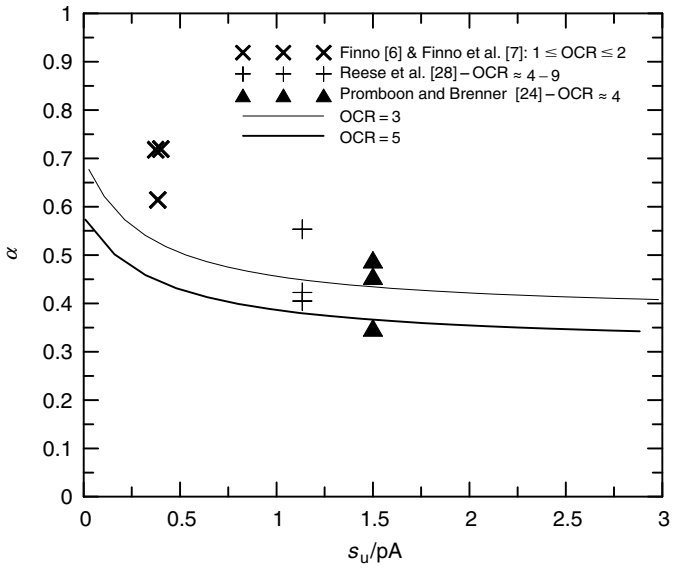

Fig. 10. Theoretical values of α and estimated values from field case histories

however, that this is the ϕ_c of the clay–silt–sand soil, not that of the clay); for clay content increasing from 25 to 52%, the residual friction angle drops towards the ϕ_r of the pure clay. For clay content greater than 52%, the residual friction angle remains stable at this minimum value. In order to account for the clay content in the calculation of α, we will assume that the α method will only be used when CF $\geq$ 25%. Based on the numbers provided by Skempton [40] on the values of CF between which ϕ_r changes from ϕ_c of the soil mix to ϕ_r of the pure clay, we can write the following approximate equation for ϕ_r as a function of CF:

$$\phi_r = \phi_r|_{\text{pure clay}} + \frac{\phi_{c,\text{ mix}} - \phi_r|_{\text{pure clay}}}{27\%} [52\% - \text{CF}(\%)] . \tag{15}$$

Values of α can now be calculated as a function of clay content. The α of soils containing mixtures of sand, silt, and clay with more than 25% clay would be expressed as:

$$\alpha = \frac{\sigma'_{\text{hds}} \tan \left\{ \phi_r|_{\text{pure clay}} + \frac{\phi_{c,\text{mix}} - \phi_r|_{\text{pure clay}}}{27\%} [52\% - \text{CF}(\%)] \right\}}{\sigma'_v [0.11 + 0.0037(\text{PI}_{\text{mix}})] \, \text{OCR}^{0.8}} \tag{16}$$

Studies on mixtures of clay, sand, and silt with high-quality data on the ϕ_c of these soils are few. The presence of sand or nonplastic silt increases ϕ_c by a few degrees. We know that the ϕ_c of most sands, nonplastic silts or mixtures of the two encountered in practice would be in the 30–35° range (e.g., [33]). The presence of clay reduces ϕ_c from that range to perhaps 28–30°. We will take 28° to be the ϕ_c of a sand–silt–kaolinite mixture with 25% kaolinite, assume

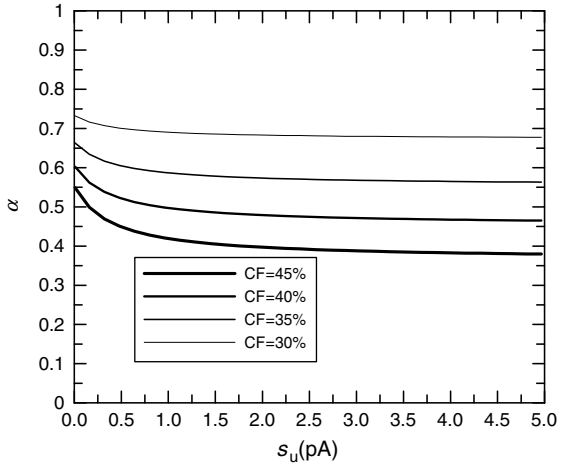

Fig. 11. Plots of α versus undrained shear strength s_u for soils with different clay content CF

it to decrease linearly with clay content as it increases from 25 to 52%, and assume, as before, that $a_r = 0$ for $3 \leq \text{OCR} \leq 5$. The PI of the soil drops significantly as CF drops from 52 to 25%. We will assume for simplicity that this drop occurs linearly and that the PI at 25% CF is equal to 10. We can now illustrate the calculation of α for soils with $25 \leq \text{CF} \leq 52\%$ using (16). Plots of α versus clay content obtained in this manner are shown in Fig. 11 for $\text{OCR} = 5$. Note that the plot for $\text{CF} = 45\%$ is very close to the corresponding plot of Fig. 10. These should be considered preliminary estimates of α, which can be refined with more elaborate determination of all the variables entering the calculations.

4 Conclusions

If pile resistance is determined using sound mechanics from a soil model that captures the essence of soil load response without reliance on empiricism or direct correlations, the fundamental basis for rigorous analysis is in place. We have shown this to be true for nondisplacement piles.

For nondisplacement piles installed in sand, the limit base resistance can be calculated with good accuracy using a cavity expansion-based analysis. We have shown using finite element analysis that the ratio of ultimate to limit base resistance is in the 0.13 (for dense sand) to 0.2 (for loose sand) range. The shaft resistance of nondisplacement piles in sand is the product of a lateral stress ratio K by the vertical effective stress and the tangent of the critical-state friction angle. We have shown that K lies between just under K_0 for loose sands to about twice K_0 for dense sands.

For nondisplacement piles installed in clay, numerical analyses (both finite element and limit analysis) have established accurate bounds on the values of limit unit base resistance. The ratio of net limit unit base resistance to undrained shear strength has been shown convincingly to be in the 10–13.5 range. The same ratio for ultimate instead of limit resistance would be less than that; some authors suggest numbers just under 10. The shaft resistance is most frequently calculated using the α method. We have shown that the value of α can be determined analytically if the critical-state and residual friction angles, as well as the relationship between the residual friction angle and the normal effective stress on the shearing plane, are known. The analysis can also be used to determine α for soils containing clay contents greater than 25%.

Acknowledgments

I am grateful to Monica Prezzi and Dimitrios Loukidis for their insightful comments and to him for his assistance with the FE analysis of shaft resistance in sands.

References

1. Abbo, A.J. and Sloan, S.W. (2000). *SNAC, User manual, Version 2.0*. Department of Civil, Surveying and Enviromental Engineering, University of Newcastle, Callaghan, Australia.
2. Atkinson. J. (1993). *An Introduction to the Mechanics of Soils and Foundations Through Critical State Soil Mechanics*. Mc Graw Hill, New York.
3. Bishop, A.W. (1971). "Shear strength parameters for undisturbed and remolded soil specimens. Stress–strain behaviour of soils." *Roscoe Memorial Symposium*, 3–58. Henley, Foulis.
4. Carraro, J.A., Bandini, P. and Salgado, R. (2003). "Evaluation of liquefaction resistance of clean and silty sands based on CPT cone penetration resistance." *Journal of Geotech. and Geoenvironmental Engineering*, ASCE, 129(12), 965–976.
5. Dafalias, Y.F. and Manzari, M.T. (2004). "Simple plasticity sand model accounting for fabric change effects." *Journal of Engineering Mechanics*, ASCE, Vol. 130, No. 6, 622–634.
6. Fahey, M. and Carter, J.P. (1993). "A finite element study of the pressuremeter test in sand using a non-linear elastic plastic model." *Canadian Geotechnical Journal*, 30(2), 348–361.
7. Finno, R.J. (1989). "Surface conditions and pile installation data." *Proceedings of the Pile Prediction Symposium*, ASCE, Foundation Engineering Congress, Northwestern University, Evanston, I.L., Finno R.J. (eds), 1–74.
8. Finno, R.J., Cosmao, T. and Gitskin, B. (1989). "Results of foundation engineering congress pile load tests." *Proceedings of the Pile Prediction Symposium*, ASCE, Foundation Engineering Congress, Northwestern University, Evanston, I.L., Finno R.J. (eds), 338–355.
9. Fleming, W.G.K., Weltman, A.J., Randolph, M.F. and Elson, W.K. (1992). *Piling Engineering*. Surrey University Press, 390pp.
10. Franke, E. (1989). Co-report to discussion, session 13: large-diameter piles. *Twelth International Conference of Soil Mechanics and Foundation Engineering*, Rio de Janeiro.
11. Franke, E. (1993). "Design of bored piles, including negative skin friction and horizontal loading." *Deep Foundations on Bored and Auger Piles* (Van Impe, ed.), Balkema, Rotterdam.
12. Gens, A. and Potts, D.M. (1984). "Formulation of quasi-axisymmetric boundary value problems for finite element analysis". *Engineering Computations*, 1(2), 144–150.
13. Ghionna, V.N., Jamiolkowski, M., Pedroni, S. and Salgado, R. (1994). "The tip displacement of drilled shafts in sands." *Proceedings of Settlement '94* (Yeung and Félio, eds.), Vol. 2, Geotechnical Engineering Division, ASCE, June, 1039–1057.
14. Houlsby, G.T. and Hitchman, R. (1988). "Calibration chamber tests of a cone penetrometer in sand." *Geotechnique* 38(1), 39–44.
15. Hu, Y. and Randolph, M.F. (2002). "Bearing capacity of caisson foundations on normally consolidated clay." *Soils and Foundations*, 42(5), 71–77.
16. Hu, Y., Randolph, M.F. and Watson, P.G. (1999). "Bearing capacity of skirted foundations on non-homogeneous soil." *Journal of Geotechnical and Geoenvironmental Engineering*, ASCE, 125(11), 924–935.

17. Jamiolkowski, M. and Lancellotta, R. (1988). "Relevance of in-situ test results for evaluation of allowable base resistance of bored piles in sands." In: Van Impe (ed), *Deep Foundations on Bored and Auger Piles*: 107–119. Balkema, Rotterdam.
18. Kenney, T.C. (1967). "The influence of mineralogical composition on the residual strength of natural soils." *Proceedings of the Oslo Geotechnical Conference on the Shear Strength Properties of Natural Soils and Rocks*, Vol. 1, 124–129.
19. Lee, J. and Salgado, R. (1999). "Determination of pile base resistance in sands." *Journal of Geotechnical and Geoenvironmental Engineering*, ASCE, 125(8), August, 673–683.
20. Maksimovic, M. (1989). "On the residual shearing strength of clays." *Geotechnique,* 39(2), 347–351 .
21. Martin, C.M. (2001). "Vertical bearing capacity of skirted circular foundations on tresca soil." *Proceeding of the 15th International Conference on Soil Mechanics and Geotechnical Engineering*, Istanbul, Vol. 1, 743–746.
22. Mayne, P.W., and Harris, D.E. (1993). "Axial load–displacement behavior of drilled shaft foundation in piedmont residuum." *Technical Report No. 41-30-2175*, Federal Highway Administration, Washington, DC
23. Meyerhof, G.G. (1951). "The ultimate bearing capacity of foundations." *Geotechnique*, 2(4), 301–332.
24. Meyerhof, G.G. (1963). "Some recent research on the bearing capacity of foundations." *Canadian Geotechnical Journal*, 1, 16–26.
25. Nemat-Nasser, S. and Okada, N. (2001). Radiographic and microscopic observations of shear bands in granular materials. *Géotechnique*, 51(9), 753–765.
26. Papadimitriou, A.G. and Bouckovalas, G.D. (2002). "Plasticity model for sand under small and large cyclic strains: a multiaxial formulation." *Soil Dynamics and Earthquake Engineering*, 22(3), 191–204.
27. Promboon, S. and Brenner, R.P. (1981). "Large diameter bored piles in Bangkok clay." *Proceedings of the International Conference on Soil Mechanics and Foundation Engineering*, Vol. 2, 815–818.
28. Randolph, M.F., Jamiolkowski, M.B. and Zdravkovic, L. (2004). "Load carrying capacity of foundations." *Advances in Geotechnical Engineering – Proceedings of the Skempton Conference*, London, 2004. (Jardine, R.J., Potts, D.M. and Higgins, K.G., eds), Thomas Telford, London, Vol. 1, 207–240.
29. Reese, L.C. and O'Neill, M.W. (1988). *Drilled Shafts: Construction and Design.* FHWA Report No. HI-88-042.
30. Reese, L.C., Touma, F.J. and O'Neill, M.W. (1976). "Behavior of drilled piers under axial loading." *Journal of the Geotechnical Engineering Division*, ASCE, 102(5), 493–510.
31. Salgado, R. (1995). "Design of piles in sands based on CPT results." *Proceedings of the 10th Pan-American Conference on Soil Mechanics and Foundation Engineering*, Vol. 3, 1261–1274, Guadalajara.
32. Salgado, R. and Prezzi, M. (2005). "Computation of cavity expansion pressure and cone resistance in sand." *International Journal of Geomechanics,* submitted.
33. Salgado, R. and Randolph, M.F. (2001). "Analysis of cavity expansion in sand." *International Journal of Geomechanics*, 1(2), 175-192.
34. Salgado, R., Mitchell, J.K. and Jamiolkowski, M. (1997). "Cavity expansion and penetration resistance in sand." *Journal of Geotechnical and Geoenvironmental Engineering*, ASCE, 123(4), 344–354.

35. Salgado, R., Bandini, P. and Karim, A. (2000). "Shear strength and stiffness of silty sands." *Journal of Geotechnical and Geoenvironmental Engineering*, ASCE, 126(5), 451–462.
36. Salgado, R., Lyamin, A., Sloan, S. and Yu, H.S. (2004). "Two- and three-dimensional bearing capacity of footings in clay." *Geotechnique*, 54(5), 297–306.
37. Simonini, P. (1996). "Analysis of behavior of sand surrounding pile tips." *Journal of Geotechnical Engineering*, ASCE, 122(11), 897–905
38. Skempton, A.W. (1951). "The bearing capacity of clays." Building Research Congress, 1, 180–189.
39. Skempton, A.W. (1957). "The planning and design of New Hong Kong airport." Proceedings of ICE, London, 7, 305–307.
40. Skempton, A.W. (1959). "Cast in situ bored piles in London clay." *Geotechnique* 9, 153–173.
41. Skempton, A.W. (1985). "Residual strength of clays in landslides, folded strata and the laboratory." *Geotechnique*, 35(1), 3–18.
42. Teixeira, C.Z., and Albiero, J.H. (1994). "A Evolução da Reação de Ponta de Estacas Escavadas Submetidas a Sucessivas Provas de Carga." *Proceedings of the 10th Brazilian Conference Soil Mechanics and Foundation Engineering*, Foz Do Iguacu, Vol. 1, 3–9.
43. Uesugi, M., Kishida, H. and Tsubakihira, Y. (1988). "Behavior of sand particles in sand–steel friction." *Soils and Foundations*, 28(1), 107–118.
44. Uesugi, M. , Kishida, H. and Uchikawa, Y. (1990). "Friction between dry sand and concrete under monotonic and repeated loading". *Soils and Foundations*, 30(1), 115–128.
45. Vardoulakis, I. and Sulem, J. (1995). *Bifurcation Analysis in Geomechanics*. Blackie, London.
46. Yu, H.S., Herrmann, L.R. and Boulanger, R.W. (2000). "Analysis of steady cone penetration in clay." *Journal of Geotechnical and Geoenvironmental Engineering,* ASCE, 126(7), 594–605.

Assessment of Uncertainties in Wellbore Stability Analysis

Y. Sheng, D. Reddish, and Z. Lu

School of Civil Engineering, University of Leeds, Leeds, UK
y.sheng@leeds.ac.uk

Abstract. Wellbore instability is a critical and costly problem in the petroleum engineering industry, which has yet to be fully understood and addressed. This is mainly because of uncertainty in some key influential parameters, such as in situ stress, rock strength, and other engineering operating parameters. These can lead to wellbore stability uncertainty, and make it very difficult for the conventional deterministic approaches to predict the risks associated with the instability problems during the drilling and production process. To account for the uncertainty involved in the wellbore stability analysis, a Monte Carlo uncertainty analysis technique has been combined with a numerical geomechanical modelling method to develop a geostatistical approach. This makes it feasible to assess not only the probability of achieving a desired degree of wellbore stability at a given mud weight, but also the effects of the uncertainty in each parameter on the stability of the wellbore. This approach has been applied to a case study of a vertical well in deepwater. The most influential parameters have been identified by a sensitivity analysis technique, and the likelihood of avoiding wellbore failure in different modes is obtained across a range of mud weights. The advantage of adopting numerical methods in this study lies in more realistic geomechanical representations of the wellbore stability problem, and less uncertainty from numerical modelling compared with the analytical models used in previous studies. Results of the analysis illustrate the potential of the approach to be used as a pre-drilling design tool to predict optimal mud weight windows for a better drilling program.

1 Introduction

Wellbore instability problems are often encountered during and after drilling in the oil and gas industry. As a consequence of this, the borehole wall may collapse or the circulation may be lost, which can lead to a stuck drill string

and consequent fishing, sidetracking and reaming operations, even a complete halt of productivity [2]. In addition to being a technical challenge, the occurrences of the wellbore instability related problems will significantly add to the already high well costs. It is estimated that at least 10% of the average well budget is used on unplanned operations resulting from wellbore instability. This cost may approach one billion dollars per year worldwide [2, 18].

Wellbore stability issues were not seriously addressed until Bradley [4] published his influential paper "Failure of Inclined Boreholes", which initiated great interest in the topic within the industry [4]. Although the application of rock mechanics has improved drilling performance, it is still not satisfactory, judging from the trends observed in recent years.

One of the most significant problems remaining, which handicaps the utilization of the advanced geomechanical and numerical models in the wellbore stability analysis, is the uncertainty of the key influences upon the instability, such as rock strength, pore pressure and the magnitude and orientation of the three principal stresses obtained in the vicinity of a drilling field. A number of deterministic techniques have been developed to predict optimal operational parameters such as mud weights or drilling trajectories [1, 4, 12, 17, 18, 20], in which either for the sake of simplicity or for lack of information, it is assumed that the geomechanical and operational parameters are the same throughout a material domain. However, in many cases, due to the intrinsic inhomogeneous nature of the rocks, the minimal exposure of the rock mass around a borehole, and the need to extrapolate available information over a depth range, the geomechanical parameters such as the in situ stresses, pore pressure, and rock strength are inevitably poorly assessed, as the required data necessary to compute their values are often not available [2, 14–16]. Furthermore, models that describe the relationships between field measured data and the required parameters for modelling are poorly calibrated. In some cases, technological or operational constraints make it impossible to acquire the information necessary to overcome these problems. An additional problem relates to the intrinsic uncertainty or error associated with each measurement. Thus, the uncertainty involved in the wellbore stability problem has a sense of the unknown due to the lack of knowledge about the properties of the rock mass and the in situ stresses rather than due to the inherent randomness in them [5].

Because of the uncertainty involved in the wellbore stability analysis, the use of averaged values for the input parameters in the deterministic approaches can lead to conclusions that significantly differ from the true behaviour of a wellbore. A good understanding of the impact of these uncertainties would definitely promote safe and economic design and help better cope with the large uncertainties and variations. Given the potential improvements to design and the already achieved successes in resource estimation, it is technically possible to utilize probabilistic methods to quantify the effects of the uncertainties on wellbore stability predictions. Although probabilistic methods have frequently been used in the oil industry, e.g. to estimate the expected value of a project, their application to wellbore stability is relatively new.

Ottesen et al. [16] presented a new statistical approach based on Quantitative Risk Analysis (QRA) that provides a means to assess uncertainties in input data and defines the results in terms of the probability to achieve a desired degree of stability as a function of mud weight [16]. McLellan and Hawkes [14] applied a similar approach to sand production prediction, utilizing poro-elastic constitutive models [14]. Moos et al. [15] adopted and modified QRA approach, and analyzed both the collapse pressure and the lost circulation pressure to derive a mud window, both at a single depth and over an entire open hole [15]. A common feature of these studies is that the probabilistic method was utilized based on a theoretical closed form or empirical solution to the linear elastic failure of the wellbore. This enables a simple and quick process of geomechanical analysis so that the repetitive probabilistic approach can be applied with limited computational resources. However, this was achieved at a price of compromising the accuracy of the analysis, because the analytical or empirical solutions have too many unrealistic assumptions to represent real problems.

In this chapter, the Monte Carlo uncertainty analysis technique and a 3D finite difference numerical modelling method were combined to address the uncertainty involved in a wellbore stability analysis. The input parameters whose uncertainty had a significant impact on the numerical model output were selected by a sensitivity analysis and then treated as random in the follow up analysis. A 3D numerical model was set up to represent the borehole and the surrounding rocks at a certain depth. Variable combinations of the key influential parameters, generated by the sampling process, were introduced in the numerical simulation to observe the geomechanical response of the wellbore. A controlling MS Visual Basic program has been developed to run the calculations in sequence with varying rock properties and geomechanical input parameters. The output uncertainty sensitivity analysis of the results was performed via a standard Monte Carlo uncertainty analysis procedure to determine the likelihood of a wellbore failure.

The probabilistic methodology developed in this chapter takes advantages of both numerical modelling and QRA therefore, the uncertainty associated with the wellbore stability analysis can be addressed. Furthermore, there are less unrealistic simplifying assumptions on the geomechanical properties at and around a wellbore in this methodology when compared with the conventional deterministic analyses and the existing probabilistic approaches.

2 Uncertainty Analysis Process

It is well known that there is considerable uncertainty with most of the data used in geomechanical analyses. Several strategies have been developed by geotechnical engineers to deal with the uncertainty [3, 5], including passive solutions like ignoring it, being conservative in design, using the observational method and recent attempts to quantify the uncertainty.

Among the large number of approaches developed for performing uncertainty studies, the Monte Carlo analysis is preferable for this research because it is not dependent on the underlying model and hence is more applicable to complex geotechnical problems. Additionally, the full coverage of each input variable and a friendly interface with a variety of sensitivity analysis techniques allows one to not only estimate the expected value and standard deviation but also obtain a full distribution of the output variable [3, 6, 7]. Theoretically a Monte Carlo analysis may require a large sample size (e.g. 10,000 samples) in order to approximate the original distribution well. Consequently, the computational cost may become a critical concern. In practice, usually a sample size of less than 1,000 is sufficient to provide an acceptable uncertainty and sensitivity analysis result [6, 8].

Before performing an uncertainty analysis, the parameters of the greatest influence must be determined by means of a proper systematic sensitivity study. A sensitivity study attempts to estimate how the uncertainty in the output of a model can be apportioned to different sources of uncertainty in the model inputs. Of a variety of sensitivity analysis techniques, the one at a time (OAAT) technique has been chosen for its effectiveness and simplicity [8]. OAAT involves a process to screen out the influential parameters and in turn vary them across their range of distribution with all other parameters set at their mean value in the geomechanical modelling process. This initial analysis gives out an idea of which parameters have the greatest influence on the chosen performance parameter of the model, such as the deformation of wellbore wall in this research. Once the parameters that contribute the most uncertainty have been identified, this knowledge in turn makes it possible to determine the amount of risk reduction that can be achieved by acquiring the data necessary to reduce the uncertainty of any or all of the input parameters.

After examination of the influential parameters the most sensitive parameters are selected and their representative distributions will be determined. The Monte Carlo approach allows sampling of data uncertainties from the actual distributions of the measured parameters as well as from functional forms for these distributions such as normal or lognormal distributions. Ideally more data should be collected for the most important parameters and an expert should be involved to determine the distribution for the most influential parameters, the least important ones may need less field data and could involve more subjective judgements. The distribution characteristics and ranges of the input parameters will directly determine the quality of the uncertainty analysis.

It is also very important in the uncertainty analysis that an appropriate sampling technique is employed to ensure reasonable accuracy with efficiency. Random sampling and Latin Hypercube sampling are the two most used techniques for the generation of samples form the distribution of the influential parameters. Random sampling is simple but requires a large sample size (e.g. 100,000 s) to ensure sufficient coverage of regions that have a low probability

of occurrence. By contrast, the Latin Hypercube sampling technique can fully cover the specified subsets with fewer samples (1,000 s or less) [9, 10], thus it has been adopted in this research.

The subsequent sampling propagation in this study consists of four steps:

- Each sample property value is transformed into a form that can be recognized by the chosen the Fast Lagrangian Analysis of Continua (FLAC) constitutive model;
- Write the normalized data for that value to a file;
- A batch file is then generated to run all the models by obtaining randomly the values of input parameters from the previously constructed normalized data files;
- Finally the key results of each model execution are written to a permanent file before the execution of the next model in the series.

A MS Visual Basic program was developed to incorporate the input data transformation, model evaluations, and model outputs extraction into a unified program package. Both pre-processor and post-processor are unified into this program package so that this can be used to provide normalized input data for the numerical model and extract required results from outputs of the numerical modelling for the uncertainty and sensitivity analysis.

3 The Application of Numerical Modelling to Uncertainty Analysis

Traditional analytical methods have been commonly used to conduct structural designs and determine appropriate design parameters, and also have been adopted in the previous uncertainty analysis of the wellbore instability problems [14–16]. However, the simple mathematical models used in an analytical analysis are usually oversimplified representations of the real problem being studied. Hence, the model employed to perform an analytical analysis is often a key source of uncertainty due to these simplifications. For instance, an analytical model may assume the rock to be elastic when in fact it has a nonlinear stress–strain characteristic. This is a key drawback of the existing uncertainty studies on the wellbore instability problems, which spent much effort to reduce the uncertainties of input parameters, whilst introducing additional uncertainty by using a simplified analytical approach in the geomechanical models.

On the other hand, the widely used powerful numerical modelling methods usually involve a smaller number of assumptions and may represent the complicated geotechnical engineering problems with a higher degree of accuracy. There are many successful examples of the applications of the numerical methods in solving geomechanical problems, all however in the deterministic way [13, 19]. Until recently it has been impractical to incorporate a Monte

Carlo type approach into the numerical techniques to study the uncertainty involved in geotechnical engineering, because of the excessive scale and complexity of the problem. However recent improvements in hardware and the use of variance reduction techniques have facilitated the feasibility to analyze the geomechanical problems such as wellbore instability in this way in a research context.

FLAC (ITASCA 2000) was chosen to execute the geomechincal models for the uncertainty analysis in this research, because FLAC provides a very powerful built-in programming language that allows the user to automatically control the repeat modelling process of thousands of runs that a Monte Carlo analysis needs [11].

4 Modes of Wellbore Failure

The wellbore is a cylindrical excavation loaded by ground stress and internally supported by the fluid pressure from the special mud used in the drilling process to remove cuttings. The mud's density can be changed by addition of heavy minerals (often barite), thus the fluid pressure can be adjusted. The occurrences of wellbore failure often appears in two modes: too little support inside the hole can lead to compressive failure, in extreme cases the sidewall may collapse; too much internal fluid pressure can also fail the hole in tension, and may thus cause lost circulation [17, 20].

4.1 Compressive Failure of Wellbore

Compressive failure occurs wherever the wellbore stress exceeds the rock strength and causes borehole breakout. In engineering practice, compressive failure can be mitigated by manipulating the borehole fluid pressure (mud weight). For example, raising the mud weight generally decreases the compressive stress around the well, resulting in a decrease in breakout, whilst, decreasing the mud weight may lead to wider breakouts. The well will be stable for finite breakouts, provided either the hole cleaning is improved, or the mud weight can be increased and maintained to an appropriate level to contain compressive failure. If the mud weight is reduced too far and breakouts surpass a critical limit such that the remaining intact section of the wellbore wall can no longer sustain the surrounding stress concentration the well will eventually collapse. For a given drilling system, the limit beyond which breakouts will jeopardize hole stability can be defined by the relationship between the initial width of a breakout and the volume of material produced, which is lithology dependent. It is very complicated in practice to determine such a limit, because many factors influence the assessment. For the purpose of numerical modelling, a criteria of the compressive failure of wellbore needs

to be defined in geomechanical terms. To avoid the introduction of complex fracture mechanics to calculate each possible breakout, which is practically impossible, the case of the wellbore collapse can be simplified into a situation that the wellbore wall deforms continuously under compressive stress until a critical state has been reached, resulting in wellbore collapse. The failure criteria can therefore be defined in terms of a critical compressive strain, or the inward radial deformation. In this research, a critical radial deformation of 10 mm has been considered as the compressive failure criteria.

4.2 Tensile Failure of Wellbore

Tensile failure due to excessive mud weight will create a hydraulic fracture at the wellbore wall, which may propagate through the near-wellbore stress concentration so that it can "link up" with a far-field fracture. This can form a path into which mud is lost. Fracture propagation requires a pressure equal or slightly in excess of the least stress, thus, lost circulation pressure is ultimately controlled by the least principal stress. The fracturing initiation and link-up pressures are functions of all three stresses and of the orientation of the well. If the static mud weight is higher than the least principal stress but lower than the initiation and link-up pressures, it is still possible to maintain circulation under ordinary circumstances. However, total lost circulation may occur without warning if there is a sudden increase in mud pressure, for example, due to surge, or while circulating out a kick. As rocks at and adjacent to the wellbore wall are in very complicated conditions (often heavily fissured), it is impossible to apply fracture mechanics directly in the assessment of the fracturing initiation and propagation in the case of tensile failure. In this chapter, the initiation of tensile strain is selected as the criteria for fracturing initiation and link-up, and thus lost circulation.

5 Modelling a Vertical Well in Deepwater

In many deepwater environments, offset data from previous wells are rare, either because there has been no previous drilling, or because the new well is drilled in an area of the field separated by faulting from that penetrated by previous wells [12,15,18]. Therefore, there is a large amount of uncertainty in the acquisition of geomechanical parameters such as the rock strength, pore pressure and the in situ stresses that are needed in analysis of the risk associated in drilling in this challenging environment. This uncertainty makes the operators very cautious in using the predicted collapse and lost circulation pressures in the pre-drill design. On the other hand, it provides an ideal opportunity for the utilization of probabilistic approaches. A few attempts have been made to tackle uncertainty in deepwater well stability [15]. Through application of the methodology developed in this research to a deepwater

wellbore, we illustrate how it is possible to utilize probabilistic analysis and numerical methods to determine the likelihood of the desired wellbore stability and identify the most influential factors associated with the uncertainty in the prediction of the wellbore instability.

First, in order to represent the geometry and the geomechanical conditions at a certain depth of the borehole, a 3D model is set up in FLAC3D, as schematically shown in Fig. 1. The model consists of a slice of the cross section of the borehole and the surrounding rock mass, in which the material properties of rocks, pore pressure, and in situ stresses can all be conveniently applied and varied in the subsequent probabilistic studies. The horizontal domain of the model has been selected as an area that stresses applied at boundaries can be regarded as the far-field stresses. The vertical stress can be computed by integrating the weight of the overburden and is directly applied to the upper surface of the model. FLAC provides a command to apply pore pressure to the rock, and the fluid pressure (mud weight) is exerted on the wellbore wall as a uniform surface pressure. The Mohr–Coulomb model was used to represent the nonlinear material behaviour of rocks, though more advanced and specific constitutive models can be developed and introduced into the numerical modelling in further research. Each set of sampling data generated in the Monte Carlo analysis will be transformed into a form that can be recognized by FLAC, and used as new values of rock properties and geomechanical parameters in the FLAC modelling. Output data are monitored and selected at the wellbore wall by extracting mechanical responses, such as deformation, stress and strain into a file. Probabilistic analysis will be carried out once all sample data have been put into FLAC in turn and the calculation results extracted. In this research, for each assumed mud weight, 500 different combinations of

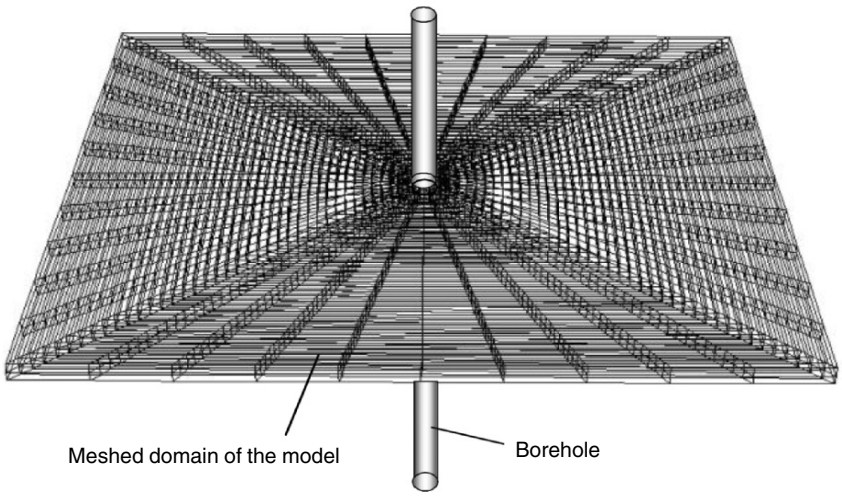

Fig. 1. Schematic figure of the numerical model in FLAC

the input parameters are introduced into the FLAC modelling. Five hundred runs of the numerical simulation are carried out to give out the corresponding distribution of the wellbore deformation. These data points are used in the subsequent probabilistic analysis to identify the probability of the wellbore failure.

6 Results and Discussion

6.1 Sensitivity Analysis of Input Parameters

A number of variables contribute to the uncertainty in the wellbore stability analysis, such as the rock strength, pore pressure, the orientations and magnitudes of all three principal stresses, and the fluid pressure (mud weight), etc. Uncertainties in any of these parameters will result in uncertainties in predictions of the wellbore instability problems. In this research, the specific parameters that contribute the most uncertainty are determined by means of the OAAT technique. Figure 2 presents a sensitivity plot of the relationship between the wellbore deformation and each parameter, holding the others fixed at mean values.

Judging from the tendency of each curve in Fig. 2, the bigger the deformation of the wellbore wall changes within the range of the studied parameter, the more uncertainty in the wellbore stability analysis can be associated with this parameter. As shown in Fig. 2a, the uncertainty in the vertical stress has very little influence on wellbore deformation. The known uncertainties in the minimum and maximum stress have relatively bigger impact on the wellbore deformation, seen in Fig. 2b,c. Figure 2d shows that uncertainty in the rock strength contributes much more to the uncertainties of the wellbore stability analysis. The range of possible pore pressures, as illustrated in Fig. 2e could lead to a large variation in the wellbore deformation. The most influential parameter, as can be seen in Fig. 2f is apparently the mud weight. With mud weight varying in a relatively small range, the deformation of the wellbore changes significantly. Thus, all the parameters studied here, with the exception of the vertical stress are associated with uncertainties in the wellbore stability analysis, and will be treated as random variables in the subsequent geomechanical and probabilistic analysis processes. This sensitivity study approach can also be employed to isolate those parameters that most contribute to the uncertainty of the results and provide critical information to guide decisions to develop a targeted program of field measurements to reduce risk in a cost-effective manner.

6.2 Quantification of the Risk of the Wellbore Failure

A key step in the data preparation before commencing sampling and the FLAC modelling process is to determine the representative distributions of the influential parameters screened out by the earlier (OAAT) sensitivity studies.

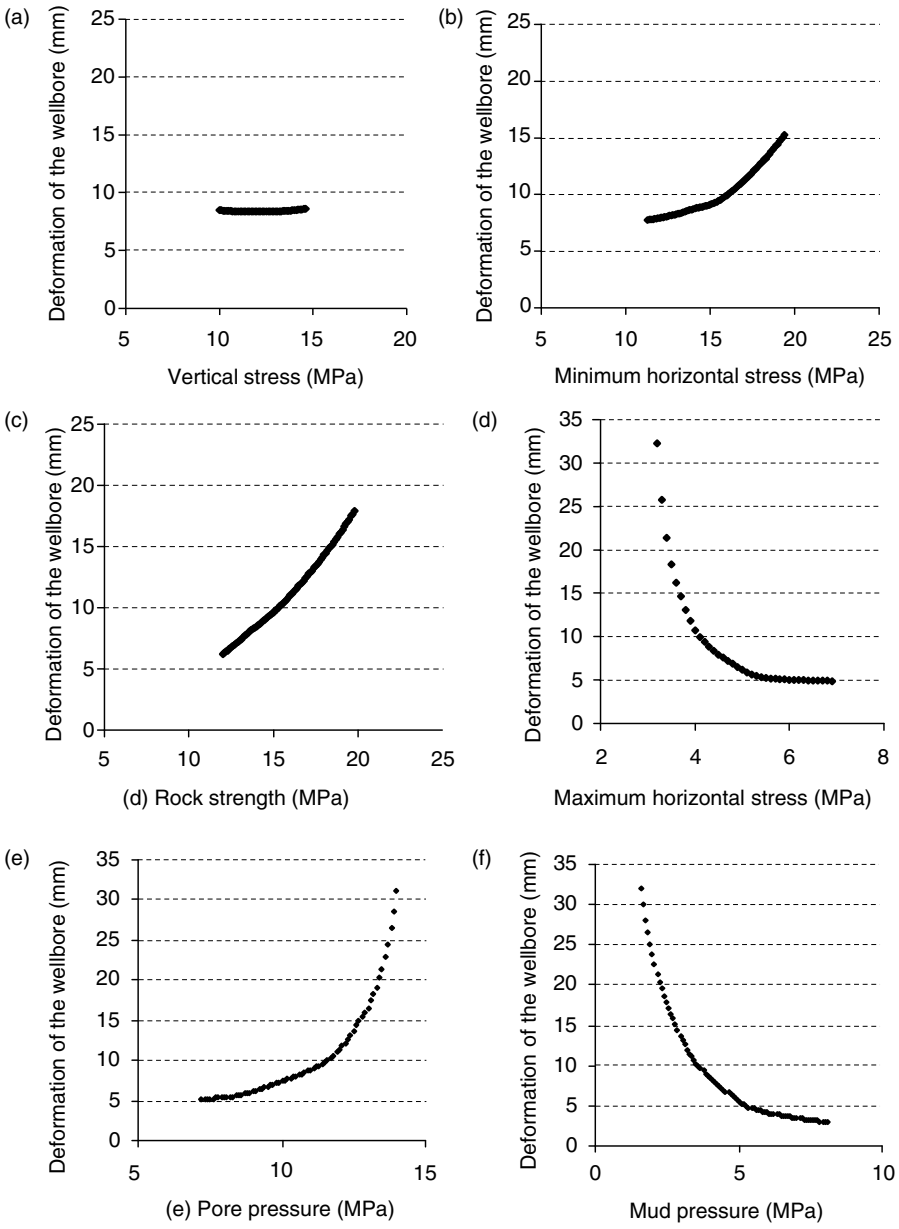

Fig. 2. Sensitivity study of input parameters

Although the representative distributions of the input parameters can be obtained through measured data, in reality, such field data are often sparse and rare, and hence not sufficient to exhibit the distribution characteristics of the input parameters. In the previous studies, the representative distributions of the influential parameters were given by probability distribution functions specified by means of the minimum, the maximum, and the mean of each parameter [15]. Similar functions are adopted in this research, as shown in Fig. 3. They are either normal or log-normal curves depending on whether the minimum and maximum values are symmetrical (e.g. pore pressure, and in situ stresses) or asymmetrical (e.g. cohesion) with respect to the mean. In either case, the functional form of the distribution is defined by the assumption that 99% of the possible values lie between the maximum and minimum input values.

Since the sample was generated by the use of the Latin Hypercube sampling technique, we can calculate the likelihood of any range of wellbore deformation based on the probability distribution function and determine the central tendency and dispersion of the output data. For more detailed information such as the probabilities of each deformation range, the histograms are plotted for the selected values of mud weight, as shown in Fig. 4. Figure 4 presents the histogram plots from the lower mud weight cases, in which the wellbore fails in the compressive mode.

With the 500 varied combinations of input parameters obtained from the sampling process, the numerical model in FLAC gives out the corresponding 500 wellbore deformations. Scores of the appearance of a certain range of deformations are counted and plotted in Fig. 4. If we take a nominal deformation (e.g. 10 mm in this research) as the tolerance limit, indicated by a dotted line in Fig. 4, beyond which wellbore will collapse, we may know the total number of the possible wellbore collapse cases, and thus the cumulative likelihood of wellbore collapse can be obtained. As can be seen in Fig. 4, as the mud weight increases, there are less numbers of cases of wellbore collapse. This indicates a decreasing possibility of the compressive failure. A similar process is applied to the analysis of the tensile failures of the wellbore (lost circulation), as illustrated in Fig. 5. Considering rock mass near a wellbore is normally heavily fissured and the residual tensile strength is very small, a very small tensile stress can cause fracturing of the rock. In this research, tensile failure is defined as wherever a tensile strain is recorded in the numerical simulations.

Reflected in the histogram plots in Fig. 5, any negative value of the deformation is counted as a case of tensile failure (lost circulation), also indicated by the dotted line here. From Fig. 5, numbers of tensile failure can be found to increase with the continuing increase of the mud weight, which indicates an increasing probability of lost circulation.

In this chapter, instead of directly using the possibility of the wellbore failure, uncertainties in the analysis of the wellbore stability are presented in terms of the cumulative likelihood of avoiding wellbore collapse and lost

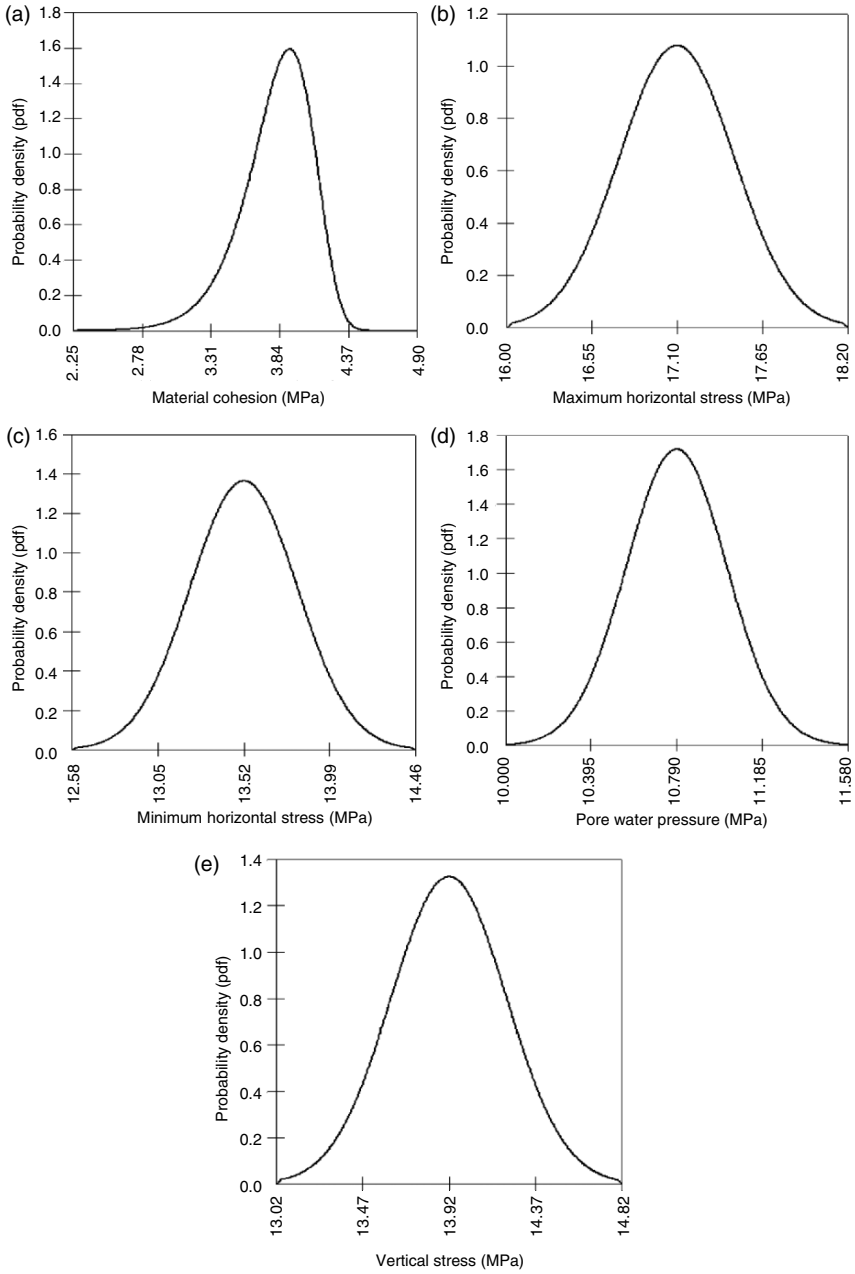

Fig. 3. The probability distribution functions of the input parameters

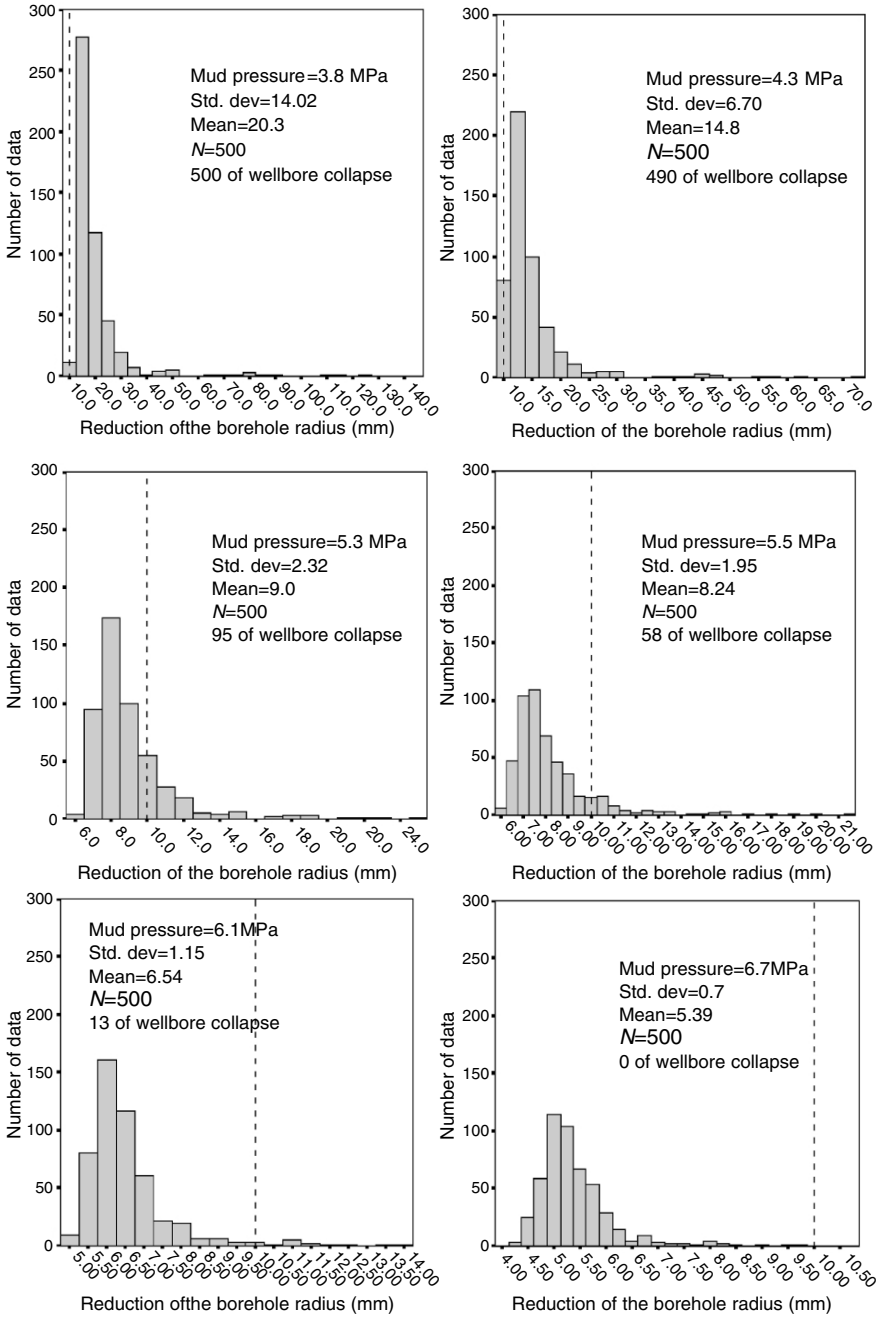

Fig. 4. Histogram plots for wellbore compressive failure (lower mud pressures)

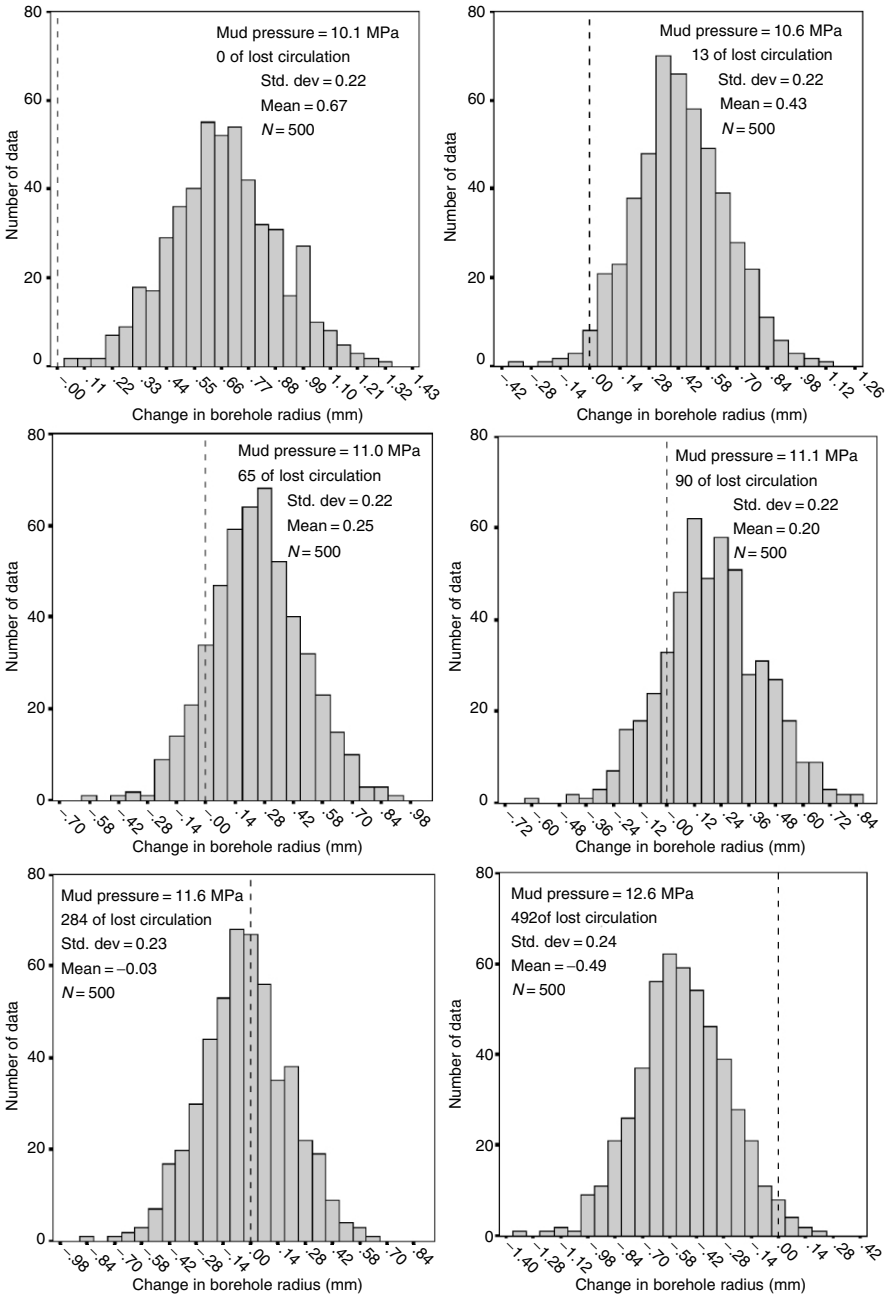

Fig. 5. Histogram plots for wellbore tensile failure (higher mud pressures)

circulation as a function of the mud weight at the depth of interest, as shown in Fig. 6. The left section of the curve represents the possibility of avoiding wellbore collapse while mud weight is kept at a lower range. While increasing mud weight till 6.7 MPa and beyond, where there is no possibility of wellbore collapse, the curve in Fig. 6 will turn into the measure of the likelihood of avoiding lost circulation. The range of safe mud weights to maintain wellbore stability lies between the wellbore collapse pressure and the lost circulation pressure. As demonstrated in Fig. 6, the horizontal line spans the range of mud weights that will simultaneously provide at least a 95% certainty of avoiding both collapse and lost circulation. This is because there is a greater than 95% certainty of avoiding collapse provided the mud weight is above 5.8 MPa. At the same time, there is a 95% certainty of avoiding lost circulation provided the mud weight is less than 10.7 MPa. The analysis result suggests that optimum stability can be achieved by manipulating a static mud weight between the lower bound value of 5.8 MPa, to upper bound value of 10.7 MPa.

The analysis carried out for the example of a deepwater well in this research revealed that there were substantial uncertainties in the predictions of the borehole instability, which can be identified by the probabilistic approach. It may be cost-effective, given the possible benefit, to acquire the data necessary to reduce those uncertainties. For example, as suggested in [15, 17], acquisition of good leak-off test data, including a careful determination of shut-in or fracture closure pressure, can be extremely valuable for a quantitative assessment of the risk associated with raising mud weight to address hole instabilities. The fact that the uncertainty in the predicted mud weight had multiple sources means that considerable additional effort would have to be devoted to improving the predictions, including the acquisition of real time data to improve the model while the well is drilled.

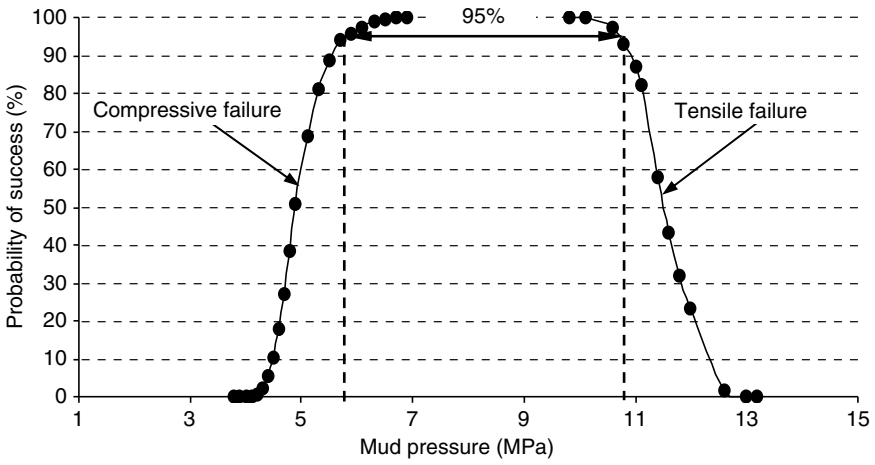

Fig. 6. Cumulative likelihood of avoiding wellbore failure

7 Conclusions

Significant uncertainties are involved in the predictions of the safe range of mud weights appropriate to avoid wellbore stability problems due to a number of factors, the most important of which are uncertainties in the acquisition of the geomechanical and operational parameters. Therefore, it is only possible to assess these uncertainties in terms of probabilistic approaches in order to reduce the risk of later drilling problems.

The earlier discussion illustrates a new approach to predict the required mud weights to avoid wellbore stability problems and also assess the uncertainty in those predictions. The advanced features of this approach that differ from previous methods are that it utilizes the probabilistic method in conjunction with numerical modelling techniques which allows determination of the uncertainties in both the collapse and the lost circulation pressures. The uncertainty introduced by using analytical solutions to the wellbore failure problems has been significantly reduced by employing an advanced numerical method. This approach also provides a measure of the effects of uncertainties in each of the input parameters on the instability predictions, thereby provides a recommendation for data acquisition that could be implemented in the course of drilling the well to reduce the uncertainty further. Analysis of the degree of risk to a well in deepwater illustrates the importance of knowing the magnitudes of the in situ stresses, the pore pressure, and the rock strength. Furthermore, they show that if it is possible to define the uncertainties in these parameters, it is possible to use that knowledge to define uncertainties in the predictions of required mud weights. The method can be applied over large intervals of open hole, where the lowest mud weight to avoid collapse and the highest mud weight to prevent lost circulation can be calculated independently for the worst case depth in each instance. This approach can definitely be modified and adopted in a pre-drilling design to predict the optimum mud weight windows and reduce the risk associated with the uncertainties in the wellbore stability problems.

References

1. Abousleiman, Y., Ekbote, S., Tare, U. (2000) Time-dependent wellbore (in) stability predictions: theory and case study, IADC/SPE 62796, Presented at the IADC/SPE Asia Pacific Drilling Technology Conference, Kuala Lumpur, Malaysia, 11–13 September
2. Aadnoy, B.S., Ong, S. (2003) Introduction to special issue on borehole stability, *J. Petroleum Sci. Eng.* **38**(3–4), 79–82
3. Baecher, G.B., Christian, J.T. (2003) Reliability and statisitics in geotechnical engineering. Wiley, New York
4. Bradley, W.B. (1979) Failure of inclined boreholes. J. Energy Resour. Technol., Trans. AIME **102**, 232–239
5. Christian, J.T., ASCE, H.M. (2004) Geotechnical engineering reliability "how well do we know what we are doing". The 39th Terzaghi Lecture

6. Davis, J.C. (2002) Statistics and data analysis in geology, Wiley, New York
7. EPA, U.S. (1997) Guiding Principles for Monte Carlo Analysis. Report, EPA/630/R-97/001
8. Helton, J.C., Davis, F.J. (2002) Illustration of sampling-based methods for uncertainty and sensitivity analysis. Risk Anal., **22**(3), 591–622
9. Helton, J.C., Davis, F.J. (2003) Latin hypercube sampling and the propagation of uncertainty in analysis of complex sysytems. Reliab. Eng. Sys. Safety, **81**, 23–69
10. Hora, S.C., Helton, J.C. (2003) A distribution-free test for the relationship between model input and output when using Latin Hypercube Sampling. Reliab. Eng. Sys. Safety, **79**, 333–339
11. ITASCA (2000) Fast lagrangian analysis of continua, version 4.0, Itasca Consulting Group Inc., Minneapolis, MN, USA
12. Ito, T., Zoback, M.D., Peska, P. (2001) Utilization of mud weights in excess of the least principal stress to stabilize wellbores: theory and practical examples. SPE Drilling and Completion **16**, 221–229
13. Jing, L., Hudson, J.A. (2002) Numerical methods in rock mechanics. Int. J. Rock Mech. Min. Sci. Geomech., **39**, 409–427
14. McLellan, P.J., Hawkes, C.D. (1998) Application of probabilistic techniques for assessing sand production and wellbore instability risks. SPE/ISRM, 47334
15. Moos, D., et al. (2003) Comprehensive wellbore stability analysis utilizing Quantitative Risk Assessment, J. Petroleum Sci. Eng., **38**(3–4), 97–109
16. Ottesen, S., Zheng, R.H., McCann, R.C. (1999) Wellbore stability assessment using quantitative risk analysis, SPE/IADC 52864. Presented at the SPE/IADC Drilling Conference, Amsterdam, The Netherlands, 9 – 11 March
17. Peska, P., Zoback, M.D. (1995) Compressive and tensile failure of inclined well bores and determination of in situ stress and rock strength. J. Geophys. Res. **100**(7), 12791–12811
18. Van Oort, E., Nicholson, J., D'Agostino, J. (2001) Integrated borehole stability studies: key to drilling at the technical limit and trouble cost reduction, SPE/IADC 67763. Presented at the SPE/IADC Drilling Conference, Amsterdam, The Netherlands, 17 February–1 March
19. Zhang, X., Last, N., Powrie, W., Harkness, R. (1999) Numerical modeling of wellbore behaviour in fractured rock mass. J. Petroleum Sci. Eng. **23**, 95–115
20. Zoback, M.D., et al. (1995) Utilization and analysis of multiple modes of borehole failure for estimation of in situ stress, *Proceedings of the International Symposium on Rock Mechanics*, Tokyo, Japan, 25–30 September

SPRINGER PROCEEDINGS IN PHYSICS

60 **The Physics and Chemistry of Oxide Superconductors**
Editors: Y. Iye and H. Yasuoka

61 **Surface X-Ray and Neutron Scattering**
Editors: H. Zabel and I.K. Robinson

62 **Surface Science**
Lectures on Basic Concepts and Applications
Editors: F.A. Ponce and M. Cardona

63 **Coherent Raman Spectroscopy**
Recent Advances
Editors: G. Marowsky and V.V. Smirnov

64 **Superconducting Devices and Their Applications**
Editors: H. Koch and H. Lübbing

65 **Present and Future of High-Energy Physics**
Editors: K.-I. Aoki and M. Kobayashi

66 **The Structure and Conformation of Amphiphilic Membranes**
Editors: R. Lipowsky, D. Richter, and K. Kremer

67 **Nonlinearity with Disorder**
Editors: F. Abdullaev, A.R. Bishop, and S. Pnevmatikos

68 **Time-Resolved Vibrational Spectroscopy V**
Editor: H. Takahashi

69 **Evolution of Dynamical Structures in Complex Systems**
Editors: R. Friedrich and A. Wunderlin

70 **Computational Approaches in Condensed-Matter Physics**
Editors: S. Miyashita, M. Imada, and H. Takayama

71 **Amorphous and Crystalline Silicon Carbide IV**
Editors: C.Y. Yang, M.M. Rahman, and G.L. Harris

72 **Computer Simulation Studies in Condensed-Matter Physics IV**
Editors: D.P. Landau, K.K. Mon, and H.-B. Schüttler

73 **Surface Science**
Principles and Applications
Editors: R.F. Howe, R.N: Lamb, and K. Wandelt

74 **Time-Resolved Vibrational Spectroscopy VI**
Editors: A. Lau, F. Siebert, and W. Werncke

75 **Computer Simulation Studies in Condensed-Matter Physics V**
Editors: D.P. Landau, K.K. Mon, and H.-B. Schüttler

76 **Computer Simulation Studies in Condensed-Matter Physics VI**
Editors: D.P. Landau, K.K. Mon, and H.-B. Schüttler

77 **Quantum Optics VI**
Editors: D.F. Walls and J.D. Harvey

78 **Computer Simulation Studies in Condensed-Matter Physics VII**
Editors: D.P. Landau, K.K. Mon, and H.-B. Schüttler

79 **Nonlinear Dynamics and Pattern Formation in Semiconductors and Devices**
Editor: F.-J. Niedernostheide

80 **Computer Simulation Studies in Condensed-Matter Physics VIII**
Editors: D.P. Landau, K.K. Mon, and H.-B. Schüttler

81 **Materials and Measurements in Molecular Electronics**
Editors: K. Kajimura and S. Kuroda

82 **Computer Simulation Studies in Condensed-Matter Physics IX**
Editors: D.P. Landau, K.K. Mon, and H.-B. Schüttler

83 **Computer Simulation Studies in Condensed-Matter Physics X**
Editors: D.P. Landau, K.K. Mon, and H.-B. Schüttler

84 **Computer Simulation Studies in Condensed-Matter Physics XI**
Editors: D.P. Landau and H.-B. Schüttler

85 **Computer Simulation Studies in Condensed-Matter Physics XII**
Editors: D.P. Landau, S.P. Lewis, and H.-B. Schüttler

86 **Computer Simulation Studies in Condensed-Matter Physics XIII**
Editors: D.P. Landau, S.P. Lewis, and H.-B. Schüttler